

**Redistribution dynamics of ultrathin vanadium oxide layers under catalytic
conditions and activation of diffusion by surface acoustic waves**

Von der Naturwissenschaftlichen Fakultät der
Gottfried Wilhelm Leibniz Universität Hannover
zur Erlangung des Grades

Doktor der Naturwissenschaften (Dr. rer. nat.)

genehmigte Dissertation
von
Bernhard von Boehn, M. Sc.

2020

Referent: Prof. Dr. rer. nat. Ronald Imbihl
Korreferent: Prof. Dr. rer. nat. Herbert Pfnür
Korreferent: Prof. Dr. rer. nat. Jens Falta
Tag der Promotion: 20.02.2020

Keywords: Vanadium oxide, methanol oxidation, surface acoustic waves

Abstract

The reaction-induced redistribution of vanadium oxide supported on noble metal single crystal surfaces (inverse model catalysts), and the influence of surface acoustic waves (SAW) on the composition of a bimetallic Rh/Pt surface are studied.

Previously, the movement and coalescence of macroscopic, two-dimensional VO_x islands on Rh(111) during catalytic methanol oxidation was explained with a polymerization / depolymerization mechanism. To investigate how general this mechanism is, the reaction dynamics of VO_x on Rh(111), Rh(110) and Pt(111) are investigated in a number of catalytic reactions. Island formation and coalescence are observed in ammonia, CO, and methanol oxidation on $\text{VO}_x/\text{Rh}(111)$ in the 10^{-4} mbar range. Exchanging O_2 by NO as oxidizing agent results in an inverse pattern, i. e. holes in a dense VO_x film instead of VO_x islands surrounded by bare Rh surface. Spectroscopic LEEM reveals, that NO influences the width of the interface VO_x island / bare Rh(111), thus indicating a change in the line tension. The line tension possibly explains the complementary types of pattern formation. Indications for a Rh surface oxide under reaction conditions are found. In the 10^{-4} mbar range on Rh(111), oscillating VO_x islands occur. A tentative mechanism is proposed, based on phase transitions inside the VO_x islands, which result from gradients in the oxygen coverage. With near ambient pressure LEEM, turbulent redistribution dynamics are observed during methanol oxidation at 0.02 mbar.

On $\text{VO}_x/\text{Rh}(110)$ island formation occurs, but no island coalescence is seen. Instead, a wealth of chemical wave pattern is found: traveling interface modulations (TIMs), traveling wave fragments and target pattern, as well as chemical waves propagating over both, the bare Rh(110) substrate and macroscopic VO_x islands. TIMs are explained by a mechanism based on the reversible creation of surface defects at the interface. The system $\text{VO}_x/\text{Pt}(111)$ is characterized by the reversible diffusion of V into the Pt bulk under reaction conditions. As a consequence, no pattern formation occurs.

A strong effect of the metallic support on the behavior of VO_x catalysts is demonstrated by the different types of pattern formation in $\text{VO}_x/\text{Rh}(111)$, $\text{VO}_x/\text{Rh}(110)$, and $\text{VO}_x/\text{Pt}(111)$. In addition to different types of pattern formation, also the selectivity and catalytic activity is strongly influenced by the support. Whereas formaldehyde is the main product in catalytic methanol oxidation on $\text{VO}_x/\text{Rh}(111)$, no formaldehyde production is detected on $\text{VO}_x/\text{Rh}(110)$ and $\text{VO}_x/\text{Pt}(111)$.

The influence of SAWs on the diffusive intermixing of a Rh/Pt surface is investigated by laterally resolved X-ray spectroscopy. The results are compared to Auger spectroscopy measurements on the thermal diffusion of Rh into the Pt bulk on a Pt(100) single crystal and on polycrystalline Pt. At 445 K, a SAW-induced intermixing of Pt and Rh is detected. In thermal diffusion experiments, the onset of Rh diffusion into the Pt bulk is found to occur around 500 to 550 K. The experiments are a first step towards verifying the working hypothesis, that structural defects caused by SAWs are the main reason for a SAW-induced increase in catalytic activity reported in literature.

Zusammenfassung

Die reaktionsinduzierte Umverteilung von Vanadiumoxid auf Edelmetall-Einkristalloberflächen (inverse Modellkatalysatoren) und der Einfluss von akustischen Oberflächenwellen (SAW) auf die Zusammensetzung einer Rh/Pt-Oberfläche werden untersucht.

Kürzlich wurde die Verschmelzung von makroskopischen, zweidimensionalen VO_x -Inseln auf Rh(111) während der Methanoxidation mit einem Polymerisations-/Depolymerisationsmechanismus erklärt. Um zu untersuchen, wie allgemein dieser Mechanismus ist, wird die Dynamik von VO_x auf Rh(111), Rh(110) und Pt(111) in einer Reihe von Reaktionen untersucht. Inselbildung und Verschmelzung werden bei der Oxidation von Ammoniak, CO und Methanol an $\text{VO}_x/\text{Rh}(111)$ im 10^{-4} mbar Bereich beobachtet. Der Austausch von O_2 durch NO als Oxidationsmittel führt zu einem umgekehrten Muster, d.h. Löcher in einem VO_x Film, anstelle von VO_x Inseln umgeben von unbedeckter Rh-Oberfläche. NO sorgt für eine Verbreiterung der Grenzfläche VO_x Insel / Rh(111), was auf eine Änderung der Linienspannung hindeutet. Die Linienspannung erklärt möglicherweise die komplementären Arten der Musterbildung. Es werden Anzeichen für ein Rh-Oberflächenoxid unter Reaktionsbedingungen gefunden. Im 10^{-4} mbar Bereich treten oszillierende VO_x Inseln auf Rh(111) auf. Ein vorläufiger Mechanismus wird vorgeschlagen, der auf Phasenübergängen in den VO_x -Inseln basiert, die sich aus Sauerstoff-Gradienten ergeben. In Near Ambient Pressure LEEM wird die turbulente Umverteilung von VO_x während der Methanoxidation bei 0.02 mbar beobachtet.

Bei $\text{VO}_x/\text{Rh}(110)$ kommt es zu Inselbildung, nicht aber zur Verschmelzung. Stattdessen findet sich eine Fülle chemischer Wellenmuster: Traveling Interface Modulations (TIMs), Traveling Wave Fragments, Target Pattern, und chemische Wellen, die sich über Rh(110) und die VO_x -Inseln ausbreiten. TIMs werden durch einen Mechanismus erklärt, der auf der reversiblen Erzeugung von Oberflächendefekten an der Grenzfläche basiert. Im System $\text{VO}_x/\text{Pt}(111)$ verhindert die reversible Diffusion von V in das Pt-Volumen unter Reaktionsbedingungen die Musterbildung. Ein starker Einfluss des Trägers auf das Verhalten von VO_x -Katalysatoren wird durch die verschiedenen Arten der Musterbildung in $\text{VO}_x/\text{Rh}(111)$, $\text{VO}_x/\text{Rh}(110)$ und $\text{VO}_x/\text{Pt}(111)$ deutlich. Daneben wird auch die Selektivität und katalytische Aktivität stark durch den Träger beeinflusst. Formaldehyd ist das Hauptprodukt bei der katalytischen Methanoxidation an $\text{VO}_x/\text{Rh}(111)$, keine Formaldehyd-Produktion wird an $\text{VO}_x/\text{Rh}(110)$ und $\text{VO}_x/\text{Pt}(111)$ festgestellt.

Der Einfluss von SAWs auf die Vermischung einer Rh/Pt Oberfläche wird durch ortsaufgelöste Röntgenspektroskopie untersucht. Die Ergebnisse werden mit Augerspektroskopie-Messungen zur thermischen Diffusion von Rh in das Pt-Volumen auf Pt(100) und auf polykristallinem Pt verglichen. Bei 445 K wird eine SAW-induzierte Vermischung von Pt und Rh nachgewiesen. Die thermische Diffusion von Rh in den Pt Kristall beginnt ab 500 bis 550 K. Die Experimente sind ein erster Schritt zur Überprüfung der Arbeitshypothese, dass SAW-erzeugte strukturelle Defekte der Hauptgrund für eine in der Literatur beschriebene Erhöhung der katalytischen Aktivität durch SAWs sind.

Für Dana, Jannes und Schnucki

Danksagung

Mein besonderer Dank gebührt Prof. Dr. Ronald Imbühl, nicht nur für die Möglichkeit in seinem Arbeitskreis zu lernen und zu forschen, sondern auch für die freundliche Unterstützung und Betreuung. Vielen Dank für all den Rat, das Vertrauen, die konstruktive Kritik und die große Freude, die mir die Arbeit bei Ihnen bereitet. Zudem danke ich für die ausführlichen Diskussionen zu dieser Arbeit.

Prof. Dr. Jens Falta möchte ich für die Übernahme eines der Gutachten und die Möglichkeit Experimente in seiner Gruppe durchzuführen danken. Mein Dank gebührt darüber hinaus seiner ganzen Gruppe, im besonderen Dr. Jon-Olaf Krisponeit für die gemeinsamen Stunden vor dem LEEM, ohne die viele Ergebnisse nie zustande gekommen wären.

Für das Interesse an unseren Forschungsergebnissen und die Übernahme eines der Gutachten bedanke ich mich herzlich bei Prof. Dr. Herbert Pfnür.

The support during many tough nights by Dr. Andrea Locatelli, Dr. Onur Mentş, Dr. Francesca Genuzio, Dr. Alessandro Sala, Dr. Lucia Aballe, Dr. Michael Foerster, Dr. Blai Casals Montserrat, Jordi Prat Albert, Dr. Luca Gregoratti, Dr. Matteo Amati and Dr. Patrick Zeller at the Nanospectroscopy, ESCA Microscopy, and CIRCE beamlines is highly appreciated. I am especially thankful for the support, hospitality and advise of Dr. Andrea Locatelli and Dr. Onur Mentş. Grazie grandissimi!

Der Firma Elmitec, Dr. Torsten Franz, Dr. Helder Marchetto, Dr. Benjamin Borkenhagen und Dr. Gerhard Lilienkamp möchte ich für die gemeinsamen Experimente am NAP-LEEM danken.

Dr. Christopher Penschke, Xiaoke Li, Dr. Joachim Paier und Prof. Dr. Joachim Sauer danke ich für die aufschlussreichen wissenschaftlichen Diskussionen und die Forschungskooperation zu $\text{VO}_x/\text{Rh}(111)$.

Meinen Kollegen im Arbeitskreis, Mathias Homann und Dr. Tim Werth, sowie den Studierenden im Forschungspraktikum, Masteranden und studentischen Hilfskräften Anika Preiss, Sarah Mehrwald, Lena Scholtz, Dennis Groeneveld, Anton Weißbach, Piotr Wemhoff und Moritz von Boehn möchte ich für die gute Stimmung, die anregenden Diskussionen und die tolle Zusammenarbeit danken. Großer Dank gebührt den Mitarbeitern der Feinmechanischen Werkstatt Wilfried Becker, Peter Mühr, Markus Köhler und Jan Kuckuck, sowie Yvonne Gabbye und Kerstin Battermann aus dem Sekretariat.

Meiner Familie möchte ich für ihren Rückhalt, die Entbehrung während so manchem Forschungsaufenthalt und die uneingeschränkte Unterstützung danken.

Contents

Abstract	i
Zusammenfassung	ii
Danksagung	iv
1 Introduction	1
1.1 The pressure and material gaps in catalysis	2
1.1.1 In situ and operando techniques	3
1.1.2 From single crystals to real catalysis	4
1.2 The inverse catalyst in heterogeneous catalysis	5
1.2.1 Technical applications of inverse catalysts	6
1.2.2 The surface science approach to inverse catalysts	7
1.3 Theoretical chemistry in heterogeneous catalysis	8
1.4 Surface acoustic waves in heterogeneous catalysis	8
1.5 Motivation	9
2 Experimental methods and theory	11
2.1 Surface sensitivity	11
2.2 Electron spectroscopy	13
2.2.1 Auger electron spectroscopy	13
2.2.2 X-ray photoelectron spectroscopy	17
2.3 Low-energy electron diffraction	19
2.3.1 Kinematic theory of diffraction	21
2.3.2 Experimental implementation of LEED	24
2.4 Cathode lens microscopy	25
2.4.1 Photoemission electron microscopy	26
2.4.2 Low-energy electron microscopy	27
2.4.3 Near ambient pressure low-energy electron microscopy	30
2.4.4 Spectroscopic low-energy electron microscopy	31
2.5 Scanning photoemission electron microscopy	33
2.6 Quadrupole mass spectrometry	35
2.6.1 Temperature programmed reaction	37

2.7	Thin film growth	38
2.8	The single crystal surfaces used in this thesis	40
2.8.1	The Rh(111) surface	40
2.8.2	The Rh(110) surface	42
2.8.3	Interaction of CO with Rh(110)	44
2.8.4	The Pt(111) surface	44
2.8.5	The Pt(100) surface	45
2.8.6	The interaction of vanadium with Rh(111), Rh(110) and Pt(111) .	45
2.9	Basics of nonlinear dynamics in reaction diffusion systems	45
3	Experimental setup	50
3.1	Sample preparation	51
3.2	Experiments with vanadium oxide layers	51
3.2.1	Thin Film Preparation	51
3.2.2	Photoemission Electron Microscopy (Hannover)	53
3.2.3	Low-Energy Electron Microscopy (Bremen)	55
3.2.4	Spectroscopic LEEM (Trieste)	56
3.2.5	Scanning Photoemission Electron Microscopy (Trieste)	57
3.2.6	Near Ambient Pressure LEEM (Clausthal)	58
4	Reaction induced redistribution of vanadium oxide	60
4.1	Vanadium oxide in fundamental catalysis research	60
4.1.1	Vanadium oxide structures on Rh(111)	62
4.2	Reaction-induced redistribution of vanadium oxide	63
5	Reaction-induced VO_x redistribution on Rh(111)	68
5.1	VO _x deposition rate calibration	69
5.2	VO _x redistribution during methanol oxidation in PEEM	75
5.2.1	The transition from a homogeneous VO _x film to islands	75
5.2.2	Evolution of VO _x pattern at constant temperature	82
5.2.3	Dependence of the VO _x island substructure on the gas phase composition	87
5.2.4	Summary of the PEEM experiments	90
5.3	VO _x redistribution during methanol oxidation in LEEM	91
5.3.1	VO _x stripe pattern formation	91
5.3.2	In situ LEED analysis	95
5.3.3	Oscillating VO _x islands	99
5.3.4	Oxidation of a VO _x island in LEEM	105
5.4	VO _x Coverage calibration during methanol oxidation	107
5.4.1	Beam damaging effects	107
5.4.2	VO _x coverage calibration	110
5.4.3	Ex situ VO _x coverage determination on oxide islands	114
5.4.4	In situ VO _x coverage determination on oxide islands	118
5.4.5	Chemical analysis of the VO _x islands	121

5.5	VO _x redistribution during other oxidation reactions	124
5.5.1	VO _x redistribution during catalytic ammonia oxidation	124
5.5.2	VO _x redistribution during catalytic CO oxidation	127
5.6	VO _x redistribution with NO as oxidizing agent in PEEM	130
5.6.1	VO _x redistribution during the CH ₃ OH + NO reaction	131
5.6.2	VO _x redistribution during the NH ₃ + NO reaction	133
5.6.3	Transformation of the “hole pattern” into an “island pattern” . . .	135
5.6.4	VO _x redistribution during the H ₂ + NO reaction	137
5.6.5	Structural changes and oxygen gradients in the oxidation reactions with NO	138
5.6.6	Catalytic activity in the oxidation reactions with NO	140
5.6.7	Conclusions from the PEEM experiments conducted with NO . . .	144
5.7	VO _x redistribution during NH ₃ oxidation in SPELEEM	144
5.7.1	VO _x coverage calibration	145
5.7.2	Ex situ VO _x coverage determination on oxide islands	148
5.7.3	In situ characterization of VO _x during the NH ₃ + O ₂ reaction . .	153
5.7.4	In situ characterization of VO _x during the NH ₃ + NO reaction . .	159
5.7.5	Oxygen distribution during ammonia oxidation with O ₂ and NO .	162
5.7.6	Discussion	164
5.8	VO _x redistribution studied with NAP-LEEM	167
5.8.1	VO _x island formation and turbulent dynamics at 0.02 mbar	168
5.8.2	Oxidation of a VO _x island in the 10 ⁻² mbar range	172
5.9	Summary	174
6	VO_x Redistribution and Pattern Formation on Rh(110)	176
6.1	Growth of vanadium and vanadium oxide on Rh(110)	177
6.1.1	The growth of vanadium on Rh(110)	177
6.1.2	The growth of vanadium oxide on Rh(110)	180
6.1.3	The stability of vanadium oxide films on Rh(110)	182
6.1.4	XPS characterization of vanadium oxide films on Rh(110)	187
6.2	Chemical wave pattern on Rh(110) and VO _x /Rh(110)	189
6.2.1	Methanol oxidation on Rh(110) and VO _x /Rh(110)	190
6.3	Traveling interface modulations on Rh(110) and VO _x covered Rh(110) . .	198
6.3.1	Traveling interface modulations on Rh(110) during methanol oxi- dation in PEEM	199
6.3.2	Traveling interface modulations on Rh(110) during methanol oxi- dation in LEEM	201
6.3.3	Traveling interface modulations on Rh(110) in other reactions . . .	205
6.3.4	Traveling interface modulations on VO _x /Rh(110) during methanol oxidation in PEEM	208
6.3.5	Traveling interface modulations on VO _x /Rh(110) during methanol oxidation in LEEM	213
6.3.6	Discussion	216

6.4	Target pattern during methanol oxidation on 0.2 MLE $\text{VO}_x/\text{Rh}(110)$. . .	220
6.5	Traveling wave fragments during methanol oxidation on $\text{VO}_x/\text{Rh}(110)$. .	225
6.5.1	Oxidation/reduction fronts and traveling wave fragments on 0.4 MLE $\text{VO}_x/\text{Rh}(110)$ in PEEM	225
6.5.2	Oxidation/reduction fronts and traveling wave fragments on 0.4 MLE VO_x on $\text{Rh}(110)$ in LEEM	229
6.6	Reaction-induced redistribution of VO_x on $\text{Rh}(110)$	232
6.6.1	VO_x redistribution on $\text{Rh}(110)$ under oxidizing reaction conditions in PEEM	232
6.6.2	VO_x redistribution on $\text{Rh}(110)$ under oxidizing reaction conditions in LEEM	237
6.7	Chemical wave patterns on patterned $\text{VO}_x/\text{Rh}(110)$ surfaces	240
6.7.1	Traveling wave fragments on micro-patterned $\text{VO}_x/\text{Rh}(110)$ surfaces in PEEM	240
6.7.2	Pattern formation on the micro-patterned $\text{VO}_x/\text{Rh}(110)$ surface in LEEM	242
6.8	Ex situ SPELEEM measurements after the reactive phase separation . . .	249
6.9	Discussion of chemical wave patterns on $\text{Rh}(110)$ and $\text{VO}_x/\text{Rh}(110)$. . .	252
6.9.1	Chemical wave pattern on the homogeneous surface	253
6.9.2	Reaction-induced VO_x redistribution at 1000 K	256
6.9.3	Chemical waves on patterned $\text{VO}_x/\text{Rh}(110)$ surfaces	256
6.10	Conclusion	258
7	VO_x Redistribution on Pt(111)	260
7.1	VO_x deposition rate calibration	261
7.2	VO_x redistribution on Pt(111) during catalytic methanol oxidation . . .	263
7.2.1	Segregation behavior of vanadium oxide on Pt(111)	266
7.2.2	Characterization of the (2×2) $\text{VO}_x/\text{Pt}(111)$ Structure	269
7.3	Catalytic activity of Pt(111) and $\text{VO}_x/\text{Pt}(111)$ in methanol oxidation . .	271
7.4	Discussion of the different VO_x structures	274
7.5	Catalytic activity and pattern formation	277
7.6	Conclusion	279
8	Surface Acoustic Wave Activated Diffusion of Surface Atoms	280
8.1	Introduction	280
8.2	Surface acoustic waves and instrumentation	282
8.3	Sample preparation and experimental set up	284
8.3.1	$\text{Rh}/\text{Pt}/\text{LiNbO}_3$ Sample Preparation	284
8.3.2	Spectroscopic LEEM (Barcelona)	287
8.4	Measurement of the SAW induced diffusion	287
8.5	Thermal diffusion of Rh on Pt/LiNbO_3	289
8.6	Thermal inter-diffusion of Rh and Pt for $\text{Rh}/\text{Pt}(110)$	295
8.7	Discussion	297
8.8	Summary	298

<i>CONTENTS</i>	ix
9 Conclusion and Outlook	300
Bibliography	303
A Vanadium oxide phases on Rh(111) reported in literature	321
B List of abbreviations	322
Curriculum vitae	324
Publikationsliste	325

List of Figures

2.1	Inelastic Mean Free Path	13
2.2	Auger Process	14
2.3	Oxidation State Determination from Auger Data	16
2.4	Cylindrical Mirror Analyzer	16
2.5	Differential photoionization cross sections of V 2p, O 1s, Rh 3p and Rh 3d	19
2.6	Exemplary XPS Spectrum	20
2.7	Ewald Sphere	23
2.8	Four grid LEED optics	25
2.9	SPELEEM Microscope	29
2.10	NAP-LEEM	32
2.11	NAP-LEEM	34
2.12	Quadrupole Mass Analyzer	36
2.13	Growth Modes	38
2.14	Growth Mode Identification by AES	39
2.15	Rh(110) Surface Structures	43
2.16	FitzHugh-Nagumo Model	48
2.17	Front velocity in bistable systems	49
4.1	Structural model for the $(\sqrt{7} \times \sqrt{7})R19.1^\circ$ VO_x phase	62
4.2	Vanadium oxide island nucleation during catalytic methanol oxidation	64
4.3	Scheme illustrating the movement of two neighboring VO_x islands	65
4.4	Scheme illustrating the diffusion of adsorbed oxygen towards a vanadium oxide island	66
5.1	Vanadium oxide structures on Rh(111) as a function of V coverage	70
5.2	V deposition rate calibration	71
5.3	V Auger intensity ratio	72
5.4	VO_x LEED pattern	74
5.5	Summary of VO_x redistribution pattern	77
5.6	VO_x stripe pattern formation	79
5.7	VO_x redistribution under strongly oxidizing conditions	80
5.8	Temporal stripe pattern evolution at 930 K under oxidizing reaction conditions	82

5.9	Reversibility of the stripe - island transition	84
5.10	Reversible stripe - island transition under reducing reaction conditions . .	85
5.11	VO _x pattern formation at constant 1020 K temperature (0.1 MLE)	86
5.12	VO _x pattern formation at constant 1020 K temperature (0.2 MLE)	87
5.13	Stability of the reduced VO _x island core as a function of methanol pressure	88
5.14	Coexistence of VO _x phases within an island at 970 K	89
5.15	Vanadium oxide stripe formation imaged with LEEM	92
5.16	Heatup of the VO _x stripe pattern in LEEM	94
5.17	Large scale LEEM image showing the substructure of an VO _x Stripe . . .	95
5.18	LEED images acquired during the VO _x stripe pattern formation	97
5.19	μLEED measurements on VO _x islands	98
5.20	Oscillating vanadium oxide island imaged with LEEM	100
5.21	DFT phase diagram of two-dimensional VO _x phases on Rh(111)	103
5.22	Mechanism explaining the oscillations of VO _x islands during methanol oxidation	104
5.23	Oxidation of a macroscopic VO _x island followed in LEEM	106
5.24	O 1s beam damage effect in OSA mode	108
5.25	O 1s beam damage effect in ZP mode	109
5.27	Overview spectra taken during the XPS calibration curve	113
5.28	V 2p, Rh 3p and O 1s core level spectra used for the XPS calibration curve.	114
5.29	Rh 3d and C 1s photoemission spectra of the calibration curve	115
5.30	V 2p / Rh 3p core level intensity ratio calibration curve	116
5.31	Ex situ XPS characterization of VO _x islands on Rh(111)	117
5.32	Ex situ XPS of VO _x islands formed during methanol oxidation	119
5.33	In situ XPS characterization of VO _x islands on Rh(111)	120
5.34	In situ XPS for the VO _x coverage determination	122
5.35	V 2p core level spectra recorded ex and in situ on VO _x islands	123
5.36	VO _x redistribution during ammonia oxidation	125
5.37	VO _x stripe pattern evolution during ammonia oxidation	126
5.38	Catalytic activity during ammonia oxidation on VO _x /Rh(111)	128
5.39	VO _x redistribution during CO oxidation	129
5.40	VO _x island core formation during CO oxidation	130
5.41	VO _x redistribution during the CH ₃ OH + NO reaction	131
5.42	VO _x stripe pattern formation during the CH ₃ OH + NO reaction at 1030 K	132
5.43	VO _x redistribution during the NH ₃ + NO reaction	134
5.44	Methanol and ammonia oxidation with oxygen on the NO-patterned surfaces	136
5.45	VO _x redistribution during the H ₂ + NO reaction	138
5.46	LEED pattern after the oxidation reactions with NO on VO _x /Rh(111) . .	139
5.47	Comparison of the oxygen gradients in ammonia oxidation with O ₂ and NO	140
5.48	Reaction rate measurement in the CH ₃ OH + NO reaction	141
5.49	Reaction rate measurements in the NH ₃ + NO reaction	142
5.50	LEED images acquired during the VO _x calibration curve	146

5.51	Rh 3p, V 2p and O 1s photoemission spectra for the V coverage determination	147
5.52	V coverage as a function of V 2p / Rh 3p core level intensity ratio	148
5.53	Ex situ LEEM- $I(V)$ analysis of macroscopic vanadium oxide islands formed during ammonia oxidation	150
5.54	μ LEED characterizarion of a vanadium oxide island obtained after ammonia oxidation	151
5.55	Ex situ XPS characterization of vanadium oxide islands obtained after ammonia oxidation	152
5.56	Vanadium oxide island coalescence during adjustment of reaction conditions	154
5.57	In situ LEED and LEEM- $I(V)$ characterization of VO_x islands and the Rh surface	156
5.58	In situ XPS characterization of vanadium oxide islands during ammonia oxidation with O_2	157
5.59	N 1s spectra taken in situ during ammonia oxidation with O_2	159
5.60	In situ XPS characterization of vanadium oxide islands during ammonia oxidation with NO	160
5.61	N 1s spectra taken in situ during ammonia oxidation with NO	162
5.62	O 1s dispersive plane XP spectra as a function of distance to the VO_x /Rh interface	163
5.63	Oxygen distribution measured during ammonia oxidation with O_2 and NO	165
5.64	In situ LEED of VO_x islands and the Rh surface during $NH_3 + NO$ reaction	166
5.65	Overview of the VO_x redistribution pattern between 10^{-7} and 0.02 mbar .	169
5.66	NAP-LEEM images showing the formation of VO_x islands at 0.02 mbar .	170
5.67	Turbulent redistribution dynamics of VO_x during methanol oxidation at 0.02 mbar	171
5.68	Oxidation of a VO_x island in the 10^{-2} mbar range.	172
5.69	Work function map of an oxidited VO_x island acquired at 1.5×10^{-2} mbar.	174
6.1	V deposition rate calibration on Rh(110)	178
6.2	LEED images acquired during the deposition of V on Rh(110)	179
6.3	LEED intensity as a function of V coverage measured on V/Rh(110) . . .	181
6.4	LEED images acquired during the reactive evaporation of VO_x on Rh(110)	183
6.5	The influence of post-oxidation on sub-monolayer VO_x films on Rh(110) .	184
6.6	The influence of post-oxidation on thick VO_x films on Rh(110)	185
6.7	V segregation upon oxygen treatment of V/Rh(110) at high temperature .	186
6.8	XPS characterization of VO_x films on Rh(110)	188
6.9	Reaction fronts in the system $CH_3OH + O_2$ /Rh(110) (PEEM)	191
6.10	LEED measurements during oxygen and methanol adsorption on Rh(110)	193
6.11	Reaction fronts in the system $CH_3OH + O_2$ /Rh(110) (LEEM)	195
6.12	Reaction rate measurements on Rh(110) and VO_x /Rh(110)	197
6.13	Traveling interface modulations on Rh(110) (PEEM)	200
6.14	In situ LEED measurements of traveling interface modulation on Rh(110)	202

6.15	Propagation of traveling interface modulations on Rh(110) (LEEM) . . .	204
6.16	LEED images acquired during the $H_2 + O_2$ reaction on Rh(110)	207
6.17	Traveling interface modulations on $VO_x/Rh(110)$	209
6.18	$x(t)$ plots taken during traveling interface modulations on $VO_x/Rh(110)$.	210
6.19	Formation of enhanced brightness at the interface	211
6.20	Traveling interface modulations on $VO_x/Rh(110)$ (LEEM)	213
6.21	In situ LEED during traveling interface modulation on $VO_x/Rh(110)$. . .	215
6.23	Target pattern during catalytic methanol oxidation on $VO_x/Rh(110)$. . .	222
6.24	Evolution of the (0,0) LEED intensity during chemical wave pattern . . .	223
6.25	LEED measurements during the transition from the oxidized into the reduced state	224
6.26	Double metastability in catalytic methanol oxidation on $VO_x/Rh(110)$. .	226
6.27	Activation of an oscillating surface defect	227
6.28	A traveling wave fragment during catalytic methanol oxidation on $VO_x/Rh(110)$ (PEEM)	228
6.29	Double metastability during catalytic methanol oxidation on 0.4 MLE $VO_x/Rh(110)$ (LEEM)	229
6.30	A traveling wave fragment during methanol oxidation on $VO_x/Rh(110)$ (LEEM)	230
6.31	LEED measurements during double metastability	231
6.32	Formation of macroscopic VO_x islands at 1000 K (PEEM)	233
6.33	PEEM intensity VO_x islands as a function of temperature	235
6.34	Oxidation and reduction of VO_x islands (PEEM)	236
6.35	Reaction-induced redistribution of VO_x on Rh(110) (LEEM)	237
6.36	LEED characterization of a VO_x hole pattern	239
6.37	Traveling wave fragments after VO_x redistribution (PEEM)	241
6.38	Reduction and oxidation of a micro-patterned $VO_x/Rh(110)$ surface . . .	243
6.39	Onset of pattern formation on a micro-patterned $VO_x/Rh(110)$ surface . .	244
6.40	Chemical wave pattern on a micro patterned VO_x Rh(110) surface (LEEM)	245
6.41	LEED on vanadium oxide rich and depleted areas	247
6.42	Propagation of reaction fronts on VO_x enriched and -depleted areas . . .	248
6.43	LEEM and XPEEM images recorded after the reactive phase separation of VO_x on Rh(110)	250
6.44	Ex situ XP spectra taken on vanadium oxide enriched and VO_x depleted areas present after reactive phase separation of VO_x on Rh(110)	251
6.45	Ex situ LEEM and LEED measurements on a macroscopic VO_x island . .	253
7.1	V deposition rate calibration on Pt(111)	262
7.2	V deposition rate calibration in LEED	264
7.3	Structural transformation and segregation of a thick VO_x film on Pt(111) upon methanol oxidation	265
7.4	Segregation behavior of VO_x on Pt(111) monitored by temperature pro- grammed AES measurements	267

7.5	Auger spectra of the reversible V diffusion into the bulk and to the surface of Pt(111)	268
7.6	VO _x Auger spectra (black) acquired after oxygen treatment	269
7.7	Characterization of the (2 × 2) apparent after the segregation of VO _x to the Pt surface	270
7.8	Temperature programmed reaction rate measurement on Pt(111) during methanol oxidation	273
7.9	AES and LEED measurements taken before and after the catalytic methanol oxidation on VO _x /Pt(111)	275
8.1	Surface Acoustic Wave	283
8.2	Samples for SAW and thermal diffusion experiments	285
8.3	SAW induced diffusion of Rh on Pt/LiNbO ₃ monitored with XPS	288
8.4	Sample and X-ray beam drift	290
8.5	Influence of sample and X-ray beam drift on the XPS measurements	291
8.6	Thermally induced Rh diffusion on Pt/LiNbO ₃ (AES)	293
8.7	Thermally induced Rh diffusion on Pt/LiNbO ₃ as a function of time and temperature (AES)	294
8.8	Thermal diffusion of Rh on Pt(100)	296

List of Tables

2.1	Total photoionization cross sections and asymmetry parameters at 650 eV photon energy	19
2.2	X-ray and atomic notation	21
3.1	Instruments used in this thesis.	52
4.1	Ordered vanadium oxide phases on Rh(111) reported in literature.	63
5.1	Results of the ex situ and in situ XPS characterization of VO _x islands on Rh(111)	121
5.2	V and O coverages obtained from ex situ recorded XP spectra of vanadium oxide islands	153
5.3	V and O coverages obtained in situ during ammonia oxidation with O ₂	158
5.4	V and O coverages obtained in situ during ammonia oxidation with NO	161
6.1	Non-linear phenomena observed during methanol oxidation on Rh(110) and VO _x /Rh(110).	254
A.1	Ordered vanadium oxide phases on Rh(111) reported in literature.	321

Chapter 1

Introduction

Abstract This introductory chapter covers developments in fundamental catalysis research relevant for this work. It is intended to help classifying the subject of this thesis, and to provide a (small) selection of literature. The chapter starts with a definition of a catalyst and the subdisciplines of catalysis research, while focusing then on heterogeneous catalysis at the solid-gas interface. The surface science approach to heterogeneous catalysis is introduced, and some disadvantages of this strategy are shown, namely the pressure and material gaps. After presenting some in situ and operando methods which enable to tackle the pressure gap, ways of increasing the complexity of catalytic model systems are described. A way of addressing the material gap is the concept of inverse catalysts. Applications of this concept in the context of surface science are treated together with recent developments towards an industrial application of inverse catalysts. Finally, the application of ultrasound in catalysis is briefly reviewed. The work done during my doctorate mainly focuses on the dynamics of inverse model catalysts during catalytic reactions in the pressure range from ultrahigh-vacuum to 0.1 mbar, and the influence of surface acoustic waves on the composition of bimetallic model catalysts.

A catalyst is a substance that accelerates a chemical reaction. The speed of the chemical reaction is increased by reducing the reaction activation energy [1]. It is important to note that the chemical equilibrium of the catalyzed reaction does not change [2, p. 155]. The catalyst thus has an influence on the reaction kinetics. Due to the higher reaction rate, it is possible to save large amounts of energy in chemical industry by applying catalysts [3, 4]. A catalyst can also catalyze the reaction path to a particular product, thus increasing selectivity. The increase in selectivity opens up further potential for saving energy and resources [5]. In nature, almost all important chemical reactions take place with the help of a catalyst. Prominent examples are the photosynthesis in plants or the conversion of food into usable energy for living organisms [6].

Many sub-disciplines have emerged in academic and industrial research on catalysis, classified according to the type of catalyst system and to their application. A distinction can be made between homogeneous catalysis – the catalyst and the substances involved in the chemical reaction are present in the same phase [2, p. 155] – and heterogeneous catalysis, in which the chemical reaction occurs at the interface of the catalyst and the reactants.

Solids are a large proportion of the used heterogeneous catalysts and the reactants are often in the gas phase. The combination of a solid catalyst and gaseous reactants has the advantage, that the interface is comparatively easy accessible for a characterization. A rigorous simplification of the catalytic reaction systems to almost perfect surfaces under vacuum conditions led to a far-reaching understanding of elementary reaction steps. Fundamental research in heterogeneous catalysis has therefore been accompanied by the development of vacuum technology and surface analysis techniques [1, 7].

1.1 The pressure and material gaps in catalysis

The desire of scientists to understand elementary steps of a heterogeneous catalytic reaction on a fundamental level, so that the properties of a catalyst can be tailored based on knowledge, is among the motivations for the so-called surface science approach to heterogeneous catalysis. In the surface science approach, a catalytic system is simplified as much as possible in order to address specific questions under well defined conditions. This simplification includes the use of single crystal surfaces as catalysts and the application of ultrahigh-vacuum (UHV) conditions [8].

The use of single crystal surfaces as catalysts has the advantage that only a small set of well defined surface sites is involved in the catalytic reaction. Industrial catalysts are often porous materials, consisting of different elements. They often can comprise contamination. The surface of such a catalyst exposes a large number of different crystal phases, and it can even be amorphous [9]. Clearly, it is challenging to ascribe an elementary step in a complex reaction mechanism to a specific site on such a surface [10]. Observations obtained in single crystal studies can in turn potentially be related to a specific surface site. UHV conditions give the ability of characterizing a clean surface, and allow for observing the interaction of a surface with a gas phase of controlled composition [6].

In the so-called surface science approach, the data obtained at low pressure with single crystal surfaces are extrapolated to the high pressure conditions of “real catalysis”, where complex polycrystalline mixtures of substances are used as catalysts. Quantitative data on adsorption and diffusion, on reaction energies, and on equilibrium and reaction rate constants obtained in surface science studies are the basis for micro-kinetic modeling of real catalytic processes. Finally, quantum chemical calculations can be compared with results of well defined surface science experiments [11].

This extrapolation is in general not valid for reasons given below, and the discrepancy between the conditions of surface science studies and applied industrial catalysis is termed “pressure and material gaps” in heterogeneous catalysis [12]. This is because

besides the problems of mass and heat transport in an industrial reactor, there are other intrinsic challenges. At elevated pressure and/or temperature other phases of the catalyst might either be thermodynamically stable or kinetically stabilized, as under UHV conditions. In addition, under the conditions of industrial catalysis, the structure and composition is largely determined by dynamic effects like restructuring, chemical transformations and segregation effects. These dynamic effects are pressure dependent: a catalytic surface under UHV conditions will be different from the surface under reaction conditions at high pressure.

Bridging the pressure and material gaps has evolved to an own research field in the past decades. It includes the development of new in situ methods applicable at high pressure for bridging the pressure gap, new model systems that better mimic the properties of real catalysts for bridging the material gap, and the theoretical tools needed for the interpretation of the data acquired under realistic or semi-realistic conditions. The ultimate goal is to gain understanding of structure-activity relations at the molecular scale, which aids in improving existing or developing new catalytic processes based on knowledge.

The difference in pressure between surface science studies and industrial catalysis can be as large as 15 orders of magnitude. An example where the surface science approach to catalysis was successful is the ammonia synthesis over iron potassium catalysts in the Haber-Bosch process [13, 14]. Nevertheless, a direct extrapolation of the results of surface science studies to industrial catalysis is rarely possible.

1.1.1 In situ and operando techniques

The latin term *in situ* can be translated to “on site” and is used to describe measurements, which are conducted while a certain process is happening. The term *ex situ* describes the characterization of a state present after a process has occurred. The characterization is often conducted in the absence of the experimental conditions, that have caused this process. The latin term *operando*, which can be translated to “working” or “operating”, has recently been introduced in catalysis literature and describes the simultaneous application of in situ methods and measurement of the catalytic activity and selectivity of a catalyst [15]. Furthermore, there is the claim, that operando studies are performed under realistic reaction conditions. In operando studies, the structure and/or chemical composition is characterized by spectroscopic and/or microscopic methods, and the catalytic activity and selectivity is recorded under operation conditions at the same time.

The development of suitable operando techniques is challenging. Several problems arise when industrial catalytic conditions are approached. The need for data on catalytic activity and selectivity sets several restrictions on the design of the catalytic reactor. Since most of the studied catalysts have a rather low active surface (except when powders are studied), the reactor volume should be as small as possible. At the same time, the reactor walls and the sample holder should be inert with respect to the investigated catalytic reaction, in order to clearly ascribe the measured reaction products to the catalyst [16].

Probably the most straightforward way to realize operando measurements is the use of photons as probe. In principle, photons can be used in a very wide pressure range, due to the negligible interference from the gas phase. Photon based techniques also do not impose strong restrictions on the catalyst morphology and even powders can be investigated. The first experimental studies termed operando used Raman spectroscopy. Other methodologies often applied include X-ray absorption and emission, surface sensitive X-ray diffraction, Mössbauer spectroscopy, electron paramagnetic resonance or nuclear magnetic resonance, and UV-VIS spectroscopy [16, 17].

All these methods have in common, that they provide integral information about the processes taking place on a surface. In most cases a microscopic analysis of the catalyst is only possible *ex situ*. The desire to gain microscopic insight into the processes occurring during a catalytic reaction under operation conditions led to the development of electron based techniques, that could be used at elevated pressures. Among the impressive developments is the ReactorSTM and ReactorAFM driven forward by Frenken and coworkers. The special scanning tunneling microscope (STM) and atomic force microscope (AFM) can be operated in gas atmospheres up to 5 bar and allow for operando studies with structural and chemical information on an atomic scale [16, 18, 19]. By reducing the width of the gas phase through which electrons have to travel to less than a few μm , transmission electron microscopy can be applied up to several bar [20, 21]. Most other electron based techniques like X-ray photoelectron spectroscopy (XPS) use an approach that uses small pressure reducing apertures together with differential pumping to separate the reaction environment from the other parts of the instrument. An example for an electron spectroscopy method is near ambient pressure XPS (NAP-XPS), that can be operated up to 100 mbar [22–25]. Examples for microscopy methods are transmission electron microscopy (TEM) and environmental scanning electron microscopy (ESEM) [26, 27], as well as near ambient pressure photoemission electron microscopy and near ambient pressure low-energy electron microscopy [28, 29]. All these microscopic methods should be regarded as *in situ* methods rather than operando methods, since reaction rates are often difficult to measure. However, in literature is many times no clear distinction between *in situ* and operando methods; partly these terms are used synonymously.

Suitable methods for operando studies exist and are continuously improved, while new methods are being developed. However, since each method only probes a certain aspect of a catalyst under operation, i. e. the geometric or electronic structure, multi-methods studies are required to obtain structure-activity relations.

1.1.2 From single crystals to real catalysis

The term “material gap” describes the discrepancy between carefully cleaned single crystals of metals or vacuum cleaved metal oxides and the industrially used catalysts, which typically are powders, nanoparticles or porous structures, and in most cases mixtures of different chemical compounds. Several different routes have been taken to approach the complexity of a real catalysts, resulting in the “concept of model catalysts”. In a model catalyst, the complexity is reduced, while still certain features of the real catalyst – those one would like to study – are retained. Typically planar model catalysts are

constructed.

The simplest model catalyst is a single crystal, which is cut in a certain crystallographic direction. Single crystals of alloys or thin metal layers deposited on single crystal surfaces serve as models for bimetallic catalysts [30]. Another way of increasing the complexity is the use of polycrystalline foils instead of single crystals. In this way several different surface orientations can be studied simultaneously (“surface structure libraries”) [31]. The Ostwald process, in which ammonia is oxidized on a Pt/Rh gauze, is an example for the application of polycrystalline foils or meshes in an industrial processes.

Not only metals, but also metal oxides are widely distributed in industrial catalysis. A metal oxide can act as a support for the catalyst or as the catalyst itself. One possible way to determine the structure and adsorption properties of oxide surfaces is the use of metal oxide single crystals. However, most electron based methods suffer charging problems when applied to insulating samples, which can complicate experiments. To overcome such charging problems, the growth of well ordered oxide layers on top of electrically conducting single crystal surfaces is subject of intense research. Thin films consisting of only a few atomic layers or even less than a monolayer have been studied. These systems exhibit interesting quantum size effects and interface stabilized oxide structures, which have no structural analogue as bulk crystals could be synthesized [32]. The electrical, magnetic and chemical properties of thin oxide films can differ considerably from the properties of bulk oxides, and thus they have the potential for technical applications [33,34]. Thicker metal oxide films, which exhibit the same surface structure as their bulk counterparts could also be grown. For example the interaction of water molecules with such surfaces is studied, or their catalytic activity in simplified model reactions [35, 36]. Metal oxide films are also used as support for small metal clusters or nanoparticles, in order to mimic the properties of supported metal catalysts used in chemical industry [37].

All model catalysts mentioned so far have in common, that they exhibit a flat surface. Further increase in complexity towards technical samples is possible if the model catalyst is extended in the third dimension. In order to facilitate in situ or operando measurements, simplified model catalysts consisting of non-porous oxides with a low surface area and metal nanoparticles deposited on the outer surface have been developed. Still, this simplifies the often highly porous and irregular structure of industrial catalysts [9]. However, such model systems have been used to study for example particle size effects in different reactions [38].

1.2 The inverse catalyst in heterogeneous catalysis

Metal oxides play an important role in heterogeneous catalysis, both as a support for the catalytically active species, or as a catalyst itself. The combination of metal oxides and metals is a well established concept in industrial catalysis. In the simplest case, the metal oxide represents an cost-effective and chemically inert support with a high surface area, which hosts catalytically active nanoparticles and which ensures the exposure of

the highest possible surface area of the catalyst to the reactants. The catalytic activity of nanoparticles varies with the used oxidic support, and systematic studies of metal-support interactions have been started. The effects causing these activity variations are manifold and should not be discussed at this point. The desire of a detailed understanding of such metal-support interactions, however, led to the concept of the inverse catalyst.

The term inverse catalyst describes a (model) catalyst in which the metal supports a metal oxide catalyst. A situation, which is just the inverse of most industrially relevant supported catalysts. The concept was first used in surface science studies. Recently a translation of the concept to more technically relevant scales took place [39].

1.2.1 Technical applications of inverse catalysts

Adsorption sites or active centers at the interface between a metal and a metal oxide play an important role in heterogeneous catalysis. The interaction of metallic and oxidic materials can lead to new catalytic properties, that are far beyond those of the two isolated materials [40]. A new strategy to incorporate this catalytic properties into technical catalysts is the deposition of an oxide, which is normally used as a support, onto the catalytic active metal. The reasons for such a synthesis strategy can be of different nature. An oxidic coating can prevent metal nanoparticles from sintering and thus stabilizes their size during a catalytic reaction. If a porous coating is used, a precise adjustment of the pore size of the coating can provide a way of controlling mass transport to the active centers of a catalyst. A comprehensive review about the recent progress in inverse catalysts can be found in reference [39].

Ways to realize inverse catalysts are for example the synthesis of core-shell nanoparticles consisting of a metal core encapsulated in an oxide shell. Another synthesis strategy developed by Haldor Topsøe A/S is the FENCETM technology. In this class of commercial catalysts for methanol synthesis, copper nanoparticles are surrounded by multiple metal oxide crystallites, which act like a fence surrounding the active metal particles. The metal oxide particles represent a support on one hand. On the other hand they prevent the particles from sintering. In this way an inverse catalyst ensures extended lifetime and stable performance of the catalyst in an industrial process [9, p. 65].

Finally, inverse catalysts can also form during a catalytic reaction, if (partial) wetting of the metal particles by the oxidic support sets in under reaction conditions. This phenomenon is commonly known as strong metal support interaction. Many systems exist, in which the formation of an inverse catalyst is assumed to occur. An example are zinc oxide overlayers on copper particles used in the methanol synthesis [41–43].

The technical application of inverse catalysts is still a young discipline of heterogeneous catalysis. Insufficient knowledge about the nature of active centers at the metal - metal oxide interface, of structure - activity relations in oxide coated catalysts, of dynamic effects under reaction conditions, and the disadvantage of blockage of active sites of the metal particle by an oxide overlayer are challenges that have to be overcome [39]. A suitable way to tackle questions concerning structure, structure - activity relations, and to some extent also dynamic effects is the surface science approach to inverse catalysts.

1.2.2 The surface science approach to inverse catalysts

Inverse model catalyst are well suited for investigating the oxide - metal interface in catalytic reactions. Furthermore, oxide phases that are not stable as bulk oxides can be stabilized in form of thin layers by a metallic support. Advantages of the surface science approach to inverse catalysts are the possibility to apply the methods commonly used for surface characterization, the large metal / oxide interface, and the accessibility of structural defects in the oxide films, which are often hidden, e. g. by metal particles, in technical samples. A comprehensive review about the structural and chemical properties of such metal oxide nanostructures by Surnev, Fortunelli and Netzer can be found in [32]. Perspectives focusing more on the application of such systems to catalysis are given by Rodriguez and coworkers [44], and by Barcara and Fortunelli [33].

The idea of an inverse catalyst was first introduced by Schwab, who studied the electronic properties of supported catalyst, both of metals deposited on oxides and carbides, and of nickel, iron and zinc oxides supported on silver or gold crystals [45]. Interestingly the strong metal support interaction has been observed just one year before by Tauster in a study of noble metals supported on titania [46,47]. The wetting of metal nanoparticles by thin layers of the supporting oxide is one of the motivations for the inverse catalyst approach.

In general, STM is the method of choice for the investigation of structure - property relationships of inverse model catalysts. It allows for a real space imaging on the atomic scale, together with the possibility of conducting a local chemical analysis (“chemical contrast”). The combination of density functional calculations based on structural models derived from STM and low-energy electron diffraction measurements (LEED) is nowadays the standard procedure for a structural characterization of ultrathin oxide layers. The chemical (for example the oxidation state of the metal) and electronic properties (like the density of states in the valence band) of such oxide films can further be characterized by means of photoemission experiments (e. g. XPS and ultraviolet photoelectron spectroscopy). The vibrational properties of oxide films can be studied with high-resolution energy electron loss spectroscopy (HREELS). As microscopical methods, besides STM and AFM, low-energy electron microscopy (LEEM) and photoemission electron microscopy (PEEM), especially in its spectroscopic variants (SPELEEM), are versatile tools for the characterization of inverse model catalysts and in situ studies [48].

The preparation of inverse model catalysts for surface science studies is mostly carried out by means of physical vapor deposition (PVD) either in ultrahigh vacuum or in an oxygen ambient. Also the use of atomic oxygen is applied in some cases. More chemical methods like chemical vapor deposition (CVD) or methods using liquid precursors are also used, but are not very common. This chemical methods find wide application in more realistic catalytic model systems. In the PVD growth of thin oxide films on metallic substrates it can be distinguished between two different methods to form an oxide: the reactive evaporation process and the postoxidation process. In reactive evaporation a metal is deposited in an oxygen atmosphere onto a substrate, which can optionally also be heated during the oxide growth. The deposition rates are typically chosen so that the growth of a monolayer takes several seconds to minutes. The oxygen partial

pressure is often in the ultrahigh or high vacuum range. In the post-oxidation process, the metal is deposited onto the metallic substrate and after the deposition is completed, an oxidation step by dosage of either molecular or atomic oxygen is performed. In both cases, in reactive evaporation and in post-oxidation, it can be beneficial for the crystallinity of the oxide film to anneal the freshly grown oxide in molecular oxygen. Due to the sometimes complex phase diagrams of the different interface stabilized oxide films, small variations in the synthesis protocols can have a huge structural impact [32].

With respect to heterogeneous catalysis, the focus of making supported metal nanoparticles accessible to the methods of surface science was complemented over the past decades by catalytic studies with ultrathin oxides as the catalytic active species. Possible model systems range from reactions on several layers thick oxide films over three-dimensional oxide particles on metal surfaces to monolayer oxides and two-dimensional islands, opening the path to two-dimensional materials and catalysis in confined space.

1.3 Theoretical chemistry in heterogeneous catalysis

Theoretical chemistry is essential for the interpretation of experimental results, for deriving and verifying mechanisms of catalytic processes, and for understanding reactivity trends, among many other fields of application. The high level of sophistication results in predictive power, and the term *in silico* is established in catalysis research [49–51]. With the methods of theoretical chemistry quantities like the heat of adsorption, bond strengths, and activation energies of elementary reactions can be calculated, structures of catalysts can be determined, and reaction pathways and transition states can be calculated [52]. Thus, theoretical chemistry is required to understand the structure of a catalyst and the reaction on the catalytic surface. Of special interest for this study are the structural characterization of two-dimensional vanadium oxide phases in the groups of Netzer (experiment) and Kresse (theory) [53–55], as well as studies on catalytic methanol oxidation on vanadium oxide surfaces in the group of Sauer [56–58].

1.4 Surface acoustic waves in heterogeneous catalysis

Besides the composition of a catalyst also external stimuli can be used to influence the catalytic performance. Examples for such external stimuli are the use of photons in photocatalysis, or electrical power in electrocatalysis. Another way to influence the catalytic activity and selectivity is the application of acoustic waves to a catalyst, a concept known as sonochemistry [59, 60].

Sonochemistry is often applied in the liquid phase but also heterogeneous systems of liquids and solids have been intensively studied. In liquid phase, the application of ultrasound causes acoustic cavitation. The formation, growth and implosion of small bubbles is responsible for several effects observed in sonochemistry. Especially the high energy transfer during the collapse of such bubbles can explain most of the observed effects [61]. Extended surfaces of metals irradiated by ultrasound in a solvent can undergo drastic morphological changes due to the implosion of cavitation bubbles at

the surface, or by solvent streams onto the surface caused by bubble collapse in close proximity. Also the application of ultrasound to a suspension of small catalyst particles (“slurry”) can change the surface morphological via inter-particle collisions caused by shock waves upon cavitation. For example, an activity increase by a factor of 10^5 has been observed in a heterogeneous sonocatalysis reaction with nickel powder [62].

Acoustic waves can be applied to a solid catalyst as surface acoustic waves (SAW) or as bulk acoustic waves. The experimental implementation is described in [63]. Bulk acoustic waves are excited by metal electrodes located at the front and backside of polarized ferroelectric crystals. If radio frequency is applied to the electrodes resonant oscillations of the crystal can be induced, and acoustic waves propagate through the crystal. The resonance frequency depends on the shape of the crystal and the orientation of the polarization axis [64]. Often the metallic electrodes are used as the catalytic surface. SAW are excited by applying radio frequency to so-called interdigital transducers which are attached to the same side of a ferroelectric crystal. The excited acoustic waves propagate on the crystal surface. Application of SAW to catalytic surfaces is realized by depositing thin metal (oxide) films in the acoustic path [63].

One of the first studies, which investigated the application of an ultrasonic excitation to a gas-solid system was reported by Dension, who attached an ultrasonic transducer to a vacuum chamber in order to desorb residual gas molecules from the vessel walls [65]. Later, desorption phenomena from better defined systems, namely the desorption from a quartz single crystal have been studied [66]. The concept of applying acoustic waves to a catalyst in a gas-solid system has been introduced by Inoue and coworkers. They observed an increase in the catalytic rates, and in some reactions an increase in selectivity upon application of bulk or surface acoustic waves to metal catalysts.

A review about the acoustic-wave induced effects on the catalytic and adsorption properties of different catalytic surfaces, including metals, alloys and metal oxides, is given in references [63,67]. Even though the remarkable effects SAW have on the catalytic activity of heterogeneous gas-solid systems, no thorough and detailed understanding of the elementary processes explaining the increased catalytic performance exists to date.

1.5 Motivation

While the structure and adsorption properties of oxide surfaces have been intensely investigated in the past few decades, little is known about the dynamics of oxide surfaces in catalytic reactions. Recently, a new ripening polymerization / depolymerization mechanism was proposed, which explains the coalescence of macroscopic vanadium oxide islands on Rh(111) during catalytic methanol oxidation [68–70]. This study aims at *i*) characterizing the reaction-induced redistribution thoroughly and *ii*) investigating whether the ripening mechanism can explain the behavior of ultrathin vanadium oxide catalysts in other reactions and on other substrates, namely Rh(110) and Pt(111). Short, we try to answer the question: How general is the polymerization / depolymerization mechanism?

In addition to catalytic methanol oxidation, ammonia, CO and H₂ oxidation are

studied on $\text{VO}_x/\text{Rh}(111)$. Furthermore, the oxidizing agent O_2 is replaced by nitric oxide in these reactions. To decipher the influence of the surface orientation of the substrate, the thermodynamically stable $\text{Rh}(111)$ surface is exchanged by the less stable $\text{Rh}(110)$ surface. The $\text{Pt}(111)$ surface is used to study the influence of the metal substrate on the properties of $\text{VO}_x/\text{fcc}(111)$ catalysts. The $\text{Pt}(111)$ surface is a thermodynamically stable $\text{fcc}(111)$ surface, but $\text{Pt}(111)$ has different adsorption properties than $\text{Rh}(111)$. For example the $\text{Pt}(111)$ surface exhibits a much lower oxygen sticking coefficient.

In order to cope with the complexity of the systems, a number of complementary analytical techniques is applied. The macroscopic redistribution dynamics are imaged with photoemission electron microscopy (PEEM). Since PEEM provides no structural and only indirect chemical information about the catalyst surface, low-energy electron microscopy (LEEM), both in its normal microscopic variant and in its spectroscopic variant, is used. LEEM enables us to *i*) image the reaction dynamics on a smaller nm length scale, and *ii*) to record diffraction images from selected areas of the catalyst under reaction conditions, thus allowing for a local structural characterization. The surface chemistry is studied by means of synchrotron X-ray photoemission experiments. Spectroscopic LEEM (SPELEEM) and scanning photoemission electron microscopy (SPEM) provide chemical information and lateral resolution required to characterize dynamic surface processes. Finally, the influence of pressure on catalytic reactions, a problem known as “pressure gap” in catalysis research, is investigated by comparing the results obtained in UHV up to the 10^{-4} mbar range with near ambient pressure LEEM (NAP-LEEM) measurements at 0.01 mbar.

A second aim of this study is to clarify the mechanistic basis for the influence of surface acoustic waves (SAW) on a catalytic surface. SAW are known to influence the activity and selectivity of catalytic reactions on metal, alloy, and metal oxide surfaces. The question of how SAW influence the catalytic performance has not been thoroughly answered. We try to validate the working hypothesis, that application of SAW leads to the creation of surface defects, which we assume to be the main reason for the altered catalytic properties. As a model system a bimetallic Rh/Pt surface is used.

Chapter 2

Experimental methods and theory

Abstract The experimental methods used in this work are introduced. The focus is on one hand on the interaction of photons and electrons with solid surfaces, on the other hand on the instrumentation. A brief overview of the different contrast mechanisms in low-energy electron microscopy and photoemission electron microscopy is given, as far as needed for the interpretation of the experimental data presented in this thesis. Besides the mentioned microscopic methods, a chemical and structural characterization was done using X-ray photoelectron spectroscopy, Auger electron spectroscopy, and low-energy electron diffraction. Fundamentals relevant for the understanding of the experimental findings are shortly presented. The catalytic activity of the model catalysts was probed with quadrupole mass spectrometry, and its application is shown as well as instrumental details. This chapter is based on, and in some parts identical to chapter 1 and 2 and section 6.1 of my master thesis [71], the presented information is taken from textbooks [6, 72–75] and scientific publications mentioned in the text.

2.1 Surface sensitivity

Surface sensitivity is a crucial property of most analytical techniques used in surface science. However, the thickness of the region called surface is not strictly defined. The “Compendium of Chemical Terminology” (IUPAC Gold Book) has three definitions for a surface: the ‘surface’ in general, the ‘physical surface’ and the ‘experimental surface’. While the first is defined as the “(...) ‘outer portion’ of the sample of undefined depth”, the second is defined as the “(...) outermost atomic layer of a sample”. The experimental surface is defined as the “(...) portion of the sample with which there is significant interaction with the particles or radiation used for excitation. It is the volume of sample required for analysis or the volume corresponding to the escape for the emitted radiation

or particle, whichever is larger.” [76]. The ‘physical surface’ can be probed only with a small number of experimental techniques, one of them is low-energy ion scattering [77]. In surface science, the term “surface sensitivity” is therefore often used for a probing depth of the topmost few atomic layers, and the term surface is used as a synonym for the IUPAC definition of an ‘experimental surface’ throughout this thesis.

The majority of surface science methods of analysis utilize electrons or photons as probing particles. Also incident ions, neutrons and sample heating is used to obtain information about the crystallographic and electronic structure or chemical composition of the surface. The underlying principle of most techniques of analysis is a primary excitation of the surface or an adsorbate by a probing particle or photon, and subsequent measurement of the resulting emission of radiation or particle(s) due to relaxation processes or scattering [73]. Surface sensitivity is thereby governed by the interaction of probing and emitted particles/radiation with the surface. The penetration/escape depth of electrons is often represented by the inelastic mean free path (IMFP) in the bulk material. The IMFP describes the mean distance that an electron can propagate in a solid until it undergoes an inelastic process [78].

In a rough approximation the IMFP λ of an electron is independent of the probed material, but a function of the electrons kinetic energy E_{kin} . The so-called “universal curve” describes the dependence of an electrons IMFP on its kinetic energy. Figure 2.1 shows λ given in monolayers as a function of electron energy above the fermi level, as calculated from equation 2.1 with the empirical parameters obtained from a least square fit of all elements investigated in [78, A_m and B_m in table 1]. (The IMFP of course varies with the material. For a precise analysis the material specific parameters should be taken into account.) The universal curve exhibits a global minimum of about two monolayers (ML) at an electron energy of about 20 to 100 eV. At lower energies the mean free inelastic path is mainly influenced by excitation of electron hole pairs and decreases approximately with E^{-2} . For higher energies also excitation of phonons or ionization can occur and the IMFP “varies roughly as the square root of electron energy” [75, 78]:

$$\lambda_i = \frac{A}{E^2} + B\sqrt{E}. \quad (2.1)$$

The fit parameters A and B have to be optimized in a least square fit to experimental data. In this work, electrons are used as probing particles in low-energy electron diffraction (LEED) and low-energy electron microscopy (LEEM), as well as in Auger electron spectroscopy (AES). The used photon-based techniques that detect emitted electrons are X-ray photoelectron spectroscopy (XPS), scanning photoemission electron microscopy (SPEM) and spectroscopic low-energy electron microscopy (SPELEEM), all are based on the photoelectric effect. In these techniques the sample is probed with radiation in the energy range of ultraviolet light or X-radiation. In all used techniques surface sensitivity is ensured by the low energy of less than 500 eV of either the incident electron beam (LEED and LEEM), or the emitted electrons (AES, XPS, SPEM, SPELEEM). Compared to a conventional X-ray cathode, the surface sensitivity can be further increased in synchrotron light excited XPS, SPEM, and SPELEEM by choosing

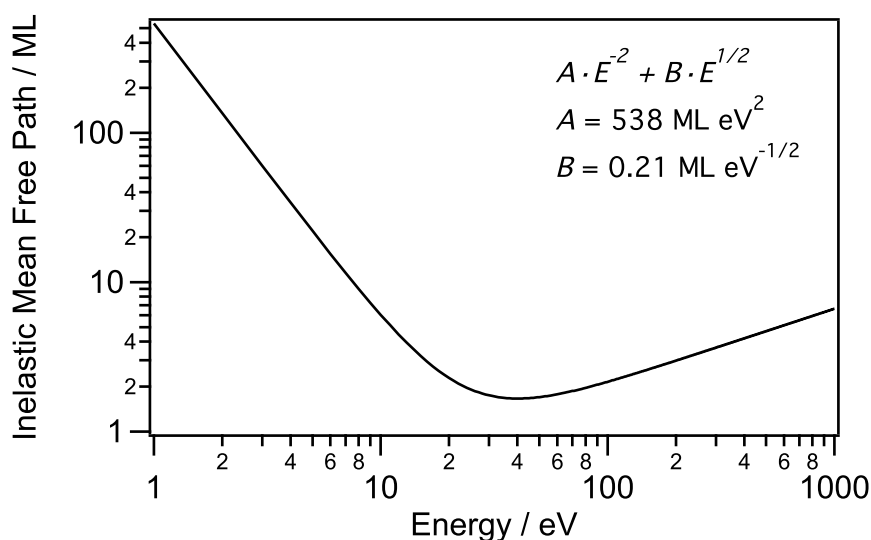


Figure 2.1: Universal curve of the inelastic mean free path of electrons in metals, given in monolayers as a function of kinetic energy above the Fermi level. The graph shows an empirical least square fit to equation 2.1 (equation 5 in [78]) of a compilation of data for different elements. The fit results A and B are taken from [78].

the photon energy in a way, that the emitted photoelectrons of interest have a kinetic energy of around 100 eV.

2.2 Electron spectroscopy

2.2.1 Auger electron spectroscopy

Auger electron spectroscopy (AES) is a surface sensitive spectroscopic method used for chemical surface analysis. AES is a non-destructive analysis technique based on the Auger-Meitner effect [79, 80]. Due to its instrumental simplicity (when an electron gun is used for excitation) compared to other techniques like XPS, AES is among the widely used surface analytical tools. The basic principle of most Auger spectrometers consists of electron beam bombardment of the sample surface and detection of the ejected Auger electrons. However, Auger transitions can also be excited with X-rays, thus Auger electrons are a natural part of an XPS spectrum.

The first step of the Auger-Meitner effect is the ionization of an isolated or bulk atom by an X-ray photon or an incident electron of sufficiently high energy. A schematic representation of the Auger-Meitner process for an isolated atom is shown in figure 2.2. Removal of an electron from an inner atomic electron shell A leads to a fast recombination by filling the core hole with an electron of an energetically higher shell B. The result is an excited atom. Relaxation can occur in one of two ways. First, the atom can emit an

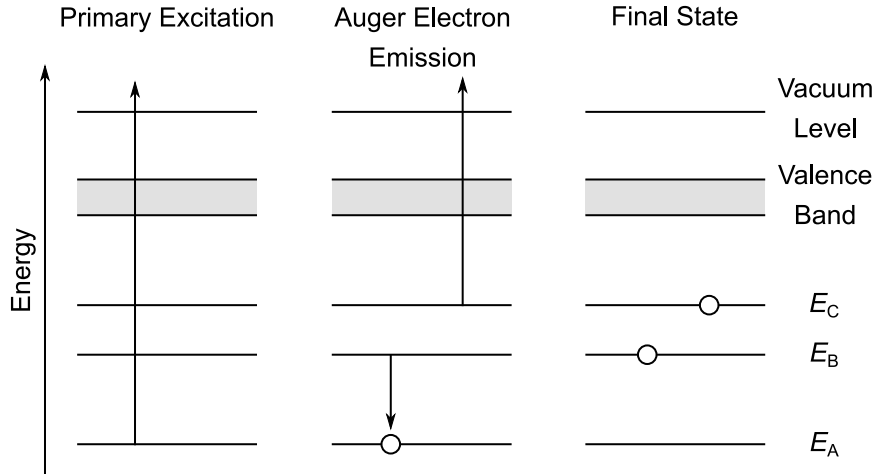


Figure 2.2: Schematic representation of the electronic levels involved in the Auger–Meitner effect. In the first step an inner shell electron is removed by a primary excitation (with an electron or an X-ray photon). Subsequently, an electron from a higher shell fills the core hole. The released excitation energy causes the emission of a so-called Auger electron from a third level. The Auger–Meitner effect is a three-state-effect, in this example involving the levels E_A , E_B and E_C . Figure adapted from [81].

X-ray photon of characteristic energy. This is the principle used in a technique called X-ray fluorescence. Since the probability of X-ray emission increases with $(h\nu)^2$, high excitation energies $E_A - E_B$ are mainly dissipated by X-rays. Alternatively, the Auger–Meitner effect can occur: the excitation energy is transferred radiation-less to another electron from the same or an higher electron shell C, which leaves the atom with the corresponding kinetic energy [75]

$$E_{\text{Auger}} = E_A - E_B - E_C - U_{\text{eff}}. \quad (2.2)$$

The extra energy needed to remove an Auger electron from the double-ionized atom is taken into account by U_{eff} . This factor includes also inner- and extra-atomic relaxation processes and interactions of the two hole-states in B and C [75, 81]. The radiation-less energy exchange happens *via* direct Coulomb interaction, and the probability of the transition depends on the orbital overlap of the two involved electrons. For this reason, core holes are often filled by electrons of the next higher energy level and Auger-electrons are often emitted from the same energy level as the hole filling electrons come from [75]. Two other important points must be considered when AES is used for analysis of condensed matter instead of isolated atoms. First, the kinetic energy of ejected Auger-electrons is diminished by the work function ϕ of the solid material. Second, the band structure of the solid must be taken into account.

In general, it is difficult to get detailed chemical information like oxidation numbers from AES data. This is, to a minor part, due to interactions of the ejected Auger

electrons with other atoms on their way out of the solid. On the other hand, a part of the chemical information is lost due to relaxation and interaction processes occurring in the Auger-Meitner effect, since three electron levels are involved. Despite this, some information about the chemical environment can be obtained if electrons from the valence band are involved [75].

For a core-core-valence transition ABV (V stands for valence band), every valence electron can be involved in the Auger-Meitner process. Since the valence band has a certain width ΔE_V , also the corresponding Auger-line has a width ΔE_V . Assuming a constant probability of transition for all electrons in the valence band, the shape of the Auger-line is reflecting the electronic density of states. In analogy, a line width of $2 \cdot \Delta E_V$ is obtained for core-valence-valence transitions AVV, and the line shape is the auto-convolution of the density of states [75]. Experimental and theoretical examples for such core-valence-valence transitions and the effect of the chemical environment on the line shape of Auger transitions can be found in literature [82–84].

Another example of chemical information obtained from Auger spectra is the determination of the oxidation state of vanadium (and other transition metals) in its oxides [85, 86]. The oxidation state of vanadium can be determined by the linearly decreasing ratio of the two Auger lines at around 473 eV and 437 eV, the V $L_{2,3}M_{2,3}M_{4,5}$ and $L_{2,3}M_{2,3}M_{2,3}$ transitions, with increasing oxidation state. Since the ratio of these two Auger transitions is specific for a spectrometer, and especially for the recording settings of the analyzer/detector system and the primary energy of the electron beam, a calibration with vanadium oxide samples of known oxidation state has to be established [87]. However, systematic trends can be observed, even though no direct assignment of an oxidation state to a V $L_{2,3}M_{2,3}M_{4,5}/L_{2,3}M_{2,3}M_{2,3}$ can be made if such a calibration is missing. As an example for the different peak ratios two spectra from the system $VO_x/Pt(111)$ are shown in figure 2.3.

Experimental implementation of AES

An experimental setup for AES by means of electron excitation consists of an electron gun, which acts as the source for the primary electron beam, an analyzer which passages only electrons of a specific kinetic energy, and a detector which detects the emitted Auger electrons. Modern Auger spectrometers are usually equipped with cylindrical mirror analyzers (CMA) [88]. Figure 2.4 shows a schematic cross-section of a CMA. Only electrons which enter the analyzer within the acceptance angle to the z -axis can pass the entrance slit, and only electrons of a specific kinetic energy are deflected onto the exit slit by the capacitor. Upon variation of the capacitor voltage $+V$, electrons of different energies can pass the analyzer and an energy spectrum can be recorded. Detection of the electrons is realized with an electron multiplier called channeltron.

The cylindrical geometry of the CMA has two benefits: The electron gun can be placed inside the analyzer, which allows bombardment of the sample at normal incidence. In this geometry electrons in (nearly) the full range of the azimuthal angle are collected, which increases the efficiency of the CMA. Since the amount of ejected Auger electrons is small compared to the elastic and inelastic backscattered electrons, the spectra typically

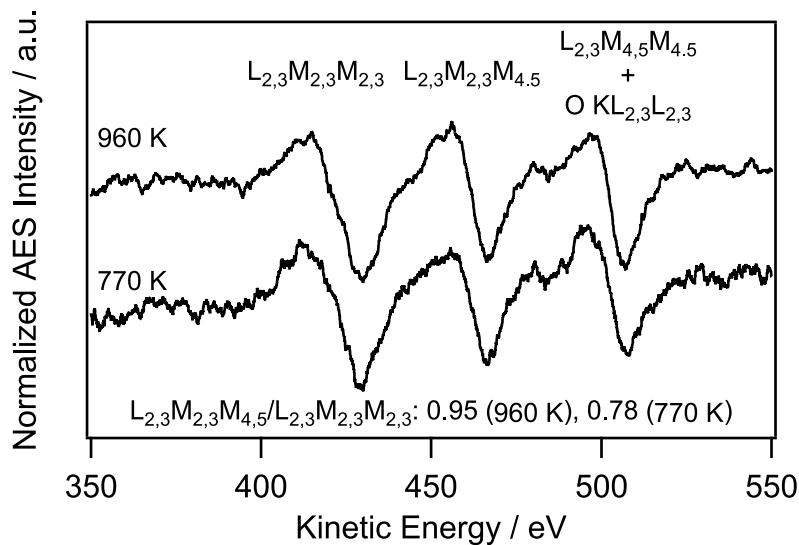


Figure 2.3: Auger spectra acquired on the same vanadium oxide film at two different temperatures in vacuum. The peak ratio $V L_{2,3}M_{2,3}M_{4,5}/L_{2,3}M_{2,3}M_{2,3}$ indicates a higher oxidation state at 770 K compared to 990 K. The spectra are recorded on the same vanadium oxide film at different temperatures in vacuum, and Auger intensity is normalized to the $V L_{2,3}M_{2,3}M_{2,3}$.

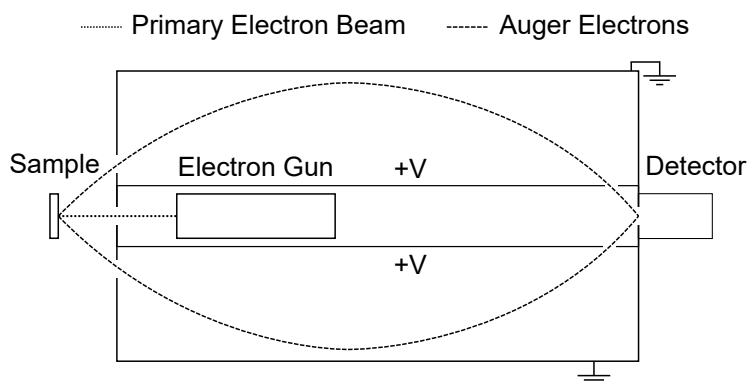


Figure 2.4: Schematic representation of the cross-section of a cylindrical mirror analyzer. The electron trajectory inside the analyzer is represented by the dashed line, the trajectory of the primary electrons is represented by a dotted line.

are measured differentially with analog lock-in technique. Another analyzer used in AES is the retarding field analyzer, which is described in chapter 2.3.2. In this work AES is used to ensure the purity of the sample surface, to measure the quantity of deposited vanadium oxide or rhodium, to roughly estimate the oxidation state of vanadium oxide films, and to investigate the segregation behavior of vanadium oxide and rhodium films.

2.2.2 X-ray photoelectron spectroscopy

In photoelectron emission experiments surface sensitivity is obtained due to the short IMFP of the emitted photoelectrons. The strong interactions of photoemitted electrons with the specimen limit the information depth to a few nm, depending on the electrons kinetic energy. If synchrotron radiation is used instead of a lab X-ray source, the surface sensitivity can be further increased by choosing a photon energy, which is about 50-100 eV higher than the Fermi energy. In this way the kinetic energy of the emitted photoelectrons is minimized to several tens to a few hundred eV, and the IMFP is minimized. Also the number of secondary electrons is reduced, resulting in a better signal to noise ratio. Since only one electron level is involved in the photoelectric effect, XPS can be used not only for element identification, but also for chemical analysis. Therefore XPS is also referred to as electron spectroscopy for chemical analysis (ESCA). In this work XPS spectra are taken using the SPELEEM III microscope (Elmitec Elektronenmikroskopie GmbH) at the Elettra electron storage ring, Nanospectroscopy beamline [89–91], at the ALBA electron storage ring, CIRCE beamline [92], and at the SPEM microscope of the ESCA Microscopy beamline (Elettra) [91, 93].

If a sample is illuminated with radiation of the energy $h\nu$, which is higher than the binding energies E_B of the electrons within a solid, excited electrons can leave the specimen and can be detected as a function of their kinetic energy E_{kin} . The binding energy of the ejected photoelectrons can be calculated as follows [75]:

$$E_B = h\nu - (E_{\text{kin}} + \phi) - \phi_{\text{sp}}. \quad (2.3)$$

In a solid the binding energy is referenced to the Fermi energy E_F , whereas the kinetic energy of the photoelectrons in vacuum is referenced to the vacuum level E_V . The Fermi energy is connected to the vacuum level by the work function $\phi = E_V - E_F$. Although the work function of a sample surface can vary locally, determining the kinetic energy of photoelectrons is simple since they are measured against the work function of the spectrometer ϕ_{sp} . In this way the measured kinetic energies are independent of local work function variations of the sample surface. Electrons emitted from core levels leave the sample with a certain characteristic energy, which can be shifted due to the chemical environment of the emitting atom (chemical shift). The binding energy is the energy difference between the electron system consisting of N electrons before photoemission, and the energy of the $N - 1$ electron system after photoemission from a certain core level [72]:

$$E_B = E_{\text{System}}(N) - E_{\text{system}}(N - 1). \quad (2.4)$$

The binding energy of an electron in a core level depends on the energy of the initial state and of the final state. The local environment can have influence on both states of the system and thus influences the binding energy. In this way information for example about the oxidation state and the identity of neighboring atoms can be obtained. The chemical shift is an initial state effect determined by the partial charge of an atom (electrostatic effect). Final state effects are determined by intra-atomic processes and the interaction of the charged core hole with the surroundings. Final state effects can show up for example as multiplet splitting or by the occurrence of so-called shake-up peaks [94].

Since the amount of emitted photoelectrons is proportional to the atom concentration in the surface region, XPS can be used quantitatively to determine the chemical composition. By taking into account the photoionization cross sections and asymmetry parameters of the measured core levels, the atomic ratio of two Elements A and B $\frac{N_A}{N_B}$ can be calculated under the assumption of a homogeneous distribution of A and B by the following equation:

$$\frac{N_A}{N_B} = \frac{I_A}{I_B} \cdot \frac{\sigma_B}{\sigma_A} \cdot \frac{T_B}{T_A}, \quad (2.5)$$

where I_i is the core level intensity, σ_i the photoionization cross section and T_i the transmission of the analyzer for electrons of specific kinetic energy. The photoionization cross section can be calculated with the energy dependent, total photoionization cross section $\sigma_{\text{tot}}(h\nu)$, the energy dependent asymmetry parameters $\beta(h\nu)$, and the angle between the ejected photoelectrons and the polarization vector of the incident X-rays θ by [95]:

$$\frac{d\sigma}{d\Omega} = \frac{\sigma_{\text{tot}}(h\nu)}{4\pi} \cdot (1 + \beta(h\nu) \cdot (3 \cos^2 \theta - 1)). \quad (2.6)$$

This equation only holds for linearly polarized light. Figure 2.5 shows the calculated photoionization cross sections for the V 2p, O 1s, Rh 3p and Rh 3d core levels.

In SPELEEMIII at the Nanospectroscopy (Elettra) and CIRCE (ALBA) beamline, the vertically mounted sample is illuminated by horizontally, linearly polarized X-ray light in grazing incidence (16°). The ejected photoelectrons are collected in the surface normal direction, giving an angle θ of 16° . In SPEM at the ESCA Microscopy beamline (Elettra), the sample is also mounted vertically, but the X-ray photons impinge in normal incidence on the surface, the ejected photoelectrons are collected under an angle of 60° . This geometry results in a value of $\theta = 30^\circ$. The values for $\sigma_{\text{tot}}(h\nu)$ and $\beta(h\nu)$ are taken from the Elettra WebCrossSections Database [96], which is based on the references [97, 98]. The transmission of the spectrometer used in this work scales as $1/E_{\text{kin}}$ in case of SPELEEM, and is unknown for the SPEM microscope. The total photoionization cross sections and asymmetry parameters used for the calculations of the differential photoionization cross sections are given in table 2.1.

In the interpretation of XPS it has to further be taken into account, that the spin orbit coupling splits all core levels with an angular momentum $l > 0$ in two components of total angular momentum $j = l \pm 1/2$. The characteristic intensity ratios of the spin

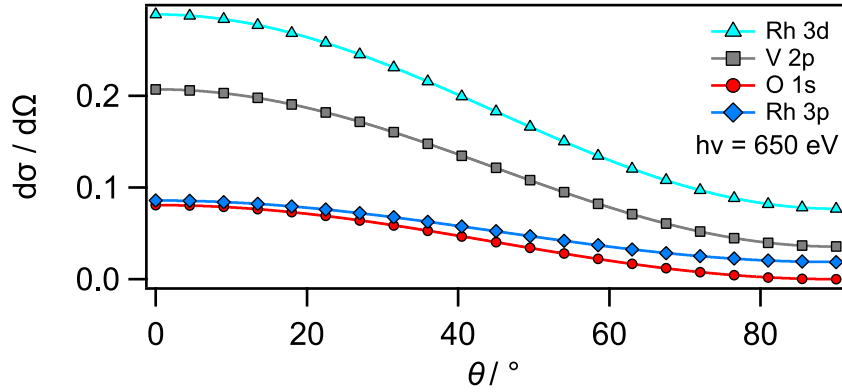


Figure 2.5: Differential photoionization cross sections of V 2p, O 1s, Rh 3p and Rh 3d calculated according to equation 2.6.

Table 2.1: Total photoionization cross sections and asymmetry parameters taken from [96] and calculated differential photoionization cross sections at 650 eV photon energy for the core levels V 2p, O 1s, Rh 3p and Rh 3d.

Core level	$\sigma_{\text{tot}}(h\nu = 650 \text{ eV})$	$\beta(h\nu = 650 \text{ eV})$	$d\sigma/d\Omega(\theta = 16^\circ)$	$d\sigma/d\Omega(\theta = 30^\circ)$
O 1s	0.3384	2	0.075	0.061
V 2p	1.165	1.233	0.194	0.164
Rh 3p	0.5162	1.089	0.081	0.069
Rh 3d	1.853	0.9582	0.273	0.236

orbit doublets is given by the degeneracy of the states $2j + 1$ [75]. Table 2.2 gives an overview of the two common notations with which atomic orbitals are labeled, as well as the degeneracy of the corresponding states. An exemplary XPS spectrum of a Rh(111) surface covered with about 1.2 monolayer equivalents of vanadium oxide is shown in figure 2.6.

2.3 Low-energy electron diffraction

Determining the atomic arrangement of a surface is an important step in understanding the physical and chemical properties of any given interface. Typically the structure of surfaces differ from bulk termination. The variations range from relaxations of the interplanar spacings to complete reconstructions with different surface densities and periodicities [6]. Low-energy electron diffraction (LEED) is a versatile method to probe the atomic arrangement of the topmost atomic layers of a crystal.

The de'Broglie wavelength λ_{el} of electrons with energies $E_{\text{el}} = eU$ ranging from a few tens to hundreds of eV (U is the accelerating voltage and e the electrons charge) lay in the same range like interatomic distances in a crystal or molecule. By taking an accelerating voltage of 100 V, the Planck constant h , and the electrons mass m_e and

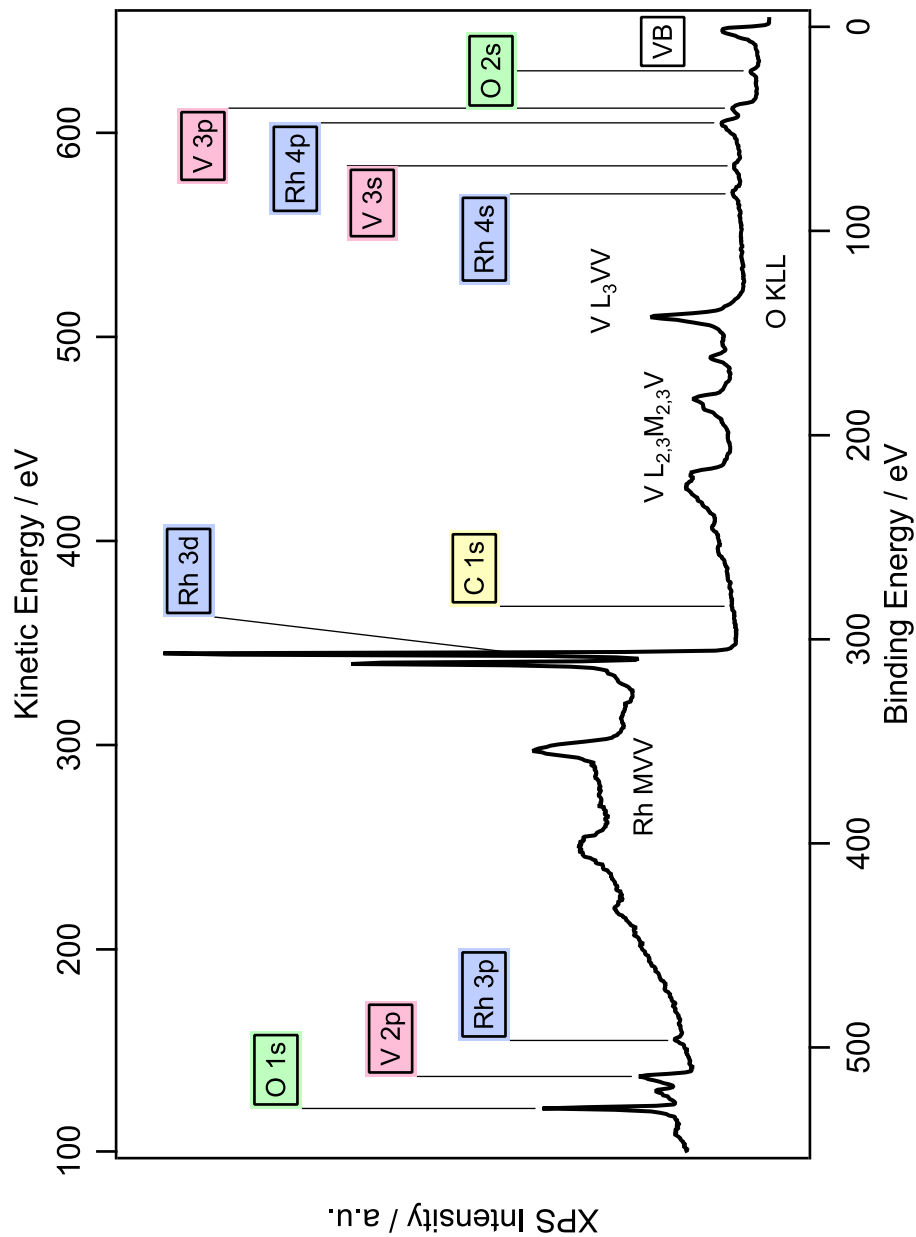


Figure 2.6: XPS spectrum of a Rh(111) surface covered with about 1.2 monolayer equivalents of vanadium oxide. The spectrum was acquired in an oxygen atmosphere of 2×10^{-7} mbar with a photon energy of 650 eV at the ESCA Microscopy beamline (Elettra). The Auger transitions as well as the V, Rh, O and C core levels are indicated.

Table 2.2: Correspondence between the X-ray notation and the atomic notation of core levels and the degeneracy of the corresponding states.

X-ray Notation X_i	K	L ₁	L ₂	L ₃	M ₁	M ₂	M ₃	M ₄	M ₅
Atomic Notation nl_j	1 s _{1/2}	2 s _{1/2}	2 p _{1/2}	2 p _{3/2}	3 s _{1/2}	3 p _{1/2}	3 p _{3/2}	3 d _{3/2}	3 d _{5/2}
Degeneracy $2j + 1$	2	2	2	4	2	2	4	4	6

charge e , a wavelength of roughly 122 pm can be calculated:

$$\lambda_{\text{el}} = \frac{h}{\sqrt{2m_e eU}}. \quad (2.7)$$

Electrons with low kinetic energy ensure a small penetration depth due to the strong interaction with the solid, thus limiting the probing depth to around 1 nm [78]. On the other hand, these strong interactions lead to multiple scattering, which complicates the interpretation of LEED data. Simple single scattering analysis (kinematic) of acquired LEED intensity vs. voltage curves ($I(V)$ -curves), like in X-ray diffraction, is not possible and costly calculations based on multiple scattering theory of diffraction (dynamical calculations) are necessary to determine the surface structure.

2.3.1 Kinematic theory of diffraction

The kinematic theory of diffraction describes the situation in which every incident electron (helium atom, photon) is diffracted only once before leaving the solid. This is a good approximation for helium atom scattering and X-ray diffraction. In LEED, however, also multiple scattering plays an important role, leading to the dynamic theory of diffraction, which is described in detail in reference [74] and which will not be discussed in this thesis. A detailed description of the kinematic theory of diffraction can be found in the textbooks [73–75], and is recapitulated briefly in the following.

In the kinematic theory of diffraction it is assumed, that an incident electron beam, described by a plane wave of wave vector \mathbf{k}_0 , is elastically scattered once, leaving the solid as a diffracted plane wave of wave vector \mathbf{k} . The momentum transfer between the incoming and diffracted plane wave is $\mathbf{s} = \mathbf{k} - \mathbf{k}_0$. Furthermore, since only elastic scattering is considered, the magnitudes of \mathbf{k} and \mathbf{k}_0 are equal. The amplitude A_{in} of the incoming mono-energetic electron beam is given by:

$$A_{\text{in}} = A_0 e^{i\mathbf{k}_0 \mathbf{r}}, \quad (2.8)$$

with \mathbf{r} a space vector. For the amplitude of the diffracted beam A_{out} follows:

$$A_{\text{out}} = A_0 \left(\sum_n \alpha f_n(\mathbf{s}) e^{i\mathbf{s} \mathbf{r}_n} \right) e^{i\mathbf{k} \mathbf{r}}. \quad (2.9)$$

The attenuation of a plane wave reflected in deeper layers is taken into account by α , and $f_n(\mathbf{s})$ is the atomic scattering factor of the n^{th} atom at position \mathbf{r}_n . If the diffracting

solid is a crystal the atomic position \mathbf{r}_n can be written as $\mathbf{r}_n = \boldsymbol{\rho}_j + m_1 \mathbf{a}_1 + m_2 \mathbf{a}_2 + m_3 \mathbf{a}_3$. The positions of N atoms within the unit cell of a crystal are given by $\boldsymbol{\rho}_j$ ($j=1,2,\dots,N$), \mathbf{a}_i are the basis vectors of the crystal lattice and m_i are integer numbers. The sum in equation 2.9 can then be written as

$$\left(\sum_j f_j e^{i\mathbf{s}\boldsymbol{\rho}_j} \right) \cdot \left(\sum_{m_1, m_2, m_3} e^{i\mathbf{s}(m_1 \mathbf{a}_1 + m_2 \mathbf{a}_2 + m_3 \mathbf{a}_3)} \right) \quad (2.10)$$

for the three dimensional case. The first sum is called the structure factor, the second is known as the lattice factor. Whereas the structure factor contains all information about the position and the chemical nature of the atoms within an unit cell, the lattice factor is only depending on the point lattice of the crystal.

Because of the short IMFP in a diffraction experiment with low-energy electrons, the crystal periodicity is only retained in two dimensions parallel to the surface. The position of the atoms are given by $\mathbf{r}_n = \boldsymbol{\rho}_j + m_1 \mathbf{a}_1 + m_2 \mathbf{a}_2$. The atomic position within the two dimensional unit cell are now represented by $\boldsymbol{\rho}_j$. Perpendicular to the surface, the unit cell extends to infinity meaning down into the solid to the depth reached by electrons. Equation 2.10 becomes

$$\left(\sum_j f_j e_j^{i\mathbf{s}_{\parallel} \boldsymbol{\rho}_j} \right) \cdot \left(\sum_{m_1, m_2} e^{i\mathbf{s}_{\parallel}(m_1 \mathbf{a}_1 + m_2 \mathbf{a}_2)} \right). \quad (2.11)$$

Since the sum over the lattice vectors is proportional to the Dirac delta function $\delta(\mathbf{s}_{\parallel} - \mathbf{g})$, only components of momentum transfer \mathbf{s}_{\parallel} parallel to the surface, that equal any vector \mathbf{g} of the reciprocal lattice, give a non-zero solution. The reciprocal lattice vector in two dimensions is defined as:

$$\mathbf{g} = h\mathbf{g}_1 + k\mathbf{g}_2 \quad (h, k \text{ are integers}), \quad (2.12)$$

with the basis vectors of the reciprocal lattice

$$\mathbf{g}_1 = 2\pi \frac{\mathbf{a}_2 \times \mathbf{n}}{\mathbf{n} \times (\mathbf{a}_1 \times \mathbf{a}_2)} \quad \text{and} \quad \mathbf{g}_2 = 2\pi \frac{\mathbf{n} \times \mathbf{a}_1}{\mathbf{n} \times (\mathbf{a}_1 \times \mathbf{a}_2)}. \quad (2.13)$$

For the Bragg conditions in two dimensions follows:

$$\mathbf{s}_{\parallel} = \mathbf{k}_{\parallel} - \mathbf{k}_{0,\parallel} = \mathbf{g}. \quad (2.14)$$

Diffraction is only possible in the directions

$$\mathbf{k}_{\parallel} = \mathbf{k}_{0,\parallel} + \mathbf{g}. \quad (2.15)$$

With equation 2.12 this directions can be indexed with the miller indices (h,k) and the surface point lattice in reciprocal space can be determined from a diffraction experiment. Due to the lack of symmetry perpendicular to the surface, virtually every momentum \mathbf{k}_{\perp} can be transferred, leading to so-called crystal truncation rods which are perpendicular

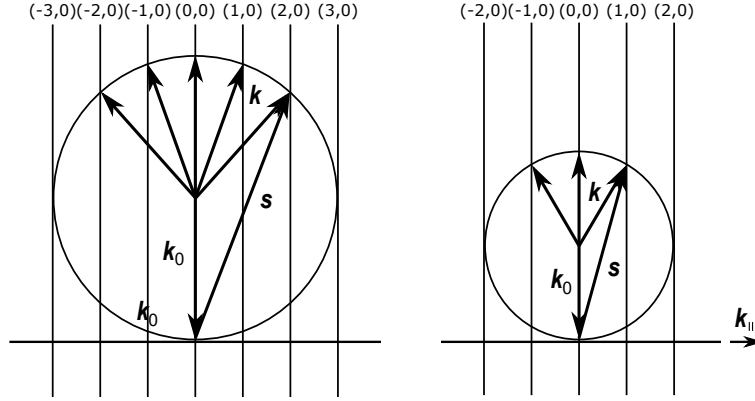


Figure 2.7: Construction of the Ewald sphere for normal incidence and two different energies. From comparing the left (higher energy) with the right side of the diagram, it follows that the number of lattice rods intersecting the Ewald sphere increases with increasing \mathbf{k}_0 (kinetic energy of the incident electron beam). The radius r of the Ewald sphere is given by $r = |\mathbf{k}_0| = 2\pi\lambda_{\text{el}}^{-1}$.

to the plane of reciprocal lattice points \mathbf{g} . Since only elastic scattering is considered, meaning $|\mathbf{k}| = |\mathbf{k}_0|$, the value of \mathbf{k}_\perp can easily be calculated:

$$\mathbf{k}_\perp = \pm \sqrt{\mathbf{k}_0^2 - (\mathbf{k}_{0,\parallel} - \mathbf{g})^2} = \pm \sqrt{\mathbf{k}_0^2 - \mathbf{k}_\parallel^2}. \quad (2.16)$$

The sign \pm represents the direction of diffraction, meaning back and forward scattering. A effective concept of showing the possible diffraction direction for a given \mathbf{k}_0 is the Ewald construction: in reciprocal space the vector \mathbf{k}_0 is drawn in a way that it points at the origin of the reciprocal lattice (0,0). A sphere of radius $r = |\mathbf{k}_0|$ is drawn around the initial point of \mathbf{k}_0 , the so called Ewald sphere. All crystal truncation rods that intersect the Ewald sphere are defining possible \mathbf{k} vectors. Since the Ewald sphere expands with increasing electron energy, or better increasing \mathbf{k}_0 , more crystal truncation rods intersect the sphere. This means that higher order diffraction becomes apparent. A schematic representation of the crystal truncation rods and the Ewald sphere for the one-dimensional case is given in figure 2.7.

In case of an adsorbate on the surface, which has a long range order and therefore forms a so called super lattice, additional diffraction vectors \mathbf{k} fulfill equation 2.15. The super lattice is also described by its basis vectors \mathbf{b}_1 and \mathbf{b}_2 . The relation between \mathbf{a} and \mathbf{b} in the reciprocal space is given as follows:

$$\begin{pmatrix} \mathbf{a}_1 \\ \mathbf{a}_2 \end{pmatrix} = \begin{pmatrix} m_{11} & m_{12} \\ m_{21} & m_{22} \end{pmatrix} \begin{pmatrix} \mathbf{b}_1 \\ \mathbf{b}_2 \end{pmatrix}. \quad (2.17)$$

For the real space the basis vectors of the super lattice can be calculated by:

$$\begin{pmatrix} \mathbf{b}'_1 \\ \mathbf{b}'_2 \end{pmatrix} = \begin{pmatrix} m_{11} & m_{21} \\ m_{12} & m_{22} \end{pmatrix} \begin{pmatrix} \mathbf{a}'_1 \\ \mathbf{a}'_2 \end{pmatrix}. \quad (2.18)$$

With known basis vectors of the substrate, the dimensions of the super lattice can be determined. The determinant

$$|m_{11}m_{22} - m_{21}m_{12}| \quad (2.19)$$

represents the size of the superstructure unit-cell given in units of the substrate unit-cell area.

The lattice factor of a clean or an adsorbate covered crystal depends only on the lattice vectors \mathbf{a}_i and the scattering vector \mathbf{s} . It holds all information about the crystal lattice since it is itself a periodic arrangement of points forming the reciprocal lattice. The geometrical properties of a diffraction pattern obtained in an diffraction experiment can be rationalized with the lattice factor. In contrast, the structure factor depends on the atomic arrangement within the unit cell, characterized by ρ_j , as can be seen in equation 2.10, and it varies with \mathbf{k}_0 . The atomic arrangement within the unit-cell can be obtained from measuring the diffraction intensity as a function of \mathbf{k}_0 of the incident electron beam, a so called LEED $I(V)$ curve. Starting from an initial structure model the theoretical LEED $I(V)$ curves are calculated. The structure is than refined in order to minimize the difference between the theoretical predicted and experimental obtained $I(V)$ curves. Due to the very strong interaction of low-energy electrons with the atoms within a crystal, multiple scattering always has to be taken into account in structure determination, leading to the application of dynamical LEED theory in calculations.

In summary, the diffraction pattern interpreted with the lattice factor in LEED theory holds the information of the crystal lattice symmetry and size, whereas the intensity variation with changing \mathbf{k}_0 ($I(V)$ curve) gives information about the atomic arrangement in the unit cell, and the type of atoms that constitute the unit cell. The analysis of a diffraction pattern in terms of spot position can be done in the kinematic limit, but a complete structure determination including a theoretical reproduction of the LEED $I(V)$ curve should be done in a dynamic calculation.

2.3.2 Experimental implementation of LEED

In this work diffraction experiments are conducted with a conventional LEED optics, as well as with LEEM. In this section the conventional LEED apparatus will be described, a description of the LEEM instrument can be found in chapter 2.4.2.

A LEED optics consists mainly of two essential elements: an electron gun which emits an almost parallel and mono-energetic electron beam, and a detection system for the backscattered electrons [99]. A schematic representation of a LEED display system is given in figure 2.8.

The incident electron beam is generated by a hot cathode, focused by a Wehnelt cylinder and a lens system, and accelerated towards the grounded sample. After interacting with the surface, the elastically and inelastically back-scattered electrons pass four hemispherical grids on their way to the hemispherical detection screen. The grid systems acts as an high-pass filter and suppresses the inelastically back-scattered electrons. To avoid electrical fields between detection system and sample, the first of the four grids is

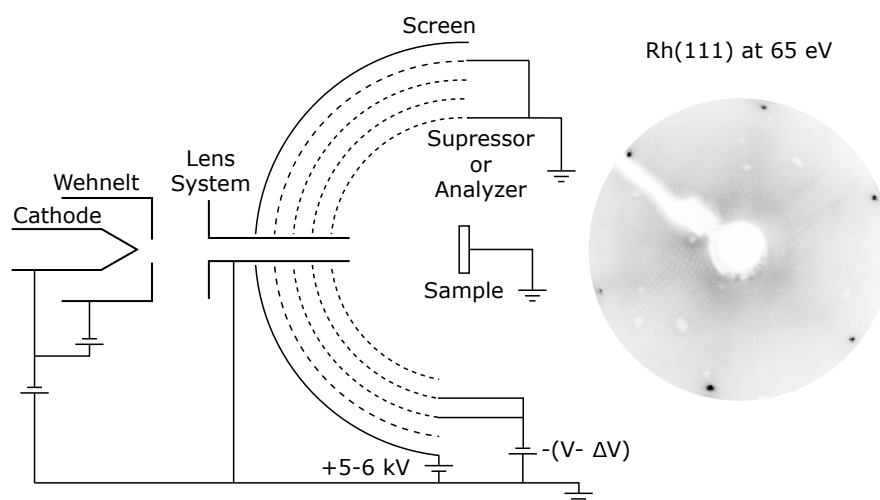


Figure 2.8: Schematic diagram of a four grid LEED optics adapted from [100] together with an example of the LEED pattern of the clean Rh(111) surface recorded at 50 eV with a rear-view LEED optics.

grounded. The second and the third grid are the so called suppressor grids. By applying a negative potential to the suppressor grids which magnitude is just below the primary energy of the electron beam, inelastically scattered electrons are repelled while elastically scattered electrons can pass. The fourth grid, which again is on ground potential, prevents the retarding field of the suppressor grids from influence of the high acceleration potential (typically around 5 to 6 kV) of the imaging screen. An arrangement of this type is called a retarding field analyzer (RFA). Modern LEED optics use hemispherical glass plates coated with thin, conducting layers of indium tin oxide, instead of metal screens to allow signal detection with a video camera mounted on the backside of the screen. In this way a direct view on the screen without having the sample obscuring the view of the camera is possible (rear view LEED).

2.4 Cathode lens microscopy

The simplest configuration of a cathode lens consists of the sample as the cathode and the objective as an anode. In cathode lens microscopy electrons are emitted from (emission microscopy) or diffracted at the sample surface, resulting in structural [101], chemical [102,103] or magnetic [104] contrast. When electrons formed by the absorption of photons are used to generate an image, the technique is called photoemission electron microscopy (PEEM). Commonly PEEM refers to the use of ultraviolet light, whereas XPEEM refers to the use of X-radiation. Compared to other microscopes, XPEEM has the advantage of providing chemical information, since the kinetic energy of the outgoing electrons is depending on the orbital from where the photoelectrons originate [105].

In low-energy electron microscopy (LEEM) elastically back-scattered electrons are

used to form an image of the surface. The combination of LEEM with an electron analyzer is called spectroscopic low-energy electron microscopy (SPELEEM). All microscopes have in common that the sample acts as the cathode of an immersion objective lens. Usually the sample is kept on a high negative potential (several kV) to accelerate the emitted electrons towards the imaging lens system [72]. However, also set-ups with a grounded sample and an optical column on high positive potential (up to 20 kV, 12 kV in this thesis) exist. One of them, the PEEM system of Engel et al. [106], is used in this thesis. The resolution of modern cathode lens microscopes is limited to 2 nm in LEEM and 5-10 nm in PEEM [107, 108]. However, a resolution of about 10 nm in LEEM and 20 nm in XPEEM is a more realistic lower limit in the type of experiments conducted in this thesis. Since both, LEEM and PEEM, are direct methods no scanning techniques are necessary and fast image acquisition is possible. The UV-PEEM instrument used in this study is described in reference [106], whereas a detailed review of the used SPELEEM can be found in reference [103]. A comprehensive textbook about the history, theory, and instrumentation of cathode lens microscopy in general, with a focus on LEEM as well as on recent applications can be found in reference [72].

2.4.1 Photoemission electron microscopy

The underlying principle of PEEM is the photoelectric effect, first mentioned by Heinrich Hertz and Wilhelm Hallwachs in 1888 [109, 110]. Theoretical treatment was given by Albert Einstein in 1905 [111]. The kinetic energy E_{kin} of an ejected electron by incident ultraviolet light of the energy $h\nu$, where ν is the frequency of light and h Planck's constant, is given by:

$$E_{\text{kin}} = h\nu - \phi. \quad (2.20)$$

With the PEEM microscope used in this work, UV-photons are used to image the local work function ϕ of a sample surface with a spatial resolution in the range of 0.1 μm and a temporal resolution in the range of 200 ms [106, 112]. The dependence of the photoemission yield on the photon energy and the work function is treated in the Fowler-DuBridge theory [72, 113, 114]. The photoelectron current density is given by:

$$J = \alpha A_0 T^2 f\left(\frac{h\nu - \phi}{k_B T}\right), \quad (2.21)$$

with a proportionality constant α , the Richardson constant $A_0 = 4\pi m k_B^2 e/h^3$ [115], the Boltzmann constant k_B , and the Fowler equation f :

$$f\left(\frac{h\nu - \phi}{k_B T}\right) \equiv f(x) = \int_{-\infty}^x \ln(1 + e^t) dt \quad (2.22)$$

$$= \frac{x^2}{2} + \frac{\pi^2}{6} - e^{-x} + \frac{e^{-2x}}{2^2} + \dots \quad \text{for } x \geq 0. \quad (2.23)$$

For interpretation of photoemission intensities, typically only the first term of the Fowler equation is taken into account [72], leading to:

$$J \approx \alpha A_0 T^2 \frac{1}{2} \left(\frac{h\nu - \phi}{k_B T} \right)^2. \quad (2.24)$$

As can be seen, the photoelectron current, and thus the PEEM intensity, is proportional to the square of $h\nu - \phi$. Surface regions with a high local work function, *e.g.* adsorbed oxygen or a metal oxide, result in a lower photoelectron current and therefore a low brightness value in PEEM. In contrast, surface regions with a low local work function, *e.g.* bare metal surfaces, adsorbed carbon species, can be identified by high brightness values in PEEM. Finally, it has to be stated, that the Fowler-DuBridge equation is based on the free electron gas approximation and therefore has limitations [72].

The imaging column of the PEEM instrument used in the experiments conducted in Hannover consists of three lenses, an objective lens, an intermediate lens, and a projective lens. The microscope is operated in a way, that the sample is grounded and the imaging column is kept on a positive potential of 12 kV to accelerate emitted photoelectrons. The lens system magnifies the generated image, and projects it onto a micro channel plate (MCP) detector. The visible image is produced by a fluorescent phosphor screen which is mounted behind the channel plate. Data acquisition is carried out with a CCD (charge-coupled device) or CMOS (complementary metal-oxide semiconductor) camera. Due to differential pumping of the PEEM housing a pressure of 5×10^{-4} mbar inside the main chamber can be realized (the pressure is limited by the main turbo pump, not by discharges in the imaging column of the microscope). Quantitative evaluation of the acquired PEEM images is done with the program package Fiji ImageJ [116], and self-written analysis procedures as well as the SPELEEM Imaging Suite (SIS) program package written by A. Locatelli and O. Mentis et al. [117] in IGOR Pro 6.37.

2.4.2 Low-energy electron microscopy

In low-energy electron microscopy (LEEM) the wave nature of electrons is used to generate a real space image with contrast mainly being produced by diffraction of an elastically backscattered electron beam at the surface of a specimen. The theory of low-energy electron diffraction is described briefly in chapter 2.3.1. Due to the large interaction cross section of electrons in the energy range below 100 eV, LEEM can be used to obtain true images without the need of scanning techniques. For energies below roughly 20 eV, the exposure time can become short enough to record images in video frame rate, thus enabling the visualization of dynamic surface phenomena like film growth, surface phase transitions, and diffusion in situ [118]. The fact that imaging contrast is provided by backscattered electrons makes it necessary to separate the illumination and imaging beams with a beam separator, which distinguishes LEEM from other emission microscopes. Despite this, LEEM can easily be combined with LEED, (X)PEEM or other emission microscopies, making it a powerful multitool for surface analysis. All LEEM images shown in this work are taken using *i)* the SPELEEM III (Elmitec Elektronenmikroskopie GmbH) at the Elettra synchrotron radiation laboratory, Nanospectroscopy

beamline, *ii*) at the ALBA synchrotron radiation laboratory, CIRCE beamline, *iii*) at the University of Bremen, or with the NAP-LEEM at Elmitec in Clausthal. The SPELEEM microscopes operated at ALBA and Elettra are a combination of a commercial LEEM microscope with energy filtered synchrotron X-ray photoemission electron microscopy (XPEEM). Therefore the following description includes all necessary parts to run the microscope in XPEEM mode. Detailed reviews of the development, instrumental details, and applications of LEEM in general and the SPELEEM in particular can be found in literature [72, 102, 103, 107, 108, 119, 120].

A schematic representation of the instrumental set-up including the electron gun, the illumination column, the beam separator, the imaging column, the energy analyzer and the detector system is given in figure 2.9. If the SPELEEM is operated in LEEM-mode electrons are needed as probing particles. A focused electron beam is produced by a LaB₆ electron gun and a focussing lens system which is summarized as the imaging column in figure 2.9. In this type of LEEM instrument, the resolution is limited by the energy dispersion of the electron gun to about 10 nm [72]. The incident electron beam is directed onto the specimen by a 60° beam separator. In the beam separator magnetic deflectors are used to deflect the incoming illumination beam and the outgoing imaging beam in two different directions. The direction of the Lorentz force \mathbf{F}_L caused by the influence of a magnetic field \mathbf{B} on a point charge q depends on the translational direction expressed by its velocity vector \mathbf{v} :

$$\mathbf{F}_L = q\mathbf{v} \times \mathbf{B}, \quad (2.25)$$

whereas the Coulomb force \mathbf{F}_C caused by an electrical field \mathbf{E} is independent of \mathbf{v} :

$$\mathbf{F}_C = q\mathbf{E}. \quad (2.26)$$

Therefore a static magnetic field is suitable to separate the illumination and the imaging beam, allowing the usage of backscattered electrons for real space imaging.

After leaving the beam separator, the electron beam interacts with the specimen. In the used LEEM III microscope the objective lens is a magnetic diode, consisting of two electrodes (the sample and the objective lens), and a magnetic field for focussing. The incoming electron beam has a kinetic energy of 10 to 20 keV, since the LaB₆ e-gun is kept at a constant negative potential U . The specimen is at a potential $U + \Delta U$ to decelerate the incoming electrons to low-energy. ΔU is the so-called start voltage (STV) and defines the kinetic energy of the electrons at the sample surface. The (in)elastically backscattered electrons are then accelerated again by the acceleration voltage U . During passing the objective lens a magnified image of the specimen is produced in the intermediate image plane, as well as an image of the diffraction pattern in the back-focal plane. The beam separator directs the imaging beam into the imaging column, where the image of the specimen is magnified by the transfer lens (TL), the field lens (FL) and the projector lens (P1), before it enters the hemispherical energy analyzer. At the entrance of the analyzer the electron beam is decelerated to the pass energy of the energy analyzer, and accelerated again before leaving the analyzer through the exit slit. After leaving the analyzer the image is projected by two projective lenses (P2 and P3) onto

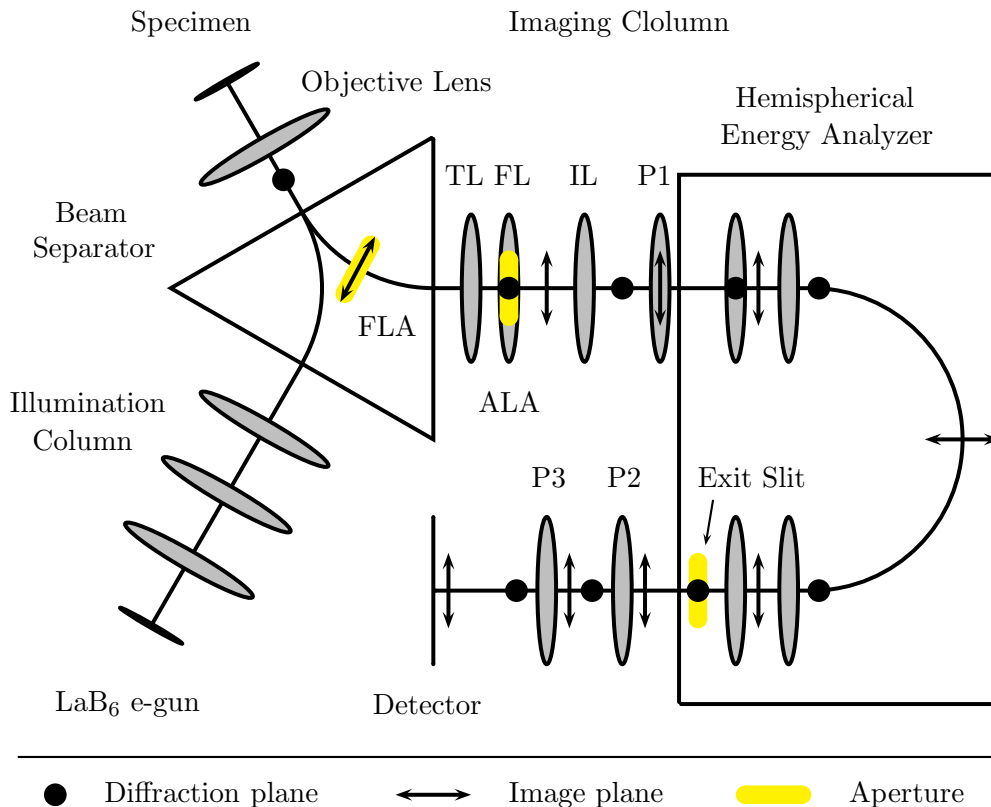


Figure 2.9: Schematic representation of the SPEELEEM instrument. Electrons emitted from the LaB₆ electron gun are accelerated by the acceleration voltage U , focused by the illumination column and directed onto the specimen by the beam separator. The specimen, which acts as the cathode of the immersion objective lens (OBJ), decelerates the electron beam to low-energy, due to the applied potential $U - \Delta U$. The backscattered electrons are then again accelerated and directed into the imaging column by the beam separator. In the imaging column a magnification of the image and diffraction plane takes place before the imaging beam enters the hemispherical energy analyzer. After leaving the analyzer the image or diffraction plane is projected by the projector lenses onto the detector system. For details and abbreviations see text; figure adapted from [121].

a detector system consisting of a double stage MCP image intensifier and a fluorescent phosphorous screen. Data acquisition is done with a digital camera [118, 121].

The imaging column can be used in two different ways to image either the intermediate image plane or the back-focal plane. If the image plane is projected onto the detector, like it is depicted in figure 2.9, a real space image of the surface is obtained. If instead the intermediate lens (IL) images the back-focal plane onto the first projective

lens (P1), the LEED pattern is projected onto the fluorescent screen. In this way LEEM enables fast switching between real and reciprocal space information. This can be used to perform selected area LEED (μ LEED) by inserting a field limiting aperture (FLA) into the image plane located inside the beam separator, or an illumination aperture in the imaging beam (not shown in figure 2.9). In this way only a small region (apertures of diameter 0.25 – 30 μm are available) of interest is selected from the real space image, which is then used to display the back-focal plane containing the LEED pattern.

Despite the capability of only probing a selected area, LEED data acquired with LEEM has the advantage of energy independent spot positions and energy independent electron flux, which simplifies the evaluation of LEED- $I(V)$ data. Both characteristics are a consequence of the deceleration/acceleration stage at the objective lense. For imaging the surface in real space an angle limiting aperture (ALA, also called contrast aperture CA) has to be inserted in the back-focal plane in order to filter out undesired diffraction beams, thus increasing image contrast. If the specular beam is used to generate an image it is referred to as the bright field image. In bright field imaging, contrast is mainly caused by the energy dependent diffraction beam intensity. If the angle limiting aperture is used to image higher order diffraction beams, the microscope is used in dark field mode. Only areas with a structure corresponding to the selected diffraction beam appear bright in the dark field image.

In another mode of operation called mirror electron microscopy (MEM) the start voltage is set in a way that the incoming electron beam has a kinetic energy of zero to a few eV, which is not high enough to reach the surface. The imaging electron beam is reflected in front of the surface, leading to a local image of the work function. Areas of high work function cause high reflectivity and therefor appear bright in MEM images. If the start voltage is increased continuously starting from 0 V (a procedure called LEEM- $I(V)$) it is possible to measure relative work function differences on the surface by comparing the local intensity evolution during the voltage scan. The MEM-LEEM transition is characterized by a sharp intensity drop.

2.4.3 Near ambient pressure low-energy electron microscopy

LEEM is a typical UHV technique since both, the electron source and the image detector are highly pressure sensitive. A pressure in the low 10^{-8} mbar range should be ensured close to these components. Two other problems are encountered when the pressure in LEEM is increased: the strong interaction of electrons with molecules or atoms from the gas phase, resulting in a considerable decrease in image intensity starting at around 1×10^{-4} mbar, and the risk of discharges between the sample and the objective lens [29]. To overcome these three problems, a dedicated reaction cell was designed by Elmitec Elektronenmikroskopie GmbH for the NAP-LEEM, which separates the high pressure region from the imaging and illumination column, and which reduces the path that electrons have to travel in the high pressure gas atmosphere to a minimum. A detailed description of the microscope, together with experimental results of CO oxidation on Pt(110) and polycrystalline Pt foil can be found in reference [29]. With the NAP-PEEM another near-ambient pressure cathode lens microscope developed by Specs GmbH exists.

Like in the Elmitec NAP-LEEM, a NAP gas cell separates the high pressure region in which the sample is located from the optical components of the microscope [28]. A cutaway schematic of the Elmitec NAP-LEEM can be found in figure 2.10.

In the Elmitec NAP-LEEM a pressure of up to 0.1 mbar can be reached, and the optical components of the microscope are separated from the NAP cell by two-stage differential pumping. The NAP cell is located in the main chamber of the LEEM microscope, as can be seen in figure 2.10. Reaction gases are introduced by a separate gas-inlet system into the NAP cell. The aperture of the second electrode of the objective lens (a magnetic triode) acts as the pin-hole of the first differential pumping stage. A small capillary of 0.6 mm diameter and 2.0 mm length inserted in the optical path in the third electrode of the objective lens (highlighted with the label “Capillary” in figure 2.10) is the pin-hole for the second differential pumping stage. The two differential pumping stages ensure a pressure in the low 10^{-8} mbar range in the illumination and imaging column. The small diameter of the capillary reduces the accessible reciprocal space in diffraction experiments to about 7 eV.

In order to reduce the electrical field strength in the sample region, the magnetic diode objective lens of a conventional LEEM III microscope is replaced by a magnetic triode lens [119]. In this way the acceleration voltage of the microscope U is reduced in two stages to ground potential at the third electrode of the objective lens. The sample is kept on the potential $U + \Delta U$ (with ΔU being the start voltage STV), whereas the second electrode of the objective lens acts as an intermediate electrode which is on the potential U_{Int} . With U_{Int} being in the range of $1 \text{ kV} \leq U_{\text{Int}} < U$, the electrical field strength between the sample and the second electrode of the objective lens can be reduced significantly compared to conventional LEEM instruments, which operate with acceleration voltages of up to 20 kV and a comparable distance between the objective lens and the sample surface. The risk of discharges during high pressure operation is reduced to a minimum, the spatial resolution can be optimized by tuning the values of U and U_{Int} .

The path that the electrons have to travel in the high pressure area can only be reduced by a design, which is as compact as possible. However, a decrease in image intensity due to scattering of electrons with the gas phase has to be weighed against practical consideration such as the possibility to illuminate the sample with UV or X-ray photons, or to attach an electron beam evaporator to the NAP cell.

2.4.4 Spectroscopic low-energy electron microscopy

In X-ray photoemission electron microscopy (XPEEM) X-ray stimulated photoelectrons are used as probing particles. Photoelectron microscopy can be done either with scanning techniques or in a full-field approach [122]. A combination of the third generation synchrotron light sources Elettra and ALBA with a LEEM microscope equipped with a hemispherical energy analyzer is utilized to perform XPEEM and XPS measurements. A detailed description of the beamline set-up of the Nanospectroscopy and CIRCE beamlines, as well as a review of the capabilities of the SPELEEM microscope, can be found in [90, 92, 103, 121, 123]. Chapter 2.2.2 shortly summarizes the physical principles of

Elmitec LEEM III Microscope and Near-Ambient Pressure Cell

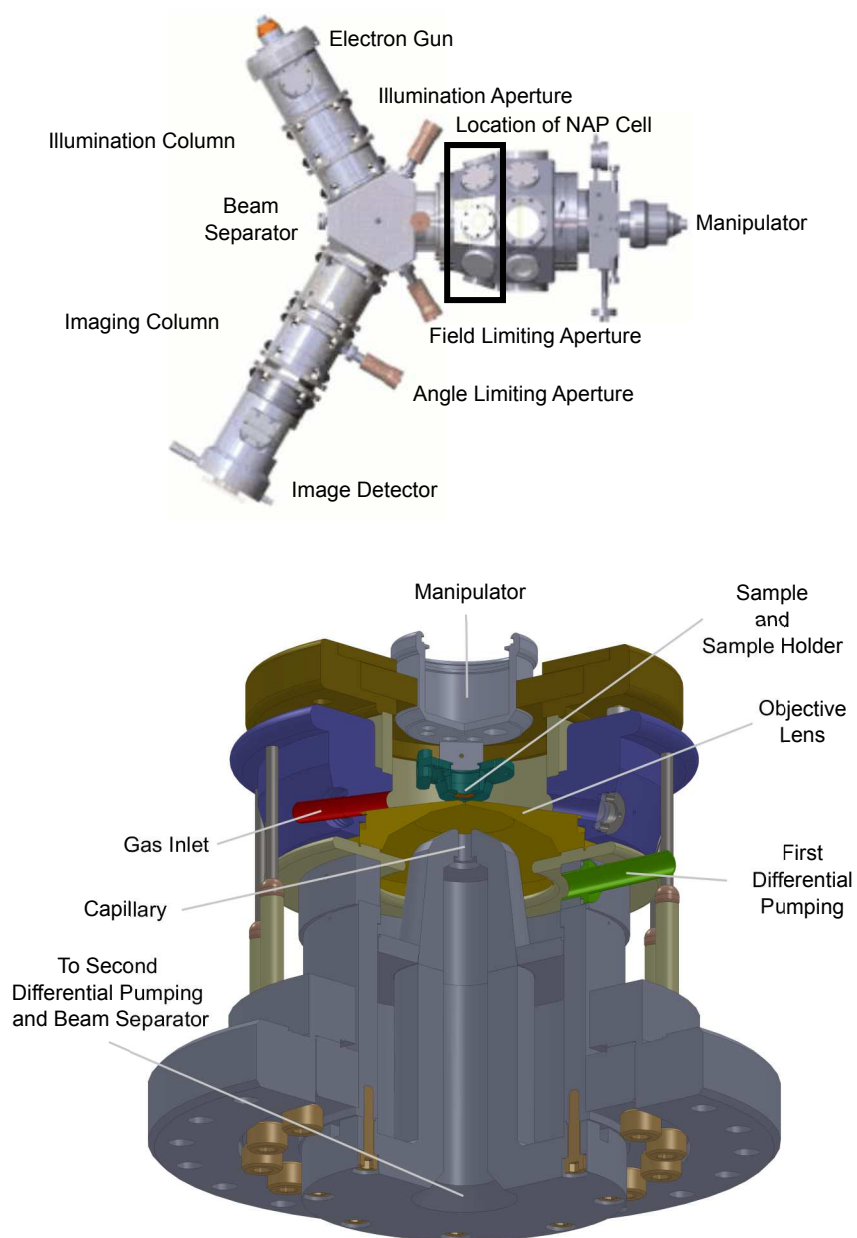


Figure 2.10: Schematic representation of an Elmitec LEEM III microscope together with a cutaway scheme of the near-ambient pressure cell of the NAP-LEEM. The location of the NAP cell within the microscope is highlighted by the solid black rectangle in the LEEM III representation. The schemes of the LEEM III microscope and of the NAP cell are reproduced with permission from Elmitec Elektronenmikroskopie GmbH.

X-ray photoemission.

A schematic representation of the microscope used in this work is given in figure 2.9. In XPEEM mode the specimen is illuminated with synchrotron radiation at a grazing incidence angle of about 16° . Since no illuminating electron beam is needed, the voltage of the photoelectrons ejected from the surface of the specimen are accelerated by the acceleration voltage U , and enter the imaging column and the hemispherical energy analyzer through the beam separator. All electron optical elements are operated in the same way like in LEEM mode. With this setting XPEEM can be carried out energy filtered in imaging, diffraction and spectroscopic modes. In imaging mode the angular acceptance of the microscope is set by the contrast aperture diameter. A small diameter suppresses aberrations and improves the lateral resolution. In diffraction mode the field limiting aperture is used to select an area of interest for spectroscopic diffraction imaging (angle-resolved photoemission spectroscopy, ARPES) or microprobe XPS (μ XPS) measurements. In the cases of diffraction and real space imaging the bandwidth which can pass the hemispherical energy analyzer can be set by the width of the exit slit placed at the exit of the analyzer, allowing proper energy filtering. The kinetic energy of the emitted photoelectrons can be calculated with equation 2.3. Spectral imaging is done by collecting images at different kinetic energies, which is practically carried out by varying the start voltage STV applied to the specimen. The resulting image stack contains the lateral resolved photoelectron spectra of the imaged area. It can be extracted by calculating the averaged XPEEM intensity for a selected area for every STV value. In this way local adsorbate coverages can be calculated, since the photoemission intensity is proportional to the number of surface emitters [118]. In the same way, by varying STV, the full k-space can be probed in ARPES, enabling the examination of the electronic structure of the surface. In a third modus of operation, the dispersive plane of the energy analyzer is projected onto the image detector. In this way a roughly 10 eV wide photoelectron spectrum can be recorded with short exposure times of only a few seconds.

2.5 Scanning photoemission electron microscopy

The advantage of a photoemission electron microscope over a conventional XPS spectrometer is the high spatial resolution, which can ultimately result in a magnified image of a sample surface with chemical contrast. In cathode lens microscopy spatial resolution is obtained by an electron optics, which magnifies the image produced by the emitted photoelectrons. Spatial resolution is obtained via projection of the emitted photoelectrons. In scanning photoemission electron microscopy (SPEM) instead, the probing X-ray beam is focussed into sub-micrometer spot size to allow high spatial resolution, and scanned over a certain area. Whereas the direct, “spectromicroscopic” approach of cathode lens microscopy produces a direct image, the “microspectroscopic” approach of SPEM needs a scanning unit, which rasters the sample surface to produce an photoelectron image [93].

The advantage of direct XPEEM imaging is (comparable) fast image acquisition.

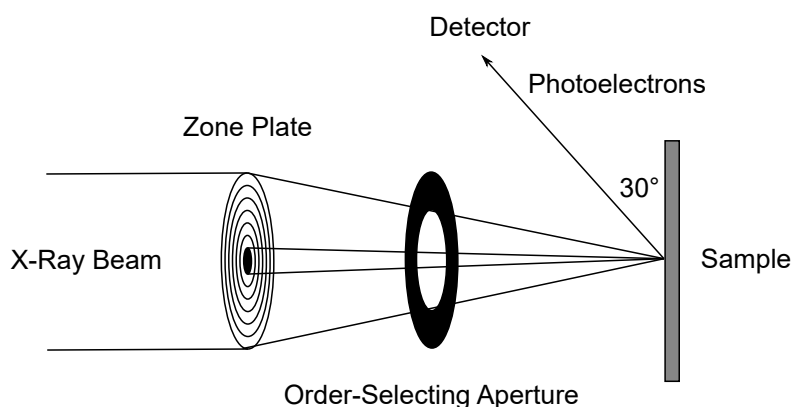


Figure 2.11: Schematic representation of the SPEM set-up consisting of a Fresnel zone plate optic system, which focuses the probing X-ray beam, the sample mounted on the two-stage motorized sample stage (not shown), and the multi-channel photoelectron detector.

However, SPLEEM has restrictions with respect to the sample. The high electrical fields applied in cathode lens microscopy require very flat surfaces (e.g. of single crystals or polished metal foils), whereas the potential free sample environment in SPEM can even tolerate technical samples with a rough surface. Also problems connected to sample charging are less critical in SPEM. In cathode lens microscopy already small charging effects lead to large field distortions between sample surface and objective lens and thus lower imaging quality.

The SPEM microscope located at the ESCA microscopy beamline of the electron storage ring Elettra consists essentially of a Fresnel zone plate optic system [124], which focuses the X-ray light, a piezo-driven sample positioning system, and a hemispherical energy analyzer. As X-ray source a 98 periods undulator is used, which produces horizontally polarised light in the energy ranges 90 to 1500 eV and 130 to 1800 eV for electron energies of 2.0 and 2.4 GeV in the storage ring, respectively.

A schematic representation of the SPEM set-up is shown in figure 2.11. The zone plate optic system comprises a zone plate (ZP) and an order-selecting aperture (OSA). In the so-called zone plate mode (ZP mode) both, the zone plate and the order selecting aperture are inserted into the X-ray optical path. The zone plate focuses the X-ray beam down to 50 nm at best, whereas the order-selecting aperture blocks unwanted diffraction order radiation. Zero-order light is additionally blocked by a circular stop mounted in the center of the zone plate. The ZP mode is the operating modus in which the highest spatial resolution can be obtained. In the so-called order-selecting aperture mode (OSA mode) the zone plate is removed from the X-ray optical path and only the OSA restricts the area illuminated by the X-ray photons [93].

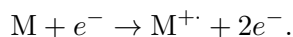
SPEM can be used to collect XPS spectra with high spatial resolution in ZP mode or with medium spatial resolution in OSA mode. Due to parallel 48-channel photoelectron detection, a roughly 10 eV wide energy spectrum can be acquired within a single

snapshot, comparable to the dispersive plain mode of SPELEEM. The fast acquisition times allow for in situ measurements of surface processes with temporal (and in ZP mode high spatial) resolution. The width ΔE of the energy spectrum that can be acquired within a single snapshot can be calculated by $\Delta E = 0.16 \cdot E_P$, with E_P being the kinetic energy of the electrons during passage of the analyzer (“pass energy”) [125]. Imaging is performed by tuning the hemispherical analyzer to a specific energy (e.g. of the desired core level), while continuously rastering the sample surface with respect to the probing X-ray beam. The sample stage consists of a double motor stage. A “coarse stage” allows for SPEM images of >1 mm, with minimum step size of $1 \mu\text{m}$, whereas a “fine stage” enables images sizes of up to 100 by $100 \mu\text{m}^2$ with a minimum step size of 1 nm (piezo motor). The coarse stage is additionally used to position the sample surface in the focal plane of the X-ray beam. Due to the mentioned multi-channel detection not only an image with chemical contrast is obtained, also a pixel-wise analysis of e.g. core-level shifts is possible by extracting the “multi-channel” photoelectron spectrum from the image data [126]. Detailed descriptions of the ESCA microscopy beamline, recent developments, and applications of the SPEM can be found in references [91,93,127–131].

2.6 Quadrupole mass spectrometry

The total pressure in a vacuum chamber is the sum of the partial pressures of all gas components. In order to measure a partial pressure it is necessary to isolate one component from the rest of the gas mixture. In quadrupole mass spectrometry (QMS) ionized atoms, molecules or molecular fragments are separated according to their mass to charge ratio m/e . Partial pressure measurement with QMS can be divided into three steps: The first step is the ionization of the gas phase. The second step is the separation of the resulting ions according to their mass to charge ratio. The last step is the quantitative registration of the species belonging to the specific mass to charge ratio, which can pass the analyzer. Therefore a quadrupole mass spectrometer consists of an ion source, a mass analyzer and a detector.

In the mass spectrometer used in this work ionization of the gas phase is achieved by electron bombardment. If a molecule M is hit by an electron with high kinetic energy (≈ 70 eV), a part of the kinetic energy is transferred to the molecule. If the transferred energy is higher than the ionization energy of the molecule, ionization can take place with a certain probability:



Double or triple ionization is also possible, depending on the electronic structure of the molecule and the kinetic energy of the incident electron. The excitation of a molecule by electron bombardment can also cause fragmentation of the molecule in two or more neutral or charged molecular fragments. Therefore every molecule shows a characteristic fragmentation pattern which has to be taken into account in QMS data analysis. The fragmentation pattern of methanol and formaldehyde are shown in the right side of figure 2.12.

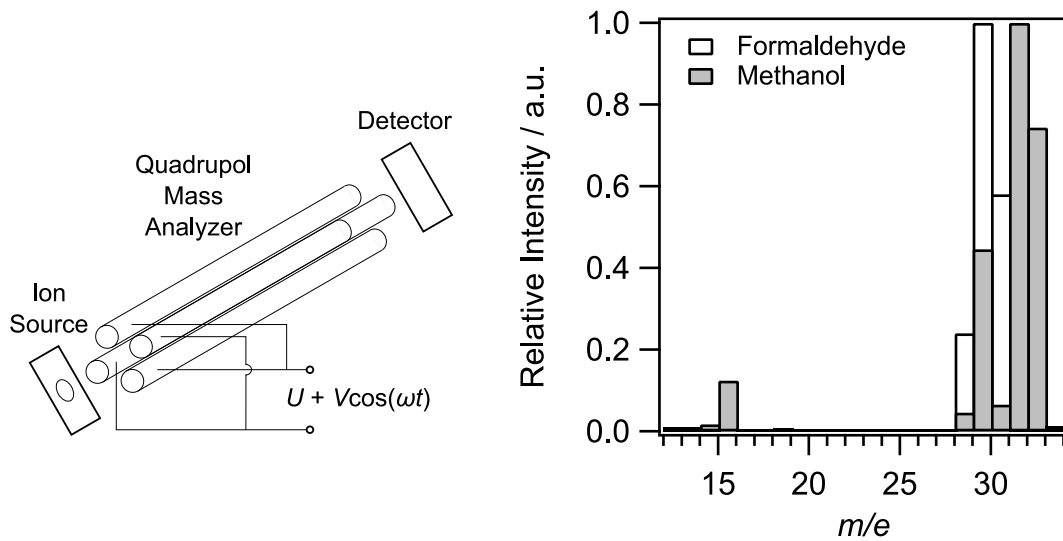


Figure 2.12: Schematic representation of a quadrupole mass spectrometer consisting of an ion source, a quadrupole mass analyzer and a detector (left). Electron ionization fragmentation pattern of methanol and formaldehyde (right). Data taken from [132].

The generated ions are accelerated and focused on the entrance of the analyzer with a well defined energy E_{kin} . A widely used mass analyzer is the linear quadrupole analyzer [133]. The benefits of this analyzer are the high transmission, the small size and the low price. A linear quadrupole analyzer consists of two pairs of cylindrical bar electrodes. They are quadratically arranged and point in the z -direction (the flight direction of the ions after leaving the ion source). The two electrodes of a pair are positioned at the opposite sites of the square arrangement [134]. A schematic drawing can be seen in the left side of figure 2.12. Each two pair electrodes are held at the same potential Φ . Thereby the potential has a constant component U and an alternating component V :

$$\Phi = U \pm V \cos(\omega t) \quad (2.27)$$

The two pairs have the same potential but opposite sign. In this way a time dependent electric quadrupole field is generated. Every ion which enters the analyzer in z -direction experiences an electrical force which changes the ions direction of motion. The equation of motion for an ion i with mass m_i and the charge ze in x - and in y -direction is:

$$\frac{\partial^2 x}{\partial t^2} + \frac{e}{m_i r_0^2} (U + V \cos(\omega t)) x = 0, \quad (2.28)$$

$$\frac{\partial^2 y}{\partial t^2} - \frac{e}{m_i r_0^2} (U + V \cos(\omega t)) y = 0. \quad (2.29)$$

Here r_0 is the shortest distance between the surface of an electrode and the center of the square formed by the four electrodes. The solution of these differential equations is given by the Mathieu-function [135]:

$$\frac{d^2x}{dt^2} + (a_x + 2q_x \cos(2\tau)) x = 0 \quad (2.30)$$

$$\frac{d^2y}{dt^2} + (a_y + 2q_y \cos(2\tau)) y = 0 \quad (2.31)$$

$$\text{with } a_x = -a_y = \frac{4zeU}{m_i r_0^2 \omega^2}, q_x = -q_y = \frac{2zeV}{m_i r_0^2 \omega^2} \text{ and } \tau = \frac{\omega t}{2}.$$

U , V and ω can be chosen in a way that a small range of $\frac{m}{z}$ can pass the analyzer. Therefore the maximum amplitude in x - and y -direction must be smaller than $2r_0$. Ions which can pass the analyzer travel on so-called stable curves. By varying the parameters U , V and ω it is possible to scan for different $\frac{m}{z}$ values. After passing the analyzer, the ions are detected by a faraday-cup (which allows a higher pressure in the experimental chamber) or a single electron multiplier (SEM, which has a higher sensitivity) detector.

In this work the production rates of different catalytic reactions are measured. Also the partial pressure of the reactants are monitored during temperature programmed reaction measurements (TPR). The fragmentation pattern of different molecules can complicate the interpretation of QMS data. An example is the simultaneous detection of methanol and formaldehyde. As can be seen in the right side of figure 2.12, the fragmentation pattern of methanol and formaldehyde overlap. Therefore the mass to charge ratio $\frac{m}{e} = 30$ is chosen to follow the formaldehyde production. The highest formaldehyde signal can be obtained using $\frac{m}{e} = 29$, but due to the fact that methanol has a high signal intensity at $\frac{m}{e} = 29$, the $\frac{m}{e} = 30$ signal is chosen to lower the influence of the methanol partial pressure on the acquired signal.

2.6.1 Temperature programmed reaction

Mechanisms of adsorption, surface reaction and desorption are important information for deciphering the mechanism of a catalytic reaction. Temperature programmed reaction measurements are a useful tool to study the processes of an ongoing reaction. Interpretation of the desorption of reaction products and unreacted reactants can reveal surface reaction mechanisms and kinetics [136]. In this work, the catalyst is exposed to a continuous gas flow of both reactants and heated with a constant heating rate β . The desorbing molecules are detected with a differentially pumped QMS which is connected to the main chamber by a cone with a small hole (6 mm diameter). The catalyst is placed directly in front of the hole, so that only molecules reflected by the catalyst surface can be detected by the QMS.

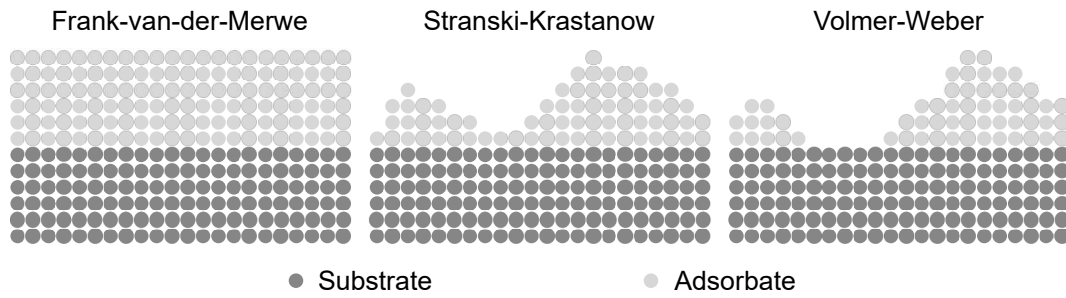


Figure 2.13: Schematic representation of different growth modes observed in thin film growth.

2.7 Thin film growth

In this thesis thin films of vanadium, vanadium oxide and of rhodium are investigated. In all cases thin films were prepared by means of electron beam evaporation (physical vapor deposition) from a high purity metal rod. Oxides are deposited by means of reactive evaporation (metal deposition at elevated sample temperature in an oxygen atmosphere), as described in detail in reference [32], whereas pure metals are deposited in vacuum. The deposition of adatoms from the gas phase onto a surface is a non-equilibrium process and thermodynamic as well as kinetic aspects govern the morphology of the deposited film. A review about the processes occurring on an atomic level in the early stages of film growth can be found in references [137, 138]. Those processes can include adatom diffusion on the surface, formation and diffusion of a stable nucleus, at- and detachment of atoms from a formed overlayer, and three-dimensional (interlayer) diffusion. In the later stages of film growth three different growth modes can be observed, the Frank-van-der-Merwe mode [139–141], the Stranski-Krastanow mode [142], and the Volmer-Weber mode [143]. These three modes are schematically depicted in figure 2.13.

In the Frank-van-der-Merwe growth mode the deposited material covers the substrate surface uniformly in a layer-by-layer fashion. The two other growth modes, the Stranski-Krastanow mode and the Volmer-Weber mode, are characterized by an agglomeration into three-dimensional clusters (often also called crystallites or islands, however, the term islands can also refer to two-dimensional islands obtained for coverages below a monolayer). These crystallites may grow directly on the substrate (Volmer-Weber mode, islands), or form after the completion of a closed, first layer (Stranski-Krastanow mode, layer and islands) [144]. From a thermodynamic perspective the different growth modes can be rationalized by taking the free interface energies γ_i of the interfaces i (substrate - vacuum: sv, substrate - adsorbate: sa, adsorbate - vacuum: av) into account [145]. Crystallite growth (Volmer-Weber growth mode) is thermodynamically favored if the sum of the interface free energies of sa and av are higher than sv:

$$\gamma_{sv} \leq \gamma_{av} + \gamma_{sa}. \quad (2.32)$$

The total free energy can thus be minimized by conserving the interface sv during

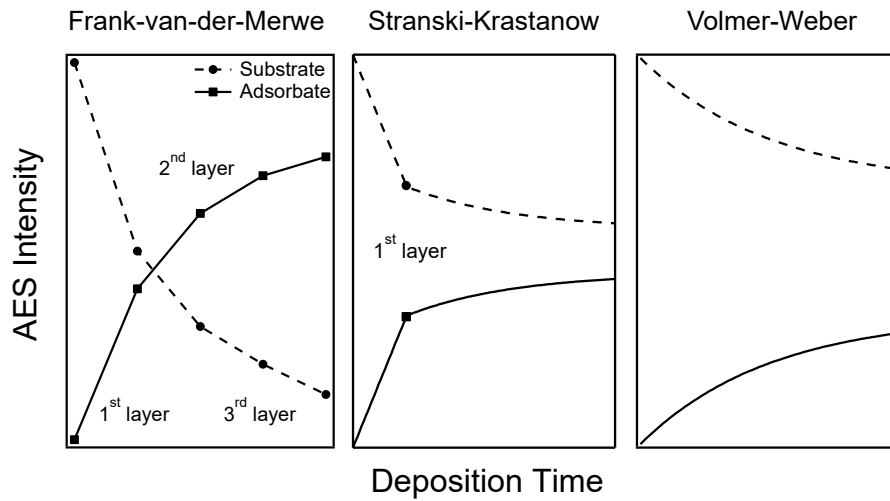


Figure 2.14: Schematic representation of the temporal Auger signal evolution (AS-t plots) during adsorbate exposure for the three different growth modes Frank-van-der-Merwe, Stranski-Krastanow and Volmer-Weber. Figure adapted from reference [148].

the growth process. If in turn the interface free energy γ_{sv} is large compared to γ_{av} and γ_{sa} a Frank-van-der-Merwe growth mode is likely to occur:

$$\gamma_{sv} \geq \gamma_{av} + \gamma_{sa}. \quad (2.33)$$

The Stranski-Krastanow growth mode, however, is an intermediate between the two extremes, the Frank-van-der-Merwe and Volmer-Weber growth mode, and can be explained by the different properties of the adsorbate in the form of a thin film (monolayer) or as a bulk material (multilayer) [145], as well as plastic and elastic strain [146], and entropy [147] effects.

Probably the easiest way to determine which growth mode is encountered in a given system of adsorbate and substrate is direct imaging with atomic resolution like it is possible with STM. However also other direct methods like LEEM and spectroscopic methods like AES and XPS can be used to identify the growth mode. An extensive review about the growth mode identification by means of Auger electron spectroscopy is given in reference [148]. The procedure will be described briefly in the following: Auger signals of the substrate and the adsorbate are recorded as a function of adsorbate exposure. This can be done either in situ during deposition or in a step-wise manner, depending of the geometrical arrangement of the Auger spectrometer and the adsorbate source. The acquired Auger intensities are then plotted against the deposition time to obtain an Auger signal vs. time plot (AS-t plot). For different growth modes different AS-t plots are obtained as schematically in figure 2.14.

The Frank-van-der-Merwe growth mode is characterized by a linear decrease of the substrate Auger signal (linear increase of the adsorbate signal) during formation of a closed layer. Upon completion of a closed layer, the slope of the signal is decreased

and further linear decrease (increase) is observed. This behavior leads to pronounced kinks in the AS-t plot, which mark the deposition time for the completion of each layer. In the Stranski-Krastanow growth mode, initially the same linear increase (decrease) is observed for the completion of the first closed layer. Subsequently the signal decrease (increase) stagnates and a plateau is found in the AS-t plot, indicating the formation of crystallites on the first adsorbate layer. In the Volmer-Weber mode no linear decrease (increase) of the substrate (adsorbate) signal can be observed. Instead a non-linear, comparably slow signal change is observed, also resulting in a plateau in the AS-t plot.

The growth mode is a function of the experimental parameters, most important of the temperature. At low temperature, the adatom mobility can be very low, leading to metastable growth modes, from which two are mentioned in reference [148], the simultaneous-multilayer growth and the monolayer plus simultaneous-multilayer growth. The simultaneous-multilayer (very low adatom diffusion) is a special case of the Frank-van-der-Merwe growth mode (very high adatom mobility), where also closed multilayers are formed, but not in a consecutive manner. The monolayer plus simultaneous-multilayer growth mode is the equivalent for Stranski-Krastanow growth. The complicated classification of a thin film growth experiment into one of the growth modes can be considerably reduced by auxiliary methods (like LEED, LEEM, STM etc.), which deliver complementary information to the AS-t plots.

2.8 The single crystal surfaces used in this thesis

In the experiments presented in this thesis rhodium and platinum single crystal surfaces with a (111), (110) and (100) orientation have been used. In the following the relevant properties of the Rh(111), Rh(110), Pt(111), and Pt(110) surfaces mentioned in literature are briefly described.

2.8.1 The Rh(111) surface

Rhodium is a transition metal of the platinum-group. Typical for the platinum-group, rhodium shows a high variety of oxidation numbers reaching from -3 to +6. The prevalent application of rhodium is the use as an alloy additive and in heterogeneous catalysis, e. g. for NO removal in environmental catalysis, or for NO production in the so-called Ostwald process. As a model system the low indexed single crystal surfaces of rhodium play an important role in fundamental catalysis research.

Rhodium crystallizes in the face centered cubic structure with a lattice parameter of 3.8034 Å [149]. The (111) orientated surface has a hexagonal lattice, with the parameters $\mathbf{a}_1 = \mathbf{a}_2 = 2.6894 \text{ \AA}$. The surface density is one atom times $4 \cdot 3^{-\frac{1}{2}} \cdot \mathbf{a}^{-2}$, which is approximately $1.59 \cdot 10^{15} \text{ atoms/cm}^2$. No reconstructions are observed for the clean surface, but in order to reduce the free surface energy, a relaxation of the first four atomic layers is reported in the literature: $d_{1/2} = 2.16 \pm 0.02 \text{ \AA}$ (the distance d between the first and the second surface layer), $d_{2/3} = 2.16 \pm 0.04 \text{ \AA}$ and $d_{3/4} = 2.23 \pm 0.04 \text{ \AA}$, with the bulk value being 2.19 Å [150]. The experimental and theoretical obtained work

function of the clean Rh(111) surface is 5.3 eV and 5.23 eV, respectively [151, 152].

The interaction of oxygen with Rh(111)

At low temperature around 100 K, oxygen adsorbs disordered on the Rh(111) surface. An irreversible ordering transition was observed upon annealing to 150 K, resulting in a (2×2) LEED pattern. The (2×2) undergoes subsequent disordering transitions upon further annealing to 280 K and 400 K, respectively [153]. Later studies revealed that the observed (2×2) LEED pattern results from three rotational domains of a (2×1) -O phase on Rh(111) [154]. The (2×1) -O is not the only oxygen phase with a (2×2) LEED pattern, as was revealed subsequently by LEED experiments: during oxygen adsorption at 273 K first a (2×2) -O structure of an ideal coverage of 0.25 ML is formed, which transformed to the mentioned (2×1) -O structure of 0.5 ML ideal coverage upon further oxygen exposure [155]. Under HV and UHV conditions, the (2×1) -O and (2×2) -O phases are the only oxygen phases that can be prepared using molecular oxygen. However, further high coverage phases become accessible when applying more oxidizing conditions: a $(2\sqrt{3} \times 2\sqrt{3})R30^\circ$ -O phase (0.66 ML ideal coverage) is obtained after molecular oxygen exposure at 400 K in 1×10^{-3} mbar (together with a Rh surface oxide at step edges) [156]. With atomic oxygen also a (1×1) -O phase of coverage 1 ML can be prepared [157]. The existence of a dense (1×1) -O phase on Rh(111) has been backed by DFT calculations [152]. For coverages close to 1 ML, also the occupation of subsurface sites by oxygen is reported [158, 159]. Temperature programmed desorption (TPD) measurements performed after adsorption of up to 13 Langmuir (L) at 120 K revealed three desorption peaks: molecular oxygen desorbs at 150 K, whereas chemisorbed oxygen exhibits two desorption peaks around 840 - 860 K and 1090 - 1325 K, depending on the oxygen exposure [160]. The initial sticking coefficient of oxygen on Rh(111) has been determined to 0.2 at 100 K with AES [153], and around 0.3 to 0.8 at 300 K (depending on the oxygen beam energy) in molecular beam experiments [161].

The formation of an (8×8) coincidence LEED pattern was observed after oxidation in 1.3 mbar oxygen at 975 K in an early study, and was attributed to the epitaxial growth of a corundum $\text{Rh}_2\text{O}_3(0001)$ surface oxide. The rhodium oxide could be reduced to a (1×1) -Rh surface again by heating to 800 K in vacuum or 1075 K in 1.3×10^{-5} mbar oxygen [154]. Further investigations in a combined STM, high resolution XPS, surface X-ray diffraction and DFT study revealed the existence of a metastable hexagonal RhO_2 surface oxide trilayer (O-Rh-O), that forms and kinetically hinders the formation of a bulk Rh_2O_3 in an intermediate pressure range up to 0.5 bar [162]. A misfit between the RhO_2 surface oxide lattice and Rh(111) causes a Moiré pattern, which can be described as a (8×8) surface oxide on a (9×9) Rh(111) unit cell. However, in DFT calculations a (7×7) surface oxide on a (8×8) Rh(111) unit cell was found to be slightly more stable [162]. In the same study, the existence of a thick corundum $\text{Rh}_2\text{O}_3(0001)$ was confirmed for a pressure above 10^{-3} mbar (800 K). Crucial for the formation of a Rh surface oxide is the penetration of oxygen into the Rh subsurface region, which is energetically favored at step edges compared to terraces.

In summary, under UHV and HV conditions molecular adsorbed oxygen forms a

(2×2) and a (2×1) phase on Rh(111). Higher oxygen coverages can be realized by adsorption of molecular oxygen in the 10^{-3} mbar range or of atomic oxygen, resulting in $(2\sqrt{3} \times 2\sqrt{3})R30^\circ$ or (1×1) phases, respectively. Also in the 10^{-3} mbar range at elevated temperature, self-limited growth of a metastable (8×8) Rh₂O₃ surface oxide on a (9×9) Rh(111) unit cell takes places, which kinetically hinders the formation of a thick Rh₂O₃(0001) oxide. The Rh₂O₃ oxide, characterized by a (8×8) LEED pattern, can be prepared at a pressure of 1 mbar or higher at a temperature around 1000 K. Details on the oxygen induced Rh 3d core level shifts, useful for the interpretation of XPS data, can be found in reference [163].

2.8.2 The Rh(110) surface

The (110) orientated surface has a rectangular unit cell with the parameters $\mathbf{a}_1 = 2.6894 \text{ \AA}$ and $\mathbf{a}_2 = 3.8034 \text{ \AA}$. The surface density is one atom times $\sqrt{2} \cdot \mathbf{a}_2^{-2}$, which is approximately $9.78 \cdot 10^{14}$ atoms/cm². For the clean surface no reconstructions are observed but, in order to reduce the free surface energy, an oscillatory relaxation of the first four atomic layers is reported: the distance between the first and the second layer shorten by $\Delta d_{1/2} = -5.4\%$, followed by $\Delta d_{2/3} = +0.9\%$ and $\Delta d_{3/4} = -0.7\%$. The work function of the clean Rh(110) surface is 4.85 eV [164]. A schematic representation of the Rh(110) surface and the oxygen induced reconstructions can be found in figure 2.15.

The interaction of oxygen with Rh(110)

Upon oxygen adsorption on a Rh(110) surface, a variety of different surface structures can form, depending on temperature and the oxygen coverage. Between 125 K and 300 K a (2×1)p2mg structure with coverages from 0.4 to 1 ML is formed. This structure turns into a (2×2)p2mg of 0.5 ML ideal coverage upon heating to 470 K [166]. Annealing or adsorption at higher temperatures results in the formation of a series of c(2×2n) structures, with $n = 3, 4, 5$ in an activated process [167]. The interaction of adsorbed oxygen with the Rh(110) surface results in an (1×n) missing-row reconstruction ($n = 2, 3, 4, 5$). The term missing row indicates that every n^{th} $[1\bar{1}0]$ row is missing. This reconstruction is favored since energetically more stable (111) orientated surfaces are formed. –Rh–O– chains along the $[1\bar{1}0]$ direction are the structural units [165]. For an increasing oxygen coverage the lattice spacing of the metal-oxygen chains, as well as their density increases, as can be seen in figure 2.15. Apart from molecular adsorption at low temperatures, temperature programmed desorption spectroscopy (TPD) revealed at least five high temperature desorption peaks of chemisorbed oxygen species at 780 K, 797 K, 835 K, 909 K, 1095 K, and 1150 K with estimated activation energies between 205 and 294 kJmol⁻¹ [168]. This is of particular interest since the maximum temperature of the experiments conducted in this work is around 1030 K. The initial sticking coefficient of oxygen on Rh(110) was determined to 0.6 to 0.7 for 310 K and 670 K, respectively, in a molecular beam experiment [168].

Besides the formation of ordered adsorbate layers also surface oxidation of Rh(110) is known for oxygen pressures in the 10^{-4} mbar range and temperatures of 750 K, as well as

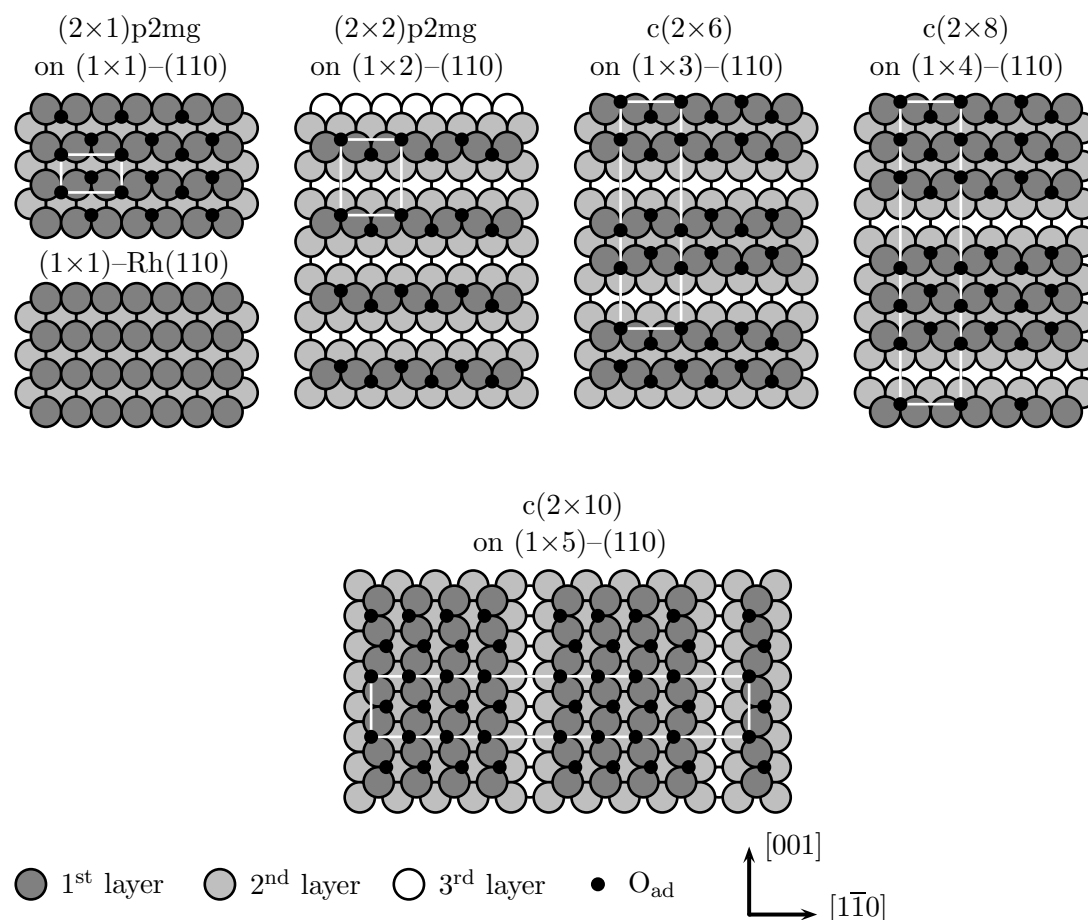


Figure 2.15: Schematic representation of the clean Rh(110) surface and of the oxygen induced $(1 \times n)$ reconstructions. Figure adapted from [165].

for oxide growth by adsorption of atomic oxygen. Oxidation of Rh(110) proceeds laterally nonuniform for oxidation with molecular oxygen. In the case of atomic oxygen, instead a homogeneous oxide film is formed. This can be explained by atomic defects on the Rh surface which favor the dissociative adsorption of oxygen, thus acting as nucleation centers for oxide growth. The rhodium surface oxide exhibits a $c(2 \times 4)$ structure and a composition close to the bulk oxide of rutile type RhO_2 . In the case of molecular oxygen also the formation of an oxygen poor phase of composition close to the corundum bulk oxide Rh_2O_3 takes place. Oxygen rich and oxygen deficient areas exhibit the same $c(2 \times 4)$ structure. The Rh surface oxide is reactive to hydrogen even if the dissociative adsorption of hydrogen is hindered on the O covered surface [169].

2.8.3 Interaction of CO with Rh(110)

Since methanol decomposition takes place on the Rh(110) surface, resulting in a CO coverage during catalytic methanol oxidation, the interaction of adsorbed CO with a Rh(110) surface is described briefly. On (1×1)-Rh(110) four different phases are observed for increasing CO coverage during adsorption at 125 K [170]. For a coverage between 0.33 ML and 0.55 ML a c(2×2) phase is observed, which turns into a (2×1)p2mg of an ideal coverage of 1 ML upon further CO exposure. In an earlier study, the occurrence of a c(2×2) has been attributed to adsorbed carbon (possibly forming a surface carbide), since it was observed after prolonged exposure of adsorbed CO to the electron beam of an Auger spectrometer [171]. CO adsorbs preferentially at on-top sites as concluded from O 1s core level photoemission spectroscopy. For a coverage near the saturation coverage, a bridging tilted adsorption geometry is proposed leading to the formation of *zig-zag* chains of CO. On the (1×2)-reconstructed surface (2×2), c(2×4) and (2×2)p2mg phases are formed for increasing CO coverages. For all these structures simultaneous occupation of on-top and bridging sites is reported [170]. In the saturation TPD spectrum of CO on (1×1)-Rh(110) three peaks occur at 390 K, 440 K and 490 K. For the (1×2)-Rh(110) surface the peaks are slightly shifted to 400 K and 485 K, one peak has vanished. In order to compare both TPD spectra one has to consider that the metastable (1×2)-reconstructed surface transforms to a (1×1) above 480 K, making a clear attribution of the high temperature peak difficult [172].

2.8.4 The Pt(111) surface

The noble metal platinum is widely used in catalysis (for example in the automotive exhaust gas catalyst), and has a prominent role in fundamental catalysis research, since CO oxidation on platinum is probably the most studied model system/reaction in heterogeneous catalysis. Platinum can have oxidation numbers reaching from -2 to +6 in its compounds.

Platinum crystallizes in the face centered cubic structure with a lattice parameter of $3.923 \pm 0.0006 \text{ \AA}$ [173]. The (111) orientated surface has a hexagonal lattice with the parameters $\mathbf{a}_1 = \mathbf{a}_2 = 2.774 \text{ \AA}$. The surface density is one atom times $4 \cdot 3^{-\frac{1}{2}} \cdot \mathbf{a}^{-2}$, which is approximately $1.49 \cdot 10^{15} \text{ atoms/cm}^2$. No reconstructions are observed for the clean surface up to 1330 K [174], but a relaxation of the first three atomic layers is reported: $d_{1/2} = 2.29 \pm 0.01 \text{ \AA}$, and $d_{2/3} = 2.27 \pm 0.03 \text{ \AA}$, with the bulk value being 2.26 \AA [175]. Above 1330 K the surface undergoes a commensurate-incommensurate transition. However, the maximum temperature reached in the experiments presented in this thesis is with 1030 K considerably lower. The experimental obtained work function of the clean Pt(111) surface is $6.1 \pm 0.06 \text{ eV}$ [176].

The interaction of oxygen with Pt(111)

Molecular oxygen forms at around 100 K a $(\frac{3}{2} \times \frac{3}{2})R15^\circ$ of 0.44 ML saturation coverage. Upon annealing to room temperature partial desorption of molecular oxygen (desorption

peak at around 160 K) and partial dissociation of adsorbed oxygen leads to the formation of a (2×2) -O phase of 0.25 ML ideal coverage. Chemisorbed oxygen often shows two desorption peaks in the TDS spectrum, a broad peak located between 600 and 1100 K with a maximum at about 800 K, and a second one above 1250 K [177]. The second (high temperature) desorption peak is associated with contamination (e. g. silicon) and does not represent a pure oxygen phase [178]. The initial oxygen sticking coefficient at room temperature is measured to 0.038 [179], and thus is markedly lower by at least one order of magnitude than the value of Rh(111).

2.8.5 The Pt(100) surface

The lattice parameters of the (100) orientated surface (square unit cell) have a value of $a_1 = a_2 = 3.923 \text{ \AA}$. The surface density is two atoms per a^2 , which is approximately $1.29 \cdot 10^{15} \text{ atoms/cm}^2$. Under UHV conditions, the (1×1) bulk terminated surface is not stable and a reconstruction with a hexagonal or rotated hexagonal lattice (0.7°) is observed [180]. The reconstruction can be lifted by adsorbing CO, resulting in a (1×1) LEED pattern. The work function of the hexagonal rotated Pt(100) surface is 5.75 eV [181].

2.8.6 The interaction of vanadium with Rh(111), Rh(110) and Pt(111)

Vanadium oxide films are supported on Rh(111), Rh(110) and Pt(111) in the experiments presented in this thesis. Vanadium oxide forms a large number of ultrathin oxide layers on Rh(111), which are reported in literature [53, 55, 182, 183]. In contrast, only one study on VO_x oxide structures is reported for Pt(111) [184], and for vanadium oxide structures on Rh(110) only a study conducted during my master and doctoral thesis exists [185].

Also alloys of vanadium with the Rh(111) and Rh(110) surfaces have been investigated, due to the industrial relevance of bimetallic catalysts [30]. Vanadium deposited on Rh(111) forms a (2×2) subsurface alloy in the coverage range between 0.4 to 2.5 ML, when heated above 823 K [186]. Oxygen adsorption at 300 K and annealing at elevated temperature resulted in the formation of a vanadium surface oxide, which means that oxygen can stabilize V on the Rh(111) surface, thus preventing surface alloying [186]. Furthermore catalytic activity towards the oxidative dehydrogenation of methanol has been reported for Rh(111)/V subsurface alloys [187]. Also for the system V/Rh(110) the formation of a near-surface alloy above 823 K, characterized by a (2×1) LEED pattern, is reported in literature [188]. Annealing at higher temperature (1023 K) results in the diffusion of V into deeper layers of the Rh bulk, stabilizing a (1×2) reconstructed Rh(110) surface.

2.9 Basics of nonlinear dynamics in reaction diffusion systems

A detailed description of nonlinear dynamics can be found for example in the textbooks [189,190], the application to chemical systems is reviewed in [191]. A brief introduction, on which this section is based together with reference [189], is given in [192].

Chemical waves in surface reactions can be described as wave patterns in a two-dimensional reaction-diffusion-system [193]. The behavior of such a system is described by the theory of nonlinear dynamics. The state of a dynamic system is characterized by its components, which vary in time [192]. In a chemical reaction-diffusion-system these components are the different chemical species, represented by their concentrations $\mathbf{c} = c_1, c_2, \dots, c_i$. Parameters like the pressure or the temperature are expressed by the parameter vector $\boldsymbol{\mu}$. A space with the coordinates \mathbf{c} is called phase space and the state of a system at the time t is represented by a point in the phase space. A possible state of a system is represented as a unique point in phase space.

In a dynamic system \mathbf{c} is not stationary and the point $\mathbf{c}(t)$ travels with the velocity $\dot{\mathbf{c}}$ on so-called trajectories in phase space. In a chemical reaction this movement in phase space is given by the rate equation:

$$\frac{\partial \mathbf{c}}{\partial t} = \dot{\mathbf{c}} = \mathbf{f}(\mathbf{c}, \boldsymbol{\mu}). \quad (2.34)$$

The vector \mathbf{f} , which is a function of the concentration itself and of the parameter vector $\boldsymbol{\mu}$, describes the temporal development of the concentration vector \mathbf{c} . Points in phase space where the velocity $\dot{\mathbf{c}}$ is zero are called fixed points. A stable fixed point is called “attractor”, an unstable fixed point is referred to as “repeller”. A fixed point or limit cycle is stable when all neighboring trajectories approach it for $t \rightarrow \infty$, and unstable if all neighboring trajectories approach it for $t \rightarrow -\infty$. A third case exists if a trajectory approaches a fixed point from one side for $t \rightarrow \infty$ and for $t \rightarrow -\infty$ from the other side. This case is called a saddle node. The position of fixed points or limit cycles in phase space can be a function of the parameters $\boldsymbol{\mu}$. If a parameter change leads to a qualitative change of the behavior of a system, it is called a bifurcation. The influence of parameter changes on the behavior of a system can be mapped out in a bifurcation diagram.

A simple example for a parameter-induced change of fixed points is the saddle node bifurcation. In an one-component system with the bifurcation parameter μ , \dot{c} may be given as:

$$\dot{c} = \mu - c^2 \equiv f(c, \mu), \quad (2.35)$$

and the fixed points c^* can be calculated as:

$$c^* = \pm\sqrt{\mu}. \quad (2.36)$$

For $\mu < 0$ there is no fixed point, for $\mu = 0$ there is one fixed point and for $\mu > 0$ two fixed points exist [194].

Also a classification of the global behavior of a dynamic system exists. For a two component system, which is dependent on two variables, already four different global behaviors can be observed: stationary, bistable, excitable and oscillatory behavior. In the FitzHugh-Nagumo model, a two-variable system is described by the equations:

$$\dot{c}_1 = \mathbf{f}(c_1, c_2) + D_{c_1} \nabla^2 c_1, \quad \dot{c}_2 = \mathbf{g}(c_1, c_2) + D_{c_2} \nabla^2 c_2, \quad (2.37)$$

where f is a cubic function with respect to c_1 , and g is a linear function with respect to c_2 [195]:

$$\mathbf{f}(c_1, c_2) = \frac{1}{\epsilon} \left(c_1 - \frac{c_1^3}{3} - c_2 \right), \quad (2.38)$$

$$\mathbf{g}(c_1, c_2) = c_1 + b - ac_2. \quad (2.39)$$

In this model ϵ , a and b are parameters, c_1 is called the activator and c_2 the inhibitor, i. e. one has two species with an antagonistic effect on the reaction: the activator species accelerates the activator production, while the inhibitor slows down the activator production. In addition to the reaction terms also diffusion is taken into account by diffusion terms of Fickian type $D_{c_i} \nabla^2 c_i$. Here D_{c_i} is the diffusion constant of species i and ∇^2 is the Laplace operator. In order to understand the global system behavior one has to have a look at the nullclines in phase space. A nullcline is a line in phase space for which either $f = 0$ or $g = 0$. The intersection of the two nullclines is a fixed point since $\dot{\mathbf{c}} = 0$. Figure 2.16 shows four solutions of the FitzHugh-Nagumo equations.

In a bistable system, two stationary states exist, which are stable against small perturbations. A transition between the stationary states can be stimulated by a large parameter change. The transition between the two stationary states occurs via reaction fronts. Figure 2.17a schematically shows the dependence of the front velocity v as a function of the bifurcation parameter (in this example the oxygen pressure), a bifurcation diagram. Only stable solutions exist (solid lines); for a low oxygen pressure reduction fronts are obtained ($v < 0$). An oxygen pressure increase can lead to the formation of oxidation fronts ($v > 0$). The point at which both front velocities are equal ($v = 0$) is the equistability point.

A parameter range of so-called ‘‘double metastability’’ may exist in bistable systems adjacent to the equistability point. Double metastability refers to a parameter range in which two stable front solutions coexist, resulting in a behavior similar to an excitable system [197, 198]. The bifurcation diagram of a bistable system with a sub-region of double metastability is shown in figure 2.17b. The stable solutions of the front velocity are shown as solid lines, whereas the unstable solution is shown as a dashed line. The turning points of the front velocity define the region of double metastability, in which reduction ($v < 0$) and oxidation ($v > 0$) fronts coexist. The main difference between double metastability and excitability is that in a double metastable system, no fixed distance between the fore- and backfront of a pulse exists, and that the formed wave pattern are therefore more irregular.

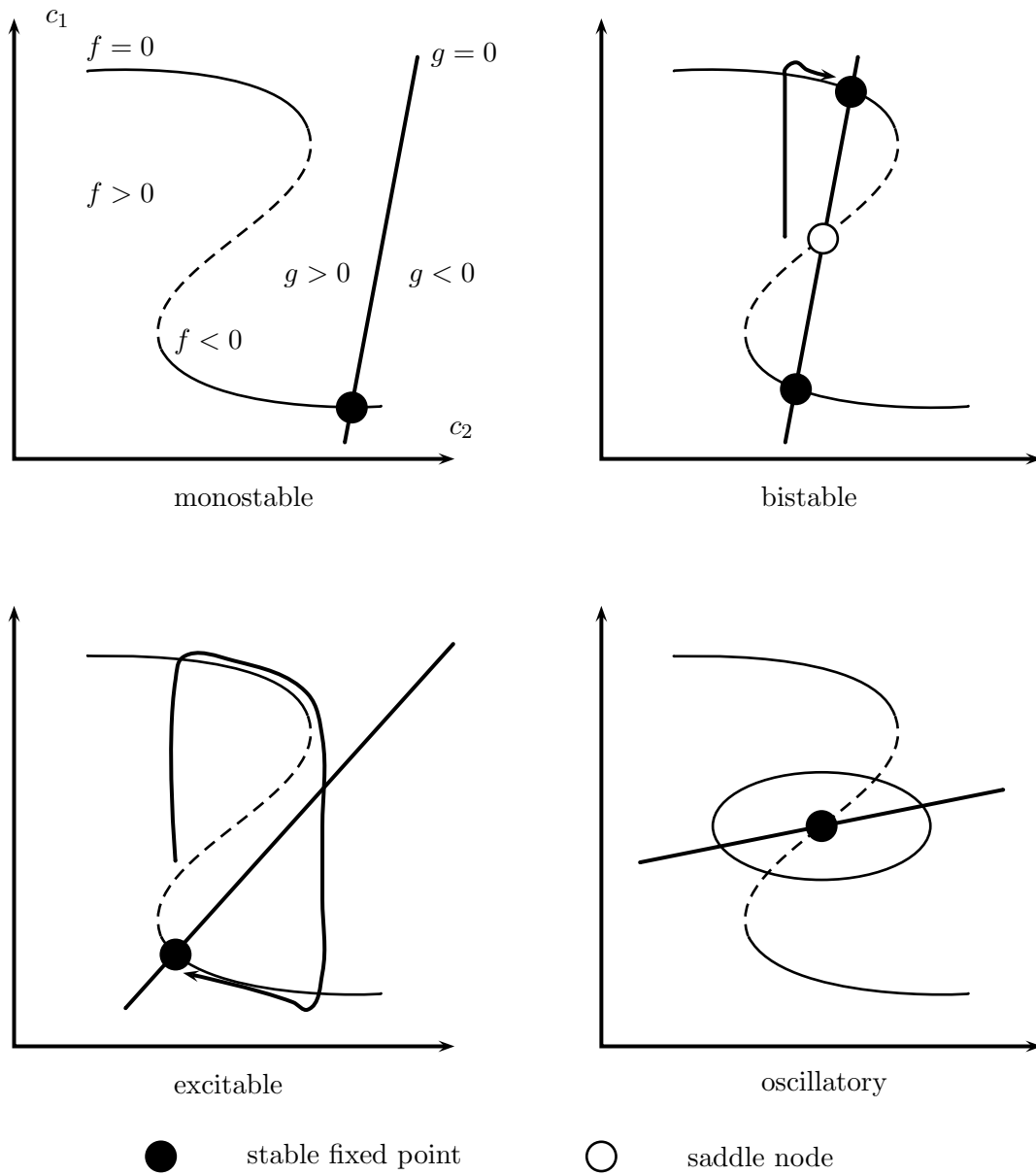


Figure 2.16: Four solutions of an activator-inhibitor model of FitzHugh-Nagumo type: a monostable, bistable, excitable or oscillatory system. The stationary points are given by the intersections of the nullclines of f and g . Figure adapted from [195]

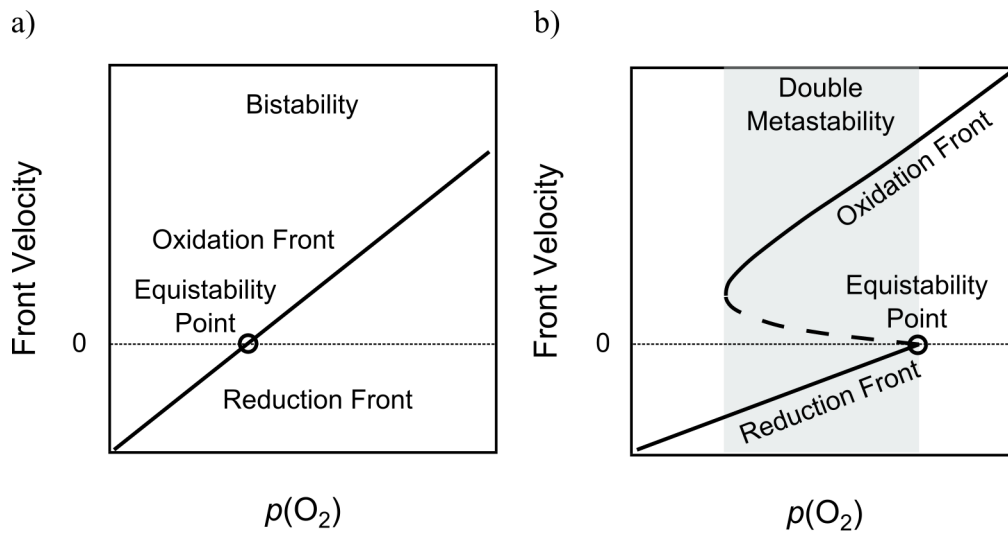


Figure 2.17: Front velocity in bistable systems with and without a double metastable regime. a) The front velocity v of a reduction front ($v < 0$) and an oxidation front ($v > 0$) is shown schematically as a function of the bifurcation parameter $p(O_2)$. The point at which the front velocity is zero is called the equistability point. Only stable solutions (solid line) exist. b) In a bistable system with a parameter range of double metastability stable (solid line) and unstable (dashed line) solutions exist. In a certain parameter range reduction and oxidation fronts are both stable simultaneously. This range is the double metastable regime. The figure is adapted from reference [196, figure 2].

In an excitable system, only one stationary state exists, which is stable against small perturbations. Excitability is characterized by a specific sequence of transitions in a response to large enough perturbations. The excitation is followed by a recovery into the stationary state. The difference between transitions in bistable and excitable systems is, that an excitable system restores its single stable state after wave propagation, i. e. after excitation and recovery the system is back in its initial state from where it can be excited again. In a bistable system instead, a front leads to the second stable state. Consequently, in a bistable system, a parameter change is required to initiate a front and this front only propagates one time through the system. In an excitable system a sequence of pulses (a pulse train) – usually in form of a rotating spiral wave or a target pattern – can be observed, provided that a trigger center exists, which periodically excites pulses. An oscillatory system undergoes periodic limit cycle oscillations and spiral waves and target pattern are seen, similar to an excitable system. In contrast to an excitable system, an oscillatory system is characterized by its own frequency [195]. Finally, if the diffusion of the inhibitor is much faster than the diffusion of the activator, a stationary concentration pattern may result, which also is called a “Turing pattern” (not shown in figure 2.16) [199].

Chapter 3

Experimental setup

Abstract The results described in this thesis were obtained in several different ultra-high vacuum systems. In this chapter, a detailed description of the used systems is given. The three sections of this chapter deal with the sample cleaning procedures, as well as the experimental setups used in the vanadium oxide projects. A description of the experimental setups used in the surface acoustic waves project can be found in chapter 8.3.

Most of the experiments are conducted at the Institute of Physical Chemistry and Electrochemistry at the Leibniz University Hannover. An UHV system equipped with a PEEM, a QMS, an AES and a four grid LEED optics is used. Since PEEM provides no structural and no or only indirect chemical information other microscopes have been applied to obtain complementary information. Imaging with chemical contrast is possible with the scanning photoemission electron microscope (SPEM) and the spectroscopic low-energy electron microscope (SPELEEM) at the electron storage ring Elettra located in Trieste, Italy. The SPELEEM microscope additionally provides diffraction contrast and the possibility to perform spatially resolved diffraction measurements (μ LEED). Both microscopes have in common, that they can only be operated up to a pressure in the low 10^{-6} mbar range. In order to image reaction dynamics at a pressure up to the 10^{-4} mbar range with diffraction contrast, and to perform in situ μ LEED measurements, a LEEM microscope located at the University of Bremen is used. The accessible pressure range is further increased into the 10^{-2} mbar range by using a newly developed near ambient pressure LEEM (NAP-LEEM) at Elmitec Elektronenmikroskopie GmbH at Clausthal. Finally the SPELEEM microscope at the electron storage ring ALBA in Barcelona is used to investigate the influence of surface acoustic waves (SAW) on catalytic surfaces. It is the only LEEM microscope at a synchrotron light source, which provides the infrastructure to apply radio frequency necessary for the excitation of SAW.

Table 3.1 summarized the applied methods, their location, and the systems which are investigated with them.

3.1 Sample preparation

All single crystals used in this thesis have been cleaned by repeated cycles of Ar^+ ion sputtering and oxygen treatment at elevated temperatures, followed by a final flash annealing step in order to desorb oxygen and to order the surface. The argon ion bombardment has been conducted at normal incidence and with varying ion energies, depending on the type of surface and the stage in the cleaning process. The following single crystals are used in this thesis, in parenthesis is the number of different samples: Rh(111) (4), Rh(110) (2), Pt(111) (1) and Pt(110) (1).

Single crystals that have been freshly polished are initially sputtered for two to five hours at an ion energy of 2 kV and at a sample temperature of 770 K, followed by a two to four hour oxygen treatment at 770 K in an oxygen pressure of 1×10^{-6} mbar. In all cleaning procedures only molecular oxygen is used as oxidizing agent.

After the initial cleaning of freshly polished samples, at least ten cycles of argon ion sputtering (1 kV, 2 - 5 μA , 5 to 9×10^{-5} mbar Ar, 20 min) and oxygen treatment at 1×10^{-6} mbar and 820 - 1020 K are applied. Each cleaning step is finished by a final flash annealing to 1100 K prior to an experiment. As an indication for a clean surface, a combined AES and LEED analysis is used. In case of Rh(111), the formation of a (2×2) LEED pattern upon exposure to an oxygen atmosphere in the 10^{-8} mbar range at room temperature [153], together with the absence of additional signals in the Auger spectrum, is taken as a sign for an atomically flat and clean surface. In the case of the Rh(110) surface, a series of oxygen induced reconstructions resulting in a $c(2 \times 8)$ LEED pattern [165,166], which can be observed in 10^{-8} mbar oxygen around 400 K, is taken as evidence for a clean surface.

3.2 Experiments with vanadium oxide layers

The behavior of ultra-thin vanadium oxide films is studied on the (111) surfaces of rhodium and platinum single crystals and on the (110) surface of a rhodium single crystal. Sub-monolayer quantities of vanadium are deposited by means of electron beam bombardment from a high purity rod.

3.2.1 Thin Film Preparation

Transition metal oxides deposited on noble metal surfaces show a wealth of different structures, especially in the two-dimensional limit of zero to five monolayer thickness [32]. Different synthesis methods have been developed in the past two decades, from which the so-called reactive evaporation is applied in this thesis. In the reactive deposition, a transition metal is evaporated in an atmosphere of oxygen onto a metal surface, which is kept at an elevated temperature.

Table 3.1: Instruments used in this thesis.

Instrument	Location	Properties	p / mbar	Application
PEEM (Photoemission Electron Microscopy)	Leibniz University Hannover	Work function contrast; LEED, AES and QMS available	$\leq 5 \times 10^{-4}$	VO _x /Rh(111) VO _x /Rh(110) VO _x /Pt(111) Rh/Pt(110) Rh/poly-Pt
LEEM (Low-Energy Electron Microscopy)	University of Bremen	Structural, work function, and topographical contrast, μ LEED	$\leq 2 \times 10^{-4}$	VO _x /Rh(111) VO _x /Rh(110)
NAP-LEEM (Near Ambient Pressure LEEM)	Elmitec (Clausthal)	Structural, work function, and topographical contrast	$\leq 10^{-1}$	VO _x /Rh(111)
SPELEEM (Spectroscopic LEEM)	Nanospectroscopy (Elettra, Trieste)	Chemical (XPEEM), structural, work function, and topographical contrast; μ XPS and μ LEED	$\leq 2 \times 10^{-6}$	VO _x /Rh(111) VO _x /Rh(110)
SPEM (Scanning Photoemission Electron Microscopy)	ESCA-Microscopy (Elettra, Trieste)	Chemical and topographical contrast, μ XPS, LEED and AES available	$\leq 2 \times 10^{-6}$	VO _x /Rh(111)
SPELEEM	CIRCE (ALBA, Barcelona)	Chemical, structural, work function, and topographical contrast, μ XPS and μ LEED, SAW excitation	$\leq 2 \times 10^{-6}$	Rh/poly-Pt

In the PEEM, LEEM, SPELEEM, and SPEM experiments on vanadium oxide supported on Rh(111) and Rh(110), ultra-thin oxide layers are grown by means of electron bombardment of a high purity V rod (Goodfellow) in an atmosphere of 2×10^{-7} mbar oxygen and a substrate temperature of 670 K. Prior and after the deposition of vanadium, the substrate is kept at 670 K and 2×10^{-7} mbar oxygen for ten minutes. In this way it is ensured, that vanadium is deposited onto an oxygen covered surface, which is free of carbon.

Vanadium is evaporated from a standard electron beam evaporator purchased from Tectra GmbH during the PEEM, LEEM and NAP-LEEM experiments. The evaporation is conducted at a filament current of 6.7 A and a bombardment voltage of 1.5 kV. These settings yielded an emission current of 15 mA. Since the evaporator is not equipped with a flux monitor, evaporation is performed under constant emission current by keeping the bombardment voltage constant and varying the filament current. From a combined LEED and AES calibration curve, which is described in detail in chapter 5.1, a deposition rate of 0.1 MLE is determined in Hannover. It turned out, that the deposition rate is constant enough to obtain reproducible results, as long as the emission current is precisely adjusted to 15 mA. A comparable procedure is applied in the SPEM experiments conducted at the ESCA microscopy beamline at Elettra. Here a filament current of 2.1 A and a bombardment voltage of 960 V is used, resulting in a flux of 12 nA. At the Nanospectroscopy Beamline, an electron beam evaporator equipped with a flux monitor (Focus GmbH) is available. There the V deposition rate is stabilized by the evaporator control unit, resulting in a flux of 20 nA with a filament current of 1.9 A and a bombardment voltage of 820 V.

In the LEEM and SPELEEM experiments, the growth of vanadium oxide could be followed with LEED. In the PEEM and SPEM experiments, vanadium oxide is deposited and a characterization with LEED and AES after the sample has been cooled down in the continuous oxygen flow until a temperature of 470 K is reached. Because of the geometry of the high pressure cell of the prototype NAP-LEEM instrument, it is not possible to deposit vanadium in the microscopes main chamber. Instead, the electron beam evaporator is mounted in the preparation chamber, where heating is not possible. Consequently, vanadium is deposited at room temperature onto the Rh(111) surface. Oxidation of the vanadium film occurred under the conditions of catalytic methanol oxidation applied subsequently. The process, in which a (transition) metal is deposited onto the metallic substrate and oxidized after the deposition is completed, is called post oxidation [32].

3.2.2 Photoemission Electron Microscopy (Hannover)

The photoemission electron microscope at the Institute of Physical Chemistry and Electrochemistry at the Leibniz University Hannover is installed in a standard UHV chamber of about 100 L volume. UHV is generated by three turbo molecular pumps and a titanium sublimation pump. Besides PEEM, also AES, a differentially pumped QMS and a LEED optics is available. The total pressure inside the vacuum system is measured with a Leybold Haereus ionization gauge (Ionivac IM 510). All pressures stated in this

thesis are given as the direct instrument readout and no correction factors are taken into account, unless something else is stated.

The spatiotemporal development of the sample surface can be followed in situ during a catalytic reaction with a differentially pumped PEEM, developed by Engel et al. at the Fritz-Haber-Institute, Berlin [106]. The differential pumping stage located in the image intensifier unit allows, in principle, the operation of the microscope up to a pressure of 1×10^{-3} mbar. However, in the used UHV system, the maximum pressure at which the PEEM can be operated is limited by the main turbo molecular pump (Leybold Haereus, 340 L s^{-1}) to about 5×10^{-4} mbar. Photoelectrons are emitted from the sample surface by photons ejected from a deuterium discharge lamp (Haereus D 200 F). The lamp has a broad spectral distribution around 6 eV, and the sample is illuminated under grazing incidence through a sapphire window with a low absorption coefficient for ultraviolet light. The lateral resolution of the microscope is about 0.1 to 1 μm , and the temporal resolution is limited by the integration time needed for sufficient image intensity. In a typical PEEM experiment the integration time is varied between 100 and 500 ms. The PEEM images are digitized by two different cameras, a CCD system (Basler acA2040-25gm) and a CMOS system (Hamamatsu Orca Spark). Both cameras are operated with a LabVIEW program package called *PEEM Imaging Suite*, which is written as a part of this thesis. The use of the LabVIEW program package has the advantage, that together with the PEEM images also a time-stamp and the current pressure and temperature values are saved in a separate text file.

The reaction rates of the investigated model catalyst systems could be followed with a differentially pumped QMS (Hiden Analytical HALO 201), located in a small vacuum chamber (5 L volume) connected through a nozzle to the main vacuum chamber. The QMS is equipped with a Faraday cup detector, which can be operated up to the 10^{-4} mbar range, and a single electron multiplier (SEM), which operates up to a pressure of 10^{-6} mbar. In addition to the QMS also an ionization gauge of the same type as used in the main chamber is installed in the small vacuum chamber. In this way a precise calibration of the gas pressure in the two vacuum chambers and the QMS readout is possible. Due to the small opening of the nozzle (around 6 mm), it is possible to measure the reactive sticking coefficient. Therefore the sample (8 to 10 mm diameter) is placed directly in front of the nozzle opening. In this way it is ensured, that all molecules that enter the QMS are in contact with the sample surface prior to detection. In principle, this setup also allows for reaction rate measurements during the acquisition of PEEM images. Due to the large volume of the main vacuum chamber, and the small sample surface a good signal to noise level is only ensured, if the sample is placed in front of the QMS nozzle. Therefore all reaction rate measurements have been conducted in separate experiments on freshly prepared samples.

For accurate measurements of reaction rates and the observation of chemical wave patterns and other pattern forming phenomena under constant parameters, a constant gas flow of the reactants (oxygen, hydrogen, methanol, ammonia, carbon monoxide, nitric oxide) into the vacuum system is crucial. A differentially pumped gas line allows for the simultaneous dosage of up to six different gases. The gases are manually introduced

via high precision sapphire sealed leak valves. Feedback-controlled mass flow regulators (MKS 250 Controller) ensure a constant gas flow of two gases (oxygen and methanol) over several hours. The purity of the gases is: 5.3 for oxygen (Linde AG), 5.0 for hydrogen, ammonia and argon (Linde AG), 3.7 for carbon monoxide (Westfalen), 2.5 for nitric oxide (Linde AG). The purity is checked with QMS. For dosing methanol, 99.8% liquid methanol is used (Sigma Aldrich). Using liquid nitrogen, Methanol is degassed by three freeze-pump-thaw cycles prior to the first experiment.

The surface structure of the sample is determined with a LEED optics (ErLEED Digital), which can be operated up to 1×10^{-6} mbar. The LEED images are captured with the same LabVIEW program package and the same cameras as the PEEM images. A chemical characterization of the sample surface is carried out by means of AES. The single pass cylindrical mirror analyzer (Staib Instruments ESA 100) is optimized for large working distances of up to 4 cm. Typically primary electron energies of 3 kV are used. The instrument can be operated up to a pressure of 1×10^{-6} mbar.

3.2.3 Low-Energy Electron Microscopy (Bremen)

A LEEM instrument suitable for measurements at elevated pressure up to 10^{-4} mbar is operated in the research group of J. Falta at the Institute of Solid State Physics at the University of Bremen. In general, all LEEM measurements are carried out with (modified) LEEMIII microscopes manufactured by Elmitec. They all have basically the same layout. Thus in this section, the basic layout of the microscope is described in detail and in the following sections only relevant changes are mentioned.

The Elmitec LEEMIII system consists of two separate chambers, a main chamber, in which the actual microscope is located, and a preparation chamber. Transfer between this chambers is possible without breaking the vacuum. This is possible because the sample is mounted on a transferable sample holder, consisting of a base plate, on which a cylinder containing a tungsten filament is mounted. The sample, which is pressed on top of this cylinder by a molybdenum or titanium cap, can be heated either radiatively by the glowing filament, or by bombardment with electrons emitted from the filament. Under UHV conditions and up to a pressure of 1×10^{-6} mbar Mo caps are used to hold the sample in place. At elevated pressure up to 1×10^{-4} mbar Ti caps can be used, in order to avoid Mo contamination of the sample at high oxygen pressure and temperature. The temperature of the sample is measured by a C-type tungsten-rhenium thermocouple, which is spot welded directly to the side of the sample, or to a tantalum ring or plate located between the sample and the underlying cylinder. The sample manipulator and the preparation chamber are equipped with receiving stations, which allow to heat the sample by passing current through the filament and applying an acceleration voltage for the emitted electrons. Sample transfer is done with magnetically coupled transfer rods.

The main chamber is pumped by an ion pump (Varian Star Cell, 300 Ls^{-1}) coupled with a titanium sublimation pump, and a turbo molecular pump, ensuring a base pressure in the low 10^{-10} mbar range. The chamber has several vacuum ports, from which some are aligned so that attached electron beam evaporators point directly to the measurement position of the microscope. The electron evaporators are inclined by 45°

with respect to the sample surface. In this way it is possible to deposit metals onto the sample surface during LEEM measurements. One of this ports is used to illuminate the sample with photons emitted from a Hg lamp, allowing, in principle, also for PEEM measurements. Since the work function of the used noble metals is higher than the energy of the emitted photons (Hg discharge lamp), PEEM is only used to facilitate the microscope alignment.

The preparation chamber is equipped with a sputter gun and high precision sapphire sealed leak valves for dosage of oxygen and argon for sample cleaning. All sample cleaning steps are performed in the prep chamber and only the final flash annealing step is carried out in the main chamber. Furthermore the preparation chamber is equipped with a load-lock system, which allows for fast sample exchange.

In normal UHV operation, the electrons in the illumination and imaging column are accelerated up to 20 keV to obtain optimal resolution. In order to avoid discharges during operation at elevated pressure, the acceleration voltage is decreased to 12 kV (for pressures up to 5×10^{-6} mbar) or 10 kV (for pressures up to 2×10^{-4} mbar).

Even though no reaction rate measurements have been conducted in the LEEM experiments, a constant gas flow is important for the observation of the reaction induced redistribution of vanadium oxide on Rh(111) and especially for the chemical wave patterns during catalytic methanol oxidation on Rh(110). Therefore the complete gas inlet system with the MKS mass flow regulators was transported from the PEEM laboratory in Hannover to the LEEM microscope in Bremen. The gas line is attached directly to the main chamber of the instrument, using one of the vacuum ports which do not point directly to the sample surface. In this way proper gas mixture in the chamber is ensured.

3.2.4 Spectroscopic LEEM (Trieste)

The spectroscopic low-energy electron microscope operated in the research group of A. Locatelli at the Nanospectroscopy beamline (Elettra) consists of an Elmitec LEEM III microscope, and a custom-built high pressure cell. A comprehensive description of the beamline layout and the endstation can be found in references [90, 103, 121, 123]. Samples can be transferred from the main chamber through the preparation chamber into the high pressure cell without braking the vacuum. In all three chambers, sample heating is possible, and only during the sample transfer heating is interrupted and gases have to be pumped off to avoid contamination of the preparation and main chambers. In the SPELEEM microscope the sample can be illuminated by X-ray photons from the electron storage ring in grazing incidence (16°). The photoelectrons are detected in surface normal direction. As X-ray photon source an undulator of the Sasaki Apple II scheme, consisting of two identical undulator sections with each 20 poles and a phase modulation electromagnet is used [90]. With the insertion device elliptically polarized light (circular, linear horizontal and vertical as special cases) in the energy range 40 - 1000 eV is available.

In this thesis, experiments are performed in the 1×10^{-4} mbar range in the high pressure cell and in the 1×10^{-10} to the 1×10^{-6} mbar range in the main chamber. A gas line with manually operated sapphire sealed leak valves (no mass flow regulation)

allows for dosing oxygen, nitric oxide, ammonia and methanol in all chambers. The total pressure in the chambers is measured with two ionization gauges located directly in each chamber. In the high pressure cell, the Leybold Heraeus Ionivac IM 510 from Hannover is installed to ensure comparable experimental conditions with the experiments conducted in Hannover. For the high pressure regime, a cold cathode ionization gauge together with Pirani and capacitance pressure sensors are located in the high pressure cell. In addition, a differentially pumped QMS (Stanford research System RGA100) connected to the high pressure cell via a small nozzle allowed for recording the partial pressures of the reactants during high pressure experiments.

Sample heating is possible via irradiative heating or electron bombardment from the backside of the sample, as described in 3.2.3. The temperature is measured with a C-type thermocouple attached to a small Ta ring on the backside of the sample. Ultrathin vanadium oxide layers could be deposited in front of the microscope, allowing for diffraction measurements during the deposition process. Deposition is carried out by electron beam bombardment of a high purity V rod in an electron beam evaporator (Focus - Omicron GmbH). Like described in section 3.2.3. The evaporator is inclined 45° with respect to the sample.

3.2.5 Scanning Photoemission Electron Microscopy (Trieste)

The scanning photoemission electron microscopy (SPEM) measurements are performed at the ESCA Microscopy beamline in the group of L. Gregoratti (Elettra). A detailed description of the SPEM microscope and the beamline can be found in the references [93, 125–129]. The end-station of the ESCA Microscopy Beamline is a multichamber setup consisting of two preparation chambers, a high pressure cell and a main chamber containing the SPEM microscope.

In this work the larger of the two preparation chambers is used to perform cleaning cycles. Also ultra thin vanadium oxide films are prepared and characterized in this chamber. In addition to an electron beam evaporator and a sputter gun, a LEED optics (Oxford Instruments) and an Auger electron spectrometer (Perkin Elmer) are available. Since no camera is available to record the LEED images, the diffraction images are digitized using a mobile phone camera (Samsung Galaxy Note 4).

Sample heating is possible by means of a boron nitride heating element (BN heater). With this heating element temperatures of over 1300 K could be reached. The sample temperature is measured with a K-type thermocouple spot welded directly to a sample edge. Sample transfer between the different parts of the measuring setup is possible without breaking the vacuum by means of linear transfer rods. Heating or dosing of gases is not possible during the transfer process.

Oxygen of purity 5.6 and Argon of purity 5.0 is introduced into the preparation chamber via high-precision leak valves. Methanol (99.8%) is filled into a Conflat steel pipe, degassed by applying two freeze-tough-pump cycles, and dosed using a high precision leak valve (no mass flow regulation). The same leak valves are used for experiments in the preparation chamber as well as in the main chamber. The total pressure in the preparation chamber and in the main chamber is measured using two ionization manome-

ters located directly in the preparation chamber and at the energy analyzer in the main chamber, respectively. In the main chamber and the preparation chamber pressures up to the 10^{-6} mbar range can be reached. The high pressure cell is used to generate vanadium oxide islands in a gas atmosphere up to the 10^{-3} mbar range.

The main chamber contains a sample stage, a hemispherical energy analyzer (Specs Phoibos 100) and a Fresnel zone plate optics for focusing the incoming X-ray beam. These three units form the basis of the SPEM microscope. The sample stage allows to scan the sample position with respect to the incoming X-ray beam and the emitted photoelectrons are detected in the hemispherical analyzer. Sample illumination is realized in normal incidence and the photoelectrons detected by the analyzer leave the surface under an angle of 60° . The detector of the hemispherical energy analyzer consists of 48 independent channels for electron detection. Due to the energy dispersion of the analyzer, a roughly 10 eV wide spectrum can be acquired, centered around the energy to which the analyzer is tuned. This is particularly useful if the SPEM microscope is used in imaging mode, since this 10 eV spectrum can be extracted pixel-wise from an SPEM image, and can be used for background correction. Additionally it yields chemical information.

3.2.6 Near Ambient Pressure LEEM (Clausthal)

The near ambient pressure low-energy electron microscope (NAP-LEEM) used in this work is a prototype instrument of Elmitec. It was recently developed by T. Franz and is a LEEM III microscope with an adapted main chamber and objective lens. A detailed description of the imaging performance in the near ambient pressure (NAP) regime together with a short description of the necessary changes for the NAP operation is given in reference [29] and chapter 2.4.3.

The set-up of the NAP-LEEM is similar to the layout of a conventional LEEM III microscope, as described in section 3.2.3. It consists of a preparation chamber with a load-lock, and a main chamber containing the high pressure cell. The preparation chamber is equipped with a sputter gun (Physikalische Instrumente), a sample station with electrical contacts for heating and temperature measurement, as well as a high precision leak valve for dosing of argon (Westphalen, purity 5.0). For the experiments described in this thesis, a standard Elmitec sample holder is used, which is equipped with a boron nitride heating element (BN heater). Titanium is chosen as the cap material. The temperature measurement is realized by means of a C-type thermocouple, which is clamped under the BN heater. The thermocouple is not in direct contact with the sample during the measurements, and rather the temperature of the heating element is measured.

For the deposition of the vanadium oxide layers the same electron beam evaporator is available in the preparation chamber as in the experiments at Hanover and Bremen. Since the sample stage, where heating of the sample is possible, is already fully occupied by the sputter gun, the evaporator is attached to an adjacent vacuum port. Thus, the vanadium deposition took place with the sample on the transfer rod in vacuum and at room temperature. In the NAP-LEEM experiments on Rh(111), the surface could

neither be analyzed with AES nor with LEED before the experiments. However, after the vanadium oxide experiments on Rh(111), a scanning Auger electron spectroscopy analysis of the sample was performed after the sample has been transferred through air in a separate UHV chamber.

The same gas inlet system that is used for the measurements at Hanover and Bremen is connected to the main chamber of the NAP-LEEM. Two feedback-controlled mass flow controllers allowed for flow regulated dosing oxygen (purity 5.6) and methanol (99.8%) into the main chamber, ensuring constant gas flow for hours. In the gas inlet system a Laybold Thermovac TM 210 S pressure sensor is located, and in the main chamber an ionization gauge, which is designed for pressure measurement up to the 10^{-4} mbar range. In the high pressure cell no pressure sensor is installed. However, a pressure calibration between the pressure measured by the Thermovac in the gas inlet system and the pressure prevailing in the high pressure cell, measured directly in the sample position, was carried out with a home-built pressure sensor of Pirani type.

To effectively pump the different parts of the microscope, a combination of turbomolecular pumps and ion getter pumps, partially equipped with a titanium sublimation pump, is used. A total of three turbomolecular pumps are available. The first turbomolecular pump is connected to the load lock / preparation chamber and can also be connected to the main chamber via an angle valve. A second turbomolecular pump is connected directly to the high-pressure cell and functions as the first differential pumping stage. The third turbomolecular pump is connected between objective lens and beam splitter of the microscope. It represents the second differential pumping stage, by means of which the high-pressure cell is separated from the illumination and imaging columns. In this way, UHV conditions can be guaranteed throughout the entire beam path outside the high pressure cell. Two ion getter pumps (Varian / Agilent Technologies) are used to pump the preparation chamber, and the imaging and illumination columns.

Chapter 4

Reaction induced redistribution of vanadium oxide

Abstract The role of vanadium oxide in fundamental catalysis research is briefly reviewed and an introduction into the preceding studies [68–70, 200–202] conducted on reaction induced redistribution of vanadium oxide is given.

4.1 Vanadium oxide in fundamental catalysis research

Vanadium oxide based catalysts find wide application in oxidation reactions in the chemical and petroleum industry, as well as in environmental catalysis. Important examples of the numerous products manufactured with the aid of vanadium oxide based catalysts are sulfuric acid (contact process), and maleic and phthalic anhydride (selective catalytic oxidation of hydrocarbons) [203]. The selective catalytic reduction of nitric oxide with ammonia (SCR process) is an effective way to remove NO from automotive exhaust gas or industrial fumes. Many SCR catalysts contain vanadium oxide [204]. The general importance of vanadium in the field of catalysis is reflected by the fact, that at the beginning of the 21st century around 5% of the annual vanadium production was related to catalysis, and that $\approx 28\%$ of the publications in the field of metal oxide catalysis found in literature between 1967 and 2000 are about vanadium oxides [203].

In many processes, supported vanadium oxide catalysts have the highest catalytic activity. The superior performance of supported vanadium oxide catalysts can be generally be considered as a consequence of the geometric and electronic variability of surface vanadium oxide phases [203]. For this reason a large number of fundamental research studies has been performed in order to understand the geometric and electronic structure

of vanadium oxide surfaces [205]. A key challenge thereby has always been to decipher the connection between the structural properties and the catalytic activity of a catalyst.

In bulk oxides, the oxidation state of vanadium can vary between +2 and +5. Besides the single valency oxides (VO, V₂O₃, VO₂ and V₂O₅) also mixed valency oxides with two different oxidation states between +3 and +5 exist (for example V₆O₁₁ or V₆O₁₃) [206]. Such mixed valency oxides are characterized by a large number of (ordered) oxygen vacancy defects. Two series of mixed valency vanadium oxide phases are known as Magnéli phases (V_nO_{2n-1}) and Wadsley phases (V_{2n}O_{5n-2}).

Surfaces of vacuum cleaved vanadium oxide single crystals have been investigated with surface science techniques, including LEED, X-ray absorption spectroscopy and XPS, and electron energy loss spectroscopy. LEED investigations of V₂O₃(0001), VO₂(011) and V₂O₅(001) surfaces indicate a bulk terminated surface [207,208]. The question of the surface termination was treated with density functional theory, and the results range from a half-metal layer termination of the V₂O₃(0001) surface [209,210] to a surface layer of vanadyl groups on a vacuum deposited V₂O₃ film [211,212]. These vanadyl groups and the existence of (subsurface) oxygen vacancies are important features of vanadium oxide surfaces [212,213]. All these findings underline the structural variety of vanadium oxides. This variability gets even more intricate in case of thin supported oxide films.

Industrially relevant vanadium oxide catalysts often consist of vanadium oxide films supported on other (metal) oxides like for example SiO₂, Al₂O₃ or TiO₂. The influence of the support material on the catalytic activity has been studied systematically by Wachs and coworkers [214,215]. The properties of supported vanadium oxide catalysts have also been the subject of the DFG Sonderforschungsbereich 546 [216]. As model systems single crystal surfaces [217], epitaxial layers [218,219], supported vanadium oxide catalysts [220,221], and gas phase clusters [222–224] have been investigated experimentally and theoretically. The partial oxidation of propane to propene and the catalytic dehydrogenation of methanol to formaldehyde has been the focus of most of the studies.

Methanol oxidation is a frequently studied catalytic model reaction of industrial importance. Among the remarkable findings of the Sonderforschungsbereich 546 are a mechanism for the methanol dehydrogenation on vanadium oxide catalysts [57,58,225,226], and the influence of the support material on the methanol dehydrogenation [56,221]. Essential for the dehydrogenation of methanol yielding formaldehyde is the formation of a methoxy intermediate through fission of the methanol O-H bond at oxygen vacancies formed by removal of vanadyl oxygen atoms. Surface defects play an important role in the adsorption of methanol and formation of formaldehyde. The support material has a huge influence on the adsorption of methanol and the subsequent reaction to formaldehyde, as was shown in the case of vanadium oxide supported on cerium oxide. Ceria is directly involved in the redox process of methanol oxidation [221].

The above mentioned results have been obtained either from vanadium oxide single crystal surfaces, from epitaxial, several layers thick vanadium oxide films on noble metal single crystals, or on supported vanadium oxide clusters. Such systems are an established way of investigating oxide catalysts with the methods of surface science [36]. An alternative concept in fundamental catalysis research is the so-called “inverse model

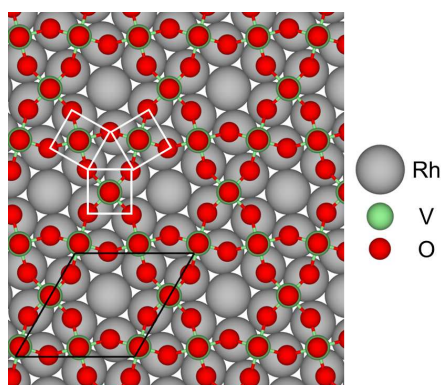


Figure 4.1: Structure model for the $(\sqrt{7} \times \sqrt{7})R19.1^\circ$ vanadium oxide phase on Rh(111). The unit cell and three VO_5 pyramid as structural units are indicated in the model by black and white lines, respectively. The figure is a courtesy of C. Penschke.

catalyst approach”, in which an oxidic catalyst is supported on a (noble) metal single crystal [227]. The thickness of the oxide catalyst is here typically less than a monolayer, so that not only the oxide surface, but also the metal surface is exposed. The inverse catalyst approach avoids typical problems like charging effects etc. associated with bulk oxides or thick films. New materials with unique properties have been discovered in this way. The structures of two-dimensional oxide films typically differ from their bulk phases [32].

4.1.1 Vanadium oxide structures on Rh(111)

A particularly well studied system is vanadium oxide supported on a Rh(111) surface, which has been characterized extensively in the group of Netzer. Based on scanning tunneling microscopy measurements and density functional theory calculations conducted in the group of Kresse, a large variety of ordered two-dimensional oxide phases has been described [53, 55, 183, 211]. In the sub-monolayer range, vanadium oxide on Rh(111) forms a number of well-ordered two-dimensional phases. These structures can be built up as a two-dimensional network in which VO_n polyhedra ($n = 3 - 6$) as structural units are connected by sharing oxygen corner atoms, as shown in figure 4.1. A summary of the $VO_x/Rh(111)$ structures reported in literature is given in table 4.1, a topical review on the growth of VO_x on Rh(111) is given in [183], a review about vanadium oxide surface studies in general can be found in [205].

Ultrathin VO_x films serve also as model catalysts in the CO and H_2 oxidation reactions [182, 228–230]. An enhanced removal of pre-adsorbed oxygen from the Rh(111) surface surrounding vanadium oxide covered areas compared to the bare Rh(111) is reported. Associated with the catalytic reaction is a mass transport of vanadium oxide during the reduction and during redox cycles. The mass transport proceeds via diffusion of small vanadium oxide clusters. The structure, stability and dynamics of V_6O_{12} clusters have been investigated [54], including the self-assembly of the clusters under

Table 4.1: Ordered vanadium oxide phases on Rh(111) reported in literature.

LEED pattern	Composition	Oxidation state	V coverage / MLE	Reference
$(\sqrt{13} \times \sqrt{13})R13.8^\circ$	VO ₃	+5	0.46	[53]
$(\sqrt{7} \times \sqrt{7})R19.1^\circ$	VO ₃	+5	0.43	[53]
$(5 \times 3\sqrt{3})$ -rect	V ₁₃ O ₂₁	+3 / +5	0.43	[55]
(5×5)	V ₁₁ O ₂₃	+3 / +5	0.44	[55]
Moiré	VO ₂	+4	0.85	[53]
(9×9)	V ₂ O ₃	+3	0.44	[55]
(2×2)	V ₂ O ₃	+3	≤ 0.5	[53, 202]
(2×2) -split	V ₂ O ₃	+3	≤ 0.5	[202]
$(\sqrt{3} \times \sqrt{3})R30^\circ$	V ₂ O ₃	+3	-	[53]
”Wagon wheel“	VO	+2	0.73	[55]
$(\sqrt{3} \times \sqrt{3})$ -Moiré	-	-	-	[70]

reducing conditions [231].

4.2 Reaction-induced redistribution of vanadium oxide

The morphology, composition, and electronic properties of a catalyst under operation typically deviate from the initial state after catalyst preparation. Such reaction-induced variations can be associated with a catalyst activation, or resulting in a so called “poisoning”, i. e. in deactivation. In order to study these processes, the interaction of VO_x/Rh(111) in catalytic model reactions like H₂ or methanol oxidation have been investigated on sub-monolayer thick vanadium oxides films. A number of in situ methods for the structural and chemical characterization of such ultrathin oxide films during catalytic reactions, including PEEM and LEEM, have been applied [68–70, 200–202].

A surprising phenomenon that has been observed is the reaction-driven formation of vanadium oxide stripe and island patterns, and the subsequent coalescence of these macroscopic vanadium oxide islands during methanol oxidation. This island coalescence is depicted in figure 4.2 [68–70]. The macroscopic VO_x redistribution is accompanied by a considerable increase of the formaldehyde production. Formaldehyde is the main reaction product in catalytic methanol oxidation. The movement of these islands towards each other and the subsequent coalescence, which can only be observed under reaction conditions, has been explained by a polymerization / depolymerization mechanism, which is governed by oxygen gradients on the surface [68–70].

The mechanism is based on the reversible aggregation of VO_x clusters into larger islands, and the reverse process, i. e. the dissolution of these large islands into small clusters. The key points of the mechanism are explained in the following: During catalytic methanol oxidation in the 10⁻⁴ mbar range at around 1000 K, vanadium oxide is distributed in form of circular oxide islands of tens to hundreds of μm diameter, surrounded

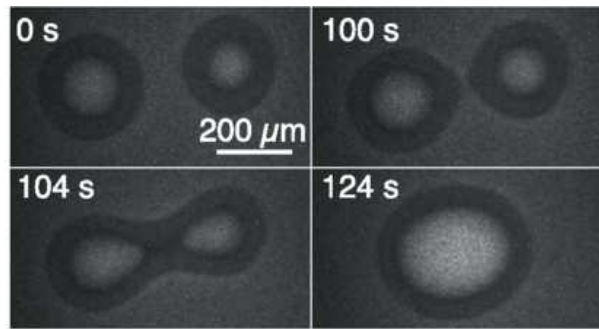
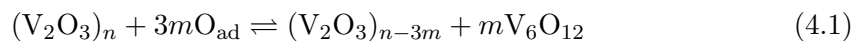


Figure 4.2: PEEM images showing different stages in the coalescence of two nearby vanadium oxide islands under reaction conditions. Experimental conditions: $\theta_V = 0.23$ MLE, $T = 1020$ K, $p(\text{CH}_3\text{OH}) = 3 \times 10^{-4}$ mbar, $p(\text{O}_2) = 1 \times 10^{-4}$ mbar. Figure reprinted with permission from [69].

by the bare Rh(111) surface. Oxygen can dissociatively adsorb on the Rh surface; the adsorption on the oxygen terminated V-oxide islands, however, is slow. Methanol in turn can easily adsorb on the VO_x covered surface and react there to formaldehyde. The oxide islands thus act as catalytic “micro reactors”, which consume oxygen needed for the catalytic reaction. The oxygen is supplied by surface diffusion from the surrounding Rh surface. The diffusive supply of oxygen from the Rh surface towards the V-oxide islands leads to oxygen gradients in the area surrounding the islands. Also inside the VO_x islands an oxygen gradient develops as oxygen diffuses from the edges of the island in the interior. Consider two neighboring islands, then the oxygen gradients overlap, resulting in a considerable lower oxygen coverage in between the two islands, compared to the rest of the surrounding Rh surface. Both islands “compete” for the same amount of oxygen located in between these two islands. This situation is sketched in figure 4.3. By taking the experimentally observed V_6O_{12} clusters [54] as representatives for the small and mobile VO_x species, one can formulate the following equilibrium between clusters and extended oxide islands, for which we assume a composition of $(\text{V}_2\text{O}_3)_n$:



According to equation 4.1, a dissolution of the VO_x islands should be observed in regions of high oxygen coverage, and an aggregation of the formed clusters to large islands should occur in regions of low oxygen coverage. The simultaneous dissolution and aggregation at different positions explains the macroscopic observation of moving islands.

Oxygen is consumed inside the vanadium oxide islands, but it is supplied only from the boundaries by diffusion from the surrounding rhodium surface. The resulting oxygen gradients in the vanadium oxide island is equivalent to a gradient in the chemical potential of oxygen, i. e. the thermodynamic conditions vary from the boundary to the center of a VO_x island. This gradient can give rise to - depending on temperature and pressure - a phase separation into a reduced VO_x phase in the center of the oxide is-

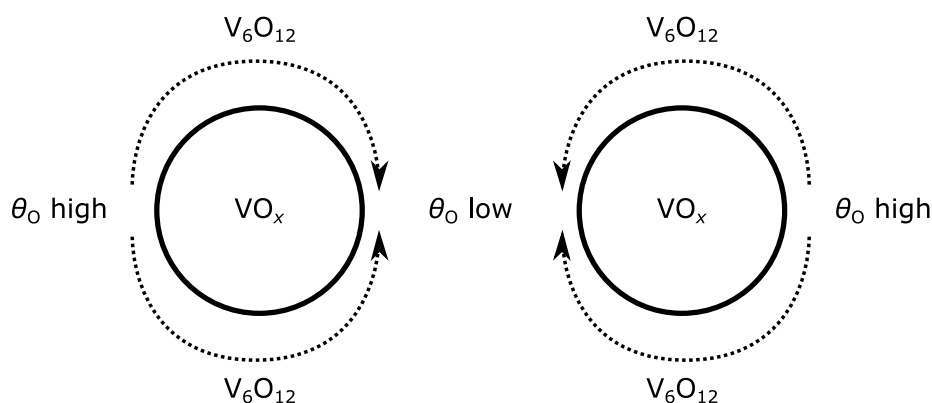


Figure 4.3: Mechanistic scheme illustrating the movement of two neighboring VO_x islands on a $\text{Rh}(111)$ surface under reaction conditions *via* a polymerization/depolymerization mechanism. The vanadium oxide island dissolves in the presence of a high oxygen coverage into V_6O_{12} clusters. These clusters diffuse to regions of lower oxygen coverage and condensate at the perimeter of the oxide island. The simultaneous dissolution and condensation of the island and the oxide clusters results in the macroscopic movement of the vanadium oxide islands.

lands and an oxidized phase at the outer parts. Experimentally, the reduced phase can be recognized by its high brightness level in the PEEM images shown in figure 4.2. A schematic representation of the oxygen gradients in and around a vanadium oxide island, and the resulting phase separation can be seen in figure 4.4. Laterally resolved XPS measurements confirm the interpretation of an inner, reduced VO_x phase and an outer oxidized VO_x phase: the reduced core consists of V in the oxidation state of mainly +3/+4, whereas the oxidized ring is better described by V species in the oxidation state +4/+5 [69, 70].

The polymerization/depolymerization mechanism represents a special ripening mechanism, which is neither pure Ostwald ripening nor Smolochowski ripening. General ripening describes a process in which the density of islands or particles decreases while the mean particle or island size increases. In Ostwald ripening larger particles/islands grow at the expense of smaller ones. Mass transport happens via cluster, molecule, vacancy or atom diffusion across terraces [232–234], but no movement of two- or three-dimensional particles or islands is described. The thermodynamic driving force of Ostwald ripening is the higher thermodynamic stability of larger particles due to a lower surface energy. Consequently small particles have a higher vapor pressure than larger particles, as expressed in the Kelvin equation.

In Smolochowski ripening, the coalescence of diffusing islands on a surface leads to a coarsening. This ripening type is only possible for islands of high surface mobility. This mobility is typically encountered for small island sizes of only a few tens to hundreds of atoms, since the island diffusivity decreases with increasing island size [235]. Quite in general ripening processes play an important role in heterogeneous catalysis, because

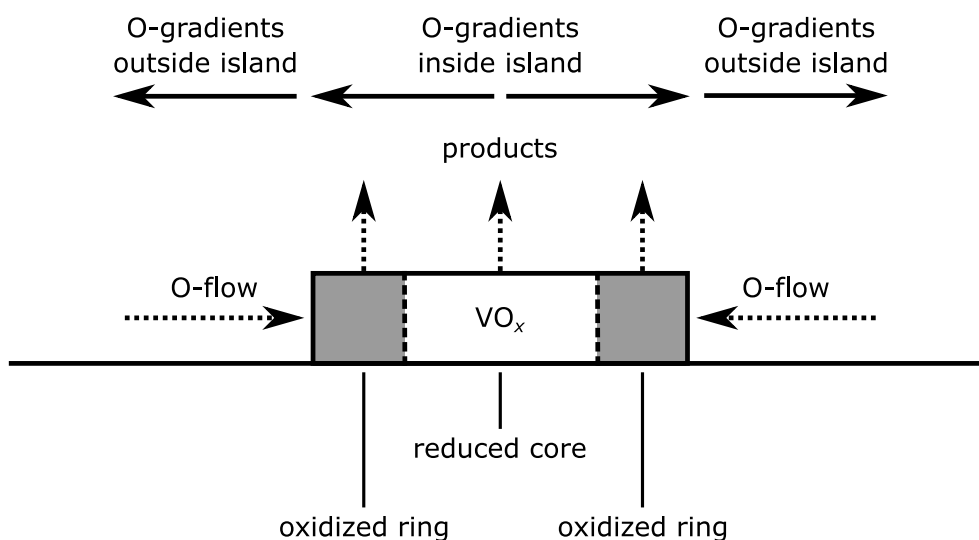


Figure 4.4: Mechanistic scheme illustrating the diffusion of adsorbed oxygen towards a vanadium oxide island. On the vanadium oxide island oxygen is consumed during the oxidation of methanol. As a result of the lateral restriction of the catalytic reaction to the vanadium oxide islands and of the oxygen adsorption to the rhodium surface, macroscopic oxygen gradients develop around and inside the vanadium oxide island. Reprinted from: Reaction dynamics of metal/oxide catalysts: Methanol oxidation at vanadium oxide films on Rh(111) from UHV to 10^{-2} mbar, B. von Boehn, C. Penschke, X. Li, J. Paier, J. Sauer, J.-O. Krisponeit, J. I. Flege, J. Falta, H. Marchetto, T. Franz, G. Lilienkamp, and R. Imbihl, *Journal of Catalysis*, **2020**, *385*, 255 - 264, Copyright (2020), with permission from Elsevier.

catalytic surfaces may restructure under reaction conditions [236, 237]. An important example is the ripening of metal nanoparticles on an oxidic support at elevated temperature [238]. Such ripening often leads to a loss in catalytic activity. On the other hand, wetting of a metal nanoparticle by its oxidic support, a phenomenon known as strong metal support interaction (SMSI) [46, 47], can be beneficial for the activity and selectivity of a catalyst [42, 239, 240]. In the system $\text{VO}_x/\text{Rh}(111)$ the formation and ripening of macroscopic vanadium oxide islands is accompanied by a significant increase of catalytic activity in formaldehyde production. The ripening mechanism presented here works only under non-equilibrium conditions, i. e. the ongoing methanol oxidation is needed for moving and coalescing vanadium oxide islands.

The reaction induced redistribution of vanadium oxide on a Rh(111) surface during catalytic methanol oxidation exhibits a new type of ripening, which is possibly also connected to the catalytic activity. These two findings make $\text{VO}_x/\text{Rh}(111)$ an interesting system for fundamental research and the results are important in the field of surface science and catalysis research. In order to investigate whether this novel phenomenon is of general importance, or whether it is restricted to catalytic methanol oxidation on

$\text{VO}_x/\text{Rh}(111)$, a series of experiments were carried out, which are described in this thesis. Firstly, only the catalytic reaction are changed, but the catalyst $\text{VO}_x/\text{Rh}(111)$ remains the same. Catalytic ammonia, carbon monoxide and hydrogen oxidation are studied on $\text{VO}_x/\text{Rh}(111)$ (section 5.5, [241]). Since oxygen gradients are of crucial importance for the oxide redistribution, the influence of a different oxygen source, nitric oxide, is investigated, and molecular oxygen is replaced by NO as the oxygen source in the methanol, hydrogen, and ammonia oxidation (section 5.6, [242]).

Spectromicroscopic experiments carried out at the electron storage ring Elettra yield results about the structure and composition of vanadium oxide during the $\text{CH}_3\text{OH} + \text{O}_2$ (section 5.7.3), the $\text{NH}_3 + \text{O}_2$, and the $\text{NH}_3 + \text{NO}$ (section 5.7.4), as well as about the V and O coverage under reaction conditions. PEEM experiments at different temperatures and gas phase compositions lead to further details of the phase separation into oxidized and reduced VO_x phases (section 5.2.3), and in situ LEEM and NAP-LEEM experiments reveal further reaction dynamics, namely a periodic expansion and contraction of vanadium oxide islands under reaction conditions (section 5.3), as well as turbulent dynamics in the 10^{-2} mbar range (section 5.8).

Finally, with Pt(111) another fcc(111) substrate is chosen as support for vanadium oxide during catalytic methanol oxidation (chapter 7). Since oxygen gradients play an important role in the dynamics of vanadium oxide, Pt(111), with its considerably lower oxygen sticking coefficient compared to Rh(111), is an instructive extension to the experiments conducted on Rh(111).

In a next step towards a generalization of the polymerization / depolymerization mechanism, the $\text{CH}_3\text{OH} + \text{O}_2$, the $\text{NH}_3 + \text{O}_2$, and the $\text{H}_2 + \text{O}_2$ reactions are studied on $\text{VO}_x/\text{Rh}(110)$ with PEEM ([243, 244]), SPELEEM (section 6.8, [245]) and LEEM. The results are presented in chapter 6. Preliminary PEEM and SPELEEM experiments are part of my master thesis [71], while a large part of the interpretation of the PEEM and SPELEEM experiments and the publication, as well as the LEEM measurements are part of this thesis.

Chapter 5

Reaction-induced VO_x redistribution on Rh(111)

Abstract The reaction-induced redistribution of sub-monolayer VO_x films on Rh(111) is investigated in a number of catalytic reactions with photoemission electron microscopy (PEEM) and low-energy electron microscopy (LEEM). For catalytic methanol oxidation, a detailed investigation of the influence of experimental parameters on pattern formation is achieved with PEEM. The reversible formation of a vanadium oxide stripe pattern or of a pattern of circular vanadium oxide is studied. Both, the stripes and the islands, can exhibit a substructure of a reduced core and an outer oxidized ring. The length scale of the pattern ranges between tens to hundreds of micrometers. A similar behavior can be seen in catalytic ammonia and CO oxidation. In situ LEEM experiments revealed a $(\sqrt{7} \times \sqrt{7})R19.1^\circ$ structure for the oxidized ring and a $(\sqrt{3} \times \sqrt{3})$ -Moiré pattern in the island core. The dependence of the oxygen gradient inside a VO_x island on the island size can cause kinetic instabilities. This leads to oscillatory changes of the VO_x island size in the 10^{-4} mbar range. The vanadium coverages in the VO_x islands previously determined [69,70] are accurately measured using in situ scanning photoemission electron microscopy (SPEM). A surprisingly high oxygen coverage suggests the presence of a Rh surface oxide under reaction conditions. Replacing O_2 by NO in methanol and ammonia oxidation results in a pattern consisting of a dense VO_x layer with holes of vanadium oxide depleted Rh surface, instead of a vanadium oxide island pattern. A pressure increase into the 10^{-2} mbar range leads to turbulent VO_x redistribution dynamics, as imaged with near ambient pressure-LEEM (NAP-LEEM).

5.1 VO_x deposition rate calibration

The deposition rate of a vanadium oxide electron beam evaporator can be determined by combined AES and LEED measurements, as described in detail in the supplemental material 1 of [69] and in [70]. Vanadium oxide growth in the Stranski-Krastanow mode is characterized by the transition from a $(\sqrt{7} \times \sqrt{7})R19.1^\circ$ structure, into a Moiré pattern, as reported by Schoiswohl and coworkers. For completion of the $(\sqrt{7} \times \sqrt{7})R19.1^\circ$ layer an experimental coverage around 0.5 - 0.6 MLE has been determined [53]. In the above mentioned study, the deposition rate was calibrated with a quartz microbalance, and the nucleation point of the second oxide layer was determined with STM. Structural models calculated with DFT in the group of Kresse predict an ideal coverage of 0.43 MLE for the $(\sqrt{7} \times \sqrt{7})R19.1^\circ$ structure, which is at slight variance to the experimentally determined coverage of 0.5 - 0.6 MLE. In this thesis, the same pressure and temperature (reactive evaporation) as in reference [53] are applied for the growth of VO_x (2×10^{-7} mbar and 670 K).

The sharp transition from the $(\sqrt{7} \times \sqrt{7})R19.1^\circ$ structure into a Moiré pattern in LEED is used for a coverage calibration. In all experiments of this thesis, the transition from the $(\sqrt{7} \times \sqrt{7})R19.1^\circ$ via an (8×8) structure into a Moiré pattern is observed in LEED upon subsequent (PEEM and SPEM) or continuous (LEEM) deposition of VO_x . This transition is demonstrated by the LEED data depicted in figure 5.1.

Figure 5.1d displays the intensity of the $(\sqrt{7} \times \sqrt{7})R19.1^\circ$ and a Moiré spot as a function of time. The sharp decrease of the $(\sqrt{7} \times \sqrt{7})R19.1^\circ$ LEED intensity around 7 min deposition time marks the completion of the first oxide layer. The small intensity plateau extending from around 7 - 8 min indicates the appearance of the (8×8) , which is followed by the development of a Moiré pattern.

The limited temporal resolution of about one minute in the SPEM and PEEM experiments (caused by the step-wise VO_x deposition and ex situ characterization), and the broad coverage range mentioned in literature for the $(\sqrt{7} \times \sqrt{7})R19.1^\circ$ structure (0.43 MLE from DFT, 0.5 - 0.6 MLE from STM [53]) are the strongest contributions to the overall error of the coverage determination. Errors related to an unstable vanadium flux of the evaporator etc. have only a minor influence on the accuracy of the vanadium oxide coverages.

As described in section 2.7, the Stranski-Krastanow growth mode is characterized by an initial linear increase (decrease) of the adsorbate (substrate) Auger signal, followed by a slower, more or less exponential signal increase (decrease). The transition from the linear to the exponential signal evolution shows up as a kink in the Auger signal vs. time (AS-t) plot. Such a kink has also been observed in AS-t plots of the system $VO_x/Rh(111)$, as described in the supplemental material 1 of [69] and in detail in [70]. The kink in the AS-t plot coincided with the vanishing $(\sqrt{7} \times \sqrt{7})R19.1^\circ$ LEED pattern. In order to calibrate the vanadium evaporator, a combined LEED and AES vanadium deposition calibration is conducted. The resulting Auger spectra of the $RhMN_{4,5}N_{4,5}$ (Rh_{302}), and of the $VL_{2,3}M_{2,3}M_{2,3}$ (V_{437}), $VL_{2,3}M_{2,3}M_{4,5}$ (V_{473}), and $VL_{2,3}M_{4,5}M_{4,5}$ and $OKL_{2,3}L_{2,3}$ ($O+V_{510}$) are shown in figure 5.2 a and b, respectively.

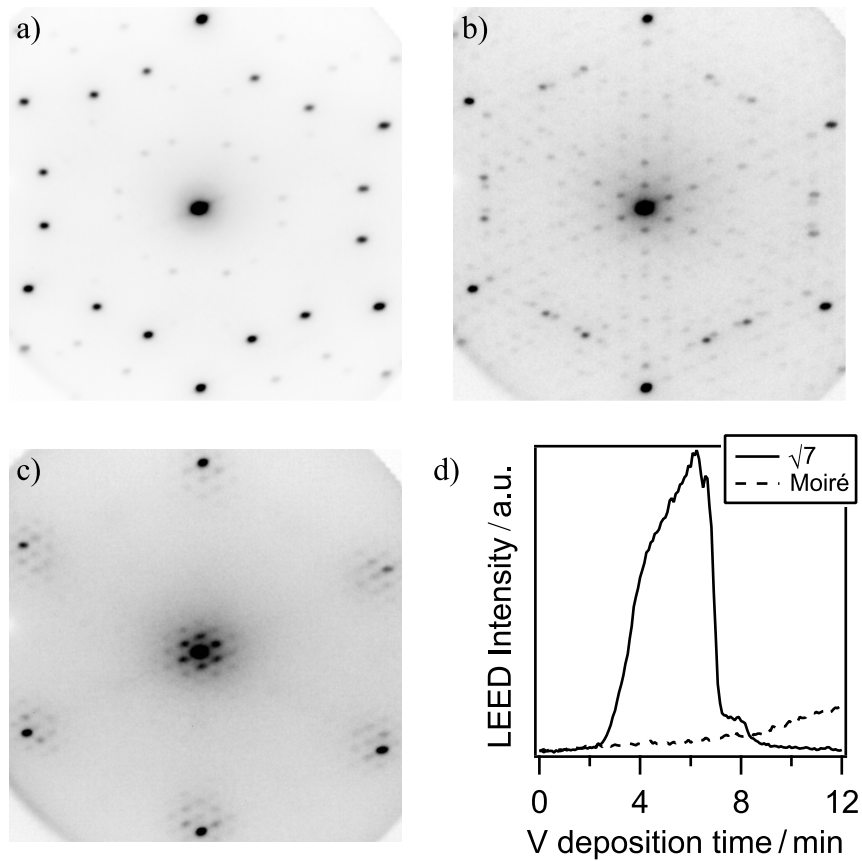


Figure 5.1: LEED images acquired during continuous VO_x deposition. a) $(\sqrt{7} \times \sqrt{7})R19.1^\circ$, (b) (8×8) and (c) Moiré pattern. d) $(\sqrt{7} \times \sqrt{7})R19.1^\circ$ (denoted as “ $\sqrt{7}$ ”) and Moiré LEED spot intensity as a function of deposition time. The LEED images are acquired at 670 K in 2×10^{-7} mbar at a start voltage of 65 eV.

Details on the VO_x growth are given in section 3.2.1. The AS-t plots constructed from the Auger data are shown in figure 5.2 c. In figure 5.2c is seen, that the V and O signals increase more or less linearly during the first 10 minutes of VO_x deposition. A change in the slope indicates completion of the first oxide layer. Subsequently, the Auger signals increase with a lower rate, as expected for the formation of three dimensional vanadium oxide crystallites on top of the first oxide layer.

As described in section 2.2.1, the oxidation state of vanadium oxide can be estimated from the V $L_{2,3}M_{2,3}M_{4,5}/L_{2,3}M_{2,3}M_{2,3}$ Auger intensity ratio. Such an analysis is conducted for the Auger data shown in figure 5.2b, and the Auger intensity ratios are depicted in figure 5.3. Because of the low Auger intensity the data point for 0.5 min deposition time is excluded from the evaluation.

Starting from a value of 1.12 for 1.5 min deposition time the V Auger intensity ratio in figure 5.3 decreases to a final value of 0.96. The average value is 0.99. The standard

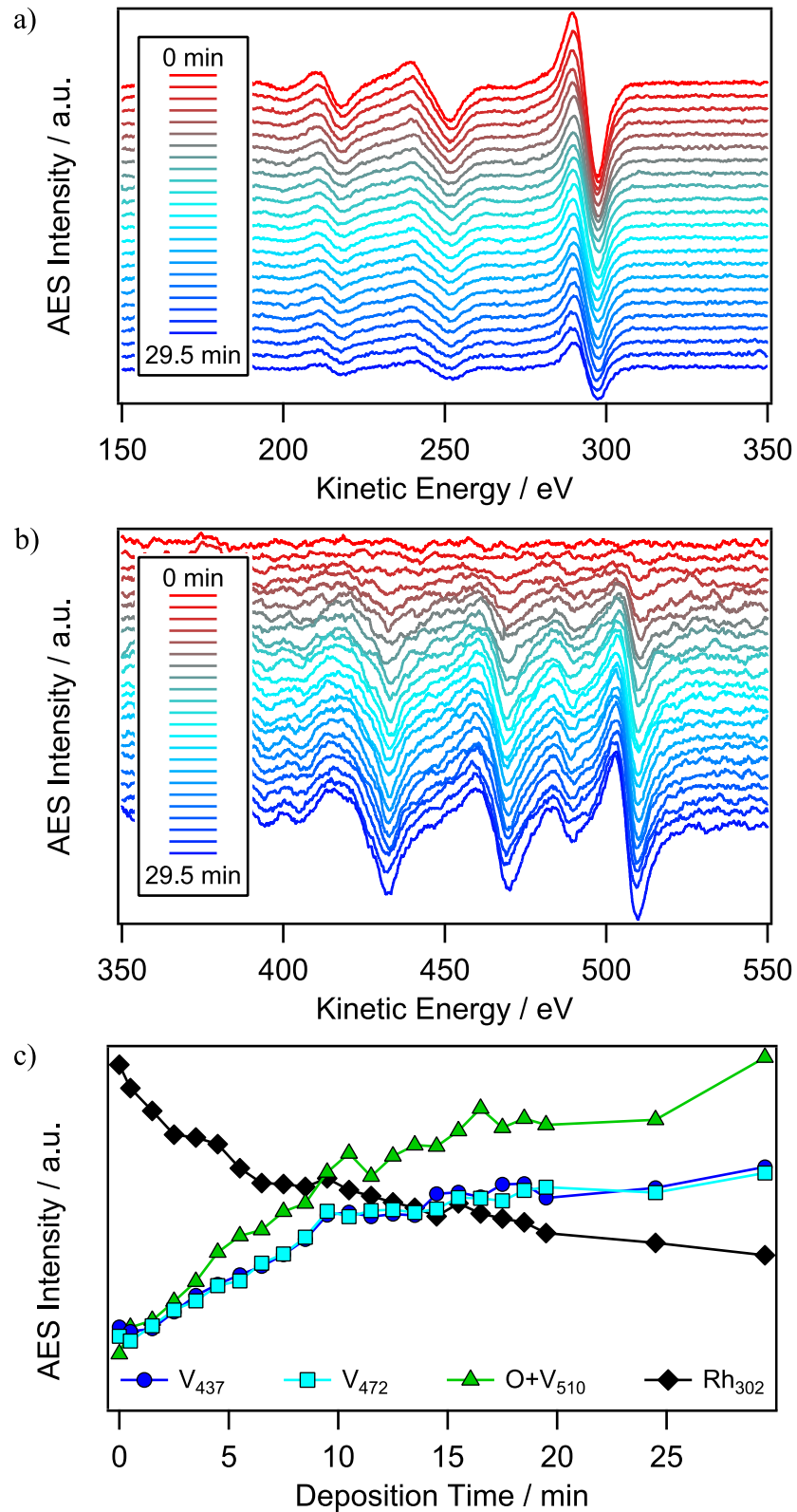


Figure 5.2: Deposition rate calibration by AES. Acquired Rh (a), and V and O (b) Auger spectra as a function of VO_x deposition time. c) AS-t plot of the $VL_{2,3}M_{2,3}M_{2,3}$ (V_{437}), $VL_{2,3}M_{2,3}M_{4,5}$ (V_{472}), $VL_{2,3}M_{4,5}M_{4,5}$ and $OKL_{2,3}L_{2,3}$ ($O+V_{510}$), and $RhMN_{4,5}N_{4,5}$ (Rh_{302}) Auger transitions.

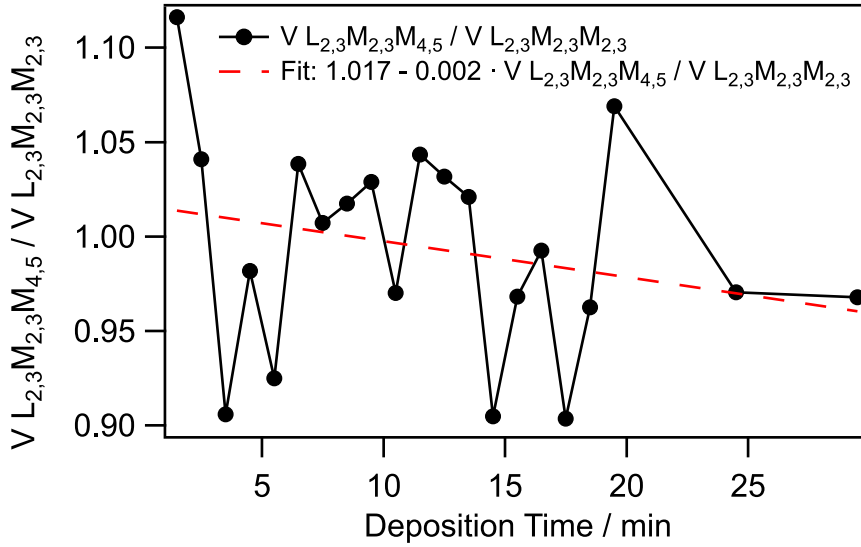


Figure 5.3: $V L_{2,3}M_{2,3}M_{4,5}/V L_{2,3}M_{2,3}M_{2,3}$ Auger intensity ratio as a function of VO_x deposition time.

deviation is with 0.05 quite high, indicating a high signal to noise ratio. The slight decrease in the $V L_{2,3}M_{2,3}M_{4,5}/V L_{2,3}M_{2,3}M_{2,3}$ Auger intensity ratio indicates an increase of the vanadium oxidation state during the deposition process. This is, however, in contradiction to literature. Experiments have revealed a gradual reduction of vanadium with increasing V coverage [53]. A decreasing oxidation state of vanadium mainly occurs during the transition from the $(\sqrt{7} \times \sqrt{7})R19.1^\circ$ structure to the hexagonal, high coverage phases in the coverage range between 0.6 and 1.2 MLE. The reduction is manifested by the appearance of a low binding energy component in the V 2p core level spectrum. XP spectra collected at the Nanospectroscopy beamline and the ESCA microscopy beamline (Elettra), presented in sections 5.4 and 5.7, indicated a gradual shift to lower binding energy of V during VO_x deposition. Apparently, the estimation of the oxidation state based on the V Auger intensity ratio fails (at least with the used spectrometer) for sub-monolayer VO_x films on Rh(111).

Together with Auger spectra, also LEED images are acquired after every deposition step. A selection of the LEED images as a function of VO_x coverage is shown in figure 5.4. Initially, the diffraction spots of a $(\sqrt{7} \times \sqrt{7})R19.1^\circ$ structure are visible together with a (2×2) pattern of chemisorbed oxygen up to a coverage of about 0.4 MLE. With increasing VO_x coverage, the (2×2) diffraction spots become weaker until they finally vanish, and only the $(\sqrt{7} \times \sqrt{7})R19.1^\circ$ LEED pattern remains at 0.5 MLE. Further deposition results in a complex LEED pattern at about 0.6 MLE, which has been identified as a $(5 \times 3\sqrt{3})\text{rect}$ in reference [70]. This structure turns into a Moiré pattern of approximately (12×12) periodicity for 0.8 MLE, with additional diffraction spots appearing at 1 MLE. At about 1.8 MLE the Moiré pattern is transformed almost completely into the so-called “wagon wheel” structure. Starting from about 2.9 MLE the $(\sqrt{3} \times \sqrt{3})R30^\circ$

spots of the oxygen terminated corundum V_2O_3 surface [211] are superimposed on the wagon wheel LEED pattern.

The VO_x coverages stated in figure 5.4 are based on a calibration in which the vanishing $(\sqrt{7} \times \sqrt{7})\text{R}19.1^\circ$ LEED pattern between 4.5 and 5.5 min deposition time is taken as a marker for a V coverage of 0.6 MLE. The assignment of a closed $(\sqrt{7} \times \sqrt{7})\text{R}19.1^\circ$ layer after 5 minute VO_x deposition and the subsequent growth of a second layer is at variance with the AS-t plot shown in figure 5.2c. The pronounced kink visible in the AS-t plot suggests the formation of a closed oxide layer after 10 min deposition time, according to the change in slope of the $\text{V L}_{2,3}\text{M}_{2,3}\text{M}_{2,3}$, $\text{V L}_{2,3}\text{M}_{2,3}\text{M}_{4,5}$, $\text{V L}_{2,3}\text{M}_{4,5}\text{M}_{4,5}$ and $\text{OKL}_{2,3}\text{L}_{2,3}$, and $\text{RhMN}_{4,5}\text{N}_{4,5}$ signals. The recorded AS-t plot is also at variance with the AS-t plot reported in [69, 70], where the change in slope coincided with the transformation of the $(\sqrt{7} \times \sqrt{7})\text{R}19.1^\circ$ into a $(5 \times 3\sqrt{3})\text{rect}$ structure.

Overall, the experimental findings are in good agreement with the growth studies reported by Schoiswohl et al. [53] and Hesse et al. [69, 70]. However, some differences exist: *i*) the characteristic structural transformations for the high-coverage VO_x phases ($\theta_V \geq 0.6$ MLE) are observed at higher V coverages than in [53]; *ii*) a considerable change in slope of the AS-t plot in figure 5.2c is seen only after deposition of about (1 MLE) VO_x , whereas a kink in the AS-t plot is reported to occur during the transformation of the $(\sqrt{7} \times \sqrt{7})\text{R}19.1^\circ$ into a $(5 \times 3\sqrt{3})\text{rect}$ structure (0.6 MLE) [69, 70].

The first point might be explained by the different analysis methods used in this study and in the experiments of Schoiswohl et al.: In [53] STM was applied to observe structural transformations, whereas in this study only LEED is available for a structure determination. Since LEED probes a much larger area than STM ($\approx 1 \text{ mm}^2$ vs 10^{-8} mm^2), STM might just happen to detect one of a number of coexisting vanadium oxide structures during the deposition. For example, the formation of the wagon wheel structure is reported to occur after deposition of 0.8 MLE VO_x together with an ‘‘oblique’’ structure, whereas in this study the formation of the wagon wheel LEED pattern is observed only after deposition of about 1.1 MLE VO_x . The same holds for the appearance of the $(\sqrt{3} \times \sqrt{3})\text{R}30^\circ$ spots belonging to the corundum V_2O_3 oxide phase. Schoiswohl et al. report the formation of V_2O_3 crystallites starting from 1 MLE, whereas in this study weak $(\sqrt{3} \times \sqrt{3})\text{R}30^\circ$ reflexes can only be observed after the deposition of 2.2 MLE. Another deviation from the experiments reported by Schoiswohl et al. is the coexistence of the wagon wheel and the $(\sqrt{3} \times \sqrt{3})\text{R}30^\circ$ V_2O_3 structure in this study. In the experiments reported in [211], the $(\sqrt{3} \times \sqrt{3})\text{R}30^\circ$ V_2O_3 structure is the only stable structure for $\theta_V \geq 2$ MLE. These differences might just reflect the different averaging processes in the two methods.

The second point, the missing change in slope in the AS-t plot after the transformation from the $(\sqrt{7} \times \sqrt{7})\text{R}19.1^\circ$ into a series of other VO_x structures can not be explained easily. The system $\text{VO}_x/\text{Rh}(111)$ is characterized by number of structural transformations and coexisting phases during the VO_x transition, until finally the V_2O_3 corundum phase becomes the only stable phase. The $(\sqrt{7} \times \sqrt{7})\text{R}19.1^\circ$ is followed by the (partially coexisting) hex- VO_2 (Moiré), the oblique structure, and the wagon wheel structure, upon continuous VO_x deposition. These structural transformations proceed

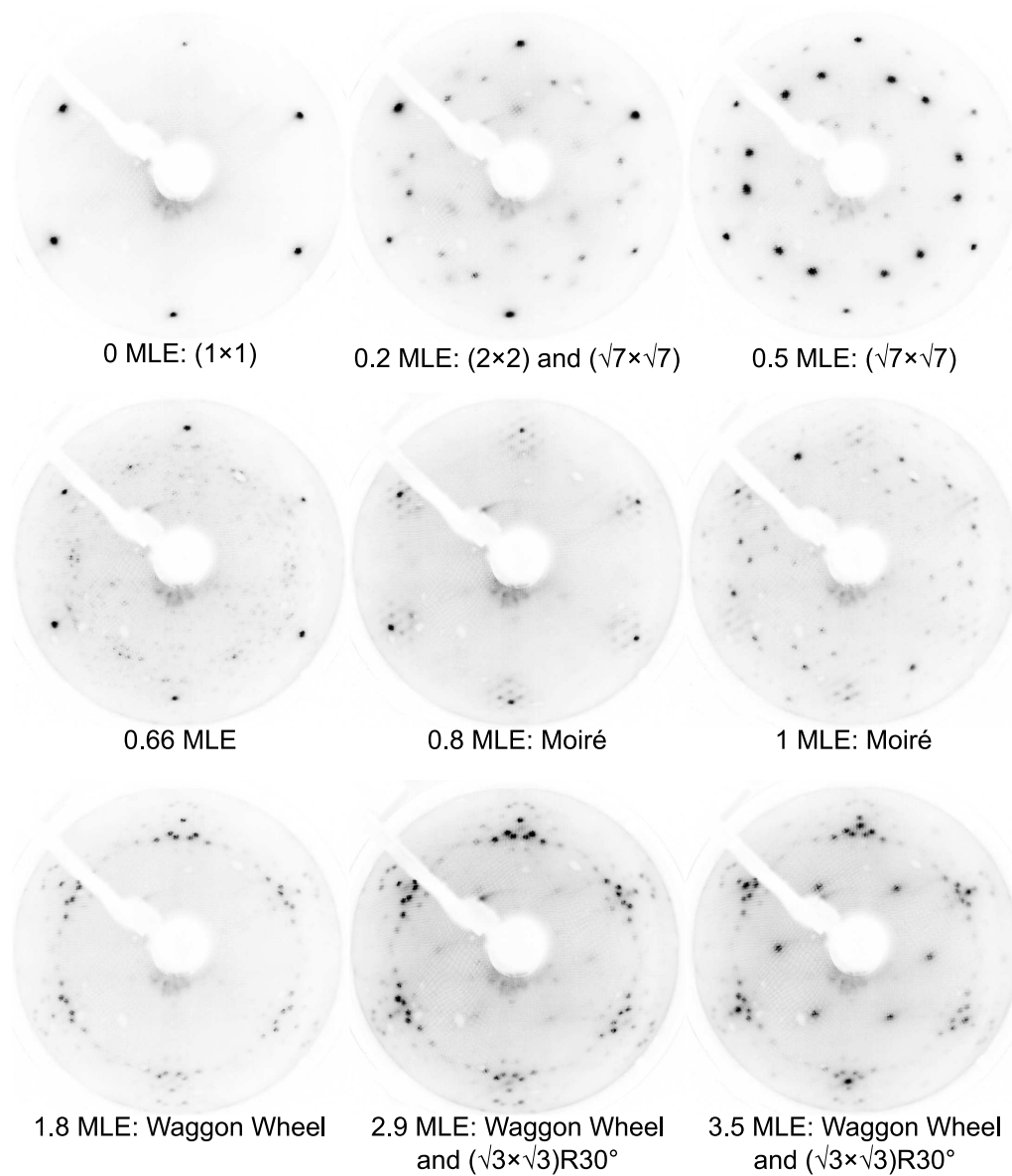


Figure 5.4: Vanadium oxide structures obtained during reactive evaporation as a function of V coverage. VO_x is deposited in a step-wise manner (1 min steps) at a sample temperature of 670 K in an oxygen atmosphere of 2×10^{-7} mbar. The LEED images are acquired at a start voltage of 65 eV after the sample is further heated in oxygen for 10 min and cooled down in continuous oxygen flow after every deposition step.

mainly by V uptake in the first oxide layer as proposed by Schoiswhl et al. [53], rather than by opening up a second layer on top of the existing one. Consequently, the V density increases upon further VO_x deposition, which explains the observed gradual reduction of V in the coverage range $0.6 \leq \theta_V \leq 1.0$ MLE. The wagon wheel structure, with a composition of VO and a formal oxidation state of +2 is thereby the last oxide structure in the first layer. Further V deposition leads to the nucleation and formation of three-dimensional V_2O_3 crystallites of a formal oxidation state of +3. The gradual increase of V density during the structural transitions may explain the missing change in slope in the AS-t plot at around 5 min. The observed kink at 10 min (about 1.0 MLE) coincides with the onset of three-dimensional oxide growth reported in [53].

5.2 VO_x redistribution during methanol oxidation in PEEM

The behavior of ultrathin vanadium oxide layers during methanol oxidation in the 10^{-4} mbar range has been described in references [68–70]. In this section details on the redistribution dynamics are shown, mainly obtained during PEEM experiments conducted at constant temperature and at variable gas phase composition. These results complement the findings described in [70, chapter 5.4.2].

In most of the preceding experiments, linear heating ramps have been applied under the conditions of catalytic methanol oxidation. Thus, the vanadium oxide redistribution pattern have been observed under transient experimental conditions. The observed pattern do not represent the equilibrium pattern, which could have been observed, if the temperature would have been kept constant for a reasonably long time. The term equilibrium is here not used in the sense of a thermodynamic equilibrium, since the system under investigation represents a dissipative system, which by definition is not a (and maybe even far from) thermodynamic equilibrium. Rather the stationary pattern that emerges after a sufficiently long time is termed “equilibrium pattern”. In the first part of this section, the transformation from a homogeneously vanadium oxide covered surface to the condensation into circular vanadium oxide islands via an intermediate pattern of VO_x stripes is described in detail. Here, the evolution of vanadium oxide stripes and VO_x islands at constant temperature is described, with a focus on the reversibility of the transition from stripes to islands. Furthermore, the influence of the gas phase composition on the redistribution patterns is studied.

5.2.1 The transition from a homogeneous VO_x film to islands

If a Rh(111) surface covered with a sub-monolayer coverage of VO_x ($\theta_V \leq 0.6$ MLE) is heated from room temperature to 1020 K in a gas atmosphere of methanol and oxygen in the 10^{-4} mbar range, a reaction induced-redistribution leads to the formation of macroscopic vanadium oxide stripes at around 800 to 900 K, which coalesce into vanadium oxide islands between 900 and 1020 K, depending on the ratio of methanol and oxygen [68–70]. In the following, in situ PEEM experiments conducted with two different gas phase compositions (“reducing reaction conditions”: $p(\text{CH}_3\text{OH}) = 3 \times 10^{-4}$ mbar,

$p(O_2) = 1 \times 10^{-4}$ mbar; “oxidizing reaction conditions”: $p(CH_3OH)$ is equal to $p(O_2) = 1 \times 10^{-4}$ mbar) are shown. Finally, pattern formation occurring with a large excess of oxygen is described.

Reducing and oxidizing reaction conditions

Figure 5.5 summarizes six experiments conducted with 0.1, 0.2, and 0.3 MLE of VO_x heated from 770 K to 1020 K under either oxidizing or reducing reaction conditions. The PEEM images in figure 5.5 reveal systematic trends in pattern evolution, as the VO_x coverage and the gas phase composition are varied. These trends are *i*) the width and density of the vanadium oxide stripes, that form in the initial stage change; *ii*) a reduced (in PEEM bright) phase inside the vanadium oxide structures appears; *iii*) the temperature at which the different stages of the redistribution occur varies; and *iv*) the transformation of the stripe pattern into an island pattern occurs, depending on the experimental parameters.

i) The width and density of the vanadium oxide stripes depends strongly on the vanadium oxide coverage. With increasing coverage the number of stripes is reduced in all stages of the ripening process. Simultaneously the average width of a single stripe increases, as seen by comparing the first PEEM images recorded at 875 K for the three different coverages under reducing reaction conditions. The same qualitative behavior is also seen for oxidative reaction conditions, but the overall width of the stripes developing under oxidizing reaction conditions is smaller compared to the stripe width obtained under reducing reaction conditions.

ii) As described in chapter 4, the formation of a reduced core inside of vanadium oxide structures can occur under reaction conditions, provided the methanol partial pressure is high enough and the oxide island radius is above a critical radius. This prerequisites are given in the case of the vanadium oxide stripes formed under reducing reaction conditions for 0.2 and 0.3 MLE at 875 K. A bright phase is seen in the thicker parts of the oxide stripes. Also under oxidizing reaction conditions, the formation of the reduced phase in the vanadium oxide structures can be observed. Starting at around 925 K, the nucleation of the reduced phase can be recognized by small, triangular shaped dark patches at the connection points of neighboring oxide stripes, as shown in the second PEEM image of the experiment conducted with 0.3 MLE VO_x . These dark patches are the boundary phase, which separates the reduced core from the oxidized outer phase. At 975 K, the nucleus has grown to an extended reduced core, which covers a large part of the oxide stripe. Similarly, for 0.2 MLE VO_x , a formation of a reduced core can be observed. The reduced core only nucleates in the last stage of the ripening process, in which the stripes coalesce into islands, thus increasing its width (or radius). This is seen in the last PEEM image of the experiment conducted with 0.2 MLE VO_x under oxidizing reaction conditions. In the experiment with 0.1 MLE VO_x , a large number of thin stripes, and later, small vanadium oxide islands is formed. In all stages of the ripening process, the radius is lower than the critical radius needed for the formation of the reduced phase. Consequently, the vanadium oxide structures comprise only a single oxidized VO_x phase.

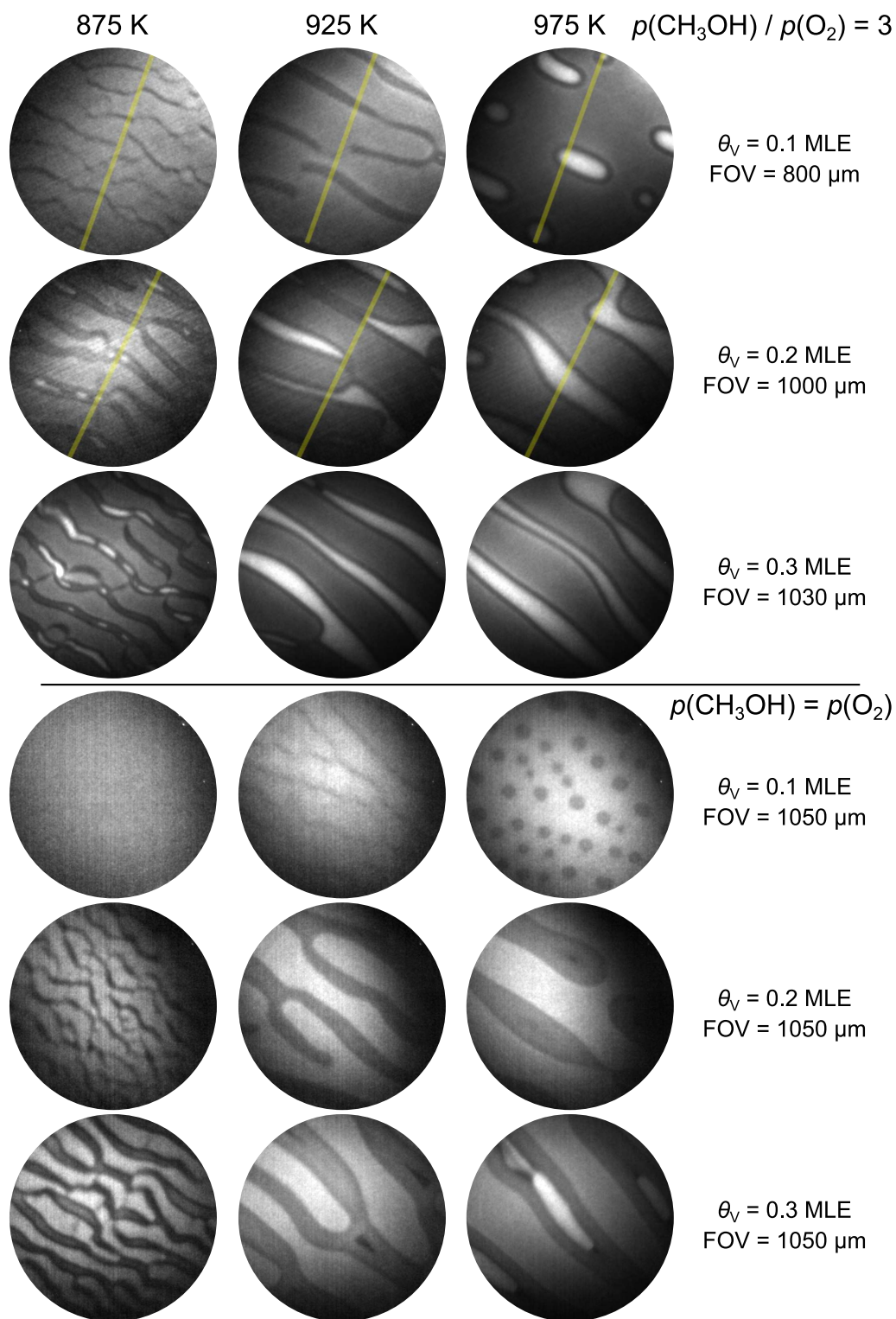


Figure 5.5: Redistribution of vanadium oxide during catalytic methanol oxidation as a function of VO_x coverage for oxidizing and reducing reaction conditions. For details please refer to the text.

iii) In general, it is difficult to exactly determine the onset temperature of the stripe formation. This has several reasons: With our PEEM system, the stripe formation can only be detected in an already advanced stage, when enough contrast is gained by a considerable separation into VO_x rich and depleted areas, and when these areas have grown to a certain size of at least a few μm diameter. The onset of stripe formation can be determined best in a set of $x(t)$ -plots shown in figure 5.6. The $x(t)$ -plots are constructed by taking line profiles from every experiment along the yellow solid lines in the first PEEM images of figure 5.5, and stacking them on top of each other.

The onset of pattern formation is found to occur at around 850, 825, and 810 K under reducing reaction conditions for a VO_x coverage of 0.1, 0.2, and 0.3 MLE, respectively. Under oxidizing reaction conditions, the stripe formation starts at 925, 850, and 840 K for a coverage of 0.1, 0.2, and 0.3 MLE, respectively. Clearly, reducing oxidation conditions lead to a stripe pattern formation at considerably lower temperature. In both sets of experiments, a shift towards lower temperature is observed for an increasing VO_x coverage.

iv) The formation of circular vanadium oxide islands. The temperature at which circular vanadium oxide islands are formed depends strongly on the vanadium oxide coverage. For a small coverage of 0.1 MLE vanadium oxide islands are already formed at around 975 K under reducing and oxidizing reaction conditions. At a higher coverage, the coalescence of neighboring oxide stripes leads to the formation of curved, elongated oxide structures, which do not reach a circular shape in the shown temperature range. These elongated oxide structures are transformed into circular oxide islands only after reaching 1020 K, or (in the case of 0.3 MLE) after prolonged exposure at 1020 K. The formation of circular islands proceeds either via a coalescence of neighboring stripes to thicker ones, or by a fragmentation of the elongated oxide structures into several more or less circular oxide islands. As long as the resulting islands have a size of less than approximately 500 μm diameter, they attain a nearly circular shape after a few minutes at 1020 K. The tendency to form circular islands indicates a strong line tension, since the interface VO_x - Rh(111) is minimized in this way. Islands larger than $\sim 500 \mu\text{m}$ do not reach a circular island size, even after several hours under reaction conditions at 1020 K.

Strongly oxidizing reaction conditions

A key question is that after a purely thermodynamic driving force for the formation of the stripe patterns and the circular islands. If these are dissipative structures generated for example by reactive phase separation, then these patterns should only form under reaction conditions. If a classic thermodynamic driving force exists, then these structures should form also in the presence of pure O_2 , i. e. without a chemical reaction. These questions are addressed in the following section.

Strongly oxidizing conditions (with a gas phase consisting only of oxygen in the limiting case) result in formation of circular vanadium oxide islands. The behavior of 0.2 MLE vanadium oxide during methanol oxidation strongly oxidizing reaction conditions is depicted in figure 5.7, together with PEEM images recorded on a surface covered

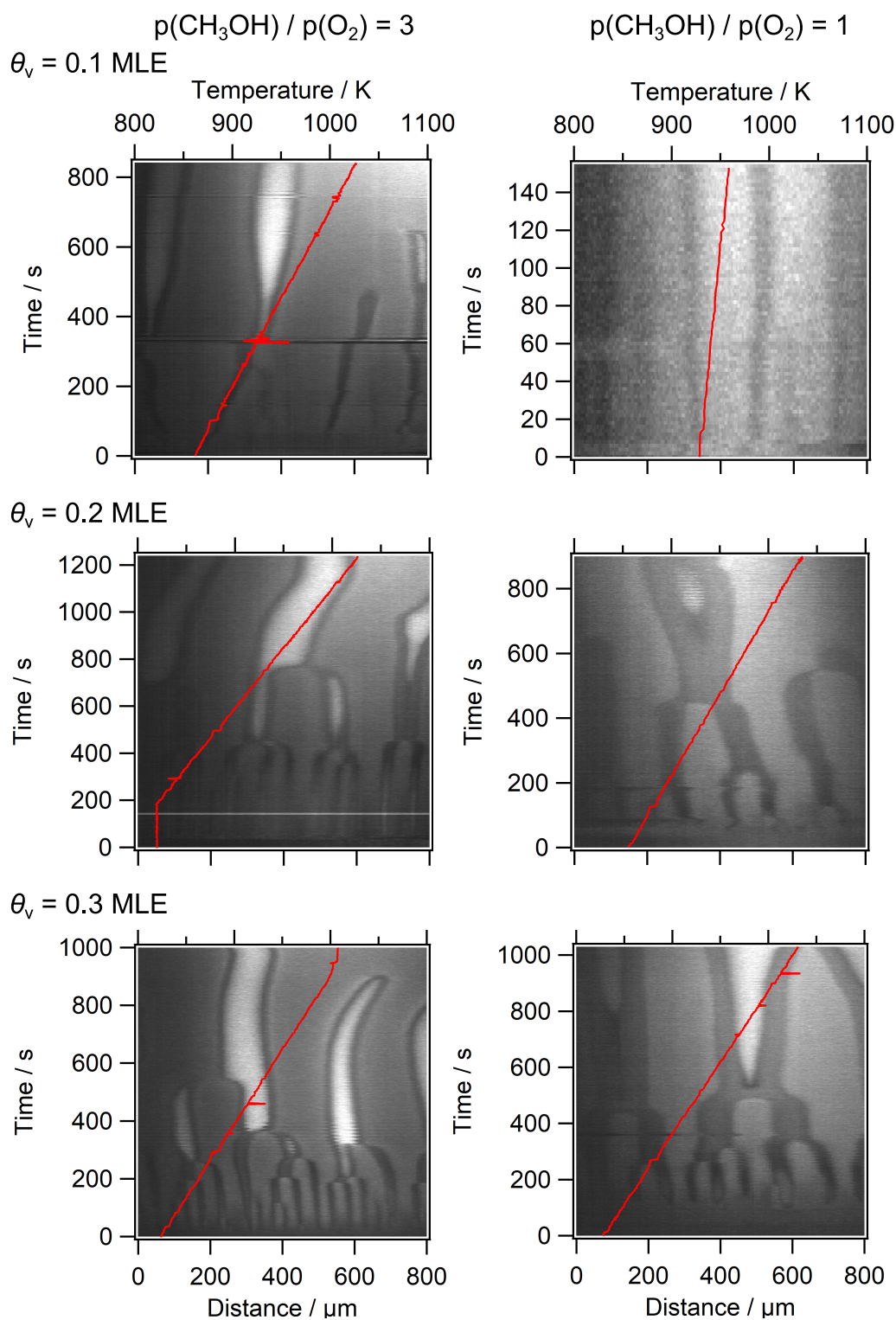


Figure 5.6: A series of $x(t)$ -plots showing the stripe pattern formation of ultrathin vanadium oxide films during catalytic methanol oxidation under reducing (left) or oxidizing (right) reaction conditions for a VO coverage of 0.1, 0.2, or 0.3 MLE. The substrate temperature is indicated by the solid red line (top axis). All samples are heated with a constant heating rate of 0.5 K s^{-1} . The line profiles are taken along the yellow lines in figure 5.5.

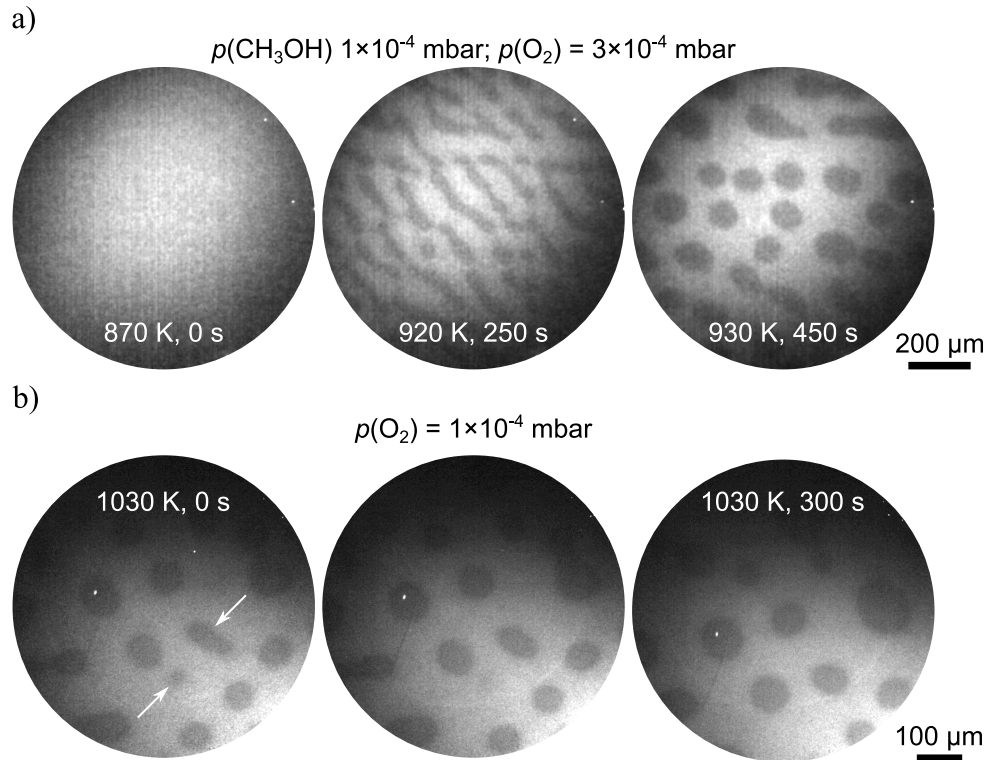


Figure 5.7: Vanadium oxide redistribution dynamics under strongly oxidizing conditions (1×10^{-4} mbar methanol and 3×10^{-4} mbar oxygen). a) A homogeneous VO_x film of 0.2 MLE coverage is transformed into a pattern of circular oxide islands via the formation of thin oxide stripes at a substrate temperature of 930 K. b) Vanadium oxide island formation in 1×10^{-4} mbar pure oxygen at 1020 K.

with 0.2 MLE, which is heated to 1020 K in pure oxygen.

Under strongly oxidizing conditions, the condensation of the homogeneous vanadium oxide film into a stripe pattern starts around 910 K. Right after the stripe formation was observed in PEEM, the heating ramp is stopped and the sample is kept at a constant temperature of 930 K. Quite fast, the stripes taper off and form circular, approximately 100 μm large oxide islands. These islands do not exhibit a reduced core.

A similar experiment conducted in 1×10^{-4} mbar oxygen is shown in figure 5.7 (b). A 0.2 MLE thick VO_x film is heated from room temperature to 1020 K. Starting at around 970 K, an island pattern evolves, as shown in the first image of the PEEM sequence. In contrast to the experiments conducted during methanol oxidation, no stripes are observed. However, due to the overall high work function in the temperature range from 400 - 970 K, the resulting lack of PEEM contrast could be responsible for the failure to observe a stripe pattern. Some interesting details of the oxide redistribution are seen in the three PEEM images shown in figure 5.7: some islands disappear, while other islands seem to coalesce at first sight, similar to the island coalescence observed during methanol

oxidation. The two white arrows in the first PEEM image highlight this behavior (the lower white arrow points to a disappearing island).

The small vanadium oxide island, indicated by the lower white arrow in the first image, is hardly visible in the second image and completely absent in the third image. The dissolution of vanadium oxide islands has already been observed during catalytic methanol oxidation under oxidizing and strongly oxidizing conditions [68,70]. It is therefore a different process than the coalescence seen during catalytic methanol oxidation. The islands do not move, but they evaporate¹. This finding can be interpreted as classical Ostwald ripening, in which small islands exhibit a higher vapor pressure than larger ones, leading to the growth of larger islands at the expense of smaller ones.

The coalescence of neighboring vanadium oxide islands in pure oxygen could not be imaged directly, but the temporal evolution of the shape of an elongated vanadium oxide island (indicted by the upper white arrow in the first image of figure 5.7), however, suggests such a coalescence event. The elliptical shape present in the first image transforms into a nearly circular shape in the third PEEM image, which is presumably the equilibrium shape obtained after the complete coalescence of two neighboring islands, which is not recorded. As explained in section 4.2, reaction-induced oxygen gradients are necessary for the coalescence of neighboring islands. The oxygen gradients may be caused by the high residual gas pressure apparent in the UHV chamber (2 to 3×10^{-8} mbar) after conducting experiments with methanol in the 10^{-4} mbar range. Another explanation for the elongated shape of the vanadium oxide island is that it can be caused by pinning at macroscopic surface defects.

The experiments conducted in pure oxygen indicate that the circular vanadium oxide island pattern is not a true non-equilibrium structure, since such a pattern also forms in the absence of a chemical reaction. The oxide redistribution and the mobility of vanadium oxide is greatly enhanced under reaction conditions. Therefore, reaction conditions might just facilitate the formation of such patterns without, however, being essential. The formation of circular vanadium oxide islands in pure oxygen can be understood by simple considerations about the energetics of an “homogeneous” VO_x film compared with macroscopic vanadium oxide islands. Since a vanadium oxide layer of 0.2 MLE consists only of half to a third of the ideal coverage of the $(\sqrt{7} \times \sqrt{7})R19.1^\circ$ structure, on a mesoscopic scale such a layer has to consist of a large number of small islands, which cannot be resolved with our PEEM. Macroscopically, the surface would occur homogeneous. However, such a morphology has a large interfacial region and is thus energetically unfavorable. By a condensation into macroscopic vanadium oxide islands, the interfacial region can be reduced. Thus a thermodynamic driving force for the coalescence of VO_x into macroscopic islands exists. Such a coalescence can only be observed at high temperature (around 1020 K) due to the low mobility at lower temperature.

¹The term evaporation refers to an equilibrium between vanadium oxide islands and a two-dimensional lattice gas of diffusing VO_x clusters, not to the evaporation of vanadium into the gas phase

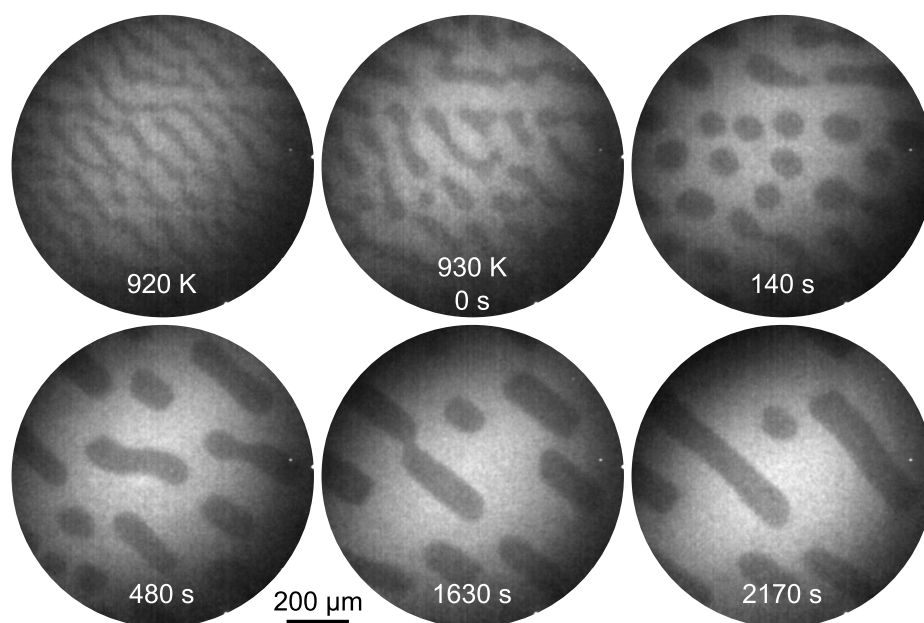


Figure 5.8: Stripe pattern evolution at a constant temperature of 930 K under strongly oxidizing reaction conditions. The linear heating ramp (0.2 K s^{-1}) is stopped at 930 K, the time in the PEEM images indicates the elapsed time at this temperature. The partial pressure of methanol and oxygen are 1×10^{-4} and 3×10^{-4} mbar, the vanadium oxide coverage is 0.2 MLE.

5.2.2 Evolution of VO_x pattern at constant temperature

Nearly all experiments that are described in this chapter so far are conducted by applying a heating ramp. This section describes the behavior of ultrathin vanadium oxide films under constant experimental conditions.

Dynamics following the interruption of the heating ramp schedule

The evolution of stripe patterns formed around 900 K is followed after stopping the heating ramp. A high partial pressure of oxygen is beneficial in a sense, that only a single vanadium oxide phase is stable, as long as the formed oxide structures do not exceed a size larger than several hundred micrometers. Also the length scale of the formed pattern is small, and the overall dynamics are quite slow, which greatly reduces problems connected to the field of view (limited to around 1 mm). In principle such experiments lead to comparable results also under oxidizing and reducing reaction conditions [70].

A series of PEEM images acquired during a heating ramp of 0.2 K s^{-1} and after the heating ramp is stopped at 930 K is shown in figure 5.8. Starting from around 900 K, the homogeneous surface state is lifted and the vanadium oxide layer is transformed into a stripe pattern. As the temperature ramp is stopped, the stripes coarsen, resulting

in a decrease in the stripe density and an increase of the average stripe thickness. After around 140 s, the merging of neighboring stripes leads to a spot pattern, consisting of circular islands. These islands can only be observed for a few minutes. This spot pattern is not stable and neighboring islands reconnect. Very large and thick stripes result. The ripening continues over a long time, and the number of stripes continuously decreases, while the length of the stripes increases. Interestingly, the width of the stripes is fairly uniform, whereas the length of the individual stripes varies. The stripe pattern formed around 900 K, thus, represents a kind of equilibrium pattern under these conditions. The formation of vanadium oxide islands only occurs after a certain reaction-condition-dependent threshold temperature is exceeded.

If a pattern is a stable structure in a certain parameter range, then it should form irrespective of how this region in parameter space is reached. In order to study whether this stripe pattern can be formed not only from a homogeneous vanadium oxide film, but also starting from a spot pattern consisting of large vanadium oxide islands, the sample is further heated (0.2 K s^{-1}) to 1030 K, and kept at this temperature for around 1000 s. The corresponding PEEM images are depicted in figure 5.9.

Soon after the linear heating ramp was started, the vanadium oxide stripes start to contract at around 960 K, resulting in an oval shape at 1000 K. The islands become circular even before the final temperature of 1030 K is reached. Besides a slight drift of the whole sample, due to the temperature change, no significant changes of the PEEM images are detected during the roughly 1000 s at 1030 K. The circular oxide islands represent the equilibrium pattern at this temperature under strongly oxidizing conditions.

Interestingly, the subsequent cool-down (0.2 K s^{-1}) to the initial temperature of 630 K reestablishes the original stripe pattern with surprising conformity. The transition from a stripe to an island pattern is fully reversible, and the resulting pattern only depends on the reaction conditions, but not on how these conditions are established. The complete reversibility imposes constraints to ex situ experiments, since obviously the local distribution and probably also the chemical composition of the surface under certain reaction conditions can not be preserved at room temperature and in vacuum.

A similar experiment is conducted with a higher methanol to oxygen ratio. The results are depicted in figure 5.10. In this case, pattern formation is additionally characterized by at least two different, coexisting vanadium oxide phases within a VO_x stripe or island. Therefore a $VO_x/\text{Rh}(111)$ surface of 0.1 MLE V coverage is heated to 1020 K under reducing reaction conditions and the formation of circular vanadium oxide islands is observed. The low vanadium oxide coverage and a sufficiently long time at 1020 K ensure the presence of small, largely separated oxide islands. In this way, the transition from the island pattern back to the stripe pattern can be observed, without disturbances due to island coalescence.

The first PEEM image in figure 5.10 shows such an isolated vanadium oxide island, after the methanol partial pressure was reduced from 3×10^{-4} to 2×10^{-4} mbar, while keeping the oxygen pressure constant at 1×10^{-4} mbar. Subsequently a cooling ramp (0.2 K s^{-1}) is started, and the change of the vanadium oxide island is followed with PEEM. Already at 890 K, an elongation of the island occurs. This elongation continues

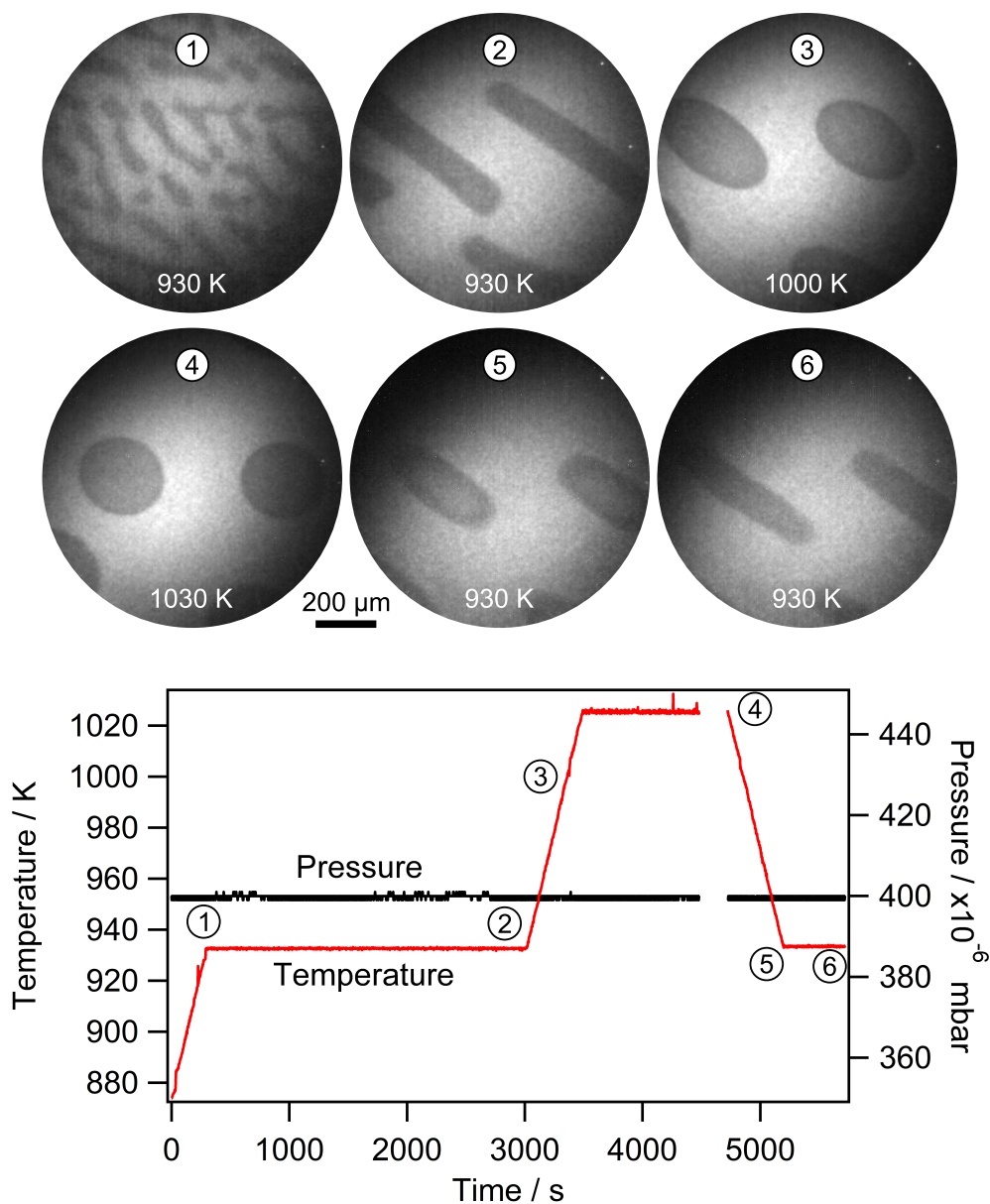


Figure 5.9: PEEM images and temporal evolution of the substrate temperature and total pressure demonstrating the reversibility of the oxide stripe - oxide island transition upon change of the reaction conditions. The stripe pattern formed at 930 K is transformed into an island pattern at 1030 K, and recovers if the temperature is lowered again. The partial pressures of methanol and oxygen are 1×10^{-4} and 3×10^{-4} mbar, the vanadium oxide coverage is 0.2 MLE.

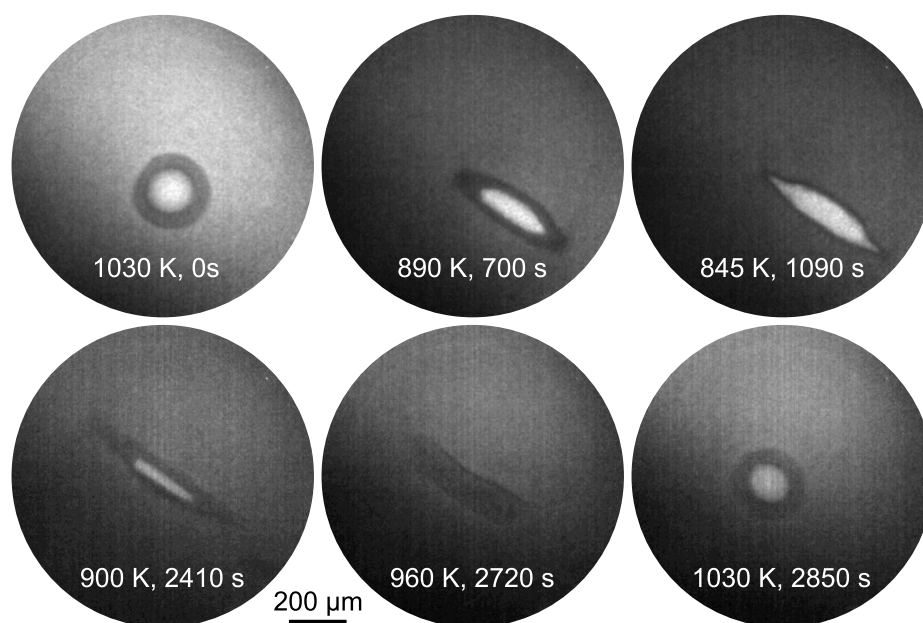


Figure 5.10: PEEM images showing a reversible stripe - island transition under reducing reaction conditions. In the first three images, the temperature is decreased from 1030 to 845 K with a rate of 0.2 K s^{-1} . Subsequently, the temperature is kept constant for 1000s before the temperature is increased again to 1030 K with the same rate.

until shortly before the heating ramp stops at 845 K. The final island shape visible in the third PEEM image of figure 5.10 does not change, even after 1000 s at constant temperature.

If a heating ramp is started again to reach 1030 K, a further elongation of the oxide island is observed starting from around 870 K. The reduced thickness of the island, which now may be better described as a stripe, leads to an oxidation of the reduced core. Finally, at 960 K, the whole VO_x stripe is oxidized, as shown in the fourth image in figure 5.10. Upon further temperature increase, the oxide stripe contracts and forms a circular island again, before 1000 K are reached. The reduced oxide phase nucleates again in the center of the vanadium oxide island, as soon as the width exceeds the critical radius for the existence of a reduced core.

Dynamics at 1020 K

Figures 5.11 and 5.12 show PEEM images acquired after a linear heating ramp was stopped at 1020 K under reducing reaction conditions on surfaces covered with 0.1 and 0.2 MLE VO_x , respectively. The main difference between this two experiments is that the low coverage oxide film forms circular vanadium oxide islands already below 1000 K, whereas the thicker oxide film is still in the stripe stage of the coarsening process after the heating ramp is finished. Another difference is the smaller diameter of the oxide

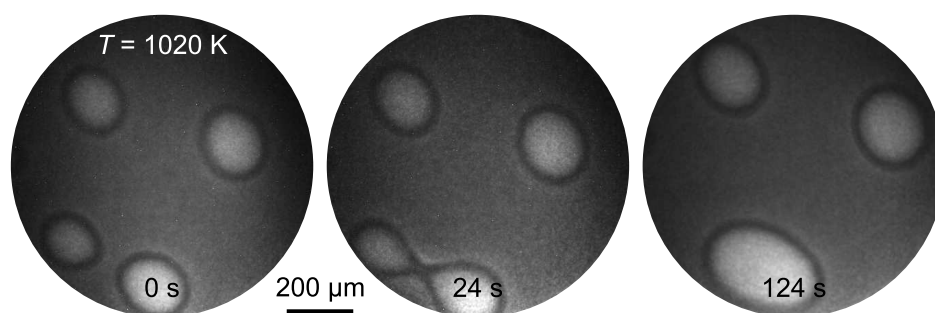


Figure 5.11: PEEM images showing the vanadium oxide island formation during catalytic methanol oxidation at a constant temperature of 1020 K with 0.1 MLE VO_x under reducing reaction conditions. The time in the images represents the time since a linear heating ramp (0.2 K s^{-1}) was interrupted at 1020 K.

islands in the experiment with only 0.1 MLE.

In figure 5.11, the approach of two neighboring islands and the subsequent coalescence is seen in the lower part of the three PEEM images. The resulting, large oxide island has a slightly deformed, elliptical shape. For smaller islands this elliptic shape slowly transforms into a circular shape again, if no other islands are within a critical distance of 100 to 200 μm . Larger islands (with a diameter typically above 200 to 300 μm , depending on the reaction conditions) retain such a deformed shape, even after hours of exposure to reaction conditions.

The PEEM images in figure 5.12 still exhibit a stripe pattern as a metastable structure up to about 400 s at 1020 K. A tapering and subsequent separation of the stripes, starting at the thinner parts, finally leads to the formation of an oval, large island at around 800 s. In the course of the experiment, the island continuously changes its shape, without becoming circular again.

In general, smaller vanadium oxide coverages and more oxidizing reaction conditions lead to the formation of circular and small oxide islands. With increasing vanadium oxide coverage, and more reducing reaction conditions, the islands become larger. Starting on freshly deposited VO_x films of a coverage around 0.3 to 0.4 MLE under reducing reaction conditions, a stripe pattern is still present after long exposure to reaction conditions at 1020 K. Large irregularly shaped vanadium oxide areas form instead of circular islands. These irregularly shaped areas do not approach an equilibrium shape, but continuously grow, coalesce and separate over a period of several hours. For a small coverage below approximately 0.2 MLE, the circular vanadium oxide islands can be seen as a kind of equilibrium structure, which can be observed for periods of several minutes to hours, as long as island coalescences have led to a large enough distance between all individual islands.

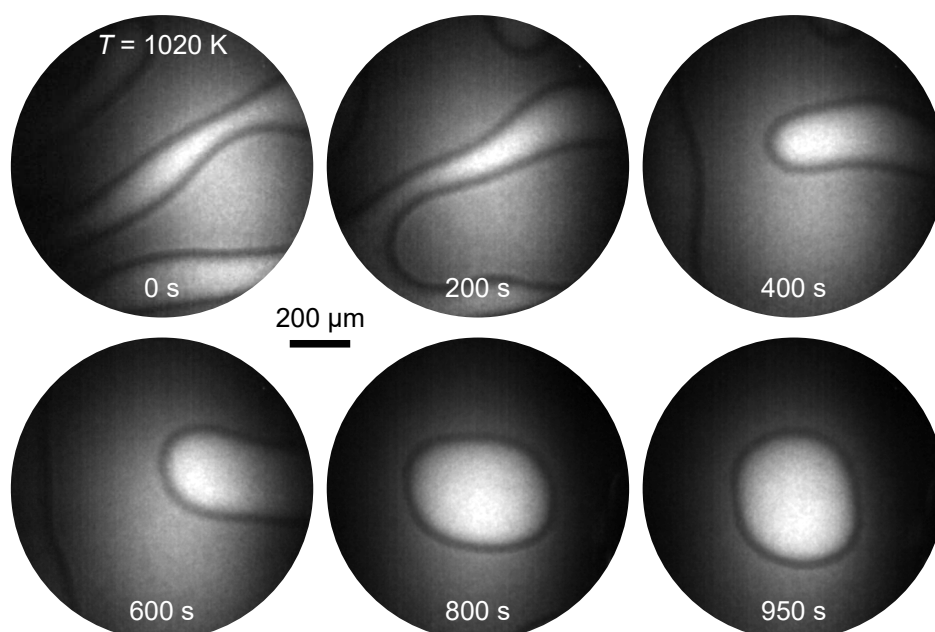


Figure 5.12: Vanadium oxide island formation at 1020 K with 0.2 MLE VO_x under reducing reaction conditions. The time in the images represents the time elapsed since a linear heating ramp (0.2 K min^{-1}) was interrupted at 1020 K.

5.2.3 Dependence of the VO_x island substructure on the gas phase composition

So far, an island substructure consisting of an oxidized rim and a reduced core has only been observed on either thin oxide stripes or on large oxide islands. The first SPELEEM measurements on the system $\text{CH}_3 + \text{O}_2/\text{VO}_x/\text{Rh}(111)$ already showed the existence of a third, a few micrometer thin boundary phase, which separates the reduced core from the oxidized ring [69, 70]. This thin boundary layer appears in most PEEM images as a thin, dark band between oxidized ring and reduced core.

Vanadium is known for a structural variety of its two- and three-dimensional oxides, and its ability to easily switch the oxidation state between +2 and +5. In order to check if this structural and chemical variability is reflected in an even larger number of coexisting oxide phases, the methanol partial pressure is varied systematically at different substrate temperatures and fixed oxygen partial pressure. The first experiment is conducted at constant 1030 K with a vanadium oxide layer of 0.1 MLE coverage. An $x(t)$ -plot taken across an approximately $250 \mu\text{m}$ wide island, together with two PEEM images of the island is shown in figure 5.13.

A close inspection of the $x(t)$ -plot reveals two characteristics of the vanadium oxide islands. Firstly, at a temperature of 1030 K only the three already known VO_x phases can be observed, the ring, the core and the thin boundary separating the two. Secondly, upon methanol pressure increase, the whole island slightly contracts, with the largest

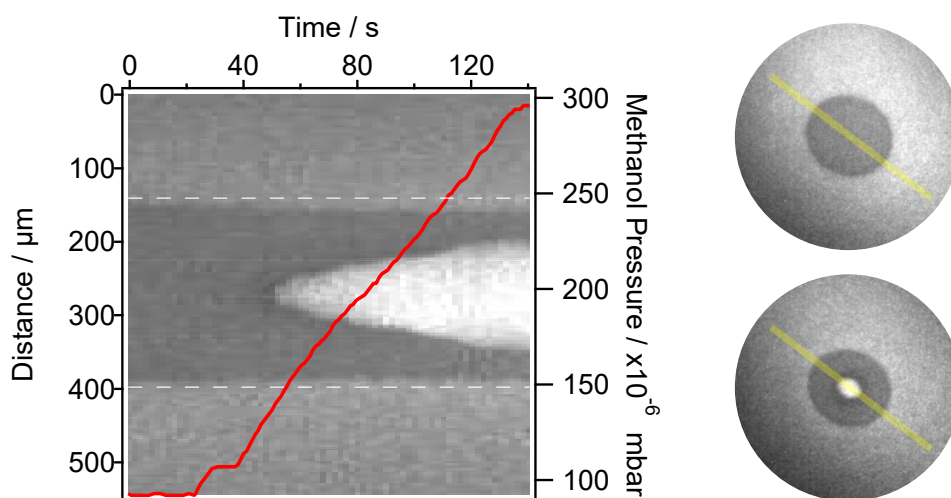


Figure 5.13: Methanol pressure dependent existence of the reduced VO_x island core observed at 1030 K during catalytic methanol oxidation on 0.1 MLE $VO_x/Rh(111)$. The $x(t)$ -plot on the left side of the figure shows intensity line profiles taken on PEEM images across the yellow line in the two PEEM images on the right side. The methanol partial pressure is indicated in the plot as a solid red line (right abscissa), the oxygen pressure is kept constant at 1×10^{-4} mbar. Two white lines are added as a reference for the readers eye in the $x(t)$ -plot.

size-change happening, when the bright phase nucleates in the island center. As a reference for the readers eye, the $VO_x / Rh(111)$ interface position at the beginning of the experiment is highlighted in the $x(t)$ -plot by two dashed white lines.

The contraction of the vanadium oxide island can easily be understood by considering, that the vanadium density of most reduced phases is higher than the V density of the oxidized phases [53, 55]. If the number of vanadium atoms in the oxide islands is conserved, a reduction of the oxide island core requires the transport of V atoms from the outer parts of the island into the center.

Similar experiments are conducted at 1000 and 970 K with a number of vanadium oxide islands of different size. The results are displayed in figure 5.14, which comprises $x(t)$ -plots and PEEM images of three vanadium oxide islands obtained by first heating 0.2 MLE VO_x to 1020 K under reducing reaction conditions, and then cooling the sample down to 970 K. The methanol partial pressure is first reduced to 1×10^{-5} mbar, resulting in a completely oxidized VO_x island. Subsequently, the methanol partial pressure is increased in steps of 1×10^{-5} mbar approximately every 2 min. The nucleation and growth of reduced vanadium oxide phases is followed in PEEM, while keeping the oxygen pressure constant at 1×10^{-4} mbar. With this procedure a surface consisting of a small number of widely separated vanadium oxide islands is obtained.

In figure 5.14 three oxide islands of different size are shown. As the methanol pressure is increased under constant conditions (970 K and 1×10^{-4} mbar oxygen), the nucleation

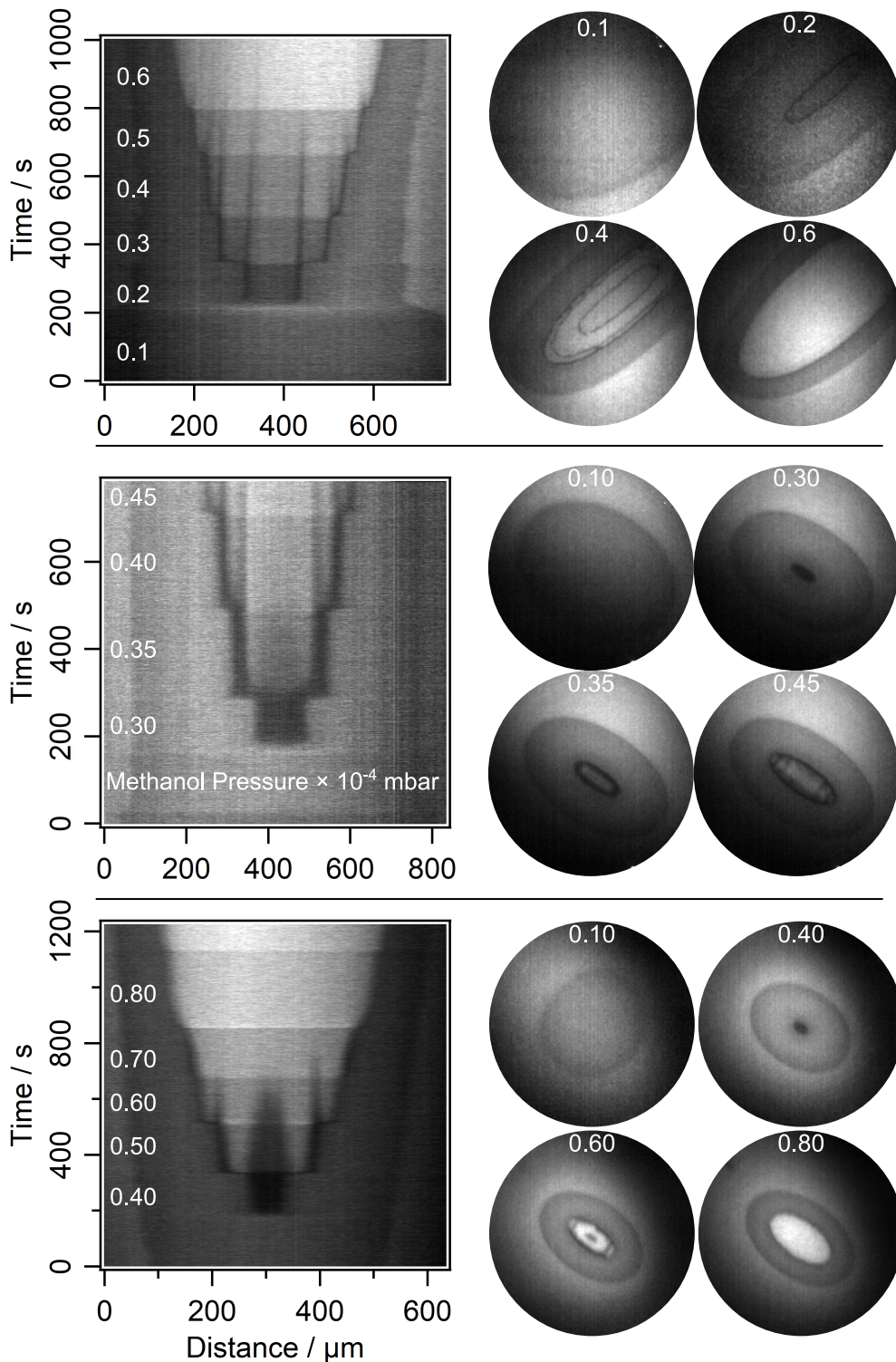


Figure 5.14: PEEM images showing the formation of different vanadium oxide phases within a VO_x island upon methanol pressure increase. Left: $x(t)$ -plots taken along the short (top experiment) and long axis (middle and bottom experiment) of elliptical oxide islands. The methanol partial pressure is indicated in the plots in units of 10^{-4} mbar. Right: Corresponding PEEM images, with the methanol pressure indicated in 10^{-4} mbar, showing different stages during the methanol pressure increase. The island size is 0.7 mm^2 (top), 0.25 mm^2 (middle), and 0.15 mm^2 (bottom). The field of view is $1100 \mu\text{m}$ (top), and $970 \mu\text{m}$ (middle and bottom), the oxygen pressure and temperature are 1×10^{-4} mbar and 970 K , respectively.

of up to four vanadium oxide phases separated by thin, dark boundary phases can be observed. In the third PEEM image in the top panel of figure 5.14, the different vanadium oxide phases show up as concentric rings of decreasing PEEM intensity. The highest PEEM intensity is observed in the center of the oxide island, whereas the lowest PEEM intensity is detected on the outermost VO_x phase. If the methanol pressure exceeds a certain threshold, which depends strongly on the vanadium oxide island size, the dark boundary phases disappear and the VO_x islands consist only of a single reduced core and an oxidized ring.

The three $x(t)$ -plots in the top, middle and bottom panel demonstrate that the methanol partial pressure at which the first reduced VO_x phase nucleates increases with decreasing island size. On the 0.7 mm^2 island (top panel), the nucleation of the first reduced phase proceeds already at a methanol pressure of 0.2×10^{-4} mbar, whereas 0.3 and 0.4×10^{-4} mbar are needed for nucleation of the reduced phase on the 0.25 and 0.15 mm^2 large islands, respectively. For nearly circular VO_x islands, the formation of the reduced VO_x phases leads to an oxide island consisting of four concentric rings. In case of an elliptical VO_x island, the four different vanadium oxide phases can only be observed along the long axis.

The occurrence of several different VO_x phases within a single vanadium oxide island is apparently a consequence of the development of macroscopic oxygen gradients under the conditions of methanol oxidation. The vanadium oxide islands act as “catalytic micro-reactors”, which consume oxygen. Due to the low sticking coefficient of oxygen on the vanadium oxide covered surface, adsorbed O atoms needed for the oxidation reaction are supplied by diffusion from the Rh(111) surface surrounding the oxide islands. Since oxygen is supplied only from the boundaries of the islands, but is consumed in the interior of the island, a gradient in the oxygen concentration develops under reaction conditions. A cross-section through an oxide island corresponds to a decrease in the chemical potential of oxygen μ_O , and should therefore represent a cross-section (isotherm) through the phase diagram of the system $VO_x/\text{Rh}(111)$ if one of the axes in the phase diagram is the chemical potential of oxygen. Such a phase diagram has been constructed with quantum chemical methods by C. Penschke, X. Li, J. Paier and J. Sauer. It will be introduced in section 5.3.3.

5.2.4 Summary of the PEEM experiments

In the preceding sections a detailed investigation of VO_x pattern formation is given. The methanol partial pressure, the temperature and the vanadium oxide coverage is varied systematically in order to decipher the influence of these parameters on the redistribution patterns.

The methanol partial pressure affects the temperature at which a condensation of the initially homogeneous VO_x film into macroscopic stripes sets in. An increasing methanol partial pressure decreases the onset temperature of pattern formation. A higher methanol partial pressure also leads to wider VO_x stripes and larger VO_x islands. Also the tendency to form an inner reduced core is increased with higher methanol partial pressures. In general island ripening proceeds via coalescence of neighboring

islands. However, also the “evaporation” of smaller islands is observed for low methanol partial pressures, e.g. under more oxidizing conditions. This latter behavior is known as Ostwald ripening.

A higher vanadium oxide coverage has a similar effect as an increased methanol partial pressure. The onset temperature for pattern formation is reduced by a higher VO_x coverage, and the width of VO_x stripes and islands increases. The shape of vanadium oxide islands differs more and more from a circular shape with increasing VO_x coverage. Pattern formation finally completely vanishes upon deposition of ≈ 0.6 MLE. The 0.6 MLE VO_x suffice to form a closed oxide layer of $(\sqrt{7} \times \sqrt{7})R19.1^\circ$, thus preventing pattern formation.

The gas phase composition has a large influence on the composition and substructure of the vanadium oxide islands and stripes. A high methanol partial pressure favors the nucleation and growth of a reduced VO_x phase in the center of the vanadium oxide islands or VO_x stripes. The existence of a reduced phase is attributed to oxygen gradients surrounding the vanadium oxide structures, but also existing in the interior of the islands / stripes. A high reaction rate causes strong oxygen gradients and therefore favors the formation of a reduced core in the oxide stripes and islands. At a temperature of 970 K up to four different vanadium oxide phases, separated by thin boundary phases, can be observed within a single island. The formation of different oxide phases upon methanol pressure variation is fully reversible.

5.3 VO_x redistribution during methanol oxidation in LEEM

Since contrast in PEEM is mainly generated by local variations of the work function, an identification of the different VO_x phases is only possible with methods which provide structural and/or chemical contrast like LEEM and SPELEEM. For this reason further experiments have been carried out at the University of Bremen in the group of J. Falta. Taking diffraction images from a small area of 5 μm diameter (μLEED) allows in principle an assignment of vanadium oxide structures to the different grey levels in PEEM. Additionally, the superior spatial resolution of LEEM enables to reveal details of vanadium oxide redistribution dynamics under reaction conditions up to a pressure in the 10^{-4} mbar range.

5.3.1 VO_x stripe pattern formation

The behavior of circular vanadium oxide islands during methanol oxidation has been investigated in a preceding SPELEEM study in the 10^{-6} mbar range [70]. In contrast to the here presented results, vanadium oxide islands have been grown in the 10^{-4} mbar range, without the possibility to follow the oxide redistribution in situ. However, with the LEEM microscope located at the University of Bremen, in situ measurements up to a pressure in the low 10^{-4} mbar are possible, and thus the complete reaction-induced redistribution process can be followed with LEED and LEEM in situ.

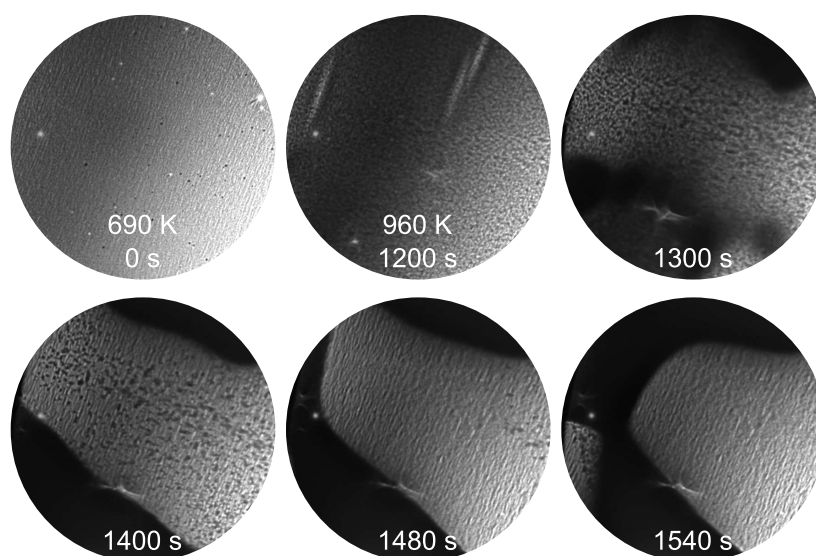


Figure 5.15: LEEM images showing the reaction-induced condensation of a homogeneous vanadium oxide film into macroscopic VO_x stripes. The $\text{VO}_x/\text{Rh}(111)$ surface ($\theta_V = 0.3$ MLE) is heated in the reaction gas atmosphere from room temperature to 960 K. Dark area is VO_x covered surface. The field of view is $50\ \mu\text{m}$ and the images are acquired at a start voltage of 2 eV.

Stripe formation is observed during a temperature ramp in a gas atmosphere consisting of 1×10^{-4} mbar methanol and 1×10^{-4} mbar oxygen, as depicted in figure 5.15. The first LEEM image shows the homogeneous $\text{VO}_x/\text{Rh}(111)$ surface as prepared after the sample was heated to 690 K. The initial VO_x coverage is 0.3 MLE, and LEED displays a $(\sqrt{7} \times \sqrt{7})R19.1^\circ$ structure after VO_x deposition. Up to 690 K no changes of the surface morphology are observed in LEEM in a field of view of $50\ \mu\text{m}$. Despite some surface defects, showing up as small dark or bright spots, the LEEM image is dominated by a large number of parallel step bunches, which run from the lower left to the upper right corner of the sample. These step bunches result from a slight (and unavoidable) miss-cut during preparation of the (111) oriented surface. These step bunches are responsible for the orientation of the macroscopic stripe pattern observable during methanol oxidation in PEEM experiments presented in section 5.2.1, as will be shown in the following.

As the sample is further heated, the homogeneous surface state is lifted and a condensation of vanadium oxide into a large number of equally spaced small islands sets in at around 750 K. Starting at around 900 K, large areas covered with a dense vanadium oxide phase form. At the chosen start voltage, vanadium oxide has a low LEEM intensity, whereas the surrounding Rh(111) surface appears as bright area. Initially, the interface between the large vanadium oxide covered areas and the Rh surface is diffuse. As the temperature is increased to 960 K, the VO_x covered regions become denser. The interface sharpens and the LEEM intensity decreases over roughly 300 s, as demonstrated in the second to fourth LEEM image in figure 5.15.

Besides ripening of the large VO_x islands, also a growth of the homogeneously spread, small vanadium oxide islands can be observed. The average size of these “micro-islands” increases, whereas their number continuously decreases. Starting from around 1350 s after 960 K is reached, the disappearance of the micro-islands in the vicinity of the larger VO_x covered regions indicates a diffusional transport of vanadium from the smaller crystallites to the extended VO_x areas. This transport continues until after ≈ 1500 s nearly all VO_x micro-islands have vanished completely. This clearly indicates an Ostwald-like ripening process during formation of the vanadium oxide stripes. Initially, nanoscopic VO_x islands grow homogeneously on the surface until a small number of these islands become large enough to finally grow into macroscopic VO_x stripes. The smaller islands initially continue to grow until they dissolve presumably into mobile VO_x clusters. The clusters condensate as the macroscopic VO_x stripes become larger and larger. The result is a nearly complete phase separation into bare Rh surface and VO_x stripes.

The last three images of figure 5.15 show that the macroscopic vanadium oxide stripes that form under reaction conditions around 700 - 800 K are not stationary structures but dynamic, forming and breaking connections over a long time. Finally they reach a quasi-stationary pattern of parallel stripes. Some details in the dynamics can be seen in the last three LEEM images in figure 5.15. In these images a connection between the upper and lower dark vanadium oxide stripe moves into the field of view from the left side. In contrast to the leading front of the moving VO_x stripe, which exhibits a sharp interface, many small dark spots surround the backside, as can be seen in the last LEEM image. A large number of small VO_x micro-islands evolves on the whole area passed by the macroscopic VO_x stripe. This indicates that a fraction the VO_x gets pinned to surface defects or step bunches. These micro-islands dissolve quickly presumably into small clusters, which cannot be resolved in LEEM. Most of the VO_x stripes are oriented perpendicular to the step bunches of the Rh(111) surface. The same behavior has been observed by Lovis et al. in a SPELEEM study conducted on ultrathin vanadium oxide films on Rh(111) during the $\text{H}_2 + \text{O}_2$ reaction in the 10^{-6} mbar range around 750 K. A step-flow mechanism of VO_x has been discussed as a possible reason for the preferential orientation of the macroscopic VO_x stripes [202].

Figure 5.16a shows a large LEEM image composed of several images². Two neighboring VO_x stripes can be seen, which just have formed a connection. The image is acquired after the sample was cooled down from 920 K, where the stripes have formed, to 820 K, where the stripes are less mobile. In this way, the coalescence of the two stripes is frozen. As a consequence of the temperature decrease, the initially sharp boundary of the vanadium oxide islands becomes fuzzy. Many excursions along the step bunches of the Rh surface occur, as shown in the first LEEM image of figure 5.16b, (area highlighted by a red circle in a). Besides a growth of the vanadium oxide stripes in the direction of the step bunches, also a morphological change of the island interior is observed. The initially homogeneous surface split up into areas of two different grey levels. These two

²The LEEM images presented in this chapter are all acquired on the same single crystal, however the large scale images composed of many single images are rotated slightly in order to fit better into the page layout.

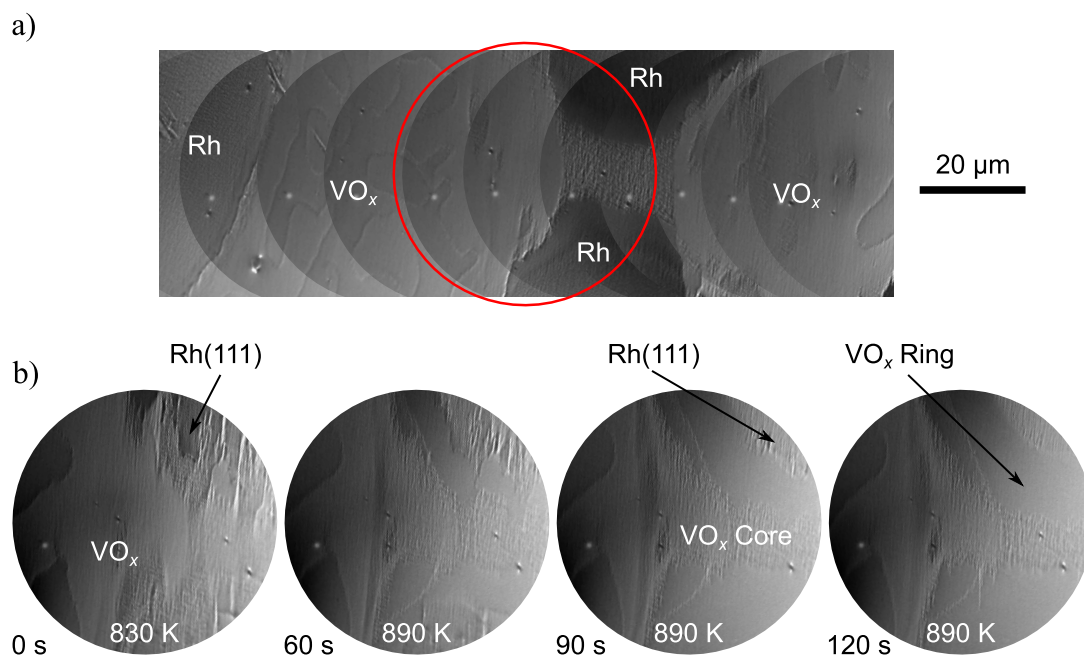


Figure 5.16: Sharpening of the $\text{VO}_x/\text{Rh}(111)$ interface upon temperature increase. a) Large LEEM image composed of several images, showing two neighboring vanadium oxide stripes, which have formed a connection to each other. The images are acquired at 820 K with a start voltage of 1.4 eV. b) Series of LEEM images acquired at 2.2 eV, showing the connection between the two VO_x stripes (highlighted by a red circle in a)) during a temperature increase of 70 K. The time elapsed since the heat-up was started, the temperature, and labels identifying the different surface areas are stated in the images.

phenomena clearly demonstrate, that a simple freezing of vanadium oxide structures by simply cooling the sample down is accompanied by drastic morphological changes on the meso-scale, which cannot be resolved clearly in PEEM.

Interestingly, the fraying of the interface upon temperature decrease is fully reversible, as demonstrated in figure 5.16b. The series of LEEM images is acquired during a temperature increase by 70 K. Within two minutes, the interface between the vanadium oxide covered area and the $\text{Rh}(111)$ surface becomes sharp again, and needle like VO_x excursions extending into the surrounding Rh surface disappear completely. Furthermore also the inner parts of the vanadium oxide covered areas are homogenized. A substructure consisting of an oxidized ring and a core known from PEEM experiments becomes visible.

An enlarged view of such a VO_x stripe consisting of a reduced core and an oxidized outer rim is depicted in figure 5.17, which comprises a large-area LEEM image composed of several images. The macroscopic VO_x stripe is oriented perpendicular to the step bunches of the $\text{Rh}(111)$ surface. A sharp interface separates the surrounding Rh

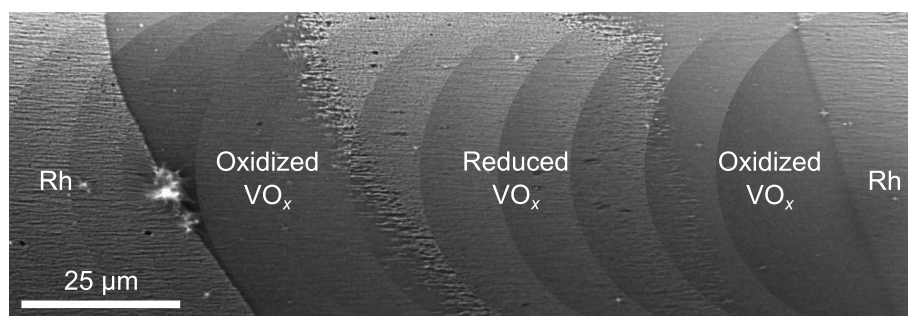


Figure 5.17: Large scale LEEM image of a VO_x stripe. The image is composed of several images. The VO_x substructure consists of a reduced and an oxidized ring. The LEEM images are acquired at 990 K with a start voltage of 1.2 eV in a gas atmosphere consisting of 1×10^{-4} mbar methanol and 1×10^{-4} mbar oxygen. The image is rotated by roughly 90° with respect to the orientation in figure 5.16.

surface from the VO_x covered area. The outer oxidized VO_x phase is characterized by a homogeneous, low LEEM intensity. Quite in contrast to the homogeneous appearance of the outer, oxidized VO_x phase is the inner, reduced area.

A fuzzy interface separates the outer and inner parts of the VO_x stripe, which seems to consist of a large number of small crystallites oriented along the step bunches. Interestingly no boundary phase can be identified in the LEEM image shown in figure 5.17. Instead the crystallite density increases over an area of about $3 \mu\text{m}$ until a more or less homogeneously bright area forms. This bright area is interrupted by dark surface defects and clearly exhibits parallel features associated to the step bunches on the surface.

5.3.2 In situ LEED analysis

The identification of the different vanadium oxide phases appearing under reaction conditions is important for deciphering the mechanism of VO_x pattern formation in catalytic methanol oxidation. An ex situ characterization of the same system has already been performed with conventional LEED [70]. In these experiments, freshly prepared vanadium oxide films have been successively heated to higher temperature under oxidizing methanol oxidation conditions in the 10^{-4} mbar range until finally 1020 K have been reached. After every heating step, the sample was cooled down fast to room temperature in a continuous gas flow. LEED images have been acquired afterwards in vacuum. For the coverage range up to 0.3 MLE, after heating to 1020 K a $(\sqrt{13} \times \sqrt{13})R13.8^\circ$ has been obtained (0.2 K s^{-1}). As an intermediate structure occurring after the sample has been heated to 793 - 828 K a Moiré pattern is reported. Both LEED images additionally showed a (2×2) pattern caused by chemisorbed oxygen on the bare Rh surface.

The mentioned LEED study has two limitations: i) structural transitions may have occurred during the cool-down of the sample; ii) a conventional LEED apparatus integrates over a large area, given by the electron beam diameter of several tens to hundreds of micrometers. VO_x covered parts and bare Rh surface are probed simultaneously.

Clearly a structural identification of the different coexisting VO_x phases that usually form under the applied reaction conditions is not possible.

Therefore an in situ LEED experiment has been performed at 900 K with SPELEEM at the Nanospectroscopy beamline (Elettra) [70]. There macroscopic vanadium oxide islands, that exhibited the substructure consisting of a reduced core and an oxidized ring, have been prepared in the 10^{-4} mbar range and were characterized in the 10^{-6} mbar range during methanol oxidation with varying partial pressures. Depending on the gas phase composition the oxidized ring and the reduced core displayed either a clean (1×1) LEED pattern or a (1×1) with faint diffraction spots belonging to a $(\sqrt{3} \times 3)R30^\circ$ Moiré. A few micrometer thin boundary layer, which separated the oxidized ring and the reduced core, displayed either a (12×12) Moiré pattern or a $(\sqrt{3} \times 3)R30^\circ$ Moiré pattern, depending on the gas phase composition.

LEED during formation of a stripe pattern

In this study, the use of the LEEM microscope located at the University of Bremen enables us to perform μ LEED in situ in the 10^{-4} mbar range during catalytic methanol oxidation. LEED images are acquired of an area of 5 μm diameter during vanadium oxide stripe formation, and on circular vanadium oxide islands. However, the redistribution dynamics of VO_x and experimental problems related to charging in the microscopes electron analyzer, as well as sample drift due to the applied high temperature rendered the experiment quite difficult. This is, for example, reflected by strongly distorted LEED images (charging in the analyzer) and the impossibility to acquire LEED- $I(V)$ measurements.

LEED images acquired during the formation of macroscopic vanadium oxide stripes are depicted in figure 5.18a and b, together with simulated diffraction pattern in c. The LEED images shown in figure 5.18a and b are taken from an LEED- $I(V)$ stack recorded on an evolving vanadium oxide stripe. Besides the integral order diffraction spots (highlighted by black circles), intense spots of the $(\sqrt{7} \times \sqrt{7})R19.1^\circ$ structure and some additional faint spots approximately at the $(2\sqrt{3} \times 2\sqrt{3})R30^\circ$ positions, better seen in the second LEED image acquired at 24 eV. Interestingly, the $(2\sqrt{3} \times 2\sqrt{3})R30^\circ$ diffraction pattern disappears within a few minutes without a parameter change and faint spots of a $(\sqrt{3} \times \sqrt{3})R30^\circ$ Moiré pattern develop additionally to the $(\sqrt{7} \times \sqrt{7})R19.1^\circ$ LEED pattern, as shown in figure 5.18b.

Figure 5.18c displays three representations of the LEED pattern depicted in figure 5.18a. The integral order diffraction spots are given as black circles, whereas the diffraction spots belonging to the $(2\sqrt{3} \times 2\sqrt{3})R30^\circ$ and $(\sqrt{7} \times \sqrt{7})R19.1^\circ$ structures are represented by green circles and blue squares, respectively. The first LEED image has the diffraction spots located at the same positions as the experimental LEED image in a. The second LEED image shows the same diffraction spots, but located at the positions of the ideal (1×1) , $(2\sqrt{3} \times 2\sqrt{3})R30^\circ$, and $(\sqrt{7} \times \sqrt{7})R19.1^\circ$ positions for comparison. The third LEED image of figure 5.18c shows a superposition of all LEED spots of the different structures.

By comparing the first and second LEED images in figure 5.18c, one notices that the

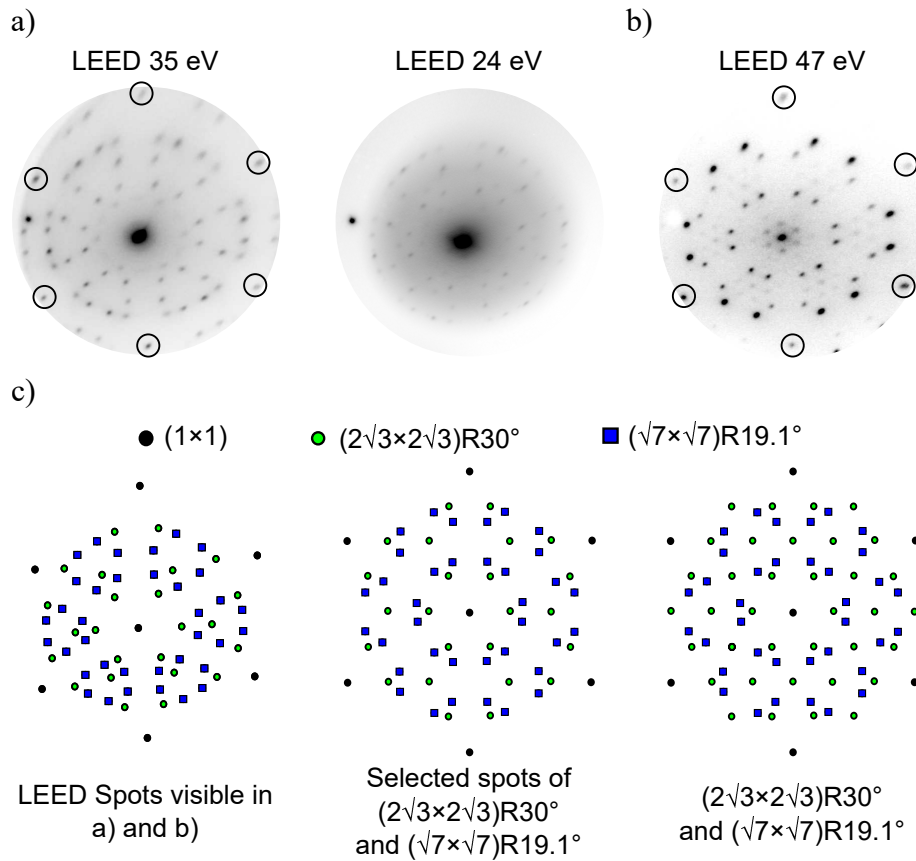


Figure 5.18: Experimentally acquired and simulated LEED images of vanadium oxide stripe formation. a) Two LEED images taken from an LEED- $I(V)$ stack at 35 and 24 eV of a vanadium oxide stripe. b) LEED image from the same $I(V)$ stack taken at 47 eV, a short time after the LEED images of (a). c) Diffraction spot positions of the experimental LEED image shown in a (left), the ideal (1×1) , $(2\sqrt{3} \times 2\sqrt{3})R30^\circ$, and $(\sqrt{7} \times \sqrt{7})R19.1^\circ$ LEED pattern with the half order diffraction spots missing (middle), and all spots of the three pattern (right). The LEED images are simulated with the program package LEEDpat Version 4.2 [246].

$(2\sqrt{3} \times 2\sqrt{3})R30^\circ$ diffraction spots located in the center of the six $(\sqrt{7} \times \sqrt{7})R19.1^\circ$ spots that occur every 60° , are shifted towards the (0,0) spot in the experimental LEED image. Since this variation occurs by more or less the same extent for each of the six LEED spots, a distortion of the LEED image can be excluded as possible reason for a changed spot position. Another difference between the experimentally observed LEED pattern and the superposition of the ideal $(2\sqrt{3} \times 2\sqrt{3})R30^\circ$ and $(\sqrt{7} \times \sqrt{7})R19.1^\circ$ patterns is the absence of all half order diffraction spots in the experimental LEED image.

Interestingly, the LEED pattern displayed in figure 5.18a can reproducibly be obtained during stripe pattern formation, but it exists for only a short period and trans-

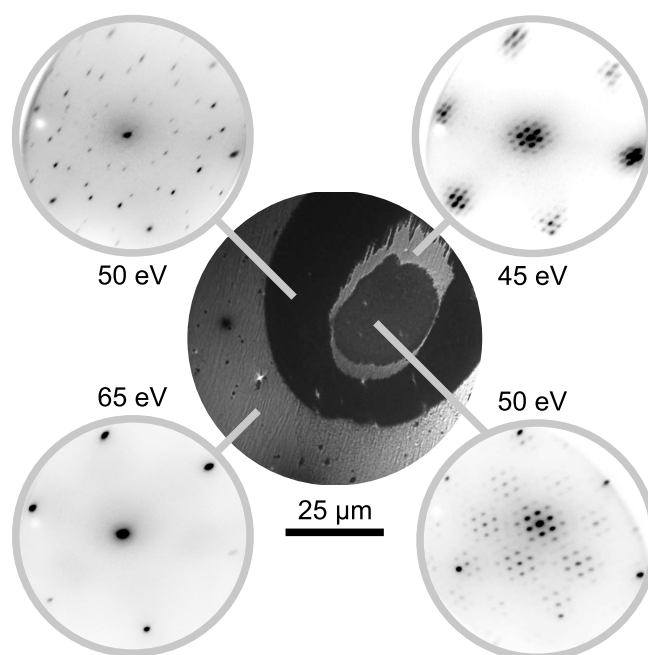


Figure 5.19: μ LEED measurements on a circular vanadium oxide island. The LEEM image acquired at a start voltage of 2.0 eV shows a representative VO_x island consisting of an oxidized ring, a reduced core, and a thin boundary phase separating the two. μ LEED measurements are performed on multiple islands and representative LEED images are shown. The images are acquired at 1030 K in 1×10^{-4} mbar methanol and 1×10^{-4} mbar oxygen.

forms quickly into a $(\sqrt{7} \times \sqrt{7})R19.1^\circ$ pattern or a $(\sqrt{7} \times \sqrt{7})R19.1^\circ$ pattern with weak $(\sqrt{3} \times \sqrt{3})R30^\circ$ Moiré diffraction spots superimposed. A possible reason for this transient LEED pattern might therefore be an ordered defect structure which is removed as the defects density is lowered and the crystallinity is increased.

LEED of circular VO_x islands

The LEEM image in figure 5.19, which is acquired at 1020 K in a gas atmosphere consisting of 1×10^{-4} mbar methanol and 1×10^{-4} mbar oxygen shows a circular vanadium oxide island with a substructure. This substructure consists of an oxidized ring of low LEEM intensity, a thin boundary phase of high LEEM intensity, and a reduced core of an intensity level between the oxidized ring and the boundary phase. Together with the surrounding Rh surface a total of four different surface phases are seen in the LEEM image. The corresponding μ LEED measurements are displayed around the LEEM image.

The Rh(111) surface surrounding the VO_x island displays a clear (1×1) pattern. The absence of an oxygen (2×2) pattern can be explained by the high temperature. The outer, oxidized ring of the vanadium oxide island displays diffraction spots belonging

to the $(\sqrt{7} \times \sqrt{7})R19.1^\circ$ structure together with six very weak Moiré spots located around the (0,0) spot. In the thin boundary phase μ LEED revealed a Moiré pattern of approximately (12×12) periodicity, whereas the reduced core exhibits a LEED pattern which can be described as a $(\sqrt{3} \times \sqrt{3})R30^\circ$ Moiré pattern of approximately (7×7) periodicity.

The obtained LEED patterns are in good agreement with the previously conducted SPELEEM study carried out in the 10^{-6} mbar range [70]. A Moiré pattern of approximately (12×12) periodicity is now identified as the structure of the boundary phase in the 10^{-6} mbar as well as in the 10^{-4} mbar range, and also the (1×1) of the surrounding Rh surface is observed in both pressure ranges. Differences between the two pressure regimes show up in the oxidized and reduced vanadium oxide phases. Whereas only a (1×1) with a considerable amount of background intensity has been observed on both phases in the 10^{-6} mbar range, a clear $(\sqrt{7} \times \sqrt{7})R19.1^\circ$ pattern is assigned to the oxidized ring under oxidizing reaction conditions at 1030 K. The reduced phase instead is characterized by a $(\sqrt{3} \times \sqrt{3})R30^\circ$ Moiré pattern of approximately (7×7) periodicity at 10^{-4} mbar. This structure has also been observed in the 10^{-6} mbar range, but only in the thin boundary phase, and only on a moving interface upon methanol partial pressure increase. The transition back to the (12×12) Moiré pattern was possible by reducing the methanol partial pressure again [70, figure 5.25]. No $(\sqrt{13} \times \sqrt{13})R13.8^\circ$ LEED pattern is observed under oxidizing reaction conditions in the temperature range from room temperature to 1020 K in the 10^{-4} mbar range.

5.3.3 Oscillating VO_x islands

Unless they are involved in a ripening process, the vanadium oxide islands normally exhibit a constant size. Under certain conditions, however, the islands are found to oscillate in a kind of breathing mode despite constant experimental parameters. During these oscillations the VO_x islands exhibit periodic variations of their size as well as of the structure of the reduced core.

Experimental observation of VO_x island oscillations

The LEEM images in figure 5.20a show an oscillating VO_x island. The first image displays a large vanadium oxide island consisting of an oxidized ring (low LEEM intensity), a thin boundary phase (high LEEM intensity), and a reduced core. Interestingly, the reduced core exhibits two different intensity levels in LEEM: a bright phase, which consists of many crystallites, coexists with another phase of lower, nearly homogeneous LEEM intensity. The brighter of the two “core phases” looks like the reduced phase observed in PEEM. The brightness in LEEM, however, depends on the start voltage, and the fact that the reduced phase is imaged as bright area in LEEM and in PEEM is pure coincidence. The reduced phase looks similar to the reduced phase in the vanadium oxide stripe pattern displayed in figure 5.17. The intensity level is almost equal to that of the thin boundary phase. This first LEEM image was acquired before the vanadium oxide island started to oscillate.

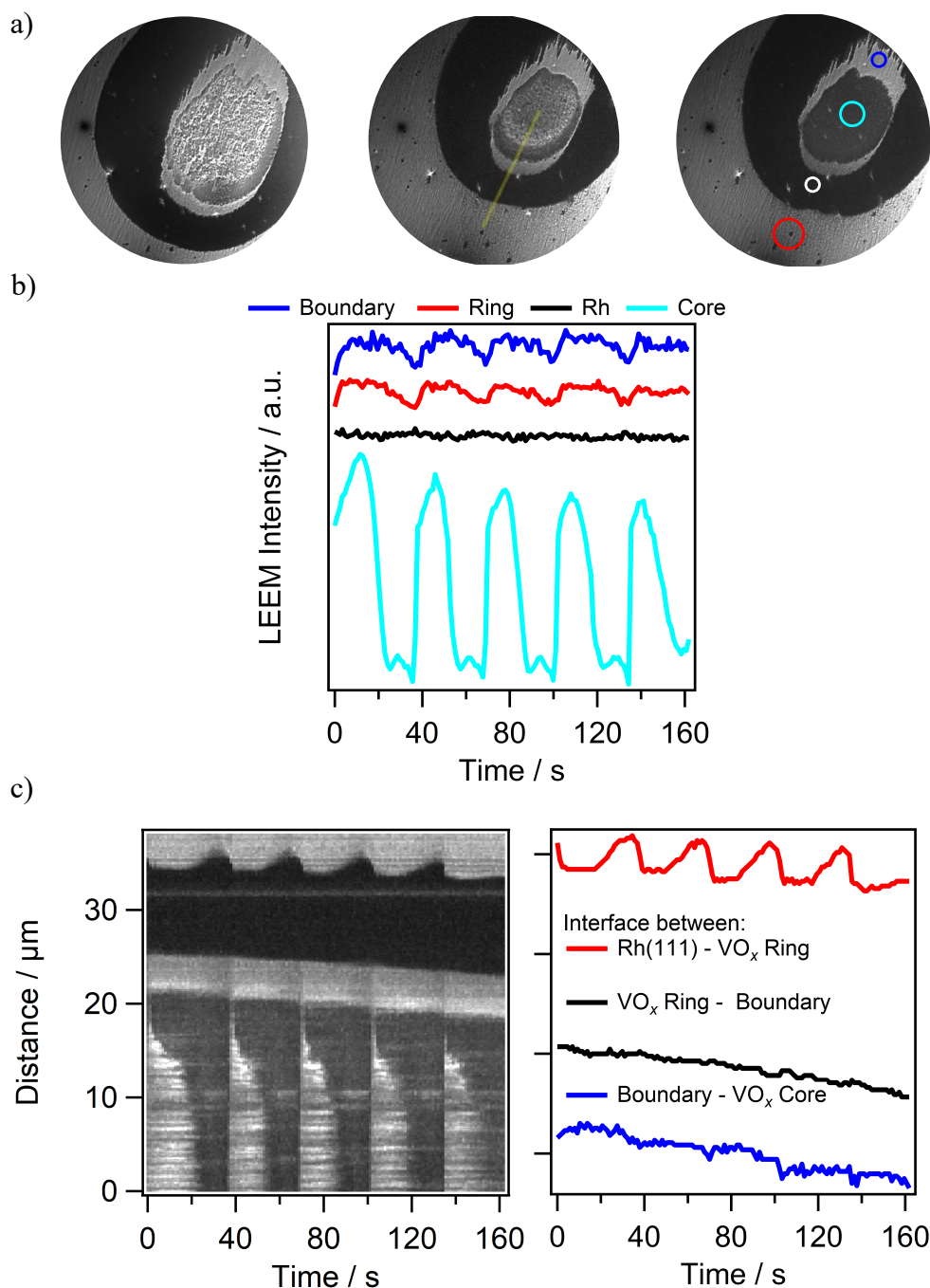


Figure 5.20: Oscillating vanadium oxide island imaged with LEEM. a) Three LEEM images acquired at a start voltage of 2.0 eV before the oscillations have started (left), during a point of smallest island size (middle), and of largest island size (right). b) Local LEEM intensity variation measured on the encircled areas in the third LEEM image of a. c) $x(t)$ -plot (left) taken along the yellow line depicted in the second LEEM image of a, together with the interface position variations of the three interfaces present in the depicted vanadium oxide island (right). Figure adapted from: Reaction dynamics of metal/oxide catalysts: Methanol oxidation at vanadium oxide films on Rh(111) from UHV to 10^{-2} mbar, B. von Boehn, C. Penschke, X. Li, J. Paier, J. Sauer, J.-O. Krispeneit, J. I. Flege, J. Falta, H. Marchetto, T. Franz, G. Lilienkamp, and R. Imbihl, *Journal of Catalysis*, **2020**, *385*, 255 - 264, Copyright (2020), with permission from Elsevier.

Upon prolonged exposure (around one hour) to the oxidizing reaction conditions – 1×10^{-4} mbar methanol and 1×10^{-4} mbar oxygen at 1020 K – the island continuously shrinks until it finally reaches a size shown in the second LEEM image. The shrinking of vanadium oxide islands observed in PEEM (for example discussed in section 5.2.1 and in [70, chapter 5.5]) happens during the ripening and coalescence process of neighboring VO_x islands around 1000 K in the 10^{-4} mbar range. The size reduction of the vanadium oxide island is accompanied by irregular intensity variations at the interface between reduced core and boundary phase. These irregular intensity variations continue to happen on larger areas extending from the boundary phase into the interior of the reduced core. Finally the whole reduced core is transformed into a state of low, homogeneous LEEM intensity. This situation is similar to the third LEEM image of figure 5.20. This phase transition in the island core is accompanied by a slight area increase of the outer oxidized ring. This transition, i. e. the disappearance of the bright phase in the reduced island core and the simultaneous size-increase of the oxidized ring, marks the onset of a periodic island oscillation. These oscillations could be observed for several minutes under constant reaction conditions. They can best be visualized in the plot of the temporal LEEM intensity variation shown in figure 5.20b.

A close inspection of the LEEM intensity variations in figure 5.20b reveals, that the core and the boundary phase of the vanadium oxide island exhibit periodic variations of their LEEM intensity, with a period of approximately 35 s. The intensity variations occur furthermore in phase: the VO_x core intensity increases together with the boundary phase and rhodium intensity. Also their relative minima coincide. Only the LEEM intensity of the oxidized ring exhibits no periodic intensity changes.

The intensity variations of the reduced island core do not proceed in a spatially homogeneous manner. The transition from a dark core into a bright core occurs via propagating fronts, which nucleate at the thin boundary phase. This can best be seen in the $x(t)$ -plot depicted in figure 5.20c (left). The initially bright core (0 s) turns dark starting from the boundary phase until, finally, at around 20 s, the whole core has a homogeneous low LEEM intensity. The transition from the dark surface back into the bright surface happens very fast, within less than a second, and spatially more or less uniform.

Remarkably, the variations of the local LEEM intensity are accompanied by a periodic contraction and expansion of the whole vanadium oxide island. These periodic size changes are depicted in the $x(t)$ -plot (left) and the plot of the interface positions as a function of time (right) in figure 5.20c. The transformation of the core from the dark into the bright state coincides with a contraction of the outer reduced core by about $2 \mu\text{m}$. As the reduced core slowly returns into the dark state, the outer ring starts to expand again until it reaches its maximum size shortly before the bright phase nucleates again in the island core.

The periodic, “breathing-like” contraction and expansion of the vanadium oxide island can be observed for several minutes until it is finally extinguished by the coalescence of the oscillating vanadium oxide island with another larger oxide island in the surrounding. The absence of any oscillation after the coalescence clearly demonstrates that the

occurrence of oscillations is an island size dependent effect, since no other parameters have changed during the coalescence.

Mechanistic explanation of the VO_x island oscillations

In order to understand the periodic, breathing like expansion and contraction of the vanadium oxide island some properties of the system $CH_3OH + OH/VO_x/Rh(111)$ are recapitulated: The ongoing catalytic reaction on the vanadium oxide island consumes oxygen. Oxygen, however, has a low sticking coefficient on the vanadium oxide covered parts of the surface, but can adsorb on the surrounding Rh surface. Adsorbed oxygen needed for the oxidation reaction is therefore supplied by surface diffusion from the surrounding Rh surface to the vanadium oxide islands. The result are macroscopic oxygen gradients, which surround the oxide islands. Since oxygen is consumed all over the island, but supplied only from the boundary, these oxygen gradients extend also inside the vanadium oxide islands. Thus, the chemical potential of oxygen is continuously decreased when one crosses the Rh/ VO_x boundary and moves into the center of the island.

As demonstrated in detail in section 5.2.3, a decreasing chemical potential of oxygen can lead to a phase transition from an oxidized vanadium oxide phase into a reduced one. A cross section through a vanadium oxide island, thus represents a cross section through the phase diagram of the two-dimensional vanadium oxide phases on Rh(111). This phase diagram (PD) has been theoretically calculated for a temperature of 900 K with density functional theory (DFT) by C. Penschke, X. Li, and J. Paier in the group of J. Sauer at the Humboldt-Universität zu Berlin. The PD is depicted in figure 5.21. A possible transition between the oxidized $(\sqrt{7} \times \sqrt{7})R19.1^\circ$ phase into a reduced phase is indicated by the dashed blue line. By comparing the vanadium oxide coverage of these two phases, one notices a difference of 0.07 MLE, or a coverage increase of 16% when reducing the $(\sqrt{7} \times \sqrt{7})R19.1^\circ$ into the $(2 \times 2) V_2O_3$ structure. A closer inspection of table 4.1 reveals a general trend: the ideal vanadium oxide coverage of a two-dimensional vanadium oxide phase increases with decreasing oxidation state of V.

A second property of the system $CH_3OH + OH/VO_x/Rh(111)$ is the existence of a “critical island radius” (if the methanol partial pressure is constant) for the existence of the reduced island core. Only if a vanadium oxide island is large enough, the chemical potential (or the stationary coverage) of oxygen is reduced far enough, so that a reduced phase can nucleate in its center³. The key elements of the mechanism explaining the oscillations of macroscopic vanadium oxide islands under constant reaction conditions are *i*) the existence of a critical radius for the nucleation of a reduced core inside the oxide islands, and *ii*) the V coverage increase upon a phase transition from an oxidized into a reduced two-dimensional VO_x phase.

A schematic representation of a possible mechanism explaining the island oscillations is given in figure 5.22. In the LEEM experiment described in the preceding section, a

³In the experiment presented in section 5.2.3 a critical methanol pressure is observed for a constant island radius, which is identical to a critical island radius at a constant methanol pressure.

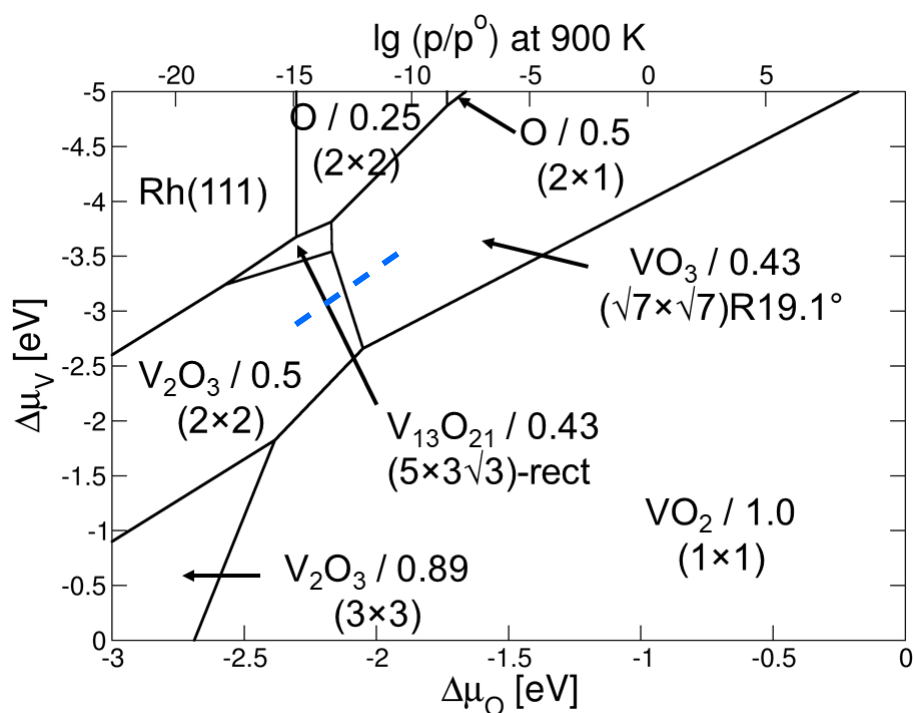


Figure 5.21: Phase diagram of two-dimensional vanadium oxide phase on Rh(111) for a V coverage of $\theta_V \leq 1$ MLE, calculated with density functional theory. The chemical potential of oxygen has been translated into a pressure scale based on tabulated data for 900 K (top axis). The composition of the different vanadium oxide phases, their coverage and their surface structure are stated in the phase diagram. A possible transition between an oxidized and an reduced phase, as observed during the island oscillations, is indicated by the blue dashed line. The phase diagram was calculated by C. Penschke, X. Li, J. Paier, and J. Sauer. Reprinted from: Reaction dynamics of metal/oxide catalysts: Methanol oxidation at vanadium oxide films on Rh(111) from UHV to 10^{-2} mbar, B. von Boehn, C. Penschke, X. Li, J. Paier, J. Sauer, J.-O. Krisponeit, J. I. Flege, J. Falta, H. Marchetto, T. Franz, G. Lilienkamp, and R. Imbihl, *Journal of Catalysis*, **2020**, 385, 255 - 264, Copyright (2020), with permission from Elsevier.

vanadium oxide island exhibiting the substructure of a reduced core (represented by the, circular white area in figure 5.22), and an oxidized ring (represented by dark grey area) continuously decreases its size until it finally undergoes the critical radius needed for the existence of the reduced core. As a consequence, the reduced core gets oxidized. The oxidation of the reduced core is connected to a decrease of the vanadium oxide coverage in the center of the island; the extra V atoms expelled during the oxidation migrate to the outer oxidized ring, which, as a consequence, increases its size. The island continues to expand until, finally, the size exceeds the critical radius. The reduction of the island center sets in and the extra V atoms needed to form the reduced VO_x phase migrate from the outer oxidized ring into the island center. The VO_x islands contracts again, and

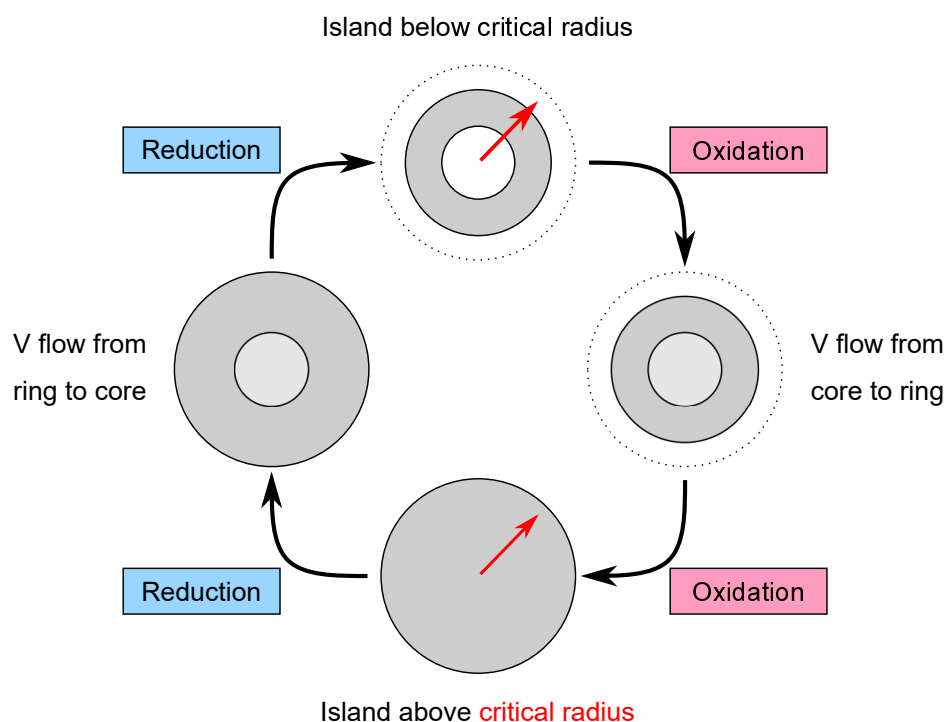


Figure 5.22: Scheme of a possible mechanism explaining the periodic, “breathing-like” expansion and contraction of a vanadium oxide island. As a vanadium oxide island with a substructure consisting of an reduced core (white) and an oxidized ring (grey) shrinks below a critical island radius for the existence of the reduced core (critical radius), the oxidation of the inner core is triggered. Since the oxidized VO_x phase has a lower V coverage than the former reduced phase, the extra V atoms expelled during oxidation migrate to the outer ring. The island expands as a consequence and is now larger than the critical radius. The reduction of the island center starts, and V atoms migrate from the outer ring into the island center to fill up empty sites in the growing reduced phase. The island contracts again, until it has a size below the critical radius, which closes the oscillation cycle.

the oscillatory cycle is closed, since a size below the critical radius triggers the oxidation of the core again.

Two different VO_x phases are clearly distinguishable in the reduced vanadium oxide core depicted in the LEEM images of figure 5.20a, a brighter phase and a darker phase. According to the mechanism sketched above, the brighter phase in the island core represents a more reduced VO_x phase, and the darker phase a more oxidized one. This is consistent with the experiment, since the vanadium oxide island in the first LEEM image clearly is larger than the critical island radius, and its core mainly consists of the brighter phase. As the island size reduces, the brighter phase is transformed more and more into the dark phase, until finally the oxidation-induced V transport in the outer

ring leads to an island expansion and the start of the oscillations.

5.3.4 Oxidation of a VO_x island in LEEM

In order to support the mechanism sketched above, an oxidation of a large VO_x island with the core-ring substructure is carried out by reducing the methanol partial pressure with all parameters being held constant. Initially the methanol pressure is increased to about 1.6×10^{-4} mbar, while keeping the oxygen pressure and the temperature constant at 1×10^{-4} mbar and 1030 K. In this way it is ensured, that a considerable fraction of the large oxide islands is transformed into a reduced VO_x phase. Subsequently, the methanol pressure is reduced in steps to 1×10^{-5} mbar. The oxidation and expansion of the large vanadium oxide island is followed in LEEM, as depicted in the six LEEM images in figure 5.23a, together with an $x(t)$ -plot in figure 5.23b, taken along the yellow line in the first LEEM image. Besides the actual oxidation of the VO_x island, also a considerable drift of the sample to the lower left side is seen in the LEEM images. Especially in the $x(t)$ -plot, the two interfaces Rh(111) / VO_x ring and VO_x ring / boundary simultaneously drift to the lower right side of the graph for $t \leq 200$ s.

As can be seen in the first LEEM image, the vanadium oxide island initially consists of a thin and dark oxidized ring, a bright and relatively thick boundary phase, and a bright island core, which seems to be composed of many small “crystallites”. By reducing the methanol pressure from its initial value to roughly 8×10^{-5} mbar (second LEEM image), the intensity level of the reduced core decreases significantly. Also the number of small crystallites in the core is reduced. At the same time, the oxidized ring expands. Only the position and the appearance of the thin boundary phase separating the core and the ring does not change, besides the above mentioned sample drift.

A subsequent reduction of the methanol pressure to 6×10^{-5} mbar (fourth LEEM image) leads to the dissolution of the thin boundary layer and a further decrease of the core-intensity. The reduced core consists now of a homogeneously dark background of roughly the same intensity as the oxidized ring with elongated bright “crystallites” on top of it. These “crystallites” slowly dissolve via a front propagating from the boundary phase towards the center of the island, as the methanol pressure is further decreased. Finally the whole VO_x island exhibits a homogeneous dark LEEM intensity (last LEEM image).

The dissolution of the small, bright islands and the disappearance of the reduced island core is accompanied by a drastic increase of the island size, as evidenced by an expansion of roughly $10 \mu\text{m}$ in the $x(t)$ -plot. This experiment clearly demonstrates, that the brighter of the two “core phases” is a more reduced VO_x phase than the darker one. With the results of the μLEED measurements presented in section 5.3.2, the $(\sqrt{3} \times \sqrt{3})R30^\circ$ structure can be assigned to the brighter of the two core phases. The boundary phase, instead, displays a Morié pattern of approximately (12×12) periodicity in LEED, whereas the outer ring has the $(\sqrt{7} \times \sqrt{7})R19.1^\circ$ structure. The dark phase in the vanadium oxide core cannot be clearly characterized with LEED, since the island oscillations were terminated by the coalescence of the two neighboring VO_x islands before a μLEED measurement could be performed. The experiment in which the VO_x

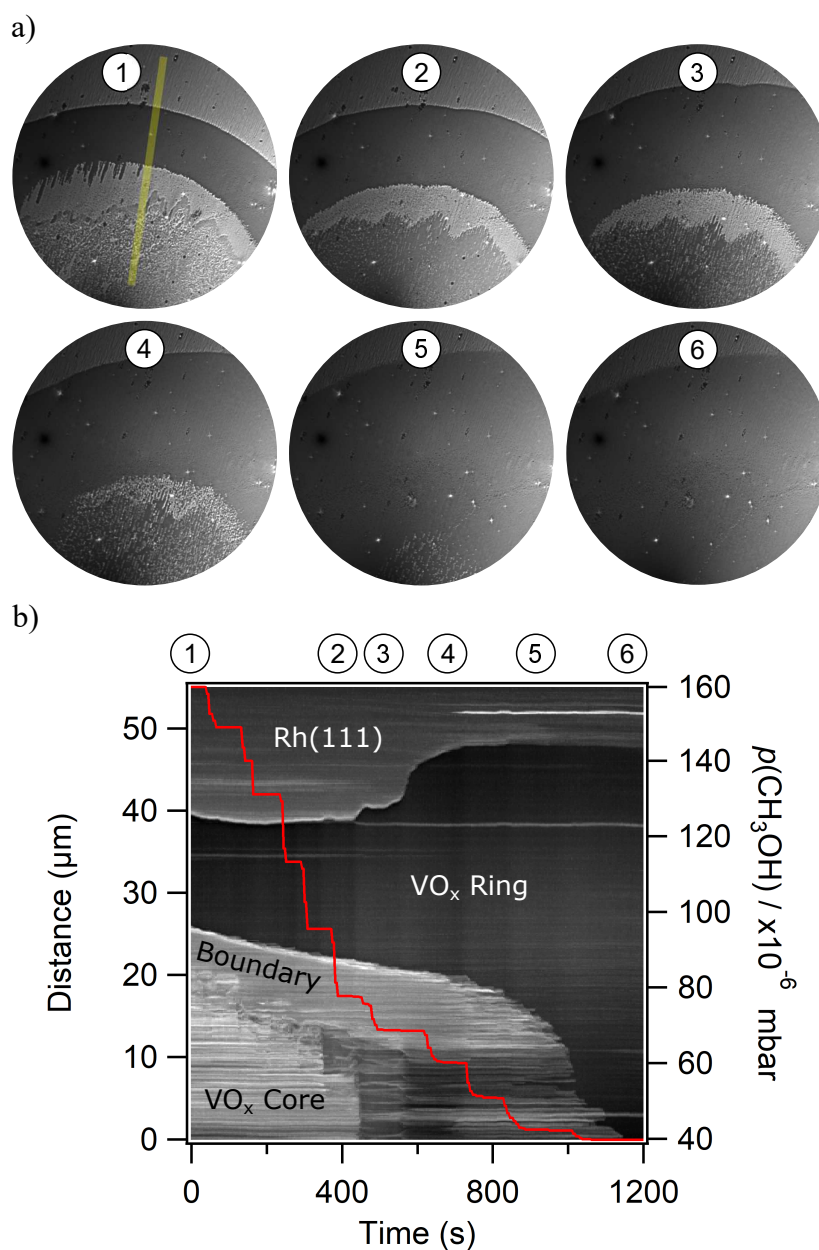


Figure 5.23: Oxidation of a VO_x island with a substructure consisting of an oxidized ring, a thin boundary phase, and a reduced core. The process is followed in LEEM. a) A series of LEEM images recorded during the step-wise decrease of the methanol partial pressure from 1.6×10^{-4} to 0.4×10^{-4} mbar, while keeping the oxygen pressure and the temperature at constant 1×10^{-4} mbar and 1030 K. The field of view is $70 \mu\text{m}$ and the images are acquired at a start voltage of 1.5 eV. b) An $x(t)$ -plot taken across the yellow line depicted in the first LEEM image of (a), together with the methanol partial pressure (solid red line, pressure scale on the right axis). The positions of the six LEEM images are highlighted by arabic numbers on top of the $x(t)$ -plot.

island was oxidized could not be repeated in LEED mode, because a discharge between the sample and the objective lens caused a contamination of the Rh(111) crystal, which made a re-polishing of the surface necessary. However, due to the similar intensity levels of the darker core phase and the outer, oxidized ring, one can assign a $(\sqrt{7} \times \sqrt{7})19.1^\circ$ structure, as proposed in the mechanism, on a tentative basis.

The in situ LEEM investigation in the 10^{-4} mbar range reveals a new kind of reaction dynamics, an oscillating vanadium oxide islands. Most of the involved VO_x phases are identified with μ LEED. Only the preparation of large vanadium oxide islands with a substructure consisting of more than three different phase, as presented in the PEEM experiments of section 5.2.3 was not possible, but only for technical reasons. Therefore it should be reproduced in future experiments.

5.4 VO_x Coverage calibration during methanol oxidation

The coverage of the different vanadium oxide phases that arise during catalytic methanol oxidation in the system $VO_x/\text{Rh}(111)$ are measured in and ex situ with scanning photoemission electron microscopy (SPEM) at the ESCA Microscopy beamline (Elettra). The principle idea of the experiment is as follows: vanadium oxide is deposited in a step-wise manner. After every deposition step a reference spectrum is acquired with XPS. Later a fresh VO_x film is prepared and the sample is exposed to the conditions of catalytic methanol oxidation in a high pressure cell at 10^{-4} mbar in order to form vanadium oxide islands. Afterwards the sample is transferred into the analysis chamber of SPEM in vacuum and an ex situ and in situ (10^{-6} mbar) characterization of the island structure is conducted by means of micro-probe XPS. The recorded spectra are then compared with the reference spectra to obtain the vanadium coverage. The coverage of oxygen in the different parts of the islands is then calculated from the O 1s / V 2p core level intensity ratio.

5.4.1 Beam damaging effects

Crucial for the interpretation of photoemission spectra is the effect of beam damage by the probing photon beam on ultrathin vanadium oxide films. The high photon flux of the focused X-ray beam emitted from the electron storage ring can have a strong impact on the oxidation state of VO_x . In general, high oxidation state compounds tend to get reduced upon exposure to high photon doses, and this problem becomes more urgent with focused X-ray beams [247]. In these experiments, the effect of beam damage is minimized by acquiring all spectra either under reaction conditions in the 10^{-6} mbar range in the presence of oxygen, or in an oxygen atmosphere of less than 2×10^{-6} mbar during the ex situ measurements. The presence of oxygen should keep VO_x in an oxidized state. Examples of beam damage effects are demonstrated in figures 5.24, 5.25 and 5.26, which show five subsequently acquired spectra (zone plate and order sorting aperture mode) of the O 1s and V 2p_{3/2} core levels.

In order to estimate the effect of beam damage, the chemical shift and the overall

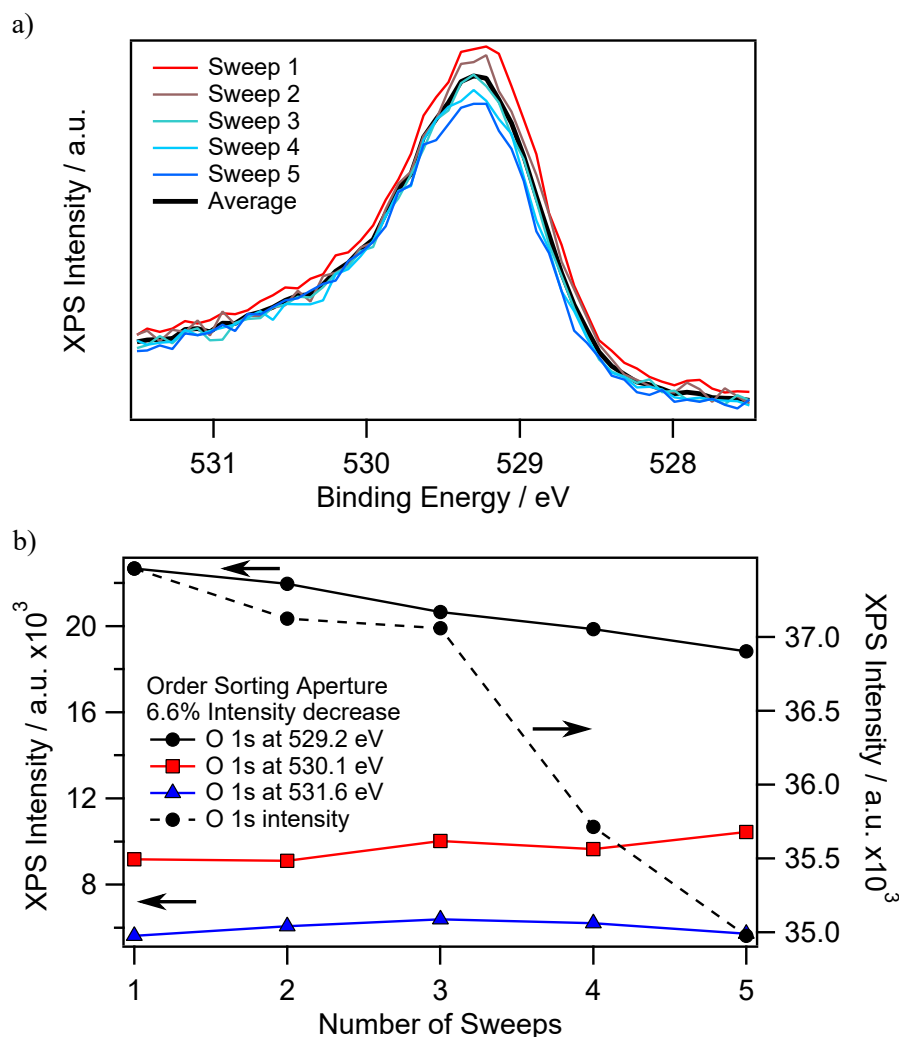


Figure 5.24: Beam damage effect on the O 1s core level during spectra acquisition in OSA mode on a 0.2 MLE VO_x /Rh(111) surface. The spectra are acquired at room temperature in an oxygen atmosphere of 1.3×10^{-6} mbar. a) Subsequently acquired O 1s core level spectra (“sweeps”) and the average spectrum. b) O 1s core level intensities obtained from a fit with three components.

signal decrease upon exposure to X-ray photons in the order-selecting aperture (OSA) and zone plate (ZP) mode are evaluated. As described in detail in chapter 2.5, the probing photon beam is focused in OSA mode by the beamline optics and the spot size on the sample is restricted by a roughly 100 μm large aperture. In ZP mode an additional zone plate optics, which focuses the X-ray beam down to ≈ 50 nm, is introduced between the beamline optics and the order-selecting aperture. Due to different flux densities in the OSA and ZP mode, also a different degree of beam damage is expected.

Figures 5.24a and 5.25a show five subsequently recorded O 1s core level spectra, so-

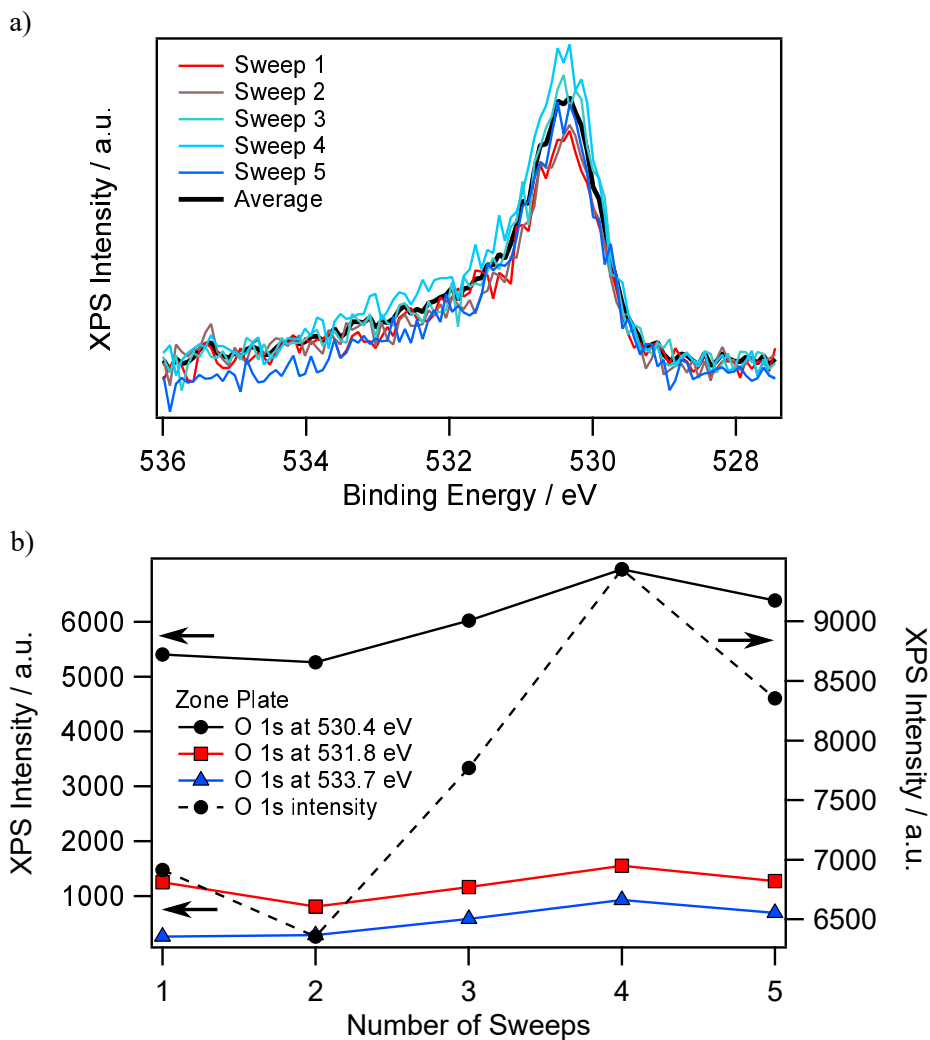


Figure 5.25: Beam damage effect on the O 1s core level during spectra acquisition in ZP mode on a Rh(111) surface covered with vanadium oxide islands obtained after catalytic methanol oxidation in the 10^{-4} mbar range. The spectra are acquired ex situ at room temperature in an oxygen atmosphere of $\leq 2 \times 10^{-6}$ mbar. Subsequently acquired O 1s spectra and the average spectrum (a), and core level intensities obtained from a fit with three components are shown (b).

called “sweeps”, that are acquired in OSA and ZP mode, respectively. In OSA mode, a constant signal decrease with every sweep is observed, resulting in a 6.6% intensity loss in the fifth sweep compared to the first one. The intensity of the average spectrum is therefore about 3 to 4% lower as expected for a situation with negligible beam damage. In ZP mode, no systematic trend in the O 1s signal intensity evolution during the five sweeps is observed, leading to the interpretation, that beam damage is negligible in zone plate mode.

The total O 1s core level intensity is obtained by a numerical fit with three components to the experimental data, after a Shirley background was subtracted. The intensity values of the three components for every sweep and the total intensity can be seen in figures 5.24b and 5.25b. In case of OSA mode (figure 5.24b), the 6.6% intensity decrease is mainly caused by the signal decrease of the low binding energy component at 529.2 eV. In ZP mode, the intensity variations shown in figure 5.25 exhibit no systematic trend, and all three O 1s components change in a similar way.

In case of the V $2p_{3/2}$ core level, no systematic trends in the total intensities can be detected, neither in OSA, nor in ZP mode. This result is depicted in figure 5.26a, which shows five sweeps and the average V $2p_{3/2}$ spectrum recorded in OSA mode. The only detectable effect of the probing photon beam on the measured core level spectra is a slight shift of the V 2p binding energy to lower values. This shift amounts to -0.06 eV/sweep in OSA mode and -0.01 eV/sweep in ZP mode. However, in case of the ZP spectra, the binding energy variations are on the noise level.

By comparing OSA and ZP spectra of the O 1s and V 2p core levels one detects no significant systematic intensity variations upon acquisition of five subsequent spectra. Only the low binding energy O 1s component measured in OSA mode shows a systematic signal decrease, resulting in a total intensity loss of 6.6%. A slight reduction of the VO_x film is furthermore indicated by a V 2p binding energy decrease of 0.3 to 0.4 eV upon acquisition of five sweeps in OSA mode. It has to be noted, that fluctuations of the probing X-ray beam cannot be detected at the ESCA Microscopy beamline during spectra acquisition, even though they modulate the signal intensity. The overall low influence of the probing photon beam on the acquired spectra allows for a reliable determination of the surface composition. Due to the superior signal to noise ratio of a spectrum averaged over five sweeps, and due to the low intensity and binding energy variations occurring during the acquisition of these five sweeps, all following spectra shown in this section are averaged over five single spectra.

5.4.2 VO_x coverage calibration

In order to assign V and O coverages to the ex and in situ measured O 1s and V 2p core level spectra of reaction-patterned samples, a calibration of the photoemission spectra is essential. From an XPS calibration curve recorded from well defined oxide phases on Rh(111), in a first step coverage dependent V $2p_{3/2}$ / Rh $3p_{3/2}$ intensity ratios are determined. In a second step, these ratios are then used to calculate the V coverage on the different parts of the reaction-patterned VO_x /Rh(111) surface. With the V coverage known, the oxygen coverage can be calculated using equation 2.5 from the O 1s / V 2p

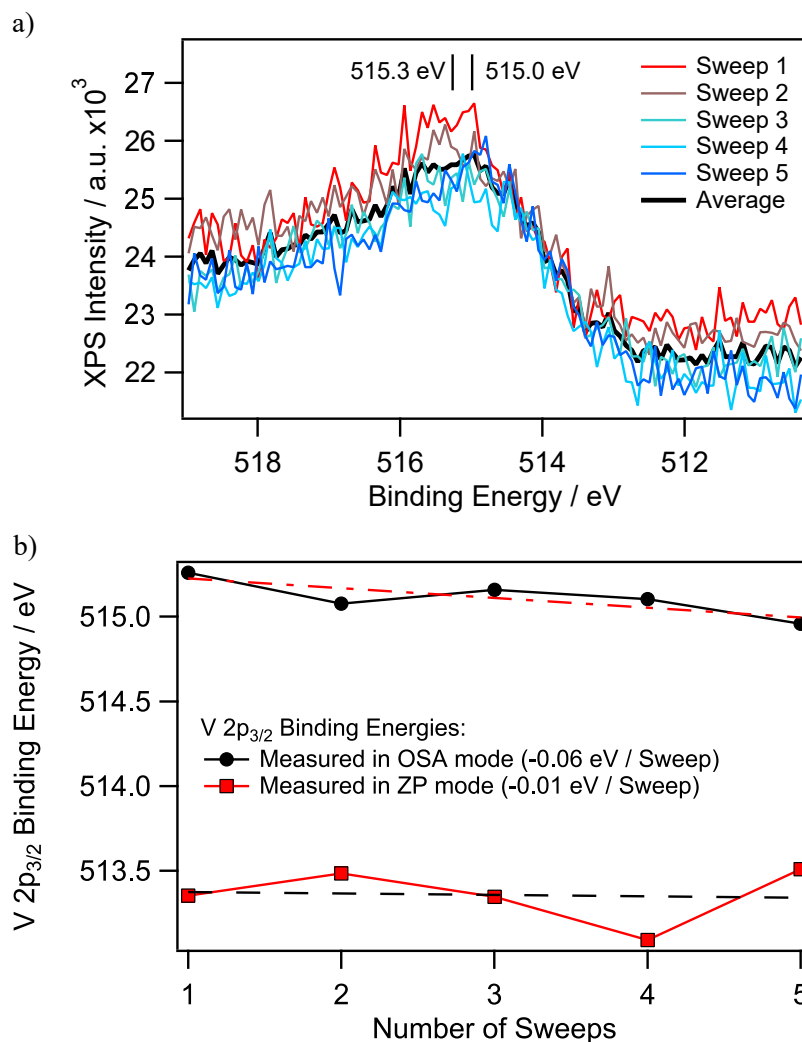


Figure 5.26: Beam damage effect on the $V 2p_{3/2}$ core level during spectra acquisition in OSA and ZP mode on a 0.2 MLE $VO_x/Rh(111)$ surface. The spectra are acquired at room temperature in an oxygen atmosphere of 1.3×10^{-6} mbar. a) Subsequently acquired $V 2p_{3/2}$ core level spectra and the average spectrum (OSA mode). b) $V 2p_{3/2}$ binding energies (OSA and ZP mode) obtained from a fit with two components. The dashed lines represent linear fits to estimate the chemical shift induced by beam damage.

intensity ratios. This method is expected to give better results than a $\text{O } 1s / \text{Rh } 3p_{3/2}$ calibration curve from homogeneous $\text{VO}_x/\text{Rh}(111)$ films, since different from V, the O coverage of the different VO_x films is not increasing linearly with deposition time, and thus is not well known. Thereby it has to be taken into account, that only the $\text{V } 2p_{3/2}$ and $\text{Rh } 3p_{3/2}$ core level intensities are obtained from the numerical fits. These values have to be multiplied by 1.5 in order to account for the specific area ratio based on the degeneracy of each spin state in the spin-orbit splitting. Survey spectra recorded on the oxygen covered $\text{Rh}(111)$ surface and on 0.4, 0.8 and 1.2 MLE thick VO_x films are shown in figure 5.27.

Homogeneous VO_x films are prepared by step-wise reactive evaporation (670 K, 2×10^{-7} mbar oxygen) of VO_x in a separate vacuum chamber. After every deposition step, a LEED and Auger characterization is performed in the preparation chamber and XPS is measured in the main chamber. Based on the vanishing $(\sqrt{7} \times \sqrt{7})\text{R}19.1^\circ$ LEED intensity as reference point, deposition of 0.6 MLE VO_x is assigned to 6 min of V evaporation time. For the XPS calibration curve, seven spectra are recorded: one of the oxygen covered $\text{Rh}(111)$ surface, and six of $\text{VO}_x/\text{Rh}(111)$ films, each recorded after every two-minute deposition step, until a total of twelve minutes deposition time (1.2 MLE vanadium oxide) is completed.

Despite a small carbon signal (probably generated by traces of surface carbonate), no contamination is detected. The $\text{C } 1s$ peak clearly visible in the first spectrum recorded on the oxygen covered $\text{Rh}(111)$ surface diminishes quickly after deposition of small amounts of VO_x . This might be explained by the oxidizing conditions during reactive evaporation of VO_x , and by the attenuation of $\text{C } 1s$ photoelectrons by the VO_x overlayer. For the XPS calibration curve, three separate spectra are acquired after every deposition step. One spectrum in the binding energy region extending from roughly 480 to 540 eV, which covers the $\text{Rh } 3p$, $\text{V } 2p$ and $\text{O } 1s$ core levels, as well as one spectrum of the $\text{C } 1s$ and of the $\text{Rh } 3d$ core levels. Figure 5.28 shows the oxygen, vanadium and rhodium signals used for the calibration, whereas the $\text{Rh } 3d$ and $\text{C } 1s$ core levels can be seen in figure 5.29a and b, respectively.

As indicated in figure 5.28, a slight shift of the $\text{V } 2p$ core level towards lower binding energy is observed with increasing VO_x coverage. This shift between 0.6 and 1.2 MLE is in good agreement with the results of Schoiswohl et al., who attributed the binding energy shift to the incorporation of additional V atoms into the initially formed $(\sqrt{7} \times \sqrt{7})\text{R}19.1^\circ$ structure during the deposition process. A reduction of V from the formal oxidation state of +5 to +2 results. The nucleation of three-dimensional V_2O_3 crystallites on top of the first oxide layer around 1.0 to 1.2 MLE leads to a slight increase of the $\text{V } 2p$ binding energy for thicker films [211].

Due to the partially overlapping $\text{V } 2p_{1/2}$ and $\text{Rh } 3p_{1/2}$ components, and some variations in the background intensity which makes a reliable numeric fit including all three core levels impossible, the $\text{O } 1s$, $\text{V } 2p_{3/2}$ and $\text{Rh } 3p_{3/2}$ components are fitted separately, after a Shirley-type background was subtracted. The resulting $\text{V } 2p / \text{Rh } 3p$ intensity ratios as a function of V coverage are depicted in figure 5.30, together with a linear fit, which allows to correlate the measured intensity ratios to the vanadium coverage.

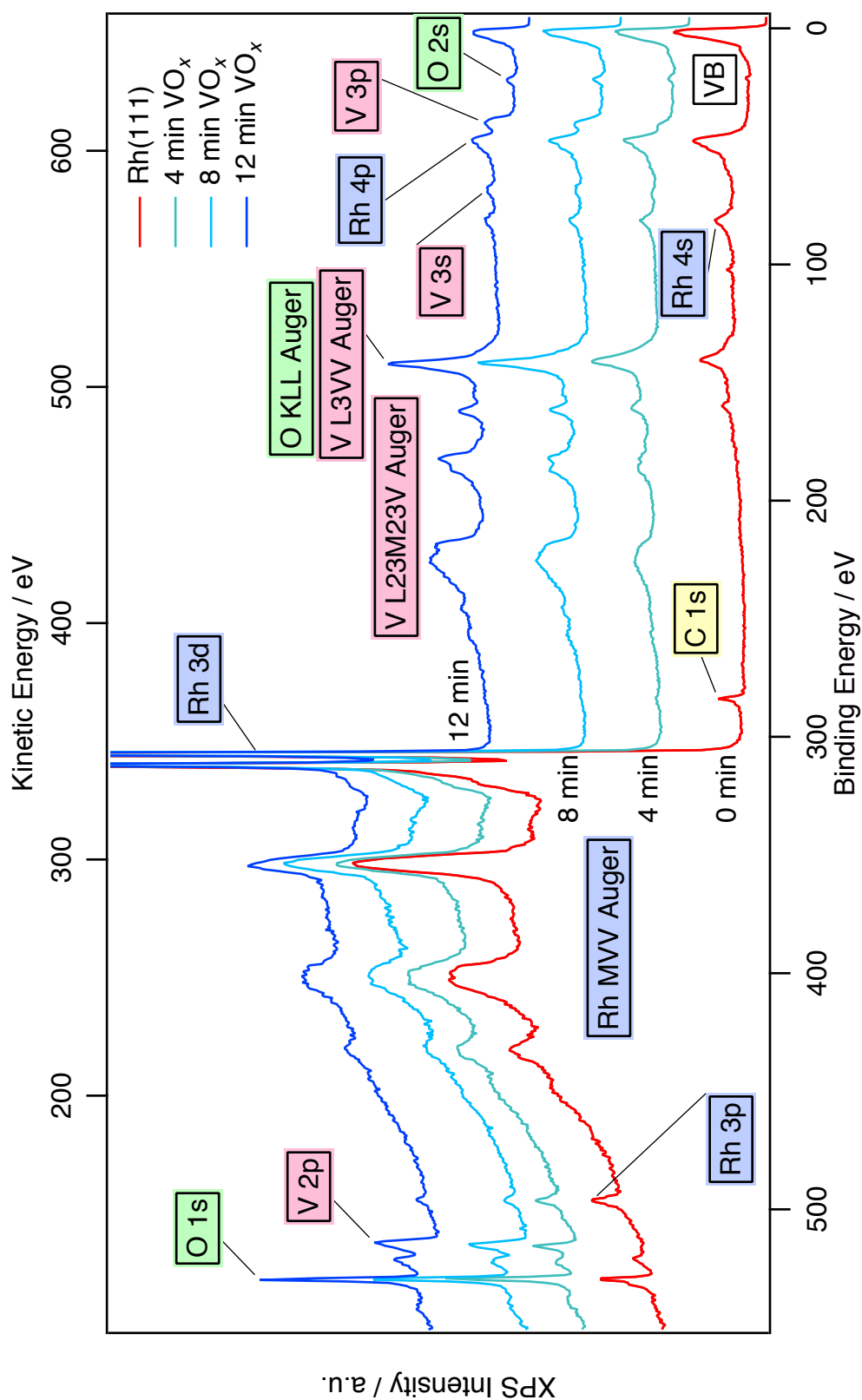


Figure 5.27: Survey spectra recorded on the oxygen covered Rh(111) surface and after step-wise deposition of VO_x . The spectra are recorded at room temperature in an oxygen atmosphere of 1×10^{-7} mbar with a photon energy of 650 eV.

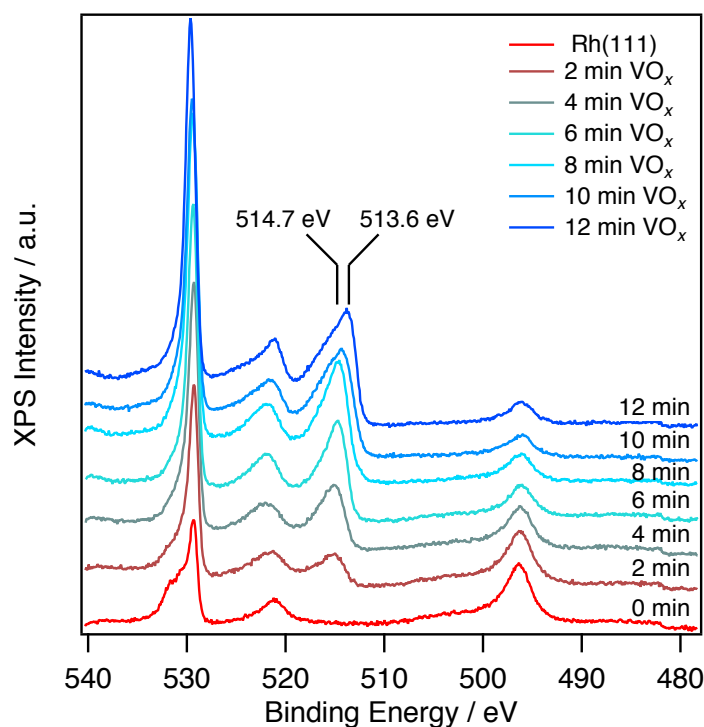


Figure 5.28: Photoemission spectra recorded during step-wise deposition of VO_x on a Rh(111) surface by reactive evaporation. The partially overlapping Rh 3p and V 2p core levels, as well as the O 1s core level are seen. The spectra are recorded at room temperature in an oxygen atmosphere of 1×10^{-7} mbar with a photon energy of 650 eV.

5.4.3 Ex situ VO_x coverage determination on oxide islands

For the coverage determination of the different VO_x phases present after the reaction-induced redistribution of VO_x on Rh(111), a freshly deposited vanadium oxide film (0.2 MLE) is exposed to the conditions of catalytic methanol oxidation in a separate high pressure cell. After in vacuo transfer of the sample, 1×10^{-4} mbar oxygen and 3×10^{-4} mbar methanol are introduced, and the sample is heated within 17 min to roughly 1000 K. The sample is cooled down again after 5 min at 1000 K and transferred into the microscope chamber without braking the vacuum. After an oxygen pressure of 4×10^{-7} mbar was adjusted, two Rh 3d_{5/2} maps are acquired, shown in figure 5.31a. The left elemental map of a size of $1.28 \times 1.28 \text{ mm}^2$ shows a large number of vanadium oxide islands, of which most have a circular shape.

The regions in which the ex situ characterization is conducted are highlighted by the roman letters **A**, **B**, and **C**. An enlarged view of the vanadium oxide island **A** can be seen in the right Rh 3d_{5/2} map in figure 5.31a. A close inspection reveals, that the circular vanadium oxide islands comprise two different intensity levels in the Rh 3d_{5/2} map: a bright core is surrounded by a thin, roughly 5 μm wide dark ring. This contrast is generated by the different vanadium oxide coverages in the island core and the island ring.

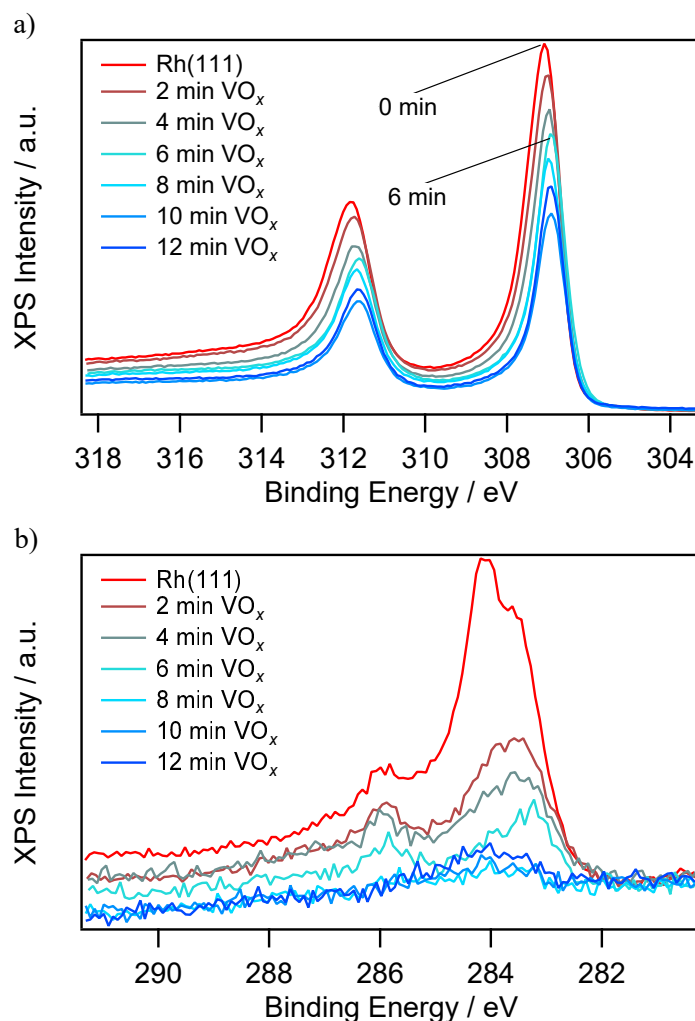


Figure 5.29: Photoemission spectra recorded during step-wise deposition of VO_x on a Rh(111) surface by reactive evaporation. a) A constant Rh 3d signal decrease is observed during VO_x deposition. b) The C 1s signal decreases upon VO_x deposition, probably caused by reactive removal under the oxidizing conditions of VO_x deposition. The spectra are recorded at room temperature in an oxygen atmosphere of 1×10^{-7} mbar with a photon energy of 650 eV.

The map evidences the successful preparation of the vanadium oxide island substructure consisting of an reduced core and an oxidized ring.

The corresponding Rh 3d spectra acquired in ZP mode in the core and the outer ring of the VO_x island **A** and on the bare Rh(111) surface are depicted in figure 5.31b. The strong image contrast between the VO_x covered and VO_x free areas of the surface is reflected by a considerable higher Rh intensity on the bare Rh(111) surface. The signal attenuation by the VO_x islands amounts to 28%. The Rh spectra acquired on the VO_x

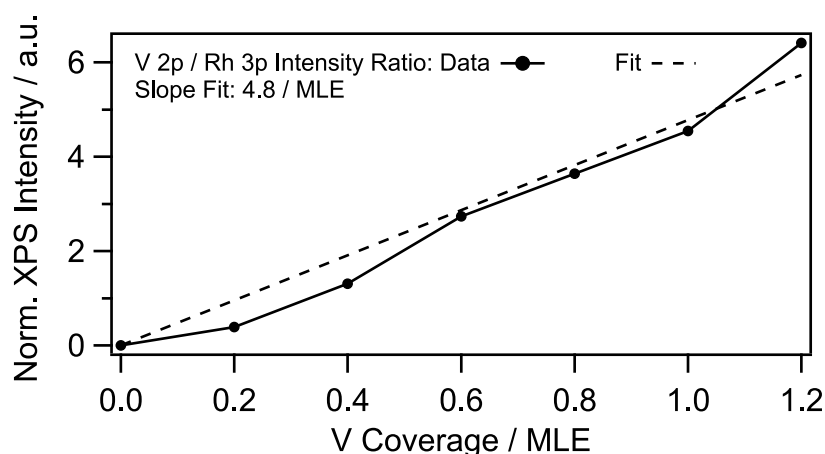


Figure 5.30: V 2p / Rh 3p core level intensity ratio calibration curve for the conversion of measured intensity ratios into V coverages. The data points are calculated from numerical fits to the V 2p_{3/2} and Rh 3p_{3/2} core levels shown in figure 5.28.

island core and outer ring have nearly the same intensity. The difference amounts to only 2 to 3%, with the higher intensity being measured in the VO_x island core. The higher Rh 3d intensity in the island core with respect to the island ring indicates a slightly lower VO_x coverage in the reduced island core. Due to the different oxygen content in the two VO_x phases, and due to the unknown inelastic mean free path of electrons in ultrathin vanadium oxide layers, the Rh 3d signal attenuation is not used to estimate the thickness of the VO_x overlayer.

The V coverages can, however, be calculated with the V 2p / Rh 3p core level intensity ratios taken from the different parts of the VO_x island, using the calibration for homogeneous VO_x films of known V coverage. Figure 5.31c shows three ZP core level spectra of the O 1s, V 2p, and Rh 3p core levels. Three characteristics of the patterned $\text{VO}_x/\text{Rh}(111)$ surface can directly be seen in the spectra: *i*) The very low V 2p intensity in the spectrum recorded on the bare Rh(111) surface indicates a nearly complete phase separation into vanadium oxide enriched islands and VO_x free Rh surface. The vanadium signal is so low, that a reasonable coverage determination is not possible. *ii*) The O 1s intensity on the bare Rh(111) surface is also nearly zero, which is surprising taking into account the oxygen atmosphere of 4×10^{-7} mbar, in which the spectra are acquired. *iii*) Despite nearly identical V 2p intensities in the core and the outer ring of the VO_x islands, a considerably higher O 1s intensity is measured on the outer VO_x ring, compared to the inner island core.

The low O 1s intensity on the bare Rh(111) surface can be explained by a considerable C 1s peak around 284 eV binding energy measured in the same region. Even though no quantitative measure for the C coverage can be given, the low signal to noise ratio indicates a substantial amount of carbon as a result of exposure to high methanol pressures. The carbon layer on the bare Rh surface is most probably caused by thermal methanol decomposition during cool-down in the high pressure cell, and it obviously

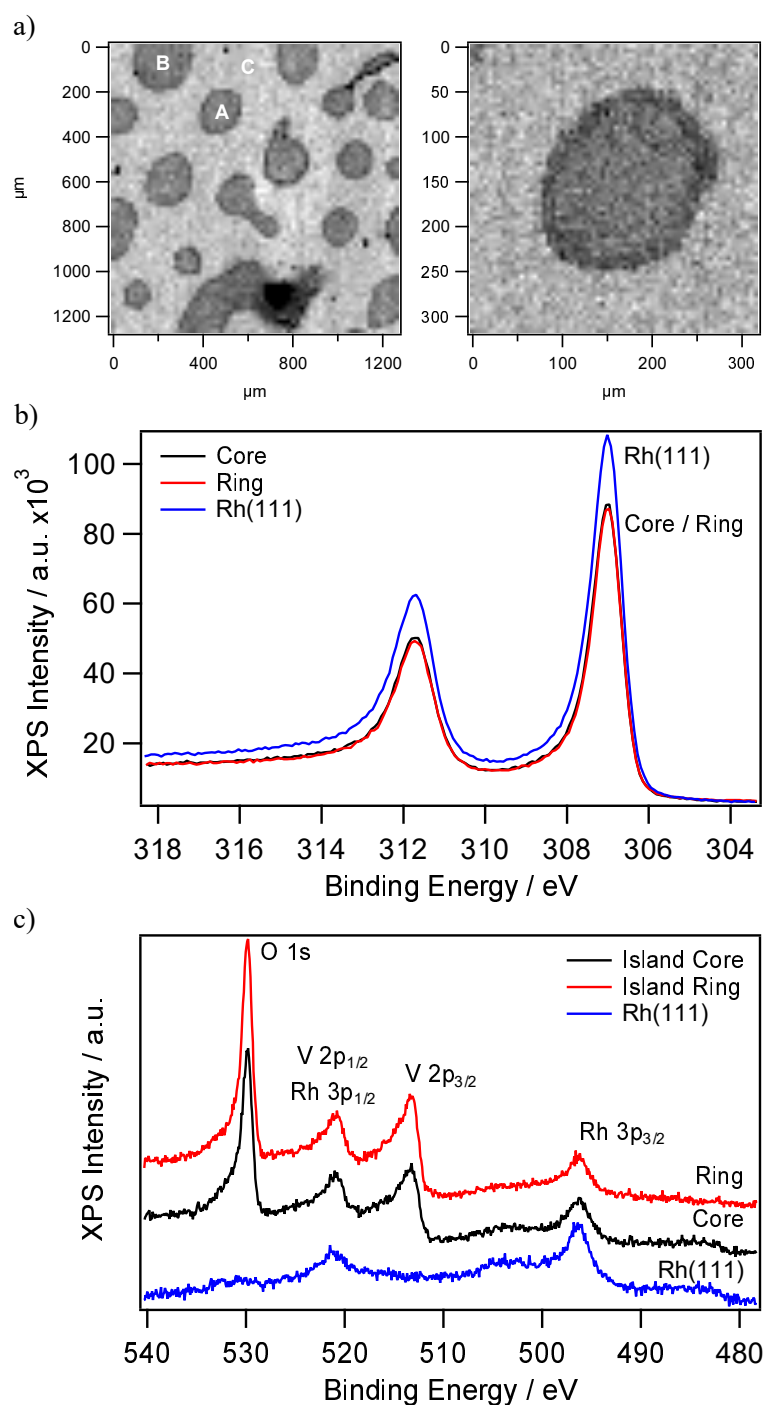


Figure 5.31: Ex situ XPS characterization of VO_x islands on Rh(111). a) Rh 3d_{5/2} maps recorded on a Rh(111) surface covered with 0.2 MLE VO_x after catalytic methanol oxidation was performed in the 10^{-4} mbar range. Shown are a large scale image (left) and a detailed image of the island marked with an **A** (right). b) Rh 3d core level spectra recorded on the core and ring of island **A**, and on the VO_x free Rh surface (position **C**). c) O 1s, V 2p, and Rh 3p core level spectra recorded at the same positions as the Rh 3d spectra in b). The spectra are acquired in ZP mode with a photon energy of 650 eV at room temperature in an oxygen atmosphere of 4×10^{-7} mbar. The binding energy is referenced to the Fermi level.

inhibits oxygen adsorption from the gas phase.

The higher O 1s intensity in the outer VO_x island ring with respect to the core corresponds well to the interpretation of the substructure as being a reduced core and an oxidized ring. This interpretation is also in line with the measured C 1s signals, which are by roughly a factor of 1.5 smaller on the vanadium oxide islands compared to the bare Rh surface. The difference in the C 1s signal measured on the outer ring and the island core amounts to roughly 5%, with the core containing more carbon, as expected for the reduced VO_x phase. However, it has to be taken into account, that only limited information about the active catalyst under reaction conditions can be drawn from carbon contamination measured in ex situ experiments.

To assign V and O coverages in MLE to the ring and the core of the vanadium oxide islands, the O 1s, V 2p_{3/2}, and Rh 3p_{3/2} core levels are extracted from the spectra shown in figure 5.31 and fitted. Due to the low V and O intensities in the spectrum measured on the uncovered Rh surface, no V and O coverages can be calculated for the VO_x depleted regions of the sample. The results of the numeric fits are summarized in table 5.1. Important for the coverage determination are the V 2p / Rh 3p ratio and the O 1s / V 2p ratio. Taking the slope of the V calibration curve shown in figure 5.30, a V coverage of 0.49 and 0.40 MLE is calculated from the V 2p / Rh 3p ratios of 2.3 and 1.9 for the island ring and island core, respectively. With equation 2.5 and the O 1s / V 2p ratios, oxygen coverages of 1.2 and 1.0 MLE are calculated for the island ring and island core. These coverages both correspond to a VO_x composition of roughly $VO_{2.5}$, which is slightly lower than the ideal composition of the $(\sqrt{7} \times \sqrt{7})R19.1^\circ$ structure, which is VO_3 .

The largest error results from uncertainties related to the numeric fits. The overall error is estimated to be ± 0.2 MLE for the oxygen coverage and ± 0.1 MLE for the V coverage. The results of the ex situ XPS characterization are summarized in table 5.1.

5.4.4 In situ VO_x coverage determination on oxide islands

After the ex situ XPS characterization of the VO_x islands present on the Rh(111) surface after exposure to catalytic methanol oxidation in the 10^{-4} mbar range, the sample is heated up to 820 K in a reaction atmosphere of 2×10^{-6} mbar oxygen and 6×10^{-6} mbar methanol. A Rh 3d map of the surface under reaction conditions is shown in figure 5.33. By comparing the Rh maps recorded ex situ (shown in figure 5.31) with the image in figure 5.33a, one notices the increased width of the outer ring of the VO_x islands. The growth of the outer ring indicates that probably more oxidizing reaction conditions prevailed during the in situ measurements, compared to the situation in the high pressure cell, in which the VO_x islands are prepared.

The Rh 3d spectra in figure 5.33b show a similar behavior as observed in the ex situ characterization. The Rh intensity is by a factor of 1.4 larger on the VO_x depleted areas, as compared to the area covered by VO_x islands. The difference between the Rh 3d signals measured on the VO_x ring and the VO_x core amounts to only 2%. However, it has to be taken into account, that the kinetic energy of the ejected Rh 3d electrons (roughly 300 eV) ensures no high surface sensitivity.

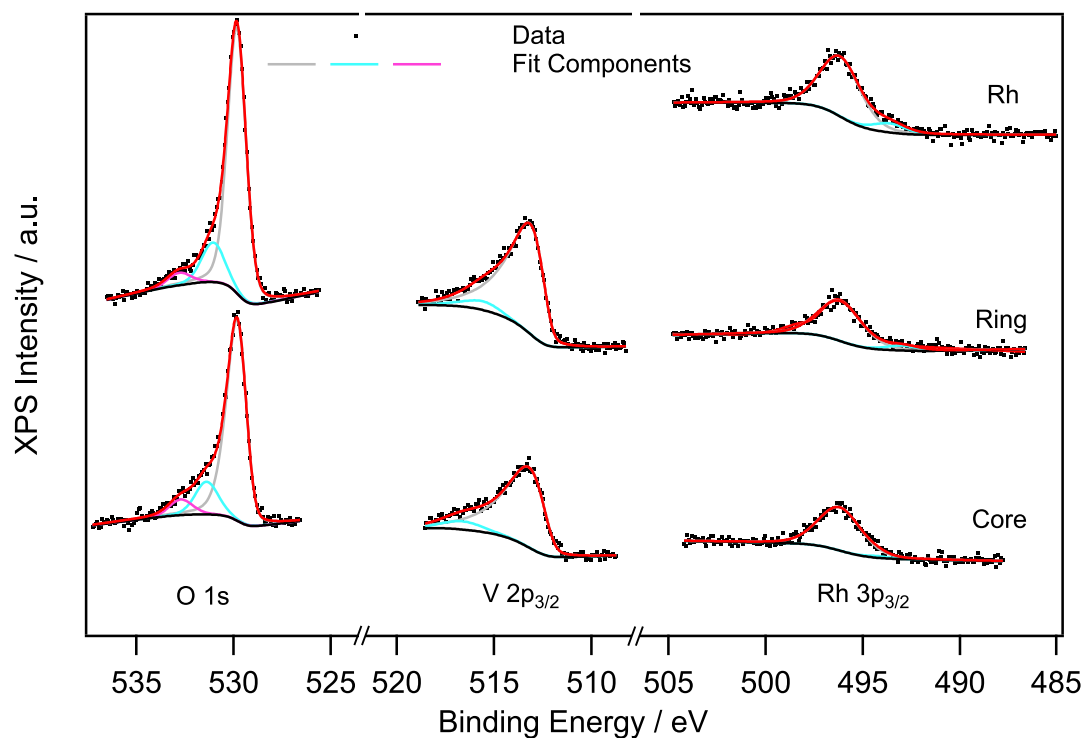


Figure 5.32: Ex situ photoemission spectra for the V and O coverage determination of VO_x islands formed during methanol oxidation in the 10^{-4} mbar range. Shown are the O 1s, V $2p_{3/2}$, and Rh $3p_{3/2}$ core levels as extracted from the spectra shown in figure 5.31. The results of the numeric fits are summarized in table 5.1. The spectra are recorded at room temperature in an oxygen atmosphere of 1×10^{-7} mbar with a photon energy of 650 eV, and are referenced to the separately measured Fermi level.

Different from the ex situ characterization, no C 1s signal is measured in ZP or OSA mode, neither on the VO_x depleted area, nor on the VO_x islands. Obviously, the stationary C concentration is below the detection limit of SPEM. As a consequence, a considerable amount of oxygen is measured on the mostly VO_x free Rh surface, as demonstrated in the XP spectra depicted in figure 5.33c. In order to calculate the V and O concentrations present on the surface under the conditions of catalytic methanol oxidation in the 10^{-6} mbar range, the O 1s, V 2p, and Rh 3p core levels are extracted from the spectra and the peak areas are determined by numeric fits shown in figure 5.34. In order to fit the V $2p_{3/2}$ core level, three fit components are used at fixed binding energies of 514.5, 515.6 and 517.0 eV. These binding energy values are reported for thin vanadium oxide films in the oxidation states +3, +4, and +5, respectively [248].

From the V 2p / Rh 3p core level intensity ratio V coverages of 0.27 and 0.41 MLE are calculated for the VO_x island core and the island ring, respectively. The results are close to the values obtained in the ex situ characterization, but slightly lower V coverages are measured in situ. From the O 1s / V 2p intensity ratios, an oxygen coverage of 1.7 MLE

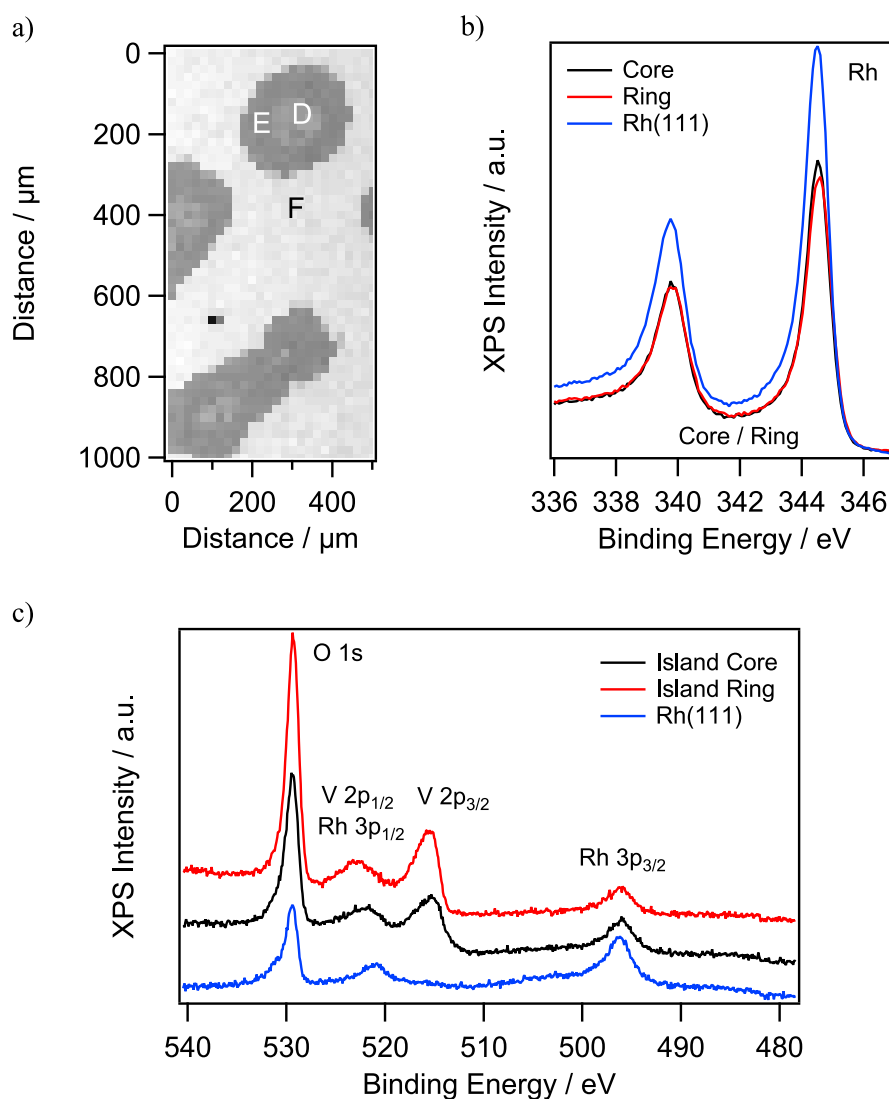


Figure 5.33: In situ XPS characterization of VO_x islands on Rh(111). a) Rh 3d map recorded on 0.2 MLE $\text{VO}_x/\text{Rh}(111)$ after catalytic methanol oxidation has been adjusted at 820 K in the 10^{-6} mbar range. The positions for the μXPS characterization are marked with the roman letters D, E, and F. b) Rh 3d core level spectra recorded on the VO_x depleted Rh surface (F), and on the core (D) and ring (E) of a VO_x island. c) O 1s, V 2p, and Rh 3p core level spectra recorded at the same positions as the Rh 3d spectra in b. The spectra are acquired in ZP mode with a photon energy of 650 eV. The binding energy scale is referenced to the Fermi level.

Table 5.1: Results of the ex situ and in situ XPS characterization of VO_x islands on Rh(111). Listed are the binding energy values of the fit components (BE), the total peak area, and the V (θ_V) and O (θ_O) coverages. The oxygen coverage θ_O is calculated from the O 1s / V 2p intensity ratio. In order to calculate the oxygen coverage from the O 1s / V 2p intensity ratios, the V 2p_{3/2} values listed below have to be multiplied by 1.5 to account for the spin orbit splitting.

	O 1s BE / eV Peak area / a.u.	V 2p _{3/2} BE / eV Peak area / a.u.	Rh 3p _{3/2} BE / eV Peak area / a.u.	Coverage θ_V, θ_O / MLE
Ex situ:				
Rh	-	-	496.2, 493.6; 4350 4350	-
Ring	529.8, 531.1, 532.8 9836	513.4, 515.7 7072	496.2, 493.6 2954	0.49, 1.2
Core	529.9, 531.4, 532.7 8189	513.5, 516.6 5801	496.2, 493.6 3068	0.40, 1.0
In situ:				
Rh	529.4, 531.0,3 5072	- -	496.2, 493.6 5238	-, 0.3
Ring	529.3, 531.0 14699	514.5, 515.6 517.0 6071	496.1, 493.6 3107	0.41, 1.7
Core	529.4, 531.2 9750	514.5, 515.6 517.0 4849	496.0, 493.6 3788	0.27, 1.0

is calculated for the outer ring, whereas a value of 1.0 MLE is obtained for the island core. Accordingly, VO_x compositions of $VO_{4.1}$ and $VO_{3.7}$ are determined for the island ring and the island core, respectively. For comparison, for the $(\sqrt{7} \times \sqrt{7})R19.1^\circ$ structure a composition of VO_3 is reported [53].

5.4.5 Chemical analysis of the VO_x islands

Under certain conditions, the vanadium oxide islands exhibit a substructure consisting of an oxidized ring and a reduced core. This substructure has been explained by the existence of macroscopic oxygen gradients in and outside the islands [69]. In this study, also a chemical shift of the V 2p core level to higher binding energy, and an increase of the O / V ratio in the oxidized ring is found. The reduced core exhibited a V 2p binding energy of 515.2 eV, whereas the V 2p core level measured in the oxidized ring is shifted

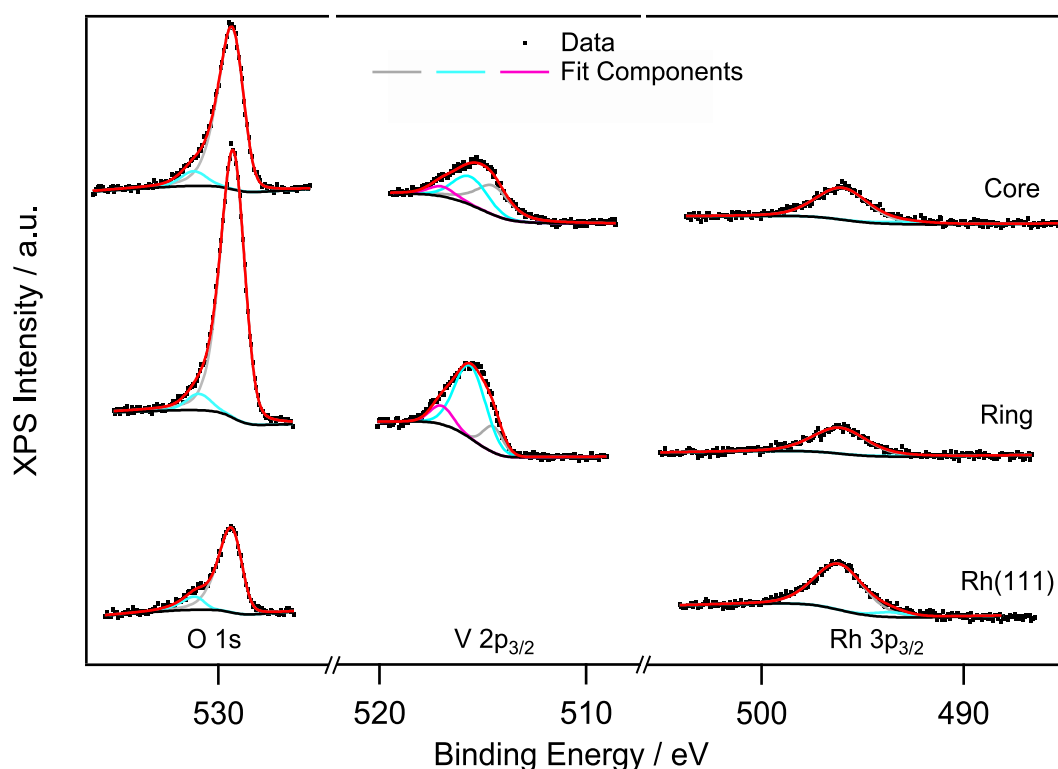


Figure 5.34: In situ photoemission spectra for the V and O coverage determination. Shown are the O 1s, V $2p_{3/2}$, and Rh $3p_{3/2}$ core levels as extracted from the spectra shown in figure 5.33. The results of the numeric fits are summarized in table 5.1. The spectra are recorded at 820 K in a reaction atmosphere consisting of 2×10^{-6} mbar oxygen and 6×10^{-6} mbar methanol with a photon energy of 650 eV. The binding energy is referenced to the separately measured Fermi level.

to 515.6 eV. Hesse et al. measured similar values of 514.9 and 515.6 eV for the core and the ring, respectively. Also the vanadium coverage in the core and the ring have with 0.27 and 0.41 MLE similar values as reported by Hesse et al. [69].

Taking the in situ coverages from table 5.1 one calculates an oxygen to vanadium ratio of 4.1 and 3.7 for the ring and the core, respectively. These values are quite high, taking into account, that the O / V ratio of the highly oxidized $(\sqrt{7} \times \sqrt{7})\text{R}19.1^\circ$ structure is three [211]. The high O coverage might be an indication for the involvement of an Rh surface oxide. On the bare Rh surface, an O coverage of 0.3 MLE is measured, which is below the saturation coverage of oxygen on Rh(111) at room temperature, which is 0.5 MLE.

Another interesting finding is the pronounced V 2p core level shift between the ex situ and in situ measured spectra depicted in figure 5.35. Despite a 20% higher coverage in the VO_x island ring compared to the island core, no dramatic differences in the peak shape of the ex situ measured V 2p spectra can be seen in the upper part of figure 5.35,

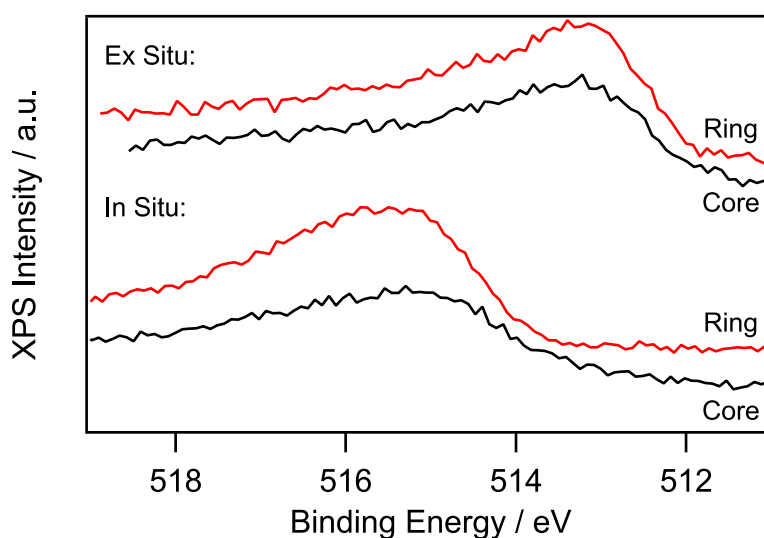


Figure 5.35: V 2p core level spectra recorded ex and in situ on the oxidized ring and the reduced core of circular VO_x islands. The ex situ spectra are acquired at room temperature in an oxygen atmosphere of 1×10^{-7} mbar with a photon energy of 650 eV. The in situ spectra are recorded at the same photon energy in a reaction atmosphere consisting of 2×10^{-6} mbar oxygen and 6×10^{-6} mbar methanol at 820 K.

whereas a binding energy difference of 0.4 eV is measured in situ between the ring and the core.

An even more pronounced shift is a difference in binding energy of roughly 2 eV between the V $2p_{3/2}$ core levels measured ex situ and in situ. Interestingly, even though a large amount of oxygen is present on the vanadium oxide covered areas of the surface (the ring and the core exhibit roughly a VO_3 composition), a low binding energy value of 513.5 eV is measured ex situ in both phases, corresponding to vanadium in a formal oxidation state between +2 and +3. On the other hand, exposure of the vanadium oxide islands to catalytic methanol oxidation resulted in a considerable oxidation of V, as evidenced by the V 2p core level positions at 515.2 and 515.6 eV in the core region and the outer ring, respectively.

A close lying interpretation for the shifted binding energy values in the ex situ spectra is a reduction of the VO_x catalyst during cool-down in the reaction gas atmosphere. This finding demonstrates the importance of in situ techniques for a reliable catalyst characterization. Furthermore, it has to be taken into account, that the total pressure at which the in situ XPS characterization is conducted, is still two orders of magnitude lower than the reaction conditions at which island formation and coalescence is observed.

5.5 VO_x redistribution during other oxidation reactions

The reaction dynamics of ultrathin vanadium oxide layers during catalytic methanol oxidation are described in detail in the preceding sections. One important question connected with the discovery of such a large-scale reaction induced redistribution of a supported oxide is: How general is this phenomenon, and how general is the derived polymerization/ depolymerization mechanism, which explains the movement of neighboring vanadium oxide islands. In a first step to answer this two questions, different catalytic reactions – ammonia, and carbon monoxide oxidation – are investigated under else identical conditions. The results are presented in the following [241].

5.5.1 VO_x redistribution during catalytic ammonia oxidation

The experiments on ammonia oxidation are conducted in a similar way as in catalytic methanol oxidation. A heating ramp (0.5 K s^{-1}) is applied in a reaction gas atmosphere from room temperature up to 1020 K. Subsequently, VO_x redistribution is observed with a spatially resolving method at constant 1020 K. Starting with a surface that is homogeneous in PEEM, this surface is transformed into a pattern of thin, parallel oxide stripes during ammonia oxidation under reducing reaction conditions ($p(\text{NH}_3) = 3 \times 10^{-4}$ mbar, $p(\text{O}_2) = 1 \times 10^{-4}$ mbar). The series of PEEM images in figure 5.36 starts at around 800 K. With increasing temperature, the stripes coarsen and form connections, resulting in a reduced number of thicker oxide stripes, similar as in catalytic methanol oxidation. At around 950 K, the stripe pattern gradually transforms into a spot pattern consisting of irregularly shaped, approximately $100 \mu\text{m}$ sized islands, which become circular at higher temperature. As in catalytic methanol oxidation, also during ammonia oxidation, the vanadium oxide islands exhibit a bright core and a dark ring at 1020 K. Also as in methanol oxidation, neighboring vanadium oxide islands move towards each other and finally coalesce into larger islands. This happens if the islands are close enough, i. e. less than around $100 \mu\text{m}$ apart.

A comparison between the patterns obtained during methanol oxidation (displayed in figure 5.5) and during ammonia oxidation demonstrates the same qualitative behavior in both reaction systems. Differences are only found in details: the length-scale of the stripe pattern is smaller in case of ammonia oxidation. This smaller length-scale continues also in the stage of island formation. In ammonia oxidation smaller islands are formed, compared to methanol oxidation under the same conditions. However, the absolute pressures of methanol and ammonia differ even if the ionization gauge readings are identical, since gas sensitivity factors of the ionization gauge have to be taken into account. The gas correction factors (referenced to the sensitivity towards N_2) for hot cathode ionization gauges reported in literature vary for NH_3 between 1.12 and 1.23, whereas a value of 1.69 is reported for methanol [249, 250]. The real pressure ratio of methanol to oxygen is therefore by a factor of 1.4 to 1.5 smaller compared to the ammonia - oxygen ratio. The fact that the pattern formation observed with ammonia is nearly identical to the pattern formation observed during methanol oxidation suggests a similar mechanism for the pattern formation.

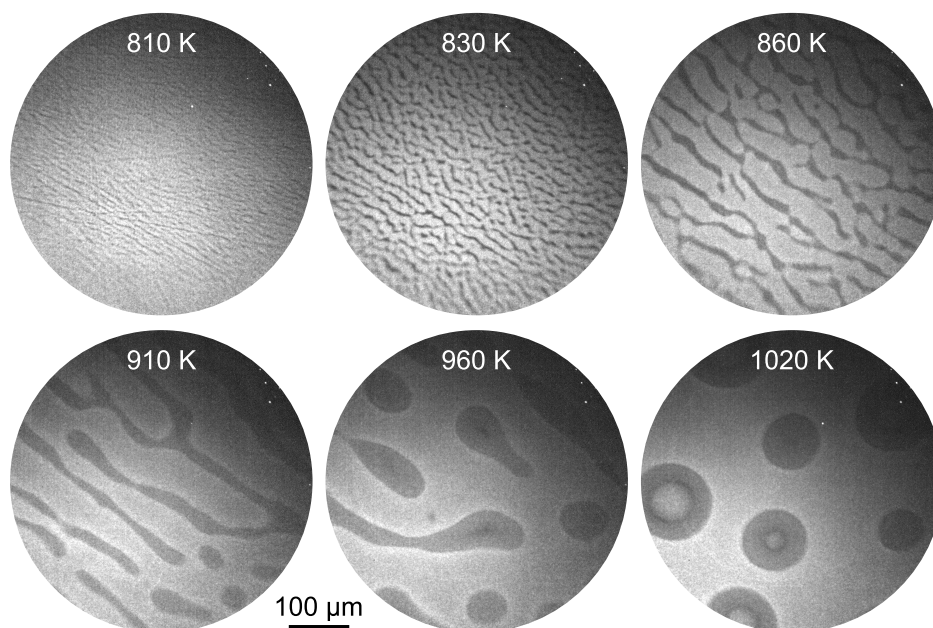


Figure 5.36: A series of PEEM images demonstrating the reaction induced redistribution of vanadium oxide during catalytic ammonia oxidation. The images are acquired during a heating ramp (0.5 K s^{-1}) from room temperature to 1020 K under reducing reaction conditions, the vanadium oxide coverage is 0.2 MLE. Figure adapted from [241].

The coarsening of vanadium oxide stripes, which occurs between 800 and 950 K, is visualized in figure 5.37, where an $x(t)$ -plot extracted perpendicular to the oxide stripes shown in figure 5.36 is presented together with the wavelength of the stripe pattern. The oxide stripe coarsening mainly proceeds in the temperature range from 820 to 880 K. As in methanol oxidation, the redistribution of VO_x is connected with a change in catalytic activity. This is demonstrated in the temperature programmed reaction measurements depicted in figure 5.38. The rate measurements are carried out under reducing reaction conditions on a clean Rh(111) surface and on a Rh(111) surface covered with 0.2 MLE VO_x during heating ramps of 0.5 K s^{-1} . In this way, the reaction rate measurements can directly be compared with the PEEM data displayed in figure 5.37.

In general, the catalytic activity on the vanadium oxide covered surface is for all reaction products shifted by about 20 K to higher temperature, compared to the clean Rh(111) surface. The overall reaction rates are higher on Rh(111), followed by the pristine $\text{VO}_x/\text{Rh}(111)$ surface and the already patterned $\text{VO}_x/\text{Rh}(111)$ surface. Nitrogen production starts beyond 470 K, and NO production at around 520 K on the Rh(111) surface. Interesting details can be obtained by comparing the reaction rates measured on the pristine $\text{VO}_x/\text{Rh}(111)$ surface and the already patterned surface. The pristine surface exhibit relative reaction rate maxima at around 810 K in NO production, at 700 - 870 K in N_2 production, and at 790 - 850 K in water formation. All these rate maxima are either absent or shifted to lower temperature in the rate measurements conducted on

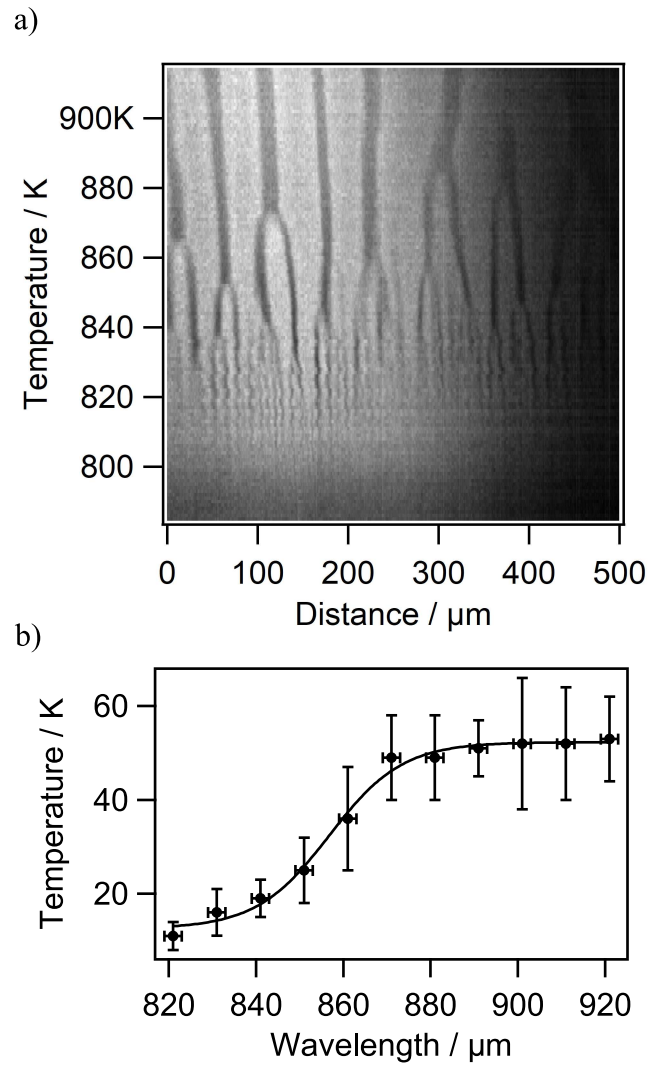


Figure 5.37: Coarsening of vanadium oxide stripe pattern during catalytic methanol oxidation. a) An $x(t)$ -plot extracted from the experiment shown in figure 5.36 as a function of temperature. b) The wavelength of the stripe pattern shown in (a) as a function of temperature. Experimental conditions as in figure 5.36. Figure adapted from [241].

the already patterned surface. Thus, the differences are a consequence of the redistribution process. The temperature range of the rate maxima of the pristine surface overlaps considerably with the temperature range of vanadium oxide stripe formation and coarsening. A similar connection between catalytic activity in formaldehyde production and the redistribution of vanadium oxide is also reported for catalytic methanol oxidation on ultrathin VO_x layers on Rh(111) [68–70].

The catalytic activity of Rh(111) is by a factor of two - three higher than the one of the patterned surface. Since a coverage of 0.2 MLE VO_x represents a surface covered by 30 to 50% with vanadium oxide (taking the ideal coverage of 0.43 MLE for the $(\sqrt{7} \times \sqrt{7})\text{R}19.1^\circ$ from DFT or the experimentally obtained 0.6 MLE for a complete layer), one can conclude that vanadium oxide is more or less inactive on the pre-patterned surface.

5.5.2 VO_x redistribution during catalytic CO oxidation

A qualitatively different behavior than in ammonia oxidation is seen in CO oxidation on $\text{VO}_x/\text{Rh}(111)$. As a surface covered with 0.2 MLE is heated from room temperature to 1020 K with a constant heating rate of 0.5 K min^{-1} under reducing reaction conditions ($3 \times 10^{-4} \text{ mbar CO}$, $1 \times 10^{-4} \text{ mbar O}_2$), no pattern formation is observed in the complete temperature range. The surface appears homogeneously dark in PEEM. In order to observe pattern formation, the partial pressure of oxygen has to be reduced to the 10^{-5} mbar range. A decrease of the oxygen pressure to about $5 \times 10^{-5} \text{ mbar}$ (while keeping the CO pressure constant) immediately leads to a lifting of the homogeneous surface state, and to the formation of parallel, thin oxide stripes with a broad interface, as can be seen in figure 5.39. After further exposure to reaction conditions, a coarsening of the stripes finally leads to elongated vanadium oxide islands. These move towards each other and coalesce, forming large and irregularly islands.

A closer look at the first three PEEM images in figure 5.39 reveals an elliptical vanadium oxide free Rh(111) area around a long surface scratch. This elliptically shaped, VO_x depleted area is the result of a preceding experiment. Quite in general, a retraction of vanadium oxide from macroscopic surface defects is observed in all experiments with heating ramps. Evidently it is the result of the different adsorption properties of defects, compared to the intact Rh(111) surface. However, the influence of such macroscopic surface defect changes with increasing temperature, as can be seen in the last three PEEM images of figure 5.39. An already formed vanadium oxide island becomes attracted by the surface scratch and finally gets pinned to it. The different behavior might also be a consequence of the defects properties being modified by the reaction.

Interestingly, no formation of a reduced core can be observed in the PEEM images, even though the nominal CO to oxygen ratio is about six. If CO oxidation does not lead to the formation of macroscopic oxygen gradients, which surround the oxide islands and extend into them, also no gradients in the chemical potential of oxygen exist, which lead to the formation of a reduced VO_x phase in the island centers.

Figure 5.40 comprises PEEM images recorded on a large vanadium oxide island at constant 1020 K and CO pressure ($3 \times 10^{-4} \text{ mbar}$) but with a variable oxygen pressure. Starting from $5 \times 10^{-7} \text{ mbar}$ in the first PEEM image, the oxygen pressure is increased

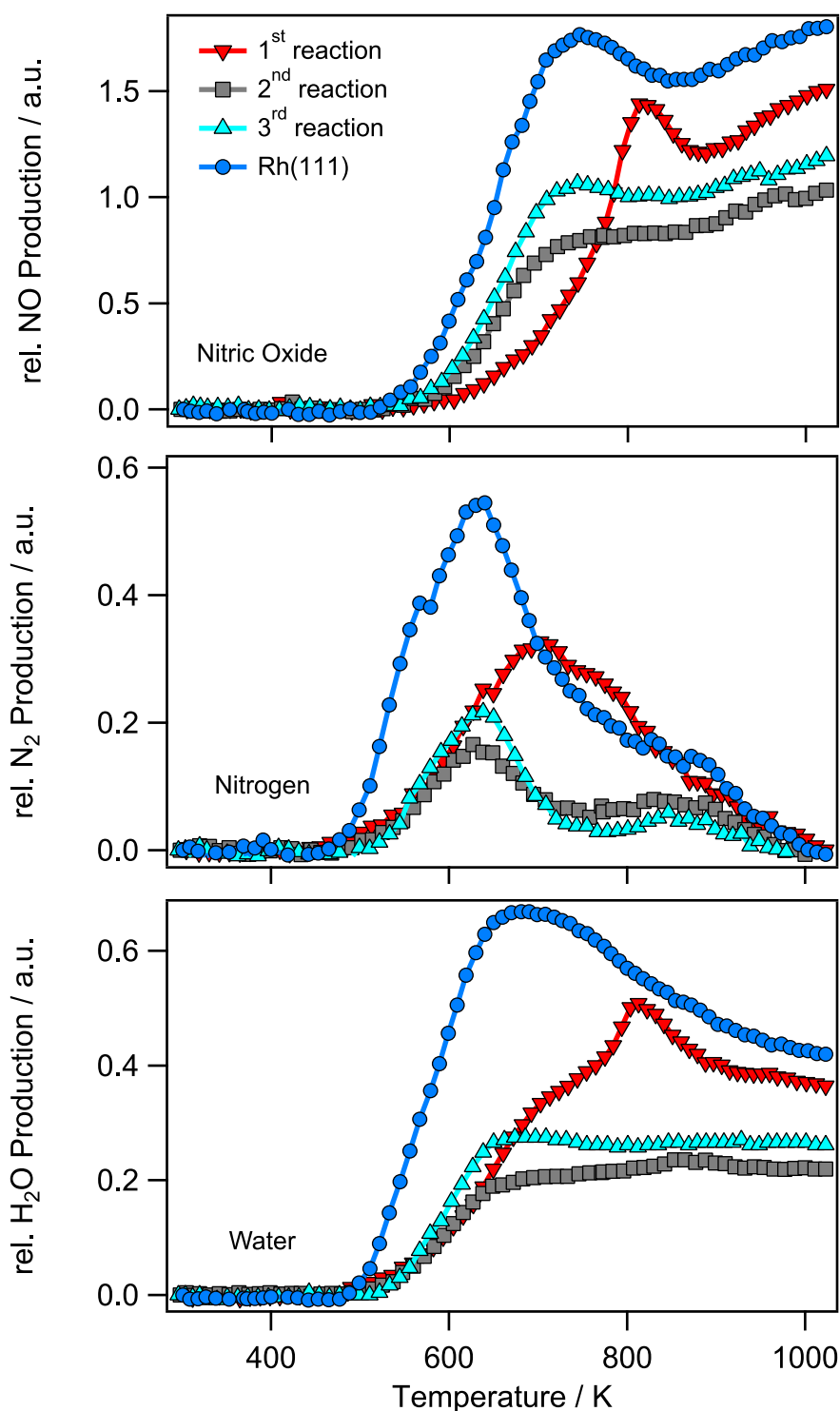


Figure 5.38: Reaction rates measured during a temperature programmed reaction experiment in ammonia oxidation over a VO_x /Rh(111) catalyst. The graphs represent the nitric oxide, nitrogen, and water production rates measured on Rh(111) (blue circles), VO_x on Rh(111) as deposited (red triangles pointing down), and the second and third time the heating ramp is applied (grey squares and light blue triangles, respectively). Experimental conditions: $\theta_V = 0.2$ MLE, $T = 350 - 1000$ K, 0.5 K s⁻¹. Figure adapted from [241].

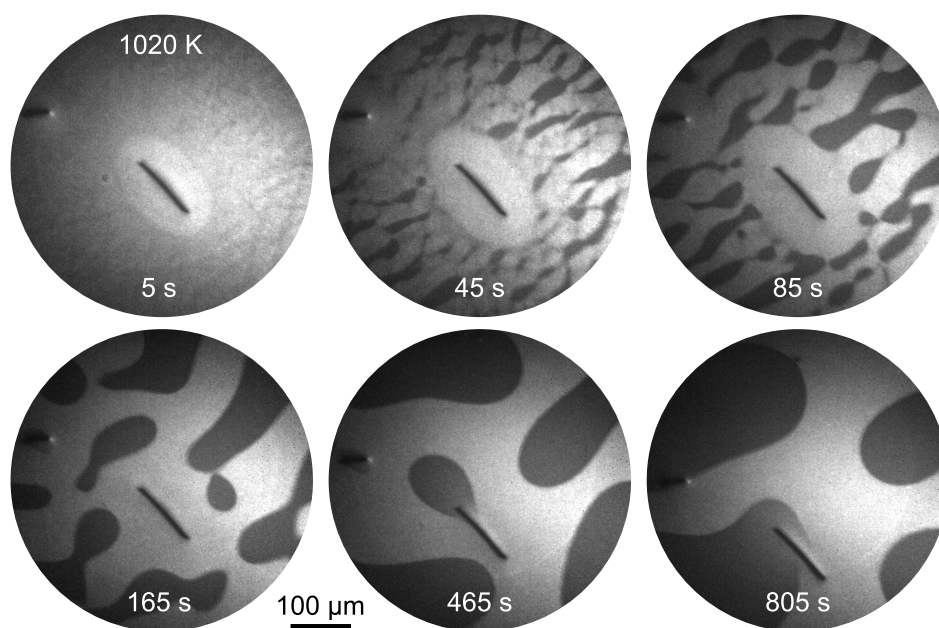


Figure 5.39: PEEM images showing the redistribution of 0.2 MLE vanadium oxide during CO oxidation at constant 1020 K. The images are acquired after a heating ramp (0.5 K s^{-1}) from room temperature to 1020 K under reducing reaction conditions (no pattern formation was observed). Subsequently, at constant 1020 K, the oxygen partial pressure is reduced into the 10^{-5} mbar range, and the PEEM images are acquired. The time in the images represents the time elapsed since 1020 K is reached. Figure adapted from [241].

step-wise up to 1×10^{-4} mbar. The first PEEM image in figure 5.40 represents a completely reduced vanadium oxide island, imaged as bright area. A thin boundary separates the free Rh surface (top) from the vanadium oxide covered parts of the surface (bottom). As the oxygen partial pressure is increased, the outer dark boundary grows, turning into a dark stripe. Finally, at about 5×10^{-5} mbar, the whole oxide island is turned into an oxidized state, characterized by a low PEEM intensity. Interestingly also the interface line between the vanadium oxide free and vanadium oxide covered area retracts with increasing oxygen pressure, as indicated by the white arrows in figure 5.40. This behavior is not observed in methanol or ammonia oxidation.

The previous experiment clearly demonstrates, that also in CO oxidation macroscopic oxygen gradients exist inside the VO_x island, as evidenced by a substructure consisting of a bright, reduced core and a dark, oxidized rim. The formation of vanadium oxide stripes is followed by a ripening process leading to vanadium oxide islands, which move on the surface under reaction conditions and coalesce. Thus, the polymerization / depolymerization mechanism can be observed in three different reaction systems and evidently is robust.

Comparing pattern formation during methanol, ammonia, and CO oxidation on

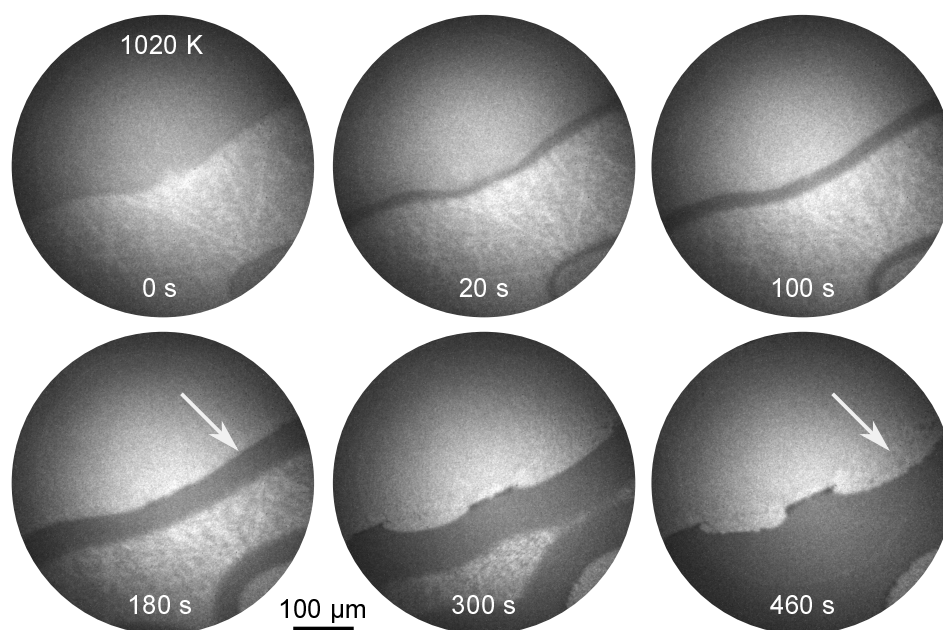


Figure 5.40: Composition of a vanadium oxide island (0.2 MLE) at varying oxygen pressure during CO oxidation. The images are acquired during the stepwise increase of $p(O_2)$ from 5×10^{-7} mbar (0 s) to about 5×10^{-5} mbar (460 s) at a constant temperature of 1020 K. Figure adapted from [241].

$VO_x/Rh(111)$, one can order the three reducing agents by their ability to reduce vanadium oxide, to induce oxygen gradients and to increase the mobility of vanadium oxide under reaction conditions. The highest VO_x mobility and the strongest oxygen gradients are observed in the methanol oxidation, closely followed by ammonia oxidation. In CO oxidation a large excess of CO is needed to form a reduced core in the vanadium oxide islands, even if they have a large size. Therefore the following ranking for the reducing effect of the reactant is proposed: $CH_3OH \geq NH_3 > CO$.

5.6 VO_x redistribution with NO as oxidizing agent in PEEM

In a second step towards a generalization of the polymerization / depolymerization mechanism, nitric oxide instead of molecular oxygen is used for oxidation. Studied is the oxidation of methanol, ammonia, and hydrogen by NO. In all experiments the vanadium oxide coverage is 0.3 MLE, resulting in a surface covered by approximately 50% with vanadium oxide. The reaction-induced redistribution is followed during linear heating ramps (0.5 K s^{-1}), and at a constant temperature of 1030 K with PEEM. In order to allow a direct comparison with the experiments conducted with molecular oxygen, the partial pressures of the reducible reactant and NO are 1.5×10^{-4} and 1×10^{-4} mbar, neglecting the different sticking coefficients of oxygen and nitric oxide. Reaction rates are measured on freshly prepared $VO_x/Rh(111)$ surfaces with QMS during linear heating

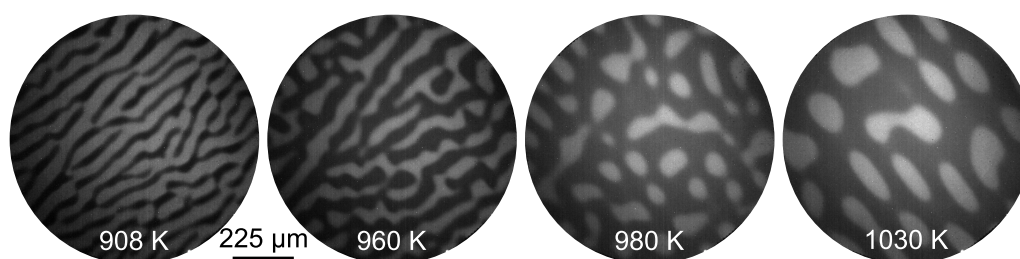


Figure 5.41: Vanadium oxide redistribution during a linear heating ramp (0.5 K s^{-1}) under reducing reaction conditions in catalytic methanol oxidation with nitric oxide. Experimental conditions: $p(\text{CH}_3\text{OH}) = 1.5 \times 10^{-4} \text{ mbar}$, $p(\text{NO}) = 1 \times 10^{-4} \text{ mbar}$, the vanadium oxide coverage is 0.3 MLE. Adapted from *Chaos* **2018**, *28*, 045117., with the permission of AIP Publishing.

ramps (also 0.5 K s^{-1}). The redistribution patterns obtained during catalytic ammonia and methanol oxidation with NO represent an inverse pattern compared to the patterns found in ammonia and methanol oxidation with molecular oxygen: They consist of a dense VO_x film containing holes, instead of vanadium oxide islands surrounded by the bare Rh surface [242].

5.6.1 VO_x redistribution during the $\text{CH}_3\text{OH} + \text{NO}$ reaction

The formation of vanadium oxide redistribution patterns during a heating ramp (0.5 K s^{-1}) under reducing reaction conditions ($1 \times 10^{-4} \text{ mbar NO}$ and $1.5 \times 10^{-4} \text{ mbar methanol}$) is depicted in figure 5.41. The initially homogeneous state obtained after deposition of vanadium oxide is lifted starting at around 870 K. A stripe pattern consisting of dark vanadium oxide stripes and bright areas of bare Rh surface develops. The temperature range, in which the redistribution of vanadium oxide is observed in the $\text{CH}_3 + \text{NO}$ reaction is nearly identical with the temperature range of pattern formation in the $\text{CH}_3 + \text{O}_2$ reaction. In the first stage of the coarsening process, the stripes only increase their width, whereas a pronounced modulation of the interface VO_x / Rh can be observed starting at around 950 K. In the further development, neighboring stripes start to form connections, while simultaneously the overall PEEM intensity increases. The ongoing connection of neighboring oxide stripes finally leads to a closed vanadium oxide film, which contains several elongated, bright holes, as shown in the last PEEM image of figure 5.41.

The stripe pattern, which forms in the $\text{CH}_3 + \text{O}_2$ reaction has a preferential orientation, caused by step bunches on the $\text{Rh}(111)$ surface. This has been confirmed by LEEM [242, Supporting Information S1]. Also the holes (third PEEM image in figure 5.41) have a preferential orientation in their elongated shape at 980 K. This preferential orientation is rotated by 90° when 1030 K is reached. Further exposure to reaction conditions at 1030 K leads to a “stretching” of the elliptical holes, the long axis of the holes grows until finally neighboring holes merge. In contrast to the islands observed in methanol oxidation with molecular oxygen, no movement of the holes in the oxide

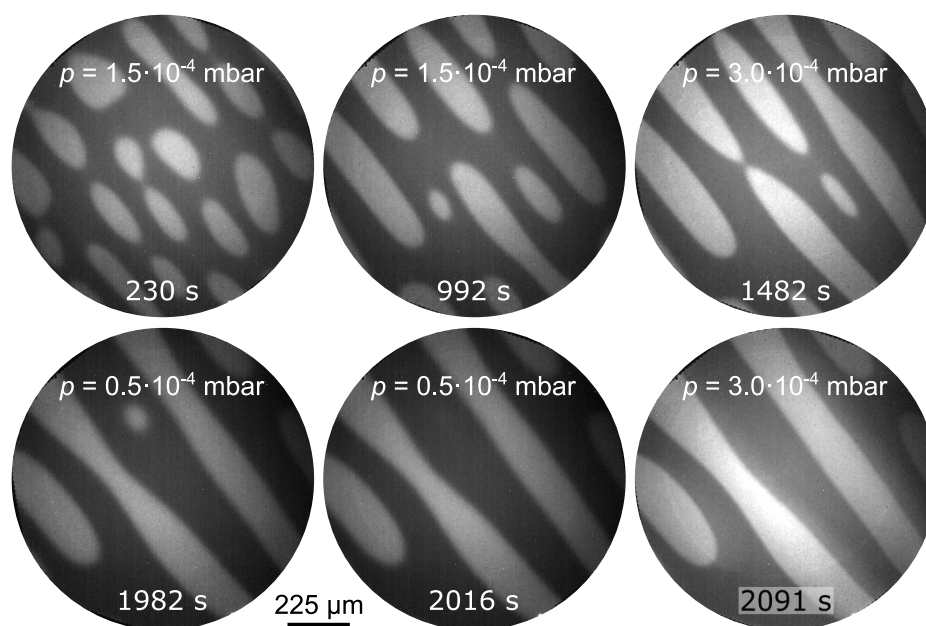


Figure 5.42: PEEM images showing the transformation of a vanadium oxide hole pattern back into a stripe pattern during prolonged exposure to the conditions of methanol oxidation with NO at constant 1030 K. The time at 1030 K and the methanol partial pressure are stated in the images. The NO partial pressure is kept constant at 1×10^{-4} mbar. Adapted from *Chaos* **2018**, *28*, 045117., with the permission of AIP Publishing.

layer can be observed in methanol oxidation with NO. Instead the holes continuously grow until they finally form a kind of stripe pattern again, as demonstrated in figure 5.42.

The influence of a varying methanol partial pressures on the redistribution pattern at 1030 K is investigated in figure 5.42. In the first two PEEM images, the methanol pressure is reduced by a factor of two for about 1000 s. Afterwards the methanol pressure is increased again to the original value of 3×10^{-4} mbar (third PEEM image). Subsequently, the methanol pressure is varied again in the same manner. No influence of the variation of the gas phase composition on pattern formation can be observed, except that the VO_x / Rh interface thickness increases with decreasing methanol pressure. The same behavior has been observed during methanol oxidation with molecular oxygen: if the gas phase contains a large amount of methanol, a well defined, sharp interface separates the vanadium oxide rich and vanadium oxide poor areas of the surface. If the amount of methanol in the gas phase is reduced, the interface smears out and gets broader. Another similarity between the methanol oxidation with NO and O_2 is the overall increase in PEEM intensity upon increase of the methanol pressure. This increase can simply be explained by a lower stationary oxygen concentration on the surface under more reducing conditions.

Comparing the third, fourth and fifth PEEM image in figure 5.42, one notices that

some smaller holes in the vanadium oxide layer disappear over time, whereas the bigger holes grow and connect, forming large stripes. This behavior can be regarded as an Ostwald-like ripening process, since the larger holes grow at the expense of the smaller ones.

In contrast to methanol oxidation with molecular oxygen, no formation of a reduced core is observed on the vanadium oxide covered parts of the surface, even not with a large excess of methanol in the gas phase. This finding clearly demonstrates the absence of large oxygen gradients in the VO_x layer. The driving force for the phase separation into a dense, vanadium oxide rich layer and vanadium oxide depleted holes is most likely thermodynamics, i. e. a minimization of surface energy and of line tension. The absence of moving holes in the NO system is apparently also a consequence of missing oxygen gradients surrounding the vanadium oxide covered parts of the surface.

5.6.2 VO_x redistribution during the $NH_3 + NO$ reaction

In order to investigate pattern formation during catalytic ammonia oxidation with NO, a similar temperature program is applied as in the $CH_3OH + NO$ reaction, with the only difference being, that the linear heating ramp is stopped already at 820 K. A further temperature increase to 1020 K destroys the vanadium redistribution patterns formed at lower temperature, and a homogeneous surface is established again. Pattern formation during ammonia oxidation occurs at lower temperature than in methanol oxidation with O_2 or in the $CH_3 + NO$ reaction. Neither methanol oxidation, nor hydrogen oxidation with NO led to a homogeneous surface at 1030 K in a wide range of methanol to oxygen and hydrogen to oxygen ratios, respectively.

PEEM images acquired after a linear heating ramp during catalytic ammonia oxidation with NO was stopped at 820 K are shown in figure 5.43a. Different from methanol oxidation with NO, no pattern consisting of vanadium oxide stripes develops. Instead, a pattern of bright stripes of vanadium oxide depleted area is formed a few seconds after the temperature ramp is stopped at 820 K. After about three minutes of constant reaction conditions, a coarsening of the stripe pattern leads to the coexistence of elongated, parallel bright stripes and small circular bright holes of a few tens of micrometers diameter. The bright stripes have the same preferential orientation as the dark vanadium oxide stripes formed during methanol oxidation with NO (figure 5.41).

After further 50 min exposure to the reaction gas atmosphere at 820 K, most of the bright, vanadium oxide depleted stripes have vanished or merged into large, almost circular holes. In contrast to the $CH_3OH + NO$ reaction, no stripe pattern develops after the formation of holes in the oxide layer. Also no preferential orientation of the elongated holes can be identified.

The response to changes in the gas phase composition is markedly different from the $CH_3 + NO$ reaction, as demonstrated by the development of the local PEEM intensity measured on vanadium oxide covered and depleted surface areas shown in figure 5.43b. For this measurement the NO and ammonia partial pressure is reduced to 4×10^{-5} mbar, and subsequently the ammonia pressure is gradually increased again. The local PEEM intensity of the vanadium oxide free surface increases in a monotonic manner and ap-

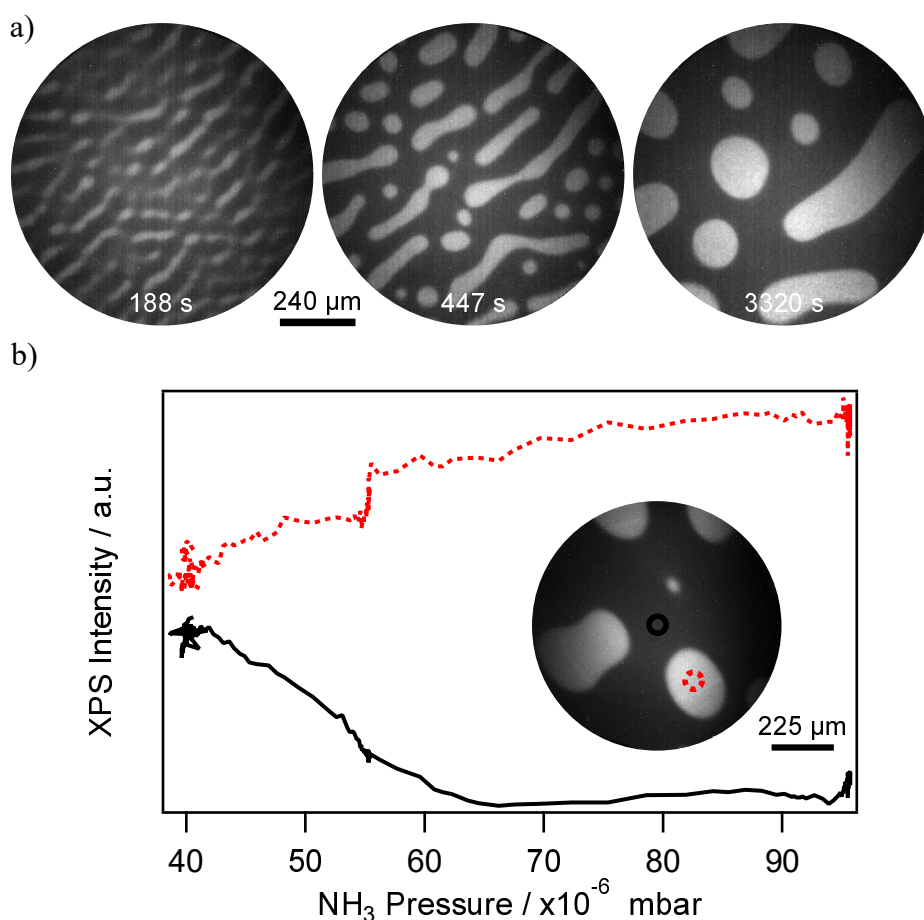


Figure 5.43: Stripe and hole pattern formation during catalytic ammonia oxidation with NO on 0.3 MLE VO_x /Rh(111) at a constant temperature of 820 K. a) Coarsening of a stripe pattern, and transition into a hole pattern as a function of time at elevated temperature. b) Local PEEM intensity as a function of ammonia partial pressure. The partial pressures of ammonia and nitric oxide are 1.5×10^{-4} and 1×10^{-4} mbar in the PEEM images of (a), respectively. The NO pressure during the experiment shown in (b) is 4×10^{-5} mbar, the ammonia pressure is varied between 4×10^{-5} and 1×10^{-4} mbar. Adapted from *Chaos* **2018**, *28*, 045117., with the permission of AIP Publishing.

proaches saturation close to a pressure of 1×10^{-4} mbar. Surprisingly, the vanadium oxide covered regions show the opposite behavior. With increasing ammonia pressure the PEEM intensity decreases linearly up to a pressure of 6.5×10^{-5} mbar, and settles then at a constant level up to 1×10^{-4} mbar ammonia. This behavior is not observed in the $CH_3 + NO$ reaction, but also in ammonia and methanol oxidation with molecular oxygen, no decrease in PEEM intensity with increasing partial pressure of the reducing agent is observed.

5.6.3 Transformation of the “hole pattern” into an “island pattern”

Up to now, the ascription of vanadium oxide and bare Rh surface solely relies on the PEEM intensity and the assumption that VO_x has a higher work function than the bare Rh(111) surface. This is the case during methanol oxidation with O_2 for the highly oxidized vanadium oxide phases. In order to verify whether the dark parts in PEEM represent vanadium oxide, the “NO-patterned” surfaces are cooled down to room temperature in the reaction gas atmosphere, and nitric oxide is replaced by molecular oxygen. Subsequently the same heating ramp (0.5 K s^{-1} up to 1030 K) is applied, and the redistribution of vanadium oxide is followed with PEEM in both reactions, methanol oxidation and ammonia oxidation.

Figure 5.44 summarizes the observations made in methanol oxidation (a) and ammonia oxidation (b) with molecular oxygen on already NO-patterned surfaces. As can be seen by the first PEEM image in (a), up to a temperature close to 800 K the original contrast obtained during the $CH_3 + NO$ reaction remains also during methanol oxidation with oxygen. The holes in the vanadium oxide layer have a lower work function than the oxide covered parts of the surface. Things change when pattern formation sets in at around 820 K. A phase separation in the vanadium oxide covered parts leads to a stripe pattern consisting of a large number of thin and parallel dark oxide stripes. As these stripes become thicker, at around 885 K, a reduced and bright phase nucleates in the center of the oxide stripes. The vanadium oxide covered parts of the surface consist now of a dark, oxidized rim, and a reduced core, as expected for an experiment carried out with methanol oxidation under reducing reaction conditions.

Upon further temperature increase, the neighboring oxide stripes start to form connections and finally end up as an extended vanadium oxide islands with a smooth interface at 1030 K. The absence of any visible vanadium oxide nuclei inside the Rh(111) holes indicates a nearly complete phase separation into vanadium oxide free and covered areas. Interestingly, the transition from the stripe into an island pattern is accompanied by a kind of interface instability, manifested as a periodic expansion and contraction of the vanadium oxide stripe borders observed for a few seconds during the heating ramp at around 970 K [242].

The PEEM images shown in (b) demonstrate a similar behavior during ammonia oxidation. A large number of thin, parallel oxide stripes form on the vanadium oxide covered regions of the surface at around 800 K. These stripes show the same preferential orientation as during the methanol oxidation experiment depicted in (a). With increasing temperature, the coarsening and interconnection of the oxide stripes finally leads to the formation of a reduced, bright appearing phase in the center of the vanadium oxide covered areas. A dark rim separates this reduced phase from the Rh(111) surface.

At variance to the results of methanol oxidation, also in the VO_x depleted holes, the nucleation of vanadium oxide stripes can be observed in the first PEEM image in (b). Also at variance to the results of methanol oxidation is the existence of a dense vanadium oxide layer with holes in it, which can be observed up to 1030 K, and which is reminiscent of pattern formation during ammonia oxidation with NO.

The PEEM images shown in figure 5.44c are recorded at a constant temperature of

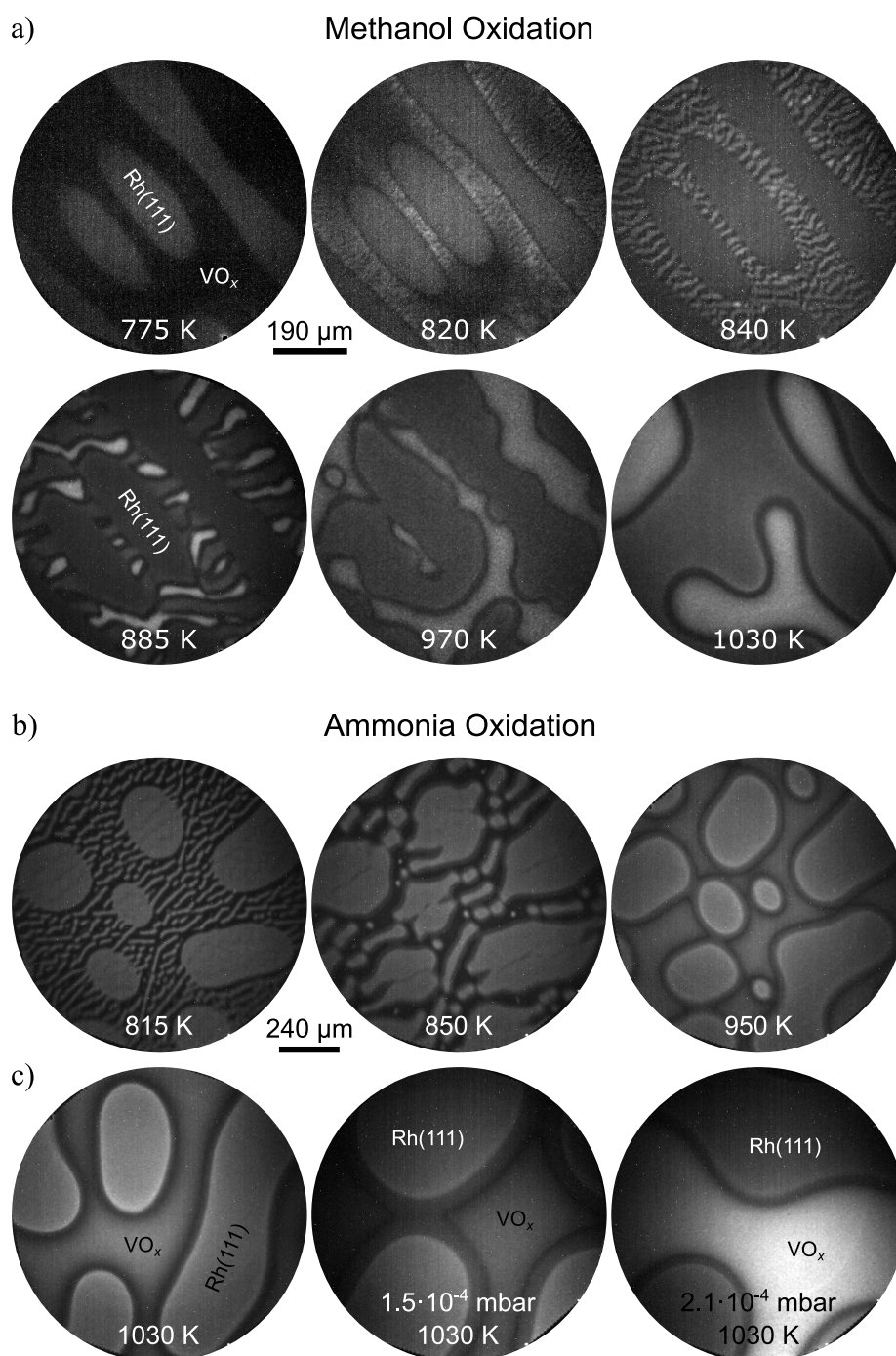


Figure 5.44: PEEM images showing the redistribution of vanadium oxide during methanol and ammonia oxidation with molecular oxygen on the “NO-patterned” surface. a) After the $\text{VO}_x/\text{Rh}(111)$ ($\theta_V = 0.3$ MLE) surface was patterned during methanol oxidation with NO , the sample is cooled down in continuous gas flow and NO is replaced by O_2 . Afterwards, a linear heating ramp (0.5 K s^{-1}) is applied during methanol oxidation with 3×10^{-4} mbar methanol and 1×10^{-4} mbar oxygen. b) The same procedure is applied with ammonia oxidation to a $\text{VO}_x/\text{Rh}(111)$ ($\theta_V = 0.3$ MLE) patterned during Ammonia oxidation with NO . c) The influence of the ammonia partial pressure on the substructure of vanadium oxide islands is investigated at constant 1030 K and 1×10^{-4} mbar molecular oxygen. Adapted from *Chaos* **2018**, *28*, 045117., with the permission of AIP Publishing.

1030 K after the heating ramp was interrupted. Only after a few minutes, the condensation of the vanadium oxide film into an island pattern is completed, as can be seen in the last PEEM image of (c). Variations of the ammonia partial pressure result in the familiar size-variation of the oxidized ring. An oxygen pressure increase leads to an increase of the dark boundary phase, surrounding the bright reduced core, and an overall decrease of the PEEM intensity, as seen in the second PEEM image of (c), in which the ammonia pressure is reduced from 3×10^{-4} to 1.5×10^{-4} mbar. A subsequent ammonia pressure increase depicted in the last PEEM image of (c) restores the former high PEEM intensity and shrinks the width of the oxidized vanadium oxide ring again. Both systems, methanol and ammonia oxidation with molecular oxygen on $VO_x/Rh(111)$, exhibit the same behavior as expected from a freshly deposited VO_x film. Each reaction system has its own characteristic type of pattern, a stripe and island pattern with O_2 as oxidizing agent and a hole pattern with NO as oxidizing agent. Both types of patterns have, however, different length scales for comparable experimental parameters.

5.6.4 VO_x redistribution during the $H_2 + NO$ reaction

Besides ammonia and methanol oxidation, also the $H_2 + NO$ reaction is investigated. The $H_2 + O_2$ reaction is the simplest oxidation reaction, that can be studied on the $VO_x/Rh(111)$ model catalyst. In contrast to methanol, ammonia, and CO oxidation neither the coexistence of different vanadium oxide phases (an oxidized rim and a reduced core), nor the movement and coalescence of vanadium oxide islands is observed in a wide temperature range under comparable experimental conditions. Instead only the formation and coarsening of a large number of parallel vanadium oxide stripes is observed, which exhibit a clear preferential orientation. The $H_2 + O_2$ reaction has been studied intensely by Lovis et al. [201, 202]. A combined PEEM and SPELEEM study revealed, that the preferential orientation of the stripes is based on the anisotropic diffusion of small vanadium oxide species (e. g. V_6O_{12}) caused by step bunches on the Rh(111) surface. The width of the oxide stripes depends strongly on the pressure ratio of hydrogen and oxygen, and on the total pressure of the reaction atmosphere.

The findings obtained during the $H_2 + NO$ reaction resemble the results described by Lovis et al. surprisingly well. Figure 5.45 shows a series of PEEM images acquired during heating a $VO_x/Rh(111)$ surface ($\theta_V = 0.3$ MLE) to 1030 K and subsequently holding it at this temperature in a gas atmosphere of 1.5×10^{-4} mbar hydrogen and 1×10^{-4} mbar NO. Starting from about 900 K, the homogeneous surface state is lifted and the formation of parallel, dark vanadium oxide stripes sets in. Different from the experiments conducted during ammonia and methanol oxidation with NO, the preferential orientation of the oxide stripes is considerably disturbed by macroscopic surface scratches. These macroscopic surface scratches can best be seen in the first PEEM image of figure 5.45, in which a decoration of these scratches with VO_x increases the PEEM contrast.

The preferential orientation of the oxide stripes finally vanishes completely at around 1000 K (third PEEM image), and a gradual reorientation of the pattern starts. During this reorientation process, the coexistence of perpendicular stripes leads to the appear-

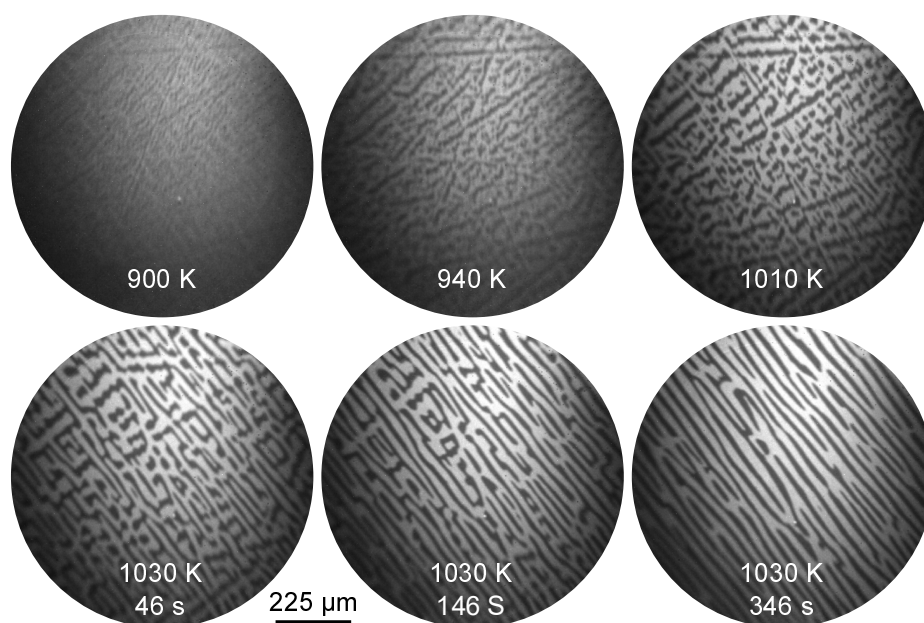


Figure 5.45: VO_x stripe pattern formation during catalytic $\text{H}_2 + \text{NO}$ reaction on 0.3 MLE $\text{VO}_x/\text{Rh}(111)$. The homogeneous $\text{VO}_x/\text{Rh}(111)$ surface is heated from room temperature to 1030 K in a reaction atmosphere consisting of 1.5×10^{-4} mbar hydrogen and 1×10^{-4} mbar nitric oxide. As 1030 K are reached, the sample is held at constant temperature for several minutes. The initially formed stripe pattern changes its orientation by 90° upon prolonged exposure to reaction conditions at 1030 K, as seen by comparing the third and last PEEM image. Adapted from *Chaos* **2018**, *28*, 045117., with the permission of AIP Publishing.

ance of square shaped vanadium oxide structures, which finally coalesce to form parallel stripes again after about 350 s at 1030 K (last PEEM image). This behavior is identical to the pattern formation observed during the $\text{H}_2 + \text{O}_2$ reaction on $\text{VO}_x/\text{Rh}(111)$ surfaces of similar V coverage [201, figure 8]. In literature it was suspected, that the reorientation of the stripe pattern may be caused by the formation of a rhodium oxide at the step bunches, which causes a different orientation of the vanadium oxide stripes. This consideration was based on the fact, that the reorientation of the stripe pattern has only been observed at a total pressure greater than 5×10^{-5} mbar.

5.6.5 Structural changes and oxygen gradients in the oxidation reactions with NO

Even though the three investigated oxidation reactions with NO, oxidized are NH_3 , CH_3OH or H_2 on 0.3 MLE $\text{VO}_x/\text{Rh}(111)$, show considerable differences in terms of pattern formation, they exhibit also common properties: In all experiments the same LEED pattern is observed after the reaction conditions were applied. In all systems no oxygen

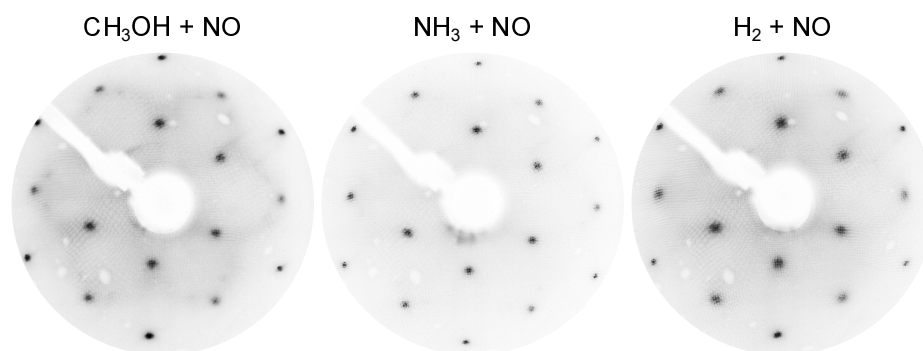


Figure 5.46: LEED pattern acquired after the pattern forming reaction conditions are applied, and the sample is cooled to room temperature. The LEED images are acquired after the $\text{CH}_3\text{OH} + \text{NO}$ reaction with 1.5×10^{-4} mbar methanol, the $\text{NH}_3 + \text{NO}$ reaction with 1.5×10^{-4} mbar ammonia, and after the $\text{H}_2 + \text{NO}$ reaction with 1.5×10^{-4} mbar hydrogen. The NO pressure is 1×10^{-4} mbar in all experiments, and 0.3 MLE vanadium oxide films are investigated. The LEED images are acquired at an electron energy of 65 eV.

gradients around the vanadium oxide structures are observed in PEEM experiments.

A series of LEED images, that are recorded after the different samples were cooled down to room temperature during a continuous flow of reactants, is shown in figure 5.46. After all three reactions, the same (2×2) LEED pattern is observed. Only after methanol oxidation, faint LEED spots of the $(\sqrt{7} \times \sqrt{7})R19.1^\circ$ are seen in the first LEED image displayed in figure 5.46. The (2×2) can be due to adsorbed oxygen. A $(2 \times 2)\text{-VO}_x$ structure has also been observed in an in situ SPELEEM study of $\text{VO}_x/\text{Rh}(111)$ during the catalytic $\text{H}_2 + \text{O}_2$ reaction by Lovis et al. [202]. XPS revealed an oxidation state of +3 for vanadium in this structure. Also in the experiments conducted during catalytic CO oxidation on $\text{VO}_x/\text{Rh}(111)$ with oxygen, a (2×2) LEED pattern is observed. This (2×2) has been clearly distinguishable from the $(2 \times 2)\text{-O}$ structure by a temperature programmed LEED experiment (0.5 K s^{-1} heating rate) conducted in 2×10^{-7} mbar [241]. The intensity of the LEED spots belonging to the (2×2) continuously decreases, starting from 400 K, until they finally vanished at around 900 K, whereas the $(2 \times 2)\text{-O}$ LEED pattern vanished already before 400 K were reached. A (2×2) vanadium oxide structure is not observed in the experiments conducted during methanol and ammonia oxidation with oxygen.

Besides different LEED pattern after reaction conditions, also the presence or absence of macroscopic oxygen gradients under reaction conditions clearly distinguishes the experiments conducted with O_2 and NO. This is demonstrated in figure 5.47, which compares two PEEM images acquired during ammonia oxidation with O_2 (a) and NO (b). The graphs show intensity line profiles taken from the interior of the vanadium oxide covered area to the bare Rh(111) surface in radial direction. In case of O_2 as oxidizing agent, the highest PEEM intensity is measured in the interior of the vanadium oxide island (the bright, reduced core). The oxidized ring is characterized by a low PEEM

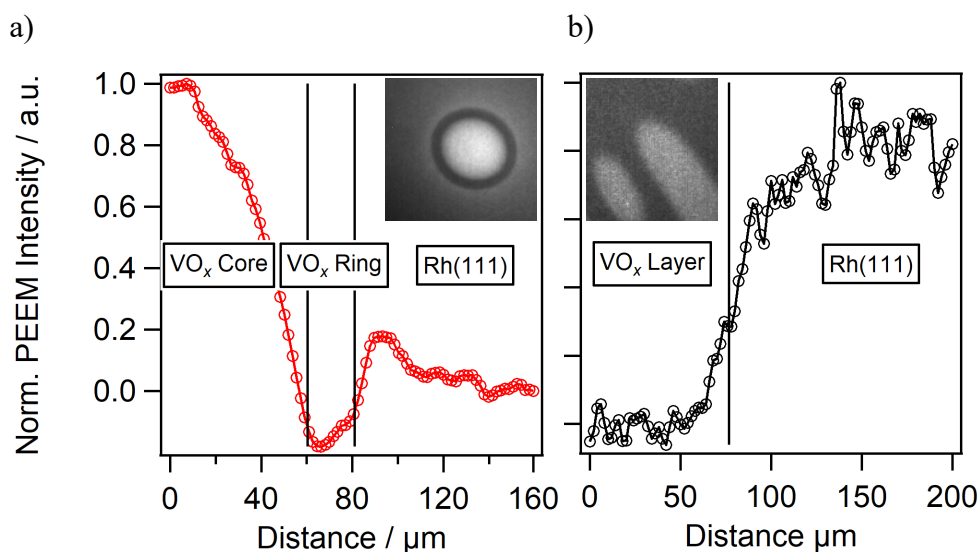


Figure 5.47: PEEM intensity line profiles taken in radial direction from the vanadium oxide covered regions to the bare Rh(111) surface during catalytic ammonia oxidation with O_2 (a) and NO (b). The PEEM images shown as insets in the graphs are taken on surfaces covered with 0.2 (a) and 0.3 MLE VO_x . The gas phase composition is 3×10^{-4} mbar ammonia and 1×10^{-4} mbar oxygen in (a), respectively 1.5×10^{-4} mbar ammonia and 1×10^{-4} mbar NO in (b).

intensity, due to its high work function. The oxidized ring can be recognized in the intensity line profile of (a) as a relative minimum at 60 to 80 μm . An increase in PEEM intensity marks the interface between the oxidized ring and the surrounding Rh(111) surface.

These gradients on the surrounding Rh(111) surface are absent or much weaker in the PEEM intensity profile from the NO reaction, displayed in figure 5.47b. The lowest (and uniform) PEEM intensity is found on the vanadium oxide covered area, whereas the highest PEEM intensity is measured on the bare Rh(111) surface, which beyond the island boundary (vertical line) exhibits a slightly increasing intensity, which then stays constant. In any case, the profile does not show an intensity that decreases with increasing distance, as observed for the reactions with O_2 (a) and which reflects an oxygen gradient away from the island. Another difference between the $\text{NH}_3 + \text{NO}$ and the $\text{NH}_3 + \text{O}_2$ reaction is the broad interface observed in the oxidation with nitric oxide.

5.6.6 Catalytic activity in the oxidation reactions with NO

The catalytic activity of different model catalysts – the bare Rh(111) surface, Rh(111) covered with 0.3 MLE vanadium oxide, and Rh(111) covered with approximately 3 MLE vanadium oxide – is studied by means of temperature programmed reaction measurements in methanol and ammonia oxidation with NO. As in the PEEM experiments, the

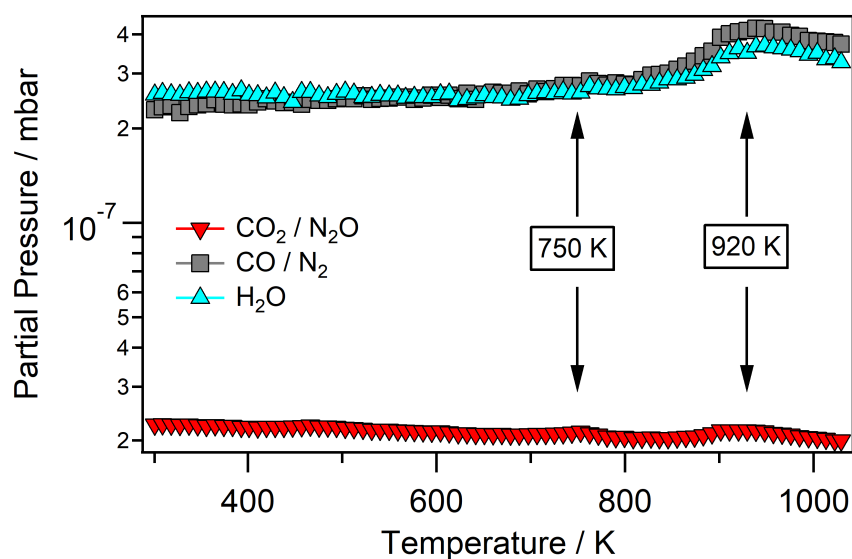


Figure 5.48: Reaction rates measured on a Rh(111) surface covered with 0.3 MLE VO_x during catalytic methanol oxidation with NO. Shown are m/e 44 (CO_2 and N_2O), 28 (CO and N_2), and 18 (H_2O). The heating rate is $0.5 K s^{-1}$, the gas phase consists of 1.5×10^{-4} mbar methanol and 1×10^{-4} mbar NO. Adapted from *Chaos* **2018**, *28*, 045117., with the permission of AIP Publishing.

samples are heated to 1030 K and subsequently cooled down to room temperature with a constant rate of $0.5 K s^{-1}$. The rate curves are shown in figure 5.48 and figure 5.49, respectively.

However, the analysis of the rate curves is complicated by the large number of overlapping mass to charge ratios of the different species occurring under reaction conditions: The already mentioned overlap of the methanol and formaldehyde fragmentation pattern is further complicated by the overlapping signals at $m/e = 30$ with nitric oxide. Also carbon monoxide and molecular nitrogen, and N_2O and carbon dioxide have the same m/e of 28 and 44, respectively. In principle, the problems connected to the overlapping QMS signals can be circumvented by isotopically labeled nitric oxide ($N^{15}O$), but such experiments could not be realized during the experiments presented in this thesis. Therefore no conclusions on formaldehyde production can be made here.

As can be seen in figure 5.48, the overall catalytic activity of the $VO_x/Rh(111)$ surface is low in the whole temperature range. Two relative production rate maxima are seen in all reaction products at around 750 and 920 K. The catalytic activity thus coincides with the occurrence of pattern formation. No signs for any catalytic activity below 750 K can be identified in the rate measurements. This is in strong contrast to the rate measurements conducted with oxygen as the oxidizing agent, where rate maxima of the CO and CO_2 production are found around 500 to 600 K. These maxima can be ascribed to the bare Rh(111) surface [68–70].

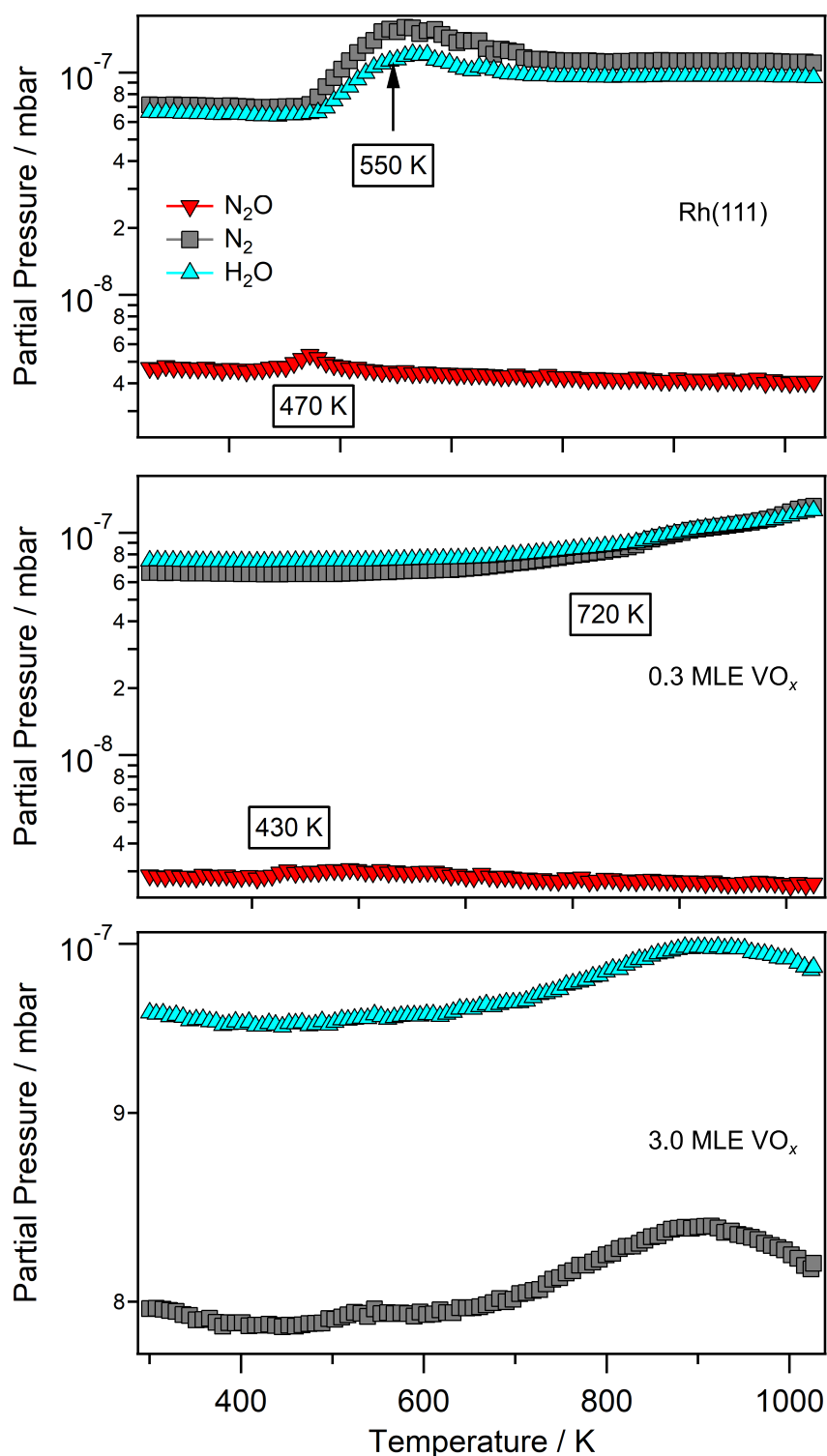


Figure 5.49: Reaction rates measured on a bare Rh(111) surface, and on Rh(111) surfaces covered with 0.3 and 3 MLE vanadium oxide during the $\text{NH}_3 + \text{NO}$ reaction. Shown are the mass to charge ratios 44 (N_2O), 28 (N_2), and 18 (H_2O). The heating rate is 0.5 K s^{-1} , the gas phase consists of 1.5×10^{-4} mbar ammonia and 1×10^{-4} mbar NO . Adapted from *Chaos* **2018**, *28*, 045117., with the permission of AIP Publishing.

Reaction rate measurements obtained during ammonia oxidation with NO are depicted in figure 5.49. The highest catalytic activity is measured on the bare Rh(111) surface, as it is also the case in the $NH_3 + O_2$ reaction. A first N_2O production peak is seen at around 470 K. This peak is shifted by about 20 K to lower temperature in the cooling branch of the experiment (not shown), indicating a slight hysteresis. The nitrogen and water production curves exhibit nearly the same curves. After passing through a relative maximum at around 550 K, the catalytic activity stays at a high level until the heating ramp is stopped at 1030 K. In contrast to the N_2O production rate, no hysteresis is found in the cooling branch of the experiment.

The deposition of 0.3 MLE vanadium oxide already completely inhibits N_2 and water formation at 550 K, and also the N_2O production peak is considerably decreased and slightly shifted to lower temperature. Only around 720 K, a gradual increase of the N_2 and water production sets in, which continues until 1030 K. Surprisingly, no hysteresis can be observed in the cooling branch, which one could expect due to pattern formation. This finding indicates an incomplete phase separation: the holes in the dense vanadium oxide layer formed under reaction conditions still contain a considerable amount of vanadium, because otherwise nitrogen and water production peaks should be observed around 550 K in the cooling branch of the TPR experiment. A closer inspection of the PEEM images in figure 5.44b already reveals the presence of a considerable amount of VO_x in the vanadium oxide depleted holes. The reaction rate measurements presented in this section demonstrate, that already this low amount of vanadium oxide completely poisons the catalytic activity of Rh(111).

The inhibitory effect of vanadium oxide is also observed on the 3 MLE thick vanadium oxide film. This surface has the lowest catalytic activity of the three investigated systems. The N_2O production is even completely inhibited. The apparent large difference in the nitrogen and water production rates is no experimental result but only a visual impression caused by the different scale of the abscissa (the first two graphs in figure 5.49 have the same scaling). The rate curves resemble the production rates measured on 0.3 MLE vanadium oxide, except a slight decrease in activity between 900 and 1030 K of the high coverage VO_x film. Different than on the thin VO_x film, the cooling branch of the TPR experiment shows a strong hysteresis, especially water formation is increased with respect to the heating branch. This trend continues, if the sample is exposed to a second TPR experiment. The increase in catalytic activity is accompanied by a decrease in the vanadium oxide coverage from 3 to approximately 1.2 MLE after completion of the second TPR experiment.

LEED images acquired after the TPR experiments show a Moiré pattern, as it is observed for a coverage around 1 MLE during vanadium oxide deposition rate calibration (figure 5.1 (c) and the fifth LEED image in figure 5.4). Evidently, the conditions of ammonia oxidation with NO suffice not to stabilize V on the Rh(111) surface at high temperature, and a part of vanadium diffuses into subsurface sites or deeper layers of the Rh(111) crystal, as reported for the in vacuo annealing of vanadium layers on Rh(111) for temperatures around 1000 K [186]. The decreased thickness of the vanadium oxide film and a potential reduction of VO_x during the TPR experiments may be the reason

for the increased catalytic activity.

In conclusion, an increase of the catalytic activity in the same temperature range where oxide redistribution takes place is observed in the oxidation reactions with NO, but the overall catalytic activity is quite low, especially compared to the bare Rh surface. Compared to the oxidation reactions with O_2 , especially with methanol oxidation, vanadium oxide seem to be more or less inert, if NO is used as oxidizing agent.

5.6.7 Conclusions from the PEEM experiments conducted with NO

The following conclusions can be made from the PEEM experiments: In catalytic oxidation of ammonia, methanol, and CO with oxygen, macroscopic vanadium oxide islands develop, which cause the formation of oxygen gradients. If the island size is above a critical radius a substructure inside the VO_x islands develops and different vanadium oxide phases coexist. If the mentioned oxidation reactions are carried out with NO instead, no island formation is observed and no detectable oxygen gradients develop. Starting from low temperature initially a stripe pattern evolves, which then is transformed into a hole pattern. A preferential orientation is imposed by step bunches on the isotropic (111) surface. In the $H_2 + O_2$ reaction, no formation of oxide islands is observed, and also no oxygen gradients can be detected on the bare Rh(111) surface or in the vanadium oxide covered regions. The catalytic rate measurements demonstrate a low catalytic activity of vanadium oxide compared to the bare Rh(111) surface in oxidation reactions with NO. The low catalytic activity of VO_x indicates that VO_x covered areas do not act as micro-reactors, consuming oxygen.

5.7 VO_x redistribution during NH_3 oxidation in SPELEEM

The exchange of molecular oxygen by nitric oxide as oxidizing agent in catalytic ammonia or methanol oxidation has a drastic impact on the reaction-induced redistribution of vanadium oxide, resulting in different macroscopic redistribution pattern: with molecular oxygen circular vanadium oxide islands of several tens to hundreds micrometer width develop close to 1000 K. Depending on the reaction conditions these islands can exhibit a substructure consisting of a reduced core and an oxidized rim. With nitric oxide as the oxidizing agent, the inverse redistribution pattern is obtained, a dense vanadium oxide film, which contains macroscopic holes of VO_x depleted area. In order to investigate the surface chemistry which causes the different behavior in terms of pattern formation, catalytic ammonia oxidation with O_2 and NO on submonolayer thick $VO_x/Rh(111)$ films is performed at the Nanospectroscopy beamline (Elettra).

A macroscopic VO_x island pattern is prepared by exposing a freshly prepared VO_x film to the conditions of ammonia oxidation (with O_2) in the 10^{-4} mbar range in a separate high pressure cell. Subsequently, the VO_x islands and the surroundings are characterized ex situ by means of μ LEED and spatially resolved XPS (XPEEM and μ XPS) before reaction conditions are adjusted for an in situ characterization. Firstly the $NH_3 + O_2$ reaction is studied in the 10^{-6} mbar range, before the oxidizing agent O_2 is

replaced by NO for further in situ measurements during the $NH_3 + NO$ reaction. Prior to the reaction studies, a V coverage calibration (similar to that described in section 5.4.2) was performed by a step-wise deposition of vanadium oxide by reactive evaporation followed by an XPS and LEED characterization.

5.7.1 VO_x coverage calibration

In order to assign vanadium oxide coverages to the ex situ and in situ measured photoemission spectra collected on the patterned $VO_x/Rh(111)$ surface, a calibration of the signals is essential. The V 2p / Rh 3p core level intensity ratio as a function of (known) vanadium coverage of submonolayer VO_x films needs to be determined. Therefore, vanadium oxide is deposited in a step-wise manner by reactive evaporation (~ 670 K, 2×10^{-7} mbar oxygen) onto the Rh(111) surface. After every deposition step, the sample is kept at high temperature for further ten minutes and cooled down in the oxygen atmosphere for the LEED and XPS characterization. The LEED images recorded as a function of VO_x deposition time and coverage are displayed in figure 5.50.

The VO_x coverage assignment is based on the disappearance of the $(\sqrt{7} \times \sqrt{7})R19.1^\circ$ diffraction spots and appearance of spots belonging to an (8×8) structure at around 14 min deposition time. A VO_x coverage of approximately 0.7 MLE is assigned, resulting in a V deposition rate of $0.05 \text{ MLE min}^{-1}$. The coverage assignment is based on a combined STM and DFT study, which reports a coverage of 0.5 to 0.6 MLE for the completion of a closed layer (STM) and an ideal coverage of 0.43 MLE (DFT) for the $(\sqrt{7} \times \sqrt{7})R19.1^\circ$ structure, respectively [53]. The decrease of the $(\sqrt{7} \times \sqrt{7})R19.1^\circ$ LEED intensity is assigned to a coverage of 0.6 MLE.

The first LEED image displayed in figure 5.50 is recorded on the vanadium oxide free, oxygen covered Rh(111) surface and displays (2×2) diffraction spots generated by adsorbed oxygen. Upon deposition of small amounts of VO_x the (2×2) spots initially become broader and weaker (0.1 MLE) until they sharpen again and additional spots belonging to the $(\sqrt{13} \times \sqrt{13})R13.8^\circ$ vanadium oxide structure appear. With increasing vanadium oxide coverage the $(\sqrt{13} \times \sqrt{13})R13.8^\circ$ becomes stronger while the (2×2) intensity decreases again. At 0.5 MLE additional spots belonging to the $(\sqrt{7} \times \sqrt{7})R19.1^\circ$ structure appeared (marked by two arrows in the sixth LEED image). The deposition of further 0.2 MLE VO_x results in the superposition of diffraction spots of the $(\sqrt{7} \times \sqrt{7})R19.1^\circ$ structure and an $(n \times n)$, with n being approximately eight.

Different from most other experiments described in this study, the reactive evaporation yields the $(\sqrt{13} \times \sqrt{13})R13.8^\circ$ VO_x phase instead of the $(\sqrt{7} \times \sqrt{7})R19.1^\circ$ for coverages ≤ 0.4 MLE. The $(\sqrt{13} \times \sqrt{13})R13.8^\circ$ and the $(\sqrt{7} \times \sqrt{7})R19.1^\circ$ VO_x structures, both having a VO_3 composition, are quite similar and ideal V coverages of 0.46 and 0.43 MLE have been determined with DFT, respectively [53]. The formation energy per VO_3 unit of the $(\sqrt{7} \times \sqrt{7})R19.1^\circ$ is reported to be slightly lower compared to the $(\sqrt{13} \times \sqrt{13})R13.8^\circ$ structure. However, the higher coverage of the $(\sqrt{13} \times \sqrt{13})R13.8^\circ$ structure results in a lower surface energy (the product of formation energy and coverage). Schoiswohl et al. concluded that the $(\sqrt{13} \times \sqrt{13})R13.8^\circ$ structure is therefore the thermodynamically more stable structure, i. e. the $(\sqrt{7} \times \sqrt{7})R19.1^\circ$ phase is

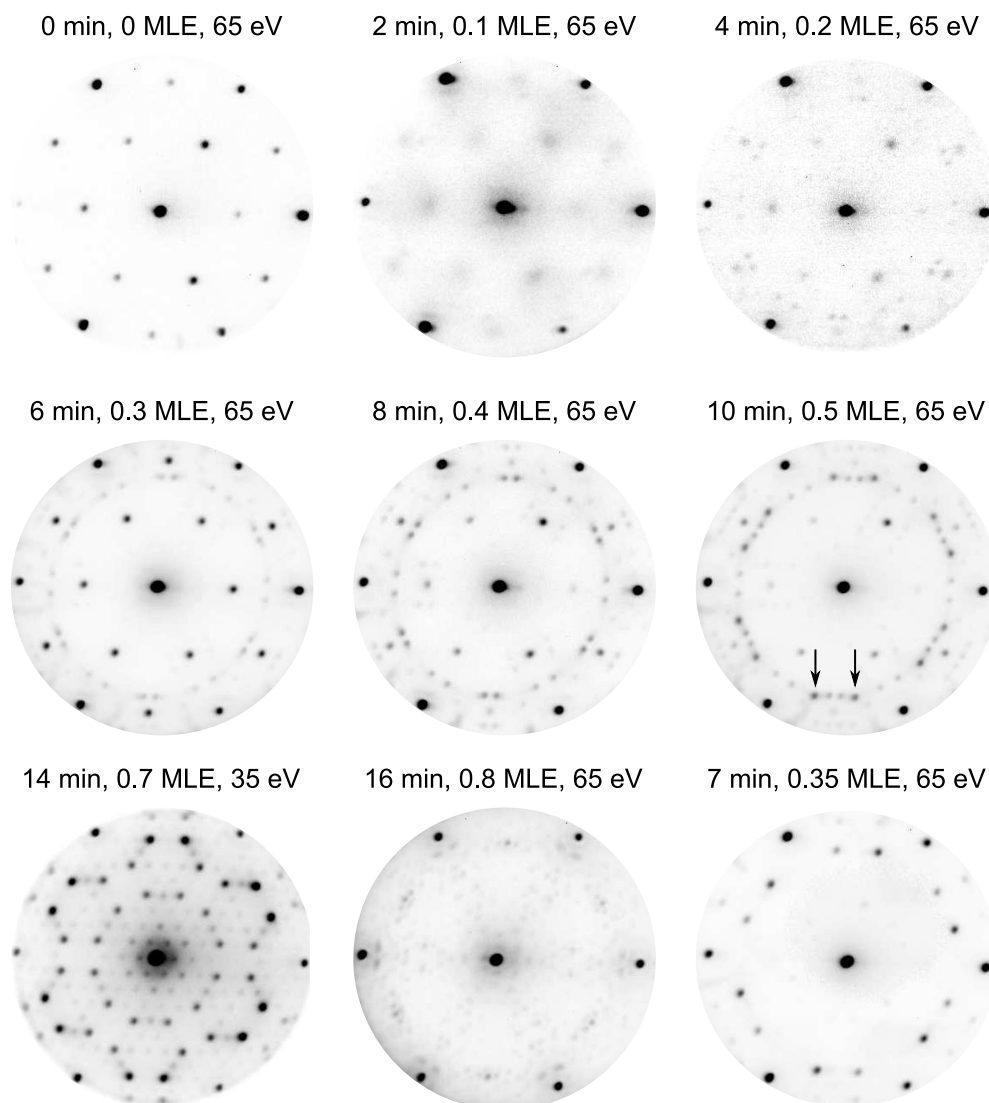


Figure 5.50: LEED images acquired during step-wise deposition of VO_x for a coverage calibration. VO_x is deposited by reactive evaporation at 640 K in 2×10^{-7} mbar oxygen. Before and after each deposition, the sample is kept at high temperature in oxygen for ten minutes. All images are acquired below 370 K. The last image shows for comparison a VO_x film grown by continuous deposition of 0.35 MLE under similar conditions.

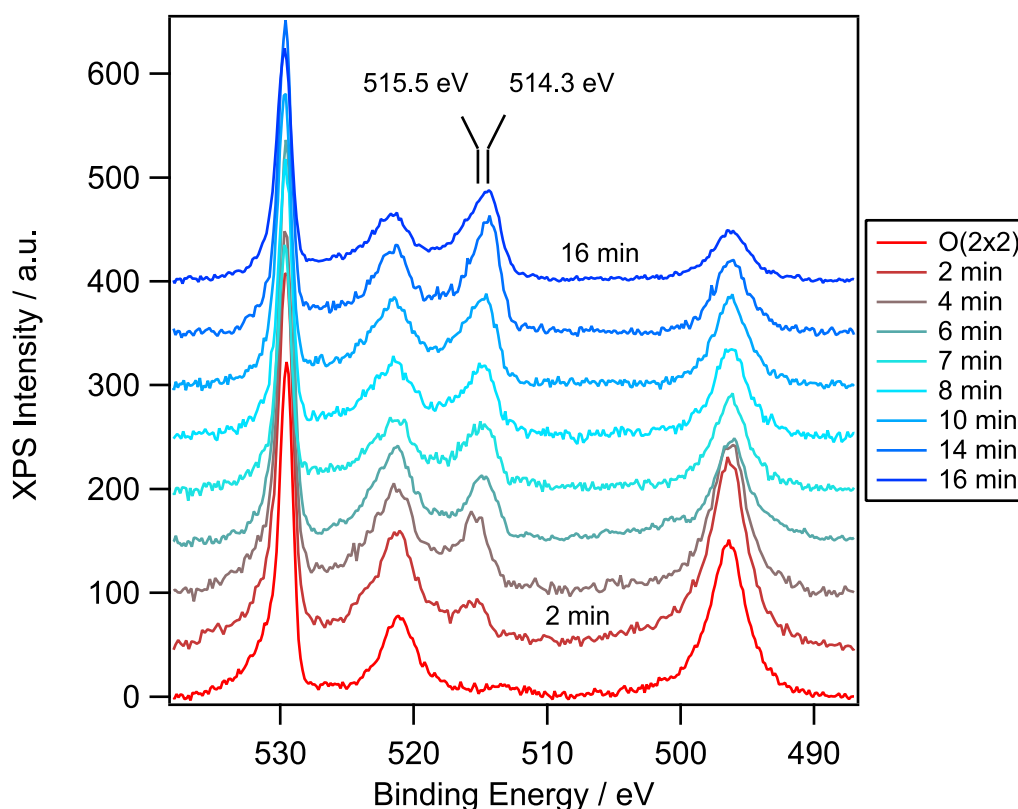


Figure 5.51: Rh 3p, V 2p and O 1s photoemission spectra (after a Shirley-type background is subtracted) for the V coverage determination. For the numeric fits a doublet-separation of 24.8 eV and 7.4 - 7.6 eV for Rh 3p and V 2p is used, respectively. The films are grown as described in figure 5.50 and the spectra are acquired in an oxygen atmosphere of 2×10^{-7} mbar after the sample was cooled below 330 K.

“only kinetically trapped, e.g. upon reactive evaporation” [53, p.155403-7]. The last LEED image displayed in figure 5.50 obtained after continuous deposition of 0.35 MLE VO_x displays only diffraction spots belonging to the $(\sqrt{7} \times \sqrt{7})R19.1^\circ$ phase. The VO_x film is grown under similar conditions as the ones prepared during the coverage calibration, and demonstrates that only small parameter changes can stabilize either the $(\sqrt{13} \times \sqrt{13})R13.8^\circ$ or $(\sqrt{7} \times \sqrt{7})R19.1^\circ$ phase. Due to the small coverage difference of only 0.03 MLE, the accuracy of the calibration curve is not significantly affected by the (co)existence of the two VO_x phases.

XP spectra recorded on the oxygen covered Rh(111) surface and after every deposition step during the coverage calibration are shown in figure 5.51. As described in literature, a binding energy shift of the V 2p core level to lower values is observed for coverages exceeding 0.5 to 0.6 MLE. This binding energy shift is caused by the incorporation of V atoms into the highly oxidized $(\sqrt{7} \times \sqrt{7})R19.1^\circ$ phase and the resulting reduction of V, starting after the Rh(111) surface is completely covered with VO_x [53].

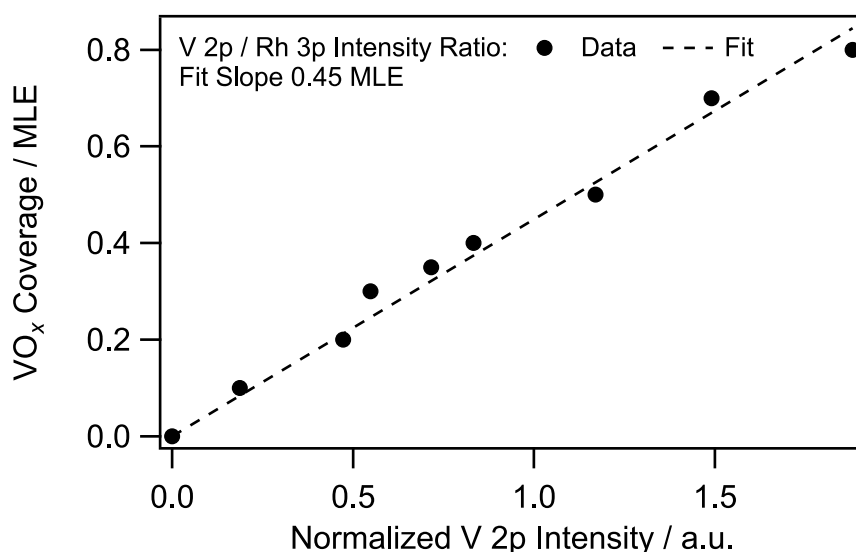


Figure 5.52: V coverage as a function of V 2p / Rh 3p core level intensity ratio. A linear fit (dashed line) yields a factor of 0.45 MLE for the conversion of V 2p / Rh 3p intensity ratios to V coverages. The data points are obtained from numerical fits to the spectra displayed in figure 5.51.

From numeric fits of the displayed spectra a linear dependence of the VO_x coverage on the V 2p / Rh 3p core level intensity ratio (“normalized V 2p intensity”) is obtained. The resulting coverage calibration curve is displayed in figure 5.52. For the numeric fits (not shown) the whole spectra are fitted with individual components for the Rh 3p, V 2p and O 1s core levels. A factor of 0.45 MLE is determined for the conversion of V 2p / Rh 3p intensity ratios into V coverages.

The conversion factor obtained from the VO_x deposition rate calibration can be used to determine (submonolayer) V coverages measured ex situ and in situ on the different parts of the vanadium oxide islands and their surroundings. In order to calculate the corresponding oxygen coverages, the O 1s / V 2p core level ratio is calculated from the numeric fits of the measured spectra. The intensity ratios are then converted into O coverages using equation 2.5 and the values listed in table 2.1 for the photoionization cross sections.

5.7.2 Ex situ VO_x coverage determination on oxide islands

A freshly prepared $VO_x/Rh(111)$ film of 0.2 MLE is transferred in vacuo into the high pressure cell in order to form a macroscopic VO_x island pattern during catalytic methanol oxidation with O_2 . Therefore, the sample is kept for 20 min at approximately 1000 K in a reaction atmosphere of 1×10^{-4} mbar oxygen and 1×10^{-4} mbar ammonia. Subsequently, the sample is cooled down to 370 K in the reaction gases and transferred into the main chamber in vacuum for an ex situ characterization.

After exposure to reaction conditions, the surface shows a large number of elongated vanadium oxide islands, which exhibit a substructure, consisting of a core, an outer ring, and a boundary phase separating the latter two. An image of such an oxide island is seen in the insets in figure 5.53a and b. At the start voltage chosen for acquisition of the MEM image in figure 5.53b, the island core and the outer ring appear as dark area, whereas the boundary phase separating the two is bright. By comparing the LEEM image with the in situ LEEM measurements conducted in the 10^{-4} mbar range during methanol oxidation (figure 5.16), the island core can be identified as the VO_x core, whereas the bright boundary phase corresponds to the oxidized VO_x ring. The interface between the oxidized ring and the Rh surface is very broad, therefore, in the following, the oxidized ring is called “inner ring”, whereas the broad interface is termed “outer ring”.

The local work function measurements displayed in figure 5.53a reveal a work function difference of 1.33 eV between the inner ring and the surrounding Rh(111) surface. In such a measurement, the start voltage is increased in imaging mode from a very low value, in which the surface is imaged in MEM mode, to a value of several eV, in which the surface is imaged in LEEM mode. The transition from MEM to LEEM mode appears as a sharp intensity decrease. The difference in start voltage at which this intensity decrease is observed in different areas of the surface corresponds to the work function difference.

An interesting behavior can be seen in the $I(V)$ curve of the island core. Instead of a single intensity decrease, a step wise decrease with a pronounced plateau phase is observed. This behavior is caused by the coexistence of (at least) two different phases, which contribute to the overall $I(V)$ curve. Interestingly, one of the two phases has a low work function close to the surrounding Rh(111) surface, whereas the other phase has a work function slightly lower than the inner ring. PEEM images acquired in the 10^{-4} mbar range during catalytic ammonia oxidation indicate a low work function in the reduced island core. The existence of a high work function phase in the island core should therefore be seen as a result of sample cooling for the ex situ characterization.

LEEM- $I(V)$ measurements conducted in the same sample area are displayed in figure 5.53b. The three $I(V)$ curves collected on the vanadium oxide covered areas of the surface show a very similar shape and differences can only be identified in the heights of the relative maxima. Only the $I(V)$ curve recorded on the VO_x depleted Rh(111) surface surrounding the oxide island differs significantly.

A pixel-wise analysis of the collected $I(V)$ stack is shown in the bottom part of figure 5.53b. In this representation (binary images), black area corresponds to the area, which generates the corresponding $I(V)$ curve. The first and second binary images represent the $I(V)$ curves measured on the Rh(111) surface and the inner ring, respectively. The $I(V)$ curve corresponding to the outer ring also contributes to the island core, as can be seen in the third binary image. Therefore also the LEEM- $I(V)$ measurements indicate the coexistence of at least two different phases in the island core.

A representative μ LEED image of an image series acquired across the Rh(111) surface and the VO_x island, displayed in figure 5.54, corroborates the assumption of a phase transition during the cool-down in the high pressure cell. As can be seen in the left

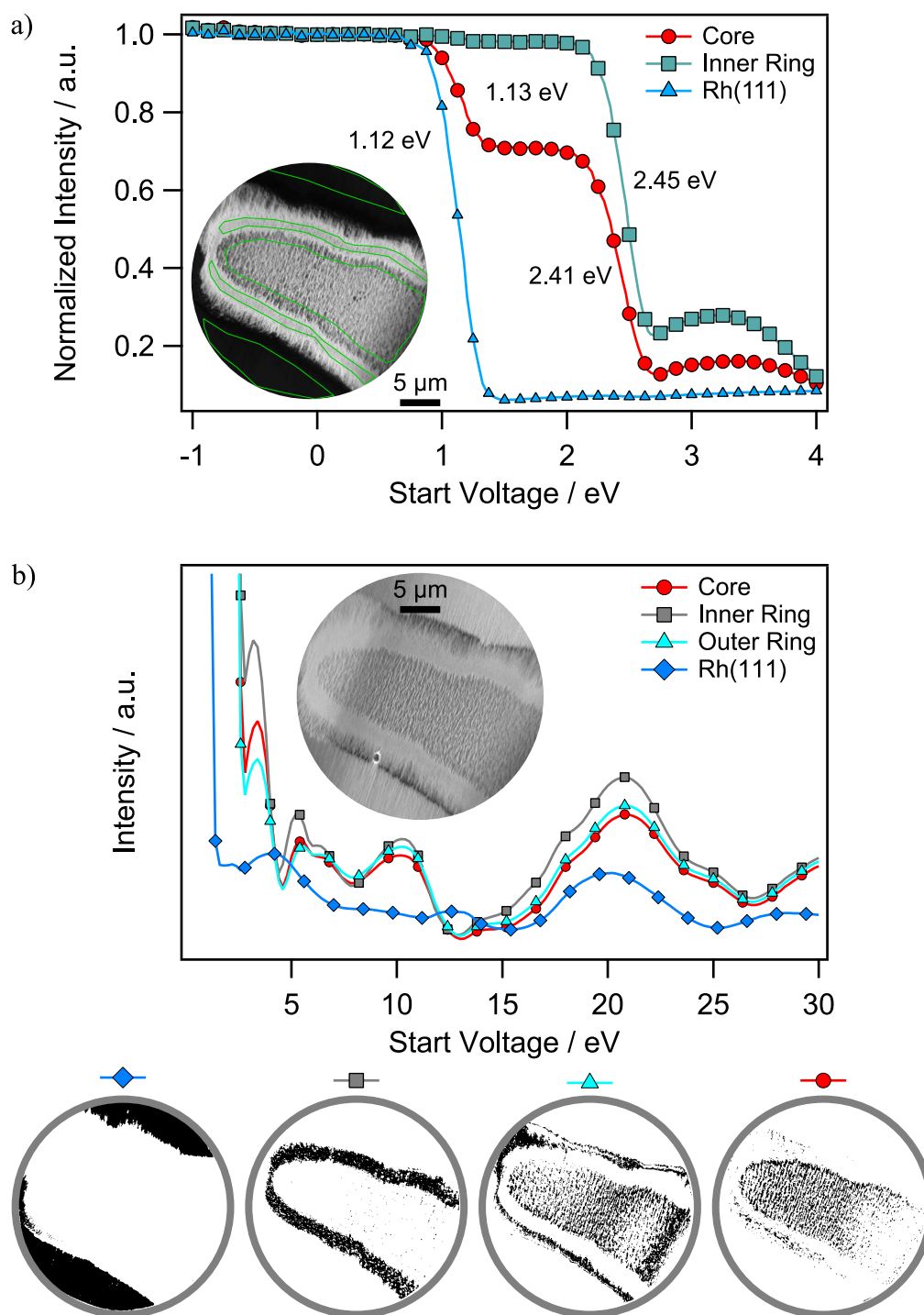


Figure 5.53: Ex situ LEEM- $I(V)$ analysis of macroscopic vanadium oxide islands formed during ammonia oxidation. a) Measurement of local work function differences in an $I(V)$ scan. The steep intensity decrease between 1 and 2.5 eV marks the transition from the MEM into the LEEM mode. The work function differences between the island core, inner ring and the surrounding Rh(111) surface is measured. The regions of interest are indicated by green solid lines in the image (2.4 eV start voltage) shown in the inset. b) LEEM- $I(V)$ measurements on the different parts of the surface. A pixel-wise evaluation (four binary images at the bottom) of the central MEM image shown in the inset reveals which areas of the surface contribute to the different $I(V)$ curves displayed in b (dark area in the binary images).

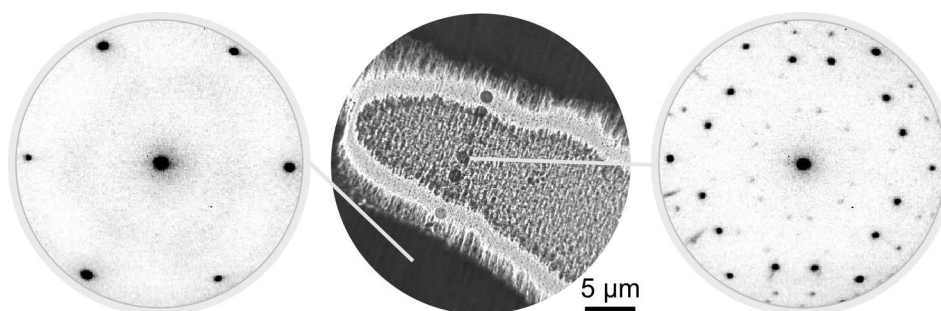


Figure 5.54: μ LEED characterization of a vanadium oxide island obtained after catalytic ammonia oxidation in the 10^{-4} mbar range. The area which is probed can be recognized as circular dark spots (beam damage) on the vanadium oxide covered parts of the surface. The shown LEED images are representative for the Rh(111) and the VO_x covered parts of the surface. Both images are acquired at a start voltage of 65 eV at room temperature in vacuum. The LEEM image is acquired at 2.3 eV.

LEED image acquired on the bare Rh(111) surface, only the integer diffraction spots are visible, together with some diffuse intensity at the half order positions. Interestingly, all μ LEED images acquired on the vanadium oxide island exhibit the same $(\sqrt{7} \times \sqrt{7})R19.1^\circ$ diffraction pattern, as shown in the left LEED image. The appearance of the $(\sqrt{7} \times \sqrt{7})R19.1^\circ$ in the center of the vanadium oxide island is surprising, since it is only observed in the outer oxidized ring in the in situ LEEM measurements in the 10^{-4} mbar range during methanol oxidation, and since it is associated to a highly oxidized VO_x phase [53].

O 1s, V 2p_{3/2} and Rh 3p_{3/2} XPEEM images of the vanadium oxide island and XP spectra extracted from the bare Rh surface, the VO_x island ring and the VO_x island core are displayed in figure 5.55a and b, respectively. The O 1s and V 2p XPEEM images reveal a nearly complete phase separation into vanadium oxide covered and free surface, and small amounts of oxygen are measured on the bare Rh(111) surface. This is reflected in the V coverages calculated from the V 2p / Rh 3p core level intensity ratios, which are 0.06 MLE on the surrounding Rh surface, and 0.31 and 0.36 MLE in the island ring and island core, respectively.

From the O 1s / V 2p intensity ratios oxygen coverages of 0.3 MLE result for the bare Rh surface, and 1.1 MLE for the island ring and island core. The vanadium oxide composition is with $VO_{3.5}$ (ring) and $VO_{3.1}$ (core) close to the ideal composition of the $(\sqrt{7} \times \sqrt{7})R19.1^\circ$ structure, which is VO_3 [53]. Interestingly, a considerably higher oxygen amount is measured in the VO_x island ring, compared to the island core, as expected for an oxidized ring and a reduced core. This is surprising, since the complete island is oxidized into the $(\sqrt{7} \times \sqrt{7})R19.1^\circ$ structure during sample cool-down. The results of the ex situ XPS characterization are summarized in table 5.2.

In addition to the O 1s, V 2p, and Rh 3p core levels, also the N 1s core level is measured. Therefore the photon energy has to be changed from 650 to 670 eV. Due to this change, only absolute N 1s intensities can be compared and not N 1s / Rh 3p intensity

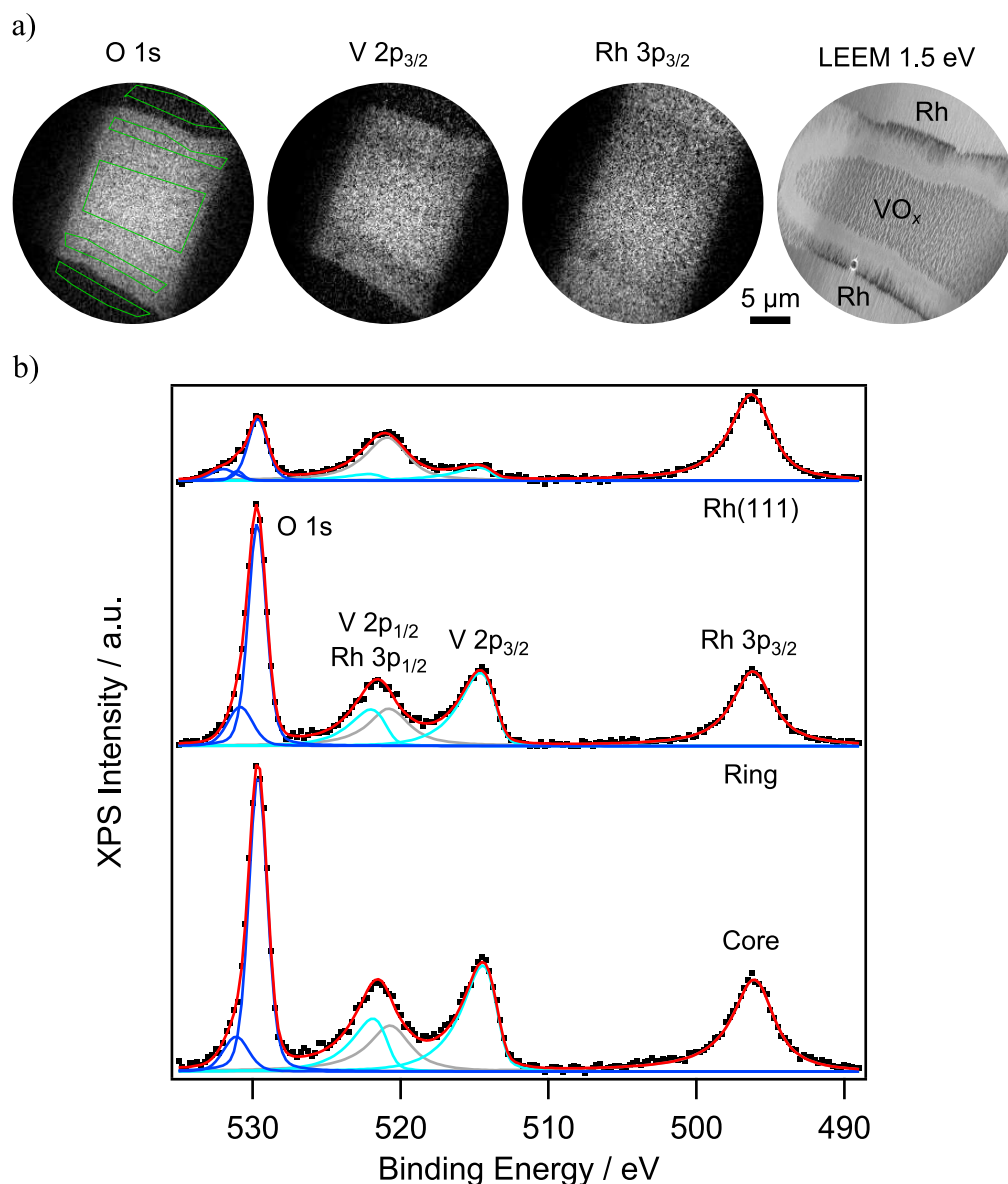


Figure 5.55: Ex situ XPS characterization of vanadium oxide islands obtained after ammonia oxidation at 1000 K in 1×10^{-4} mbar oxygen and 1×10^{-4} mbar ammonia, the deposited V coverage is 0.2 MLE. a) O 1s, V 2p_{3/2} and Rh 3p_{3/2} XPEEM images and a LEEM image acquired on a vanadium oxide island and the surrounding Rh surface. b) XP spectra (Shirley-type background subtracted) extracted from the data shown in (a) on the island core, the island ring, and the surrounding Rh surface, together with numeric fits. The regions of interest are indicated in the O 1s image by solid green lines. The spectra are acquired at room temperature in vacuum with a photon energy of 650 eV.

Table 5.2: V and O coverages obtained from ex situ recorded XP spectra of vanadium oxide islands shown in figure 5.55b. Shown are the binding energies (BE) and areas of the individual fit components, as well as the calculated vanadium and oxygen coverages θ_V and θ_O .

	O 1s BE / eV Peak area / a.u.	V 2p BE / eV Peak area / a.u.	Rh 3p BE / eV Peak area / a.u.	θ_V, θ_O / MLE
Rh	529.7, 531.1, 532; 128	514.8; 68	496.3; 533	0.06, 0.3
Ring	529.7, 530.9; 396	514.6; 319	496.2; 463	0.31, 1.1
Core	529.7, 531.1; 499	514.4; 476	496.1; 594	0.36, 1.1

ratios. The largest nitrogen signal is measured on the VO_x depleted Rh surface, followed by the island core with roughly 10% less intensity. The lowest N signal is measured on the island ring. Compared to the bare Rh surface, only 70% of the N 1s intensity is measured on the island ring. The nitrogen distribution is thereby similar to the carbon distribution measured ex situ after methanol oxidation (section 5.4.3). The highest amounts are measured on the Rh surface. However, different from the situation apparent after methanol oxidation, a considerable amount of oxygen is present on the bare Rh surface after ammonia oxidation. The pressure of oxygen during the cool-down might be an explanation for the oxidation of the whole VO_x island, resulting in the formation of the $(\sqrt{7} \times \sqrt{7})R19.1^\circ$ structure not only in the oxidized ring, but also in the core.

In general, the above described characterization of the macroscopic vanadium oxide islands formed during ammonia oxidation, and the comparison with in situ LEEM measurements in the 10^{-4} mbar range reveal, that a number of processes occur during the cool-down of the catalytic surface, which render a translation of the ex situ obtained results to the properties of the catalyst active under reaction conditions difficult.

5.7.3 In situ characterization of VO_x during the $NH_3 + O_2$ reaction

In order to obtain information about the lateral distribution of oxygen during ammonia oxidation with molecular oxygen and nitric oxide as the oxidizing agent, in situ SPELEEM measurements are performed in the 10^{-6} mbar range. Even though the original phenomenon of circular vanadium oxide islands and the formation of a dense VO_x layer with holes is observed with PEEM in the 10^{-4} mbar range, for technical reasons SPELEEM had to be taken at lower pressure in the 10^{-6} mbar range.

For the in situ measurements, the sample is heated within ten minutes to 910 K in an oxygen and ammonia atmosphere in the low 10^{-6} mbar range. Afterwards, the sample is kept at this temperature for the rest of the experiment. Heating the sample

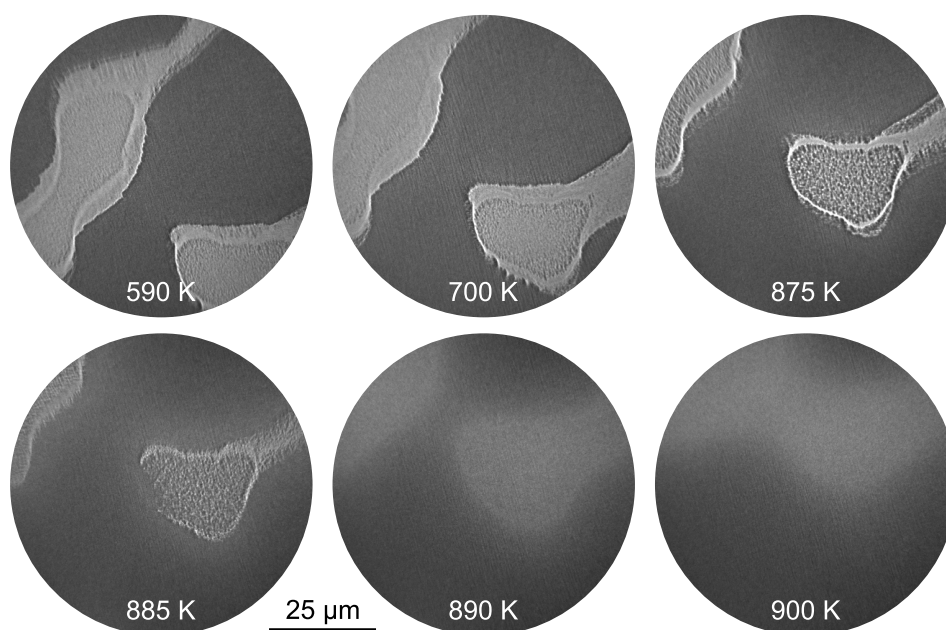


Figure 5.56: LEEM images showing vanadium oxide island coalescence during adjustment of ammonia oxidation reaction conditions. Vanadium oxide islands can be recognized as bright objects on the dark Rh(111) surface. The series of LEEM images is acquired over a period of 4.5 min with a start voltage of 1.6 eV. The gas phase consisted of 4×10^{-7} mbar oxygen and 2.4×10^{-6} mbar ammonia.

up to such a high temperature is connected with a continuous drift, resulting from thermal expansion of the sample holder and the manipulator⁴. This sample drift makes a reliable XPS characterization nearly impossible, since not only lateral movement is encountered, but also vertical movement towards or away from the objective lens. Since the incoming photon beam impinges on the sample surface in grazing incidence (16°), any vertical movement is associated with a movement of the X-ray beam on the sample, which drastically affects the measured photoemission intensity. Consequently, the XPS characterization can only be performed after a several hours long thermalization period.

Figure 5.56 shows a series of LEEM images acquired during the heat-up of the sample in a continuous flow of the reaction gases. Two bright, neighboring vanadium oxide islands / stripes can be identified on the dark Rh surface (first image). Both islands exhibit a substructure consisting of an island core and an island ring. As a consequence of the temperature increase, the “outer ring” (the broad interface between the VO_x island and the Rh surface) and the “inner ring” that were present at room temperature merged, resulting in a single oxidized ring. Starting at around 500 K, the initially fuzzy interface between the vanadium oxide covered and vanadium oxide depleted area sharpens slightly.

A further temperature increase to 875 K results in a stronger contrast between the

⁴This sample drift can be seen by comparing the first and the last LEEM image depicted in figure 5.56

island core and the island ring, as seen in the third image of figure 5.56. Simultaneously, the island ring spreads out so that the initially sharp boundary becomes fuzzy. Finally, at 890 K, the whole vanadium oxide covered area looks homogeneously in LEEM with a diffuse boundary (fifth image). Obviously, the temperature increase from room temperature to 900 K drastically increased the mobility of VO_x , as evidenced by the coalescence of the two neighboring oxide islands, that can be seen in the last three images.

After about thirty minutes at 910 K, the coalescence of neighboring vanadium oxide islands results in a small number of very large (several tens to hundreds of μm diameter), homogeneous oxide islands. The VO_x covered area is separated from the surrounding Rh surface by a sharp, less than 5 μm wide interface, as displayed in the LEEM image in figure 5.57a.

The corresponding LEED images taken on the VO_x depleted area (dark in LEEM, right LEED image) and on the VO_x covered area (bright area in LEEM, left LEED image) indicate, that a structural transition occurred during heating the sample up in the reaction atmosphere to 910 K. At room temperature, the Rh(111) surface exhibited only the integer diffraction spots and some diffuse intensity at the half order positions in LEED. The right LEED image in figure 5.57a displays, besides a diffuse (2×2) , also weak diffraction spots belonging to a $(\sqrt{3} \times \sqrt{3})$ -Moiré pattern. The same Moiré pattern is also present in the LEED image taken on the VO_x covered area, but the diffraction spots are more intense and sharper on VO_x . The diffuse (2×2) is absent in the LEED images taken on the vanadium oxide island. Even though both, the vanadium oxide enriched and depleted surface, exhibit a similar LEED pattern, their LEEM- $I(V)$ curves differ considerably, as can be seen in figure 5.57b. The different $I(V)$ curves demonstrate, that the surface structure of the VO_x enriched and VO_x depleted surface areas differ, even though they generate similar diffraction pattern.

A $(\sqrt{3} \times \sqrt{3})$ -Moiré pattern is also observed in the reduced vanadium oxide island core during the in situ LEEM measurements conducted in the 10^{-4} mbar range (methanol oxidation) presented in section 5.3. Different from the results here, the oxidized ring of the vanadium oxide island exhibits a $(\sqrt{7} \times \sqrt{7})R19.1^\circ$ structure, whereas a (1×1) is measured on the surrounding Rh surface. Obviously, the lower total pressure in the 10^{-6} mbar range does not suffice to stabilize *i*) the core-ring structure of the vanadium oxide islands, and *ii*) the $(\sqrt{7} \times \sqrt{7})R19.1^\circ$ structure, which was initially present after ammonia oxidation in the high pressure cell.

For the further characterization, the ammonia pressure is reduced while keeping the oxygen pressure constant, in order to slow down the vanadium oxide island movement. XP spectra (together with numeric fits) taken on the vanadium oxide islands and on the surrounding surface two and 18.5 hours after reaction conditions were adjusted are displayed in figure 5.58a and b, respectively. The core level binding energies and intensities obtained from the numeric fits are summarized in table 5.3, together with the calculated vanadium and oxygen coverages.

By comparing the photoemission spectra collected two hours after the reaction conditions were adjusted with the spectra taken after 18.5 h, one notices two main differences: *i*) the V 2p core level measured after two hours under reaction conditions is much more

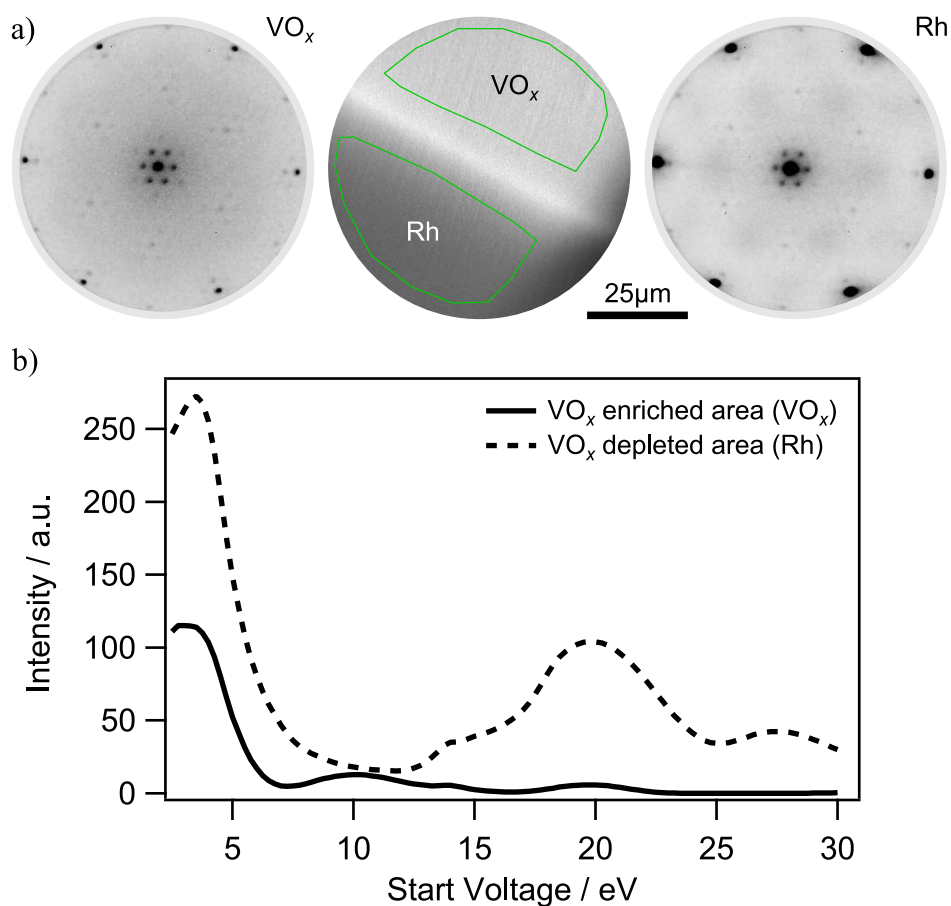


Figure 5.57: In situ LEED and LEEM- $I(V)$ characterization of VO_x islands and the Rh surface in the 10^{-6} mbar range. a) LEED images taken on the vanadium oxide covered (left) and VO_x depleted (right) area visible in the central LEEM image. The LEEM image is acquired at a start voltage of 13 eV at 910 K in 4×10^{-7} mbar oxygen and 2.4×10^{-6} mbar ammonia. The LEED images are acquired at 37 eV start voltage. b) LEEM- $I(V)$ characterization of the VO_x enriched and VO_x depleted surface area.

intense than the after 18.5 h. This is reflected also in the calculated V coverages, which reduce from an initial value of 0.54 MLE to 0.15 - 0.17 MLE after 18.5 h. The strong decrease in V coverage upon prolonged exposure to reaction conditions in the 10^{-6} mbar range demonstrates a reduced cohesion of the VO_x islands, apparently as a consequence of the two orders of magnitude lower pressure compared to the 10^{-4} mbar range. At 10^{-4} mbar compact, dense VO_x islands are observed. The VO_x composition of roughly $\text{VO}_{3.3}$ is close to the ideal value of the $(\sqrt{7} \times \sqrt{7})\text{R}19.1^\circ$ structure [53]. The O to V ratio, however, increases to a high value between eight and nine after 18.5 h exposure.

ii) In the early stage, most of the O 1s core level intensity belongs to a component of 529.5 - 529.6 eV binding energy. Later, after 18.5 h, a second component at ≈ 531.6 -

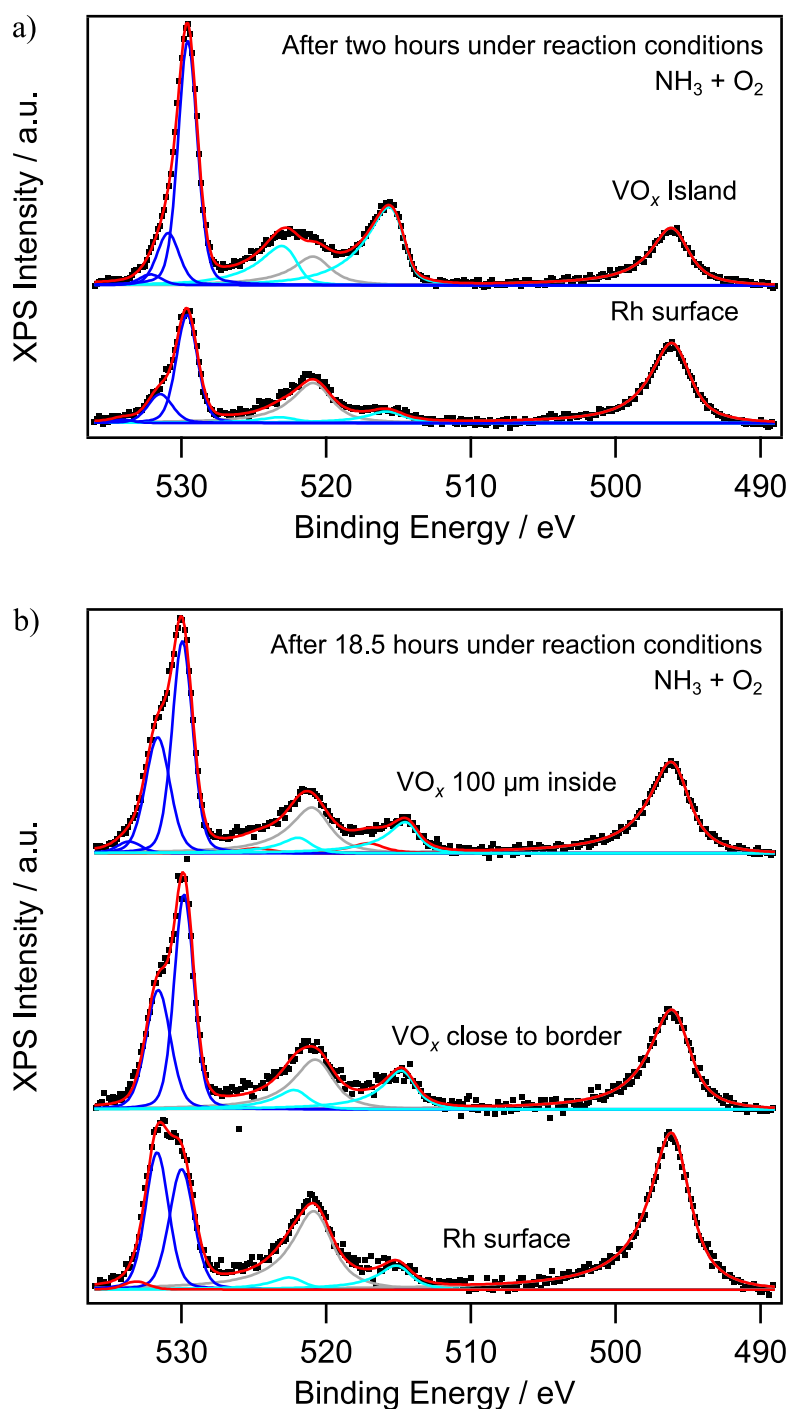


Figure 5.58: In situ XPS characterization of vanadium oxide islands and the surrounding Rh surface during ammonia oxidation with O_2 . a) XP spectra (Shirley-type background subtracted) taken after two hours under reaction conditions on a vanadium oxide island and on the surrounding Rh surface. b) Photoemission spectra (Shirley-type background subtracted) taken after 18.5 h under reaction conditions on the bare Rh surface, on a VO_x island close to the border to the Rh surface, and 100 μm inside the VO_x island. For the fits, three O 1s components are used, the binding energies are at 529.5 - 529.9 eV, 530.9 - 531.7 eV, and above 532 eV (very low intensity). The spectra are acquired at 910 K in 4×10^{-7} mbar oxygen and 1.2×10^{-6} mbar ammonia with a photon energy of 650 eV.

Table 5.3: V and O coverages obtained from in situ XP spectra recorded on a vanadium oxide island and on the surrounding Rh surface (figure 5.57). The corresponding spectra are shown in figure 5.58a and b. Shown are the binding energies (BE) and peak areas of the individual fit components, as well as the calculated vanadium and oxygen coverages θ_V and θ_O . The O 1s areas and coverages in brackets refer to the O 1s component with a binding energy below 530 eV.

	O 1s BE / eV Peak area / a.u.	V 2p BE / eV Peak area / a.u.	Rh 3p BE / eV Peak area / a.u.	θ_V, θ_O / MLE
After 2 h:				
Rh	529.6, 531.4, 534; 53 (39)	515.8; 15	496.2; 107	0.06, 0.6 (0.5)
VO_x	529.5, 530.9, 532.2; 106 (82)	515.7; 92	496.2; 76	0.54, 1.8 (1.4)
After 18.5 h:				
Rh	529.9, 531.7, 533.1; 320 (150)	515.2; 82	496.2; 644	0.06, 0.7 (0.3)
VO_x border	529.8, 531.6; 361 (213)	514.9; 132	496.1; 395	0.15, 1.2 (0.7)
VO_x inside	529.9, 531.7, 533.6; 378 (219)	514.6, 517.1; 138	496.2; 372	0.17, 1.3 (0.8)

531.7 eV dominates the spectrum recorded on the bare Rh surface. The same component also contributes significantly to the spectra taken on the vanadium oxide enriched surface area. The first O 1s component below 530 eV can be related to oxygen in the VO_x lattice. The O 1s binding energies reported for V_2O_3 , VO_2 and V_2O_5 range between 530.1 and 529.8 eV [251, table 1]. The question is, what is the origin of the second O 1s component located around 531.6 eV? Considering the low V coverage and high oxygen coverage after 18.5 h reaction conditions, one can suspect the formation of a Rh surface oxide. This surface oxide would explain the high O / V ratio of around 8 measured inside the vanadium oxide covered area. O 1s binding energy values of 200 nm thick Rh_2O_3 and RhO_2 films range between 529.9 and 531.1 eV [252]. However, no chemical shifts could be measured in the Rh 3p core levels. Separating the contributions of oxygen in the VO_x lattice and of oxygen in a Rh surface oxide, one can calculate oxygen coverages associated to VO_x alone. The corresponding θ_O values are listed in brackets in table 5.3.

N 1s spectra taken at the same positions, but with a different photon energy as the XP spectra of figure 5.58, are depicted in figure 5.59. The spectra reveal, that a considerable amount of nitrogen is present on the vanadium oxide parts of the surface under reaction conditions at 910 K, whereas no nitrogen could be measured on the surrounding, bare

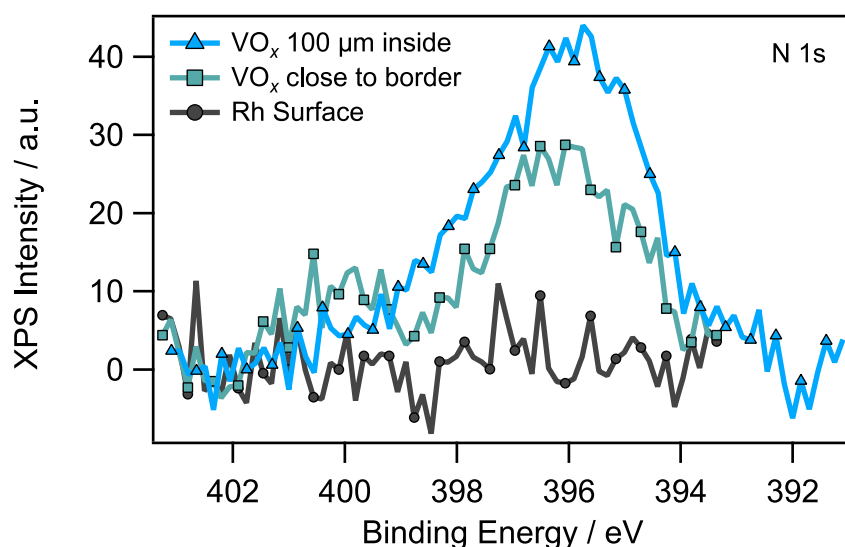


Figure 5.59: N 1s spectra taken in situ during ammonia oxidation with O_2 on the vanadium oxide depleted Rh surface and on a vanadium oxide island close to the border to the surrounding Rh surface, and 100 μm inside the oxide island. The experimental conditions are as stated in figure 5.58, the spectra are acquired at a photon energy of 670 eV.

Rh surface.

Interestingly, the N distribution is not homogeneous on the vanadium oxide covered parts of the surface. Instead, a roughly 30% higher N 1s signal is measured in the center of the island. The surplus of nitrogen measured in the island center is in agreement with the idea of vanadium oxide islands acting as catalytic micro-reactors. The existence of macroscopic oxygen gradients surrounding and extending inside the vanadium oxide islands is explained by a preferential adsorption of the educt which will be oxidized (methanol, ammonia) on the vanadium oxide islands, and supply of adsorbed oxygen from the surrounding Rh surface. Since the reaction takes place on the whole vanadium oxide island and since oxygen is supplied only from the sides, an oxygen concentration gradient should develop across the macroscopic oxide island. Consequently, also the ammonia coverage should vary along the island diameter, with the highest concentration in the island center. This situation is what can be seen in the N 1s core level spectra of figure 5.59.

5.7.4 In situ characterization of VO_x during the $NH_3 + NO$ reaction

For the in situ characterization of the vanadium oxide islands during catalytic ammonia oxidation with NO, oxygen in the gas phase is replaced by NO. All further measurements are performed on the same sample surface under the same experimental conditions, namely 910 K, 1.2×10^{-6} mbar ammonia and a NO pressure of 4×10^{-7} mbar. After further 13h under reaction conditions (a total of 32h at 910 K in the reaction

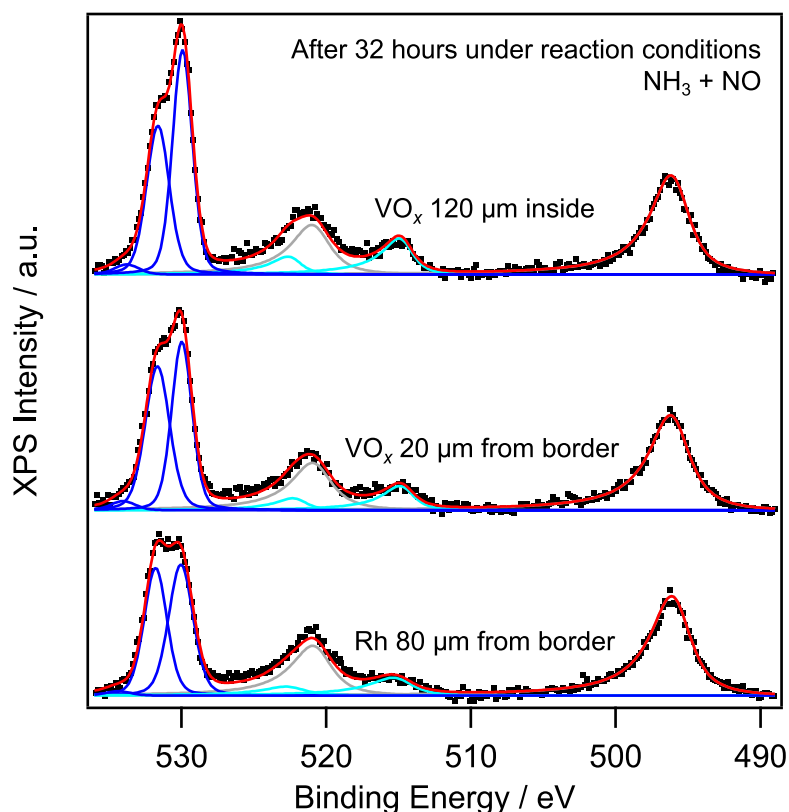


Figure 5.60: In situ XPS characterization of vanadium oxide islands and the surrounding Rh surface during ammonia oxidation with NO. XP spectra (Shirley-type background subtracted) taken after 32 h under reaction conditions (13 h $NH_3 + NO$ reaction) on a vanadium oxide island and on the surrounding Rh surface. The positions at which the spectra are acquired are stated in the graph. For the fits, three O 1s components are used, with binding energies at 530.0 - 530.1 eV, 531.6 - 531.8 eV, and above 533 eV (very low intensity). The spectra are acquired at 910 K in 4×10^{-7} mbar nitric oxide and 1.2×10^{-6} mbar ammonia with a photon energy of 650 eV.

atmosphere) an XPS characterization of the vanadium oxide covered and of the VO_x depleted surface is performed. The long waiting period between the replacement of O_2 by NO and measurement is chosen to let the system adjust to the new conditions. The O 1s, V 2p and Rh 3p XP spectra are depicted in figure 5.60.

For the V and O coverage determination during the $NH_3 + NO$ reaction, spectra on three different positions are acquired: 120 μm inside a vanadium oxide island, 20 μm inside the same oxide island, and 80 μm away from the oxide island on the surrounding Rh surface. As described above, the O 1s core level is fitted with three components. In ammonia oxidation with NO, the low binding energy component of O 1s is shifted by 0.5 eV to 530 and 530.1 eV in all spectra. The results of the numeric fits are summarized in table 5.4, together with the calculated V and O coverages.

Table 5.4: V and O coverages obtained from in situ XP spectra recorded on a vanadium oxide island and on the surrounding Rh surface during the $NH_3 + NO$ reaction. The corresponding spectra are shown in figure 5.60. Shown are the binding energies (BE) and peak areas of the individual fit components, as well as the calculated vanadium and oxygen coverages θ_V and θ_O . The O 1s areas and coverages in brackets refer to the 530 eV component.

	O 1s BE / eV Peak area / a.u.	V 2p BE / eV Peak area / a.u.	Rh 3p BE / eV Peak area / a.u.	θ_V, θ_O / MLE
After 32 h:				
Rh	530.1, 531.8, 534.4; 71 (37)	515.4; 18	496.1; 90	0.09, 1.0 (0.5)
VO_x border	530.0, 531.7, 534; 82 (39)	514.9; 18	496.3; 88	0.09, 1.2 (0.6)
VO_x inside	530.0, 531.6, 533.8; 92 (50)	515.0; 27	496.2; 88	0.14, 1.4 (0.7)

Compared to the values determined during the $NH_3 + O_2$ reaction, with 0.09 MLE a slightly higher V coverage is measured on the Rh surface, whereas with 0.09 and 0.14 MLE roughly 20% lower V coverages are measured close to the VO_x island border and 120 μm inside, respectively. The oxygen coverages on the vanadium oxide covered parts of the surface during ammonia oxidation with NO have similar values as during the reaction with O_2 . However, a considerably higher O coverage is measured on the bare Rh surface during ammonia oxidation with NO. The O coverage increases from 0.7 MLE in the $NH_3 + O_2$ reaction to 1.0 MLE when NO is used as oxidizing agent.

Also the nitrogen distribution differs significantly in both reactions. N 1s spectra acquired on different parts of the sample surface are depicted in figure 5.61. The nitrogen spectra are acquired on two different vanadium oxide islands 120 and 140 μm from the border to the Rh surface, respectively. Three additional spectra are recorded on the vanadium oxide covered part, close to the border, and on the Rh surface 80 and 90 μm away from the two vanadium oxide islands.

Two main differences exist in the nitrogen distribution between the oxidation with O_2 and the oxidation with NO. Firstly, no nitrogen can be detected on the bare Rh surface in the reaction with O_2 , but a considerable N signal is present in the two spectra recorded on the Rh surface with NO, displayed in figure 5.61. Secondly, no significant differences in the N intensity can be measured at the different positions on the vanadium oxide covered surface. All three spectra acquired on the VO_x island look quite similar. In contrast, during ammonia oxidation with NO a roughly 30% higher N signal is measured in the core of the oxide island compared to the signal in the outer part of the VO_x covered area.

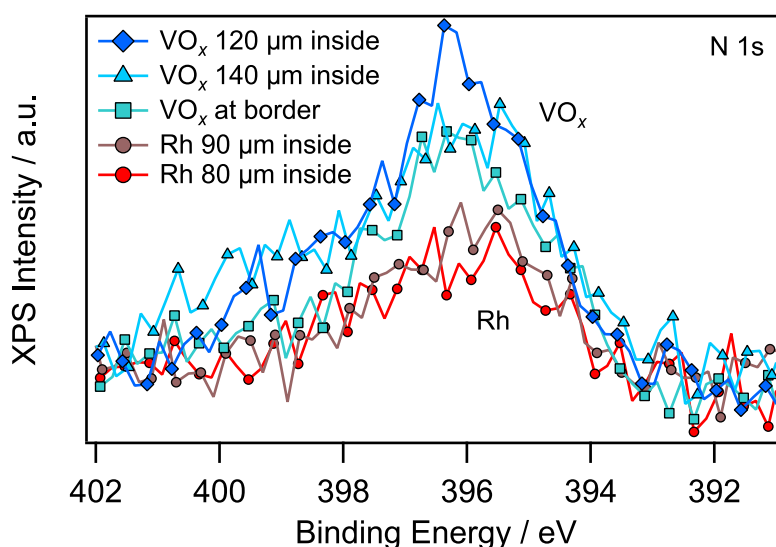


Figure 5.61: N 1s spectra taken in situ during ammonia oxidation with NO on the vanadium oxide depleted Rh surface and on a vanadium oxide island close to the border to the surrounding Rh surface, and 120 and 140 μm inside the oxide island. The experimental conditions are as stated in figure 5.60, the spectra are acquired at a photon energy of 670 eV.

5.7.5 Oxygen distribution during ammonia oxidation with O_2 and NO

The lateral distribution of oxygen turned out to play an essential role for explaining the VO_x redistribution during catalytic methanol oxidation in the 10^{-4} mbar range [69,70]. It is therefore interesting to characterize the oxygen coverage as a function of distance to the border between the vanadium oxide enriched and vanadium oxide depleted surface. The concentration profiles of ammonia oxidation with O_2 are compared with the concentration profiles of ammonia oxidation with NO. Therefore dispersive plane O 1s spectra are acquired every 20 μm starting 100 μm away from the interface on the Rh surface and ending 100 μm inside the VO_x island. The O 1s spectra acquired during ammonia oxidation with O_2 and with NO are shown in figure 5.62a and b, respectively.

The O 1s spectra are dominated by two contributions, a low binding energy component slightly below 530 eV, and two high binding energy components located around 531 and 532 eV. Interestingly, the high binding energy component has a similar intensity in all spectra, independent whether they are acquired on vanadium oxide enriched or on vanadium oxide depleted areas of the surface. Different is the situation for the low binding energy component: going from the bare Rh surface to the VO_x island, a sharp intensity increase occurred between the fourth and fifth spectra (counted from the bottom, “on Rh”) in figure 5.62a. This intensity jump marks the transition from the bare Rh surface to the vanadium oxide covered area. In ammonia oxidation with NO, this jump is less pronounced. Rather than an abrupt intensity increase of the O 1s low binding energy component, a gradual increase can be seen, starting from the fourth

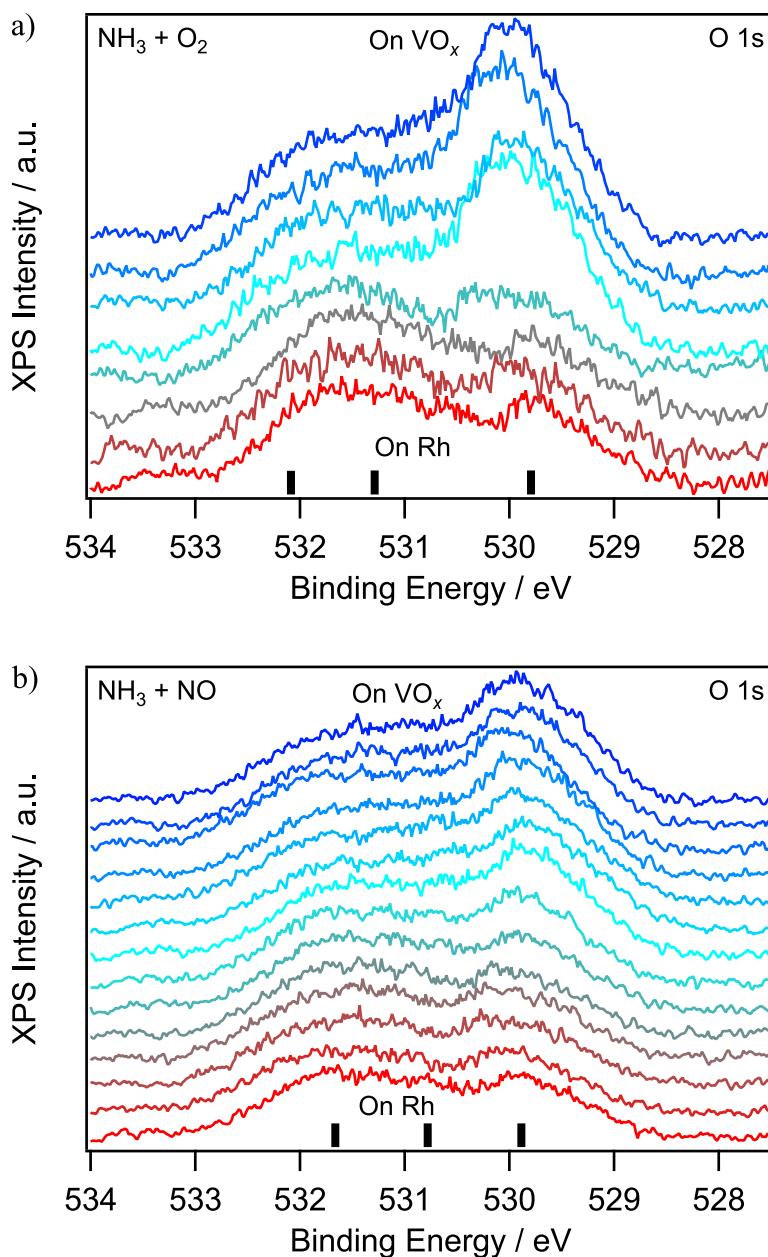


Figure 5.62: O 1s dispersive plane XP spectra as a function of distance to the VO_x/Rh interface. The O 1s spectra acquired during ammonia oxidation with O_2 are displayed in (a), whereas the corresponding spectra recorded during ammonia oxidation with NO are shown in (b). The spectra are acquired at different positions varying in steps of $20\ \mu\text{m}$. The binding energies of the three O 1s components used for the numeric fits (not shown) are indicated as solid black line at the bottom of the graphs. All spectra are acquired at 910 K in 1.2×10^{-6} mbar oxygen and 4×10^{-7} mbar O_2 (a) or NO (b). The photon energy is 650 eV.

spectra in figure 5.62b.

In order to better visualize the oxygen distribution on the surface, a plot of the total O 1s intensity as a function of distance from the border Rh/ VO_x is shown in figure 5.63a. In this representation, clear differences between the oxygen distribution in the two oxidation reactions can be seen. Whereas the interface between the bare Rh surface and the VO_x island is with $\approx 100 \mu\text{m}$ very broad in the $NH_3 + NO$ reaction, a roughly ten times narrower interface appears during ammonia oxidation with O_2 . Furthermore, the total O 1s intensity measured on the bare Rh surface is considerably lower during ammonia oxidation with O_2 compared to the oxidation reaction with NO. This result is in line with the oxygen coverages in tables 5.3 and 5.4, which amount to 0.7 MLE during the $NH_3 + O_2$ reaction, and to 1.0 MLE in the $NH_3 + NO$ reaction. If we interpret the large differences in interface width as reflecting a different line tension of the vanadium oxide islands, then the exchange of O_2 by NO would cause a large loss in line tension. Since later on the VO_x islands dissolves, the diffuse interface is a clear sign for a reduced line tension.

The surprisingly high oxygen to vanadium ratio measured in the vanadium oxide covered parts of the surface in both reactions, together with the existence of two O 1s components with considerable intensity suggests the presence of a Rh surface oxide. A decomposition of the total O 1s intensity into the low binding energy component and the sum of the two high binding energy components for the two oxidation reactions is depicted in figure 5.63b and c, respectively. The high binding energy components have a constant intensity through out the whole probed surface area, independent of the vanadium oxide coverage. In contrast, a large intensity variation can be seen in the intensity of the low binding energy component. It turns out, that the intensity increase visible in the total O 1s intensity in figure 5.64a is almost completely caused by the intensity increase of the low binding energy component.

This corroborates the interpretation of oxygen in the VO_x lattice as being responsible for the intensity contribution below 530 eV. Obviously, the high binding energy component is independent of the V coverage and thus related to the Rh surface, i. e. it should be due to Rh oxide. A high binding energy component of the O 1s core level is reported for 200 nm thick Rh oxide films [252].

LEED images of the VO_x covered and VO_x depleted surface taken after the sample is cooled down to 490 K subsequent to the XPS characterization are shown in figure 5.64. Similar to the LEED characterization conducted during ammonia oxidation with O_2 (figure 5.57a) also during the $NH_3 + NO$ reaction a $(\sqrt{3} \times \sqrt{3})$ -Moiré pattern characterizes the bare Rh surface as well as the vanadium oxide islands. The superstructure is more intense on the VO_x covered area.

5.7.6 Discussion

The SPELEEM measurements conducted during ammonia oxidation with O_2 and NO revealed a number of details important for explaining the different patterns as the oxidizing agent is changed. Firstly, if the reaction is carried out with molecular oxygen, nitrogen can only be detected on the vanadium oxide islands while the stationary N

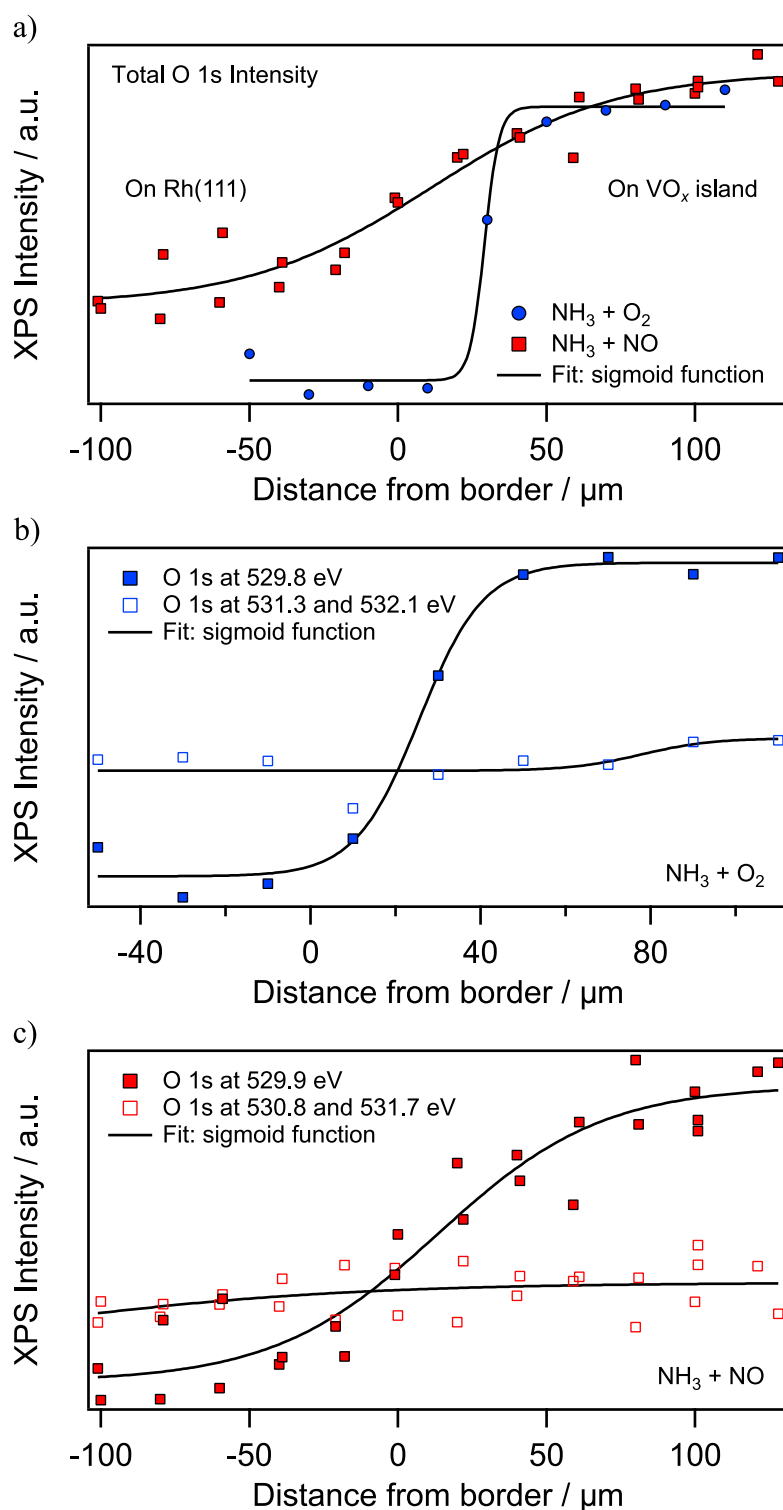


Figure 5.63: Oxygen distribution measured during ammonia oxidation with O_2 and NO . a) The total O 1s intensity as a function of distance from the interface Rh/VO_x obtained from numerical fits with three components to the spectra shown in figure 5.62a and b. b) The intensity of the O 1s component at 529.8 eV and the sum of the high binding energy components as a function of distance from the border of the VO_x island measured during ammonia oxidation with O_2 . c) The intensity of the O 1s low and high binding energy components measured during the $NH_3 + NO$ reaction. The black solid line represent numeric fits (sigmoid function) to the experimental data. The experimental conditions are as stated in figure 5.62.

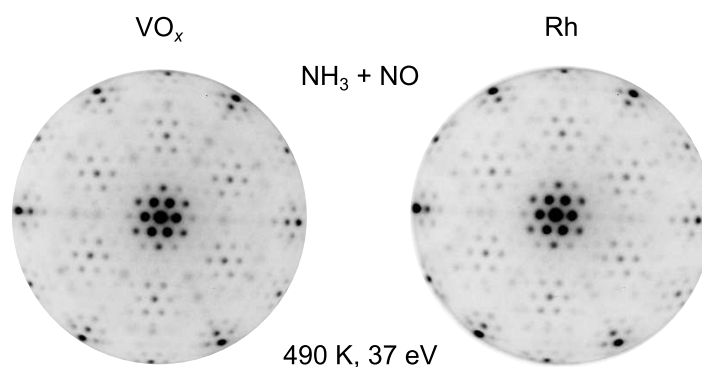


Figure 5.64: In situ LEED characterization of VO_x islands and the bare Rh surface in the 10^{-6} mbar range during ammonia oxidation with NO. The gas phase composition is as stated in figure 5.60.

coverage on the bare Rh surface is below the detection limit of XPS. If the reaction is carried out with NO instead, nitrogen can be detected on the vanadium oxide islands as well as on the bare Rh surface. The presence of nitrogen on the Rh surface can be explained with the ability of Rh to easily dissociate NO. The different adsorbate coverages in the reaction with O_2 and NO, oxygen vs. oxygen coadsorbed with nitrogen, will influence the surface energy of the bare Rh surface [253]. Secondly, the lateral oxygen distribution reveals a broad interface between the bare Rh and the vanadium oxide islands of $\approx 100 \mu m$ width in the $NH_3 + NO$ reaction. In ammonia oxidation with oxygen an interface width of only $10 \mu m$ is determined. The different interface widths could indicate a much lower line tension of the vanadium oxide islands in the oxidation reaction with NO compared to the reaction with oxygen.

Energetically, the lateral distribution of vanadium oxide on the Rh surface is determined by the interface energies γ_i of the three interfaces Rh / VO_x , Rh / gas phase, and VO_x / gas phase, as well as by the line tension of the vanadium oxide islands. In a first approximation, it can be assumed that the interface energies Rh / VO_x and VO_x / gas phase do not change significantly upon exchange of O_2 by NO. In both reactions, similar LEED patterns are observed and also the vanadium oxide coverage is in the same range. Then, the question whether vanadium oxide islands or vanadium oxide depleted holes in a dense VO_x layer are formed is largely determined by the interplay between the vanadium oxide island line tension and the surface energy of the surrounding Rh surface. The exchange of O_2 by NO reduces the line tension of vanadium oxide islands, but the influence of the different adsorbate phases on the surface energy of the bare Rh surface is not known. For this reason, the question whether holes or island pattern evolve cannot be decided on the basis of known interfacial energies.

The situation is further complicated by the assumption of a Rh surface oxide being present on the catalytic surface under reaction conditions. Based on O 1s binding energies of Rh_2O_3 and RhO_2 films reported in the literature [252], the appearance of a high binding energy component in the O 1s core level upon prolonged exposure to reaction

conditions in the 10^{-6} mbar range is taken as an indication for the formation of such a Rh oxide. The intensity of this high binding energy component is independent of the vanadium oxide coverage, whereas the low binding energy O 1s intensity correlates with the V coverage. Surprisingly, no core level shifts in the Rh 3p and Rh 3d core levels can be detected. The high kinetic energy of ≈ 340 eV of electrons emitted from the Rh 3d core level reduces the surface sensitivity, and therefore the contribution of a surface oxide to the overall spectrum. However, the kinetic energy of Rh 3p electrons is with ≈ 150 eV close to the minimum of the inelastic mean free path. The reason for the absence of a considerable chemical shift in the Rh spectra remains an open question.

The self limited growth of a thin oxide layer is described to occur on Rh(111) in the 10^{-4} mbar range. This surface oxide is characterized by a Moiré LEED pattern, which is “described as an (8×8) hexagonal Rh oxide on a (9×9) Rh(111) surface unit cell” [162, p.126102-2]. Since on both, on the vanadium oxide enriched surface ($\theta_V = 0.14 - 0.17$ MLE) and on the VO_x depleted surface ($\theta_V = 0.06 - 0.09$ MLE), a considerable amount of vanadium exists, one could also envision the formation of a mixed Rh/V surface oxide. This would explain the similar LEED pattern, a $(\sqrt{3} \times \sqrt{3})$ -Moiré pattern, recorded on the bare Rh and on the VO_x covered surface. The same $(\sqrt{3} \times \sqrt{3})$ -Moiré pattern is also observed in the vanadium oxide island core during in situ methanol oxidation experiments conducted in the 10^{-4} mbar range. Also the different LEED pattern as reported in literature for the Rh(111) surface oxide would then find a plausible explanation. The low V coverage on the bare Rh surface together with identical LEED pattern on the VO_x islands and on the surrounding Rh surface suggests that the $(\sqrt{3} \times \sqrt{3})$ -Moiré represents a minority phase, which covers only a small fraction of the surface. However, different from the Rh 3d binding energies reported in literature for Rh oxide films and a Rh surface oxide [162, 252], no significant chemical shifts could be detected in the Rh 3p and Rh 3d spectra. The missing chemical shift of the Rh core levels might be caused by the contribution of vanadium in the mixed surface oxide. To our best knowledge, for the Rh(111) surface such a mixed V/Rh surface oxide has not been described in literature yet.

5.8 VO_x redistribution studied with NAP-LEEM

An important aim of this study is to bridge a large part of the pressure gap for the system VO_x /Rh(111). Cathode lens microscopy is a typical UHV technique, electric gas discharges and the collision of electrons with gas molecules prevent the use at elevated pressure. However, by differential pumping in the electron optics, and by using a lower electrical field strength between sample and objective lens, already with conventional LEEM and PEEM microscopes a pressure up to the 10^{-4} mbar can be reached. The development of a new near ambient pressure LEEM⁵ (NAP-LEEM) by Elmitec Elektronenmikroskopie GmbH extends the accessible pressure into the 10^{-2} mbar range, enabling to image the reaction induced redistribution in situ from UHV up to 0.02 mbar.

⁵Details on the design of the NAP-LEEM microscope can be found in chapter 2.4.3.

Key elements for the construction of a NAP-LEEM are extensive differential pumping and feeding the electron beam through a thin capillary, the replacement of the magnetic diode objective lens with an objective lens of magnetic triode configuration to reduce the electrical field strength at the sample surface, and a reduction of the volume of the reaction cell [29].

The dynamics of ultrathin vanadium oxide layers on Rh(111) during methanol oxidation depend strongly on the total pressure at which the catalytic reaction is carried out. Preceding PEEM and LEEM experiments have shown, that the reaction dynamics can vary between a simple phase separation into vanadium oxide rich and depleted areas in the 10^{-7} mbar range, and the formation of dynamic stripe and island pattern in the 10^{-4} mbar range. These macroscopic vanadium oxide islands can furthermore move towards each other and coalesce, or periodically change their size, as long as reaction conditions prevail. The VO_x islands exhibit a substructure in which several different vanadium oxide phases coexist, but this substructure exists only at elevated pressure. Four representative PEEM images recorded under reducing reaction conditions between 4×10^{-7} and 4×10^{-4} mbar total pressure summarize this trend in figure 5.65. This overview is complemented by a NAP-LEEM image, acquired under oxidizing reaction conditions at a total pressure of 0.02 mbar. This image shows three circular vanadium oxide island.

The PEEM and NAP-LEEM images in figure 5.65 display two trends: first, the length scale of the VO_x redistribution pattern gets smaller with increasing total pressure; second, the tendency to form a substructure of a reduced core and an outer, oxidized ring gets stronger with increasing total pressure. Moreover, the temperature at which the redistribution of vanadium oxide sets in considerably decreases as the total pressure is increased.

5.8.1 VO_x island formation and turbulent dynamics at 0.02 mbar

The behavior of ultrathin vanadium oxide layers ($\theta_V = 0.2$ MLE) is investigated in the 10^{-2} mbar range in a similar manner as in the PEEM experiments described in section 5.2.2, with one difference: The NAP-LEEM measurements are started on a Rh(111) surface homogeneously covered with 0.2 MLE of metallic vanadium, instead of vanadium oxide. In the NAP-LEEM system, V deposition is only possible at room temperature, thus ruling out reactive evaporation. Consequently, V deposition is carried out in vacuum.

After deposition, the V/Rh(111) sample is transferred in vacuum into the analysis chamber. A continuous flow of methanol and oxygen, with a partial pressure of 0.01 mbar of each gas, is introduced. Subsequently, the sample is heated from room temperature to 660 K in roughly 20 minutes in the continuous gas flow. Afterwards the sample is kept at constant 660 K, while the redistribution dynamics of VO_x are observed. A series of NAP-LEEM images acquired in the MEM (first three images) and LEEM mode are displayed in figure 5.66. The area of lenticular shape with considerably lower LEEM intensity in the upper left corner of the LEEM images is caused by a defect of the microchannel plate detector in the image intensifier unit. Also the four small, black spots located in the

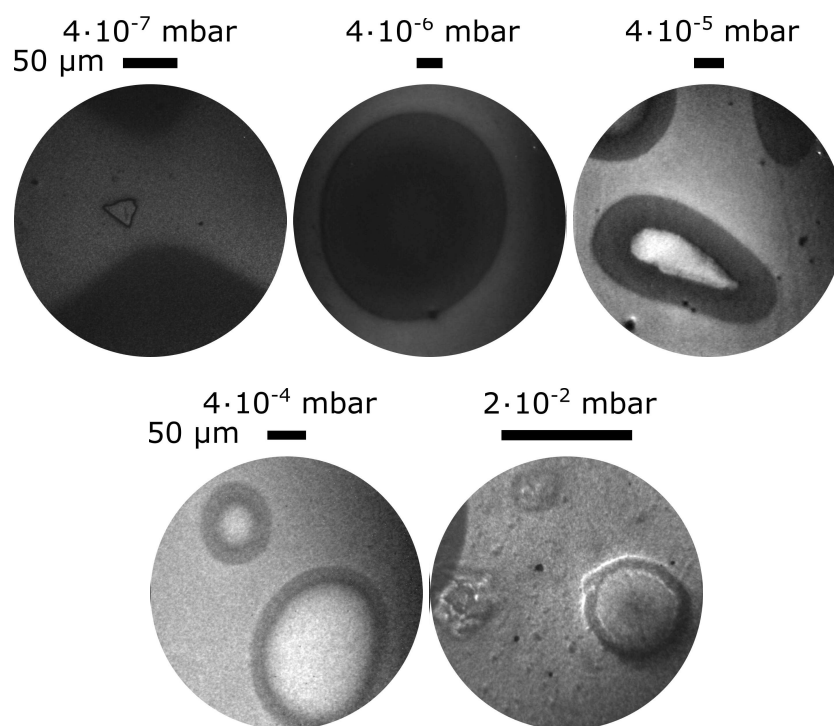


Figure 5.65: PEEM and NAP-LEEM images recorded at different pressure under reducing (threefold excess of methanol, PEEM) and oxidizing (equal amounts of methanol and oxygen, NAP-LEEM) reaction conditions. The images show the transition from a simple phase separation in the 10^{-7} mbar range to the appearance of dynamic vanadium oxide islands at elevated pressure.

center of the LEEM images and on the left side, best visible in the four central LEEM images in figure 5.66, represent defects in the microchannel plate.

Starting with a homogeneous surface at room temperature, the formation of a large number of small dark spots is observed in MEM mode, starting at around 400 K. With increasing temperature, the average size of these particles increases homogeneously, until at around 600 K the growth of four islands is observed. The contrast in MEM is mainly caused by the local work function, so that areas of low work function have a low MEM intensity, and, conversely, high work function areas appear bright. However, other effects like topography also play a similar important role in image formation in MEM mode. Consequently, an assignment of the small dark spots to areas of low work function is not possible.

As the target temperature of 660 K is reached (and kept constant over the rest of the experiment), the imaging mode is changed from MEM to LEEM by an increase of the start voltage from the 2.5 to 3.1 eV. This change takes place in the fourth image depicted in figure 5.66. Due to the change in the contrast mechanisms, the small dark spots, which are homogeneously distributed on the surface in MEM mode, are not visible anymore.

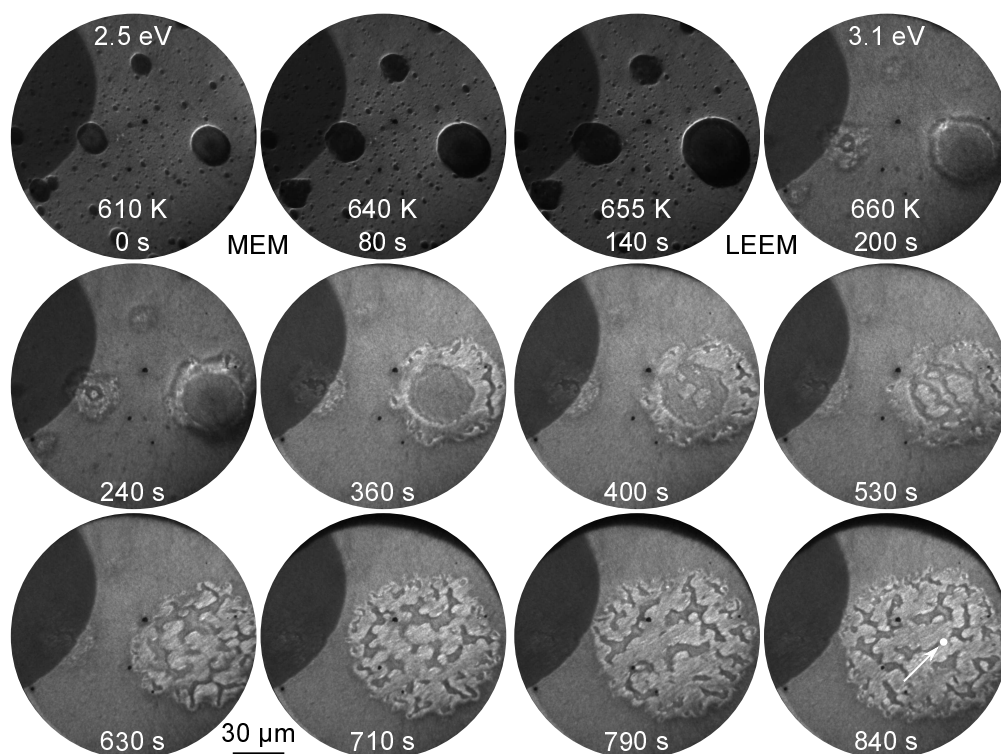


Figure 5.66: NAP-LEEM images acquired in MEM (first three images) and LEEM mode, showing the formation of macroscopic vanadium oxide islands during catalytic methanol oxidation at 0.02 mbar. The images are acquired at a start voltage of 2.5 (MEM mode) and 3.1 eV (LEEM mode). The sample is heated up in a continuous gas flow of 0.01 mbar methanol and 0.01 mbar oxygen to 660 K. The VO_x coverage is 0.2 MLE.

This indicates a very small size of these particles. The appearance of the larger VO_x islands also has changed upon increasing the start voltage. A substructure consisting of a grey core, an outer dark ring and a bright boundary phase separating the two can clearly be identified in the fourth image in figure 5.66. The smaller island on the left side of the image has a less homogeneous outer ring and a bright feature in the center of the dark core.

Interestingly, also the outer ring of the large island loses its homogeneous appearance at prolonged exposure to reaction conditions. In the fifth and sixth image, a bright phase nucleates in the outer ring of the large VO_x island. The nucleation and growth of this bright phase in the outer ring is accompanied by a considerable size increase of the whole island. Simultaneously, a third small island in close vicinity of the two larger islands, continuously decreases its size and finally vanishes. The growth of larger islands, and the disappearance of small islands can be taken as an indication for Ostwald ripening. The observation, that after the initial growth of a large number of small crystallites only

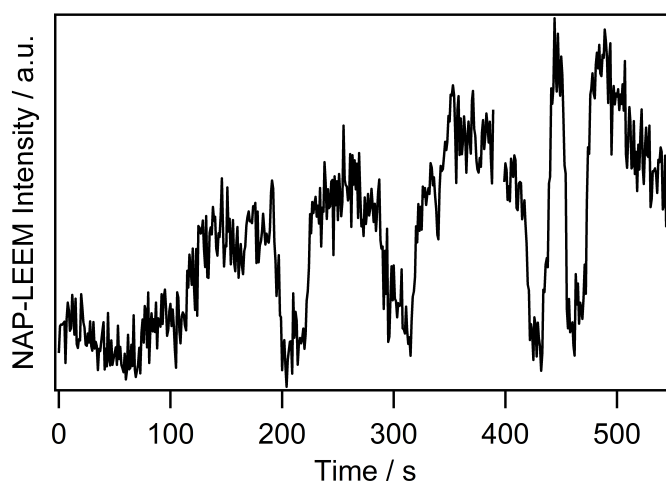


Figure 5.67: Local NAP-LEEM intensity time series recorded on a circular area of $3\ \mu\text{m}$ diameter, which is shown in the last NAP-LEEM image of figure 5.66. The time series is started at 450 s. Figure adapted from: Reaction dynamics of metal/oxide catalysts: Methanol oxidation at vanadium oxide films on Rh(111) from UHV to 10^{-2} mbar, B. von Boehn, C. Penschke, X. Li, J. Paier, J. Sauer, J.-O. Krisponeit, J. I. Flege, J. Falta, H. Marchetto, T. Franz, G. Lilienkamp, and R. Imbihl, *Journal of Catalysis*, **2020**, *385*, 255 - 264, Copyright (2020), with permission from Elsevier.

few VO_x islands grow to a size of several micrometers supports this interpretation.

After about 400 s, a bright phase nucleates also in the center of the island, and quickly grows over the whole core, except some channel-like structures of low LEEM intensity. Already at 630 s (ninth image in figure 5.66), no distinction between an outer ring and an inner core can be made. The whole VO_x island consists of a bright phase pervaded by channels of a dark phase.

Upon further exposure to reaction conditions, the largest VO_x island continues to grow, while the second largest island considerably loses LEEM contrast. At the same time, a turbulent dynamics is observed in the VO_x covered parts of the surface. The dark channels in the bright phase start to meander on the surface, forming and breaking connections with each other. The dynamics and irregular character of the structural transformations is visualized in a time series of the local LEEM intensity depicted in figure 5.67, acquired in an area indicated by the small white circle in the last LEEM image.

The local NAP-LEEM intensity shows strong, non-periodic variations with time. A stable stationary distribution of the different vanadium oxide phases can evidently not be maintained in the 10^{-2} mbar range. Instead, a turbulent redistribution of VO_x is observed. A possible explanation for the different behavior upon pressure increase from 4×10^{-4} to 0.02 mbar might be connected to the oxygen gradients between oxygen adsorbing on the metallic phase and oxygen in the oxide phase becoming too strong. Another factor might be, that due to the higher gas pressure, the reaction can no longer

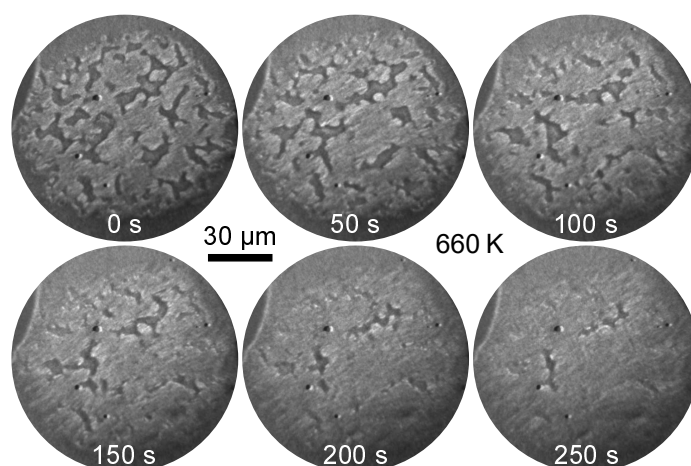


Figure 5.68: Oxidation of a macroscopic VO_x island in the 10^{-2} mbar range at a constant temperature of 660 K followed with NAP-LEEM. At $t = 0$ s the methanol pressure is decreased from 0.01 to 5×10^{-3} mbar, while keeping the oxygen pressure and the temperature constant at 0.01 mbar and 660 K, the VO_x coverage is 0.2 MLE.

be considered as isothermal. In catalytic CO oxidation on Pt single crystal surfaces, the threshold in pressure where the reaction heat is no longer negligible lies in the 10^{-3} to 10^{-2} mbar range [254–256]. As a consequence, temperature gradients might evolve, in addition to concentration gradients on the surface. However all these explanations need experimental confirmation in future experiments.

5.8.2 Oxidation of a VO_x island in the 10^{-2} mbar range

Similar to the experiments carried out with LEEM and PEEM in the 10^{-4} mbar range, also at 0.02 mbar initially a core-ring substructure is formed in the VO_x islands. As the temperature is increased, this core-ring structure becomes unstable and first the outer ring disintegrates, followed by the core at higher temperature. The result is an island consisting of a bright and a dark phase, exhibiting a dynamic, channel-like structure. A simple way to check which of the two phases, i. e. the bright or the dark, is the oxidized one, is to decrease the methanol pressure. Due to the higher oxygen content in the gas phase, the oxidized phase should grow at the expense of the reduced phase. Figure 5.68 shows the temporal evolution of a large vanadium oxide island as a response to a continuous methanol pressure decrease from 0.01 to 5×10^{-3} mbar at 670 K over ≈ 150 s, while keeping the oxygen pressure constant at 0.01 mbar.

As a consequence of the reduced methanol pressure, the turbulent redistribution dynamics considerably slows down. The same phenomenon is also observed in the PEEM and LEEM experiments conducted in the 10^{-4} mbar range: the mobility of vanadium oxide stripes and islands is maximized (up to a certain extent) by increasing the amount of methanol in the gas phase. Simultaneously, the area covered by the bright VO_x phase grows, while the dark phase slowly disappears. Therefore, the bright phase can

be associated with a higher oxidation state of V and the dark phase can be regarded as a reduced VO_x phase.

By comparing the LEEM images depicted in figures 5.66 and 5.68, with the LEEM images in figure 5.20 (section 5.3) acquired in the 10^{-4} mbar, one notices two things: *i*) the contrast between the oxidized and the reduced phase is inverted in the LEEM images acquired at 10^{-4} and 10^{-2} mbar (at 10^{-4} mbar the oxidized phase is dark and the reduced phase bright), and *ii*) the LEEM/MEM transition is shifted by more than an eV to higher start voltage upon pressure increase. The shift of the LEEM/MEM transition upon pressure increase indicates a higher work function in the NAP regime. A possible explanation for the higher work function might be the involvement of a Rh surface oxide. The self-limited growth of a rhodium oxide tri-layer on Rh(111) has been observed already at an oxygen pressure in the 10^{-4} mbar range. However, the LEEM/MEM transition depends also on other parameters like the sample alignment with respect to the probing electron beam. Comparing the LEEM/MEM transition at different instruments is therefore connected with uncertainties.

Even after prolonged exposure to a reaction atmosphere with oxygen in excess, the reduced dark phase does not disappear completely, but after about 40 min no redistribution dynamics can be observed anymore. In order to gain further information, LEEM- $I(V)$ measurements are performed. In a LEEM- $I(V)$ experiment, the start voltage is continuously increased from a value below the LEEM/MEM transition to several tens of eV. Since this measurement takes some minutes, it is only possible on a surface which changes slowly. From the obtained image stack, the start voltage at which the LEEM/MEM transition occurs can be calculated for every pixel, resulting in a work function map, which gives the work function difference of every pixel to a reference point (absolute work function measurements are not possible without a calibration in LEEM). Figure 5.69 displays such a work function map of the oxidized VO_x island shown in figure 5.68.

The work function clearly shows a granular structure inside the VO_x island, consisting of large elliptical shaped areas of low work function (dark), surrounded by areas of higher work function. The existence of large areas of low work function fits well with the assignment of a reduced VO_x species to the dark channels in the LEEM images presented in figures 5.66. Also in PEEM experiments, the reduced vanadium oxide phases always have a lower work function than the more oxidized phases.

The experimental findings obtained with the NAP-LEEM at 10^{-2} mbar in principle resemble the behavior of VO_x during catalytic methanol oxidation in the 10^{-4} mbar range. The formation of macroscopic, circular vanadium oxide islands is observed. As long as the temperature is around 600 K, also the familiar core-ring substructure can be observed for larger islands. However, as the temperature is further increased, this substructure is not stable anymore and a turbulent redistribution dynamics leads to a phase separation into a bright oxidized and dark reduced VO_x phase in LEEM. Spatially resolved measurements reveal strong work function variations within a VO_x island. In contrast to the low pressure experiments, now O-gradients could be directly measured inside the vanadium oxide islands.

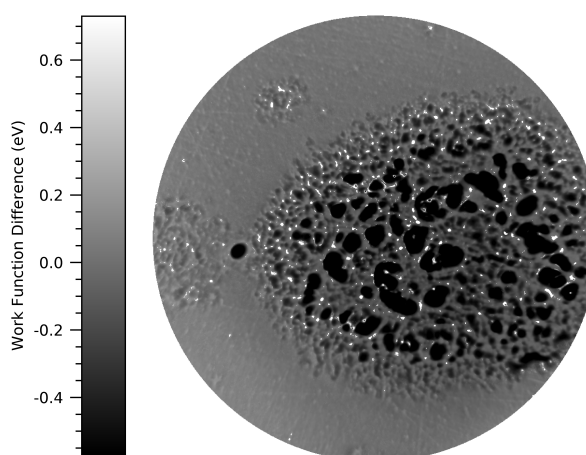


Figure 5.69: Work function map acquired after the oxidation of an oxidized VO_x island in a gas atmosphere consisting of 5×10^{-3} mbar methanol and 5×10^{-3} mbar oxygen at 660 K. The work function map shows the work function difference of every pixel in the image to a reference point indicated by a small white point. The VO_x coverage is 0.2 MLE.

One major conclusion that can be drawn from the NAP-LEEM experiments is that the vanadium oxide redistribution on Rh(111) is strongly pressure dependent, i. e. the often claimed pressure gap actually exists for $\text{VO}_x/\text{Rh}(111)$ catalysts. The catalyst looks different in each pressure range from static VO_x islands at 10^{-7} mbar, to moving and coalescing VO_x islands in the 10^{-4} mbar range, and, finally, to turbulent redistribution dynamics at 10^{-2} mbar.

5.9 Summary

The reaction-induced redistribution of ultrathin vanadium oxide layers ($\theta_V \leq 0.6$ MLE) was investigated in a number of catalytic reactions with PEEM and LEEM. In a detailed study, the influence of experimental parameters on pattern formation was determined for catalytic methanol oxidation. Depending on temperature, a reversible formation of a vanadium oxide stripe pattern or a pattern consisting of circular vanadium oxide islands occurs. The vanadium oxide stripes exhibit a substructure consisting of a reduced core and an oxidized ring. The development of this substructure depends on a critical island radius. The length scale of the patterns ranges from tens to hundreds of micrometers.

LEEM experiments revealed structural details of the different vanadium oxide phases inside a VO_x island. Under reaction conditions in the 10^{-4} mbar range, the oxidized ring has a $(\sqrt{7} \times \sqrt{7})\text{R}19.1^\circ$ structure. In the core a $(\sqrt{3} \times \sqrt{3})$ -Moiré pattern was seen.

The dependence of the oxygen gradient on the VO_x island size can cause kinetic instabilities, as the conditions for the thermodynamic stability of VO_x phases change inside a VO_x island. This leads to oscillatory size changes of VO_x islands in the 10^{-4} mbar

range. With LEEM a periodic expansion and contraction of a VO_x island was imaged. Such oscillations can only be observed if the island radius is close to the critical radius for the existence of the reduced island core.

The vanadium coverages in the oxidized island ring and the reduced core previously determined in situ during methanol oxidation in the 10^{-6} mbar range with SPELEEM [69, 70] are measured accurately using SPEM. Different from a previous study considerably higher oxygen coverages are measured on all parts of the catalytic surface. The high amount of oxygen on the surface suggests the presence of a Rh surface oxide under reaction conditions.

Besides catalytic methanol oxidation, a reaction-induced redistribution of VO_x was studied in catalytic ammonia and CO oxidation on $\text{VO}_x/\text{Rh}(111)$. Different from methanol oxidation, in both reactions the catalytic activity of VO_x is lower than the activity of the bare Rh(111) surface. Redistribution patterns very similar to the ones observed in methanol oxidation are observed in catalytic ammonia oxidation and in catalytic CO oxidation. However, the vanadium oxide islands in CO oxidation do not reach a circular shape.

Oxygen gradients play an essential role in the formation and coalescence of circular vanadium oxide islands under reaction conditions [69, 70]. Therefore the oxidizing agent O_2 was replaced by NO in methanol and ammonia oxidation. As a consequence, instead of an vanadium oxide island pattern, a pattern consisting of a dense VO_x layer with holes of vanadium oxide depleted surface evolved in the $\text{CH}_3\text{OH} + \text{NO}$ and $\text{NH}_3 + \text{NO}$ reactions. SPELEEM measurements in the 10^{-6} mbar range revealed, that the exchange of O_2 by NO in catalytic ammonia oxidation drastically reduces the line tension of the vanadium oxide islands. Furthermore, on the bare Rh surface co-adsorbed nitrogen and oxygen could be detected in the oxidation reaction with NO. No nitrogen was found on the Rh surface as the reaction was carried out with O_2 as oxidizing agent. The question whether an island or a hole pattern develops in the oxide layer is apparently determined by thermodynamic quantities like interfacial energies and the line tension.

The assumption of a Rh surface oxide being present under reaction conditions was further corroborated by high oxygen coverages measured with SPELEEM during ammonia oxidation with O_2 and NO. A high binding energy O 1s component was associated with Rh oxide, and the intensity of this O 1s component was found to be *i*) independent of the V coverage, and *ii*) constant on the whole probed area. LEED revealed the same $(\sqrt{3} \times \sqrt{3})$ -Moiré pattern for the VO_x enriched and for the VO_x depleted area. The same structure was observed in LEEM experiments during methanol oxidation in the 10^{-4} mbar range.

With the successful operation of a NAP-LEEM, the dynamics of VO_x on Rh(111) during methanol oxidation could be followed up into the 10^{-2} mbar range. Different from the experiments in the 10^{-4} mbar range and at lower pressure, turbulent dynamics are obtained in the near ambient pressure regime. Apparently, dynamic effects become increasingly important during catalytic reactions at elevated pressure.

Chapter 6

VO_x Redistribution and Pattern Formation on Rh(110)

Abstract A number of intriguing chemical wave pattern is observed during methanol oxidation on the unpromoted and VO_x covered Rh(110) surface. At temperatures above 680 K, the reaction is bistable. The existence of traveling interface modulations on Rh(110) and on the 0.1 MLE VO_x covered Rh(110) surface in the 10⁻⁴ mbar range indicates, that a parameter range of double metastability exists, adjacent to the equistability point of the bistable system. In situ LEEM/LEED reveals, that the transition from the oxidized into the reduced state is accompanied by a phase transition from the (1 × 1) surface into the c(2 × 8) missing-row reconstructed surface of adsorbed oxygen. The traveling interface modulations have been explained by a defect generation mechanism, in which the reversible formation of surface defects during the phase transition between the unreconstructed and reconstructed surface play an essential role. A higher VO_x coverage up to 0.4 MLE results in target pattern and traveling wave fragments. A reaction induced redistribution of VO_x around 1000 K leads to either a macroscopic VO_x island pattern, or a hole pattern of VO_x depleted areas surrounded by VO_x enriched surface. Moreover, a fractal growth mode of dendritic VO_x islands occurs during methanol oxidation. The propagation of traveling wave fragments on the VO_x island pattern and inside the holes is seen. Target pattern and chaotic patterns appear on the VO_x enriched surroundings of the holes. Adsorbate induced reconstructions play presumably an essential role in the chemical wave patterns. Indications for the possible involvement of a V/Rh (sub)surface alloy are also found. The PEEM and SPELEEM experiments described in this chapter were performed as part of my master thesis [71] and are recapitulated here.

Ultrathin layers of VO_x on Rh(111) exhibit an enormous structural variety, thoroughly characterized in a number of studies [53, 55, 183]. In contrast, only few inves-

tigations on the growth of V on the Rh(110) surface have been conducted [188], and no results have been published on the growth of vanadium oxide on Rh(110) prior to this study. The study of catalytic methanol oxidation on a Rh(110) surface [71, 243] and sub-monolayer VO_x films on Rh(110) [71, 244, 245] is important for a detailed understanding of the redistribution dynamics of VO_x under reaction conditions. In the system $\text{VO}_x/\text{Rh}(111)$ the formation and coalescence of macroscopic vanadium oxide islands is observed in a number of catalytic reactions. The redistribution dynamics have been explained by a polymerization / depolymerization equilibrium, that is sensitive to gradients in the oxygen coverage [69]. In order to evaluate whether this process can be generalized to other substrates, the V and VO_x growth was extended to the thermodynamically less stable and more open Rh(110) surface [71, 185]. A characterization of the different vanadium and vanadium oxide structures that form on the Rh(110) surface constitutes the basis for the interpretation of reaction dynamics observed on $\text{VO}_x/\text{Rh}(110)$ model catalysts during catalytic methanol oxidation in the 10^{-4} mbar range with LEEM and PEEM. It will be distinguished between chemical wave pattern observed on the unpromoted and on the VO_x covered Rh(110) surface.

6.1 Growth of vanadium and vanadium oxide on Rh(110)

The growth of vanadium oxide on the (111) oriented surface of rhodium is characterized by a large number of different two-dimensional structures in the sub-monolayer coverage range. Already a low oxygen pressure in the 10^{-7} mbar range suffices to form highly oxidized VO_x phases, as evidenced for example by the $(\sqrt{7} \times \sqrt{7})\text{R}19.1^\circ$ structure formed upon reactive evaporation of up to 0.6 MLE VO_x [53]. In many cases, the heteroepitaxial growth on the more open (110) surface of fcc metals is more complex. Surface alloying and the diffusion of the deposited metal into deeper substrate layers can occur [257]. In a preceding growth study of vanadium on Rh(110), the formation of an ordered vanadium near surface alloy could be observed upon V deposition and subsequent annealing above 800 K [188]. In this study, the growth of vanadium and vanadium oxide is investigated in the temperature range between 370 and 770 K for a V coverage up to 4 MLE. The experiments presented in this section have been conducted using the SPELEEM microscope located at the Nanospectroscopy beamline (Elettra), and the PEEM system located in Hannover and are part of my master thesis [71] and are published in [185, 244, 245].

6.1.1 The growth of vanadium on Rh(110)

As has been described in chapter 2.7, Auger signal vs. time (AS-t) plots are a reliable way to determine the deposition rate during metal or metal oxide growth, as long as the growth can be described as a Stranski-Krastanow or Fank-van-der-Merwe mode. Also structural transitions, that may occur for example upon completion of a complete layer, are useful to obtain a coverage calibration. In the experiments presented in this chapter, the V coverage is assigned in monolayer equivalents (MLE) based on the growth of metallic vanadium onto the Rh(110) surface at 380 K in vacuum, which is monitored

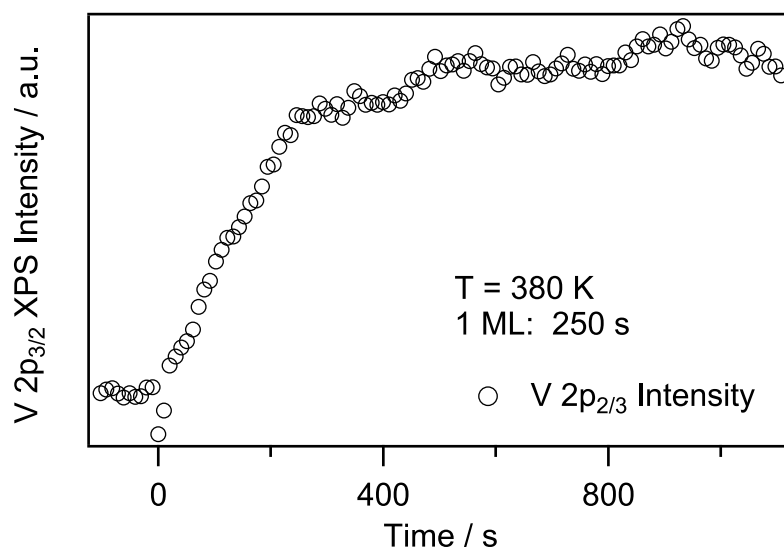


Figure 6.1: V deposition rate calibration on Rh(110) monitored by the V 2p_{3/2} photoemission signal as a function of deposition time. V is evaporated in UHV at 380 K, the photon energy is 650 eV. The change in the slope occurring at around 250 s deposition time marks the completion of the first monolayer of metallic V on Rh(110). Reproduced in part with permission from *J. Phys. Chem. C* **2017**, *121*, 19774 – 19785. Copyright 2017 American Chemical Society.

with XPS. The temporal evolution of the V 2p_{3/2} core level intensity as a function of deposition time is depicted in figure 6.1. In order to maximize the surface sensitivity of the XPS measurement, a photon energy of 650 eV is chosen, resulting in a kinetic energy of the ejected V 2p_{3/2} photoelectrons of about 135 eV, which is close to the minimum of the inelastic mean free path. The completion of the first layer of metallic V deposited on the Rh(110) surface can be recognized by the pronounced change in slope of the V 2p_{3/2} intensity at around 250 s in figure 6.1. After the initial steep and linear signal increase between zero and 250 seconds deposition time, a moderate increase is observed upon further V deposition. It has to be noted, that the coverage calibration obtained from the temporal V 2p_{3/2} intensity variation assumes the formation of a first flat vanadium layer. Since such a growth mode can only be verified by STM or low-energy ion scattering measurements, and since the growth of V on Rh(110) at 380 K is characterized by a high structural disorder as will be shown in the following, the coverage calibration has to be seen as tentative.

LEED images acquired during the growth of metallic V at 380 K indicate a considerable structural disorder with increasing V coverage, as evidenced by a high background intensity in the acquired LEED images. For the first two monolayers of vanadium, a pseudomorphic growth of V is observed, and a faint (1 × 2) LEED pattern develops during the growth of the third layer. The corresponding half-order diffraction spots are strongly elongated in the [001] direction. A strong disorder in the [001] direction is a

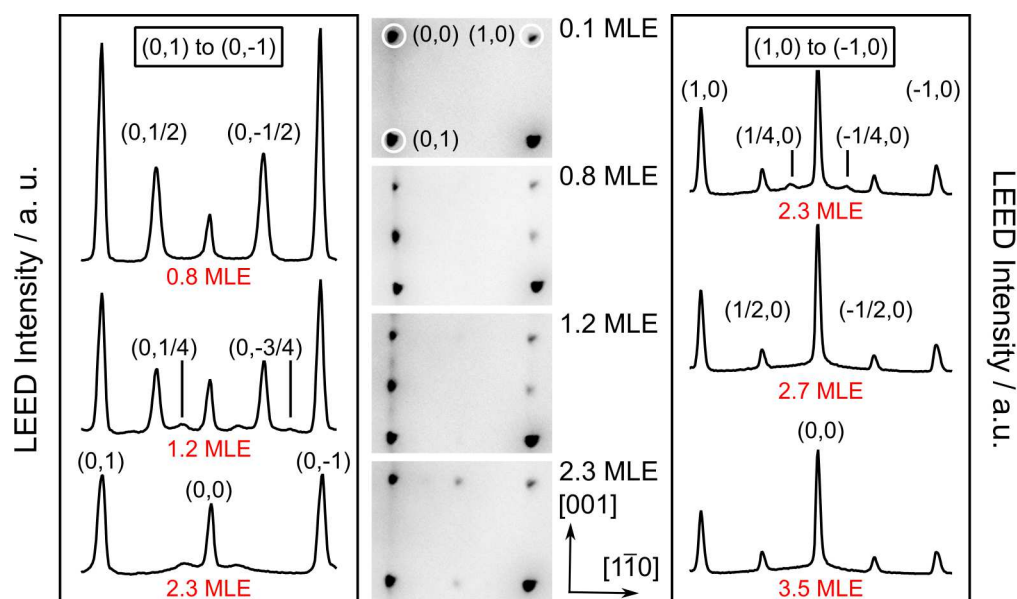


Figure 6.2: LEED images (center) and LEED spot intensity line profiles (left and right) acquired during the deposition of V on Rh(110) at 600 K in UHV. Reproduced in part with permission from *J. Phys. Chem. C* **2017**, *121*, 19774 – 19785. Copyright 2017 American Chemical Society.

possible reason for the elongation, or the formation of an incommensurable arrangement in this direction. The simultaneous occurrence of faceting is indicated by the broad (0,0) spot. UHV annealing of the (1×2) structure at 620 K leads to a transition into a weak (1×3) structure.

V deposition at 600 and 770 K, which is still far below the annealing temperatures of 973 and 1073 K reported for the formation of a (2×1) surface reconstruction with V located in the second layer and a (1×2) missing row reconstruction with V located in deeper layers of Rh(110) [188], results in a sharper LEED image, as demonstrated in figure 6.2. The higher substrate temperature does not only result in a higher structural order of the formed V film, but also different structures evolve as a function of V coverage. At 600 K the (1×2) phase starts to form already at around 0.2 MLE and reaches a maximum LEED intensity at 0.9 MLE. Starting from 1.0 MLE the formation of additional weak diffraction spots at the quarter positions indicate the formation of a (1×4) structure. Further deposition leads to a decrease of the $(0, \frac{1}{2})$, $(0, \frac{1}{4})$ and $(0, \frac{3}{4})$ spot intensities, until at around 2.0 MLE, the (1×2) and the LEED intensity at the quarter positions has disappeared completely. The removal of the (1×2) and (1×4) LEED spots is followed by the development of a (4×1) structure for $\theta_V > 2$ MLE, until finally a (2×1) remains at 3.5 MLE.

The growth of V is highly temperature dependent, as can be seen by comparing the (0,0) diffraction spot intensity as a function of V coverage recorded at 380, 600 and 770 K shown in figure 6.3a. Whereas a nearly linear decrease up to the deposition of

2 MLE is observed at 380 K, the deposition of V onto Rh(110) at 600 K is characterized by a much faster intensity decrease and a relative minimum at 1 MLE, followed by an intensity increase. If V deposition is carried out at 770 K, a similar behavior is observed, with the difference, that the first relative minimum at 1 MLE is followed by a relative maximum at around 1.2 MLE and a further decrease of the (0,0) spot intensity. The differences between the intensity variation observed at 600 and 770 K indicate, that additional processes, which possibly involve the Rh(110) substrate, occur at deposition temperatures above 600 K.

The 170 K difference between 600 and 770 K does also lead to a much faster removal of the (1×2) , as can be seen in figure 6.3b, which compares the $(0, \frac{1}{2})$ LEED intensity measured during V deposition at the two different temperatures. Whereas the (1×2) diffraction spot can be observed up to 2 MLE upon V deposition at 600 K, it already nearly disappeared upon completion of the first V layer if the deposition is carried out at 770 K. For further deposition, only a sharp (1×1) LEED pattern is observed. With the obtained experimental data, it cannot be explained, that the different behavior is caused by the formation of a V/Rh (sub)surface alloy, or bulk diffusion of V during the deposition process at 770 K.

6.1.2 The growth of vanadium oxide on Rh(110)

The growth of vanadium oxide on Rh(110) is carried out by reactive evaporation in an oxygen atmosphere at 2×10^{-7} mbar. The substrate temperature is varied between 370 and 670 K. If the VO_x deposition is carried out at 370 K, a similar sequence of LEED pattern is obtained, as upon deposition of metallic V at 600 K. Initially, a (1×2) LEED pattern appears, which reaches a maximum intensity close to a V coverage of 1 MLE. Upon further VO_x deposition, additional, slightly stronger diffraction spots of a (2×1) structure appear, reaching an intensity maximum around 1.5 MLE. In contrast to the growth of V on Rh(110) at 600 K, no spots belonging to the (1×4) and (4×1) are observed. Also the initially formed (1×2) LEED pattern does not vanish completely, resulting in a streaky (2×2) pattern after the deposition of 2.5 MLE VO_x at 370 K. The pronounced streaks at the half positions and integral order diffraction spots indicate a high degree of structural disorder at this substrate temperature.

A better structural ordering is obtained, if the VO_x deposition is conducted at at least 620 K substrate temperature. In order to be consistent with the VO_x deposition procedure applied in the system $\text{VO}_x/\text{Rh}(111)$, a temperature of 670 K is used for the deposition of ordered VO_x films onto the Rh(110) surface. As described in detail in chapter 2.8.2, the exposure of the Rh(110) surface to oxygen at elevated temperature leads to a sequence of oxygen induced reconstructions. Consequently, VO_x is deposited onto the $c(2 \times 8)$ reconstructed Rh(110) surface during the reactive evaporation at 670 K in 2×10^{-7} mbar oxygen.

Figure 6.4 comprises seven LEED images taken before the VO_x deposition is started (first image) and during the VO_x growth. The oxygen exposure in L is given in the figure together with the VO_x coverage of the corresponding LEED images. The $c(2 \times 8)$ LEED pattern caused by the oxygen covered, reconstructed Rh(110) surface is lifted

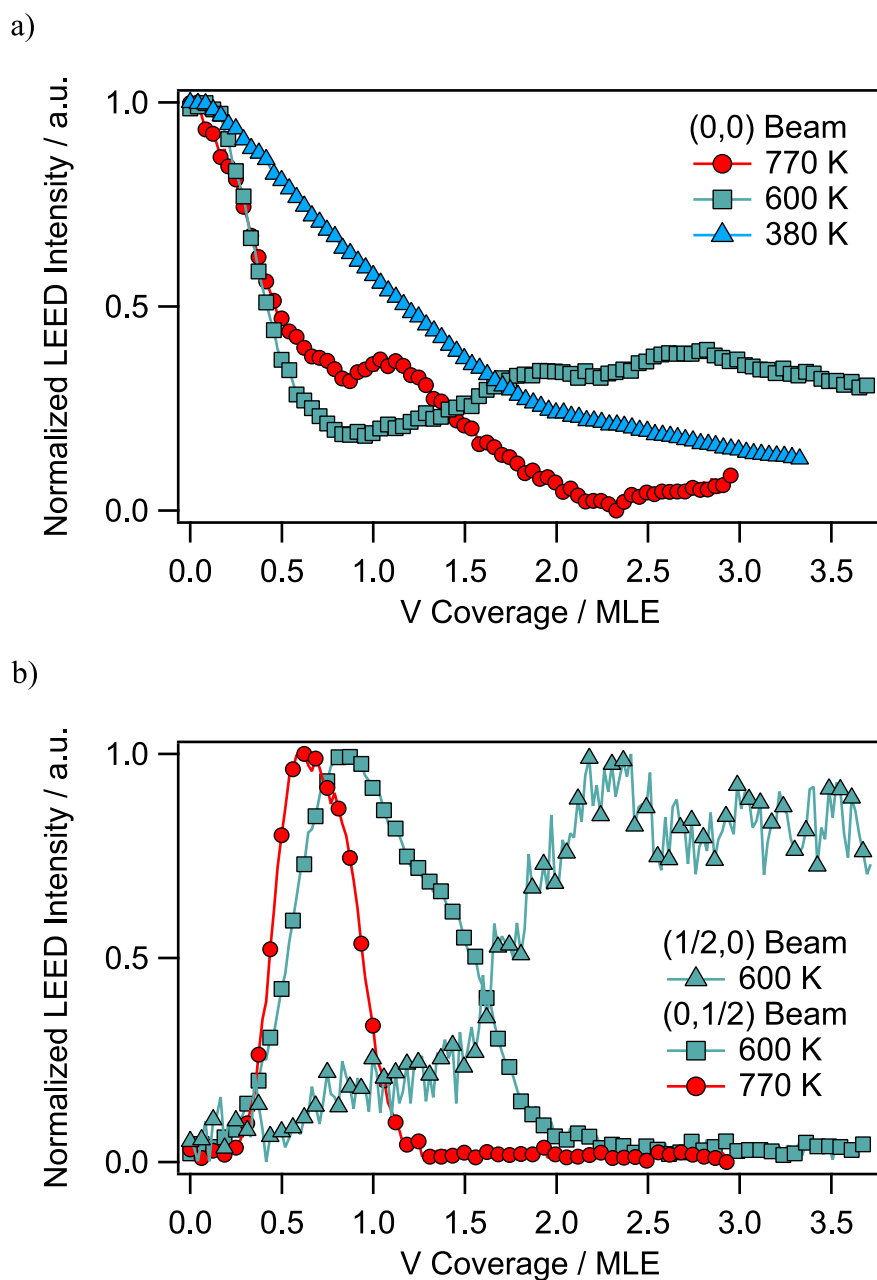


Figure 6.3: LEED intensity as a function of V coverage measured during V deposition onto Rh(110) at 380, 600 and 770 K. a) Comparison of the (0,0) diffraction spot intensity measured as a function of V coverage for the three different temperatures. b) $(\frac{1}{2},0)$ and $(0,\frac{1}{2})$ spot intensity as a function of V coverage measured during the deposition at 600 and 770 K. The LEED measurements are conducted at 43 eV. Reproduced in part with permission from *J. Phys. Chem. C* **2017**, *121*, 19774 – 19785. Copyright 2017 American Chemical Society.

upon deposition of 0.5 MLE VO_x and a (1×4) pattern appears in LEED. This (1×4) pattern is transformed into a (1×2) , as the VO_x coverage reaches 0.7 MLE. Close to the deposition of 1.0 MLE additional spots of a (2×1) structure evolve, while the streaky features around the $(\frac{1}{8}, 0)$ and $(\frac{7}{8}, 0)$ positions completely disappear. At a coverage of 1.1 MLE, weak features at the $(\frac{1}{4}, 0)$ and $(\frac{3}{8}, 0)$ positions appear, leading together with the (1×2) and (2×1) to a LEED pattern similar to a (4×2) structure. Upon deposition of 1.8 MLE, the LEED image is transformed into a strong (3×1) pattern together with weak (1×2) intensity. Finally, at 2.8 MLE the superposition of a (6×5) and the (3×1) pattern can be seen in the last LEED image of figure 6.4. The (4×2) structure obtained after the deposition of roughly 1 MLE (which gets stronger upon post-oxidation) has been used to assign a VO_x coverage to the VO_x films grown on Rh(110) in the PEEM experiments conducted in Hannover, since an AS-t plot obtained by a step-wise VO_x deposition yielded no clear evidence for the completion of the first monolayer [185].

The LEED pattern shown in figure 6.4, which are obtained in situ during the VO_x deposition, are not the thermodynamic equilibrium structures¹. This can be demonstrated by an interruption of the deposition process followed by a ten minute post-oxidation at the same conditions at which the deposition is carried out. Figure 6.5 shows LEED images acquired just after the deposition of 0.4 (a) and 0.8 MLE VO_x in 2×10^{-7} mbar oxygen at 620 K is terminated (left), and after additional ten minutes of post-oxidation (right). The initial streaky LEED pattern obtained after 0.4 MLE VO_x deposition is transformed into a strong (1×2) LEED pattern with additional streaky intensity at the $(\frac{1}{2}, 0)$ position upon post-oxidation. In a similar way, the (1×2) LEED pattern with diffuse, streaky intensity at the quarter positions obtained for 0.8 MLE deposition is replaced by a (4×2) pattern after ten minutes of further oxygen treatment. The large influence of post-oxidation on the structural ordering indicates a low mobility of VO_x on the surface and thus kinetic limitations in formation of ordered structures.

6.1.3 The stability of vanadium oxide films on Rh(110)

If post-oxidation is conducted at an elevated temperature and at higher oxygen pressure, drastic changes of the spatial distribution and the structure of the deposited vanadium oxide layers occur. By shortly heating up a 2.8 MLE thick VO_x film deposited at 350 K, characterized by a (2×2) LEED pattern, to 750 K in the presence of 2×10^{-7} mbar oxygen, a sharp (12×1) LEED pattern forms as the temperature reaches 690 K. The (12×1) LEED pattern obtained after post-oxidation is shown in figure 6.6a, together with LEED intensity cross sections taken during the temperature increase in 6.6b. After the sample was cooled down, the surface exhibits a grainy structure caused by inhomogeneities on the length scale of tens of nanometers in LEEM, as can be seen in figure 6.6c.

If a freshly evaporated, 3 MLE thick vanadium oxide film is exposed to an oxygen pressure of 2×10^{-7} mbar at a substrate temperature of 670 K for ten minutes instead of a short heat up, a similar structural transition as described above occurs, resulting in the

¹In this context, thermodynamic equilibrium refers to equilibrium between the surface layer and the gas atmosphere. The bulk phase of Rh(110) is excluded in this regard.

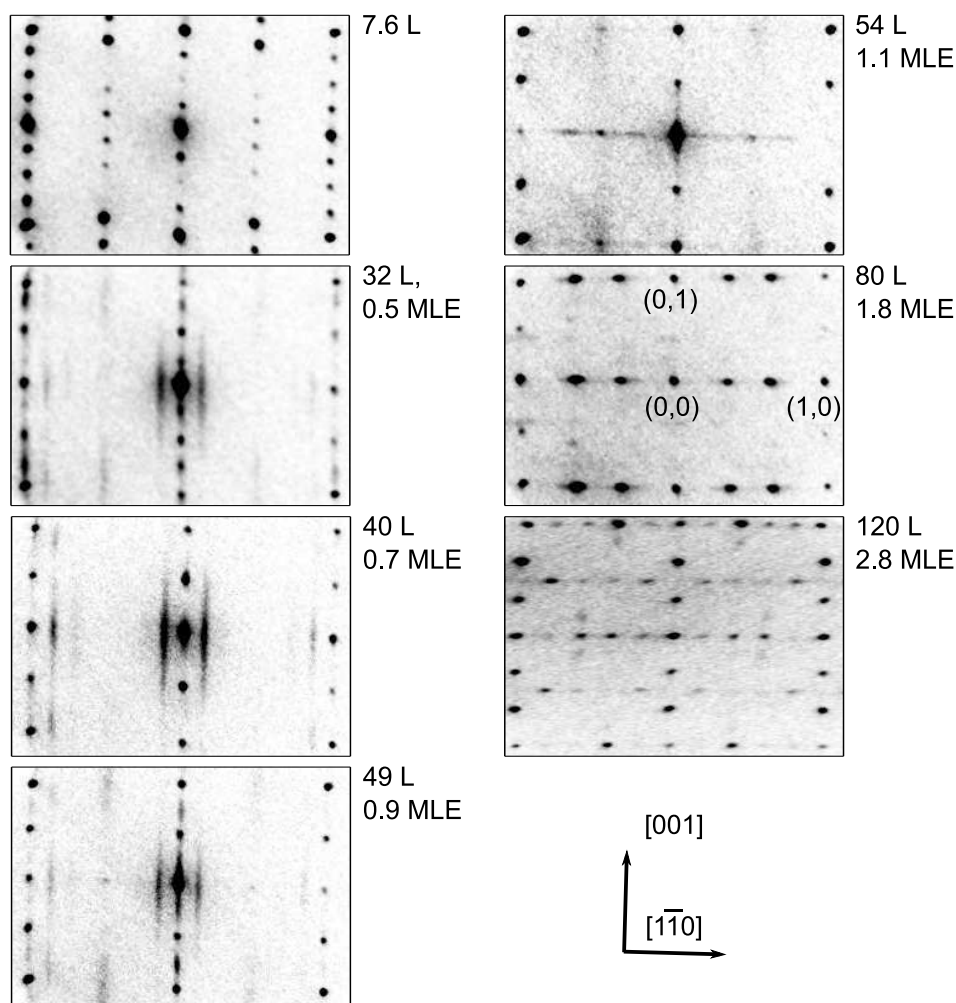


Figure 6.4: LEED images acquired during the reactive evaporation of VO_x at 670 K. The oxygen dose as well as the vanadium oxide coverage are stated with every LEED image. All LEED images are acquired at an energy of 50 eV in 2×10^{-7} mbar O_2 . Reproduced in part with permission from *J. Phys. Chem. C* **2017**, *121*, 19774 – 19785. Copyright 2017 American Chemical Society.

coexistence of a (2×2) LEED pattern with the above mentioned (12×1) pattern. The LEEM image depicted in figure 6.6d demonstrates, that prolonged post-oxidation leads to a phase separation into two phase, which appear as dark and bright at the chosen start voltage of 16 eV. A further increase of the oxygen pressure to 9×10^{-6} mbar at 670 K results in the growth of the bright phase at the expense of the dark phase, as can be seen by comparing the two LEEM images in figure 6.6d and e taken before and after the second post-oxidation at elevated oxygen pressure. A μLEED and $\text{LEEM-}I(V)$ analysis of the two phases reveals, that the bright phase exhibits the (12×1) LEED pattern and has a 260 meV lower work function than the dark phase, which is generating the (2×2)

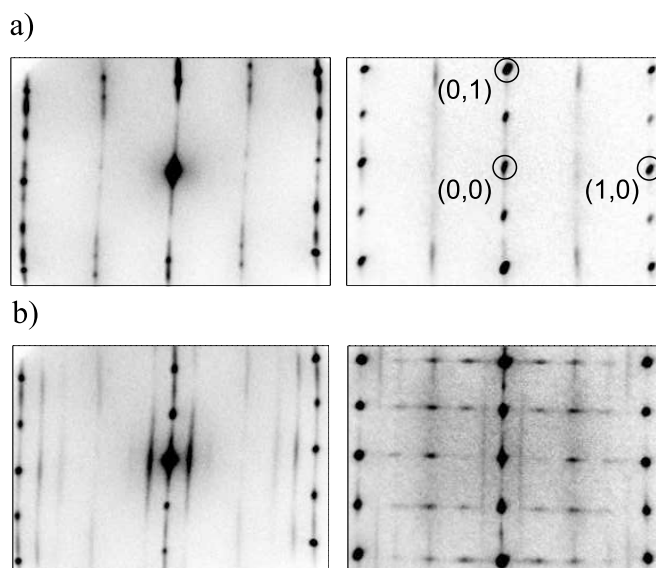


Figure 6.5: The influence of post-oxidation on the VO_x films deposited on Rh(110). a) LEED images acquired after the deposition of 0.4 MLE VO_x (left) and after the subsequent ten-minute post-oxidation (right). b) LEED images taken after the deposition of 0.8 MLE VO_x and ten minutes of post-oxidation. The LEED images have been acquired at 40 (left) and 50 eV (right), respectively. Reproduced in part with permission from *J. Phys. Chem. C* **2017**, *121*, 19774 – 19785. Copyright 2017 American Chemical Society.

diffraction spots [185].

In order to investigate whether the phase separation into the (2×2) and (12×1) structures upon high temperature oxygen treatment is accompanied by a diffusion of a part of the V present after VO_x deposition into deeper layers of the Rh(110) crystal, two thick metallic V films (2 and 6 MLE) are exposed for 40 min to an oxygen atmosphere of 1×10^{-6} and 1×10^{-5} mbar at 670 and 870 K, respectively. Auger spectra acquired before and after the oxygen treatment on both films are displayed in figure 6.7. For both films, the formation of a strong (12×1) LEED pattern is observed after the oxygen treatment, with no signs for the (2×2) structure visible in LEED.

Starting with the 2 MLE thick V film on Rh(110), one notices a slight decrease of the Rh_{302} signal, a nearly unchanged V_{437} signal and a strongly increased $\text{O}+\text{V}_{510}$ signal as a consequence of the prolonged oxygen treatment at 670 K. The signal changes are better visualized in the central inset of figure 6.7 (left). The nearly unchanged V_{437} intensity indicates that no or only small amounts of vanadium diffuse into the Rh bulk at the applied temperature. On the other hand, the strong increase of the $\text{O}+\text{V}_{510}$ and the decrease of the $\text{V}_{472}/\text{V}_{437}$ ratio by 23% is a result of the oxidation of the vanadium film to vanadium oxide. Taking into account the oxidation of the V layers, also the decrease of the Rh_{302} intensity can be explained by the additional attenuation of the ejected Auger electrons by the oxygen atoms present after the oxygen treatment.

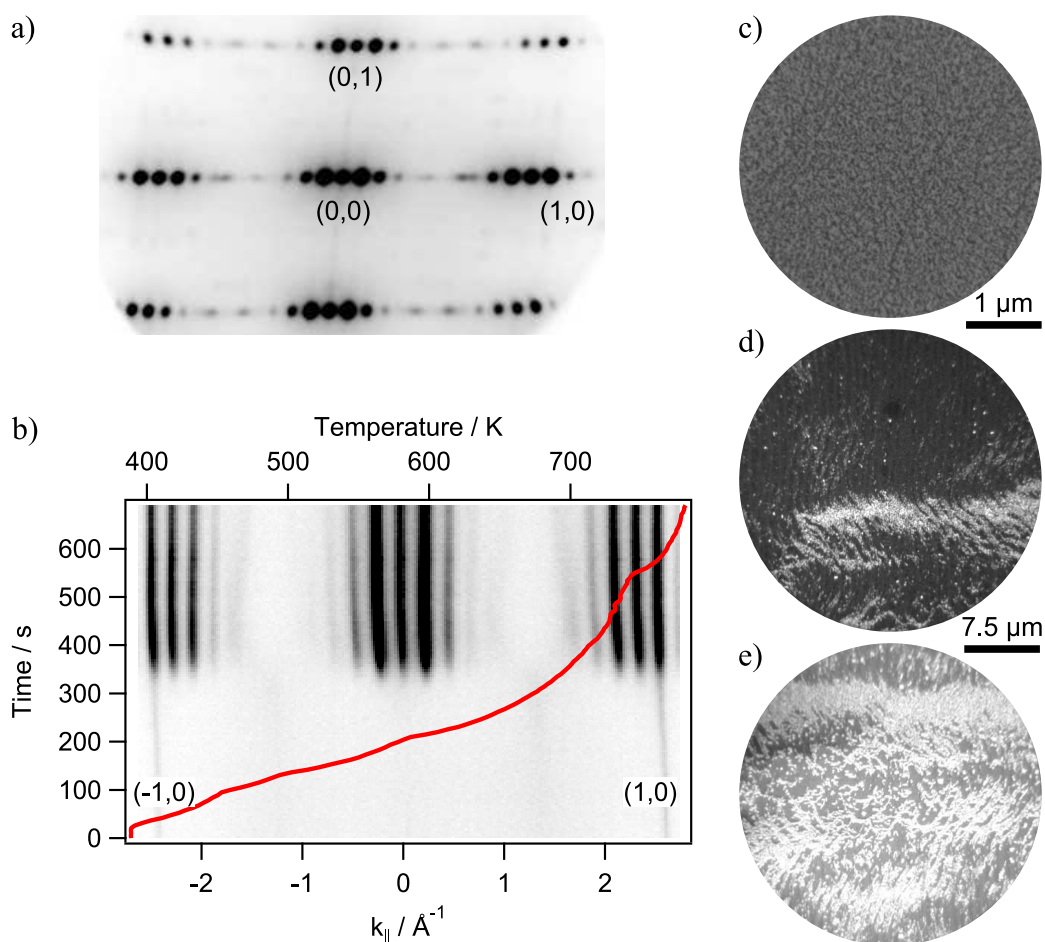


Figure 6.6: The influence of post-oxidation on thick vanadium oxide films on Rh(110). a) LEED pattern acquired at 40 eV after a short heat up to 750 K in 2×10^{-7} mbar oxygen of a 2.8 MLE VO_x film deposited at 350 K in 2×10^{-7} mbar oxygen. b) LEED intensity cross sections taken during the heatup described in a. The temperature is indicated as a solid red line (top axis). c) LEEM image acquired with a field of view of $4 \mu\text{m}$ after the heat up in oxygen. d) and e) LEEM images acquired with a field of view of $30 \mu\text{m}$ after a first post-oxidation for ten minutes at 2×10^{-7} mbar and 670 K (d), and after 25 min at 9×10^{-6} mbar and the same temperature (e). All LEEM images are acquired at a start voltage of 16 eV. Reproduced in part with permission from *J. Phys. Chem. C* **2017**, *121*, 19774 – 19785. Copyright 2017 American Chemical Society.

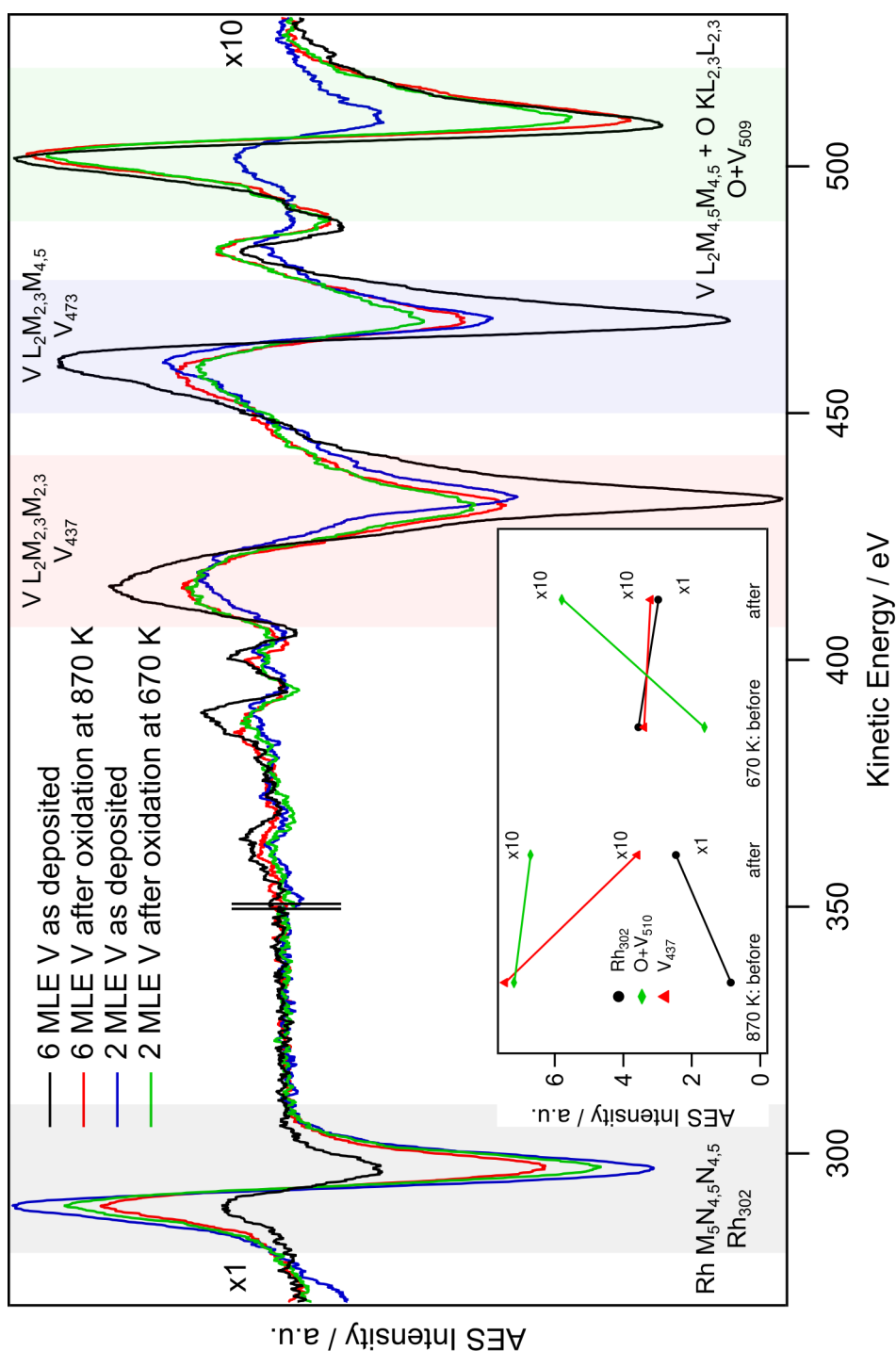


Figure 6.7: V segregation upon oxygen treatment of thick vanadium layers on Rh(110) at high temperature studied with AES. The vanadium films of 2 and 6 MLE thickness are deposited at 470 K onto the Rh(110) substrate and exposed to a 40 min oxygen treatment at 670 K and 1×10^{-6} mbar (2 MLE), and 870 K and 1×10^{-5} mbar (6 MLE). The shown Auger spectra are acquired before and after the oxygen treatment at room temperature in vacuum. The intensity measured in the energy range from 350 to 550 eV is magnified by a factor of ten for better visibility. The inset shows the Auger peak intensity variations of the Rh, V and O transitions upon oxygen treatment. Reproduced in part with permission from *J. Phys. Chem. C* **2017**, *121*, 19774 – 19785. Copyright 2017 American Chemical Society.

For the 6 MLE thick V film, a different behavior is observed as a result of the 200 K higher temperature of 870 K during the oxygen treatment. The initially low Rh₃₀₂ signal increases by a factor of almost three, whereas roughly 50% of the V₄₃₇ intensity present after the V deposition is lost upon oxidation at 870 K and 1×10^{-5} mbar for 40 min. The simultaneous increase of the substrate signal Rh₃₀₂ and decrease of the adsorbate V₄₃₇ signal is a clear sign for the thermally induced bulk diffusion of vanadium during the oxygen treatment.

Interestingly, also a slight decrease of the O+V₅₁₀ signal can be recognized in the inset of figure 6.7. This decrease can be rationalized by the simultaneous decrease of the intensity of the V L_{2,3}M_{4,5}M_{4,5} transition due to bulk diffusion of vanadium, and increase of the O KL_{2,3}L_{2,3} intensity originating from oxygen in the formed vanadium oxide. Both transitions produce Auger electrons with a similar kinetic energy, so that they overlap in the spectrum. An oxidation of V is not only indicated by the formed (12 × 1) LEED pattern and the nearly unchanged O+V₅₁₀ intensity, but also by a 10% decrease of the V₄₇₂/V₄₃₇ peak ratio. However, the smaller peak ratio decrease of only 10% compared to the measured 23% of the 2 MLE film indicates a lower overall oxidation state for the 6 MLE film, and might be a consequence of metallic V in subsurface sites and deeper layers of the Rh crystal, contributing to the Auger spectrum.

The diffusion of excess V into deeper layers of the Rh(110) crystal is consistent with the literature. Píš et al. describe the formation of a V near surface alloy upon annealing of V layers on Rh(110) at 973 K. Whether the roughly 2 MLE thick VO_x film of the formed (12 × 1) structure is the maximum V coverage that can be stabilized by oxygen at pressures up to 1×10^{-5} mbar is not clear. However, clearly oxygen has a stabilizing effect on surface V at elevated temperature.

6.1.4 XPS characterization of vanadium oxide films on Rh(110)

In order to chemically characterize the prepared vanadium oxide films, XPS is applied to freshly deposited 0.4 and 0.8 MLE thick VO_x films on Rh(110), and to the (12 × 1) structure prepared by 6 minutes of post-oxidation at 700 K in 2×10^{-7} mbar oxygen after reactive evaporation of 3 MLE VO_x. XPS is conducted at a photon energy of 650 eV in an oxygen background of 2×10^{-7} mbar to avoid beam damage. Figure 6.8 displays the spectra acquired on the 0.8 MLE thick VO_x film (a) and on the (12 × 1) structure obtained after post-oxidation (b). The binding energy (BE) values of vanadium and vanadium oxides mentioned in literature range between 515.2 and 515.9 eV for V in the oxidation state +3 in V₂O₃ [251, 258, 259], between 515.2 and 516.65 eV for V in the oxidation state 4+ in VO₂ [251, 259, 260], and between 516.9 and 517.7 eV for the highest oxidation state +5 in V₂O₅ [251, 259–261]. The BE of metallic V is reported to be between 512.16 and 512.7 eV [260, 262]. Due to interaction of the substrate with thin oxide layers and due to final-state effects, the corresponding binding energies in thin films can vary from their bulk counterparts. For thick vanadium oxide films supported on highly oriented pyrolytic graphite BE values of 514.5, 515.6, and 517.0 eV are mentioned in the literature for the oxidation states +3, +4, and +5, respectively [248].

For the two sub-monolayer VO_x films a V 2p_{3/2} binding energy of 514.4 eV results

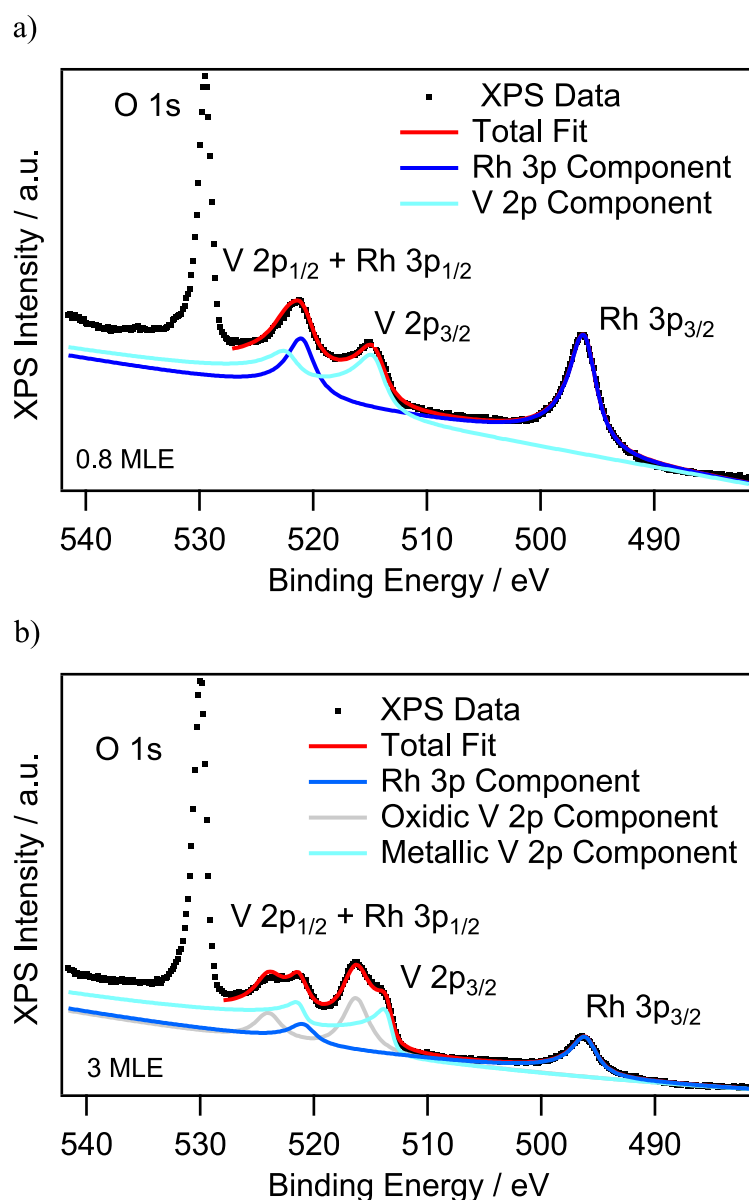


Figure 6.8: XPS characterization of VO_x films of 0.8 and 3 MLE coverage on Rh(110). Photoemission spectra acquired on (a) a 0.8 MLE VO_x film grown at 620 K in 2×10^{-7} mbar oxygen, and (b) on a 3 MLE thick VO_x film, which has been exposed to 6 min oxygen treatment at 700 K in 2×10^{-7} mbar after the reactive evaporation has been terminated. The spectra have been acquired at 340 K (a) and at room temperature (b) in an oxygen ambient of 2×10^{-7} mbar to reduce beam damage. Peak fitting of the V 2p core level has been conducted with a fixed doublet splitting of 7.7 eV after a Shirley background has been subtracted. Further fit parameters have been: (a) a Lorentzian width of 2.18 eV, an asymmetry parameter of 0.38, and (b) a Lorentzian width of 2.66 eV for the oxidic and 0.72 eV for the low BE component, and asymmetry parameters of 0 (oxidic component) and 0.6 (low BE component). The Gaussian width has been determined from the Fermi edge to be 660 meV. Reproduced in part with permission from *J. Phys. Chem. C* **2017**, 121, 19774 – 19785. Copyright 2017 American Chemical Society.

from peak fitting with a single component. This BE is close to the literature values of vanadium in the oxidation state +3 in thin films. By taking the ionization cross sections and asymmetry parameters of the V 2p_{3/2} and O 1s core levels into account, it is possible to calculate the composition of the VO_x structure with equation 2.5, assuming a homogeneous distribution of V and O atoms. An oxygen to vanadium ratio of 2.0 and 1.6 is determined in this way for the 0.4 and 0.8 MLE thick films. For an ideal V₂O₃ film, this ratio would be 1.5, which is close to the experimentally obtained value for the 0.8 MLE film. Even though the measured BE of both films is equal, an excess of oxygen compared to the ideal composition is measured for the 0.4 MLE film. The surplus of oxygen can be explained by atomic oxygen adsorbed on the VO_x uncovered parts of the surface, taking into account that the deposited coverage of 0.4 MLE is not sufficient to cover the surface completely. Accordingly, a V₂O₃ composition with V in the oxidation state +3 is tentatively assigned to the (1 × 2) and (4 × 2) structures obtained after reactive evaporation of 0.4 and 0.8 MLE VO_x onto the Rh(110) surface.

The photoemission spectrum depicted in figure 6.8b, originating from the (12 × 1) structure, can best be fitted with two V 2p_{3/2} components located at 513.4 and 516.3 eV BE. The high BE component corresponds to vanadium in the oxidation state between +4 and +5, and thus a much higher oxidation state is found on the multilayer VO_x phase, compared to the sub-monolayer films discussed above. The low BE component lies with 513.4 eV between the values reported for metallic V and V in the oxidation state +3. A possible explanation for the low BE component would be that a part of the vanadium is alloyed with the Rh(110) substrate. Another possible explanation is the existence of a second (possibly disordered) VO_x phase with V in a low oxidation state. The LEEM and μLEED measurements presented in figure 6.6 indicate that the (12 × 1) structure does not necessarily is the only VO_x phase present after short post-oxidation. An example for a reduced vanadium oxide phase of VO composition and a formal oxidation state of +2, which has a similar BE of 513.2 eV, is the so-called “wagon-wheel” structure of VO_x on Rh(111) [55].

The oxygen to vanadium ratio obtained by equation 2.5 from the V 2p_{3/2} and O 1s core level intensities of the (12 × 1) is with 1.57 close to the value obtained for the 0.8 MLE film, indicating rather a V₂O₃ composition than a highly oxidized VO_x phase, as the high BE of 516.3 eV suggests. If, however, only the high BE component is taken into account in the composition calculation, an O to V ratio of 2.48 results, which is close to the ideal value of a V₂O₅ oxide phase. Since, the nature of the low BE component and the atomic structure of the (12 × 1) phase is not known, this assignment should be seen as tentative, and the possibility of a VO₂ composition should not be ruled out.

6.2 Chemical wave pattern on Rh(110) and VO_x/Rh(110)

Different from the reaction dynamics observed in the system VO_x/Rh(111), which are characterized by a large scale redistribution of VO_x under the conditions of catalytic methanol oxidation, not only dynamic VO_x distribution pattern form in the system VO_x/Rh(110), but also chemical wave patterns can be observed, namely traveling wave

fragments, target pattern, and traveling interface modulations [71, 243–245]. Accordingly one distinguishes between experiments showing solely chemical wave patterns (sections 6.13, 6.4 and 6.5), and experiments that also include a macroscopic redistribution of VO_x in addition to chemical wave patterns (sections 6.6 and 6.7).

The structural variety of the Rh(110) surface, reflected in a large number of adsorbate-induced reconstructions [263], is responsible for a large variety of chemical wave pattern that can be observed in a number of catalytic reactions like the H₂ + O₂ or the H₂ + NO reactions [264–266]. In this study traveling interface modulations are observed. The traveling interface modulations occurring in the systems CH₃OH + O₂/Rh(110) and CH₃OH + O₂/VO_x/Rh(110) are a novel type of interface instability, that has first be observed during catalytic ammonia oxidation on a Rh(110) surface [267, 268]. Besides traveling interface modulation also target pattern and traveling wave fragments are seen on homogeneously VO_x covered Rh(110) films.

6.2.1 Methanol oxidation on Rh(110) and VO_x/Rh(110)

Prior to the chemical wave patterns and the VO_x redistribution under reaction conditions, the catalytic activity of Rh(110) and VO_x/Rh(110) is presented in this section. The system CH₃OH + O₂/Rh(110) is a bistable system in the 10⁻⁴ mbar range at elevated temperature above roughly 680 K. Depending on the methanol to oxygen pressure ratio and temperature, two stable states can be attained: in excess of oxygen the oxidized Rh(110) surface is the stable state, characterized by a very low PEEM intensity; under more reducing conditions the reduced surface becomes stable, which appears bright in PEEM. The different PEEM brightness is a consequence of the local work function, which is increased by adsorbed oxygen, but remains low on a surface with negligible oxygen coverage. Transitions between these two stable states can be induced either by a temperature change or by a change in the gas phase composition. If the transition occurs from the reduced into the oxidized state, it is called an oxidation front. A reduction front is observed during the transition from the oxidized into the reduced state.

The two stable states coexist in the parameter range of bistability. Typically, a hysteresis is observed when going from one stable state into the other and back. Oxidation and reduction fronts nucleate typically at structural defects. Therefore, the surface topography has a strong effect on the observed behavior. By slowly approaching the point in parameter space at which both states are equally stable – the equistability point – the velocity of the propagating front can be reduced, until it finally becomes zero when the equistability point is reached.

Examples of oxidation and reduction fronts observed in PEEM during catalytic methanol oxidation in the 10⁻⁴ mbar range at 830 K are shown in figure 6.9. The nucleation of the oxidation fronts takes place at surface defects as a response to a methanol pressure decrease from 3 × 10⁻⁴ to 2.8 × 10⁻⁴ mbar. This can be clearly seen in the three PEEM images denoted as “Oxidation Front”. In the first and second PEEM image, also diffusional anisotropy can be observed. Instead of a circular oxidation front expected for a surface with isotropic surface diffusion, an elliptically shaped, dark area evolves in the lower part of the PEEM images. The anisotropic Rh(110) surface is characterized

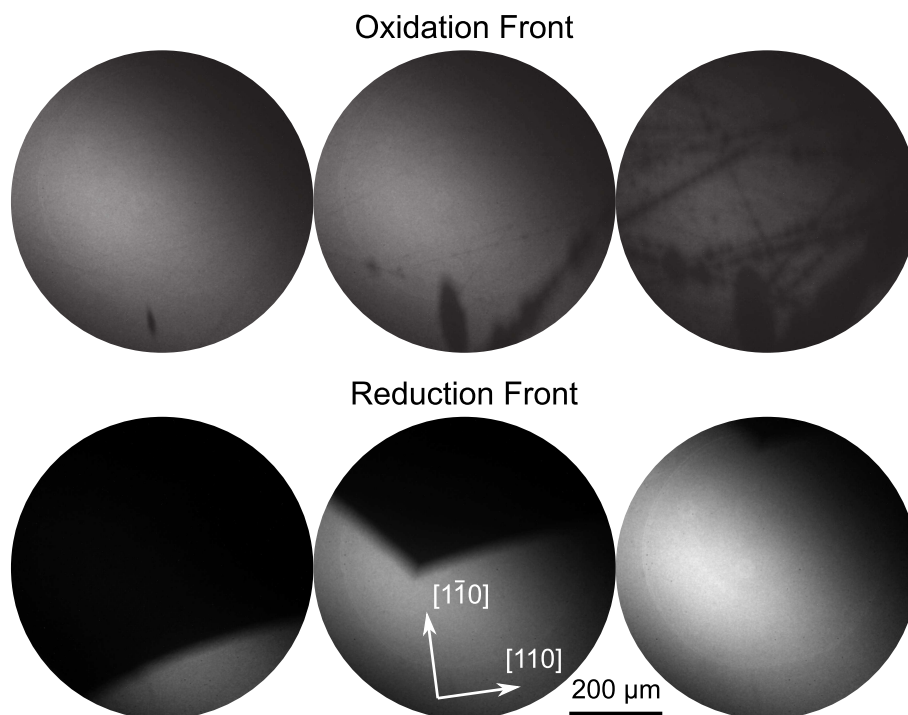


Figure 6.9: PEEM images showing reaction fronts in the system $\text{CH}_3\text{OH} + \text{O}_2/\text{Rh}(110)$ at 830 K. Dark oxidation fronts nucleating at surface defects are observed in a gas atmosphere consisting of 2.8×10^{-4} mbar methanol and 1×10^{-4} mbar oxygen. The surface defects often are macroscopic scratches. A bright reduction front appears upon subsequent increase of the methanol pressure to 4×10^{-4} mbar. The time elapsed between two images is 2 s. Adapted from [71].

by troughs and close packed rows of Rh atoms in the $[\bar{1}10]$ direction. Assuming that the activation energy for surface diffusion is determined by the geometric corrugation, oxygen diffusion should be fastest in direction of the troughs and slowest perpendicular to this direction. This is in fact seen as evident from the shape of the oxygen covered areas in PEEM.

Upon subsequent increase of the methanol partial pressure to 4×10^{-4} mbar a reduction front propagates through the imaged area and turns the surface into a reduced state, bright in PEEM. A close inspection of the interface line separating the oxidized and reduced surface areas reveals three different grey levels: the bright surface belonging to the reduced state, the dark surface of the oxidized state, and a thin band of medium intensity separating the two. The adsorption of oxygen leads to a series of different surface structures, depending on the oxygen coverage [165]. A close-lying explanation for the intermediate intensity at the interface is that the transitions between the oxidized and reduced surface state does not proceed in a single step, but involves at least two different phases of adsorbed oxygen.

In order to verify this hypothesis, adsorption experiments with methanol and oxygen are conducted under similar reaction conditions as in figure 6.9 with LEEM and LEED. Therefore the Rh(110) surface is heated in an oxygen atmosphere of 6.7×10^{-5} mbar from room temperature to 880 K. As 880 K is reached, LEED displays a $c(2 \times 10)$ diffraction pattern originating from adsorbed oxygen on the (1×5) missing-row reconstructed Rh(110) surface [165]. The corresponding LEED image is depicted as the first image in figure 6.10. This structure is the last of a series of $c(2 \times 2n)$ ($n = 3, 4, 5$) structures formed by adsorbed oxygen on the reconstructed Rh(110) surface at elevated temperature. In these structures every n th row is missing. The $c(2 \times 10)$ is the structure with the highest oxygen coverage, i. e. close to 1.0 MLE [269].

Subsequently, methanol is added to the gas phase to induce a transition from the oxidized surface state into the reduced state. Interestingly, up to a methanol pressure of 6.7×10^{-5} mbar, which corresponds to an 1:1 ratio of methanol and oxygen, no change in the surface structure can be observed in LEED, as demonstrated by the second LEED image in figure 6.10. Only when additionally the oxygen pressure is reduced to roughly 1×10^{-6} mbar, a reduction begins, which turns the $c(2 \times 10)$ into a (1×1) LEED pattern (third image in figure 6.10). However, the (1×1) surface is not stable under the applied conditions, and a $c(2 \times 2)$, shown in the fourth image, gradually develops over a few minutes. In the literature, a $c(2 \times 2)$ structure was observed upon CO adsorption on Rh(110) at 125 K [170] and upon electron induced CO dissociation, resulting in a carbon covered Rh(110) surface [171]. Due to the high temperature of 880 K and the resulting low surface residence time, the formation of an ordered CO layer on Rh(110) is unlikely. A $c(2 \times 2)$ structure has also been observed with STM during the catalytic oxidation of hydrogen on Rh(110). Based on the STM results and DFT calculations, two structures of a mixed H and O coadsorbate layer were proposed [270]. These experiments have been carried out between 200 and 270 K, and the $c(2 \times 2)$ structure has been described as a precursor towards water formation and thus complete reduction of the surface. The high temperature of more than 800 K applied in this study make it also unlikely, that the structures reported by Africh et al. are responsible for the $c(2 \times 2)$ LEED pattern observed during catalytic methanol oxidation. However, the formation of a carbon layer on Rh(110) due to methanol decomposition as the reason for the gradual formation of the $c(2 \times 2)$ pattern is plausible. The LEED results shown so far demonstrate, that the reduced state of the surface, can either be the unreconstructed (1×1) surface, or a $c(2 \times 2)$ superstructure, depending on the experimental parameters.

The oxidized state is further investigated by increasing the oxygen pressure again, while following the development in LEED. As the oxygen to methanol ratio reaches a value of 1:10, a fast removal of the $c(2 \times 2)$ superstructure and simultaneous appearance of a (1×2) pattern in LEED takes place (fifth LEED image). This transition occurs within less than a second, and also the (1×2) can be observed for only around one second, before it is transformed into the oxygen induced $c(2 \times 6)$ reconstruction. The (1×2) is most probably generated by adsorbed oxygen on the (1×2) reconstructed Rh(110) surface. At temperatures below 750 K, 0.5 ML adsorbed oxygen on the (1×2) reconstructed Rh(110) surface arrange in a $(2 \times 2)p2mg$ structure, but for higher temperatures a reversible

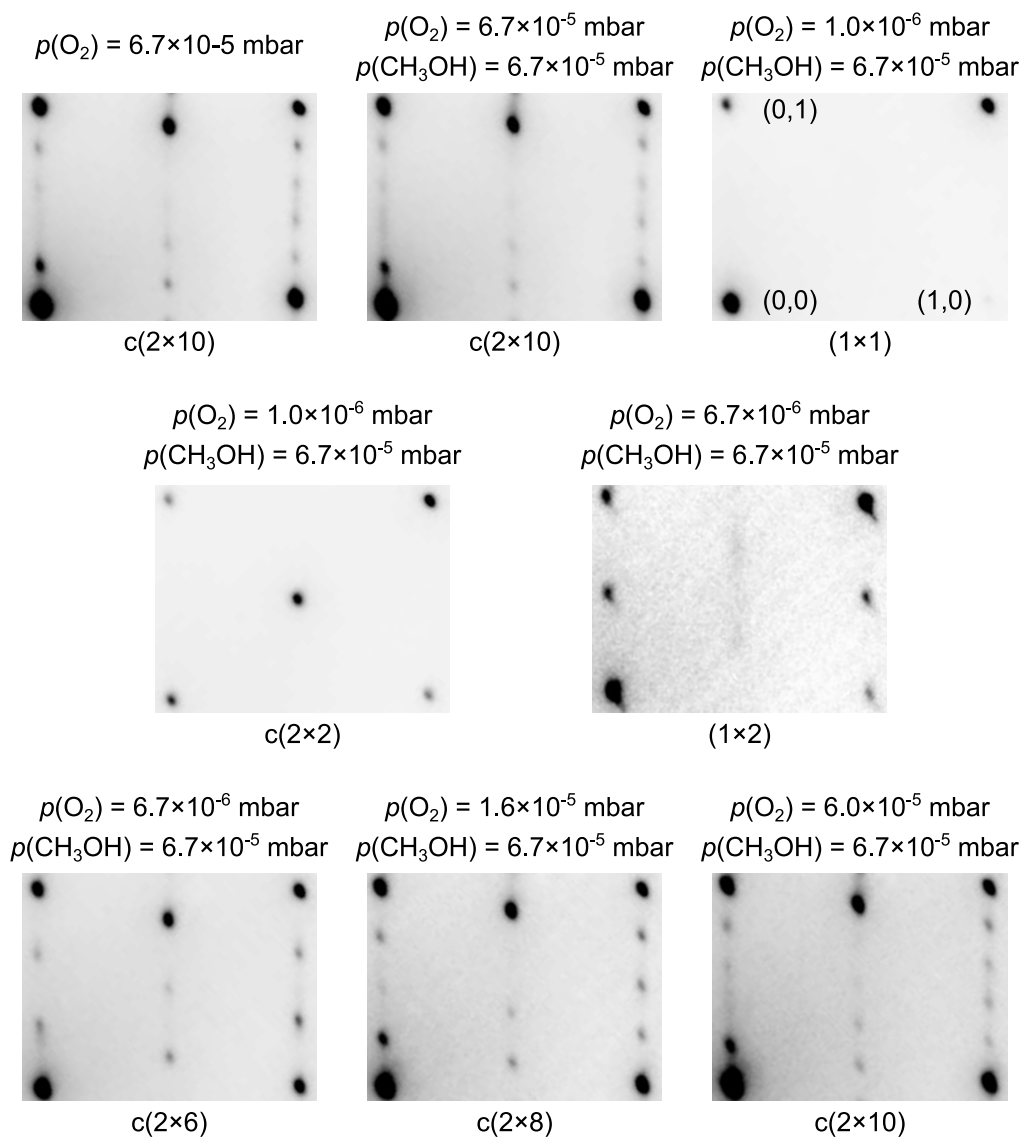


Figure 6.10: LEED characterization of the different surface structures occurring during oxygen adsorption and during reaction with methanol on Rh(110) at 880 K. All LEED images are acquired with a start voltage of 40 eV.

order-disorder transition into a (1×2) is reported by Bellman et al. [271]. Further increase of the oxygen partial pressure to 1.6×10^{-5} and 6.0×10^{-5} mbar results in the formation of the $c(2 \times 8)$ and $c(2 \times 10)$ structures. However, even with very slow pressure changes, it is not possible to stabilize the (1×2) structure under stationary experimental conditions. It might therefore represent a kind of precursor state, which directly leads to the formation of the $c(2 \times 6)$, or even higher oxidized structures, depending on the oxygen partial pressure.

LEEM images showing the transitions between the oxidized and reduced state (oxidation and reduction fronts) are depicted in figure 6.11. The images are acquired at a start voltage of 1.3 eV, which is close to the LEEM / MEM transition. By choosing a start voltage close to the LEEM / MEM transition, the image contrast is maximized. The oxidized surface state, which is characterized by a high work function, is imaged bright in MEM mode. As the surface is transformed into the reduced state, the work function decreases considerably. The probing electron beam has now enough energy to overcome the work function barrier and the electrons start to interact with the surface. The reduced state is thus imaged in LEEM mode and exhibits a low intensity in the images in figure 6.11.

By comparing the LEEM images with the LEED images in figure 6.10, one can assign surface structures to the different intensity levels in LEEM. The $c(2 \times 10)$ structure is excluded from this assignment, since it only develops far away from the equistability point, and should therefore not occur in the parameter range in which reaction fronts can be excited (except for the trivial case, that the experiment is started with the $c(2 \times 10)$ being present on the surface).

A propagating oxidation front is depicted in the upper three images. By carefully inspecting the interface depicted in the middle LEEM image, one can distinguish at least four different phases. Starting from the left side of the image, a homogeneously dark surface is visible, which corresponds, according to the adsorption experiment presented in figure 6.10, to the $c(2 \times 2)$ structure. On the far right side of the image, a despite some surface scratches homogeneous area of dark gray intensity can be recognized. This dark gray intensity level corresponds to the $c(2 \times 8)$ structure of adsorbed oxygen on the missing-row reconstructed Rh(110) surface. These two areas are separated by a thin, very bright line. On the right side of this line, the oxidized side, is an additional thin band of bright grey intensity, which probably represents the $c(2 \times 6)$ phase of adsorbed oxygen. On the left side of the bright interface line, the reduced side, is another thin band of slighter higher intensity as the rest of the reduced surface. Whether this thin band represents another surface phase cannot be determined from the experimental data. However, either the very bright interface line or the thin band of slightly higher intensity on the left side has to correspond to the (1×2) LEED pattern, which occurs in LEED during the transition from the reduced to the oxidized state.

The lower three LEEM images in figure 6.11 show a reduction front propagating with a considerably higher velocity than the oxidation front across the surface. By carefully inspecting the interface separating the oxidized and reduced surface areas, one can again identify three different intensity levels: very low intensity on the right, reduced

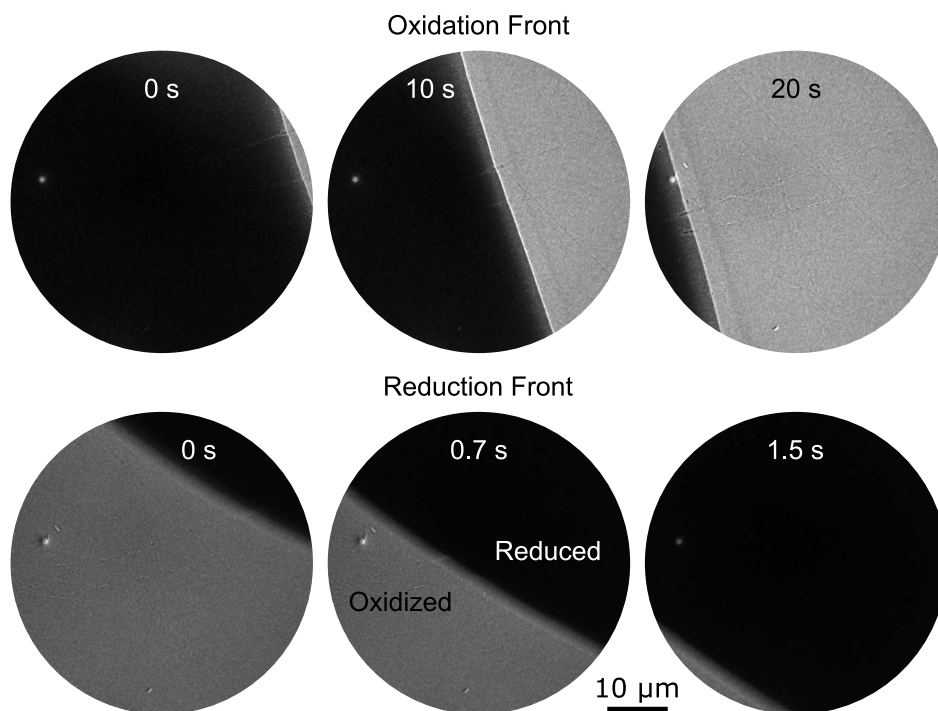


Figure 6.11: LEEM images showing oxidation (top) and reduction (bottom) fronts in the system $\text{CH}_3\text{OH} + \text{O}_2/\text{Rh}(110)$ at 890 K in a gas atmosphere consisting of 6.7×10^{-5} mbar methanol and 1.3×10^{-5} mbar oxygen. The LEEM images are acquired at a start voltage of 1.3 eV.

side, a bright band, and a dark grey intensity level on the left, oxidized side. The dark LEEM intensity of the reduced state corresponds to the (1×1) LEED pattern. Since it takes several seconds to minutes, depending on the reaction conditions, for the $c(2 \times 2)$ structure to develop, after the surface is transformed into the reduced state, it is unlikely that the dark area seen in the LEEM images is caused by the $c(2 \times 2)$ structure. The dark grey intensity level on the oxidized site can be associated with the $c(2 \times 8)$ structure of adsorbed oxygen. The thin band separating the two cannot be related to a LEED pattern, since upon reduction the $c(2 \times 8)$ of the oxidized state is directly replaced by the (1×1) of the reduced state.

A close lying interpretation of the thin band separating the oxidized and reduced surface areas is the strong gradient in surface potential at the interface, caused by the work function difference of the two adjacent surface states, leading to a blurring of the interface. In other words, due to the reduced resolution caused by the local work function difference, the interface appears wider than it really is. In the case of the oxidation front, such a blurring effect cannot clearly be observed. This might be caused by the sequential oxidation via the different structures of adsorbed oxygen, which lower the local work function gradients.

By comparing the oxygen partial pressure at which the $c(2 \times 10)$ vanishes (second

and third LEED image in figure 6.10) with the pressure at which the re-oxidation starts (fourth and fifth image), one notices a hysteresis of 5×10^{-6} mbar. If one compares the disappearance of the $c(2 \times 10)$ with the subsequent formation of the $c(2 \times 10)$, this value increases even to roughly 6×10^{-5} mbar. At the same time, the reduction of the oxidized state seem to happen in one step, directly from the $c(2 \times 10)$ into the (1×1) phase, or at least faster than the temporal resolution of the LEEM instrument, which is 0.1 s. The oxidation, instead, proceeds in a step-wise manner and includes the (1×2) , $c(2 \times 6)$, $c(2 \times 8)$, and $c(2 \times 10)$ structures. The strong hysteresis observed for the transition between the oxidized and reduced state, and the very fast reduction of the oxygen covered surface indicate, that methanol adsorption is inhibited on the oxygen covered surface.

Catalytic activity of Rh(110) and VO_x/Rh(110) during methanol oxidation

Due to the bistable character of the systems CH₃OH + O₂/Rh(110) and CH₃OH + O₂/VO_x/Rh(110) reaction rate measurements are performed with different gas compositions, ensuring that both states, the oxidized and the reduced state are investigated. The reaction rate measurements are performed by applying heating ramps between room temperature and 1020 K with constant heating rates of 0.5 K s^{-1} at a fixed methanol pressure of 3×10^{-4} mbar and a variable oxygen pressure. The VO_x coverage is varied between zero, 0.2 and 0.4 MLE.

Figure 6.12 displays the results of temperature programmed reaction measurements conducted with an oxygen to methanol ratio of 1:3 and 1:5, measured on the bare Rh(110) surface, and with a ratio of 1:3 on the 0.2 and 0.4 MLE VO_x covered surfaces. The main reaction products formed on the unpromoted Rh(110) surface are carbon monoxide and water. To a much lower extent also carbon dioxide is formed. During the experiment conducted with an oxygen to methanol ratio of 1:3, the catalytic activity sets in at around 400 K, and stays at a high level until around 900 K is reached. Upon further temperature increase, the CO, H₂O and CO₂ production decreases first moderately, before it completely disappears close to 1000 K. If the reaction atmosphere is more reducing (oxygen to methanol ratio 1:5), a similar behavior is observed. Starting from around 500 K, the formation of water and CO sets in, but the overall reaction rate is roughly 20% lower, compared to the more oxidizing conditions. In contrast to the activity decrease observed under more oxidizing reaction conditions, the CO and H₂O formation rates stay high up to 1020 K.

The different behavior observed for the two different gas compositions can be explained by a temperature-induced transition from the reduced into the oxidized state, which happens for the 1:3 oxygen to methanol ratio around 900 K. For the more reducing gas atmosphere, the reduced Rh(110) surface is the only stable state up to 1000 K. Accordingly, the reduced surface state can be assigned to the catalytically active state, whereas the oxidized state exhibits nearly no catalytic activity, as evidenced by the drastic decrease of the reaction products in figure 6.12a. The temperature dependence of the transition from a reduced to an oxidized surface is a consequence of the fact that the elementary steps of adsorption, desorption and reaction are activated, included the

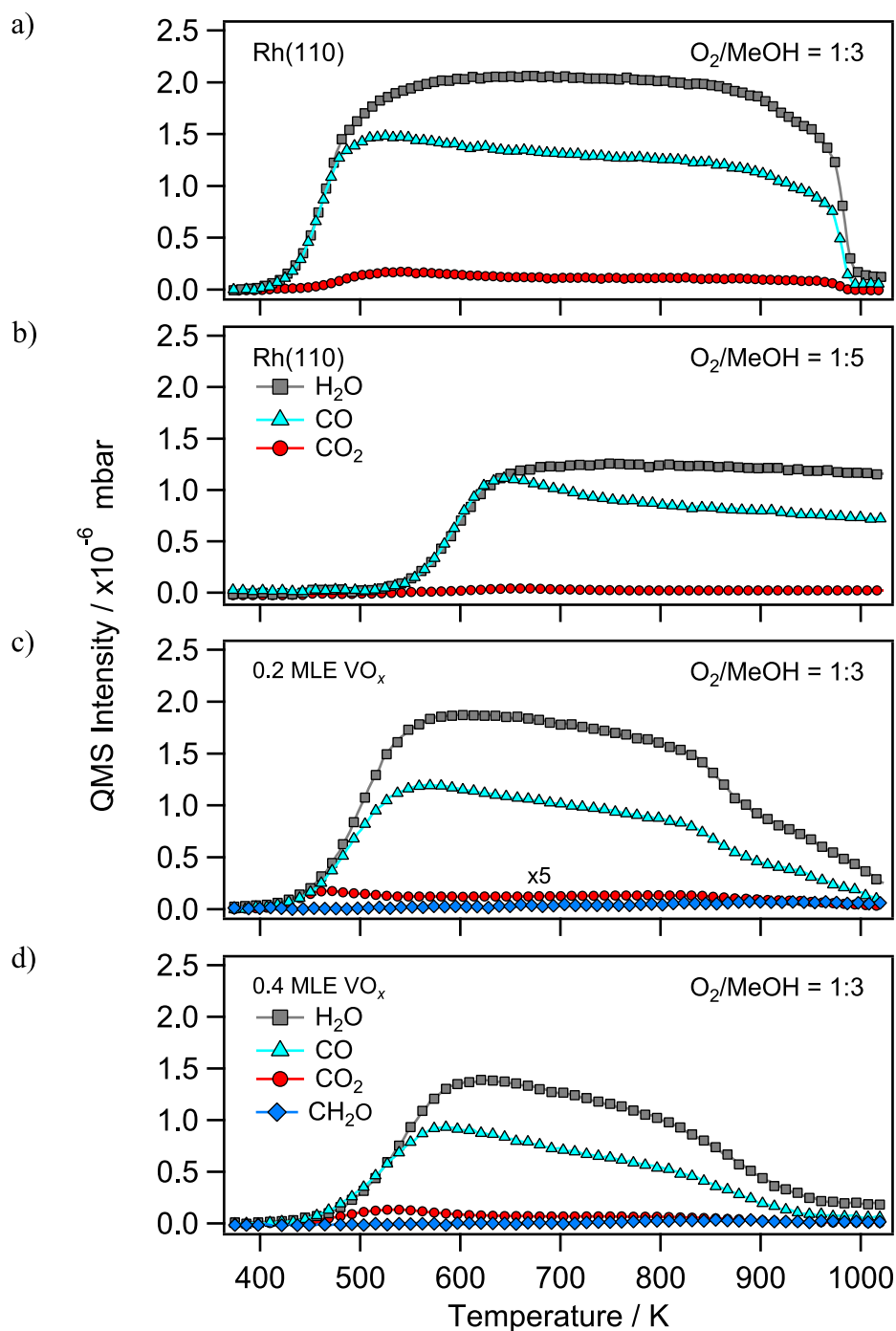


Figure 6.12: Reaction rate measurements conducted in the 10^{-4} mbar range on Rh(110) and VO_x/Rh(110) during catalytic methanol oxidation. TPR measurements on Rh(110) are shown in (a) and (b). The corresponding measurements on VO_x/Rh(110) are depicted in (c) and (d). The gas phase composition, as well as the VO_x coverage are stated in the graphs. The methanol partial pressure is 3×10^{-4} mbar in all experiments, and the heating rate is 0.5 K s^{-1} . Reproduced in part with permission from *J. Phys. Chem. C* **2018**, *122*, 12694 – 12703. Copyright 2018 American Chemical Society. Adapted from [71]

sticking of oxygen and methanol.

The drastic decrease of product formation upon transition from the oxidized into the reduced state (visible in figure 6.12a) clearly indicates an inhibitory effect of adsorbed oxygen on methanol adsorption. A similar finding is also observed in the methanol and oxygen adsorption experiment followed in LEED, presented in the previous section. In turn, the slight decrease in catalytic activity visible under more reducing reaction conditions (figure 6.12b) might be caused by the formation of adsorbed carbon, which blocks active sites. The $c(2 \times 2)$ structure obtained under reducing reaction conditions in the same LEED experiments corroborates this hypothesis.

Comparing the reaction rate measurements conducted on the bare Rh(110) surface with the measurements on the surfaces covered with 0.2 and 0.4 MLE VO_x, one realizes that sub-monolayer amounts of vanadium oxide do not alter the qualitative behavior, since the same reaction products are formed in a very similar temperature range. The most obvious difference between the measurements on Rh(110) and on the VO_x covered surface is, that the catalytic activity is reduced by roughly 10 and 30%, as can be seen by comparing the water and CO rates depicted in figure 6.12c and d, with the rate curves shown in figure 6.12a. The lower reaction rates measured on the VO_x covered surfaces suggests a low activity of VO_x on Rh(110). If the reaction rate measurement is repeated on the same VO_x covered surface, the activities measured on the two VO_x films is with a decrease of 20 and 40% even lower.

6.3 Traveling interface modulations on Rh(110) and VO_x covered Rh(110)

A reaction front in a bistable system is one of the most simple structure one can find in a reaction-diffusion system. Bistable systems are characterized by two stable states; a parameter-change induces transitions from one state into the other state via a propagating wave front. Depending on the parameter choice, the more stable state pushes out the less stable state, and only at the equistability point, both states coexist, separated by a stationary front [272, 273]. Traveling interface modulations are one type of chemical wave patterns observable in the system CH₃OH + O₂/VO_x/Rh(110). Traveling interface modulations have been first observed during catalytic ammonia oxidation on an unpromoted Rh(110) surface [267, 268]. A traveling interface modulation is a perturbation of the average interface position, which propagates in a pulse-like manner along the interface separating the two stable states of a bistable system. In this study, traveling interface modulations are observed during methanol oxidation on the clean Rh(110) surface and on a Rh(110) surface covered with a small amount (0.1 MLE) of vanadium oxide. A higher VO_x coverage leads – under similar experimental conditions – to different chemical wave pattern, namely target pattern and traveling wave fragments, described in sections 6.4 and 6.5.

6.3.1 Traveling interface modulations on Rh(110) during methanol oxidation in PEEM

An interesting property of the system CH₃OH + O₂/Rh(110) is, that traveling interface modulations are observed instead of a stationary interface as the equistability point is approached. At 680 K, traveling interface modulations can be adjusted, starting from the reduced state, by first carefully decreasing the methanol partial pressure until oxidation fronts nucleate. As soon as the oxidation front have nucleated, the methanol partial pressure is increased again slightly, to slow down the propagating oxidation fronts until they finally are brought to a halt. The temperature and pressure values at which the propagation speed reaches zero mark the equistability point of the bistable system. Experimentally it is not possible to precisely adjust the equistability point, and slowly moving interfaces result as a consequence.

As can be seen in figure 6.13a and b, the interface separating the oxidized (dark) and reduced (bright) state is not stationary, but triangular shaped interface modulations propagate in a pulse like manner along the interface. The velocity of the interface itself, and of the traveling interface modulations can be evaluated from $x(t)$ -plots taken parallel and perpendicular to the interface line, respectively. Such $x(t)$ -plots are displayed in figure 6.13c. The velocity of the interface modulations is obtained by measuring the slope of the needle like, dark excursions visible in the left plot, and an average velocity of $22.1 \pm 2.4 \mu\text{m s}^{-1}$ is calculated.

In the same way, the velocity of the interface can be calculated by taking the slope of the solid white line drawn in the right plot. A mean velocity of $0.8 \pm 0.1 \mu\text{m s}^{-1}$ is determined for the propagation of the oxidation front. The non-zero propagation velocity of the interface is caused by a slightly too low methanol pressure, i. e. the system is not exactly at the equistability point. In different experiments, propagating oxidation fronts as well as reduction fronts are observed during the existence of traveling interface modulations. No qualitative change in the behavior of the interface modulations can be identified for a slowly advancing (oxidation front) or retracting (reduction front) interface. Also no clear dependence of the interface position with respect to the crystallographic directions of the anisotropic Rh(110) surface is determined.

A closer inspection of the two $x(t)$ -plots depicted in figure 6.13c reveals other interesting properties of the system. On one hand, the size of the interface modulations grows with time, but no change in the propagation velocity of the modulations is measured. On the other hand, different from expected for a bistable system not two intensity levels can be differentiated in the left $x(t)$ -plot, but three: dark gray between zero and roughly 80 μm , bright grey between 80 μm and 250 μm on the parts of the surface not covered by traveling interface modulations, and nearly black for the oxidized surface state.

Since PEEM only provides work function contrast, and since no in situ LEED measurements are possible at the elevated pressure of up to 5×10^{-4} mbar in the used PEEM system, other experimental techniques are necessary to obtain complementary information required to understand the phenomenon of traveling interface modulations.

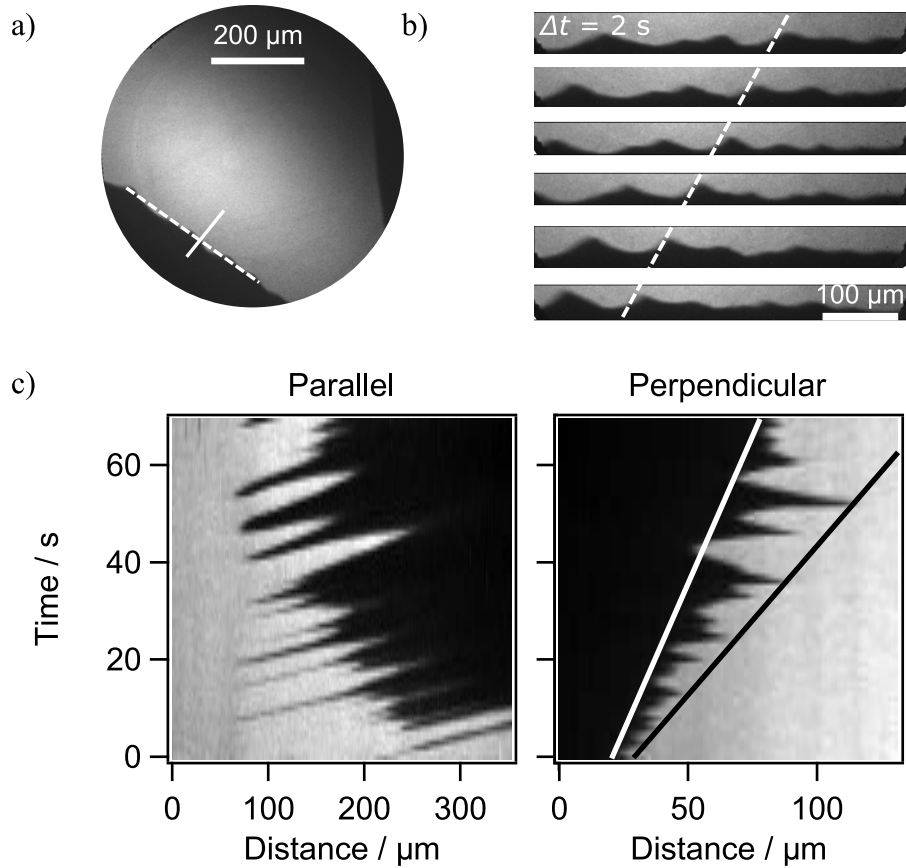


Figure 6.13: PEEM images showing traveling interface modulations during methanol oxidation on Rh(110) in the 10^{-4} mbar range. a) PEEM image acquired at the equistability point, showing the coexistence of the oxidized (dark) and reduced (bright) surface. The solid and dashed white lines mark the positions at which intensity line profiles shown in (c) and (d) are taken. b) Series of PEEM images showing the propagation of traveling interface modulations. The time between two images is 2 s and the propagation direction is indicated by the dashed white line. c) $x(t)$ -plots taken parallel (left) and perpendicular (right) to the interface shown in (a). The velocity of $0.8\ \mu\text{m s}^{-1}$ of the interface is calculated from the slope of the white line in the right $x(t)$ -plot. The temperature is 830 K, 2.8×10^{-4} and 1.0×10^{-4} mbar are adjusted for the methanol and oxygen partial pressure, respectively. Figure adapted from [243].

6.3.2 Traveling interface modulations on Rh(110) during methanol oxidation in LEEM

The superior lateral resolution and the different contrast mechanisms, together with the ability to perform laterally resolved LEED measurements in situ up to the 10^{-4} mbar range predestine LEEM as the method of choice for traveling interface modulations observed during methanol oxidation on Rh(110). However, also some difficulties exist, caused by the small field of view ($\leq 100 \mu\text{m}$) of LEEM, relative to the large length scale and high propagation velocities of the chemical wave pattern.

Traveling interface modulations are excited in a similar manner as in the PEEM experiments described above. The Rh(110) surface is heated in an oxygen atmosphere of 6.7×10^{-5} mbar to 880 K. Subsequently, methanol is added to the gas phase until the surface is turned into the reduced state, notable by the pronounced shift of the LEEM / MEM transition to lower start voltage, due to the lower work function of the surface in the reduced state. As the reduced state is established, the oxygen partial pressure is increased again slowly, until the propagation of an oxidation front is visible in LEEM.

Due to the small field of view, the nucleation of an oxidation front is typically not observed and only after formation, propagating oxidation fronts are slowed down by a parameter change. The problems related to the considerable smaller field of view are further complicated by the slow response time to changes in the gas phase composition, which is in the order of seconds. This makes it impossible to exactly adjust equistability. Despite these experimental difficulties, it is still possible to generate slowly propagating oxidation and reduction fronts, and also traveling interface modulations can be observed, as shown in figures 6.14 and 6.15.

The temporal evolution of the intensity of selected LEED spots acquired under constant reaction conditions of 885 K, 6.7×10^{-5} mbar methanol and 1.3×10^{-5} mbar oxygen is depicted in figure 6.14a. The corresponding LEED images are acquired in an area of $5 \mu\text{m}$ diameter at a start voltage of 40 eV. Shown are the intensities corresponding to the $(\frac{1}{2}, \frac{1}{2})$ spot of the $c(2 \times 2)$, the $(1, \frac{1}{2})$ spot of the (1×2) , the $(1, \frac{1}{3})$ spot of the $c(2 \times 6)$, the $(1, \frac{1}{4})$ spot of the $c(2 \times 8)$ structure, together with the (0,0) diffraction spot intensity.

It has to be noted, that due to the proximity in reciprocal space a considerable amount of (2×8) intensity is therefore apparent in the traces representing the $c(2 \times 6)$ structure. In a similar manner $c(2 \times 8)$ intensity contributes also to the trace representing the (1×2) structure, since both structures have a diffraction spot at the $(1, \frac{1}{2})$ position used to monitor the (1×2) structure. Also the $c(2 \times 2)$ structure is affected by intensity originating from the $c(2 \times 6)$ and (2×8) structures.

The position of the probing electron beam on the sample surface is chosen in a way, that mainly the reduced surface state is probed, and that from time to time an oxidation front passes through the probed area. The times at which the surface is in the reduced and oxidized state are highlighted by **R** and **O** in the graphs depicted in figure 6.14. Two excerpts of the time series in figure 6.14a, showing the transition from the reduced into the oxidized state (left) and back again(right), can be seen in figure 6.14b. As the system is transformed into the reduced state, all intensity belonging to the structures

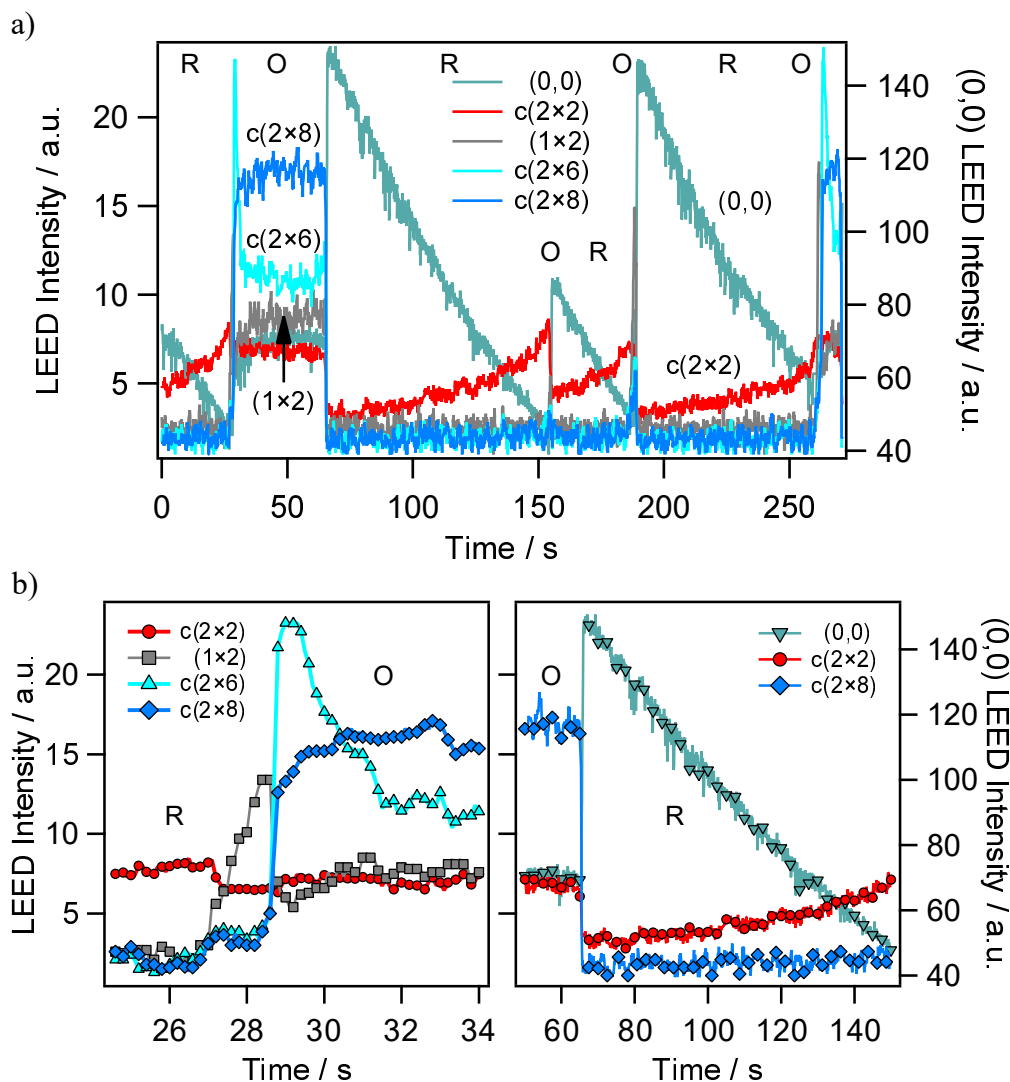


Figure 6.14: Surface structures during traveling interface modulations. Shown is the intensity evolution of selected LEED spots acquired in situ during the propagation of traveling interface modulations in methanol oxidation. The intensity of all super structure spots is scaled on the left ordinate, whereas the (0,0) diffraction beam intensity is scaled on the right ordinate. The reduced and oxidized surface states are indicated by R and O, respectively. a) Temporal evolution of the LEED intensity during the propagation of traveling interface modulations. b) Subsets of the experiment shown in a, demonstrating the transitions from the reduced into the oxidized state (left) and from the oxidized into the reduced state (right). The measurements are performed at 885 K in 6.7×10^{-5} mbar methanol and 1.3×10^{-5} mbar oxygen at a start voltage of 40 eV.

of adsorbed oxygen disappears within less than 0.1 s, while simultaneously the intensity of the (0,0) diffraction beam reaches a relative maximum. In the following, the (0,0) intensity decreases with time, while the intensity of the $c(2 \times 2)$ starts to increase in a progressive manner.

An oxidation of the surface sets in as soon as the $c(2 \times 2)$ surpasses a certain value. Interestingly, this intensity value is fairly constant in the four oxidation fronts observed during the time period depicted in figure 6.14. Upon oxidation, the $c(2 \times 2)$ structure is removed within 0.2 s, while the (1×2) structure forms over a period of 0.8 s, as can be seen in the left graph of figure 6.14b. Only 0.2 s after a maximum intensity is reached, the (1×2) structure transforms within 0.1 s into the $c(2 \times 6)$ structure, which is further transformed into the $c(2 \times 8)$ structure in roughly 1.5 s. The surface stays in the oxidized state for 30 s, until it is abruptly transformed back into the reduced state as shown in figure 6.14b. The complete disappearance of the $c(2 \times 8)$ intensity (and therefore also some $c(2 \times 2)$ intensity) and the simultaneous increase of the (0,0) intensity mark the passing of a reduction front through the area probed with LEED.

By comparing the reduction fronts turning the surface from the oxidized state back into the reduced state at roughly 70, 160, and 190 s one notices that the (0,0) intensity reaches its maximum intensity only in the first and last reduction, while only 40% of this intensity is restored in the second reduction at 160 s. At the same time, the $c(2 \times 2)$ intensity decreases to almost zero after the surface has left the oxidized state at 70 and 190 s, whereas quite some intensity belonging to the $c(2 \times 2)$ structure remains after the oxidized state has vanished at 160 s. The main difference between the three mentioned reduction fronts is the lifetime of the oxidized state: with 37 and 2 s the oxidized state lasted much longer before the reduction at 70 and 190 s compared to the 0.7 s lifetime before the reduction at 160 s. Additionally, in the latter case only the formation of the (1×2) structure is observed.

The behavior of the (0,0)-beam demonstrates that at least one slow process is involved with a time constant of several tens of seconds. This process is only active in the reduced state of the surface. Under the assumption, that the $c(2 \times 2)$ LEED pattern originates from adsorbed carbon due to methanol decomposition, this behavior can be explained. As the surface is turned into the reduced state, it is initially nearly adsorbate free, resulting in a maximum intensity of the (0,0) diffraction beam. Due to incomplete oxidation of methanol on Rh(110), carbon accumulates on the surface with time, as indicated by the increasing $c(2 \times 2)$ intensity. The growing carbon layer is responsible for the decreasing (0,0) intensity. As the surface is transformed into the oxidized state, all carbon on the surface is removed by oxidation and the original (0,0) intensity is attained after subsequent transition back into the reduced state. If, however, the oxidized state is not long enough stable to remove all adsorbed carbon, the (0,0) intensity does not reach its maximum value upon reduction and some $c(2 \times 2)$ intensity remains, as can be seen at around 160 s in figure 6.14.

LEEM images that are acquired shortly after the LEED analysis at the same experimental conditions are depicted in figure 6.15a, together with the development of the integral LEEM intensity shown in figure 6.15b. The upper four LEEM images show the

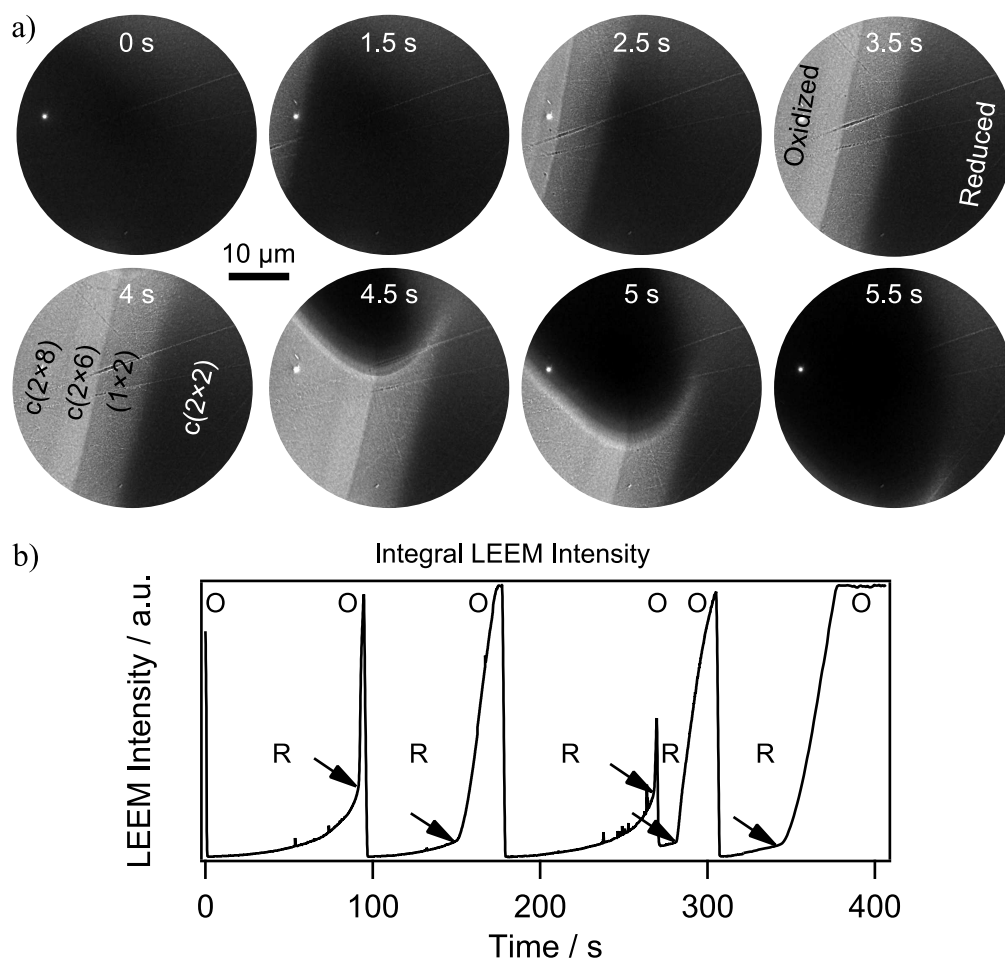


Figure 6.15: LEEM images and intensity development acquired during the propagation of traveling interface modulations in methanol oxidation on Rh(110). a) LEEM images showing an advancing oxidation front. At 4.5 s a traveling interface modulation propagates along the interface and turns the whole imaged area into the reduced state. b) Integral LEEM intensity evolution acquired over the whole imaged field of view of 50 μm. The reduced and oxidized surface states are indicated by R and O, respectively. The experimental conditions are as in figure 6.14.

transition from the reduced surface state, characterized by a low LEEM intensity, into the oxidized surface state, appearing as bright area. The lower four LEEM images show the propagation of a traveling interface modulation along the interface line from the top of the image to the bottom, until finally the whole surface is transformed back into the reduced state again.

Interestingly, the four different surface phases are much better defined in this experiment, compared to the oxidation front depicted in the upper three LEEM images of figure 6.11. Based on the LEED intensity analysis presented above, an assignment of

surface structures to the different LEEM intensity levels can be made, as indicated in the fifth image in figure 6.15a. The reduced state, characterized by a $c(2 \times 2)$ LEED pattern is transformed into a $c(2 \times 8)$ via the intermediate phases (1×2) and $c(2 \times 6)$. Again, for the reduction front, no assignment of surface structures to the different intensity levels can be made, except that the slightly lower LEEM intensity of the interface modulation, which propagates from the top of the images to the bottom, represents the (1×1) surface, and the slightly brighter LEEM intensity on the right side of the image, which is not oxidized, represents the $c(2 \times 2)$ surface phase.

Further support for the different LEEM intensity levels comes from the temporal evolution of the integral LEEM intensity shown in figure 6.15b. The time periods in which the sample is in the reduced state and the oxidized state are again highlighted by **R** and **O**, respectively. Additionally, the onset of oxidation is highlighted by the black arrows in the graph. By comparing the temporal evolution of the integral LEEM intensity with the $c(2 \times 2)$ intensity in figure 6.10a in the time frame between the transition into the reduced state and the propagation of an oxidation front, one notices that the formation of the $c(2 \times 2)$ carbon layer is accompanied by an increase of the LEEM intensity. Taking into account, that the LEEM images are recorded with a start voltage just at the LEEM / MEM transition, the increasing LEEM intensity due to the formation of the $c(2 \times 2)$ structure can be explained by a slightly increasing work function. Accordingly, the (1×1) Rh(110) surface has the lowest work function, followed by the $c(2 \times 2)$ structure. A drastic increase of the work function is encountered as the surface is transformed into the oxidized state.

Experimentally, a work function of 5.1 eV is reported for the Rh(110) surface [274], whereas a value of 4.98 eV is given for a poly-crystalline Rh film [275]. Adsorption of oxygen leads to a linear increase of the work function until a saturation of 730 meV work function difference to the clean Rh(110) surface is reached at 0.5 ML [168]. In the system O/Co(10 $\bar{1}$ 0) it was furthermore found, that a missing-row reconstruction occurring upon transition from a $c(2 \times 4)$ to a $p(2 \times 1)$ structure (both with an oxygen coverage of 0.5 MLE leads to a slight decrease of the work function [276]. Apparently, the substrate reconstruction has only a small effect on the work function of the adsorbate. The work function of carbon is with 5.0 eV very close to that of Rh [277]. Based on the work function values reported in the literature, the assignment of the surface phases to the different LEEM intensity levels seems reasonable. Whether the slight intensity difference between the (1×1) and the $c(2 \times 2)$ can be explained simply by the different work function of the mostly adsorbate free Rh(110) surface and the carbon covered surface cannot be decided from the work function values reported in the literature. However, quite in contrast to PEEM, where differences in the local work function constitute the main contrast mechanism, in LEEM diffraction contrast is the main contrast mechanism and the work function contributes only as a minor factor.

6.3.3 Traveling interface modulations on Rh(110) in other reactions

Traveling interface modulations on Rh(110) have first been observed during catalytic ammonia oxidation monitored with PEEM [267]. A subsequent LEEM study revealed

a transition from the $c(2 \times 6)$ structure of adsorbed oxygen on Rh(110) into a $c(2 \times 4)$ structure associated with a mixed nitrogen and oxygen adlayer via reaction fronts [268]. Apparently, the existence of traveling interface modulations cannot be coupled to the formation of a $c(2 \times 2)$ layer of adsorbed carbon, even though the results presented above suggest such an assumption. Traveling interface modulations can be adjusted in the absence of carbon containing species. In order to further limit the number of possible explanations for the existence of traveling interface modulations, the $H_2 + O_2$ reaction is studied on Rh(110) in PEEM and LEEM.

The bistable system $H_2 + O_2 / Rh(110)$ is a well studied system and a number of non-linear phenomena have been investigated in the past, including (parameter dependent) anisotropy of front propagation [264, 278–280]. In contrast to catalytic methanol and ammonia oxidation, no traveling interface modulations could be observed in the $H_2 + O_2$ reaction in a wide parameter range up to 1000 K and a total pressure of up to 5×10^{-4} mbar. As the equistability point is approached, propagating reaction fronts slow down, until they finally reach a halt. The result is a stationary interface, as expected for a bistable system. In order to find differences between ammonia and methanol oxidation, in which traveling interface modulations are observed, and the $H_2 + O_2$ reaction, in situ LEEM and LEED experiments are conducted in the 10^{-5} mbar range.

Propagating reaction fronts can be adjusted in the $H_2 + O_2$ reaction at 845 K in LEEM by first increasing the oxygen pressure from UHV to 2.7×10^{-5} mbar, resulting in a $c(2 \times 10)$ diffraction pattern in LEED, and subsequently introducing hydrogen until the propagation of a reduction front is observed. In order to stabilize the oxidized state, the hydrogen pressure is again decreased slightly until the whole imaged area is oxidized. Figure 6.16 shows six LEED images acquired after the oxidized state was established (first image), and after further changes in the gas phase composition.

As can be seen in the first image of figure 6.16, the oxidized state (close to the equistability point) is characterized by the same (1×2) LEED pattern, that also occurs shortly in the transition from the reduced into the oxidized state during methanol oxidation. Different from methanol oxidation, this (1×2) structure does not transform into one of the other missing-row reconstructed oxygen structures, even not after five minutes in the oxidized state. After the mentioned five minutes, the hydrogen pressure is slightly increased to 0.8×10^{-5} mbar to induce the transition back into the reduced state, which is characterized by a (1×1) LEED pattern, as shown in the second image in figure 6.16. Different from methanol oxidation, the (1×1) LEED intensity remains more or less constant over roughly 400 s, and no formation of the $c(2 \times 2)$ diffraction image is observed. The absence of any trace of the $c(2 \times 2)$ diffraction pattern corroborates the assignment of an carbon adlayer to the $c(2 \times 2)$ structure. If the $c(2 \times 2)$ would be the result of a mixed H and O adlayer, as observed in [270], it should also occur during the $H_2 + O_2$ reaction, which is not the case.

The oxidized state can only be obtained again by changing the gas phase composition. Upon slight hydrogen pressure decrease the (1×2) structure forms again, as demonstrated in the third LEED image in figure 6.16. Again, the (1×2) is the only super structure visible for 200 s, until another hydrogen pressure decrease to 0.1×10^{-5} mbar

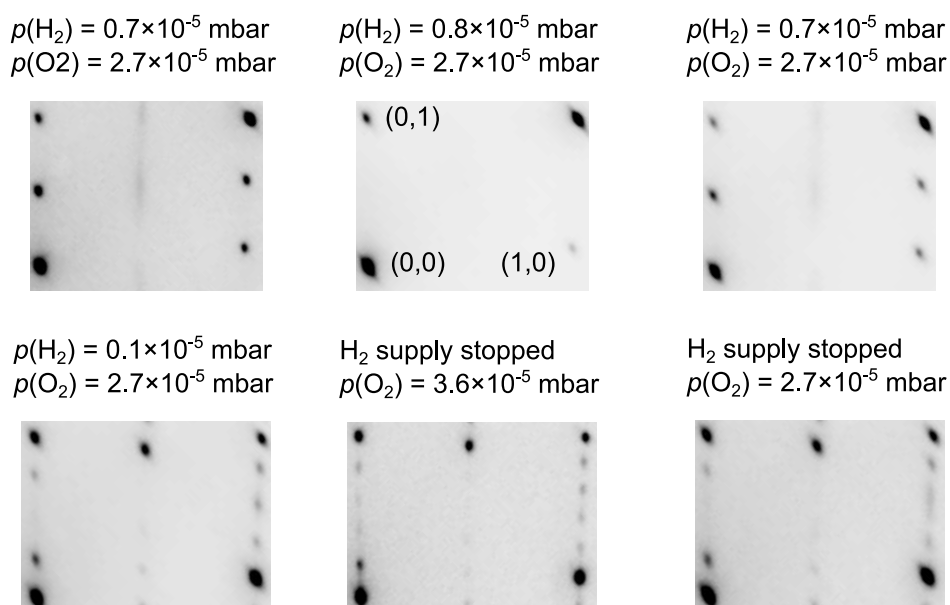


Figure 6.16: LEED images acquired during the H₂ + O₂ reaction on Rh(110) at 845 K in an area of 5 μm diameter. The partial pressures at which the single LEED images are acquired are indicated in the figure. The start voltage is 40 eV in all images.

results in a $c(2 \times 8)$ structure in the fourth image. Due to the slow image acquisition rate of 0.5 frames per second, it cannot be determined, whether the $c(2 \times 8)$ is formed directly or via a shortly existing $c(2 \times 6)$ intermediate. Interestingly, even by completely closing the hydrogen leak valve, no formation of the $c(2 \times 10)$ structure can be observed, probably caused by the residual hydrogen apparent in the UHV chamber due to the comparatively low pumping rate of turbomolecular pumps for light gases (no ion pump is used). The $c(2 \times 10)$ can only be formed by further increasing the oxygen pressure to 3.6×10^{-5} mbar (fifth LEED image). A subsequent pressure decrease back to 2.7×10^{-5} mbar results in a partial reduction back into the $c(2 \times 8)$ structure, as seen in the last LEED image of figure 6.16 by the diffuse intensity between the $(1, \frac{2}{5})$ and $(1, \frac{3}{5})$ positions.

The different behavior observed in the methanol and ammonia oxidation, and in the H₂ + O₂ reaction allows for two conclusions: *i*) The $c(2 \times 2)$ structure, probably caused by adsorbed carbon, does not play an essential role in the excitation mechanism, since it was not observed in ammonia oxidation. *ii*) The absence of traveling interface modulations in the H₂ + O₂ reaction is related to the ability of hydrogen to react with adsorbed oxygen, even though the surface is in the oxidized state. This can be understood by taking into account, that the catalytic activity in methanol oxidation drastically decreases as the oxidized state is entered (see figure 6.12), and that the $c(2 \times 10)$ structure could be observed even at equal partial pressures of methanol and oxygen (see figure 6.10). Obviously, the adsorption of methanol and the subsequent reaction with adsorbed oxygen

is strongly inhibited in the oxidized state. A deactivation of the Rh(110) surface by oxygen was, to a certain degree, also observed in rate measurements during ammonia oxidation [281], and the oxidized state, characterized by a $c(2 \times 6)$ structure of the bistable system $\text{NH}_3 + \text{O}_2/\text{Rh}(110)$ was described as unreactive [267]. In turn, the facts that even residual hydrogen present after completely turning off the hydrogen supply prevents the formation of the $c(2 \times 10)$ structure in the presence of 2.7×10^{-5} mbar oxygen, and that only the (1×2) structure is found close to the equestability point demonstrate, that hydrogen can adsorb on and react with a closed layer of adsorbed oxygen.

The main difference between the two systems in which traveling interface modulations have been observed (methanol and ammonia oxidation on Rh(110)) and the $\text{H}_2 + \text{O}_2$ reaction is, that in the former case adsorption of the reducing agent is strongly inhibited in the oxidized state, whereas in the $\text{O}_2 + \text{H}_2$ reaction we observe only a partial inhibition of H_2 adsorption by the oxygen adlayer. As will be shown below, a mathematical model that reproduces well the traveling interface modulations provides a consistent explanation why no traveling interface modulations are seen in the $\text{H}_2 + \text{O}_2$ reaction on Rh(110). This explanation is based on the asymmetric position of the equestability point relative to the boundaries of the bistability range [196].

6.3.4 Traveling interface modulations on VO_x/Rh(110) during methanol oxidation in PEEM

The addition of small amounts of VO_x (0.1 MLE) to the Rh(110) surface does not alter the principle behavior observed during catalytic methanol oxidation above 680 K. Many observations made on the unpromoted Rh(110) surface also occur on VO_x/Rh(110), as will be shown in the following. Also on the partially vanadium oxide covered surface traveling interface modulations can be observed close to the equestability point of the bistable system. Similar to the experiments on the pristine Rh(110) surface, traveling interface modulations can be excited at 820 K by first inducing a transition from the oxidized state into the reduced state (by decreasing the oxygen partial pressure), and subsequently slowing the propagating reduction fronts down by increasing the oxygen pressure again. Compared to methanol oxidation on the clean Rh(110) surface, the traveling interface modulations observed in the presence of a small amount of vanadium oxide have a considerably higher amplitude of up to several hundred micrometers, and they can be maintained over longer periods.

The PEEM images depicted in figure 6.17 show some particularly large interface modulations that could be observed in a reaction atmosphere consisting of 3×10^{-4} mbar methanol and 0.8×10^{-4} mbar oxygen on the VO_x covered Rh(110) surface. The oxidized state, characterized by very low PEEM intensity, is separated by a sharp interface from the reduced surface state, appearing as bright area in PEEM. The first four PEEM images depicted in figure 6.17a show the propagation of seven interface excitations, which propagate from the left to the right side of the field of view. The direction of propagation is indicated by a white arrow in the first PEEM image.

Similar to the interface modulations observed on the unpromoted Rh(110) surface, a

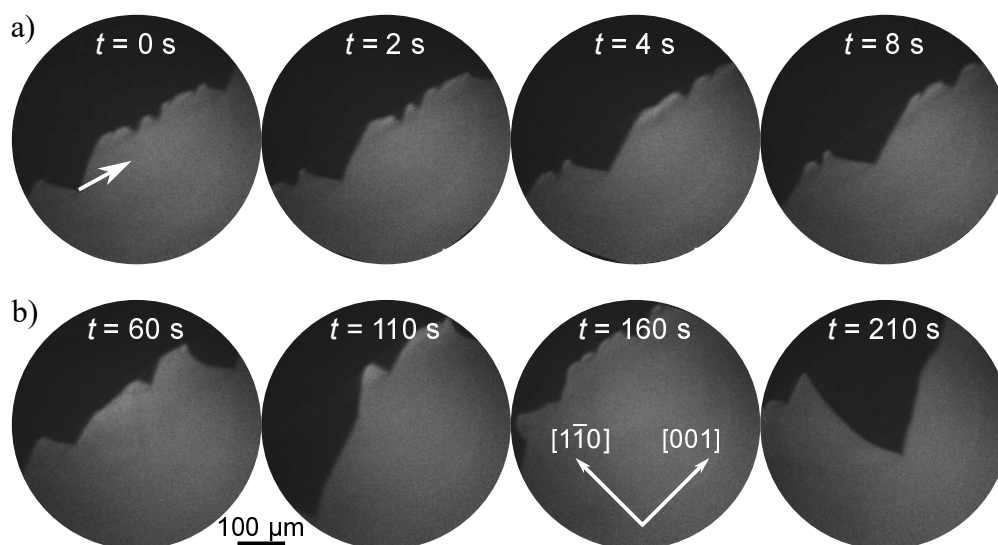


Figure 6.17: PEEM images showing traveling interface modulations on VO_x/Rh(110) during methanol oxidation. The VO_x coverage is 0.1 MLE and a gas phase composition of 3×10^{-4} mbar methanol and 0.8×10^{-4} mbar oxygen is adjusted at 820 K. Figure adapted from [243].

constant velocity of the traveling interface modulations is observed. From the slope of the dark traces in an $x(t)$ -plot shown in figure 6.18 (left side), which is constructed from line profiles taken parallel to the interface on the reduced side in figure 6.17, one can calculate an average propagation speed of $16.8 \pm 2 \mu\text{m s}^{-1}$. An $x(t)$ -plot taken perpendicular to the surface (right side) reveals, that the interface, which separates the oxidized form the reduced state, retracts with an average velocity of $0.6 \pm 0.15 \mu\text{m s}^{-1}$, with the reduced state expanding.

Different from the experiments on the Rh(110) surface, the velocity of the retracting interface is not constant but varies with the amplitude of the traveling wave fragments that propagate parallel to it. As can be seen in the $x(t)$ -plot in figure 6.18 taken perpendicular to the interface, a propagation of the reduction front happens only when no or small interface modulations are visible. As soon as a large interface modulation appears in the $x(t)$ -plot (for example at roughly 120 s) the reduction front stops, showing up by a vertical course of the interface line. Also in case of the VO_x promoted Rh(110) surface, the orientation of the interface close to the equistability point is independent on the crystallographic direction of the crystal surface. However, it should be noted that traveling interface modulations can be observed for longer times when the interface is roughly aligned with the [001]-axis.

The $x(t)$ -plot shown on the right side of figure 6.18 reveals a slight intensity increase of the reduced state close to the interface line. This enhanced PEEM intensity in the area surpassed by the traveling interface modulations is also observed on the VO_x free Rh(110) surface (left graph in figure 6.13). It can either be caused by *i*) a mostly adsorbate free

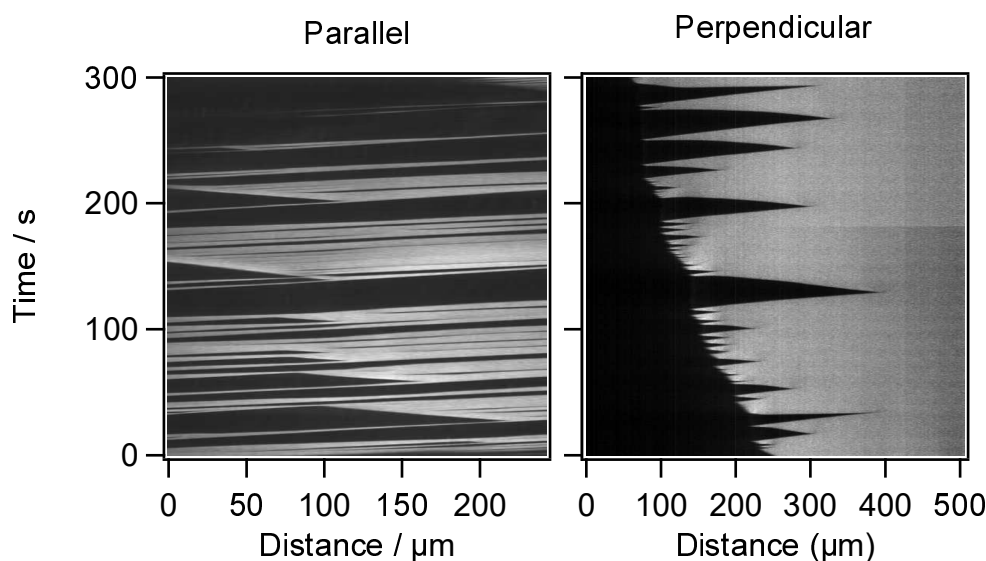


Figure 6.18: $x(t)$ plots taken parallel (left) and perpendicular (right) to the interface separating the oxidized and reduced VO_x/Rh(110) surface during the existence of traveling interface modulations. Both graphs are scaled on the same ordinate, the experimental conditions are identical to figure 6.17. Figure adapted from [243].

(1 × 1) surface, *ii*) a large number of surface defects, which roughen the surface, or *iii*) a chemical modification of the surface.

A visualization of the local PEEM intensity in the proximity of the interface is given in figure 6.19a. Two intensity line profiles are taken from the oxidized state to the reduced state across the interface. The corresponding PEEM image, a snapshot of a moving interface modulation, is shown in the background of the graph, and the positions of the line profiles are indicated by dashed black lines. One of these line profiles is taken across a traveling interface modulation of roughly 100 μm amplitude (filled squares), while the other one is taken when no modulation is located at the interface (open circles).

In both cases, the transition from the oxidized into the reduced state is characterized by a relative intensity maximum, as highlighted by the two arrows in the graph. When no interface modulation is present, the enhanced PEEM intensity decays over about 25 μm to the intensity level of the reduced state. If a modulation is present, the PEEM intensity settles at a slightly higher value as on the left, oxidized side of the interface, which is still considerably lower than the intensity of the reduced surface. The different intensity levels of the permanently oxidized regions and the traveling interface modulations is not observed on the unpromoted Rh(110) surface, and is thus related to the presence of vanadium oxide.

The enhanced PEEM intensity at the interface line can be caused by several (simultaneous) processes. *i*) As is proposed in the preceding sections, a carbon adlayer, which forms over a period of tens of seconds to minutes on the reduced surface, can increase the work function. This carbon layer gets reactively removed by oxidation fronts, and

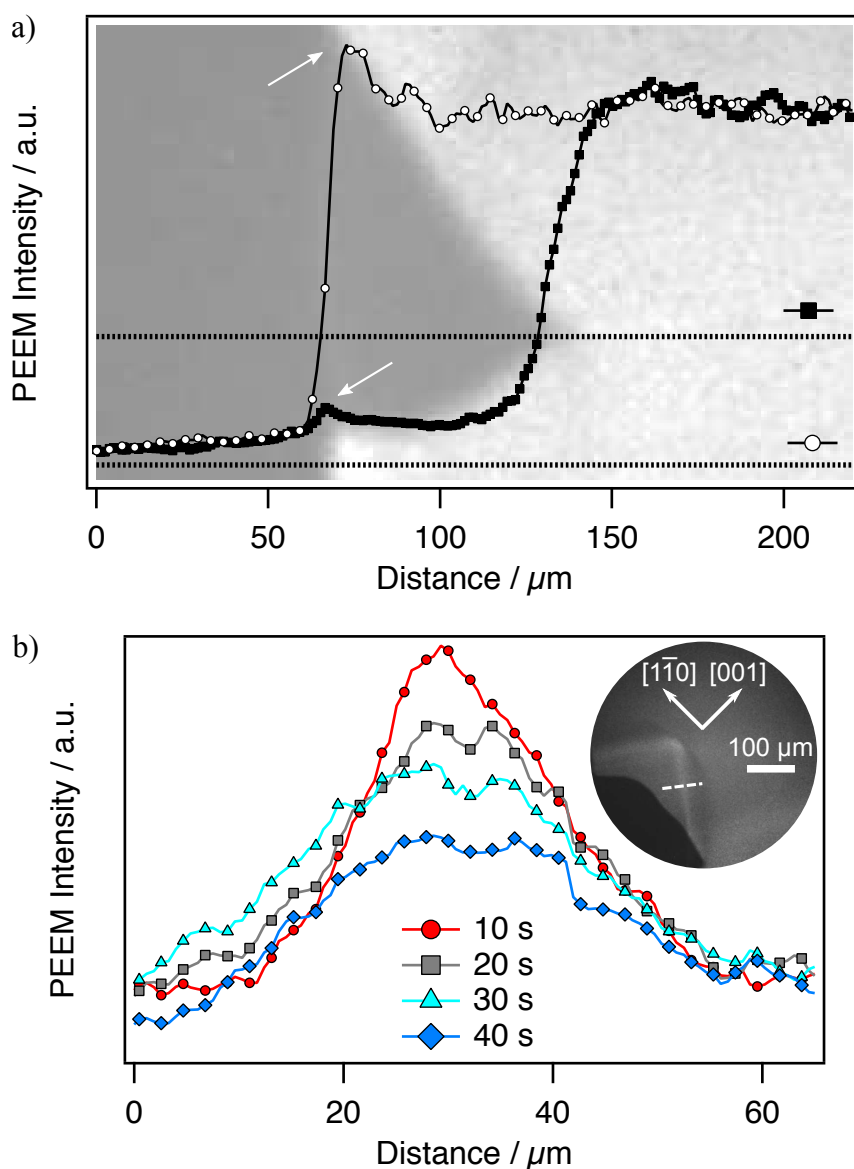


Figure 6.19: Formation of enhanced brightness at the interface. PEEM intensity cross section taken across the interface separating the reduced and oxidized VO_x/Rh(110) surface during catalytic methanol oxidation. a) Snapshot of a propagating interface modulation superimposed with two intensity line profiles taken along the dashed dark lines. The relative intensity maxima evidence a work function increase at the interface. b) Relaxation behavior of the enhanced brightness. Temporal evolution of the enhanced PEEM intensity at the former interface between oxidized and reduced area, after the interface moved away due to a spreading of the reduced state. The inset shows a PEEM image of the bright trace left by the interface line and the propagating reduction front. The experimental conditions are identical to figure 6.17. Figure (part b) adapted from [243].

when a reduction front subsequently removes the adsorbed oxygen, a mostly adsorbate free Rh(110) surface is exposed. The absence of adsorbed carbon is one of the possible explanations for the enhanced PEEM intensity.

ii) Another explanation invokes the formation of defects in the Rh(110) surface due to the fast oxygen induced reconstruction occurring during the transition between the two stable states of the system. These reconstructions are connected to a considerable mass transport of Rh atoms on the surface, and thus a roughening of the surface can easily happen. Generally, such a roughening decreases the work function of a surface, a phenomenon known as Smoluchowski effect [282]. Since the enhanced brightness at the interface occurs in both systems, during methanol oxidation on the bare Rh(110) surface and on the partially VO_x covered surface, vanadium does not play an essential role in the formation of these low work function areas.

iii) Also the presence of electropositive contamination like metals could in principle be an explanation of areas of decreased work function. Due to the strong affinity of such electropositive contaminants to oxygen, it is unlikely that they stay at the former interface position as the reduced state pushes out the oxidized state. Rather an accumulation of for example alkali metals in the oxidized surface area should occur, as has been demonstrated recently [283]. Furthermore, no signs for contamination are found with AES, but one has to be aware of the fact that small amounts of alkali metals are often difficult to detect with Auger electron spectroscopy.

Further information on these low work function areas can be gained by the relaxation behavior when displacing the interface. Such a displacement happens in an experiment, in which a propagating reduction front is pinned for 40 s at a surface defect before it detaches again. During the 40 s, in which traveling interface modulations propagated along the pinned interface, a zone of high PEEM intensity develops in the reduced state close to the interface line. As the reduction front further propagates, it leaves a bright trace, shown in the inset of figure 6.19b, together with intensity line profiles taken across this bright trace taken every ten seconds. From the intensity line profiles taken during the decay of the enhanced brightness one calculates a time constant for the 50% intensity decrease of 20 s. Furthermore a slight broadening of the high PEEM intensity area can be recognized by comparing the line shapes recorded 10 and 40 s after the oxidized state vanished, respectively.

On the unpromoted Rh(110) surface low work function areas are only observed in the area surpassed by traveling wave fragments close to the interface. If 0.1 MLE VO_x are added, the low work function areas have much larger decay times, and can in special cases also be observed detached from the interface. The addition of VO_x therefore has a stabilizing effect on the area of low work function. The observed decay may be caused by a thermal annealing of surface defects formed during the structural transitions, or by the formation of a nearly adsorbate free (1 × 1) which is then covered again by adsorbates. Vanadium oxide possibly influences the thermal healing kinetics (for example by stabilizing defects in the Rh(110) surface).

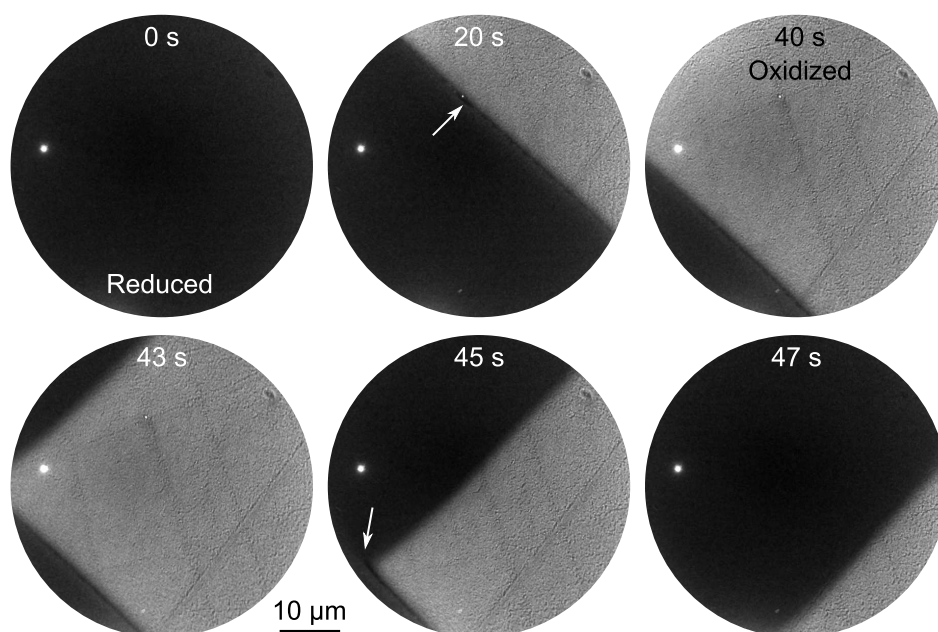


Figure 6.20: LEEM images showing a traveling interface modulation on a Rh(110) surface covered with 0.1 MLE VO_x during methanol oxidation. First an oxidation front propagates from the top right to the bottom left side of the field of view. Later a traveling interface modulation transformed the whole imaged area back into the reduced surface state. The images are acquired at 840 K in a reaction atmosphere of 9.3×10^{-5} mbar methanol 2.9×10^{-5} mbar oxygen. The start voltage is 1.7 eV.

6.3.5 Traveling interface modulations on VO_x/Rh(110) during methanol oxidation in LEEM

In order to investigate the differences between the unpromoted Rh(110) surface and Rh(110) covered with a small amount of VO_x, in situ LEED and LEEM measurements are performed during catalytic methanol oxidation on VO_x/Rh(110) with a V coverage of 0.1 MLE. Figure 6.20 shows a series of LEEM images acquired at 840 K in the low 10^{-4} mbar range. The first LEEM image displays the surface in the reduced state. Due to the chosen start voltage of only 1.7 eV, and due to the low work function of the reduced surface state, the oxidized and reduced state are imaged with different contrast mechanisms, i. e. the oxidized state in the MEM mode and the reduced state in the LEEM mode, appearing as dark area. Starting from the second image, an oxidation front propagates from the top right to the lower left side of the field of view. The oxidized state is imaged in MEM mode. Due to the considerable higher work function, and therefore characterized by a high brightness value. The oxidation front spreads with roughly $1 \mu\text{m s}^{-1}$, until after around 40 seconds a traveling interface modulation propagates along the interface line and turns the whole imaged surface back into the reduced state within 6 s.

The principle behavior is quite similar to that observed for the unpromoted surface, as described in section 6.3.2. However, also some differences can be identified. Firstly, the partially VO_x covered Rh(110) surface appears not as homogeneous as the uncovered Rh(110) surface displayed in figure 6.15. Instead some granular features are spread all over the surface. Also the contrast of surface scratches and defects is strongly enhanced. Secondly, the interface between the oxidized and the reduced surface state shows no substructure. In contrast, on the uncovered Rh(110) surface, the interface consisted of well defined, thin bands of different intensity levels, which are ascribed to the (1 × 2) and c(2 × 6) structures observed as intermediates between the c(2 × 2) of the reduced state and the c(2 × 8) of the oxidized state. Since the imaging conditions (for example the exact value of the start voltage), have a huge impact on the intensity levels in LEEM/MEM, it cannot safely be concluded that the thin bands around the interface are completely absent.

Upon careful inspection of the oxidation front in the second, third and fourth image of figure 6.20, one recognizes a thin band of very low LEEM intensity on the left (reduced) side of the interface (highlighted by a white arrow in the second image). This thin dark band does not cover the complete interface line, but is interrupted at some points. Interestingly, as the traveling interface modulation propagates along the interface line, it removes the thin dark band, as indicated by a second white arrow in the fifth image. Such a behavior is not observed on the VO_x free Rh(110) surface.

Even though no bands of different intensity levels can be recognized at the interface on the VO_x covered Rh(110) surface, a temporal evolution of the LEED intensity of the (0,0) reflex and selected spots of the (1 × 2), c(2 × 2), c(2 × 6), and c(2 × 8) structures shown in figure 6.21a and b, displays the exact same structural transformations upon oxidation and reduction of the surface, as observed on the unpromoted Rh(110) surface. The oxidized state is characterized by the c(2 × 8) structure of adsorbed oxygen. Upon reduction, this c(2 × 8) is transformed within less than 0.1 s into a (1 × 1) LEED pattern. Within about a minute the (0,0) intensity continuously decreases, while a faint c(2 × 2) develops. An oxidation pulse leads to a fast replacement of the c(2 × 2) by a (1 × 2) structure, which can be observed for less than a second before it is transformed into first the c(2 × 6) and only half a second later into the c(2 × 8).

Different from the experiments conducted on the unpromoted Rh(110) surface, the c(2 × 2) LEED pattern does not develop considerable intensity (as can be seen in figure 6.21a), and is barely distinguishable from the background intensity. Also the (0,0) intensity does not decrease in such a smooth and monotonous way, as observed on the pure Rh(110) surface. On the 0.1 MLE VO_x covered surface, the (0,0) intensity reduces to roughly 35-40% during the time in the reduced state. On the pure Rh(110) surface, a similar intensity decrease resulting in 30-40% of the original intensity is observed.

The low intensity of the c(2 × 2) LEED pattern and the granular appearance of the VO_x/Rh(110) surface, together with the decrease of the (0,0) intensity suggests, that the surface is characterized by some structural disorder. If the lower intensity of the c(2 × 2) would be caused by a smaller amount of adsorbed carbon, than also a lower decrease of the (0,0) intensity would be expected, which is not observed in the experiments. More

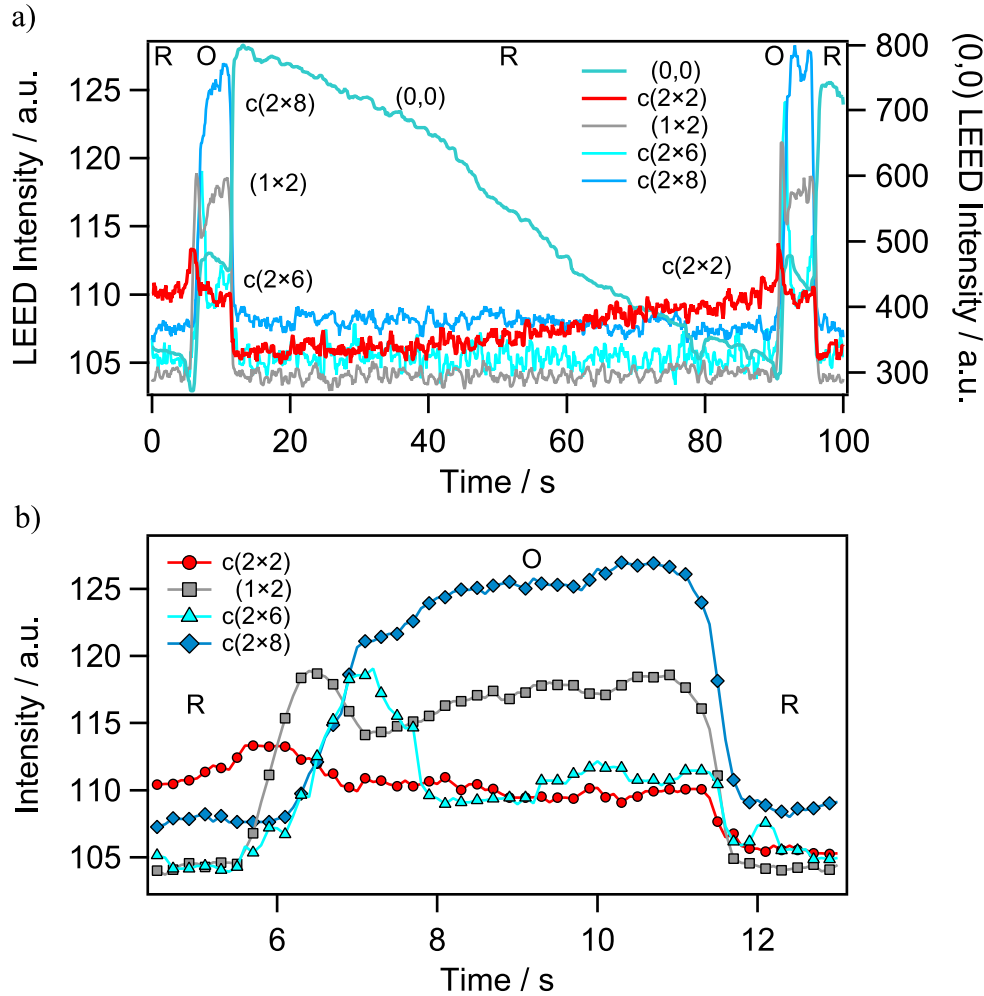


Figure 6.21: Intensity evolution of LEED data acquired during the propagation of traveling interface modulations on Rh(110) covered with 0.1 MLE VO_x. The Intensity of the super structure spots is scaled on the left, the (0,0) intensity on the right ordinate. R and O indicate the reduced and oxidized surface states, respectively. a) LEED intensity evolution during the propagation of traveling interface modulations. b) Excerpt of the time series shown in a, showing the transition from the reduced into the oxidized state and back. Identical LEED spots as in figure 6.14 are analyzed and the experimental conditions are as in figure 6.20.

likely is that the presence of V or VO_x in the reduced state inhibits the formation of an ordered C layer of $c(2 \times 2)$ structure.

6.3.6 Discussion

Front instabilities in bistable systems are an important component in many pattern formation phenomena, which have been investigated experimentally and theoretically [284–288]. Propagating interfacial waves have been observed at the oil-water interface [286]. In a reaction diffusion system, traveling interface modulations have first been observed on the unpromoted Rh(110) surface during ammonia oxidation [267, 268]. The excitability localized at the interface of the two adsorbate domains was explained by diffusive intermixing of the two adlayers, resulting in a $c(4 \times 2)$ mixed phase of oxygen and nitrogen. Hence, it was suspected, that the coexistence of oxygen and nitrogen induced reconstructions at the interface are responsible for the localized excitability and thus, the traveling interface modulations. The qualitative behavior observed in a PEEM study was reproduced with a general 3-variable model [267].

The fact, that traveling interface modulations can also be observed during catalytic methanol oxidation on an unpromoted Rh(110) surface and on a 0.1 MLE covered Rh(110) surface indicates, that the coexistence of different adsorbate induced surface reconstructions caused by diffusive intermixing at the interface cannot be the explanation for the traveling interface modulations, since neither carbon nor hydrogen induced reconstruction are known for Rh(110). An alternative mechanism is developed based on the observation of an enhanced intermediate brightness in PEEM at the interface during catalytic methanol oxidation on Rh(110) and VO_x/Rh(110) [71, 243]. The enhanced brightness, which is higher than that of the reduced state, is present for a few tens of seconds after the passage of traveling interface modulations.

This third intensity level, which slowly decays to the intensity of the reduced surface state after an interface modulation has passed, can be interpreted as being due to structural defects. The interface between the oxidized and reduced state separates the non-reconstructed (1×1) surface from the surface reconstructed due to adsorbed oxygen. For Rh(110) a series of oxygen induced reconstructions is known, which are all based on the “missing-row” principle [165]. In the oxygen induced (2×2)p2mg, $c(2 \times 6)$ and $c(2 \times 8)$ structures every second, third and fourth $[1\bar{1}0]$ -row is missing, respectively. The different reconstructions are connected with different Rh surface densities, and as a consequence every structural change between the unreconstructed (1×1) and one of the reconstructed surfaces is connected with a mass transport of Rh atoms. In the in situ LEEM experiments presented in this study, the transformation from the unreconstructed (1×1) surface into a $c(2 \times 8)$ reconstructed surface via a (1×2) and a $c(2 \times 6)$ is observed during the propagation of traveling interface modulations on the unpromoted Rh(110) surface. The principle behavior does not changed if 0.1 MLE VO_x are added to the surface.

These structural variations at the interface between the oxidized and reduced state may lead to a certain roughening of the surfaces, caused by the rearrangement of Rh atoms. Roughening decreases the work function of a surface, a phenomenon known as

Smoluchowski effect [282]. This roughening is therefore a possible explanation for the enhanced PEEM intensity observed after the propagation of traveling interface modulations. Since thermal reordering will tend to flatten the surface, the roughening is reversible. The slow decay of the high PEEM intensity to the level of the reduced state can be interpreted as the thermal healing of the roughened surface.

One can assume, that the reaction-induced surface roughening amplifies fluctuations in the adsorbate coverage close to the interface between the oxidized and reduced state, because surface defects typically enhance the reactivity of a surface. If a positive feedback between the interface fluctuations and the density of structural defects exists, an excitation mechanism localized to the interface can be derived, which explains the formation and propagation of interface modulations. The ideas of this defect creation mechanism were further elaborated by Makeev and Imbihl, resulting in a three-variable reaction-diffusion model [196], which reproduces all essential features observed in the PEEM experiments described above. The physical basis of this mechanism, i. e. the reversible creation of structural defects still needs to be proven experimentally.

The simulations revealed a number of interesting properties of the traveling interface modulations [196]: First of all, double metastability turned out to be essential for the existence of traveling interface modulations. Traveling interface modulations can only be observed in a narrow parameter range around a point at which the oxidation and reduction front, which constitute a traveling interface pulse, are equally stable. This point does not coincide with the equistability point of the bistable system, but is close to it.

A bifurcation diagram calculated for a one dimensional reaction diffusion system [196] is shown in figure 6.22a. It shows the front velocity as a function of the oxygen partial pressure. The range of double metastability, in which two stable solutions exist, is limited by the two turning points of the front velocity. A reduction front is characterized by a negative front velocity, whereas an oxidation front has a positive front velocity. At the equistability point, which is one of the two turning points of the front velocity, reduction and oxidation fronts have the same velocity, which equals to zero. Experimentally, the narrow parameter range in which traveling interface modulations can be observed is confirmed.

The front velocities obtained for a variation of the simulation parameters α and k_6 are shown in figure 6.22b. The former parameter defines the influence of surface defects on the adsorption of oxygen, the latter parameter varies the rate of defect formation and surface reconstruction. Both parameters have an effect on the width of the double metastable range, as shown by the four different solutions in figure 6.22. For details on the simulations please refer to reference [196].

Depending on the orientation of the interface between the oxidized and reduced state with the crystallographic axes of the Rh(110) surface, a variation in the shape of traveling interface pulses was observed in the simulations, but diffusional anisotropy turned out to be not essential for the existence of traveling interface modulations. This result is in good agreement with the experimental findings obtained in the LEEM and PEEM experiments, in which traveling interface modulations are observed at interfaces which are

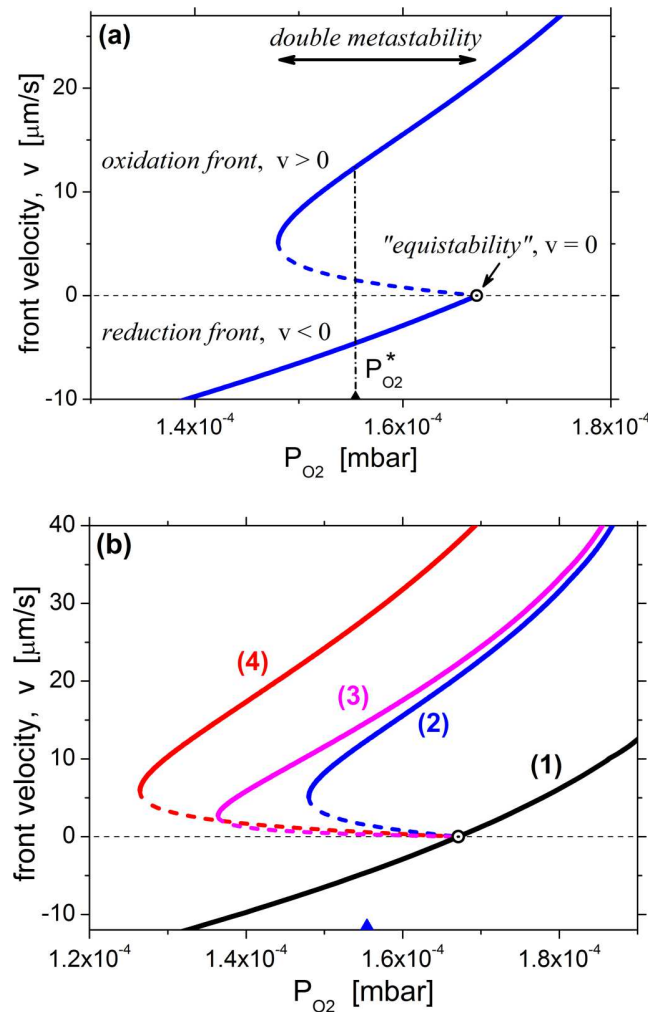


Figure 6.22: Bifurcation diagram obtained from the simulation of a one dimensional reaction diffusion system, showing the dependence of the front velocity on the oxygen partial pressure. Stable and unstable solutions are represented by solid and dashed lines, respectively. a) Results for a set of model parameters in which a region of double metastability exists. The oxygen pressure at which traveling interface pulses of stationary size exist is indicated by the vertical dash-dotted line. b) A set of solutions obtained upon variation of the model parameters α and k_6 , demonstrating the dependence of the width of the double metastable regime on the defect formation and surface reconstruction rate (k_6), and on the influence of surface defects on the oxygen adsorption (α). For details please refer to reference [196]. Reprinted figure with permission from Alexei Makeev and Ronald Imbihl, Phys. Rev. E 100, 042206, 2019 (<http://dx.doi.org/10.1103/PhysRevE.100.042206>). Copyright (2019) by the American Physical Society.

not aligned with a specific crystallographic direction. Obviously, the surface anisotropy – and therefore diffusional anisotropy – plays only a minor role in the phenomenon of traveling interface modulations.

The LEEM experiments in which traveling interface modulations are observed further corroborate the defect generation mechanism as a plausible explanation for the existence of excitation localized at the interface of the two states of a bistable system. On the unpromoted Rh(110) surface, the reduced state is characterized by a (1×1) and a $c(2 \times 2)$ LEED pattern. Upon transition from the reduced into the oxidized state, first the (1×1) appears, followed by the $c(2 \times 2)$, which has weak and diffuse $(\frac{1}{2}, \frac{1}{2})$ reflexes. The formation of the $c(2 \times 2)$, which is attributed to the formation of carbon layer due to the decomposition of methanol on the Rh(110) surface, is accompanied by a steady decrease of the (0,0) spot intensity and a slight increase of the work function of the surface. However, since the appearance of the $c(2 \times 2)$ is not coupled to the existence of traveling wave fragments, it is regarded as not essential for the excitation mechanism.

As the reduced state transforms into the oxidized state, a series of structural transitions takes place, which finally result in the $c(2 \times 8)$ structure of adsorbed oxygen. Prior to the $c(2 \times 8)$, a (1×2) and the $c(2 \times 6)$ structure is observed for tenths of seconds. The $c(2 \times 6)$ and $c(2 \times 8)$ structures are generated by oxygen adsorbed on a (1×3) and (1×4) , respectively. The (1×2) is most probably caused by an order-disorder phase transition of the $(2 \times 2)p2mg$ structure of oxygen adsorbed on the (1×2) reconstructed Rh(110) surface. The phase transition from the $(2 \times 2)p2mg$ into the (1×2) is reported to occur close to 750 K [271]. The order in which the sequence of LEED patterns is observed is consistent with the oxygen coverage which increases from 0.5 over 0.66 to 0.75 for the $(2 \times 2)p2mg$, the $c(2 \times 6)$ and the $c(2 \times 8)$ [289], respectively.

The observation that three different adsorbate induced reconstructions are passed through during the transition from the reduced into the oxidized state corroborate the defect generation mechanism. The formation of the $(1 \times n)$ missing-row reconstructions is associated with a substantial mass transport of Rh atoms. A STM study has revealed, that this mass transport can proceed via different mechanisms. At a temperature around 400 K, the diffusion of isolated Rh-O units, which detach from atomic steps, was observed for an oxygen coverage below ≈ 0.1 ML [290]. For a higher O coverage missing rows are reported to be dug along the $[1\bar{1}0]$ rows. Also the direct formation of troughs on terraces and the condensation of the removed atoms in the neighborhood of the troughs was observed in this study. Clearly, such effects might be connected to the formation of defects in the Rh surface, especially by taking into account the time scale of tenths of seconds in which the different reconstructions are passed through. On the other hand, the diffusion of isolated Rh atoms or Rh-O units may be a pathway for the healing of such defects.

Of particular interest is the absence of traveling interface modulations in the hydrogen oxidation on Rh(110) and on the 0.1 MLE VO_x promoted Rh(110) surface. The most obvious difference between ammonia and methanol oxidation, which generate traveling interface modulations, and the hydrogen oxidation, which yields no traveling interface modulations, is the absence of the $c(2 \times 6)$ and $c(2 \times 8)$ structures in the H₂ + O₂ reaction.

Close to the equistability point only a transition between the (1×2) and the (1×1) structures can be observed. In order to generate the $c(2 \times 6)$ -O structure, an excess of oxygen has to be adjusted, which is far away from the conditions at which the propagation of chemical waves can be adjusted. More drastically, after completely stopping the H_2 supply even traces of hydrogen prevent the formation of the $c(2 \times 10)$ structure, which can be observed at equal pressures of methanol and oxygen. Hydrogen can still adsorb on the oxidized surface and react with oxygen, thus preventing a higher oxygen coverage, which would result in the $c(2 \times n)$ surface structures of adsorbed oxygen. Evidently, the nearly complete inhibition of ammonia and methanol adsorption on the oxidized surface results in the sequence of different missing row reconstructions in the transition from the oxidized to the reduced state.

The simulations have demonstrated that the occurrence of traveling wave fragments is linked to the existence of a region of double metastability. Due to the asymmetric location of the equistability point in the bistable range of $\text{H}_2 + \text{O}_2/\text{Rh}(110)$, the double metastable region in this system is so small, that it will be practically impossible to observe it experimentally. The asymmetric location of the equistability point, which is close to the upper boundary of, and not roughly in the middle of, the bistable range ($p(\text{H}_2)$ as the bifurcation parameter) might be a consequence of the incomplete inhibition of hydrogen adsorption by the high oxygen coverage phases on $\text{Rh}(110)$. On the other hand, the simulations of Makeev et al. revealed, that double metastability is a necessary prerequisite for the occurrence of traveling interface modulations. Double metastability, however, has not been observed in the system $\text{H}_2 + \text{O}_2/\text{Rh}(110)$.

The addition of a small amount of VO_x results in a considerable amplitude increase of the traveling interface modulations and longer observation times with respect to the unpromoted $\text{Rh}(110)$ surface. Interestingly, no additional structures are found during the transition from the reduced into the oxidized state and back upon addition of small amounts of vanadium oxide. However, the intensity of the $c(2 \times 2)$ structure apparent in the reduced state is drastically decreased, and the decay of the $(0,0)$ diffraction spot is less regular. The influence of vanadium oxide could be a modification of the defect formation and/reordering kinetics, which facilitates the formation of traveling interface modulations.

6.4 Target pattern during methanol oxidation on 0.2 MLE $\text{VO}_x/\text{Rh}(110)$

If the vanadium oxide coverage is increased new phenomena are observed. The deposition of 0.2 MLE of vanadium onto the $\text{Rh}(110)$ surface results in the formation of target patterns during catalytic methanol oxidation. If a $\text{Rh}(110)$ surface covered with 0.2 MLE VO_x is heated to 770 K in an atmosphere of 1.2×10^{-5} mbar oxygen and 1.1×10^{-4} mbar methanol, it is initially in the reduced surface state. An increase of the oxygen pressure to 2.6×10^{-5} mbar results in the transition from a reduced into an oxidized state. Upon subsequent oxygen pressure decrease, the ignition of several, seemingly randomly nucleating reduction fronts is triggered.

The reduction fronts are followed by an oxidation front restoring the original grey level of the surface. That is one has pulses. Pulses can occur in excitable and oscillatory systems, but also in bistable systems in the regime of so-called double metastability. The difference to the former two types of systems being that the pulses can be quite irregular in double metastability. Here the following development is observed. Oxidation fronts nucleate just after the reduction fronts, resulting in a more or less chaotic wave pattern of simultaneously propagating oxidation and reduction fronts. After a period of several minutes, the number of newly nucleating oxidation and reduction fronts reduces and the overall appearance becomes more regular.

A series of LEEM images showing such chemical wave pattern is depicted in figure 6.23a. In the first LEEM image a broad reduction front can be identified by its low LEEM intensity (the propagation direction is indicated by the white arrow in the first LEEM image). In the top right and lower left corner of the image, two oxidation fronts can additionally be seen. On the forefront, the reduced state is separated by a narrow and bright interface line from the oxidized state. On the backfront a broader interface phase of intermediate LEEM intensity separates the two states of the system. Furthermore the reduction front exhibits a gradual LEEM intensity increase from its forefront to the back.

As can be seen well in the third and fifth LEEM image of figure 6.23, the width of the oxidation and reduction fronts is not constant. Especially, the width of the oxidation front varies drastically. The two reduction fronts visible in the fifth LEEM image are separated only by a thin and bright line on a large part of the image. In the upper left corner of the image, the width of the oxidation front increases, giving rise to an extended area of the oxidized state.

This situation is better visualized in the plot of the temporal LEEM intensity evolution shown as the upper trace figure 6.23b, measured on a small circular area. The periods, in which the surface is in the reduced and oxidized state are highlighted by **R** and **O**, respectively. The reduction fronts are characterized by a more or less linearly increasing LEEM intensity. At the same time, the LEED intensity of the (0,0) diffraction spot, shown as the lower trace in figure 6.23b, decreases over time. As soon as the oxidation front enters the probed area, the LEEM intensity and the LEED intensity increases, until it reaches a plateau phase (first and third fronts at 20 and 70 s²). After reaching its maximum LEEM intensity at the transition from the oxidized in the reduced state, the local LEEM intensity drops abruptly to its minimum value. This drop in LEEM intensity is accompanied by an instantaneous decrease of the (0,0) LEED intensity to an intermediate level, from which it further decreases in a linear fashion, until the next oxidation front propagates across the probed surface area. The second imaged oxidation front, represented by a sharp increase of the LEEM intensity at about 60 s, is very narrow instead. The LEED intensity of the (0,0) diffraction spot does not reach its maximum intensity level, compared to a wide oxidation front, as can be seen

²The LEEM and LEED data shown are recorded subsequently and are therefore not synchronized. They have been shifted on purpose in order to create a similar appearance to facilitate the description in the text.

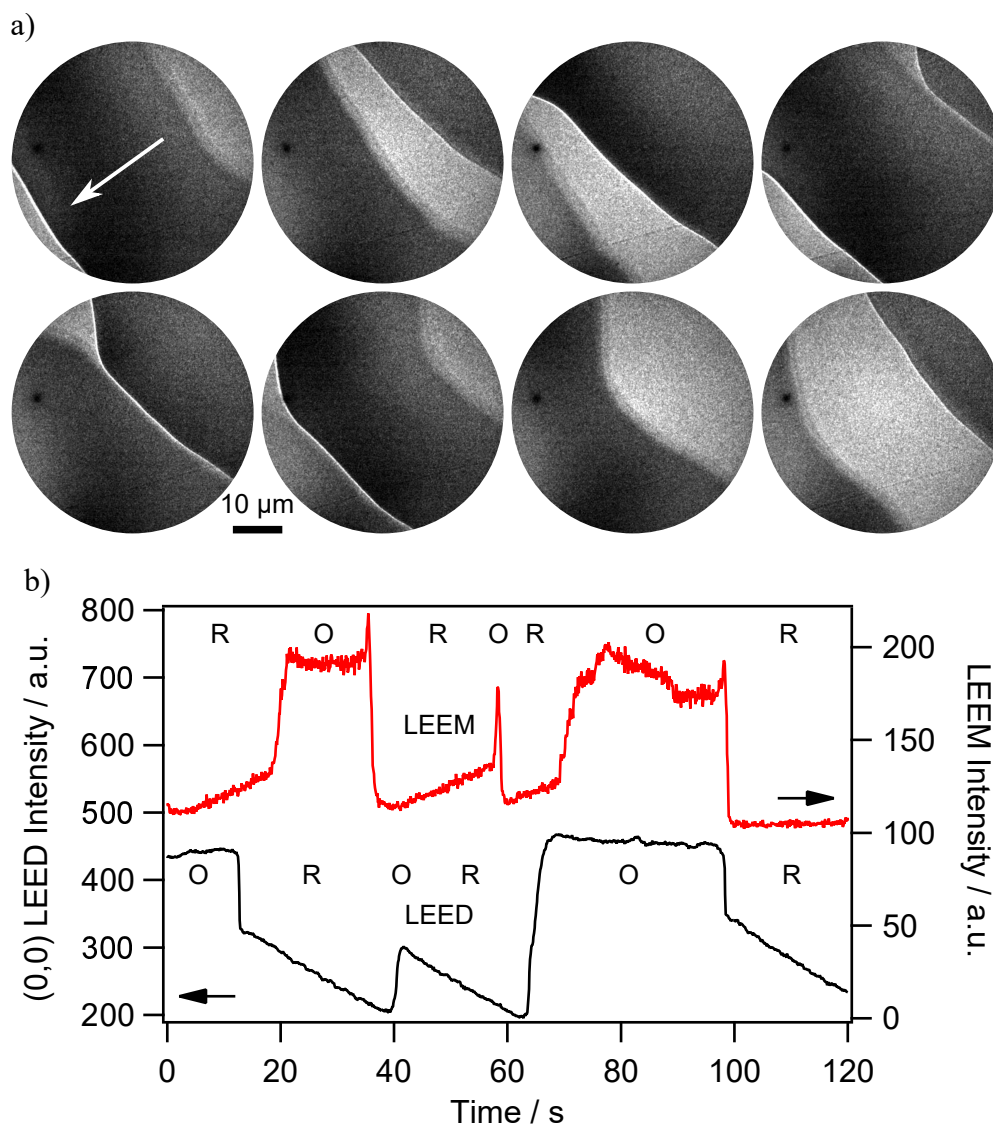


Figure 6.23: A LEEM and LEED characterization of target pattern during catalytic methanol oxidation on 0.2 MLE $\text{VO}_x/\text{Rh}(110)$. a) A series of LEEM images showing the propagation of alternating reduction (dark) and oxidation fronts (bright). b) Temporal evolution of the local LEEM and (0,0) LEED intensity. The LEEM intensity is measured on a circular, roughly $2\ \mu\text{m}$ wide spot. The LEED data is acquired in the same experiment before the LEEM images are recorded. The periods, in which the surface is in the reduced and oxidized state are highlighted by R and O, respectively. The experiment is conducted at 770 K in 1.2×10^{-5} mbar oxygen and 1.1×10^{-5} mbar methanol at a start voltage of 1.6 eV. The LEED data is recorded at 40 eV.

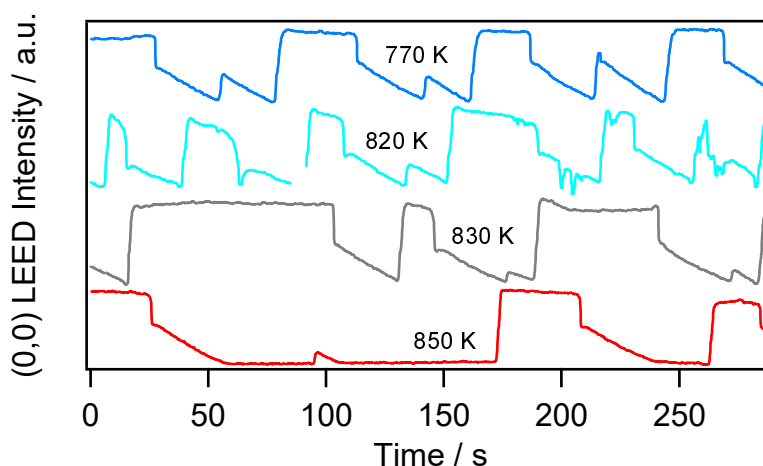


Figure 6.24: Temporal evolution of the (0,0) LEED intensity acquired at different temperatures during chemical wave pattern in catalytic methanol oxidation. The experiment is conducted in 1.2×10^{-5} mbar oxygen and 1.1×10^{-5} mbar methanol at a start voltage of 40 eV.

at around 40 s.

The regularity of the observed chemical wave pattern strongly depends on the substrate temperature, even though the principle behavior does not change in the observed temperature range. The most regular sequence of oxidation and reduction fronts is observed at 770 K, as can be seen by comparing the temporal evolution of the (0,0) LEED intensity acquired at varying temperatures depicted in figure 6.24. With increasing temperature, the width of oxidation and reduction fronts strongly increases. Additionally, the intensity increase of the (0,0) LEED intensity upon propagation of thin oxidation fronts is less pronounced, as can be seen for example in LEED intensity acquired at 850 K around 100 s.

By comparing the series of LEED pattern observed during the alternating propagation of oxidation and reduction fronts, it is in principle possible to assign diffraction pattern to the different LEEM intensity levels visible in figure 6.23. Starting from the reduced state attained directly after the transition from the oxidized state, the following LEED patterns are observed at 850 K: $(1 \times 1) - c(2 \times 2) - (1 \times 2) - c(2 \times 8) - (1 \times 2) - (1 \times 1)$. At 770 K the series of LEED pattern is reduced to the sequence: $(1 \times 1) - (1 \times 2) - c(2 \times 8) - (1 \times 1)$. Accordingly, the reduced state (low LEEM intensity in figure 6.23) can be assigned to the (1×1) that slowly transforms into the $c(2 \times 2)$. The boundary phase separating the oxidized and reduced state belongs to a (1×2) diffraction pattern, and the oxidized state represents the $c(2 \times 8)$ structure.

The temporal evolution of the different LEED pattern during the transition from the oxidized state into the reduced state, recorded at 770 (top) and 850 K (bottom), is shown in figure 6.25. By interpreting the different LEED intensity levels it has to be taken into account, that the $(0, \frac{1}{2})$ and $(1, \frac{1}{2})$ spots belong to the (1×2) and the $c(2 \times 8)$

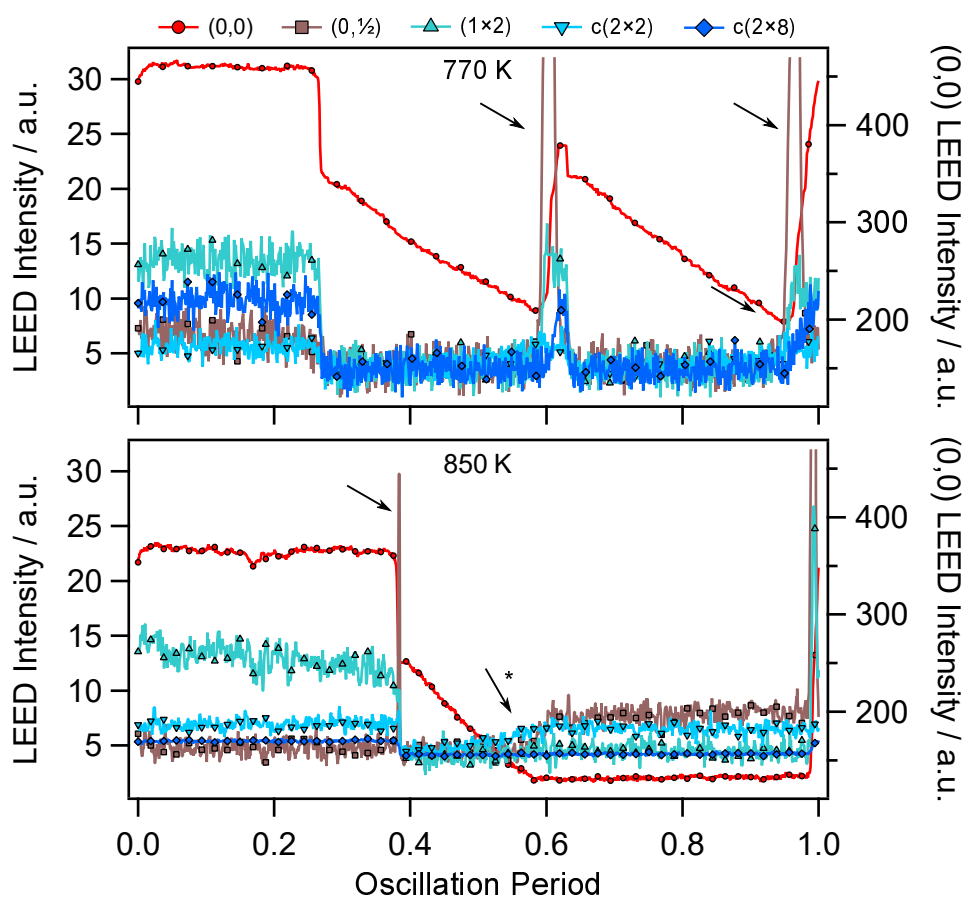


Figure 6.25: Sequence of LEED patterns during the target pattern in methanol oxidation. The LEED intensities mark the transitions from the oxidized into the reduced state and vice versa. Shown are the $(0,0)$ spot, the $(0, \frac{1}{2})$ and $(1, \frac{1}{2})$ spots of the (1×2) pattern, the $(\frac{1}{2}, \frac{1}{2})$ spot of the $c(2 \times 2)$ pattern, and the $(1, \frac{3}{4})$ spot of the $c(2 \times 8)$ pattern. The experiment is conducted in 1.2×10^{-5} mbar oxygen and 1.1×10^{-5} mbar methanol at a start voltage of 40 eV.

structures. The same holds for the $(\frac{1}{2}, \frac{1}{2})$ spot of the $c(2 \times 2)$ structure, which is also close to diffraction spots of the $c(2 \times 8)$.

At 770 K, the oxidized state, characterized by a $c(2 \times 8)$ LEED structure is directly transformed into a (1×1) LEED pattern upon reduction. During the complete period in the reduced state, no intensity increase of the $c(2 \times 2)$ LEED pattern is observed. The abrupt intensity increase of the $(0, \frac{1}{2})$ (indicated by the black arrows in figure 6.25) and $(1, \frac{1}{2})$ diffraction spots mark the transition into the oxidized state. Remarkably, the intensity increase of the $(0, \frac{1}{2})$ spot is much more pronounced than the increase of the $(1, \frac{1}{2})$ spot.

In chemical wave patterns at 850 K, a different behavior is observed. Firstly, the $c(2 \times 8)$ intensity is considerably lower, as compared to the measurements at 770 K. Secondly,

during the transition from the oxidized state into the reduced state, a sharp increase of the $(0, \frac{1}{2})$ diffraction spot intensity is observed, as indicated by the black arrow in the bottom graph of figure 6.25. The intensity increase of the $(0, \frac{1}{2})$ spot is accompanied by an intensity decrease of the $(1, \frac{1}{2})$ spot intensity. Since both diffraction spots, the $(0, \frac{1}{2})$ and the $(1, \frac{1}{2})$ spot, belong to the same (1×2) superstructure, the simultaneous intensity increase and decrease suggests that two different structures attribute to the (1×2) LEED pattern. Thirdly, during the time in the reduced state, first the $c(2 \times 2)$ intensity increases, followed by a slight increase of the $(0, \frac{1}{2})$ spot intensity (highlighted by the black arrow with asterisk) and unchanged $(1, \frac{1}{2})$ spot intensity. Even though the sequence of LEED pattern differs slightly for the two temperatures, no qualitative difference in the appearance of the oxidation and reduction fronts can be observed, except the different regularity described above.

A classic pulse consists of a sequence of resting state, excited state, and refractory state, which leads back to the resting state. With an oxidation pulse, the resting state is the reduced surface with a (1×1) , and the excited state the oxidized surface with a $c(2 \times 8)$ -O. But the question is, what represents the refractory state? The slowly decaying $(0,0)$ -intensity in figure 6.25 should reflect the refractory period. The gradual growth of the $c(2 \times 2)$ due to carbon from methanol decomposition would be a plausible candidate for the refractory period. Due to the varying width and the missing regularity in the observed chemical wave pattern, the target pattern are probably the result of a system in the double metastable state, rather than of an excitable or oscillatory system.

6.5 Traveling wave fragments during methanol oxidation on $\text{VO}_x/\text{Rh}(110)$

Traveling wave fragments have been observed on $\text{Rh}(110)$ surfaces covered with 0.4 MLE vanadium oxide at temperatures above 700 K in the 10^{-4} mbar range [71, 244]. The vanadium oxide distribution is spatially homogeneous at the length scale of PEEM (μm) and LEEM (in the field of view of $50 \mu\text{m}$ and larger). On a microscopic scale, the VO_x distribution is probably inhomogeneous.

6.5.1 Oxidation/reduction fronts and traveling wave fragments on 0.4 MLE $\text{VO}_x/\text{Rh}(110)$ in PEEM

After deposition of 0.4 MLE VO_x by reactive evaporation onto the $\text{Rh}(110)$ surface, the freshly formed vanadium oxide film is exposed to a reaction gas mixture consisting of 3×10^{-4} mbar methanol and 1×10^{-4} mbar oxygen (reducing reaction conditions) and heated with a constant heating rate of 0.5 K s^{-1} , until at around 700 K a region of the so-called “double metastability” or “dynamic bistability” is entered, which extends to roughly 850 K under the given conditions.

An example of the chemical wave pattern that can form in a system of double metastability is shown in figure 6.26. The simultaneous existence of a spreading oxidation front, imaged as a dark ellipse in PEEM, and a reduction front, which propagates

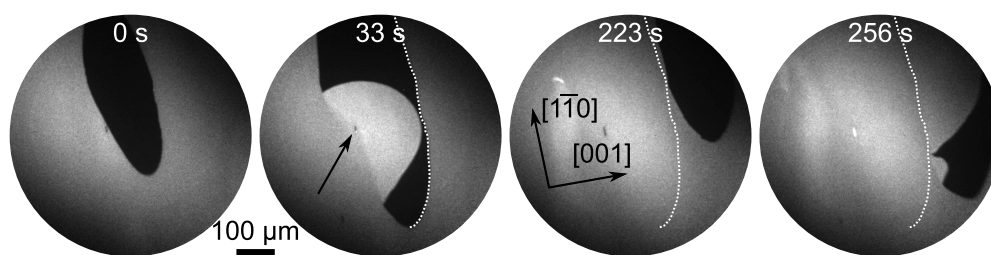


Figure 6.26: Double metastability imaged with PEEM during catalytic methanol oxidation on 0.4 MLE $\text{VO}_x/\text{Rh}(110)$. A spreading oxidation front collides with a surface defect (highlighted by the black arrow in the second PEEM image), resulting in a reduction front, which reacts off the oxygen in the oxidized area and turns the surface in a refractory state. Subsequent oxidation fronts cannot propagate on the surface in the refractory state, as shown by the second and third PEEM image (the former interface between the oxidized and reduced surface is indicated by the white dotted line). The PEEM images are recorded at 790 K under reducing reaction conditions. Reproduced in part with permission from *J. Phys. Chem. C* **2018**, *122*, 12694 – 12703. Copyright 2018 American Chemical Society. Figure adapted from [71]

only in the oxidized regions and which appears as bright area in PEEM, is shown. The elliptical shape of the oxidation and reduction fronts is caused by the anisotropy of the $\text{Rh}(110)$ surface. The diffusivity of adsorbed particles varies with respect to the crystallographic directions. In case of adsorbed oxygen, the diffusion is fastest along the $[1\bar{1}0]$ direction, and slowest along the $[001]$ direction. However, in the reduction front, the diffusion is fastest in the $[001]$ direction and slowest in the $[1\bar{1}0]$ direction instead. In general, the anisotropy of the diffusion does not only depend on the geometric corrugation of the surface, and is therefore influenced by adsorbate-induced reconstructions, but can also be a function of the adsorbate coverage and temperature – a phenomenon called state-dependent anisotropy [264, 265, 291, 292].

The first PEEM image in figure 6.26 shows an elliptical oxidation front, which propagates across the surface towards a small defect, which is highlighted in the second image. As soon, as the oxidation front reaches the defect, a reduction front nucleates and reactively removes the adsorbed oxygen in the oxidized area, turning the surface in a state of high PEEM intensity. The propagation of the reduction front is restricted to the oxidized surface area, a spreading into the reduced surface state, characterized by a medium PEEM intensity level, is not observed.

Subsequently propagating oxidation fronts, shown in the third PEEM image, cannot propagate on the surface area of high PEEM intensity left by the reduction front. As soon as the second oxidation front touches this area, reduction fronts nucleate at the entering points and turn the whole oxidized area into a state of very high PEEM intensity.

Based on the different intensity levels in PEEM, and the behavior described above, three different surface states can be identified: an oxidized state of very low PEEM intensity, a reduced state of medium PEEM intensity and a refractory state of very high

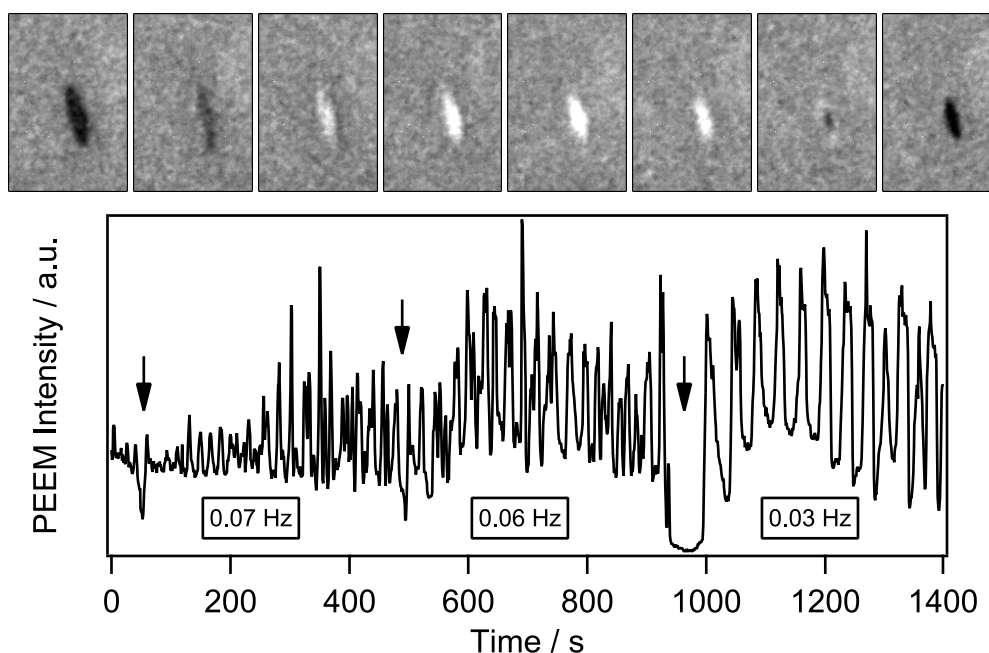


Figure 6.27: Activation of an oscillating surface defect by collision with chemical waves imaged with PEEM. The series of images shows an oscillation period of the surface defect depicted in figure 6.26. The temporal evolution of the defects PEEM intensity is shown in the graph below the PEEM images. With every collision of an oxidation front with the surface defect (highlighted by black arrows in the graph, the oscillation frequency decreases. The images are recorded under the same experimental conditions as in figure 6.26, the field of view is $62 \times 77 \mu\text{m}$. The time between two images varies between 1 and 9 s, the time between the first and the last image is 21 s. Reproduced in part with permission from *J. Phys. Chem. C* **2018**, *122*, 12694 – 12703. Copyright 2018 American Chemical Society. Figure adapted from [71]

PEEM intensity. The assignment of a refractory state to the very high PEEM intensity left by a reduction front is based on the observation, that subsequent oxidation fronts can only propagate on the surface in the refractory state, if its PEEM intensity level approaches the value of the reduced state after a period of tens of seconds to minutes (roughly five minutes in this experiment).

The surface defect depicted in figure 6.26 plays an important role in pattern formation, since it provides the stimuli needed to trigger a chemical wave. A closer inspection of the defect of figure 6.26 reveals, that the defect itself exhibits an oscillatory behavior, as shown in figure 6.27. The large size of the surface defect enables to see that the transition from the oxidized, dark state into the reduced, bright state proceeds via a reduction front, that nucleates on the left side (second and third image). The transition back into the oxidized state starts in the center of the defect, and an oxidation front propagates outwards instead (seventh and eighth image).

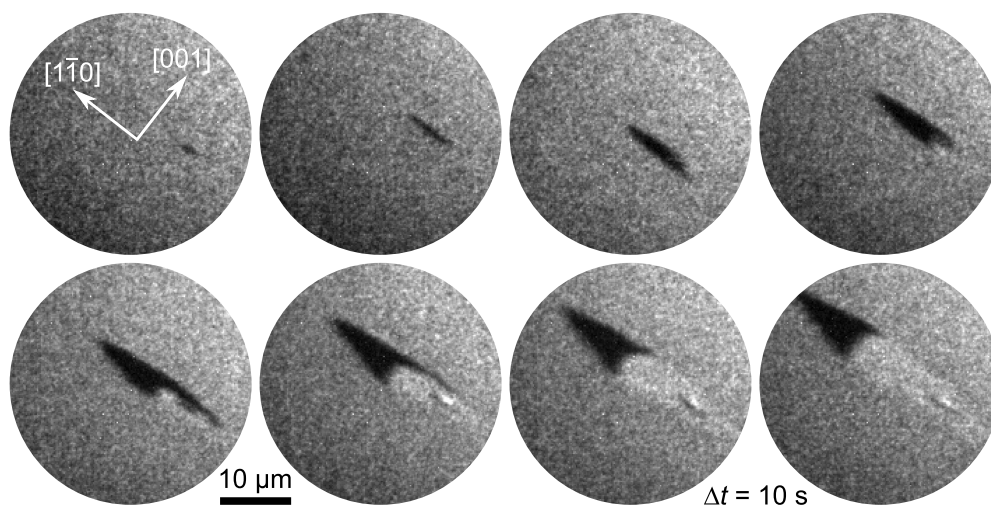


Figure 6.28: A wave fragment traveling in the $[1\bar{1}0]$ direction imaged with PEEM during catalytic methanol oxidation on 0.4 MLE $\text{VO}_x/\text{Rh}(110)$. The PEEM images are acquired at 740 K under reducing reaction conditions. Reproduced in part with permission from *J. Phys. Chem. C* **2018**, *122*, 12694 – 12703. Copyright 2018 American Chemical Society. Figure adapted from [71].

Interestingly, the oscillations of the defect are initiated by a collision with a front, and their frequency changes upon further collisions of the defect with oxidation fronts. The influence of the collisions with oxidation fronts can be seen in the temporal evolution of the defects PEEM intensity shown in the lower part of figure 6.26. At around 500 s, a first collision of an oxidation front with the defect (highlighted by the first arrow in the graph) initiates the oscillations with a period of roughly 0.07 Hz. A second and third collision at 450 and 950 s with other oxidation fronts slows the oscillations down to 0.06 and 0.03 Hz, respectively. The decrease in oscillation frequency is accompanied by an increase in amplitude and overall more regular oscillations. The influence of oxidation fronts on the oscillatory behavior of a surface defect might be explained by structural and/or chemical modifications.

Another phenomenon occurring in the region of double metastability are traveling wave fragments. In general, if an isolated pulse propagates in an isotropic medium, its free ends would curl in, resulting in the formation of a pair of counter-rotating spiral waves [272]. If the medium exhibits state-dependent anisotropy, the curling-in can be prevented, resulting in a wave fragment, which travels with a constant velocity along a certain crystallographic direction [292]. Also during catalytic methanol oxidation on the $\text{Rh}(110)$ surface covered with 0.4 MLE traveling wave fragments can be observed, as demonstrated in figure 6.28.

The traveling wave fragment nucleates at a small surface defect as an elliptical oxidation front, shown in the first PEEM image. After the oxidation front has grown to a certain size, a reduction front nucleates at the surface defect and starts to react off a

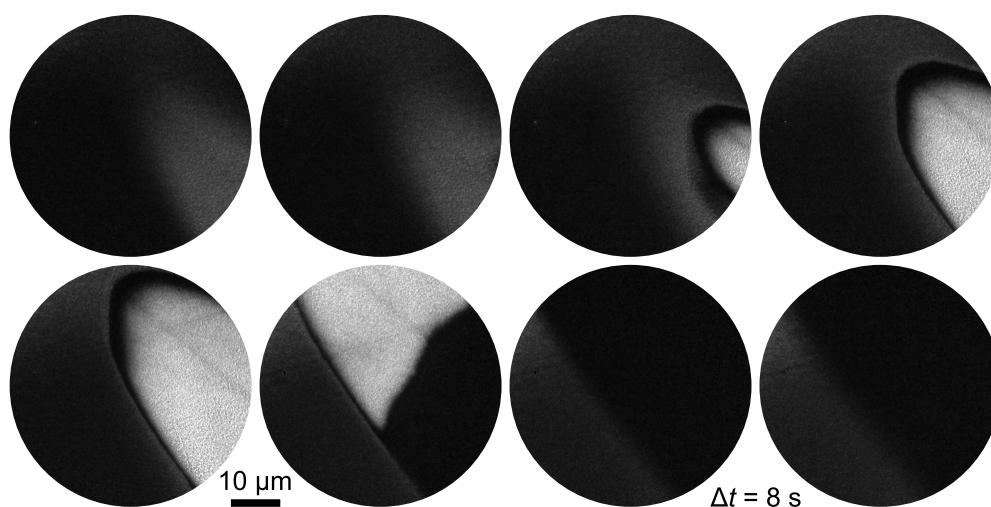


Figure 6.29: Double metastability imaged with LEEM during catalytic methanol oxidation on 0.4 MLE $\text{VO}_x/\text{Rh}(110)$. An oxidation front propagates across the imaged area and turns the reduced state (intermediate LEEM intensity) in the oxidized state (high LEEM intensity). A few seconds later a reduction front spreads on the oxidized area, reactively removing adsorbed oxygen and turning the surface into the refractory state (very low LEEM intensity). The images are recorded in an atmosphere of 1.3×10^{-5} mbar oxygen and 1.1×10^{-4} mbar methanol at 820 K with a start voltage of 2 eV.

part of the oxygen in the oxidized area. The oxidation front and the following reduction front have the same propagation velocity of roughly $2 \mu\text{m s}^{-1}$, resulting in a stable wave fragment that travels along the $[1\bar{1}0]$ direction. Such traveling wave fragments are observed under reducing reaction conditions in the temperature range between 720 and 850 K.

6.5.2 Oxidation/reduction fronts and traveling wave fragments on 0.4 MLE VO_x on $\text{Rh}(110)$ in LEEM

In LEEM a $\text{Rh}(110)$ surface covered with 0.4 MLE vanadium oxide is prepared and conditions are adjusted, so that the double metastable regime is entered. In contrast to the PEEM experiments above, in LEEM a roughly 100 K higher temperature is chosen. Due to the higher temperature more methanol is needed in order to observe pattern formation.

The coexistence of an oxidation front and a reduction front during methanol oxidation is shown in figure 6.29. The series of LEEM images depicts in the first five images an elliptical oxidation front, which propagates from the lower right side to the upper left side, turning the reduced, dark surface state into the bright oxidized state. The interface between the oxidized and reduced state is characterized by a thin, dark band.

A few seconds after the oxidation front has propagated across the imaged area, a reduction front spreads over the oxidized area and reactively removes the adsorbed

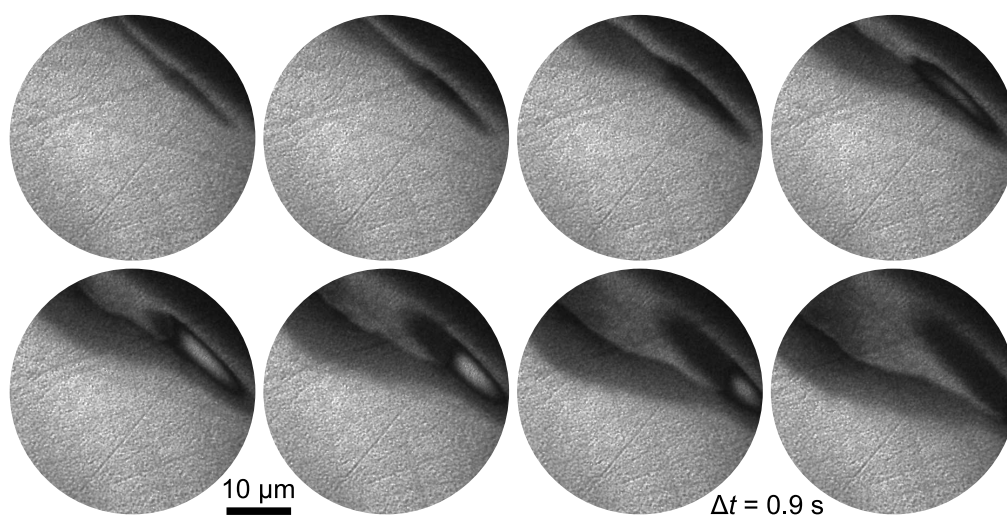


Figure 6.30: A wave fragment traveling in the $[1\bar{1}0]$ direction imaged with LEEM during catalytic methanol oxidation on 0.4 MLE $\text{VO}_x/\text{Rh}(110)$. The images are acquired at 830 K in a reaction atmosphere of 1.3×10^{-5} mbar oxygen and 1.1×10^{-4} mbar methanol, the start voltage is 2 eV.

oxygen. The former bright, oxidized surface is transformed into a homogeneously dark area (seventh and eighth image of figure 6.29).

In the LEEM measurements three different intensity levels can clearly be identified (ignoring the thin band at the interface between the oxidized and reduced state). One can assign the bright LEEM intensity to the oxidized state, the intermediate LEEM intensity to the reduced state and the very low LEEM intensity generated by reduction fronts to the refractory state. As in the PEEM experiments, the refractory state in LEEM slowly approaches the intensity level of the reduced state within tens of seconds. The faster transition from the refractory state in the reduced state (which takes a few tens of seconds in LEEM and which can take up to five minutes in PEEM) is possibly caused by the considerably higher temperature in the LEEM experiments. In LEEM also traveling wave fragments are imaged during catalytic methanol oxidation on 0.4 MLE $\text{VO}_x/\text{Rh}(110)$. An example of such an traveling wave fragment is depicted in figure 6.30.

A traveling wave fragment develops in the grey, reduced surface state close to an area in the refractory state, recognizable by its low LEEM intensity (first frame of the images). A growing ellipse is seen, which has a homogeneously low LEEM intensity until it reaches a certain size of about $10 \mu\text{m}$ (fourth frame of figure 6.30). The interior of the traveling wave fragment exhibits the bright LEEM intensity associated with the oxidized state. After further 3 s, a reduction front nucleates at the same place where the oxidation front had nucleated, and spreads over the oxidized surface area, following the oxidation front. The different curvature of the reduction and oxidation front reflects the same diffusional anisotropy, which is described in section 6.5.1. The oxygen diffusion is fastest in the $[1\bar{1}0]$ direction, whereas the reduction front propagates with the lowest

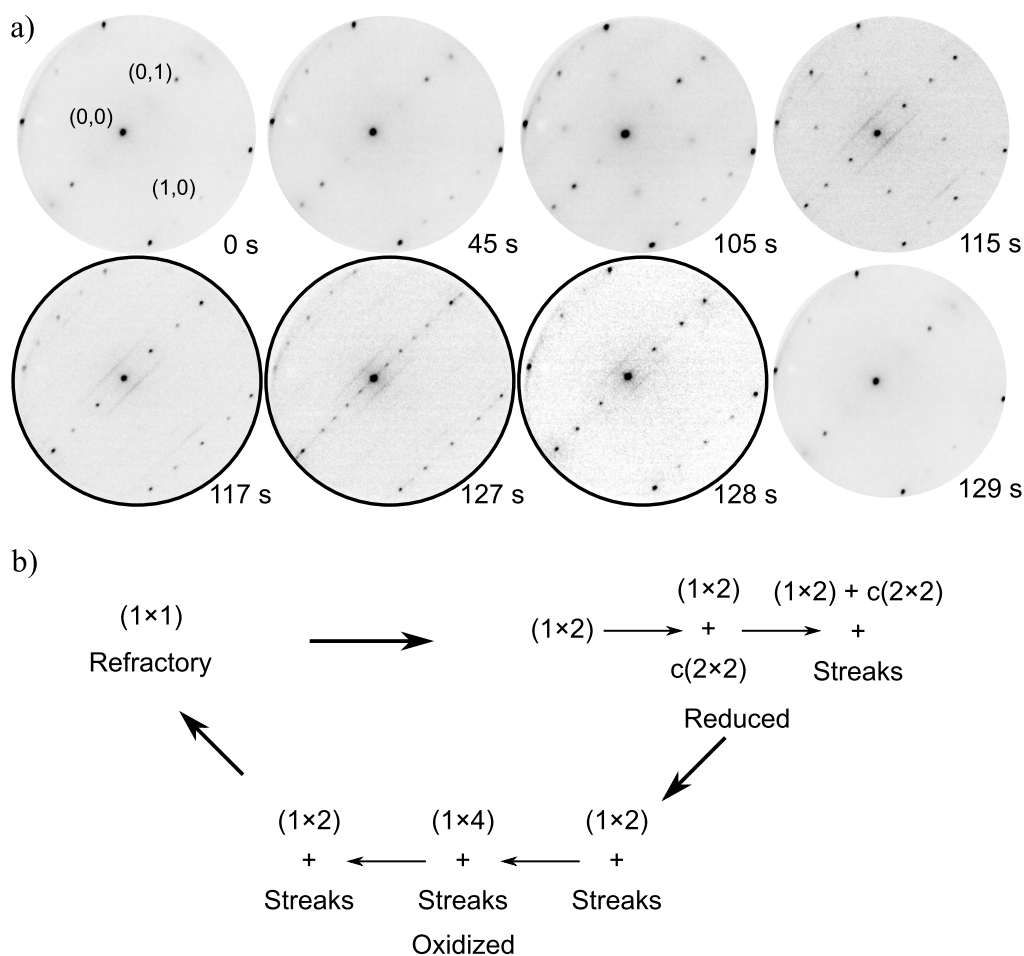


Figure 6.31: LEED images acquired during simultaneous propagation of oxidation and reduction fronts on a $\text{Rh}(110)$ surface covered with 0.4 MLE vanadium oxide. a) The LEED images encircled with a solid black line correspond to a surface in the oxidized state, the other LEED image are acquired during the transition from the refractory state (first and last LEED image) into the reduced state (second, third, and fourth image). The measurements are conducted on an area of $5 \mu\text{m}$ diameter in 1.3×10^{-5} mbar oxygen and 1.1×10^{-4} mbar methanol at 830 K. The start voltage is 40 eV in all LEED images. b) Scheme illustrating the sequence of LEED structures.

velocity in this direction. Due to the nearly identical propagation speed of the oxidation and reduction front, the traveling wave fragment moves out of the imaged surface area as a stable object, leaving a narrow stripe of very low LEEM intensity, (refractory state, last frame of figure 6.30). In order to further characterize the chemical wave pattern in the region of double metastability, an in situ μLEED measurement (probing area of $5 \mu\text{m}$ diameter) is conducted. The resulting LEED images are depicted in figure 6.31a.

This series of LEED images is acquired just after the surface was transformed from

the oxidized state into the refractory state by a propagating reduction front. As can be seen in the first LEED image, the surface directly after a reduction front has passed is characterized by a (1×1) LEED pattern. As time progresses, first weak spots of a (1×2) structure develop (second image) within 45 s, which are accompanied by additional spots of the $c(2 \times 2)$ after about one second (third LEED image). Right before the next oxidation front propagates across the probed surface area, streaky features, elongated in the $[001]$ direction, appear around the $(0,0)$ and $(1,0)$ diffraction spots. Only 2 s later, the $c(2 \times 2)$ vanishes, and the existence of a (1×2) diffraction pattern together with streaky features around the $(0,0)$ and $(1,0)$ spots mark the transition from the reduced state into the oxidized state. The (1×2) structure is rapidly transformed into a (1×4) , whereas the streaky features around the integral order diffraction spots remain unchanged. After a few seconds in the oxidized state, the surface is transformed via the (1×2) structure, which is visible for 1 s, back into a (1×1) . Interestingly, no $c(2 \times 6)$ and $c(2 \times 8)$ structures are observed, which is probably a consequence of the high vanadium oxide coverage. A scheme illustrating the sequence of LEED structures is shown in figure 6.31b.

The comparison of the temporal evolution of the diffraction pattern with the LEEM images presented in figures 6.29 and 6.30 allow for an assignment of the (1×1) phase to the refractory state and of the (1×4) structure to the oxidized state. Possibly, the thin, dark interface that separates the oxidized from the reduced surface area constitutes a (1×2) structure, since it is shortly observed before the (1×4) is established. The transition from the refractory into the reduced state is accompanied by the sequential formation of a (1×2) and a $c(2 \times 2)$ structure.

6.6 Reaction-induced redistribution of VO_x on $\text{Rh}(110)$

All experiments described so far have in common, that they are conducted either on an unpromoted $\text{Rh}(110)$ surface, or on a $\text{Rh}(110)$ surface homogeneously (on the μm scale) covered with vanadium oxide. The wave patterns described in the preceding section do not lift the spatial homogeneity of the VO_x covered surface. For comparison, the dynamics of catalytic methanol oxidation on $\text{VO}_x/\text{Rh}(111)$ are dominated by a reaction induced redistribution of vanadium oxide in VO_x -rich and VO_x -depleted areas. On $\text{Rh}(111)$, the redistribution of VO_x is observed at temperatures above roughly 820 K, whereas no VO_x redistribution could be observed on $\text{Rh}(110)$ up to 850 K. In order to investigate whether a reaction-induced VO_x redistribution can also be observed on $\text{Rh}(110)$ during catalytic methanol oxidation, the temperature range was extended to 1020 K [244, 245].

6.6.1 VO_x redistribution on $\text{Rh}(110)$ under oxidizing reaction conditions in PEEM

All experiments presented in this section are conducted on $\text{Rh}(110)$ surfaces covered with 0.4 MLE of vanadium oxide. After a fresh VO_x film is deposited on the $\text{Rh}(110)$, the surface is heated in a reaction atmosphere consisting of 3×10^{-4} mbar methanol

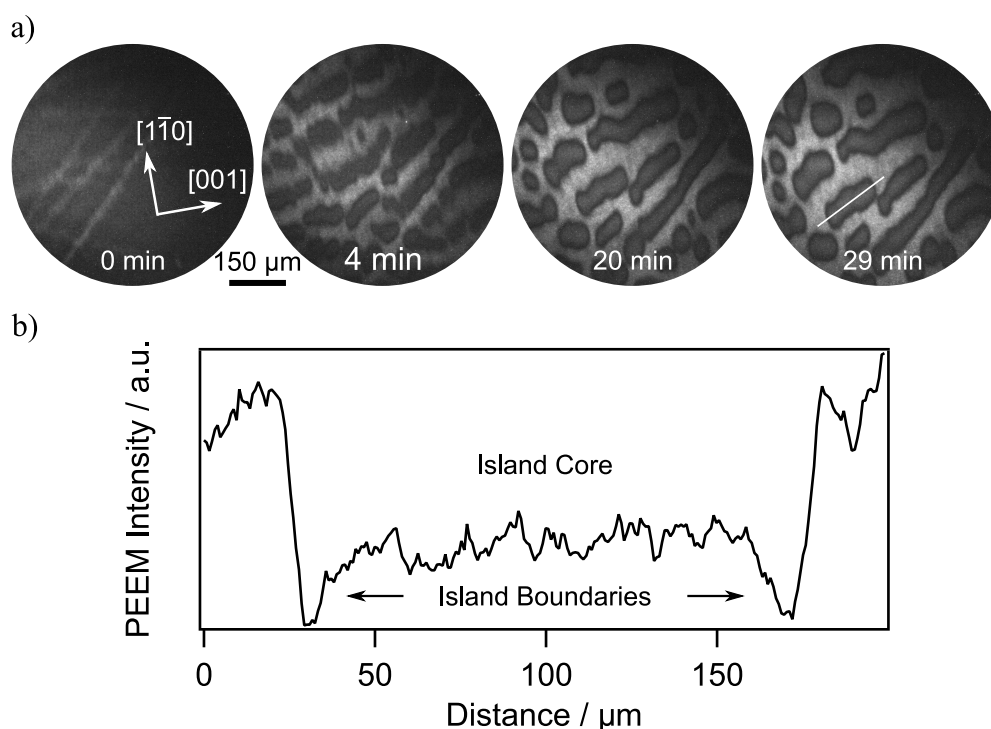


Figure 6.32: PEEM images showing the formation of macroscopic VO_x depleted and -enriched areas during catalytic methanol reaction at 1020 K on 0.4 MLE $\text{VO}_x/\text{Rh}(110)$. a) The formation and ripening of macroscopic, dark appearing islands recorded under reaction conditions in an atmosphere of 3×10^{-4} mbar methanol and 1×10^{-4} mbar oxygen. b) An intensity line profile taken across the solid white line in the last PEEM image of a, revealing the existence of a substructure consisting of a brighter core and a darker boundary within the formed islands. Reproduced in part with permission from *J. Phys. Chem. C* **2018**, *122*, 12694 – 12703. Copyright 2018 American Chemical Society. Figure adapted from [71].

and 1×10^{-4} mbar oxygen from room temperature to 1020 K. After passing through the regime of double metastability, in which the nucleation and propagation of travel wave fragments is observed until, at 870 K the whole surface is in the oxidized (in PEEM dark) state. Starting at roughly 930 K, a retraction of VO_x from surface scratches sets in, resulting in the formation of macroscopic vanadium oxide rich and -depleted areas. This is demonstrated by the series of PEEM images shown in figure 6.32a.

A further temperature increase to 1020 K finally leads to well separated, dark islands, surrounded by a homogeneously bright surface. Since PEEM only provides indirect chemical information (the main contrast mechanism is the local variation of the work function), a clear assignment of VO_x enriched and depleted area to the PEEM images is difficult. Some indications for VO_x islands surrounded by VO_x depleted area can be derived from the response of the surface to changes in the gas phase composi-

tion. However, the assignment of the dark islands being vanadium oxide enriched area rather than VO_x depleted holes has to be taken as tentative, since neither structural nor chemical information can be gained from the PEEM images. Furthermore, As will be shown by an XPS/XPEEM study described in section 6.8, different from the system $\text{VO}_x/\text{Rh}(111)$ only an incomplete phase separation is observed on $\text{VO}_x/\text{Rh}(110)$, and substantial amounts of V can be measured also on the VO_x depleted areas.

As time progresses, an Ostwald-like ripening leads to an expansion of the larger islands, while smaller islands disappear. At the same time, the contrast between the dark elongated islands, and the surrounding surface increases. As can be seen in figure 6.32a, the dark islands show a preferential orientation, which is not related with one of the crystallographic direction of the surface. Instead, the orientation of the evolving islands is governed by macroscopic surface scratches present on the $\text{Rh}(110)$ surface. This orientation along surface scratches indicates a large nucleation barrier and a low mobility of VO_x on $\text{Rh}(110)$, compared to $\text{Rh}(111)$. On $\text{Rh}(111)$, the original orientation of VO_x stripes formed around 820 K is also governed by surface scratches. As the temperature is increased, the stripes transform into nearly circular islands, which move on the $\text{Rh}(111)$ surface under reaction conditions, indicating a quite high mobility of VO_x at temperatures between 900 and 1000 K.

An intensity line profile taken across a roughly 100 μm wide island is shown in figure 6.32b. The line profile reveals, that the islands are not homogeneously dark but exhibit a substructure consisting of an inner bright core, and an outer dark ring, very similar to the VO_x islands formed during catalytic methanol oxidation on $\text{Rh}(111)$ [69]. Based on the relative PEEM intensities of the islands and their surroundings, their similarity to the islands on $\text{Rh}(111)$, and their behavior with respect to changes in the gas phase composition, the islands are assigned to the vanadium oxide rich areas of the surface, whereas the surroundings are assigned to VO_x depleted area on a tentative basis.

After a period of roughly 30 min no significant changes in the VO_x redistribution pattern are observed and the sample is cooled with 0.5 K s^{-1} . Initially, the PEEM intensity homogeneously decreases. As 680 K is reached the cooling ramp is stopped, because reduction fronts nucleate at the interface of the vanadium oxide islands and their surroundings. These fronts propagate, until after about 6 min at a constant temperature of 680 K, the original contrast from at 1020 K (dark islands on bright surroundings) is inverted. A series of PEEM images showing the initial PEEM intensity increase and the brightening of the islands, together with the temporal evolution of the PEEM intensity measured in the islands and the surrounding surface is shown in figure 6.33a. A separate temperature programmed reaction experiment conducted under similar conditions reveals, that the brightening of the islands is accompanied by a sharp increase in the CO, CO_2 and water production rates [71, 244].

The PEEM images shown in figure 6.33b are taken from the same experiment at a constant temperature of 680 K, but the image contrast is strongly enhanced. In this way, the changes that occur on the surface surrounding the bright islands (saturated in the PEEM images) are better visualized. Interestingly, the slight increase of PEEM intensity measured in the surroundings (figure 6.33a) does not proceed in a spatially

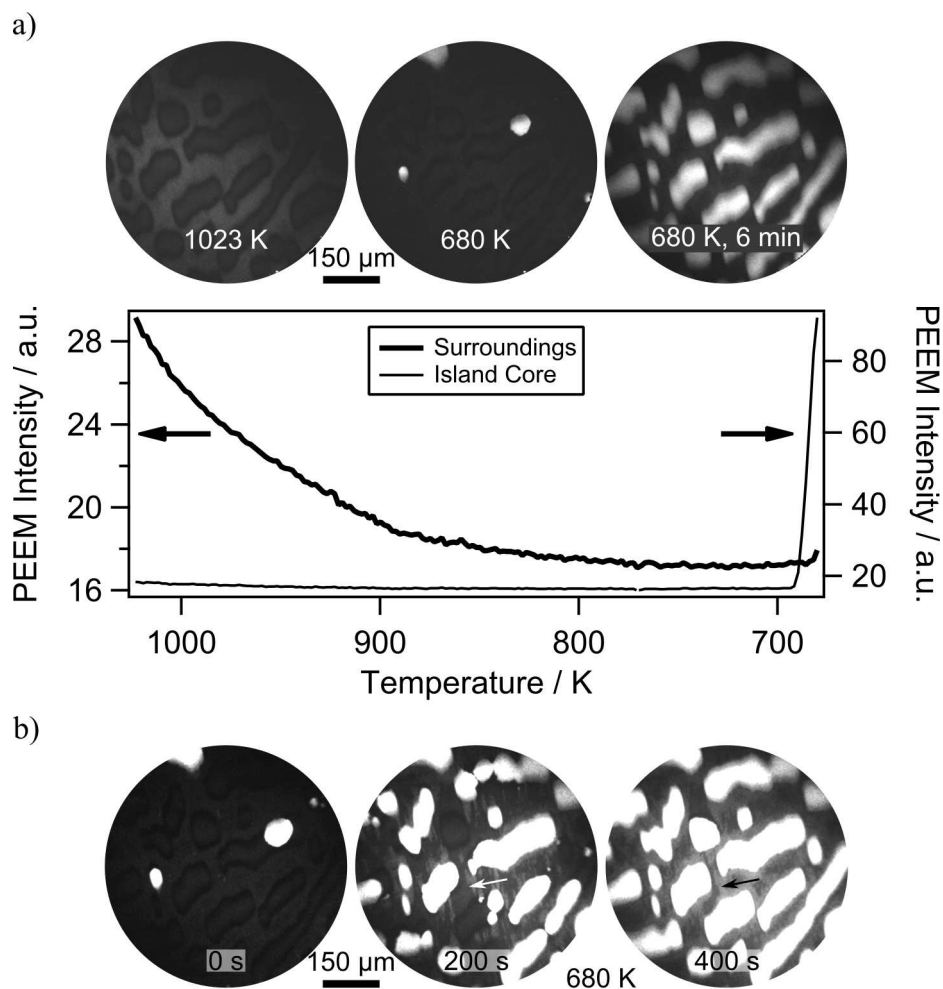


Figure 6.33: Contrast reversal in PEEM during cooling down VO_x on Rh(110) under reaction conditions. a) PEEM images and local PEEM intensity of the islands and their surroundings as a function of temperature. b) PEEM images from the same experiment, taken at 680 K with strongly enhanced contrast, show the changes in the surface surrounding the bright islands. The cooling rate is 0.5 K s^{-1} . The cooling was stopped as reduction fronts led to an intensity increase of the islands at 680 K. The gas phase composition and initial VO_x coverage is identical to the experiment in figure 6.32. Reproduced in part with permission from *J. Phys. Chem. C* **2018**, *122*, 12694 – 12703. Copyright 2018 American Chemical Society. Figure adapted from [71].

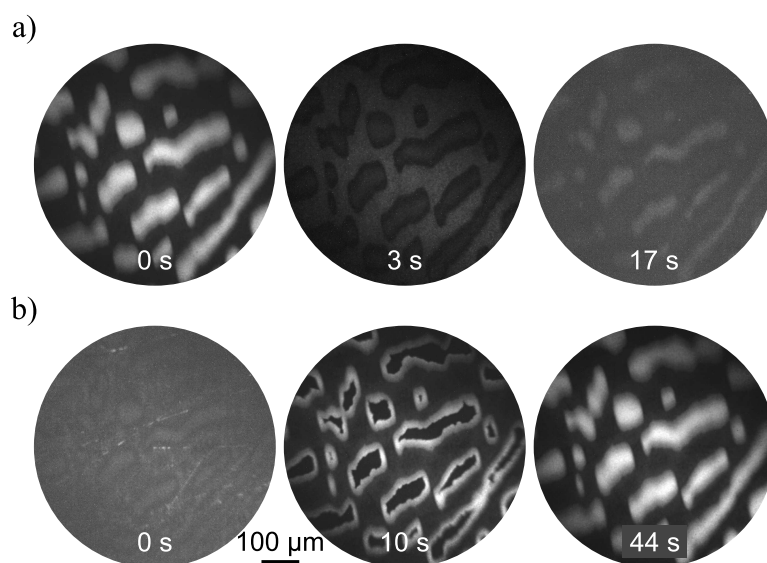


Figure 6.34: Oxidation and reduction of the macroscopic islands formed during methanol oxidation at 1020 K. a) At 0 s, the methanol pressure is reduced from 3×10^{-4} to 1×10^{-4} mbar, resulting in the fast oxidation of the islands by propagating oxidation fronts. b) A methanol pressure increase back to the initial value of 3×10^{-4} mbar cause the reduction of the islands by propagating reduction fronts. Reproduced in part with permission from *J. Phys. Chem. C* **2018**, *122*, 12694 – 12703. Copyright 2018 American Chemical Society. Figure adapted from [71].

homogeneous way. Instead the nucleation and propagation of reduction fronts is also observed on the surface around the islands. This can be seen for example by comparing the positions highlighted by the white and black arrows in the second and third PEEM images. Obviously, both surfaces, the vanadium oxide rich and poor are active towards methanol oxidation at temperatures around 680 K. This is evidenced by the simultaneous propagation of reduction fronts. However, the surrounding surface responds much slower and to a lower extend to the temperature change.

In order to investigate if the substructure of the vanadium oxide islands responds in a similar manner to changes in the gas phase composition, as observed for the VO_x islands on $\text{Rh}(111)$, the methanol partial pressure is varied. Figure 6.34a shows a series of PEEM images acquired before and after the methanol pressure is reduced from its original value of 3×10^{-4} to 1×10^{-4} mbar. As a consequence, oxidation fronts nucleating at the boundaries of the bright islands and propagate towards the center, turning them dark. A subsequent methanol partial pressure increase back to 3×10^{-4} mbar initiates the transformation via reduction fronts back into the bright state. Interestingly, the propagation speed of the oxidation fronts is with $12 \mu\text{m s}^{-1}$ considerably faster than the reduction front, which spreads with only $2.2 \mu\text{m s}^{-1}$. The surface surrounding the bright islands does not respond to changes in the gas phase composition.

In addition to the formation of elongated islands during exposure to reaction condi-

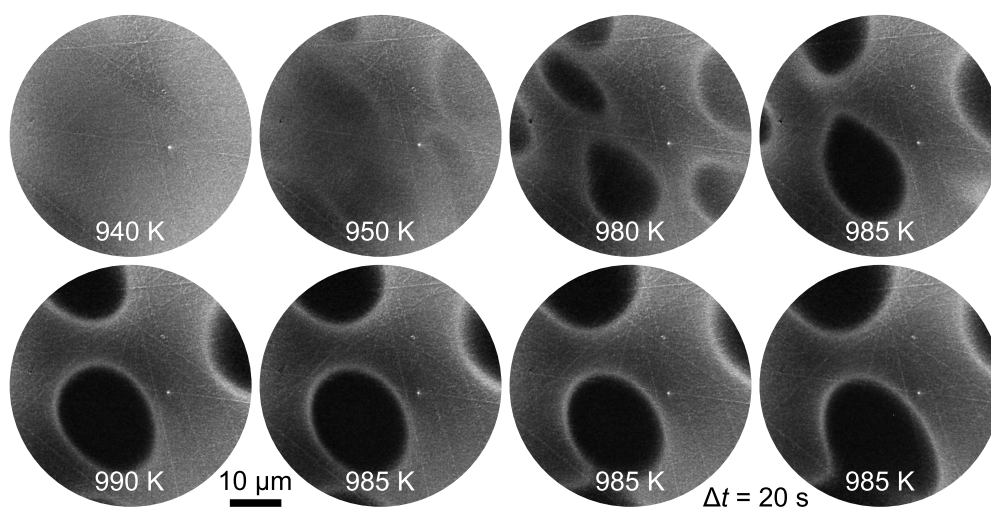


Figure 6.35: LEEM images showing the reaction-induced redistribution of VO_x on $\text{Rh}(110)$ during catalytic methanol oxidation. Upon temperature increase to 980 K, the formation of oval shaped areas of low LEEM intensity sets in. Prolonged exposure to reaction conditions results in a ripening process, which includes the coalescence of neighboring islands. The LEEM images are recorded in a gas atmosphere consisting of 2.6×10^{-5} mbar oxygen and 1.1×10^{-4} mbar methanol at a start voltage of 1.8 eV.

tions at 1020 K, a second growth mode, resulting in dendritic vanadium oxide islands, has been observed. The principle difference is that in the former case the surface is in the oxidized state, whereas in the dendritic growth mode reducing conditions are applied. The dendritic growth mode is described in detail in references [241] and [244].

6.6.2 VO_x redistribution on $\text{Rh}(110)$ under oxidizing reaction conditions in LEEM

A similar experiment as described in the preceding section is conducted with LEEM in order to further characterize the different structures that arise during the reaction-driven phase separation into vanadium oxide rich and VO_x depleted areas. Therefore, a $\text{Rh}(110)$ surface covered with 0.4 MLE vanadium oxide is heated in a gas atmosphere of 2.6×10^{-5} mbar oxygen and 1.1×10^{-4} mbar methanol to 990 K. The resulting phase separation is shown in figure 6.35.

As soon as the temperature reaches 940 K, the initially homogeneous surface state in the first LEEM image is lifted and dark, oval shaped areas develop in the seconds image. These areas are separated from the surrounding surface by a thin interface of high LEEM intensity. Upon prolonged exposure at elevated temperature to reaction conditions, the contrast between the dark and bright areas increases. At the same time, a ripening process sets in, in which smaller islands disappear, while larger ones grow in size. A coalescence of neighboring dark islands is observed, as can be seen in the last two images of figure 6.35.

The behavior observed in LEEM differs considerably from island formation observed in PEEM. In PEEM the formation of dark (high work function) elongated islands proceeded via the condensation of a homogeneous VO_x film, retracting from scratches. In the LEEM images depicted in figure 6.35 oval shaped dark islands appear by gradually increasing contrast with respect to the surrounding surface. After this initial stage, the disappearance of small islands and the growth of the larger islands sets in (as also observed in PEEM). Also the coalescence of neighboring islands can be observed, an effect well known from $\text{VO}_x/\text{Rh}(111)$, but which is not seen in any of the PEEM experiments on $\text{RhVO}_x/(110)$. In the LEEM experiment described here, the island size is with around 20 to 50 μm considerably smaller than in the PEEM experiment, where islands of up to several hundred micrometer size are common.

μLEED measurements recorded in the interior of the dark areas and in the thin bright ring reveal, that the dark areas exhibit a (1×2) LEED pattern, whereas the boundary phase and the surrounding surface are both characterized by a (1×2) diffraction pattern with the same streaky features around the $(0,0)$ and $(1,0)$ diffraction spots, which are elongated in the $[001]$ direction. Since a (1×2) LEED pattern is observed on the unpromoted $\text{Rh}(110)$ surface, as well as on a partially VO_x covered surface, no assignment of vanadium oxide rich and VO_x depleted area to the different intensity LEEM levels can be made on the basis of the μLEED measurement. Therefore the LEEM and LEED measurements are repeated at a lower temperature of 810 K.

Figure 6.36a shows a series of LEEM images acquired during the cool-down of the $\text{VO}_x/\text{Rh}(110)$ surface within 200 s, together with LEED images of the different surface phases. An overview composed of several LEEM images is given in figure 6.36b. One recognizes three changes: *i*) the overall intensity of the LEEM images slightly increases with decreasing temperature. *ii*) The initial homogeneous boundary phase, which separates the dark island from its surroundings at 990 K, splits up into two boundary phases, which grow upon temperature decrease. At the same time, their interfaces sharpen. *iii*) the initially homogeneous surroundings start to exhibit a granular morphology at around 850 K.

The changes visible in LEEM are accompanied by structural transitions, as can be seen in the five LEED images shown in figure 6.36b, acquired on the surrounding, granular surface, on the two boundary phases, in the dark island close to the boundary, and inside the dark island. At 990 K, only two different LEED pattern can be observed, a (1×2) in the dark island core, and a (1×2) with elongated streaks around the integral order diffraction spots on the boundary phase and the surrounding surface. The temperature decrease of nearly 200 K results in the formation of a (4×2) structure in the surrounding and the first boundary phase, a (3×2) in the second boundary phase, an (1×2) in the dark core close to the boundary, and a $c(2 \times 8)$ inside the dark core. The only difference, that can be seen between the (4×2) LEED pattern measured on the surrounding surface and the first boundary phase are some streaky features elongated in the $[001]$ direction, that are present around the $(0,0)$ spot in the LEED image taken on the surroundings.

With the LEED images one can assign the vanadium oxide depleted area to the dark

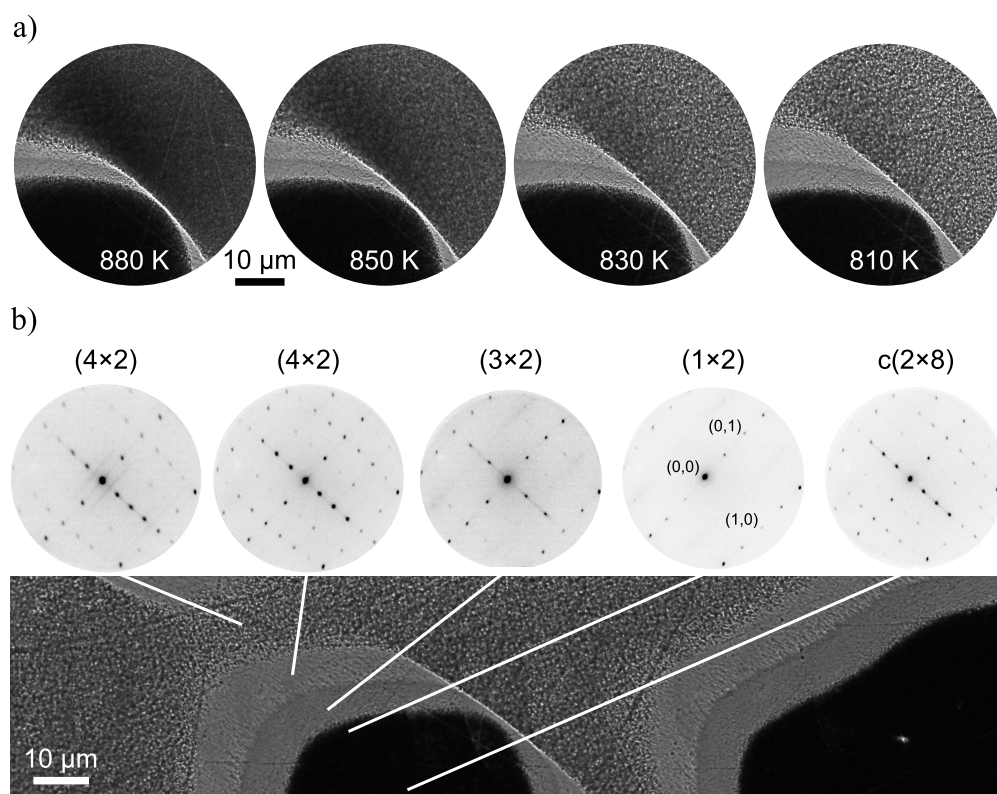


Figure 6.36: LEEM and LEED images taken on a VO_x redistribution pattern consisting of oval shaped holes in a dense VO_x film. a) LEEM images recorded at different temperatures during the cool-down from 985 K. b) μLEED images taken on the different phases distinguishable in LEEM and an overview image composed of several LEEM images. The LEEM and LEED measurements are conducted at 800 K (if nothing else is stated in the images) in an atmosphere of 2.6×10^{-5} mbar oxygen and 1.1×10^{-4} mbar methanol. The start voltage of the LEEM images is 1.9 eV, LEED is performed at 40 eV.

islands, and the vanadium oxide rich area to the boundary phases and the surroundings. The $c(2 \times 8)$ is of adsorbed oxygen on the $\text{Rh}(110)$ surface, but no such pattern has been reported for $\text{VO}_x/\text{Rh}(110)$ [185]. The (4×2) is observed in the growth experiments of vanadium oxide on $\text{Rh}(110)$. It is seen after post-oxidation of a 0.8 MLE thick VO_x film in 2×10^{-7} mbar oxygen at 620 K [185]. Apparently, the vanadium oxide redistribution pattern formed during methanol oxidation at 990 K is a hole pattern in the sense, that instead of VO_x islands surrounded by VO_x depleted area, the inverse structure is created.

The experiments conducted on 0.1 MLE and 0.2 MLE, in which traveling wave fragments and target pattern are observed, demonstrate that small amounts of vanadium do not inhibit the formation of the oxygen induced reconstructions. The dark islands visible in the overview LEEM image in figure 6.36b therefore represent a oxygen covered $\text{Rh}(110)$ surface, eventually covered with small amounts of VO_x .

This finding seems to be in contradiction with the interpretation of the macroscopic islands arising during the PEEM experiments as being vanadium oxide islands, described in section 6.6.1. However, there is no real contradiction, because the two sets of experiments differ in the pressure, which is by a factor of four higher in the PEEM experiments. Also the length scale of the holes/islands differs by roughly one order of magnitude from the island pattern in PEEM. Furthermore, a qualitatively different behavior is seen in both sets of experiments. A coalescence of neighboring holes is only observed in LEEM, whereas the islands in PEEM do not change their position. Apparently, such a complex system as $\text{CH}_3 + \text{O}_2/\text{VO}_x/\text{Rh}(110)$ allows for qualitatively different solutions, depending on parameter space and, perhaps, also depending on the history of the reaction treatments. The complexity of the system is also illustrated by XPS results (section 6.8) showing that reaction conditions do not lead to a complete phase separation [185].

6.7 Chemical wave patterns on patterned $\text{VO}_x/\text{Rh}(110)$ surfaces

The reaction induced redistribution of vanadium oxide leads to the interesting situation, that areas covered with a considerable amount of VO_x (more than 0.4 MLE) coexist with areas, that are vanadium oxide depleted. Both surfaces, the VO_x covered $\text{Rh}(110)$ surface and the unpromoted $\text{Rh}(110)$ surface have shown a variety of different chemical wave pattern including traveling interface modulations and traveling wave fragments, and target pattern. It can therefore be assumed that also on the “micro-patterned” $\text{VO}_x/\text{Rh}(110)$ surface apparent after exposure to reaction conditions at 1000 K pattern formation may occur in the parameter space in which double metastability is observed on the homogeneous $\text{VO}_x/\text{Rh}(110)$ surfaces.

6.7.1 Traveling wave fragments on micro-patterned $\text{VO}_x/\text{Rh}(110)$ surfaces in PEEM

Starting with a surface consisting of macroscopic vanadium oxide islands (figure 6.33), this pre-patterned surface is cooled under reducing reaction conditions from 1020 to 680 K. Reduction fronts form, transforming the whole surface in a reduced state. If such a surface is heated up again slowly into the parameter range of double metastability, the nucleation and propagation of traveling wave fragments can be observed, as shown in figure 6.37. This happens first on the island surroundings at 790 K and later, at 830 K also on the islands.

As can be seen in the enlarged section of the central PEEM image in figure 6.37, elliptically shaped oxidation fronts nucleate and spread on the bright islands, as soon as an oxidation front moves from the surrounding surface to the islands boundary. The long axis of these elliptical oxidation fronts is thereby inclined with the $[\bar{1}\bar{1}0]$ crystallographic direction of the surface. As observed on the homogeneous $\text{VO}_x/\text{Rh}(110)$ surface in the regime of double metastability, elliptical oxidation fronts are followed by reduction

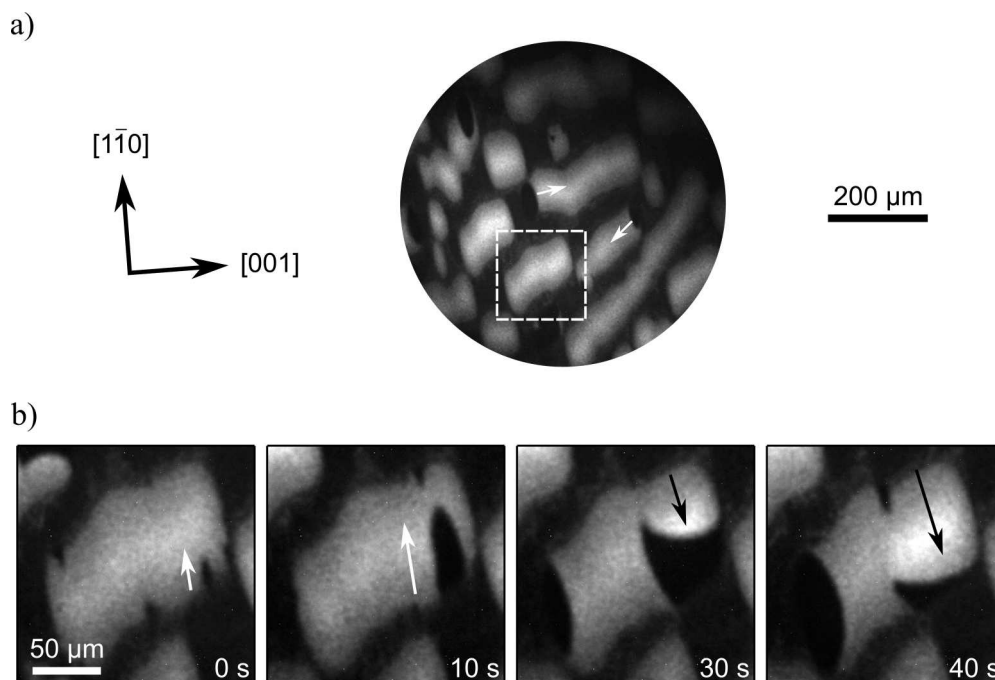


Figure 6.37: PEEM images showing traveling wave fragments, which propagate on a micro-patterned surface present after the reaction induced redistribution of 0.4 MLE VO_x on $\text{Rh}(110)$. a) A PEEM image showing the nucleation of large wave fragments at the boundary of the bright islands. The propagation direction is indicated by white arrows. b) Enlarged view of the square section indicated by a dashed white line in a, highlighting the propagation of oxidation and reduction fronts on an island. The images are recorded at 830 K under reducing reaction conditions. Reproduced in part with permission from *J. Phys. Chem. C* **2018**, *122*, 12694 – 12703. Copyright 2018 American Chemical Society. Figure adapted from [71].

fronts, whose anisotropy is rotated by approximately 90° . Interestingly, oxidation and reduction fronts nucleate in most cases at the boundary of the bright islands.

A closer inspection of the four magnified PEEM images in figure 6.37b shows, that three different PEEM intensity levels on the bright islands can be distinguished. These intensity levels can be associated with a reduced, an oxidized and a refractory state. On a tentative basis the dark area in PEEM is assigned to an oxidized state, and medium intensity to a reduced state. Starting from the boundary, a dark oxidation front nucleates and grows within 15 s across a bright island. As soon as it touches the opposite boundary, a bright reduction front nucleates at the interface and reactively removes the whole oxidized area within 15 s. The area passed by a reduction front exhibits a higher PEEM intensity as the reduced state, and no further propagation of oxidation fronts can be observed on these bright areas. Within tens of seconds, the initially bright area turns into the same intensity level as the reduced state. It is then active again for further

oxidation fronts. Therefore, the very bright area is assigned to a refractory state in a pulse.

The behavior of traveling wave fragments on the bright islands resembles the behavior on homogeneous VO_x films on $\text{Rh}(110)$ (0.4 MLE) observed under similar reaction conditions. Due to the low PEEM intensity and the small length scale no detailed analysis of the wave pattern apparent on the surroundings of the bright islands can be conducted. However, the similarity of the wave pattern observed on the bright islands and on homogeneous 0.4 MLE VO_x films on $\text{Rh}(110)$ leads to the assignment of VO_x islands and a mostly VO_x depleted surrounding. Neither the existence of a refractory state nor traveling wave fragments can be observed on $\text{Rh}(110)$ surfaces covered with less than 0.2 MLE VO_x .

6.7.2 Pattern formation on the micro-patterned $\text{VO}_x/\text{Rh}(110)$ surface in LEEM

The interface between the vanadium oxide enriched and vanadium oxide depleted areas is shown in the LEEM images presented in figure 6.38. The images show the response of a dark hole (VO_x depleted area with a $c(2 \times 8)$ diffraction pattern) and the surrounding surface (VO_x enriched area with a (4×2) diffraction pattern) to changes of the gas phase composition.

Starting from the situation after the redistribution pattern was formed at 1000 K in 2.6×10^{-5} mbar oxygen and 1.1×10^{-4} mbar methanol, the surface is cooled down. As 810 K is reached, the temperature is stabilized and the oxygen pressure is reduced in order to transform the surface from the oxidized state into the reduced state. A progressive reduction of the surrounding VO_x covered surface can be seen by a LEEM intensity decrease, starting at a large distance from the dark hole on the lower left side on the images. As the oxygen pressure is further decreased to $0.5 - 0.4 \times 10^{-5}$ mbar (fifth and sixth LEEM images in figure 6.38a), the surface surrounding the hole is in a homogeneous state of low LEEM intensity and the phase boundary starts to get reduced. The oxidized state exhibits a granular morphology in LEEM, as can be seen in the first image of figure 6.38a. The reduced state instead has an almost homogeneous appearance, as seen in the fifth and sixth image. As soon as the complete boundary phase has turned into low LEEM intensity, oxidation fronts nucleate at the interface between the surroundings and the boundary phase, as well as between the boundary phase and the hole. An oxidation front rapidly spreads across the boundary phase and the surrounding surface and turns the reduced surface back into the oxidized state. Interestingly, the oxidation front nucleates and spreads without any parameter change.

As time progresses, the oxidized surface state slowly turns back into the reduced state. The transition occurs, however, not via reduction fronts, but in a more or less homogeneous manner. This process is demonstrated in the first two LEEM images of figure 6.38b. Shortly before the whole surroundings and the boundary phase are turned into the reduced state, the oxygen pressure is increased from 0.3 to 0.9×10^{-5} mbar. Instantly, a large oxidation front nucleates at the interface between the hole and the boundary phase (second and third image of figure 6.38b). At the same time, the reduction

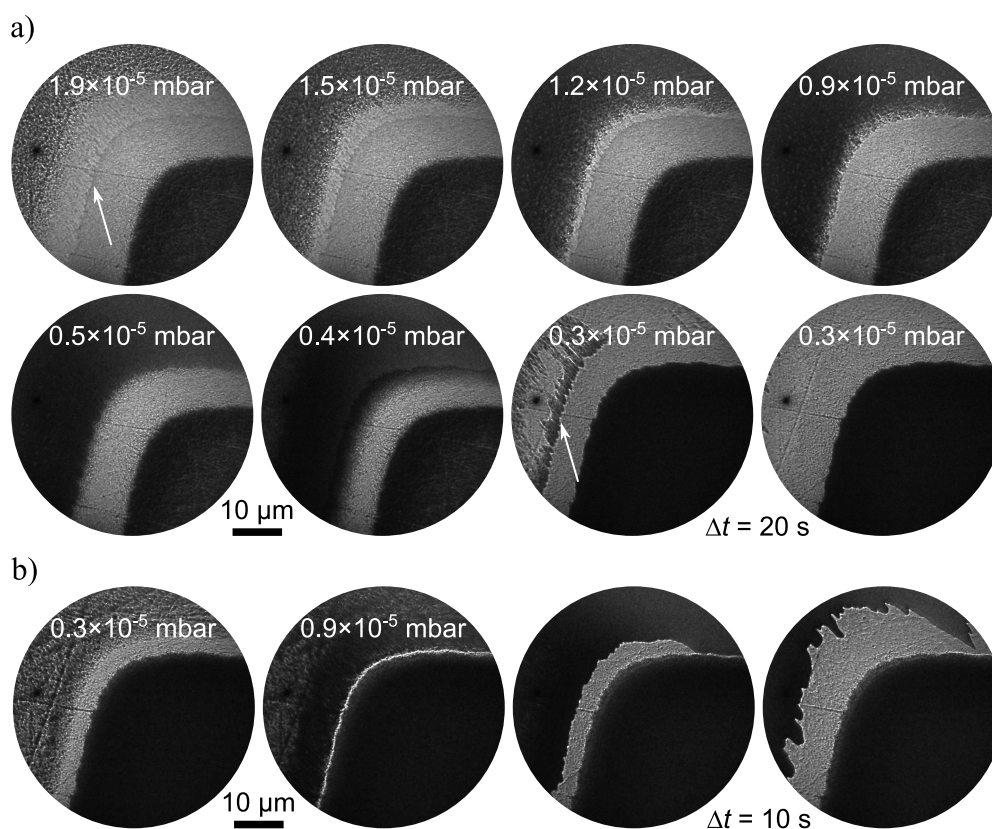


Figure 6.38: LEEM images showing the reduction and subsequent oxidation of a micro-patterned $\text{VO}_x/\text{Rh}(110)$ surface. a) Upon continuous oxygen pressure decrease from 2.6×10^{-5} to 0.3×10^{-5} mbar the reduction of the vanadium oxide covered parts of the surface is observed, followed by subsequent a re-oxidation without parameter change. b) After further 35 s a gradual reduction of the surface is observed, until an oxygen pressure increase to 0.9×10^{-5} mbar leads to the simultaneous propagation of oxidation and reduction fronts. The LEEM images are acquired at 1.8 eV and 810 K with a constant methanol pressure of 1.1×10^{-4} mbar.

proceeds in the surrounding surface and a homogeneously dark phase is established.

The simultaneous formation of oxidation and reduction fronts indicate that the oxygen pressure increase causes the system to enter a double metastable regime. Double metastability, i. e. the simultaneous presence of oxidation and reduction fronts allows for pulse-like solutions. This is demonstrated by the LEEM images in figure 6.39, recorded 30 s after the last image of figure 6.38b. The series of LEEM images shows the same dark hole on the lower left side, which is separated by a bright oxidation front from the surrounding surface, which is in the dark, reduced state. Interestingly, the oxidation front is very sinuous and exhibits many excursions. These excursions are reduction fronts, which propagate from the surrounding surface towards the hole, as can be seen by

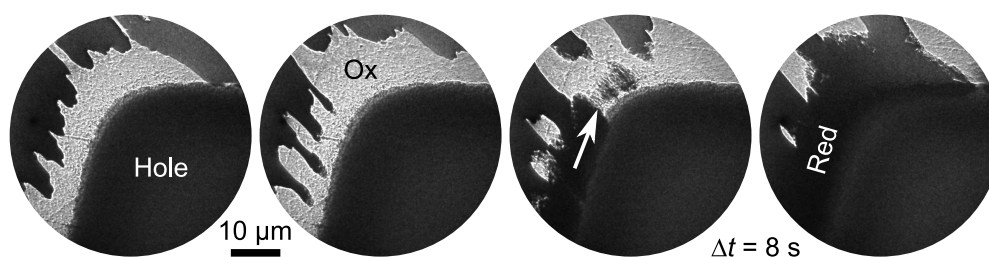


Figure 6.39: LEEM images showing the onset of pattern formation on a micro-patterned $\text{VO}_x/\text{Rh}(110)$ surface. The simultaneous propagation of oxidation and reduction fronts leads to a sinuous interface with several excursions between the reduced and oxidized surface state. As soon as a reduction front reaches the boundary between the vanadium oxide rich depleted area, it reacts off oxygen bound at the perimeter of the VO_x depleted hole, resulting in the propagation of isolated wave fragments. The LEEM images are recorded with 1.8 eV at 810 K in 1.1×10^{-4} mbar methanol and 0.9×10^{-5} mbar oxygen.

comparing the first and second LEEM image. As soon as the reduction fronts reach the hole, they start to spread along the interface and reactively remove the oxygen bound at the perimeter of the VO_x depleted region. As a consequence, the propagating oxidation front gets detached from the dark hole and travels as an isolated wave fragment across the vanadium oxide enriched surroundings. This detachment of the oxidation front and the formation of traveling wave fragments as a consequence is the onset of a target pattern like behavior observed on the surface surrounding the VO_x depleted holes.

Figure 6.40a displays a series of LEEM images taken at another position on the sample. A VO_x depleted hole is seen on the lower left side, and alternating oxidation (bright) and reduction (dark) fronts travel across the VO_x enriched surroundings. Due to the large size, the pattern cannot fully be imaged with LEEM. Some features reminiscent of target pattern and spiral waves can be observed. The dark hole on the lower left side acts like a source for the arms of a rotating spiral wave. The tips of bright oxidation fronts are attached to the VO_x depleted area. As the oxidation fronts move around the hole, they finally detach.

The wave pattern is surprisingly periodic, as can be seen in figure 6.40b by a plot of the local LEEM intensity. The period of a cycle consisting of an oxidation and a reduction front is quite constant and has a value of 35.5 ± 2.4 s. Interestingly, the local LEEM intensity passes through a relative minimum during an oxidation front (high intensity), and continuously decreases during a reduction front. Both observations differ from the pattern formation seen on homogeneous $\text{VO}_x/\text{Rh}(110)$ surfaces, in which the LEEM intensity of an oxidation pulse is more or less constant.

The LEED patterns observed during the propagation of oxidation and reduction fronts differ significantly from the ones observed during pattern formation on a homogeneous surface. In case of traveling wave fragments on 0.4 MLE VO_x a (1×2) and a (4×2) is observed. The traveling interface modulations are characterized by the appearance of

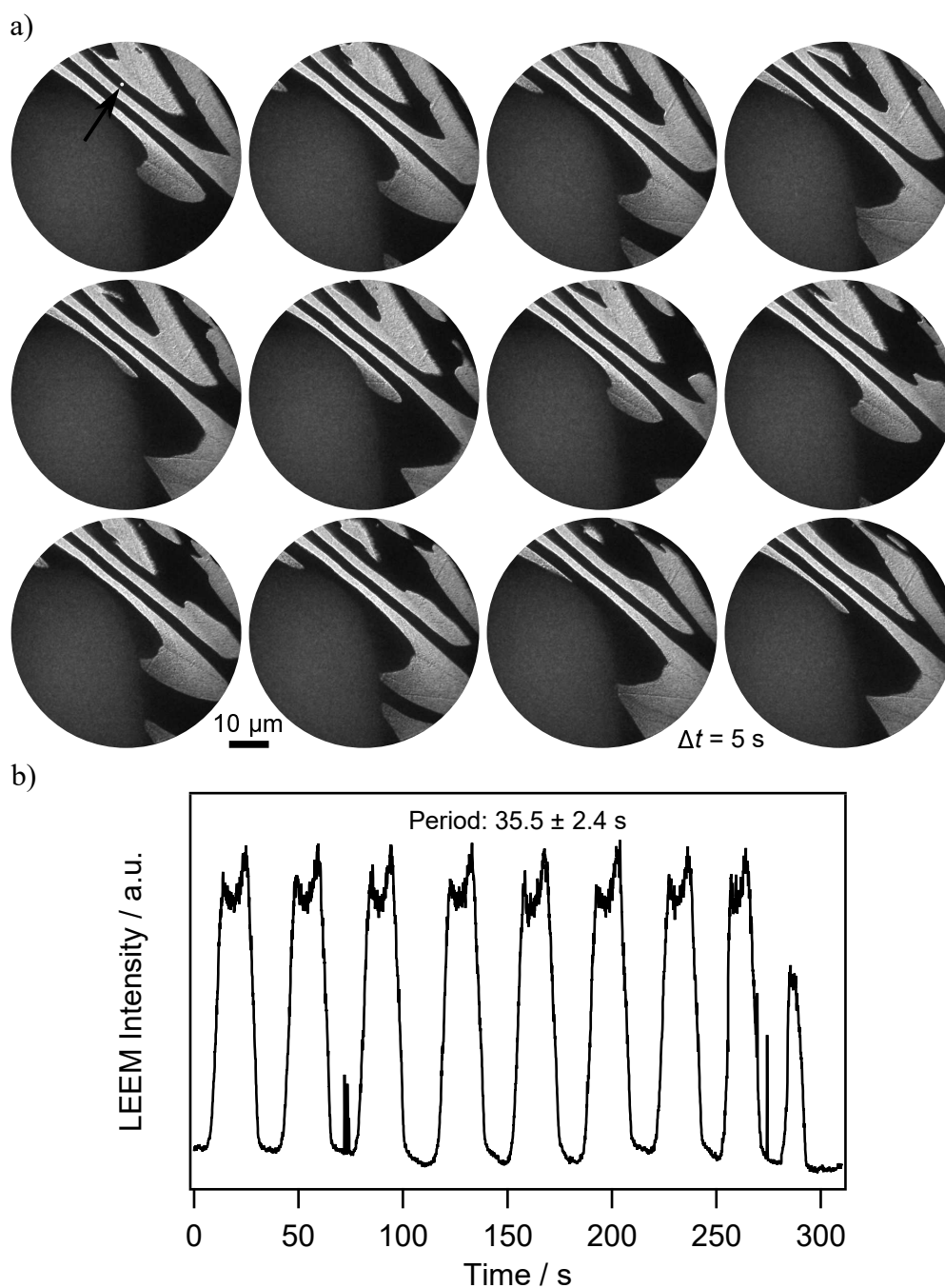


Figure 6.40: LEEM images showing chemical wave patterns similar to target pattern or spiral waves during catalytic methanol oxidation at 810 K. a) Alternating propagation of oxidation (bright) and reduction (dark) pulses around an oval VO_x depleted area (lower right side). b) Temporal evolution of the local LEEM intensity measured on a approximately $2\ \mu\text{m}$ large spot, indicated in the first image of a by a black arrow. The gas phase consisted of 0.9×10^{-5} mbar oxygen and 1.1×10^{-5} mbar methanol. The LEEM images are acquired at 1.8 eV start voltage.

(1×2) , $c(2 \times 6)$, and $c(2 \times 8)$ structures. In all chemical wave pattern observed so far, the reduced state always exhibited a (1×1) and a (weak) $c(2 \times 2)$ LEED pattern. The chemical wave pattern observed on the V_x enriched area surrounding the VO_x depleted holes exhibit only alternating (1×2) LEED pattern with and without streaky features elongated along the $[001]$ direction around the $(0,0)$ and $(1,0)$ diffraction spots. The VO_x depleted hole exhibits the superposition of a $c(2 \times 2)$ and a weak (1×2) LEED pattern. No significant intensity variations can be measured during propagation of oxidation and reduction pulses in the surroundings. This is surprising, since one would expect the occurrence of one of the VO_x related structures (for example the (4×2)) for the oxidized state, and a (1×1) for the reduced state.

The oxygen pressure is systematically varied to observe the associated changes in the surface structure on both, the VO_x rich surroundings and the VO_x depleted holes. The corresponding LEED images are depicted in figure 6.41, together with a LEEM image in which the positions of the μLEED measurements are highlighted.

At an oxygen pressure of 2.6×10^{-5} mbar, the surface is in its oxidized state and far from the conditions in which chemical wave pattern can be observed. The vanadium oxide covered parts exhibit a (4×2) LEED pattern, whereas a diffuse $c(2 \times 8)$ is seen on the VO_x depleted hole. Upon decreasing the oxygen pressure to 0.4×10^{-5} mbar, on the VO_x enriched area first a (1×2) LEED pattern with streaks around the integral order spots evolves, which transforms into a (1×2) without streaks after approximately 35 s. The VO_x depleted area displays a (1×1) structure under similar conditions. Based on the response of the LEED patterns to the oxygen pressure variations, the (1×2) with streaks is assigned to the bright oxidation fronts, and the (1×2) without streaks to the dark reduction fronts.

Pattern formation on VO_x rich and VO_x depleted areas at lower temperature

LEEM experiments are conducted at a similar temperature as the PEEM experiments of section 6.7.1. In contrast to the PEEM experiments, no propagation of oxidation or reduction fronts can be observed on the VO_x depleted area. In the PEEM experiments, small scale reaction fronts propagate on the area surrounding the macroscopic VO_x islands and initiate the nucleation and propagation of larger reaction fronts on the VO_x islands. In order to verify whether reaction fronts can also be observed in the LEEM experiments on both phases apparent after reactive phase separation at 1000 K, the temperature is lowered from its initial value to 790 K.

Figure 6.42 shows a series of LEEM images, in which an elongated, VO_x depleted hole is visible as a large stripe in the center of the images. The surrounding, VO_x enriched area is characterized by two different grey levels, assigned to the oxidized (bright) and reduced (dark) state. Similar to the experiments conducted at 810 K, local LEED measurements reveal a (1×2) LEED pattern for the reduced state and a (1×2) with elongated streaks around the integral order diffraction spots for the oxidized state. The streaks at $1/7$ or $1/8$ positions reflect a one-dimensional disorder along the $[001]$ -direction. Interestingly, different from the high temperature experiments, in which reaction pulses are found to propagate only on the VO_x enriched surroundings, at 790 K also the propagation of

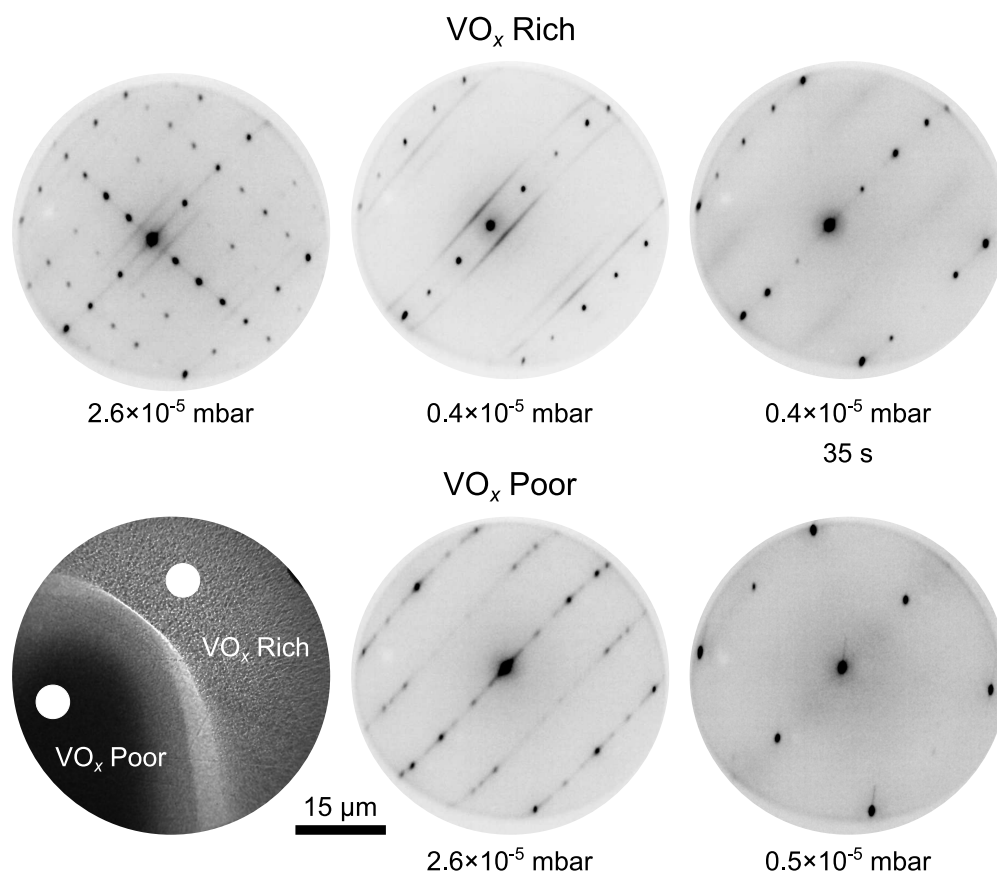


Figure 6.41: LEED pattern as a function of the gas phase composition on vanadium oxide rich (top) and depleted (bottom) areas. The oxygen partial pressures are stated below the corresponding LEED images, the position of the μLEED measurements on the surface is depicted in the LEEM image. All measurements are conducted at 810 K at a constant methanol pressure of 1.1×10^{-4} mbar. The LEED data is acquired at 40 eV start voltage, and the initial VO_x coverage is 0.4 MLE.

reaction fronts on the VO_x depleted hole can be observed.

In the first image of figure 6.42a, the nucleation of an elliptical area of high LEEM intensity is seen. This oxidation front grows until it touches the VO_x depleted hole, as depicted in the second image. As soon as the front propagates on the VO_x poor area, it slightly slows down over the VO_x hole. The oxidized zone behind the front exhibits a grainy structure. Shortly after the passage of the oxidation front, a dark reduction front nucleates at the boundary of the VO_x depleted hole and expands on the oxidized area (sixth frame). The direction of fastest propagation velocity is rotated by approximately 90° with respect to the fast direction of the oxidation front. As can be seen in the seventh and eighth image of figure 6.42a, the dark reduction front only propagates on the area, which has been turned into the oxidized state by the preceding reaction front.

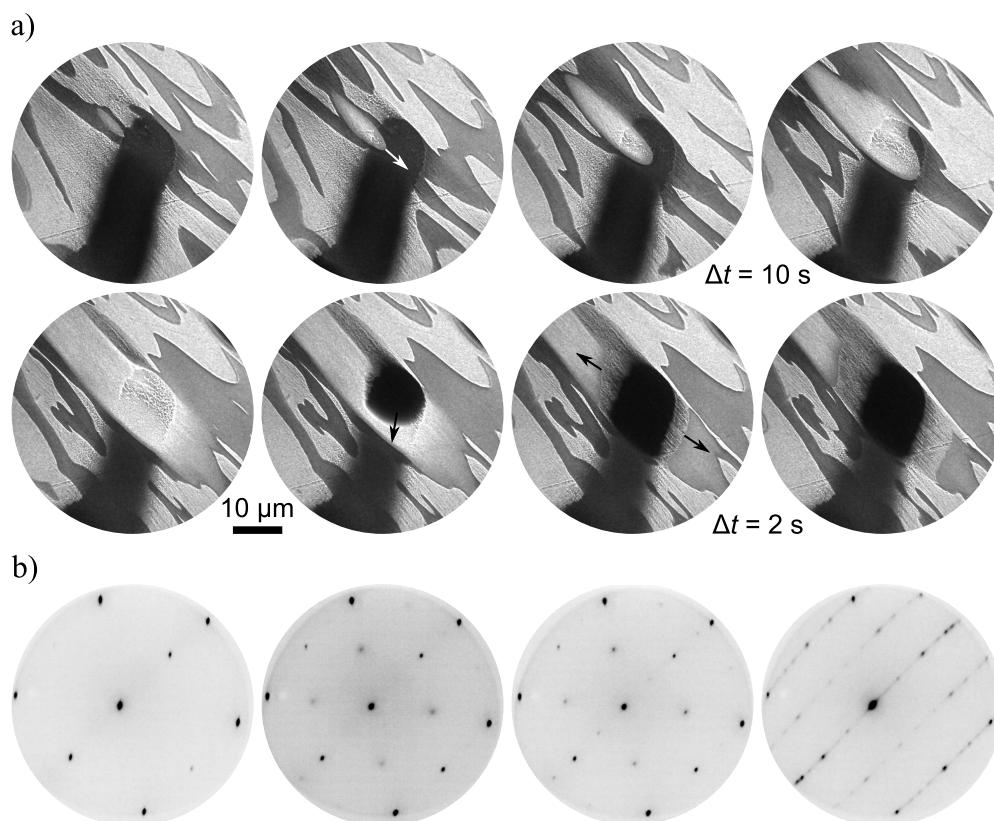


Figure 6.42: LEEM and LEED images acquired during the simultaneous propagation of reaction fronts on the VO_x enriched and -depleted areas of $\text{VO}_x/\text{Rh}(110)$ during catalytic methanol oxidation at 790 K. a) LEEM images showing a dark, elongated hole of VO_x depleted area, surrounded by the VO_x enriched area on which oxidation (bright) and reduction fronts (dark) are propagating. A bright oxidation front propagates across the VO_x depleted area. Subsequently, a reduction front removed the oxidized state. b) μLEED images recorded during the propagation of oxidation and reduction fronts on the VO_x depleted hole, showing diffraction images of the reduced (first three images) and oxidized state (last image) of the VO_x depleted hole. The LEEM images are acquired at a start voltage of 1.6 eV, the LEED images at 40 eV. The reaction atmosphere contained 1.1×10^{-4} mbar methanol and 0.5×10^{-5} mbar oxygen.

The expansion happens on both, the VO_x depleted hole and the VO_x rich surroundings.

The different LEED pattern, that can be observed on the VO_x depleted hole during the transition from the reduced into the oxidized state are shown in figure 6.42b. The first LEED image is taken directly after a reduction front moved across the probed area. It shows the (1×1) diffraction pattern, of the probably mostly adsorbate free $\text{Rh}(110)$ surface. Then, first a $c(2 \times 2)$ evolves, to which later faint spots of a (1×2) are superimposed. Shortly after the additional (1×2) diffraction spots appear, the surface

is transformed into the oxidized state, characterized by a $c(2 \times 8)$ superstructure of adsorbed oxygen.

The series of LEED patterns during the propagation of oxidation and reduction fronts is very similar to the LEED structures observed on the unpromoted and 0.1 MLE VO_x covered surfaces in the range of double metastability close to the equistability point. On such a surface traveling interface modulations are observed. This similarity corroborates the assignment of VO_x depleted area to the elongated stripe in the LEEM images in figure 6.42.

6.8 Ex situ SPELEEM measurements after the reactive phase separation

The original motivation to use SPELEEM was that the “spectromicroscopic” techniques available at Elettra can be used for an in situ chemical and structural characterization of the chemical wave patterns. SPELEEM should thus help to obtain a mechanistic understanding of this complex system. Unfortunately, this plan does not work since SPELEEM is restricted to a pressure range below 10^{-5} mbar, whereas the chemical wave patterns only show up at a pressure higher than 1×10^{-4} mbar. The way out of this was to use SPELEEM as an ex situ technique for structures prepared in a high pressure chamber in the 10^{-4} mbar range. An in situ characterization of chemical wave pattern is not feasible in this way, but one should be able to characterize the surface after reactive phase separation [71, 245].

In order to redistribute VO_x a Rh(110) surface homogeneously covered with 0.4 MLE of vanadium oxide is heated to approximately 1000 K for 30 min in a reaction atmosphere consisting of 1×10^{-4} mbar methanol and 1×10^{-4} mbar oxygen (oxidizing reaction conditions). The reaction conditions are applied in a separate high pressure reaction cell, since SPELEEM can only be operated up to a pressure of 1×10^{-6} mbar, in order to avoid contamination of the beamline optics. Transfer between the microscope chamber and the high pressure cell is possible without breaking the vacuum. However, the sample has to be cooled down to 470 K and the reaction gases have to be pumped off for the transfer. The ex situ XPEEM and LEEM characterization is performed at 370 K in an oxygen atmosphere of 2×10^{-7} mbar to reduce beam damage effects.

LEEM and XPEEM images recorded after exposure of the $\text{VO}_x/\text{Rh}(110)$ surface to reaction conditions are depicted in figure 6.43. A reaction-induced redistribution resulted in macroscopic, VO_x depleted and VO_x enriched areas, as can be seen in the three LEEM images in figure 6.43. Different from the in situ experiments presented in the preceding sections, no closed VO_x film is found. Instead, the vanadium oxide covered area seems to consist of a large number of several hundred nanometers large, dark VO_x islands. The different morphology may be a consequence of the cooling process associated with the sample transfer from the high pressure reaction cell to the microscope chamber.

The assignment of VO_x to the dark islands is based on the XPEEM images shown in the bottom part of figure 6.43. By comparing the three XPEEM images with the central LEEM image (all have a $10 \mu\text{m}$ field of view and are recorded on the same position), one

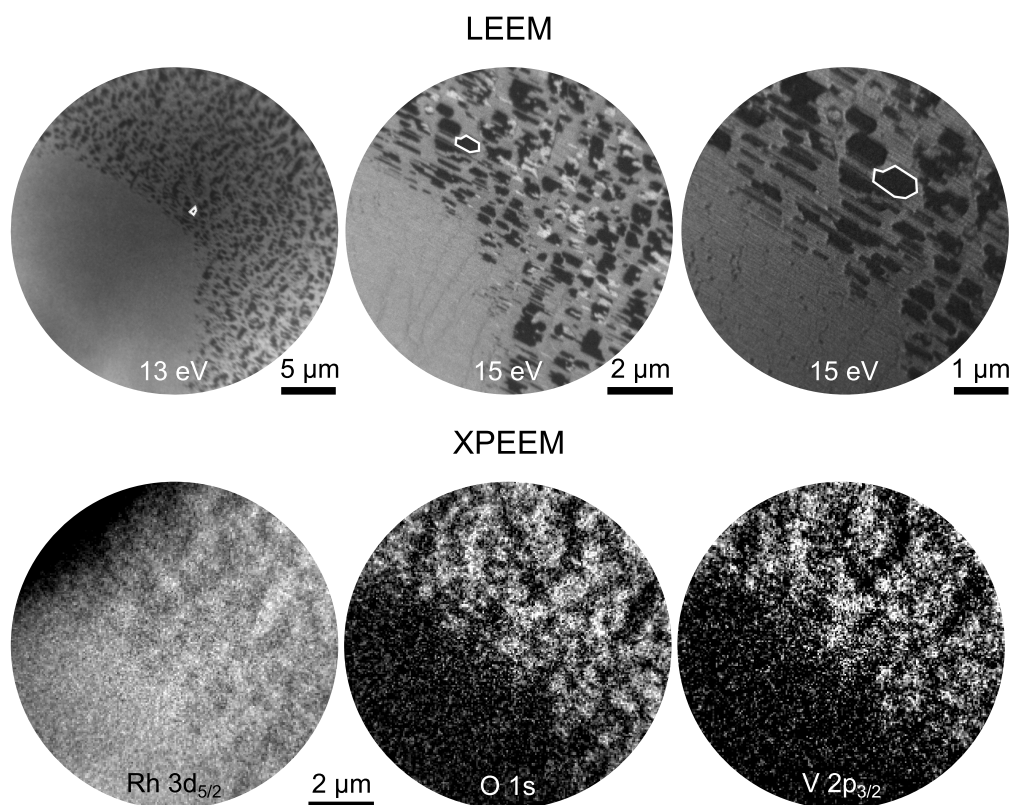


Figure 6.43: LEEM (top) and XPEEM (bottom) images recorded after the reactive phase separation of 0.4 MLE VO_x on Rh(110). The LEEM images demonstrate, that exposure of the sample to catalytic methanol oxidation in the 10^{-4} mbar range resulted in a phase separation into VO_x depleted (left side) and VO_x enriched (right side) areas. The corresponding Rh $3d_{5/2}$, O $1s$ and V $2p_{3/2}$ XPEEM images are shown in the bottom part of the figure. The images are acquired at 370 K in 2×10^{-7} mbar oxygen. The initial VO_x coverage is 0.4 MLE. Reproduced in part with permission from *J. Phys. Chem. C* **2018**, *122*, 10482 – 10488. Copyright 2018 American Chemical Society. Figure adapted from [71].

sees a slight attenuation of the Rh $3d_{5/2}$ intensity together with O $1s$ and V $2p_{3/2}$ intensity in the areas covered by the dark islands. A decomposition of the XPEEM data shown in figure 6.44 into components reveals, that also outside the dark VO_x islands on the VO_x depleted areas a substantial concentration of vanadium and oxygen exists. This indicates, that no complete phase separation takes place, even not after 30 min under reaction conditions at 1000 K. The spectrum of the VO_x depleted area is extracted from the whole vanadium and oxygen poor region visible in the second and third XPEEM image of figure 6.43, whereas the spectrum of the VO_x enriched areas is extracted from all visible VO_x islands.

From a numerical integration of the background-corrected V $2p_{3/2}$ and O $1s$ core levels,

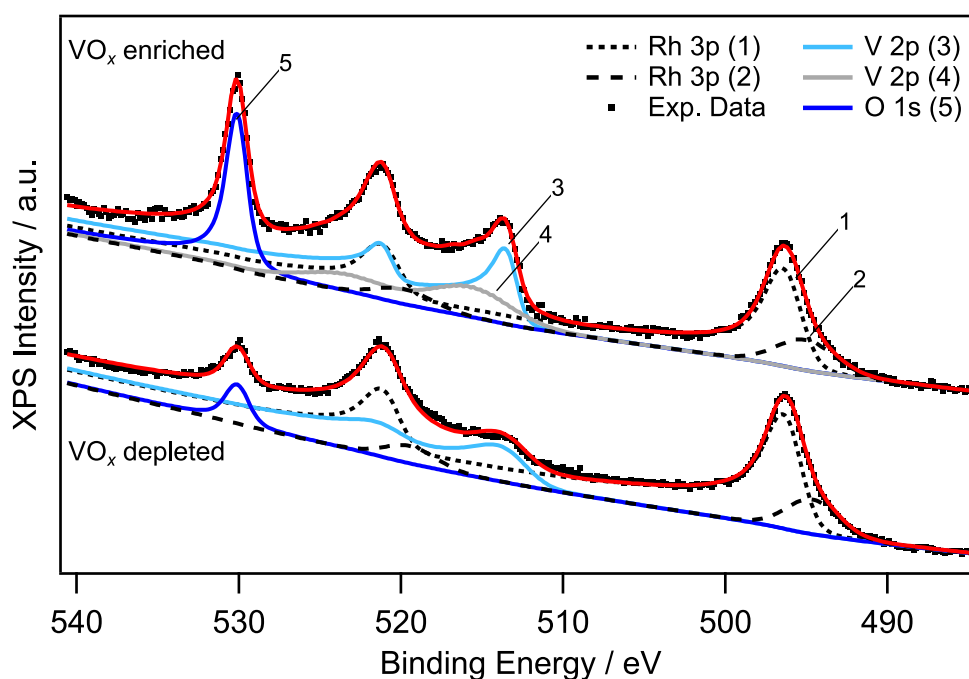


Figure 6.44: Ex situ XP spectra taken on vanadium oxide enriched and VO_x depleted areas present after reactive phase separation of VO_x on Rh(110). The spectra are extracted from the XPEEM measurements depicted in figure 6.43. The arabic numbers refer to the core levels of Rh, V and O. The binding energies determined on the VO_x enriched area are 530.0 eV for O 1s, 515.5 eV and 513.0 eV for V $2p_{3/2}$, and 496.0 eV and 495.0 eV for Rh $3p_{3/2}$. The corresponding values for the VO_x depleted area are 530.1 eV for O 1s, 513.0 eV for V $2p_{3/2}$, and 496.0 eV and 494.6 eV for Rh $3p_{3/2}$. In both cases, the Rh $3d_{5/2}$ core level is measured to 307.3 eV binding energy. All values are referenced to the Fermi edge, measured separately. Reproduced in part with permission from *J. Phys. Chem. C* **2018**, *122*, 10482 – 10488. Copyright 2018 American Chemical Society. Figure adapted from [71].

an enrichment factor of 7 and 3.4 is calculated for vanadium and oxygen, respectively. The V 2p core level is fitted with a single component in the case of the VO_x depleted surface, yielding a binding energy of 513.0 eV. This value is between the binding energy of metallic V (512.2 eV, [262]), and that of vanadium in the so-called “wagon wheel” structure (513.2 eV) of VO_x on Rh(111), to which an oxidation state of +2 was assigned [55]. The oxygen to vanadium ratio, calculated from the O 1s/V 2p peak ratio using equation 2.5, amounts to only 0.3. The low binding energy of vanadium, together with the low oxygen to vanadium ratio indicates, that V is present in a low oxidation state or possibly alloyed with the Rh surface. From the experimental data it cannot be clearly identified whether the measured oxygen signal is due to V being present as an oxide or due to adsorbed oxygen from the 2×10^{-7} mbar oxygen atmosphere maintained to reduce beam damage effects.

In the spectrum acquired on the VO_x enriched surface, the V 2p core level is fitted with two components, peaking at 513.0 and 515.5 eV. The high binding energy component corresponds to V in the oxidation state +3. Binding energies reported for vanadium +3 bulk oxides lay in the range between 515.2 and 515.9 eV [258, 260, 261]. The oxygen to vanadium ratio is calculated to be 0.8. The coexistence of a high and a low-binding energy component in the V 2p signal, together with the small O/V ratio and the low Rh attenuation on the VO_x covered regions leads to the interpretation, that pattern formation on VO_x/Rh(110) involves alloying of V with the substrate Rh. Probably also the population of Rh subsurface sites with V atoms occurs. According to Piš et al., temperatures above 820 K are needed for bulk diffusion of vanadium into Rh(110), if annealing is carried out in vacuum [188].

Further structural information is obtained from another experiment, in which 0.8 MLE of VO_x on Rh(110) are exposed for 30 min to the conditions of catalytic methanol oxidation with an oxygen pressure of 1×10^{-4} mbar and a methanol pressure of 3×10^{-4} mbar at 1000 K in the high pressure reaction cell. An overview of the surface, composed of different LEEM images, and LEED measurements recorded ex situ after the catalytic reaction are shown in figure 6.45a and b, respectively. The overview image in figure 6.45a shows a central stripe of medium LEEM intensity marked by a **4**, which is separated by two bright stripes marked by a **2** from the surrounding surface, which has a low LEEM intensity at the chosen start voltage of 44 eV, and which is marked by a **1**. A closed vanadium oxide film in the form of a macroscopic vanadium oxide island, with a substructure consisting of an inner core and an outer ring, is obtained.

This result is in contrast to the VO_x distribution pattern obtained after 0.4 MLE VO_x are exposed to reaction conditions, where the VO_x rich phase consisted of small islands of 0.1 to 1 μm size, as shown in figure 6.43. The formation of a coherent vanadium oxide island is also somehow in contrast to the in situ LEEM experiments presented in the preceding section, where a hole pattern formed.

Based on the LEED images shown in figure 6.45b, an assignment of the different grey levels in LEEM to surface structures is possible. The dark area marked with a **1** exhibits a (1×1) diffraction pattern and is therefore assigned to the bare Rh(110) surface. The bright stripe marked by a **2** is characterized by a (1×2) , whereas the central region, phase **4**, has a (4×2) or (4×1) diffraction pattern. Additionally, a very thin boundary phase **3** between phases **4** and **2** can be identified, which shows a (2×2) LEED pattern. The (4×2) and (1×2) are both LEED pattern, that are also observed during catalytic methanol oxidation around 800 K.

6.9 Discussion of chemical wave patterns on Rh(110) and VO_x/Rh(110)

Surface reactions exhibit a large variety of different non-linear phenomena, including chemical wave patterns and reaction rate oscillations. Most of the wave phenomena / rate oscillations could be reproduced with well established mathematical models, that were based on experimentally verified mechanisms: in catalytic CO oxidation on Pt the “phase

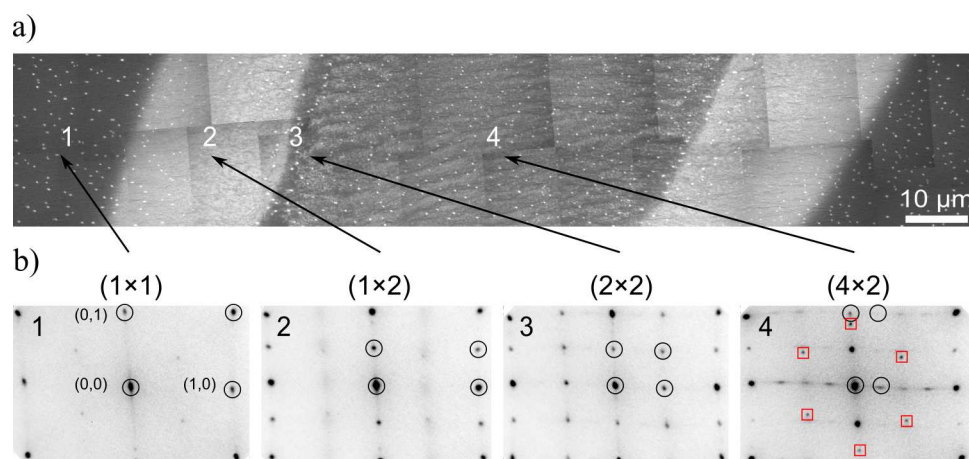


Figure 6.45: Ex situ LEEM and LEED measurements on a macroscopic VO_x island obtained after catalytic methanol oxidation in the 10⁻⁴ mbar range on Rh(110). a) Overview image composed of several LEEM images recorded at 44 eV, showing a cross section through a macroscopic VO_x island. Four different phases, marked by arabic numbers 1 - 4, can be distinguished by their intensity levels. b) μLEED images taken on the four different phases at 40 eV (phase 1), 48 eV (phases 2 and 3), and 44 eV (phase 4). The initial VO_x coverage is 0.8 MLE and the measurements are conducted in vacuum at room temperature. Reproduced in part with permission from *J. Phys. Chem. C* **2018**, *122*, 10482 – 10488. Copyright 2018 American Chemical Society. Figure (part b) adapted from [71].

transition” model at low pressure / “oxide” model at high pressure ($\geq 10^{-3}$ mbar), in catalytic CO oxidation on Pd the “subsurface oxygen” model, for NO-reducing reactions on Pt the “vacancy” model, and for the NO + H₂ reaction on Rh(110) the “repulsive-interaction” model. An overview of the models can be found in reference [254], for details please refer to the literature cited in [254]. Methanol oxidation on VO_x/Rh(110) differs from all of the above mentioned systems in so far, as it is structurally and chemically much more complex. For this reason, here no excitation / oscillation mechanism for methanol oxidation on VO_x/Rh(110) is presented, but an overview of the different phenomena and of the results obtained with different surface analysis techniques is given. The different non-linear phenomena observed on VO_x/Rh(110) in this study are summarized in table 6.1. In the following we distinguish between wave patterns on a surface that is macroscopically ($\geq 1 \mu\text{m}$) homogeneous and wave patterns on a surface that exhibits macroscopic islands/holes.

6.9.1 Chemical wave pattern on the homogeneous surface

The dynamics observed during catalytic methanol oxidation on vanadium oxide covered Rh(110) surfaces are very complex and depend on a number of factors, among which the temperature and the VO_x coverage are the most important ones. At a low VO_x

Table 6.1: Non-linear phenomena observed during methanol oxidation on Rh(110) and VO_x/Rh(110).

$\theta_{\text{VO}_x} /$ MLE	$p(\text{CH}_3\text{OH}), p(\text{O}_2) /$ mbar, T / K	Phenomena	LEED patterns	Analytical technique
0	$2.8 \times 10^{-4}, 1.0 \times 10^{-4}, 830$	Traveling interface modulations	-	PEEM
0	$6.7 \times 10^{-5}, 1.3 \times 10^{-5}, 885$	Traveling interface modulations	$(1 \times 1) - c(2 \times 2) - (1 \times 2) - c(2 \times 6) - c(2 \times 8)$	LEEM
0.1	$3.0 \times 10^{-4}, 0.8 \times 10^{-4}, 820$	Traveling interface modulations	-	PEEM
0.1	$9.3 \times 10^{-5}, 2.9 \times 10^{-5}, 840$	Traveling interface modulations	$(1 \times 1) - c(2 \times 2)^* - (1 \times 2) - c(2 \times 6) - c(2 \times 8)$	LEEM, * $c(2 \times 2)$ weak or absent
0.2	$1.1 \times 10^{-4}, 1.2 \times 10^{-5}, 770 - 850$	Target pattern	$(1 \times 1) - c(2 \times 2) - (1 \times 2) - c(2 \times 8) - (1 \times 2)$	770 K: LEED $(1 \times 1) - (1 \times 2) - c(2 \times 8)$
0.4	$3.0 \times 10^{-4}, 1.0 \times 10^{-4}, 790$	Traveling wave fragments	-	PEEM, refractory state, oscillating surface defect involved
0.4	$1.1 \times 10^{-4}, 1.3 \times 10^{-5}, 830$	Traveling wave fragments	$(1 \times 1) - (1 \times 2) - (1 \times 2) + c(2 \times 2) - (1 \times 2) + \text{streaks}, (1 \times 4) - (1 \times 2)$	LEEM
0.4	$3.0 \times 10^{-4}, 1.0 \times 10^{-4}, 1020$	VO _x redistribution: island pattern or dendritic growth	-	PEEM
0.4	$1.1 \times 10^{-4}, 2.6 \times 10^{-5}, 1000$	VO _x redistribution: hole pattern	$(4 \times 2), (3 \times 2)$ (islands); $(1 \times 2), c(2 \times 6), c(2 \times 8)$ (holes)	LEEM; LEED at 850 K
0.4	$3.0 \times 10^{-4}, 1.0 \times 10^{-4}, 830$	Traveling wave fragments (islands and surroundings)	-	PEEM
0.4	$1.1 \times 10^{-5}, 0.9 \times 10^{-5}, 810$	Target pattern (surroundings)	$(1 \times 2) - (1 \times 2)$ with streaks	LEEM
0.4	$1.1 \times 10^{-5}, 0.9 \times 10^{-5}, 790$	Target pattern (surroundings), traveling wave fragments (holes)	$(1 \times 2) - (1 \times 2)$ with streaks (surroundings); $(1 \times 1) - c(2 \times 2) - c(2 \times 2) + (1 \times 2) - c(2 \times 8)$ (holes)	LEEM

coverage around 0.1 MLE the reaction system is bistable, but with traveling interface modulations an interesting type of behavior is seen. A mathematical model based on a defect generation mechanism (section 6.3.6) has been proposed by A. Makeev and R. Imbihl, that reproduces well the experimental observations [196]. At higher VO_x coverage, on 0.2 MLE and 0.4 MLE thick VO_x films, target pattern are observed between 770 and 850 K, that are characteristic for excitable and oscillatory media. Such patterns may, however, also occur in bistable media, provided that a parameter range of double metastability is present. At a slightly higher temperature of 820 K, traveling wave fragments can be recorded with LEEM on 0.4 MLE VO_x. In PEEM such wave fragments can be seen in a wide parameter range at the same VO_x coverage of 0.4 MLE. The existence of traveling wave fragments was shown to be linked to a state-dependent anisotropy [292]. With the numerous reconstructions that exist in this system, a requirement is probably fulfilled.

The series of LEED pattern that can be observed in target pattern with 0.2 MLE VO_x is very similar to the LEED sequence observed during propagation of traveling interface modulations with only 0.1 MLE vanadium oxide. For the traveling interface modulations, a (1 × 1) together with a slowly developing c(2 × 2) is observed during a reduction state. An oxidation pulse consists of a (1 × 2), followed by a c(2 × 6), finally resulting in a c(2 × 8). In target pattern, also the (1 × 1) together with a slowly developing c(2 × 2) is observed. However, the existence and intensity of the c(2 × 2) is depending on temperature. The (1 × 2) phase is interpreted as 0.5 ML of oxygen adsorbed on the (1 × 2) reconstructed Rh(110) surface [271]. The overlayer structures in this V coverage range are thus either related to oxygen ((1 × 2), c(2 × 6), c(2 × 8)), or caused by atomic carbon (c(2 × 2)). No overlayer structure of VO_x on Rh(110) is seen.

Upon further increasing the vanadium oxide coverage to 0.4 MLE, traveling wave fragments are observed in LEEM and PEEM around 800 K. Interestingly, different LEED patterns are observed during the propagation of traveling wave fragments. The c(2 × 6) and c(2 × 8) structures of adsorbed oxygen are absent. The reduced state exhibits the following sequence of LEED structures: (1 × 1) → (1 × 2) → (1 × 2) + c(2 × 2) + streaks around the integral order diffraction spots. Upon transition into the oxidized state, first the c(2 × 2) disappears, and shortly afterwards the (1 × 2) transformed into a (1 × 4). The reduced state is attained again via the transition from the (1 × 4) over a (1 × 2) into the (1 × 1). A (1 × 2) structure is formed in the reduced state. This is surprising since it appears in the other experiments only in the oxidized state. The (1 × 2) is therefore interpreted as generated by adsorbed oxygen on the reconstructed Rh(110) surface. Two different (1 × 2) structures, one with oxygen and one without oxygen, must therefore exist. A scheme illustrating the sequence of LEED structures is given in figure 6.31b.

A (1 × 2) structure was also found upon diffusion of V into the subsurface region of a Rh(110) crystal upon vacuum annealing above 973 K [188]. The (1 × 2) was attributed to a missing row reconstruction of the Rh(110) surface, caused by the electronic interaction of surface Rh atoms with vanadium atoms in the second subsurface layer. An XPS characterization of vanadium oxide films on Rh(110) conducted in this study indicates

the existence of low oxidation state V or V alloyed with the Rh surface. However, vacuum annealing of V on Rh(110) at 923 K resulted in a (2 × 1) structure [188], which is not seen in our experiments. Nevertheless, the formation of a (sub)surface V/Rh alloy should not completely ruled out. The different adsorption properties and catalytic activity of such a V/Rh surface alloy might be important for an excitation mechanism.

6.9.2 Reaction-induced VO_x redistribution at 1000 K

If the VO_x covered surface is heated to 1000 K under reaction conditions, a redistribution of VO_x into a macroscopic island pattern can be observed. Under different conditions, holes of low VO_x concentration are found. The assignment to VO_x rich and VO_x depleted areas in PEEM is based on indirect arguments, since neither direct chemical nor structural information is available from PEEM, and in situ experiments with “spectro-microscopic” techniques are not possible in the 10⁻⁴ mbar range. The situation becomes more complicated because, first of all, ex situ XPS experiments demonstrate an incomplete phase separation into vanadium oxide enriched and depleted area. Secondly, bulk diffusion of V is encountered.

The number of different redistribution pattern that can occur upon exposure of a homogeneous VO_x film on Rh(110) to the conditions of catalytic methanol oxidation around 1000 K demonstrate the complexity of the redistribution process. Different from the VO_x redistribution on Rh(111) under similar conditions, surface alloying of V and Rh might play an important role. Also the mobility of VO_x is lower on the corrugated Rh(110) surface, compared to the flat Rh(111) surface. The situation is further complicated by the bistability, which is still present at around 1000 K. The VO_x redistribution can occur in the oxidized state, as well as in the reduced state. Exposure of VO_x on Rh(110) to 1000 K to strongly reducing conditions results in the diffusion of V into the Rh bulk and no redistribution pattern can be observed. Due to the absence of considerable catalytic activity of VO_x on Rh(110), the development of macroscopic oxygen gradients, causing a phase separation into oxidized and reduced VO_x phases within an island, is therefore unlikely.

6.9.3 Chemical waves on patterned VO_x/Rh(110) surfaces

If a VO_x/Rh(110) surface exhibiting an island or hole pattern is cooled down from 1000 K to around 800 K under reaction conditions, chemical wave patterns are observed. Target pattern and spiral wave like structures, as well as traveling wave fragments occur either on the VO_x rich or depleted areas, or on both simultaneously. The traveling wave fragments can be explained as an result of double metastability, since oxidation and reduction fronts are simultaneously stable.

In the PEEM and LEEM experiments, the interface between the VO_x rich and depleted area plays an important role in pattern formation. Oxidation fronts often nucleate at the interface, or get pinned as soon as they get in contact with it. This behavior can lead to the formation of a spiral waves, with the hole being the center around which pulses rotate. At 810 K the spiral waves are very regular and have a period of 35 s. In-

terestingly, in LEEM no propagation of chemical waves is observed on the VO_x depleted areas, which is in contrast to the above described PEEM experiments.

Initially, the VO_x enriched area exhibits a (4×2) diffraction pattern, which transforms into a (1×2) pattern, as the parameter range in which chemical wave patterns can be observed is approached. The LEED patterns observed in target pattern on the patterned VO_x/Rh(110) surface differ dramatically from the LEED sequences recorded during chemical wave pattern on the homogeneously VO_x covered surface. The propagation of oxidation and reduction fronts on the VO_x enriched surroundings of VO_x depleted holes causes the transition between a simple (1×2) LEED pattern, and a (1×2) together with streaky intensity elongated in the [001] direction. The (1×2) without streaky features is attributed to the reduced state, the (1×2) with streaky intensity in the [001]-direction to the oxidized state.

The deposition of metallic V on the Rh(110) substrate at 600 K results in a (1×2) LEED pattern between 0.2 and 1.0 MLE. Therefore, also a surface phase of metallic V on Rh(110) can be involved in the pattern formation. The interpretation of V stabilizing a (1×2) reconstructed Rh(110) surface even in the absence of adsorbed oxygen implies, that V diffuses into the subsurface region of Rh(110). The (4×2) present before pattern forming conditions are adjusted, however, is a vanadium oxide structure (figure 6.1). If vanadium is located in the subsurface sites during pattern formation, it has to diffuse there during the initiation of chemical waves. This process might take place as the (4×2) vanishes during adjusting less oxidizing conditions.

A further temperature decrease to 790 K strongly reduces the regularity of the target pattern, to an extent that one could probably classify it as a chaotic pattern. At the same time, the nucleation and propagation of traveling wave fragments can be observed on the VO_x depleted holes. However, the classification as traveling wave fragments is not as clear as in the case of the PEEM experiments, since the simultaneous propagation of oxidation and reduction fronts is not observed. In a first step, an oxidation front turns the VO_x depleted hole into the oxidized state. Subsequently, a reduction front turns the oxidized state into a refractory state, on which no further oxidation fronts can propagate for a period of tens of seconds to minutes. The fact, that the simultaneous propagation of oxidation and reduction fronts is not observed can also be a consequence of the small size of the holes, which is only about 10 μm. Probably, the time needed for an oxidation front to turn the whole VO_x depleted area into the oxidized state is simply too short for the nucleation of a subsequent reduction front. For a reduction front followed by an oxidation front LEED measurements conducted on the VO_x depleted area reveal a (1×1) → c(2×2) → (1×2) + c(2×2) → c(2×8) sequence. This LEED sequence is similar to that observed for a 0.2 MLE VO_x covered surface, where in addition also a c(2×6) as an intermediate phase is present before the c(2×8) develops.

If we take catalytic CO oxidation on Pt(100) and Pt(110) as an example for a reconstruction-driven oscillation mechanism, then the core of the mechanism lies in the different catalytic activity of the (1×1) and the reconstructed phases. In the system VO_x/Rh(110) different reconstruction phases exist, but practically nothing is known about their different catalytic activity. An even more basic problem is, that no struc-

tural models for the different VO_x phases exist. A third and very difficult to solve problem is the possible participation of vanadium in subsurface sites of the Rh(110) crystal.

What is achieved in this study is to demonstrate that a plethora of different chemical wave patterns and of reaction-induced redistribution structures exist in methanol oxidation on $\text{VO}_x/\text{Rh}(110)$. This is also the first time, to our best knowledge, that chemical wave patterns on supported oxide catalysts are observed. Interestingly, the dynamics of the reaction system are quite different on Rh(110) and Rh(111). With respect to the catalytic activity, the basic difference is that VO_x on Rh(111) is much more active than VO_x on Rh(110). This is probably a consequence of the flat and thermodynamically stable Rh(111) surface stabilizing VO_x structural units with a high oxidation state of vanadium, i. e. vanadyl species. These vanadyl species might be missing on the more open Rh(110) surface, which might be the reason for the lower catalytic activity of $\text{VO}_x/\text{Rh}(110)$. This hypothesis needs to be checked in future experiments. With respect to pattern formation one can conclude, that most of the activity probably stems from the metallic Rh(110) surface with VO_x probably only modulating that activity.

6.10 Conclusion

Catalytic methanol oxidation over a VO_x covered Rh(110) surface represents a bistable system in a wide temperature range starting from roughly 680 K in the 10^{-4} mbar range up to 1000 K. The existence of double metastability is responsible for the existence of chemical wave pattern, including traveling interface modulations, traveling wave fragments, and target patterns. Traveling wave fragments are observed also on the unpromoted Rh(110) surface and on a 0.1 MLE covered Rh(110) surface during methanol oxidation in the 10^{-5} and 10^{-4} mbar range with PEEM and LEEM. The occurrence of traveling interface modulations in different surface reactions proved that a more general mechanism has to exist, explaining the excitation localized to the interface between the two stable states. The traveling interface modulations were explained with a mathematical model [196] that is based on the reversible formation of structural defects at the interface.

The reduced surface state of the bistable system is catalytically more active, than the oxidized state. Interestingly, only negligible catalytic activity in the formation of formaldehyde is found. This finding is in strong contrast to ultrathin layers on Rh(111), on which a reaction induced redistribution is accompanied by a considerable formaldehyde production. On a tentative basis, the absence of substantial amounts of formaldehyde within the reaction products is explained by the absence of vanadyl groups in the VO_x films on Rh(110). However, since no structural identification of the different surface phases of VO_x on Rh(110) exists, this interpretation needs to be experimentally confirmed.

The observation, that the passage of traveling interface pulses leaves a slowly decaying area of high PEEM intensity inspired the formulation of a defect generation mechanism. Transition between the unreconstructed (1×1) surface and oxygen induced

reconstructions of the missing-row type during the transition between the oxidized and reduced surface state result in the reversible formation of surface defects. A positive feedback between the generation of such defects and adsorbate fluctuations of the interface results in the formation and propagation of traveling interface pulses. The defect formation mechanism is further corroborated by in situ LEEM/LEED measurements, which exhibited very fast structural transition under reaction conditions.

At higher VO_x coverages up to 0.4 MLE, more complex chemical wave pattern including target pattern and traveling wave fragments can be observed. The existence of traveling wave fragments is characteristic of a region of double metastability, and of a so-called state-dependent anisotropy, i. e. of an anisotropy that varies depending on the surface reconstruction. In situ LEED measurements revealed a sequence of diffraction patterns during target patterns, which is similar to that observed during the propagation of traveling interface modulations at 0.1 MLE VO_x .

Exposure of the homogeneous VO_x films on Rh(110) to oxidizing reaction conditions around 1000 K leads to the formation of either a macroscopic VO_x island pattern, or to a pattern of several tens of μm large VO_x depleted holes surrounded by VO_x enriched surface, depending on the conditions. Ex situ studies demonstrate, that the phase separation into VO_x enriched and depleted areas is not complete, and that substantial V concentrations can also be found in the VO_x depleted areas. Furthermore, the existence of a low binding energy component in the V 2p spectra suggests the existence of V in a low oxidation state or even metallic state in which V is probably alloyed with the Rh surface. Under more reducing reaction conditions, V diffusion into the subsurface region or deeper layers of the Rh(110) surface results, and no redistribution pattern is formed on the surface.

Chemical wave patterns are observed on a $\text{VO}_x/\text{Rh}(110)$ surface with an island or hole pattern. On the VO_x enriched area surrounding the VO_x depleted holes target patterns are seen. Traveling wave fragments either on VO_x islands or on the VO_x depleted holes are observed, depending on the reaction conditions. Oxidation and reduction fronts tend to nucleate at the boundary of VO_x depleted and VO_x enriched area.

The system $\text{CH}_3\text{OH} + \text{O}_2/\text{VO}_x/\text{Rh}(110)$ exhibits a very complex non-linear behavior. For a further understanding of the elementary processes governing the chemical wave pattern and the catalytic activity on $\text{VO}_x/\text{Rh}(110)$ catalysts, the development of structural models, for example by combined STM and DFT studies, is essential. A big challenge is the pressure range of 10^{-5} and 10^{-4} mbar, which still makes the application of in situ imaging XPS techniques impossible. The successful development of a NAP-LEEM opens the path to a technique, that allows to use “spectromicroscopy” up to a pressure of 0.1 mbar in the near future.

Chapter 7

VO_x Redistribution on Pt(111)

Abstract Ultrathin vanadium oxide layers ($\theta_{\text{VO}_x} \leq 12 \text{ ML}$) are grown by reactive deposition onto the Pt(111) surface. As low coverage ($\theta_{\text{VO}_x} \leq 1 \text{ ML}$) phases a (2×2) structure and a structure of the Moiré type are identified. With multilayer thick VO_x films, a $(\sqrt{3} \times \sqrt{3})R30^\circ$ pattern appears in LEED, probably caused by the (0001) oriented surface of corundum V_2O_3 . Under reducing conditions VO_x gets reduced and V diffuses into the Pt bulk, starting at around 750 K. Exposure to 870 K and an oxygen pressure above 1×10^{-5} mbar leads to the diffusion of V back to the surface and the formation of a roughly 1 ML thick (2×2) VO_x phase. In contrast to the system $\text{VO}_x/\text{Rh}(111)$ no pattern formation can be observed in PEEM under the conditions of methanol oxidation in the 10^{-4} mbar range. Partially and completely VO_x covered Pt(111) surfaces are very unreactive in methanol oxidation in the 10^{-4} mbar range, even though the clean Pt(111) surface catalyzes CO_2 and formaldehyde production between 350 and 620 K.

One motivation of this thesis is to evaluate whether the polymerization / depolymerization mechanism, which explains the movement and coalescence of macroscopic vanadium oxide islands under reaction conditions, can be generalized to other reaction systems. Therefore, the behavior of ultrathin VO_x layers on Rh(111) is investigated in other oxidation reactions and with NO as the oxygen source instead of molecular oxygen. It turned out, that on $\text{VO}_x/\text{Rh}(111)$ also other oxidation reactions with O_2 display the same behavior as in methanol oxidation. However, with NO no island coalescence is seen. In a second step, the studies are extended to the Rh(110) surface, to investigate the influence of a more open, and thermodynamically less stable surface on the pattern formation. On Rh(110), ultrathin vanadium oxide layers form macroscopic islands under reaction conditions, similar to $\text{VO}_x/\text{Rh}(111)$. In addition, also chemical wave pattern are observed, related to the different oxygen induced reconstructions, that the Rh(110) surface can undergo.

The experiments on Pt(111) are conducted to investigate whether the formation, movement and coalescence of macroscopic vanadium oxide islands also happens on a non-reconstructing (111) oriented surface of another metal of the platinum group. The two surfaces, Rh(111) and Pt(111), however, differ strongly in their reactivity towards O_2 . The formation of oxygen gradients under reaction conditions is crucial for the VO_x pattern formation on Rh(111) during catalytic reactions. As evidenced by molecular beam experiments, the Pt(111) surface has with 0.06 at 300 K and 0.025 at 600 K a much lower oxygen sticking coefficient s_{O_2} [293] than the Rh(111) surface, where s_{O_2} varies between 0.1 and 0.9 at 300 K, depending on the primary energy of the incident oxygen beam [161]. Furthermore, catalytic reaction rate measurements during methanol oxidation on the VO_x covered and unpromoted Pt(111) surface are conducted. Some experiments on the growth of VO_x on Pt(111) are published in literature [184, 294, 295]. The results can be compared with the systems $TiO_x/Pt(111)$ [296–300], $VO_x/Pd(111)$ [301, 302], and $VO_x/Rh(111)$ [53, 55, 183], that have been extensively characterized with LEED, STM, DFT calculations and other methods.

7.1 VO_x deposition rate calibration

A combined LEED and AES calibration is applied in order to investigate the growth mode of VO_x on Pt(111). VO_x is deposited by reactive evaporation (a temperature of 670 K and an oxygen pressure of 2×10^{-7} mbar) in half minute steps up to a total deposition time of 5.5 min. Afterwards the deposition is continued in larger steps ranging between one and ten minutes. The results can be seen in the AS- t plot depicted in figure 7.1c. After every deposition step, the sample is kept at elevated temperature in oxygen for further ten minutes, before it is cooled to room temperature in oxygen for a characterization with AES and LEED in vacuum. The acquired Auger spectra are depicted in figure 7.1a and b, respectively. LEED images of the deposited VO_x film shown in figure 7.2 are recorded in vacuum after every deposition step.

The AS- t plot in figure 7.1c shows a linear increase of the $VL_{2,3}M_{2,3}M_{2,3}$ (V_{437}), $VL_{2,3}M_{2,3}M_{4,5}$ (V_{473}), $VL_{2,3}M_{4,5}M_{4,5}$ and $OKL_{2,3}L_{2,3}$ ($O+V_{510}$) peak intensities for the first 2.5 min deposition time. Simultaneously, the peak intensity of the Pt_{60} transition decreases linearly. At 2.5 min deposition time a change in the slope of the V and O, and Pt Auger intensities can clearly be recognized. Upon further VO_x deposition, the V and O peak intensities increase with a considerably lower rate than in the first 2.5 min.

The pronounced change in slope of the V, O, and Pt Auger signals, and the non-linear behavior after the initially linear increase (Pt signal decrease) are indications for a growth mode of the Stranski-Krastanow type under the conditions of reactive evaporation. The linear increase (Pt signal decrease) of the Auger intensities is caused by the formation of a closed monolayer of vanadium oxide on the Pt(111) surface during the first 2.5 min deposition time. Upon further VO_x dosage, the nucleation and growth of three-dimensional crystallites on the first, flat VO_x layer results in a lower signal increase (Pt signal decrease) in the AS- t plot. One can therefore assign one monolayer (ML) of VO_x to a deposition time of 2.5 min.

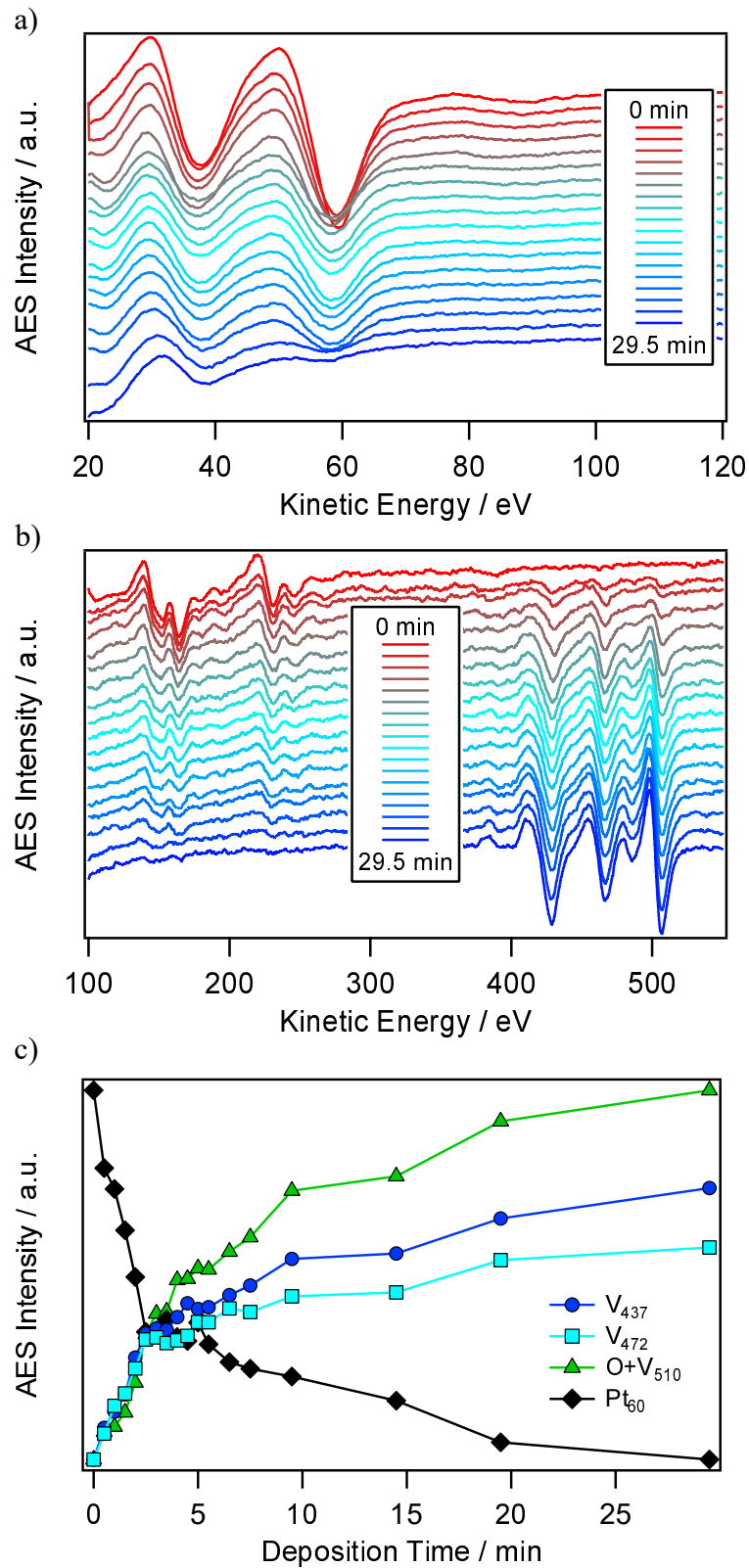


Figure 7.1: Deposition rate calibration obtained by AES. Acquired Pt (a) and vanadium (b) Auger spectra as a function of VO_x deposition time. c) AS-t plot of the $VL_{2,3}M_{2,3}M_{2,3}$ (V_{437}), $VL_{2,3}M_{2,3}M_{4,5}$ (V_{473}), $VL_{2,3}M_{4,5}M_{4,5}$ and $OKL_{2,3}L_{2,3}$ ($O+V_{510}$), and Pt_{60} intensities.

The LEED images in figure 7.2 support a Stranski-Krastanow growth mode. Up to a coverage of 1 ML, the formation of a diffuse Moiré-like LEED pattern is observed. Since the exact structure of the first layer of VO_x is not known, no V coverage in MLE (as in the preceding chapters, with 1 MLE being the same number of V atoms, as Pt atoms are present in the topmost Pt(111) layer) can be given.

Further deposition of more than 1 ML leads to the appearance of weak diffraction spots belonging to a $(\sqrt{3} \times \sqrt{3})R30^\circ$ structure, as can be seen in the third LEED image in figure 7.2. With increasing VO_x dosage, the $(\sqrt{3} \times \sqrt{3})R30^\circ$ diffraction spots become stronger and, starting after about 1.4 ML, additional spots of a (2×2) structure evolve. Interestingly, the sudden appearance of the (2×2) is neither followed by a considerable intensity increase, nor by a noticeable change of the spot shape upon further VO_x deposition. After the deposition of approximately 8 layers of VO_x , the (2×2) LEED pattern has nearly vanished again, while the $(\sqrt{3} \times \sqrt{3})R30^\circ$ pattern becomes sharper and stronger, until finally at around 12 ML almost only diffraction spots belonging to the latter structure are visible in LEED.

Presumably, the LEED images in figure 7.2 can be interpreted as follows: For a low V coverage, VO_x grows as a poorly ordered flat oxide, up to the point at which the first monolayer is completed. Subsequently, small crystallites of a vanadium oxide of $(\sqrt{3} \times \sqrt{3})R30^\circ$ structure nucleate and grow on top of the poorly ordered first layer. As further VO_x is deposited, either the first oxide layer orders and forms a (2×2) structure, or the growth of a (possibly flat) second VO_x phase on the areas not covered by the $(\sqrt{3} \times \sqrt{3})R30^\circ$ crystallites starts. Finally, after the deposition of a large amount of VO_x , only the most stable structure, the $(\sqrt{3} \times \sqrt{3})R30^\circ$ phase, is present on the surface.

7.2 VO_x redistribution on Pt(111) during catalytic methanol oxidation

The dynamics of ultrathin vanadium oxide layers on Pt(111) during catalytic methanol oxidation are investigated with PEEM in the 10^{-4} mbar range under oxidizing reaction conditions. In a first experiment, a freshly deposited VO_x film of 0.4 ML coverage has been heated within a few minutes to 870 K in an oxygen atmosphere of 1×10^{-4} mbar. As 870 K are reached, methanol is introduced in the 1×10^{-5} mbar range. Even though, the methanol pressure was varied between 1×10^{-5} and 1×10^{-4} , no pattern formation can be observed in PEEM. The only response to the change of the gas phase composition is a homogeneous increase or decrease of the PEEM intensity with increasing or decreasing methanol pressure. A temperature programmed reaction experiment (heating and cooling rate $\beta = 0.2 \text{ K s}^{-1}$ up to 1020 K) conducted on a roughly five layers thick vanadium oxide film in a gas atmosphere of 1×10^{-4} mbar methanol and 1×10^{-4} mbar oxygen does not result in any pattern formation in PEEM.

Interestingly, the initial diffuse $(\sqrt{3} \times \sqrt{3})R30^\circ$ LEED pattern, obtained after the reactive evaporation of vanadium oxide is transformed into a sharp (2×2) pattern during exposure to reaction conditions. The corresponding LEED images acquired before (first

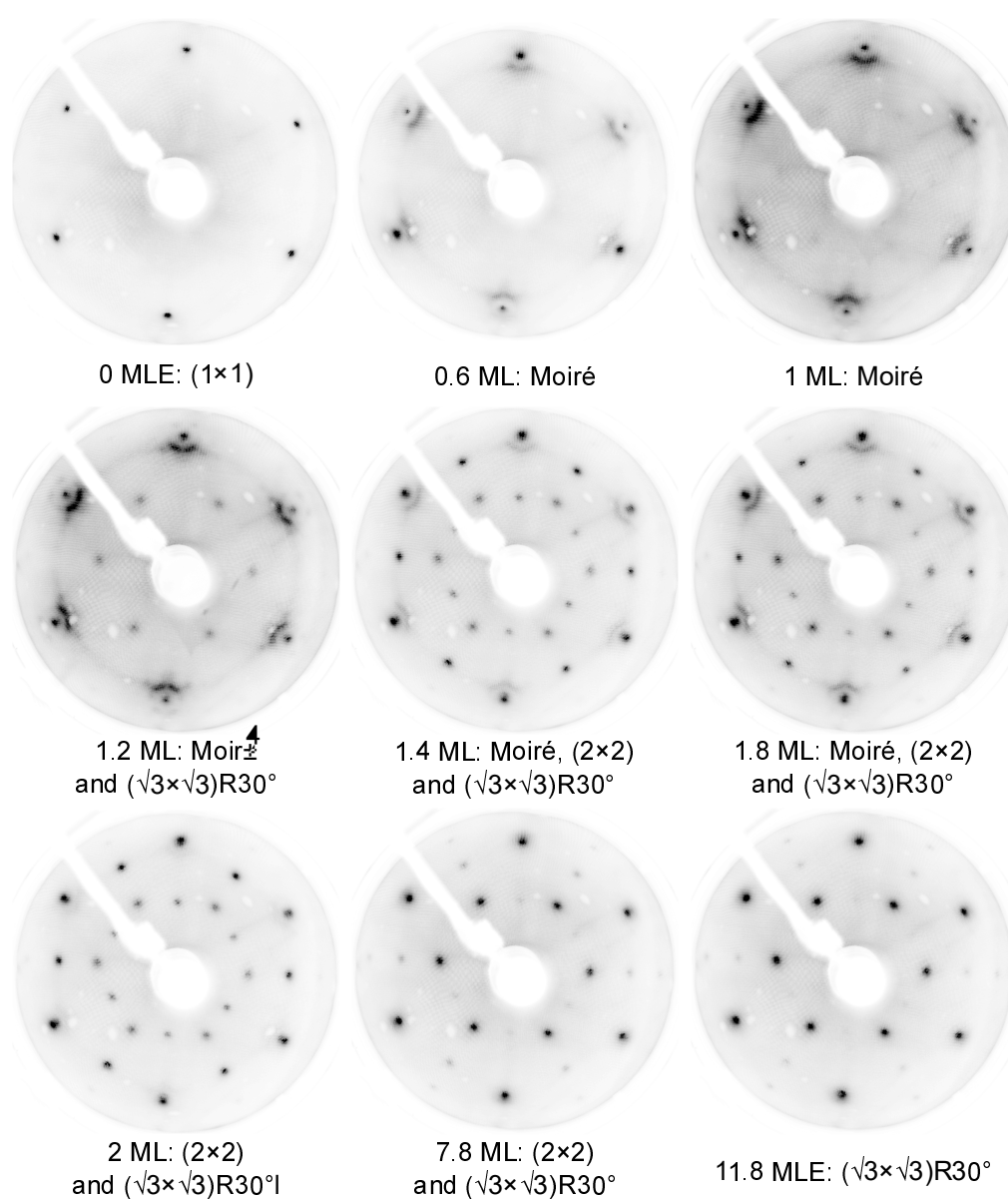


Figure 7.2: Vanadium oxide structures obtained during reactive evaporation on Pt(111) as a function of V coverage. VO_x was deposited in a step-wise manner (0.5 min steps up to 5.5 min, then larger time steps between one and ten minutes) at a sample temperature of 670 K in an oxygen atmosphere of 2×10^{-7} mbar. The LEED images are acquired at an electron energy of 65 eV at 300 K after the sample is further heated in oxygen for 10 min and cooled down in continuous oxygen flow after every deposition step.

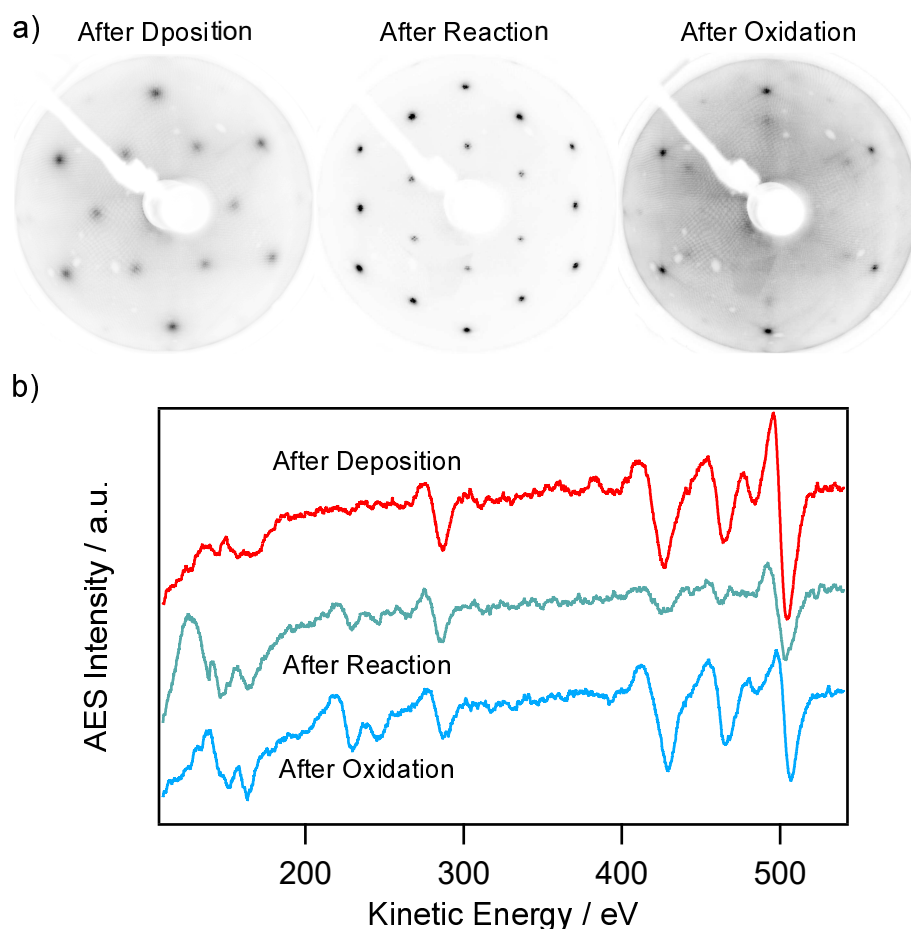


Figure 7.3: Structural transformation and segregation of a thick VO_x film on $\text{Pt}(111)$ upon methanol oxidation in the 10^{-4} mbar range. a) LEED images acquired after the reactive evaporation of roughly 5 ML of VO_x on $\text{Pt}(111)$ (left), after the application of a temperature programmed reaction experiment under oxidizing reaction conditions (0.2 K s^{-1} up to 1020 K) (middle), and after subsequent oxidation for 40 min at 870 K in 1×10^{-4} mbar oxygen. b) Auger spectra of the sample acquired together with the LEED images shown in (a).

image) and after exposure to the reaction (second image) are shown in figure 7.3a.

The $(\sqrt{3} \times \sqrt{3})R30^\circ$ is identified as a thermodynamically stable high coverage phase of VO_x on $\text{Pt}(111)$, since it is the only structure that remains on the surface if thick films (≥ 10 ML) are deposited at 670 K in 2×10^{-7} mbar oxygen. The (2×2) instead coexists with the $(\sqrt{3} \times \sqrt{3})R30^\circ$ only for a coverage between roughly one and ten monolayers. This leads to the assumption, that the presence of the reducing agent methanol and the high temperature of up to 1020 K results in diffusion of a part of vanadium into the Pt bulk.

This hypothesis is substantiated by the Auger spectra depicted in figure 7.3b acquired

after the deposition of VO_x , and after catalytic methanol oxidation. The 78% intensity decrease of the V_{437} Auger peak¹ upon exposure of VO_x to reaction conditions, clearly shows a loss of a considerable amount of V. The presence of the (2×2) pattern in LEED, and the still large peak at around 510 eV caused by Auger transitions of oxygen and vanadium, indicate that a part of V is still present on the surface as an oxide.

On the Rh(111) surface already low oxygen partial pressures in the 10^{-7} mbar range are known to stabilize vanadium at high temperatures up to 1000 K, preventing the diffusion of V into the bulk or the formation of a (sub)surface alloy. Accordingly, the VO_x /Pt(111) surface, after part of V has vanished, is subsequently oxidized for 40 min at 870 K and 1×10^{-4} mbar. The LEED pattern and the Auger spectrum acquired after the oxidation are depicted in figure 7.3a and b, respectively. A (1×1) LEED pattern with a large, diffuse background intensity and faint features close to the integer diffraction spots resulted. However, in similar experiments, in which V diffused back to the surface upon oxygen treatment, the surface exhibited a (2×2) pattern in LEED. The disorder in the LEED pattern in figure 7.3a might be a consequence of a considerable amount of carbon present on the surface, identified by the Auger peak at around 270 eV. This peak was absent in the other experiments, in which a (2×2) pattern appeared in LEED after O_2 exposure. In AES, nearly the complete V_{437} intensity is recovered upon the oxygen treatment.

7.2.1 Segregation behavior of vanadium oxide on Pt(111)

The above presented results clearly demonstrate the reversible diffusion of vanadium into the Pt bulk under reducing conditions, and back to the surface under oxidizing conditions. In order to further quantify the segregation behavior of V/ VO_x on Pt(111), temperature programmed AES measurements are performed in vacuum. Therefore, the VO_x /Pt(111) sample is heated in steps of 100 K starting from room temperature to 1020 K. Every 100 K an Auger spectrum is acquired over a period of 20 min, before the sample is heated to the next temperature within about two minutes. The resulting V_{437} , V_{472} , $V+O_{510}$ and Pt_{60} peak intensities as a function of sample temperature are depicted in figure 7.4.

For temperatures below 770 K no clear decrease in the V and O Auger signals can be seen in figure 7.4. Interestingly, the Pt_{60} intensity increases moderately already from the beginning of the measurement. A pronounced change in slope of the Pt_{60} and all V and O signals sets in, as the sample is at 870 K. This intensity decrease is taken as an indication for the diffusion of V into deeper layers of the Pt crystal. Finally, at 1020 K, more than 50% of the original V_{437} intensity is lost due to the migration of V into the bulk.

Auger spectra acquired at room temperature before and after the temperature programmed Auger experiment are depicted in figure 7.5, together with two more spectra taken after a second annealing step for 20 min at 1020 K in vacuum, and a subsequent

¹The V_{437} Auger transition is used to estimate the amount of V that has diffused into the Pt bulk, since it is neither influenced by the oxidation state of V, nor overlapping with the O KLL Auger transitions.

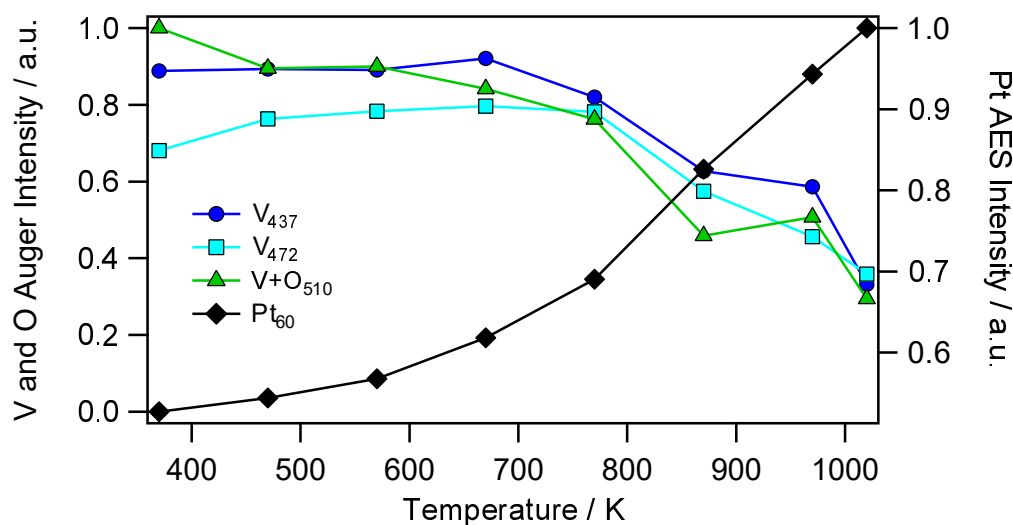


Figure 7.4: Segregation behavior of VO_x on Pt(111) monitored by temperature programmed AES measurements. Shown are the normalized Auger intensities, with the highest intensity of V (left axis) and Pt (right axis) set to unity. The VO_x sample obtained after exposure of roughly 10 ML to the conditions of catalytic methanol oxidation and subsequent 40 min oxidation in 1×10^{-4} mbar oxygen at 870 K was heated in vacuum in 100 K steps. At each step an Auger spectrum was acquired over a period of 20 min.

oxidation for further 40 min in 1×10^{-4} mbar oxygen at 870 K. The second UHV annealing step decreased the V_{437} intensity by another 57% so that only about 20% of the original value are present.

From the inelastic mean free path of an electron of 437 eV kinetic energy in the Pt bulk, one could in principle calculate the depth into which V has diffused from the signal attenuation, provided that all of the vanadium would reside in a single layer of well defined depth. In practice, V is distributed over several layers with part of the V still being on the surface. For this reason, no such analysis is conducted. However, the strong intensity decrease after the second annealing step is an evidence for a substantial diffusion depth over at least several layers, taking into account, that the initial deposited V coverage is around 5 ML.

As can be seen by comparing the last Auger spectrum depicted in figure 7.5 with the topmost spectrum acquired before the UHV annealing steps, nearly 90% of the V and O signal is restored upon oxidation for 40 min at 870 K and 1×10^{-4} mbar. Also the Auger peak intensity ratio of the two V Auger peaks at 437 and 472 eV, which is a measure of the oxidation state of V [85, 86], is identical in both measurements. The nearly identical V signal intensities present after the two oxygen treatments leads to the assumption, that V can only accumulate on the surface up to a certain threshold coverage as a response to oxygen exposure at high temperature.

In order to check this hypothesis, four Auger spectra acquired on four different VO_x

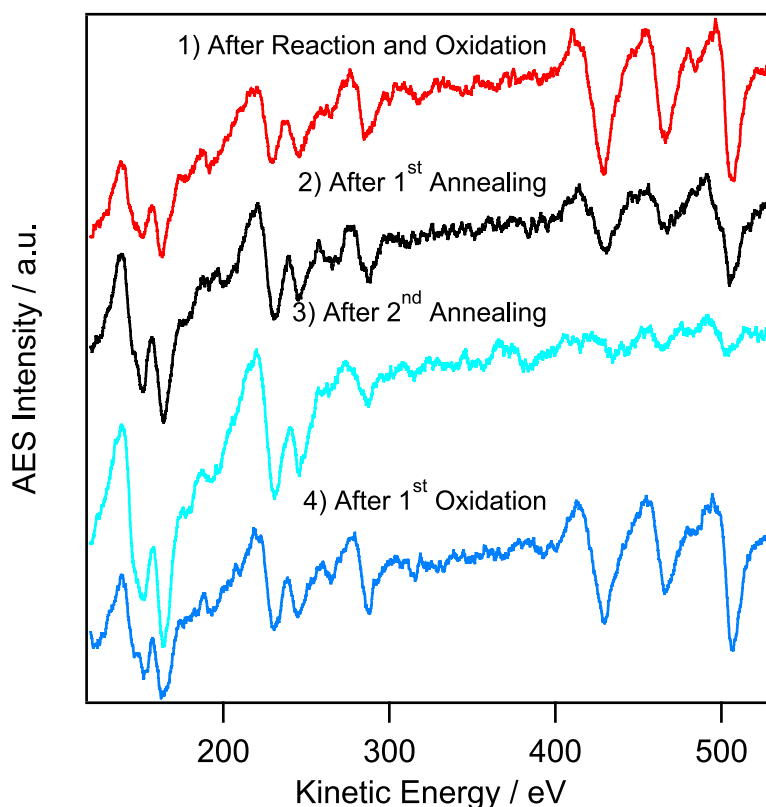


Figure 7.5: Auger spectra demonstrating the reversibility of V diffusion into the bulk and to the surface of $\text{Pt}(111)$ upon repeated UHV annealing and oxidation steps. The UHV annealing is carried out at 1020 K for 20 and 40 min, respectively. The oxygen treatment is conducted for 40 min at 870 K in 1×10^{-4} mbar.

films, which were exposed to different conditions (including Ar^+ ion sputtering in a regular cleaning cycle) before the oxidation at 870 K and 1×10^{-4} mbar is carried out, are displayed in figure 7.6 together with two Auger spectra acquired during the VO_x deposition rate calibration at 0.8 and 1.2 ML (section 7.1).

All four spectra show similar V_{437} peak intensities (the standard deviation is 15% of the mean value) and are similar to the reference spectra of 0.8 and 1.2 ML VO_x on $\text{Pt}(111)$. Despite the fact, that after the oxygen treatment V is not only present on the surface but most likely distributed over several layers of the $\text{Pt}(111)$ crystal, and that the formed VO_x (2×2) structure not necessarily has to exist as a flat oxide, the nearly identical Auger spectra apparent after the oxygen treatment suggest, that V segregates to the surface, forming an oxide, until a closed two-dimensional vanadium oxide phase has formed, which blocks further V segregation.

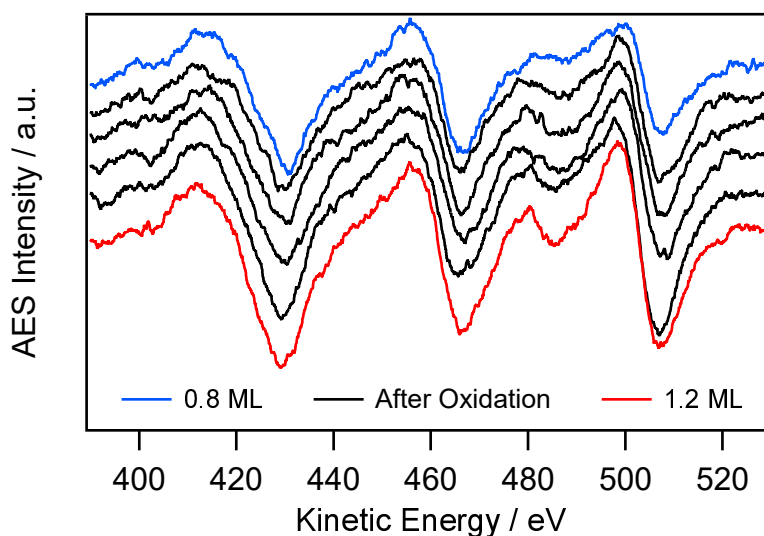


Figure 7.6: VO_x Auger spectra acquired after oxygen treatment of four samples on which V has diffused into the Pt bulk for different reasons. As a reference to estimate the VO_x coverage, two spectra acquired during the VO_x deposition rate calibration presented in section 7.1 at 0.8 ML (blue, topmost spectrum) and 1.2 ML (red, lowermost spectrum) are added.

7.2.2 Characterization of the (2×2) $\text{VO}_x/\text{Pt}(111)$ Structure

The $(\sqrt{3} \times \sqrt{3})R30^\circ$ appears to be a stable high coverage phase that is formed during the reactive evaporation process of VO_x at 670 K in 2×10^{-7} mbar oxygen. It is therefore surprising that the (2×2) structure is observed after the exposure of the sample to elevated temperature in an atmosphere consisting only of oxygen, or a mixture of oxygen and methanol, and after the oxygen induced segregation of V back to the surface. This can be explained by the stabilization of only a roughly 1 ML thick oxide layer on the surface, i. e. by the formation of a one monolayer thick surface compound.

In order to further characterize this (2×2) structure, LEED- $I(V)$ measurements are performed on a $\text{Pt}(111)$ surface, covered with about 1 ML VO_x , prepared by O-induced segregation of V dissolved in the Pt bulk. This involved a 40 min oxygen treatment at 870 K in 1×10^{-5} mbar oxygen. After the LEED- $I(V)$ measurements, the sample is heated to 1020 K with a constant heating rate of 0.5 K s^{-1} in vacuum, while continuously acquiring LEED images. The LEED pattern before the LEED- $I(V)$ measurement (left) and after the UHV annealing (right) are depicted in figure 7.7a. The results of the LEED- $I(V)$ measurements are shown in figure 7.7b. Two Auger spectra acquired before and after the high temperature treatment, are displayed in figure 7.7c.

As can be seen in the first LEED image in figure 7.7a, the oxygen induced segregation of V to the $\text{Pt}(111)$ surface results in the formation of a weak (2×2) diffraction pattern. The LEED image is characterized by diffuse intensity between the integer diffraction spots of Pt and the (0,0) spot. Upon UHV annealing, the intensity of the (2×2)

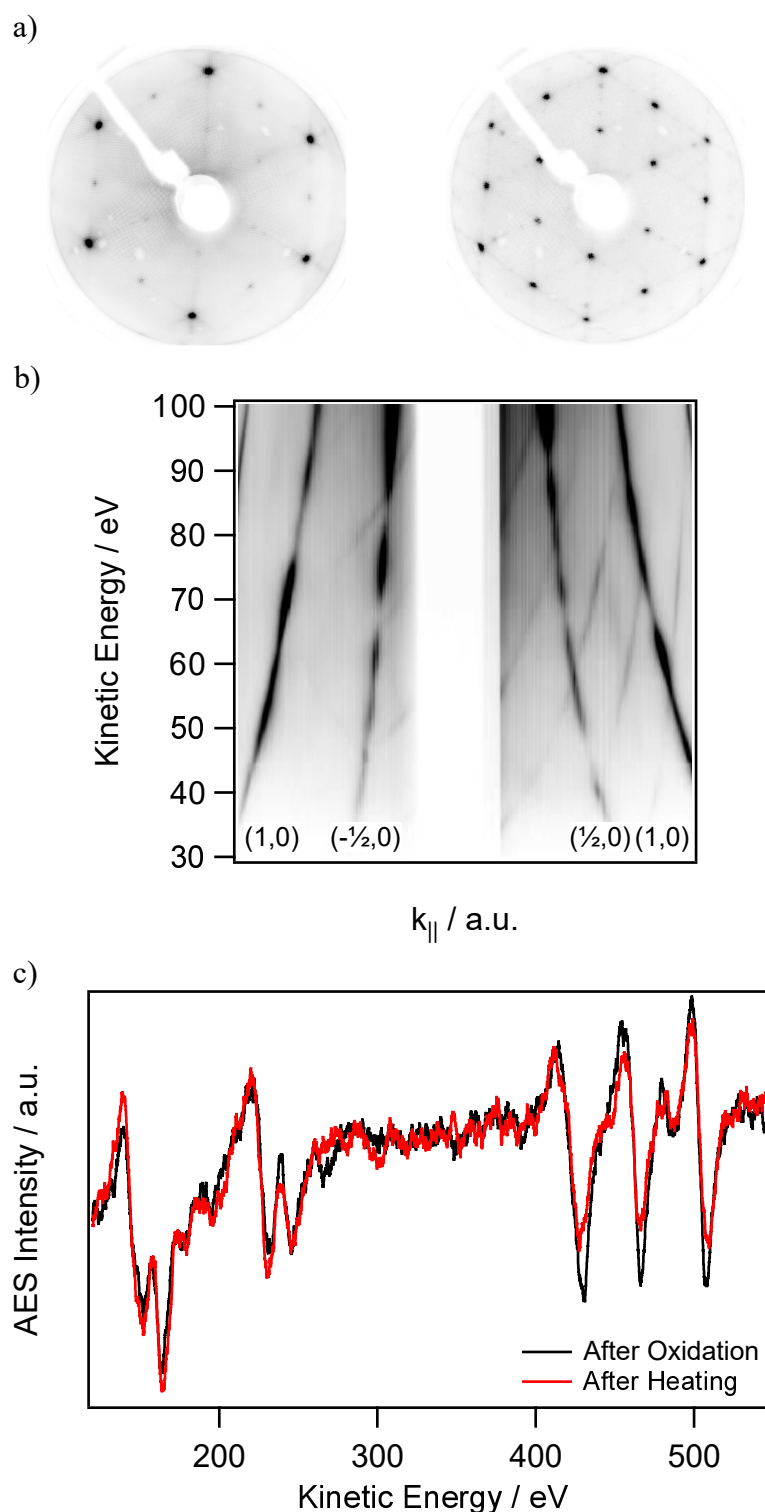


Figure 7.7: Characterization of the (2×2) apparent after segregation of VO_x to the Pt surface upon oxygen treatment. a) LEED images acquired at 65 eV before (left) and after (right) the sample is heated to 1020 K with a constant heating rate of 0.5 K s^{-1} . b) Waterfall plot of LEED- $I(V)$ measurements revealing signs of facetting. The $I(V)$ -data are acquired before UHV annealing. The $(0,0)$ spot is obscured by the electron gun of the LEED instrument (central white area). c) Auger spectra acquired before and after the UHV annealing, demonstrating a loss of about 20% of V presumably due to bulk diffusion.

diffraction spots increases drastically and the initial diffuse intensity between the Pt diffraction spots is replaced by weak spots belonging to the three rotational domains of an (8×1) LEED pattern.

The LEED- $I(V)$ measurements depicted in figure 7.7b which were conducted before UHV annealing, clearly show signs of either three-dimensional particles on the surface or facetting. The displayed graph is constructed by taking intensity line profiles across the LEED image from the $(-1,0)$ to the $(1,0)$ diffraction spot, and stacking them on top of each other as a function of the kinetic energy of the electron beam. One notes intensity lines crossing the trajectories of the regular beams. These dark lines which apparently represent beams which do not converge towards the $(0,0)$ beam of Pt(111) with increasing energy, indicate facetting and/or three-dimensional crystallites.

Vacuum annealing of the poorly ordered (2×2) structure not only leads to a considerable structural improvement, but also to the disappearance of the facet spots. This was shown in subsequent LEED- $I(V)$ measurements. The absence of the facet spots after the vacuum annealing indicates the spreading of the three-dimensional particles into a flat (2×2) wetting layer. Interestingly, the (2×2) diffraction spots can be observed in LEED up to 1020 K, indicating a high stability of the corresponding VO_x phase.

By comparing the Auger spectra before and after the high temperature treatment in figure 7.7c one notes that the intensity of the V₄₃₇ Auger peak decreased by 20% and that the V₄₇₂/V₄₃₇ peak ratio increased slightly. This indicates a loss of V and a slight reduction of the VO_x film. A possible explanation would be the spreading of the three dimensional particles and the diffusion of surplus vanadium into deeper layers of the Pt crystal upon vacuum annealing.

7.3 Catalytic activity of Pt(111) and VO_x/Pt(111) in methanol oxidation

The catalytic activity of the ultrathin vanadium oxide layers and of the metallic substrate is of crucial importance for the redistribution dynamics observed on VO_x/Rh(111). Since catalytic methanol oxidation to formaldehyde is restricted to the vanadium oxide covered parts of the surface, the macroscopic vanadium oxide islands, act as “catalytic microreactors”, i. e. as sinks for oxygen adsorbed on the metal surface surrounding the VO_x islands. This causes the formation of extended oxygen gradients on the surrounding Rh surface. The reaction-induced oxygen gradients are the reason for the phenomenon of traveling and coalescing vanadium oxide islands, observed in several different catalytic reaction on VO_x/Rh(111) [68–70, 241].

To investigate whether the considerable catalytic activity towards formaldehyde production of submonolayer VO_x films on Rh(111) is also observed in the system VO_x/Pt(111), temperature programmed reaction measurements are performed on freshly deposited vanadium oxide films of 0.6 ML and 4 ML coverage, and on the clean Pt(111) surface. The sample is heated from room temperature to 1020 K and back with a constant heating/cooling rate of 0.2 K s^{-1} . The composition of the reaction atmosphere was varied between 1×10^{-5} , 5×10^{-5} , and 1×10^{-4} mbar methanol at a constant oxygen pressure

of 1×10^{-4} mbar. A large excess of oxygen was chosen firstly because of the low oxygen sticking coefficient on the Pt(111) surface, and secondly because of the tendency of V to diffuse into deeper layers of the Pt crystal under reducing conditions.

The result of such a temperature programmed reaction rate measurement, performed in a gas atmosphere consisting of 1×10^{-5} mbar methanol and 1×10^{-4} mbar oxygen, is shown in figure 7.8a. The main products of methanol oxidation on the bare Pt(111) surface are carbon dioxide and water. To a lower extent also formaldehyde is formed. Interestingly, no production of CO is identified in the investigated temperature range. The catalytic activity of the Pt surface is initiated by a sharp, small CO₂ production peak, appearing between 350 and 360 K, which is shown in the inset of figure 7.8a. Broad H₂O and CO₂ production peaks are observed at around 470 K in the heating branch. In the cooling branch, these rate maxima are shifted by about 30 K towards lower temperature.

The formaldehyde production accounts for less than 50% of the formed, carbon-containing reaction products and is characterized by a very broad production peak, with maximum intensity around 510 K in the heating branch and 490 K in the cooling branch. No catalytic activity is found at a temperature higher than roughly 620 K, probably as a consequence of the decreasing oxygen sticking coefficient at increasing temperature.

The result of the same experiment conducted on the VO_x/Pt(111) surface (0.6 ML VO_x) instead of the clean Pt(111) surface depicted in figure 7.8b shows negligible catalytic activity. The deposition of already small amounts of VO_x (0.6 ML VO_x correspond to less than a closed oxide layer) suppresses any catalytic activity measurable within the sensitivity of the used experimental setup. The only variation of the product partial pressures are caused by a slight drift of the educt pressures and an accumulation of water in the UHV chamber, most probably produced by methanol decomposition at hot filaments. The low catalytic activity is already evidenced from the different ordinate scaling of the reaction products in figures 7.8a and b, which differ by more than a factor of ten. Essentially the same result is obtained with both VO_x coverages, 0.6 and 4 ML, independent of the composition of the reaction atmosphere. Apparently, the deposition of thin VO_x films passivates the Pt(111) surface with respect to methanol oxidation.

In order to characterize reaction-induced changes of the surface, Auger and LEED measurements are performed before and after every TPR experiment. The results are displayed in figure 7.9a and b, respectively. By comparing the Auger spectra measured before and after the TPR experiments, two trends become evident. On one hand, the V loss, reflected by the V₄₃₇ intensity decrease, grows with increasing amount of methanol on the gas phase, i.e. with reducing conditions. On the other hand, the V₄₇₂/V₄₃₇ peak ratio, which is a measure for the oxidation state of V, decreases in the experiments with a high excess of oxygen and increases for equal amounts of methanol and oxygen. These changes indicate an oxidation of the 0.6 ML film during methanol oxidation with 1×10^{-5} mbar methanol and 1×10^{-4} mbar oxygen, and a slight reduction of the VO_x film with 1×10^{-4} mbar methanol and 1×10^{-4} mbar oxygen. For the 4 ML thick VO_x film exposed to reaction conditions with 1×10^{-5} mbar methanol and 1×10^{-4} mbar oxygen, an increase of the V peak ratio results from a slight reduction of V under

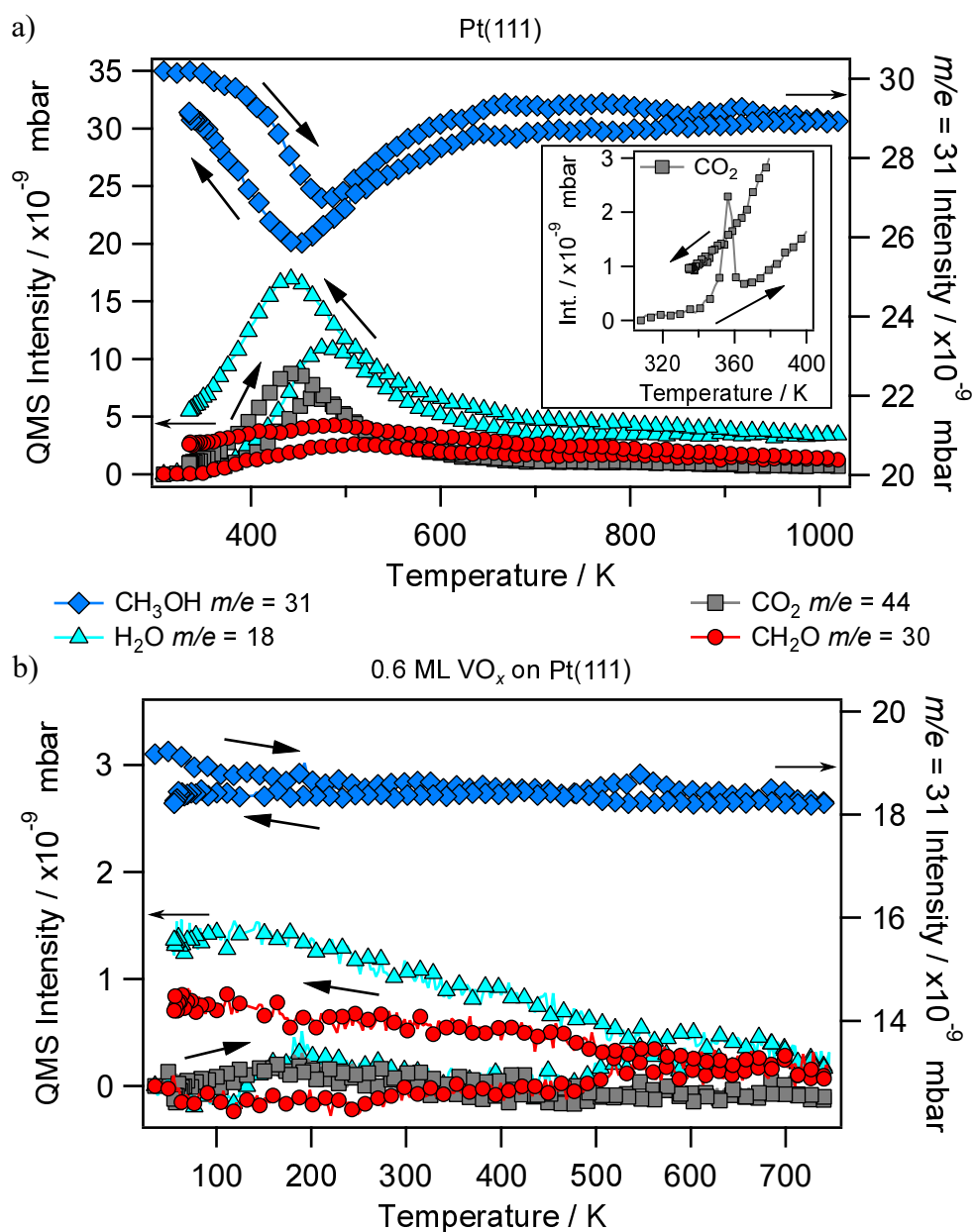


Figure 7.8: Temperature programmed reaction measurement on Pt(111) during catalytic methanol oxidation in the 10^{-4} mbar range. a) The heating and cooling branches (indicated by the black arrows) of a TPR experiment conducted with a heating rate of 0.2 K s^{-1} on the clean Pt(111) surface. The inset shows a magnified subset of the CO₂ signal. b) The same TPR experiment conducted on a freshly prepared VO_x/Pt(111) surface with $\theta_{\text{VO}_x} = 0.6 \text{ ML}$. The gas composition is 1×10^{-5} mbar methanol and 1×10^{-4} mbar oxygen in both experiments. The partial pressures of the products are scaled on the left ordinate, the partial pressure of the educt methanol on the right. Please note the different scaling of the axes.

reaction conditions.

The loss of V signal under reaction conditions can easily be traced back to the diffusion of V into the subsurface region of the Pt crystal. In the preceding sections, oxygen was shown to stabilize monolayer films of VO_x . The amount of V diffusing into the Pt bulk increases with more reducing conditions. The largest V loss is measured in the experiment with a thick VO_x film. The V_{437} intensity decrease of 73% matches quite well the coverage difference between the four deposited monolayers and the roughly 1 ML, that can be stabilized even at high temperature in the presence of oxygen.

For the interpretation of the V intensity peak ratios V_{472}/V_{437} one has to take into account, that not only V on the surface produces a V signal, but also metallic V in the subsurface region of the Pt bulk. The increased ratio with increasing amount of methanol in the gas phase might therefore not only be caused by a reduction of the VO_x surface layer, but also from the contribution of metallic V in the bulk region of the Pt crystal.

The freshly prepared $VO_x/Pt(111)$ surfaces of 0.6 ML coverage displayed LEED images similar to the second image in figure 7.2: a Moiré type pattern with diffuse intensity around the integer diffraction spots. The 4 ML thick VO_x film displayed only diffuse diffraction spots of the $(\sqrt{3} \times \sqrt{3})R30^\circ$ structure. After catalytic methanol oxidation, a sharp (2×2) LEED pattern is seen on all surfaces. An example is shown in the second LEED image of figure 7.9b. Only in the case of the 0.6 ML VO_x film exposed to methanol oxidation with 1×10^{-5} mbar methanol and 1×10^{-4} mbar oxygen, additional faint spots belonging to the three rotational domains of a (8×1) structure are visible (top LEED image in figure 7.9b).

7.4 Discussion of the different VO_x structures

Several studies on the growth and structure of ultrathin films of transition metal oxides on (111) oriented metal surfaces of the platinum group have been conducted². The systems $TiO_x/Pt(111)$ [296–300] and VO_x on $Rh(111)$ [53, 55, 183] are particularly well studied, but the growth of ultrathin VO_x layers on $Pd(111)$ [301, 302] and $Pt(111)$ [184, 294, 295] has also been investigated.

Vanadium oxide shows a variety of different two-dimensional structures for the coverage range between zero and 1 MLE. Important for this discussion is a (2×2) LEED pattern, that was observed as a V_2O_3 phase in the system $VO_x/Rh(111)$ during the $H_2 + O_2$ reaction [202]. For higher coverages a $(\sqrt{3} \times \sqrt{3})R30^\circ$ structure is obtained in the reactive deposition of more than 1 MLE of V on $Rh(111)$. This structure is assigned to the (0001) oriented surface of the corundum V_2O_3 phase [53]. This $(\sqrt{3} \times \sqrt{3})R30^\circ$ LEED pattern of the V_2O_3 corundum (0001) surface is also reported for thick (5 ML) vanadium oxide

²In this section, the different systems are compared to find structural similarities. It has to be taken into account, that the VO_x coverage is given in the unit used in the original publications, ML or MLE. Nominally equal coverage expressed in ML and MLE do not have to refer to the same number of V atoms, since this quantity is typically not known if the unit ML (of an oxide layer) is used.

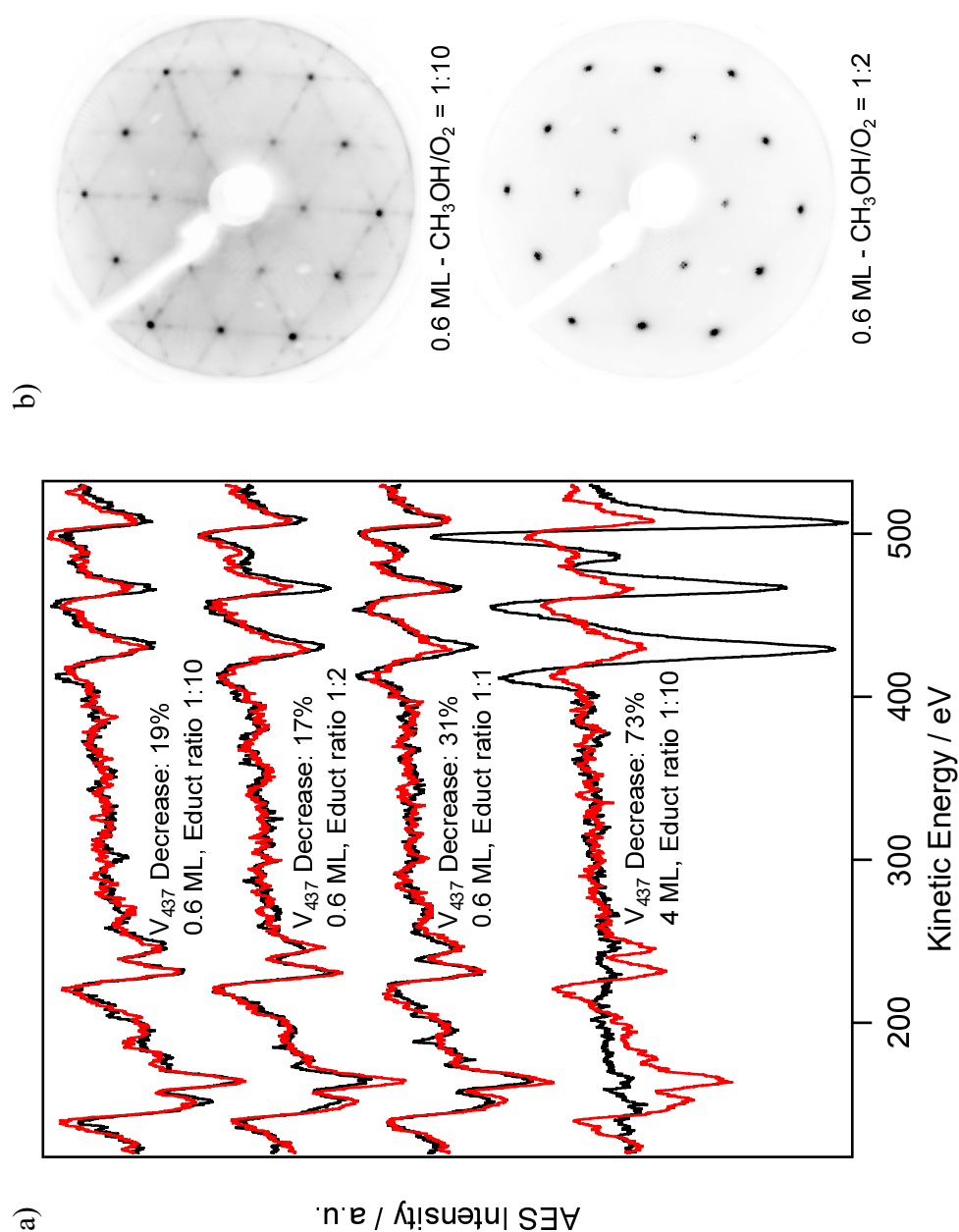


Figure 7.9: AES and LEED measurements taken before and after a TPR experiment with the catalytic methanol oxidation on VO_x /Pt(111). Different gas phase compositions and different VO_x coverages are shown. a) Auger spectra of the freshly prepared VO_x /Pt(111) surfaces covered with 0.6 ML (top three) and 4 ML VO_x , and of the surfaces present after exposure to the reaction. The educt ratios are indicated in the graph, the oxygen pressure is always 1×10^{-4} mbar. b) LEED images acquired after the TPR experiment with 0.6 ML VO_x in a reaction atmosphere with a methanol to oxygen ratio of 1:10 and 1:2, respectively. The LEED images are acquired at 65 eV.

films on Pd(111) [301]. Upon vacuum annealing to 620 K, three-dimensional crystallites of VO_2 composition on Pd(111) form a (2×2) VO wetting layer [301]. The vanadium oxide phase was identified as a surface V_2O_3 phase (s- V_2O_3) in which vanadium binds directly to the Pd(111) substrate [303].

In the system $VO_x/Pt(111)$, epitaxial VO_x films of rocksalt structure with $0.8 \leq x \leq 1.3$ (ideal composition: VO) were grown in a water atmosphere of 1×10^{-9} mbar on Pt(111) [294, 295]. Since these V^{2+} films easily get oxidized to V^{3+} species, even by the residual gas, their structure is not relevant for the results of this chapter obtained under oxidizing conditions. Another growth study on $VO_x/Pt(111)$ reports the formation of a (2×2) V_2O_3 phase for the coverage range between 0.5 and 1 ML, as well as a $(3\sqrt{3} \times 6)$ bi-layer, and a complicated tri-layer structure as high coverage phases [184]. Based on high-resolution electron energy loss spectroscopy measurements and on the similarity with the system $VO_x/Pd(111)$, the (2×2) pattern was attributed to the s- V_2O_3 phase, in which V binds directly to the metallic substrate [184].

In this study, the deposition of less than 1 ML of VO_x on Pt(111) by reactive evaporation at 670 K substrate temperature and 2×10^{-7} mbar oxygen results in diffuse intensity in LEED around the integer diffraction beams of Pt(111), reminiscent of the diffraction pattern of a Moiré-type structure. This LEED pattern is replaced by diffraction spots belonging to a $(\sqrt{3} \times \sqrt{3})R30^\circ$ and a (2×2) structure, at a VO_x coverage above 1 ML. Beyond a VO_x coverage of 12 ML, only diffraction spot of the $(\sqrt{3} \times \sqrt{3})R30^\circ$ remain.

A (2×2) VO_x phase is also observed after catalytic methanol oxidation on VO_x films of varying thickness. Moreover the oxygen-induced segregation of V dissolved in the Pt crystal back to the Pt(111) surface resulted always in the formation of a VO_x film of (2×2) structure. Estimated from the V and O Auger peak intensities a monolayer coverage was assigned to the (2×2) . In some experiments the original LEED spots attributed to three-dimensional VO_x crystallites disappeared as an intense (2×2) formed. For this reason, the (2×2) is tentatively assigned to a two-dimensional oxide phase.

As stable high coverage phase, a $(\sqrt{3} \times \sqrt{3})R30^\circ$ VO_x on Pt(111) is obtained in this study. The $(\sqrt{3} \times \sqrt{3})R30^\circ$ structure is referred to as stable high coverage phase, since it is the only structure that remains on the surface if thick films (≥ 10 ML) are deposited at 670 K in 2×10^{-7} mbar oxygen. If the VO_x deposition is carried out in a step-wise manner, like in the deposition rate calibration, this $(\sqrt{3} \times \sqrt{3})R30^\circ$ phase coexists with the (2×2) phase up to about 12 ML. If thick VO_x films with a coverage above 3 ML are deposited in a single step instead, already at lower coverage the $(\sqrt{3} \times \sqrt{3})R30^\circ$ is the only VO_x phase present, even though the diffraction spots are more diffuse in LEED.

The results obtained in this study differ in some points from the results reported in [184]. The differences can be explained by the preparation procedures applied by Tang et al. and in this study. Different from the procedure here, they evaporated metallic V at room temperature and applied an oxygen treatment at 623 K and 1×10^{-7} Torr for 10 min afterwards. The growth of VO_x is thereby conducted in a step-wise manner. Metallic V was evaporated on the already present VO_x film, and exposed to oxygen treatment afterwards. In this study, V is deposited by reactive evaporation at 670 K in

2×10^{-7} mbar oxygen, followed by 10 min of post oxidation under identical conditions. Typically, the growth of ultrathin transition metal oxide films on noble metal surfaces is kinetically controlled, and the preparation procedure therefore has a dramatic impact on the oxide phases that are formed [32]. The main difference, however, between the procedure applied in reference [184] and the one used here is that the formation of surface phases in [184] starts on a metallic surface, whereas here oxygen is present from the beginning.

For a coverage between 1.0 and 2.0 ML a $(3\sqrt{3} \times 6)$ structure is reported as a bi-layer structure of VO_x on Pt(111) [184]. A LEED pattern similar to the $(3\sqrt{3} \times 6)$ structure, but very diffuse, is observed in this study for a coverage range between roughly 0.5 and 1.2 ML. The appearance of diffuse LEED intensity around the integer diffraction beams, reminiscent of the $(3\sqrt{3} \times 6)$ LEED pattern, below 1 ML in this study is, however, in contradiction to the results presented in [184]. In the growth study of Tang et al., the (2×2) structure was the only sub-monolayer phase that could be observed, and the $(3\sqrt{3} \times 6)$ phase was assigned to a bi-layer structure. However, the low structural order of the LEED pattern acquired in the submonolayer range in this thesis (figure 7.2) make it hard to compare the observed structures at $\theta_V \leq 1$ ML with the bi-layer $(3\sqrt{3} \times 6)$ structure reported in [184].

In a combined LEEM and μ LEED study of the system $\text{TiO}_x/\text{Pt}(111)$, a LEED pattern very similar to the second and third LEED image in figure 7.2 has been observed with 0.6 MLE TiO_x . It was considered as a precursor phase P- TiO_x [304]. The presence of the P- TiO_x phase shows, that not necessarily more than 1 ML VO_x has to be present on the surface to obtain a LEED pattern reminiscent of a Moiré-type structure.

The $(\sqrt{3} \times \sqrt{3})R30^\circ$ was formed in this study as a stable high coverage phase. Due to the similarities between the systems $\text{VO}_x/\text{Pt}(111)$, $\text{VO}_x/\text{Pd}(111)$, and $\text{VO}_x/\text{Rh}(111)$ one can assume, that also on Pt(111) the corundum V_2O_3 phase is formed during the reactive deposition of thick VO_x films. The $(\sqrt{3} \times \sqrt{3})R30^\circ$ structure, which was formed here under a variety of experimental conditions was not observed by Tang et al. [184]. The different preparation procedure might explain the absence of the $(\sqrt{3} \times \sqrt{3})R30^\circ$ structure in their study. Similar to the results of this study is the appearance of the (2×2) phase for a VO_x coverage around 1 ML, which Tang et al. assigned to the s- V_2O_3 phase.

The (2×2) LEED pattern is the stable structure in a coverage range of up to around 1 ML of VO_x . As in the study of Tang et al., the (2×2) structure is assigned to the s- V_2O_3 phase first reported for VO_x on Pd(111) [303]. However, further STM measurements and DFT calculations are required to confirm this assignments.

7.5 Catalytic activity and pattern formation

The high catalytic activity of the system $\text{VO}_x/\text{Rh}(111)$ turned out to be essential for the reaction induced redistribution of VO_x . Based on the polymerization / depolymerization mechanism explained in chapter 4.2, the reversible depolymerization of large vanadium oxide islands into small, mobile VO_x clusters, and the condensation of these clusters back

into large vanadium oxide islands leads to the phenomenon of travelling, macroscopic vanadium oxide islands. In the system $\text{VO}_x/\text{Pt}(111)$ instead, practically no catalytic activity and no large scale redistribution of VO_x can be observed. Apparently, the absence of any pattern formation in PEEM in the $\text{VO}_x/\text{Pt}(111)$ catalysts is a consequence of the low catalytic activity of VO_x on $\text{Pt}(111)$. In the absence of catalytic activity on the vanadium oxide covered parts no oxygen gradients can develop.

In the reaction rate measurements, the highest reaction rates are measured on the clean $\text{Pt}(111)$ surface. The main reaction product is carbon dioxide, and only a small amount of formaldehyde is formed in methanol oxidation. The deposition of vanadium oxide, even if the $\text{Pt}(111)$ surface is not fully covered, deactivates the surface. One reason for the low activity of $\text{VO}_x/\text{Pt}(111)$ is probably the low oxygen sticking coefficient, which on the bare $\text{Pt}(111)$ surface is more than one order of magnitude lower than on $\text{Rh}(111)$ [161, 179]. A second cause is the absence of vanadyl groups, which according to references [56, 57, 305–307] are required for VO_x films being catalytically active in formaldehyde production.

Similar low catalytic activities were obtained during propane oxidation on $\text{VO}_x/\text{Pt}(111)$ model catalysts [308]. In a 1:1 mixture of oxygen and propane at a total pressure of 4 Torr at 373, 423, and 473 K, CO_2 and water were measured as the main reaction products on the clean $\text{Pt}(111)$ surface. For 423 and 473 K an increased catalytic activity relative to the clean $\text{Pt}(111)$ surface is reported upon deposition of up to 0.3 ML VO_x . For thicker VO_x films, the catalytic activity decreases again. This led to the conclusion that the VO_x - $\text{Pt}(111)$ interface comprises the catalytically active sites. Furthermore, the involvement of vanadyl groups in the reaction mechanism was discussed. In situ infrared reflection absorption spectroscopy (IRAS) revealed that the reaction conditions suffice to oxidize the initial s- V_2O_3 film to a vanadyl-group containing V_2O_5 phase. On sub-monolayer films, this oxidation proceeds at a lower temperature than on a several layers thick film. This threshold in pressure would explain why the catalytic activity decreases with increasing VO_x coverage on $\text{Pt}(111)$ in the 10^{-4} mbar range.

Vanadyl group containing VO_x species have been observed only as isolated $\text{O}=\text{VO}_x$ clusters for a coverage below 0.5 MLE. However, the clusters are reported to condense into the (2×2) s- V_2O_3 structure even upon CO adsorption at room temperature. Moreover, the vanadyl groups appeared in the third layer of a tri-layer structure formed for a VO_x coverage above 3 ML. The third layer of the tri-layer structure is not stable at high temperature and “desorbed from the bi-layer surface upon annealing above 673 K” [184]. The reduced vanadium oxide films are reported to be stable with respect to oxidation up to oxygen pressures of 5×10^{-5} Torr. The formation of highly oxidized vanadium oxide phases on $\text{Pt}(111)$, which contain vanadyl groups, requires oxygen in the mbar range [184]. Quite in contrast, on $\text{Rh}(111)$ the highly oxidized $(\sqrt{7} \times \sqrt{7})R19.1^\circ$ phase already forms in the 10^{-7} mbar range.

7.6 Conclusion

The experiments presented above demonstrate a strong influence of the preparation conditions on the structure of vanadium oxide films on Pt(111). The growth of VO_x by reactive evaporation results in the formation of a Moiré type structure for a VO_x coverage of less than a monolayer. A (2×2) structure is tentatively assigned to a two-dimensional s- V_2O_3 film, and a $(\sqrt{3} \times \sqrt{3})R30^\circ$ structure is attributed to the (0001) oriented surface of corundum V_2O_3 .

Compared to the system $\text{VO}_x/\text{Rh}(111)$ practically no catalytic activities can be measured in methanol oxidation on the partially and fully VO_x covered Pt(111) surfaces in a wide range of oxygen to methanol ratios. The low catalytic activity can in part be explained by the reactive sticking coefficient $s(\text{O}_2)$, which is on Pt(111) more than one order of magnitude lower than on Rh(111). Another factor is the absence of vanadyl groups in the vanadium oxide films on Pt(111), because vanadyl groups are known to be active in formaldehyde formation on VO_x catalysts.

Vanadium shows a strong tendency to diffuse into the Pt bulk at elevated temperature above roughly 750 K. This diffusion into the Pt bulk is reversible. Exposure of a Pt(111) surface with V incorporated in subsurface sites to oxygen pressures in the 10^{-5} or 10^{-4} mbar range at 870 K results in the formation of a roughly 1 ML thick vanadium oxide film exhibiting a (2×2) structure. A (2×2) results also if a several layers thick VO_x film is exposed to the same oxidative conditions. This indicates, that under oxidizing conditions and high temperature a vanadium surface oxide of about one monolayer thickness owns a particularly high thermodynamic stability on the Pt(111) surface. A general conclusion is that the metallic substrate has a large influence on the catalytic activity of deposited vanadium oxide layers.

Chapter 8

Surface Acoustic Wave Activated Diffusion of Surface Atoms

Abstract The influence of surface acoustic waves (SAW) on the vertical diffusion of Pt through an ultrathin (≈ 5 ML) Rh film is investigated by spatially resolved XPS. The results are compared to AES measurements on the thermal diffusion of Rh into the Pt bulk on a Pt(100) single crystal and on a 50 nm thick Pt film supported on LiNbO₃. At 445 K, the SAW induced diffusion of Pt through the Rh overlayer is detected by monitoring the ratio of the Pt 4f core level intensity of Pt underneath a Rh patch and of an uncovered Pt stripe during SAW treatment of the sample. In the thermal diffusion experiments, the onset of Rh diffusion into the Pt bulk on the LiNbO₃ sample is found to occur around 500 to 550 K.

8.1 Introduction

Tuning the activity or selectivity of a catalyst by varying an external parameter like an electric potential has always been an elusive goal of chemical engineers. Bulk and surface acoustic waves have shown a substantial, non-thermal influence on the catalytic activity and selectivity in a number of partial and total oxidation reactions on different metals, alloys, and metal oxide surfaces [63]. Even though a large number of systems has been investigated with different techniques of analysis, including infrared adsorption spectroscopy, laser doppler measurements and PEEM, no satisfactory explanation for the increase of catalytic activity by surface acoustic waves has been established yet. Since the power applied to generate SAW on a piezoelectric surface also causes heat dissipation, a non trivial question is whether the observed influence on the catalytic

activity is caused by the SAW itself or by heating up the catalyst surface.

The effect of SAW on the work function of metals including Cu, Au and Pd was studied Nishiyama and Inoue [309]. A decrease of the work function of Cu low index planes was observed during application of SAW in on-off experiments. In contrast, the work function of Cu high index planes was increased upon SAW excitation [310]. In an infrared reflection absorption spectroscopy study (IRAS) it was shown that SAW have a pronounced influence on CO bonding on Cu surfaces [311]. The intensity of the CO stretching mode varied and a frequency shift was observed during on-off experiments. The different population of high index and low index planes of the Cu surface with CO was interpreted as a consequence of a SAW induced work function change. An increase of the work function on low index planes results in weaker bonding, whereas a decrease of the work function at high index planes increases the amount of adsorbed CO. The SAW-induced catalytic promotion was attributed to electronic effects [311].

In a high-resolution acoustic wave resonance spectroscopy study Kelling et al. it could be shown, that a six-fold reaction rate increase observed during CO oxidation on Pt(110) was caused by acoustic waves, and not thermally induced [312]. In a PEEM study Kelling and Cerasari et al. reported a SAW-induced work function decrease in catalytic CO oxidation on Pt(110), which is accompanied by a reaction rate increase of CO₂ formation [313, 314]. Both, the work function decrease and the activity increase start simultaneously after an induction period of about 1 min after the SAW excitation has been started. Additionally, a considerable degradation of the Pt crystal surface is reported upon SAW treatment over several hours. The mentioned induction period together with the strong crystal degradation leads to the assumption, that the catalytic enhancement may be caused by the creation of reactive sites by a structural rearrangement or restructuring of the catalytic surface by SAW. This hypothesis implies that SAW should promote the diffusion of surface atoms.

A SAW-induced 19-fold increase in diffusivity of gold clusters on a Si(111) surface, was recently observed by Zhigilei et al. [315]. SAW were excited with laser heating and the experiments were conducted at ambient pressure. Molecular dynamics simulations of SAW-induced increase of adatom diffusion by a factor of up to 4500 [316]. As a reason for the promotional effect, dynamic coupling of SAW to vibrational state of the adsorbed species are mentioned. Anharmonic contributions of the SAW to the high-frequency vibration are important. Also surface strain-induced variation of diffusion barriers and adiabatic changes of the surface temperature are discussed [316].

The long time constants with which the catalytic activity and the work function responded to the excitation of SAW in some experiments, together with the results on SAW promoted surface diffusion suggests, that the SAW-induced creation of surface defects might be the main reason for the effect of SAW on catalytic surface reactions, rather than electronic effects. Also in the creation of surface defects by SAW, anharmonic contributions should play an important role, since in ideal SAW all atoms remain in place and no defects should be created.

A problem is that if SAW induces the lateral diffusion over only a few lattice constants, this would be far beyond the lateral resolution of spatially resolving techniques

like PEEM or LEEM. STM should work but the implementation as in situ technique would pose enormous technical difficulties. A way out of this dilemma is to consider vertical diffusion.

In a first step to experimentally verify the hypothesis of SAW-induced restructuring, the vertical diffusion of Pt atoms through an ultrathin Rh layer was investigated by x-ray photoemission electron microscopy (XPEEM) in this study. Pt and Rh are perfectly miscible in the bulk. The surface composition in equilibrium favors a Pt surface, because of its lower surface energy (2598 J cm^{-2} for Rh(111) and 1656 J cm^{-2} for Pt(111) [317]). If we assume that SAW just cause some intermixing in the Rh/Pt layer, then we should see an increase in the Pt signal as Pt segregates to the surface. As a control experiment, the influence of the temperature on the segregation of Rh on Pt surfaces is studied on Pt(100) and on a 50 nm thick poly-crystalline Pt film to determine whether the effects observed in the SAW experiments are non-thermal processes or just thermally induced segregation. The question here is: do SAW alter the composition of a bimetallic surface?

8.2 Surface acoustic waves and instrumentation

A surface acoustic wave (SAW) is an acoustic wave which propagates in the surface plane of a solid. The amplitude of such a wave decays exponentially with the depth in the solid (z -direction), and the penetration depth is in the order of a few wavelengths λ_{SAW} . Experimentally SAW can be excited on a piezoelectric crystal by applying an alternating electric signal to interdigital transducer (IDT) electrodes located on the crystal surface [318], or by a periodic stimulation with a laser [315]. A schematic representation of such an arrangement and the displacement caused by a surface acoustic waves in an idealized piezoelectric solid can be seen in figure 8.1. Acoustic waves can also be applied as bulk acoustic waves. The experimental implementation is described in [63]. Bulk acoustic waves are excited by metal electrodes located at the front and backside of a piezoelectric crystal. If radio frequency is applied to the electrodes resonant oscillations of the crystal can be induced, and acoustic waves propagate through the crystal. The resonance frequency depends on the shape of the crystal and the orientation of the polarization axis [64].

In the experiments performed in this thesis a 128° Y -cut LiNbO_3 single crystal (cut along the $(0\bar{1}4)$ crystal plane) [319] has been used in a custom sample environment at the CIRCE beamline of the electron storage ring ALBA. The crystal is further doped with carbon in order to slightly increase the conductivity, and thus to reduce charging effects during photoemission experiments. A detailed description of the principles of imaging SAW in LEEM and XPEEM is given in [320], whereas details about the sample holder needed for SAW excitation in LEEM/XPEEM can be found in [321]. In brief, the principles of SAW excitation, the experimental application at the CIRCE beamline, and the contrast mechanism in LEEM and XPEEM are recapitulated in the following.

SAW can be excited by applying an alternating electric signal (radiofrequency) to the IDT electrodes on a suitable piezoelectric material. The wavelength λ_{SAW} of the SAW is determined by the spacing of the periodic IDT electrodes L_x , and the propagation

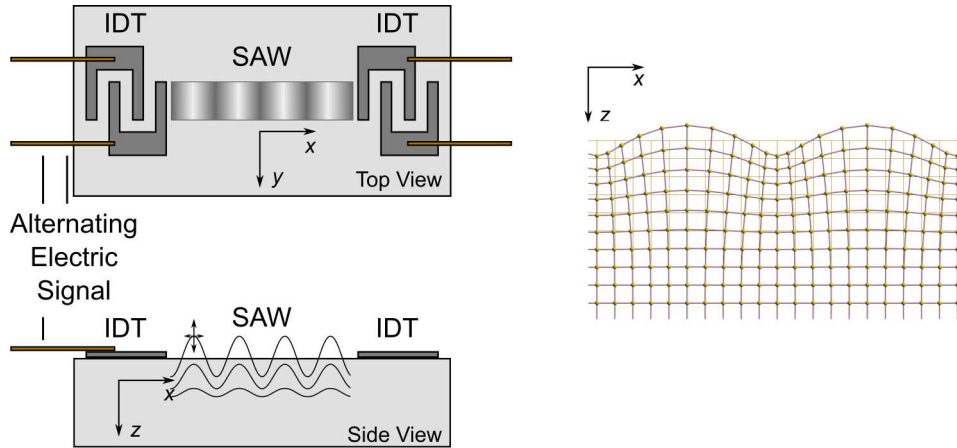


Figure 8.1: Schematic representation of the experimental set-up needed to excite surface acoustic waves on a piezoelectric material (left) and of the displacement caused by a SAW in a rectangular grid of atoms from idealized piezoelectric solid (right). The figure is adapted from [318], the right scheme is a courtesy of T. Alznauer.

velocity of the SAW v (3980 m s^{-1} for the used LiNbO_3 crystal) according to:

$$\lambda_{\text{SAW}} = \frac{v}{\nu} = \frac{L_x}{n}, \quad (8.1)$$

with ν being the excitation frequency and n a positive integer number. In general, the wavelength and the excitation frequency are thus determined by the piezoelectric material (because v is a material specific parameter), and by the geometry (L_x) of the IDTs. Typically values of ν in the range of MHz to GHz are applied, resulting in wavelengths in the range of micrometers to nanometers. At the CIRCE beamline, the periodic X-ray pulses produced by the electron storage ring are used to image the sample surface in a stroboscopic way. The repetition rate of the X-ray pulses is about 500 MHz, and L_x of the IDTs is chosen so that the fourth harmonic ($n = 4$, 125 MHz fundamental frequency) results in a frequency, which matches the synchrotron frequency [320]. In such a configuration, a SAW propagates over a distance of exactly one wavelength between two X-ray pulses. This means, every X-ray pulse produces an image of a (standing or traveling) SAW in the same phase, since the pulse duration is with 20 ps short compared to the period of the SAW.

In the experimental set-up, two IDTs are placed on the opposite sites of the LiNbO_3 crystal, and every IDT can be addressed independently. If a radio frequency signal is applied to one of the two IDTs, a traveling SAW is produced. Because of partial reflection at the other IDT, this traveling SAW also has a standing wave component. If a radio frequency signal (of the same frequency) is applied to both IDTs, a standing SAW is generated (which also has a small traveling wave component) [320].

On an isolating material SAW can be imaged in LEEM and (X)PEEM because the displacement of lattice atoms by a SAW causes a change in the surface potential (piezo-

electric surface potential). In cathode lens microscopy such a variation of the surface potential varies also the kinetic energy of the probing electrons. Thus a change in the samples surface potential shifts the spectrum of the probing electrons. If the spectrum of the probing electrons (intensity as a function of STV) is non-linear, contrast can be gained by variations in the surface potential. In LEEM and (X)PEEM, electrons at the LEEM-MEM transition and the secondary photoelectrons can be used for imaging SAW, respectively. Especially at the LEEM-MEM transition and at the onset of secondary electron photoemission small changes in the surface potential lead to a considerable intensity change, thus providing strong imaging contrast of SAW [320]. However, this contrast mechanism is only possible on isolating surfaces. On conducting surfaces no SAW induced surface potential changes should exist, since a conducting surface is an isopotential surface.

8.3 Sample preparation and experimental set up

The influence of surface acoustic waves on the composition of a Pt/Rh surface is investigated using the SPELEEM microscope located at the CIRCE beamline at the synchrotron source ALBA in Barcelona. Experiments on the thermal diffusion of similar samples are conducted at the Institute of Physical Chemistry and Electrochemistry at the Leibniz University Hannover.

8.3.1 Rh/Pt/LiNbO₃ Sample Preparation

The LiNbO₃ substrates equipped with interdigital transducers (IDT) were manufactured in the Paul-Drude-Institut für Festkörperelektronik Berlin. The photolithographic micro-patterning with thin 20 to 50 nm thick Pt stripes was carried out by F. Macià at the Institut de Ciència de Materials de Barcelona. For the photolithography, the substrate was covered with a light sensitive resist, and illuminated through an optical mask. After the light-exposed resist was removed, Pt was deposited by magnetron sputtering from a Pt target, followed by a wet-chemical removal of the remaining (Pt coated) resist. The micropatterned LiNbO₃ samples are used for SAW experiments at the CIRCE beamline. For experiments on thermal diffusion of Rh on a Pt film, a LiNbO₃ substrate was homogeneously covered with an about 50 nm thick Pt layer by direct magnetron sputtering. Figure 8.2 shows photographs of the two sample set-ups used for SAW experiments at ALBA and Hannover.

In the SPELEEM experiments conducted at the CIRCE beamline, the LiNbO₃ substrate is mounted with silver paste onto an UHV compatible printed circuit board (PCB, Curamik[®]). In order to heat the sample, a resistive heating element is glued between the PCB and a thin metal foil (which purpose is to ensure a homogeneous heat distribution) underneath the sample. The PCB provide the necessary six contacts for sample heating, the thermocouple, and SAW excitation. The sample set-up is mounted onto a home-built sample holder, which is compatible with the Elmitec LEEM III microscope [321]. Connection between PCB and IDTs on the LiNbO₃ substrate is realized with a wire

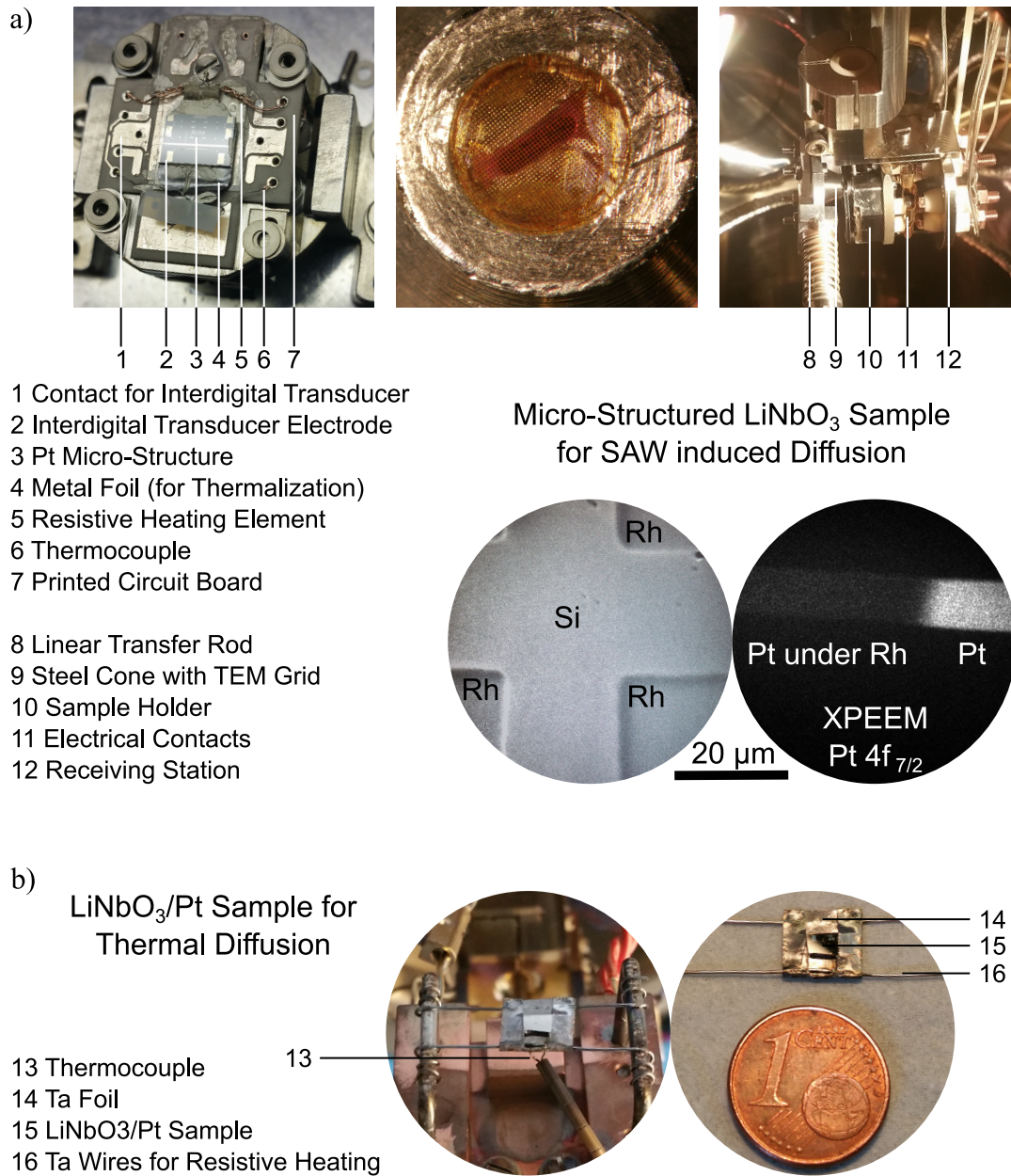


Figure 8.2: Sample and sample holder set-ups used for measurement of SAW and thermally induced diffusion of Rh into Pt. a) Top: Photographs of the sample holder (left, cap removed), the tip of a steel cone covered with a TEM grid used for Rh patterning (middle), and the cone-sample holder configuration used during deposition of Rh (right, the Rh evaporator is located on the left side of the image and not visible). Bottom: LEEM (left) and Pt 4f XPEEM (right) images of Rh squares deposited onto a Si surface and onto a micro-structured Pt/ LiNbO_3 sample, demonstrating the result of Rh deposition through the TEM grid. b) Photographs of the LiNbO_3 sample homogeneously covered by ≈ 50 nm Pt mounted on the sample holder of the Hannover PEEM system (left), and with only Ta wires for heating being connected (right).

bonder available at ALBA. Sample mounting and all related modifications of the sample holder are done by J. Prat and M. Foerster at the CIRCE beamline.

Cleaning of the micropatterned Pt/LiNbO₃ samples is done by repeated cycles of Ar ion sputtering and oxygen treatment. Special care has to be taken during sample preparation. Ar ion sputtering is carried out in 15 min steps at an ion energy of 500 V and under an angle of 45°. Carbon contamination are removed by oxygen treatment at a temperature lower than 470 K. In this way it is ensured, that the lithium niobate substrate is not reduced and that the platinum microstructures are not destroyed during the cleaning.

In order to measure the SAW-induced segregation of Pt through thin Rh films on the Pt micro-structures, a Rh micro-patterning is necessary. A Rh free part of the Pt surface as a reference, and a Rh covered part of the Pt surface have to be imaged simultaneously in the 50 μm wide field of view. The Rh micro-patterning is done by electron beam evaporation of a high purity Rh rod through a custom build shadow mask, consisting of *i*) a stainless steel cone mounted onto an Elmitec sample holder base plate, and *ii*) a Cu transmission electron microscopy grid glued onto the opening of the steel cone. An optical micrograph of the cone opening is shown in figure 8.2a (top middle image). To further confine the region onto which Rh is deposited, a Cu foil with a small slit is glued underneath the TEM grip.

For the Rh deposition, the micro-patterned Pt/LiNbO₃ sample is placed in the preparation chambers receiving station and the shadow mask is kept on the linear transfer rod of the UHV system. The cone opening covered with the TEM grid is mechanically pressed onto the LiNbO₃ substrate and Rh is deposited through the steel cone onto the sample surface. Rh deposition is carried out in UHV (residual gas pressure below 3×10^{-9} mbar during evaporation) with a deposition rate of $\approx 0.5 \text{ \AA min}^{-1}$, as determined by a quartz micro-balance. The conditions used for the Rh deposition are 5.4 A filament current and a bombardment voltage of 2 kV, resulting in an emission current of 23 mA. This procedure yields well defined, square Rh patches of approximately $50 \times 50 \mu\text{m}$ size with an interface of less than 100 nm width, as can be seen in the LEEM image of Rh patches deposited onto a Si dummy sample in figure 8.2a (lower left image). However, even though the resulting Rh patches are well defined, special care has to be taken during the deposition process: too much mechanical stress onto the LiNbO₃ substrate can easily brake the fragile ceramic sample, and also the thin Au wires, which connect the IDTs, are easily detached during approaching the sample surface with the steel cone. The thickness of the investigated Rh film is 5 ML.

For the thermal diffusion experiments conducted at Hannover no Rh micro-patterning is needed, since the used Auger spectrometer only yields spatially averaged information. Thus Rh deposition is carried out by standard electron beam deposition from a high purity Rh rod (Goodfellow) with the same Tectra electron beam evaporator used for the vanadium oxide film preparation discussed in the preceding chapters. A filament current of 6.4 A and a bombardment voltage of 1.5 kV, yielding an emission current of 20 mA, is used for Rh deposition in vacuum at room temperature. The deposition rate is estimated to be roughly 0.1 ML min^{-1} from an AES deposition calibration curve (AS-t

plots of the Rh signal at 302 eV and the Pt signals around 60 eV and 170 eV). The Rh film thickness is 3 ML in the experiment on Pt/LiNbO₃ and varies between 1.5 and 3 ML in the experiments on Pt(100).

8.3.2 Spectroscopic LEEM (Barcelona)

The SPELEEM installed in the group of L. Aballe as end-station of the CIRCE beamline (ALBA) consists of an Elmitec LEEMIII microscope and a sample preparation chamber. The sample preparation chamber, which is located between the standard load-lock/preparation chamber and the main chamber, comprises a home built electron beam evaporator, a quartz micro-balance, a sputter gun, and high-precision leak valves for oxygen and argon dosage. Additionally, a halogen lamp, which enables irradiative heating of the sample, is mounted at a view port. The lamp is used to mildly degas freshly glued samples prior to the direct heating with the resistive heating element.

The main chamber of the CIRCE end-station comprises a standard SPELEEM III and electron beam evaporators for metal deposition. Instead of the standard receiving station with four electrical connections, a receiving station with six electrical connections is mounted. A thorough description of the CIRCE beamline and the SPELEEM endstation can be found in reference [92], the custom sample holders are reported in [321]. A special modification is implemented in the high voltage rack of the SPELEEM microscope. In order to apply the radio frequency signal needed to excited SAW synchronized to the X-ray pulses of the storage ring, two function generators (independent in amplitude and phase) are connected by an optical fiber (non-conducting) to an amplifier located in the high voltage (HV) rack. A galvanic separation of the function generators and the amplifier in the HV-rack is needed, since every signal applied to the sample is referenced on the start voltage ΔU generated on top of the acceleration voltage U , which is 10 kV during the experiments.

In order to synchronize the SAWs with the pulsed synchrotron light, a vector signal generator receives a master clock signal from the storage ring timing system and produces a phase locked, sinusoidal radio frequency signal. This analog signal is converted to an optical signal and transmitted into the high voltage rack by the optical fibers, where it is amplified by an radio frequency amplifier (and converted to an analog signal again) and sent through a coaxial cable to the sample. The optical communication system is thereby configured to input/return, which allows to measure the radio frequency transmission through the sample (needed for testing the IDTs and to characterize the SAW). The maximum radio frequency power that can be applied to the sample is around 100 mW. A detailed description can be found in [321, sections 4-5] and [320, section 2].

8.4 Measurement of the SAW induced diffusion

As an indicator for the diffusion of Pt through the Rh overlayer (or Rh into the Pt bulk), the intensity ratio of the Pt 4f core level intensity measured on Rh covered and uncovered Pt is used. At room temperature no systematic variation of this intensity ratio is

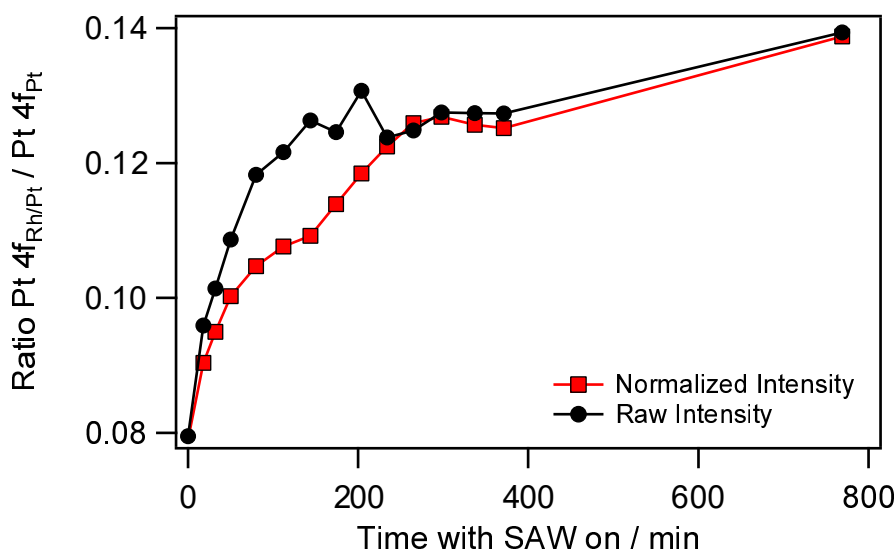


Figure 8.3: Pt 4f core level intensity ratio of the Rh covered and pristine Pt area as a function of SAW treatment time. The intensity is integrated over the whole Rh covered and uncovered Pt area shown in the XPEEM image in figure 8.2a. The raw signal as measured from the mikro-channel plate detector is shown, together with the Pt 4f intensity ratio normalized to compensate for inhomogeneities of the MCP detector.

measured at an exposure of the sample surface to SAW at 125 MHz and at the maximum power output for several hours. Therefore the sample is heated up to 400 K and held at this temperature for about 12 hours before the experiment is started. Due to this long time at constant temperature, the whole sample holder and manipulator can thermalize. In this way the thermal drift of the sample during the measurements is minimized. This is necessary, because the XPS intensity is very sensitive to the sample position. When surface acoustic waves are excited at 125 MHz and approximately 0.1 W power, the sample temperature increases from 400 to 445 K. Since the microscope cannot be operated during the excitation of SAW with such a high output power for technical reasons, photoemission spectra are acquired after approximately 30 min intervals of acoustic wave treatment. After the SAW excitation is stopped, the temperature decreased to around 410 K within 11 min. The resulting Pt 4f intensity ratio as a function of time with SAW excitation is shown in figure 8.3.

As can be seen in figure 8.3, the intensity ratio increases by a factor of ≈ 1.75 . However, the intensity ratio of Rh covered Pt and uncovered Pt remains quite small, indicating that only a weak effect is detected here. In order to see whether this result is due to the diffusion of Pt atoms through the Rh layer to the surface, or whether it is an experimental artifact related to sample and beam drift, the influence of the X-ray beam position and of the sample position is studied.

For determining the sample drift, the positions of the regions of interest (ROIs) during the analysis are evaluated. The ROIs are placed manually in every XPEEM

data set to account for the unavoidable sample movement during the measurements. The center of the X-ray beam is determined by a lorentzian fit of the beam profile visible in the XPEEM images, whereas the width of the beam is measured by fitting the edges of the X-ray spot with sigmoid functions. In figure 8.4a the ROI positions for the Rh covered and uncovered Pt areas as a function of time with SAW treatment are depicted. Figure 8.4b displays the center and the edges of the X-ray beam during the measurements.

Figure 8.5 depicts the Pt 4f core level intensity ratio of the Rh covered and uncovered Pt area as a function of the x, y -displacement of the ROI positions (a and b), and as a function of the X-ray beam position (c). For an intensity ratio up to 0.12 a clear correlation between the increasing intensity ratio and the sample movement in x as well as in y direction is visible. At higher intensity ratios (which correspond to longer application of SAW) no correlation is seen anymore. The dependence of the Pt 4f intensity ratio on the beam position shows no correlation at all, neither in the MCP uncorrected nor in the MCP corrected analysis.

The fact that both, the MCP corrected and the MCP uncorrected analysis, result in a similar dependence of the Pt 4f intensity ratio on the sample position demonstrates, that the measured ratio increase is not an experimental artifact caused by sample and/or beam drift during the measurement period of 760 min. The initial correlation between the intensity ratio and the x, y -displacement will be discussed further in section 8.7.

Regardless the fact, that the measured intensity variations are a real effect, the question of what has induced the Pt diffusion through the Rh overlayer – SAW or sample warming due to the applied ultrasonic power – still is not answered. Therefore, the segregation behavior of homogeneous, ultrathin Rh layers on Pt(110) and on a ~ 50 nm thick Pt film supported on a LiNbO₃ crystal is described in the next section.

8.5 Thermal diffusion of Rh on Pt/LiNbO₃

For the thermal-diffusion experiments ~ 50 nm Pt were homogeneously sputter-deposited onto a LiNbO₃ crystal. In order to avoid charging problems, to ensure isothermal conditions and a precise temperature measurement during the Auger experiments, the LiNbO₃ crystal is partially wrapped in Ta foil. A K-type Ni/CrNi thermocouple is spot welded to the Ta foil directly behind the sample, and heating is done by passing current through two Ta wires spot welded to the ends of the Ta foil. A picture of the sample as prepared (left) and as mounted on the sample holder of the UHV system (right) is shown in figure 8.2b.

Using the same substrate and the same Pt thickness as in the SAW-induced-diffusion experiments carried out in Barcelona, the temperature program applied there is reproduced in Hannover in order to follow in situ the Rh distribution in the first surface layers as a function of temperature. Around 3 ML of Rh are deposited, and Auger spectra covering the energy range from 20 to 550 eV are acquired at 300, 350 and 375 K. After every measurement, the sample is heated up within about 2 min to the next temperature, and immediately after reaching the temperature a spectrum is acquired. The acquisition

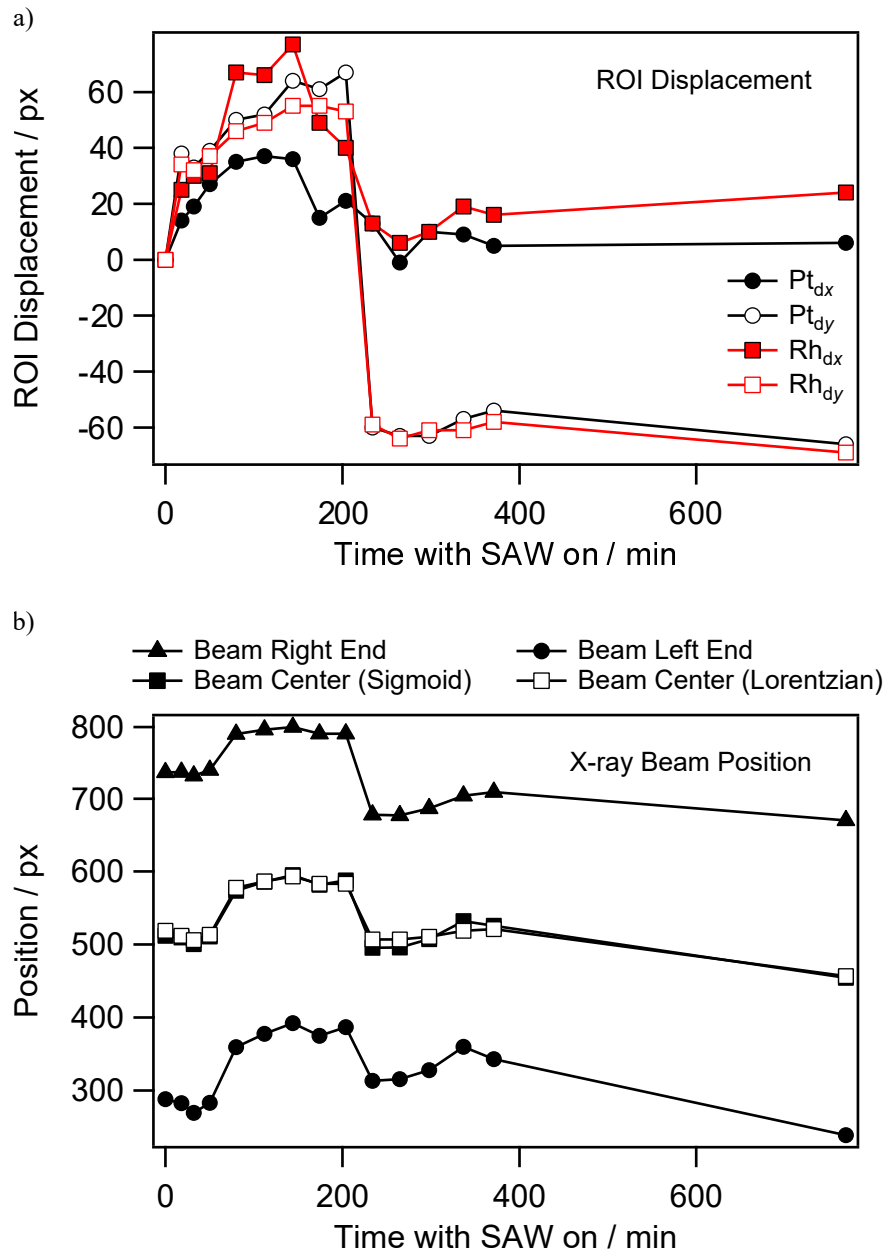


Figure 8.4: Manual adjustment of the ROI positions during data analysis and X-ray beam drift during the measurements. a) The x, y -displacement of the two regions of interest (ROI) used in order to measure the Pt 4f core level intensity on the Rh covered (Rh_{dx} and Rh_{dy}) and pristine part of the Pt stripe (Pt_{dx} and Pt_{dy}) during SAW treatment. The ROIs are adjusted manually in every measurement point to compensate for the sample drift. b) Position of the X-ray beam during the measurement. Shown are the center of the beam as determined from a lorentzian fit, and the edge positions of the beam obtained by two sigmoidal fits of the beam spot profile. Additionally, the beam center is calculated as the center between the beam edges (filled squares).

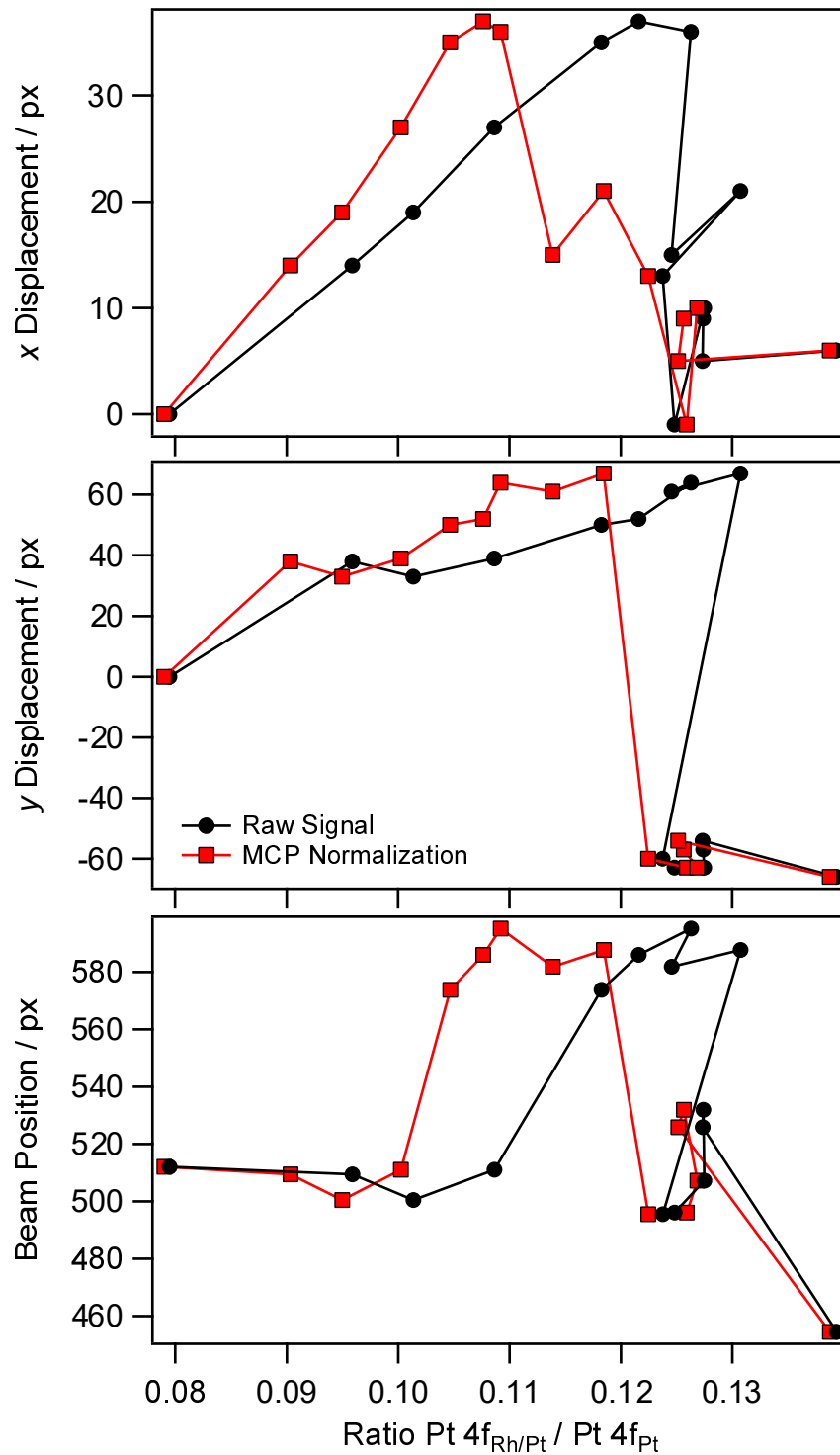


Figure 8.5: L

Pt 4f core level intensity ratio of the Rh covered and pristine Pt stripe as a function of x, y -ROI position (of the Pt ROI, top and middle graph) and X-ray beam position (bottom). Shown is the intensity ratio extracted without normalization for inhomogeneities in the MCP detector (circles) and with normalization (squares).

time of such a spectrum is approximately 20 min.

Subsequently, the sample is heated up to 400 K and kept at this temperature for 1200 min. The first 170 and the last 60 min, every 20 min a spectra is acquired. Afterwards the sample is heated up to 445 K within two minutes, and kept at this temperature for further 240 min. Every 20 min an Auger spectrum is acquired. Finally, the sample is heated in 50 K steps to 975 K, and an Auger spectrum is acquired at every step over a period of 20 min. This complex temperature program mimics, in the first stage, the experimental conditions applied during the SAW measurements carried out at the CIRCE beamline. In the second stage, the temperature is increased linearly in order to investigate the thermal segregation behavior of Rh on the Pt film.

The normalized Pt₆₀, C₂₇₀, Rh₃₀₂, and Ag₃₅₆ intensities as a function of temperature and time are shown in figure 8.6a and b. In this representation normalized means, that the average Pt₆₀ and Rh₃₀₂ intensities at 445 K are set to unity. In case of C₂₇₀ and Ag₃₅₆, the maximum intensity during the experiment is set to unity, instead. In this way the evolution of the different signals as a function of time and temperature can be easily recognized, despite quite large differences in the absolute intensity values.

In figure 8.6b one notes an exponential decrease of the Pt and Rh signals at the beginning and after 1170 min. This intensity decrease is mainly an experimental artifact related to an unstable electron beam. All spectra are acquired without switching the spectrometer off, except before the mentioned 1200 min period at 400 K. At around 1500 min the temperature is further increased towards its maximum value of 975 K. Together with this temperature increase a significant decrease of the Rh signal, accompanied by an increase of the Pt signal starts to occur around 475 K to 500 K. This sharp decrease of the Rh intensity is caused by the diffusion of Rh into deeper layers of the Pt film.

A critical point is the behavior of Rh on the Pt film around 445 K, since this is the temperature at which the migration of Pt through the Rh patches is observed during the measurements carried out at the CIRCE beamline. In order to exclude experimental artifacts related to the warm-up of the Auger spectrometer as good as possible, the intensity ratios Rh₃₀₂/Pt₆₀ and Rh₃₀₂/Pt₁₇₀ are displayed as a function of time in figure 8.7, together with the Rh₃₀₂, Pt₆₀ and Pt₁₇₀ Auger intensities as measured. In order to additionally display the temperature of the sample, a color scale is used in the representation of the Rh₃₀₂ intensity. By comparing the intensity evolution of the Rh raw intensity with the Auger ratios of Rh and Pt (light and dark grey), one recognizes a nearly constant value for the time period starting at 1170 min and ending at around 1500 min. These data points are acquired at 400 and 445 K. Within the large noise level, the nearly constant value of the Auger intensity ratios indicates, that no thermal diffusion of Rh is observed for temperatures below 475 K on the poly-crystalline Pt film supported on LiNbO₃.

In addition to the Rh and Pt signals also the characteristic Auger transitions for carbon at around 270 eV and silver at 356 eV are followed. At elevated temperatures around 500 eV and prolonged exposure to the electron beam of the Auger spectrometer, a considerable carbon signal is recorded, as can be seen in figure 8.6a and b. The silver

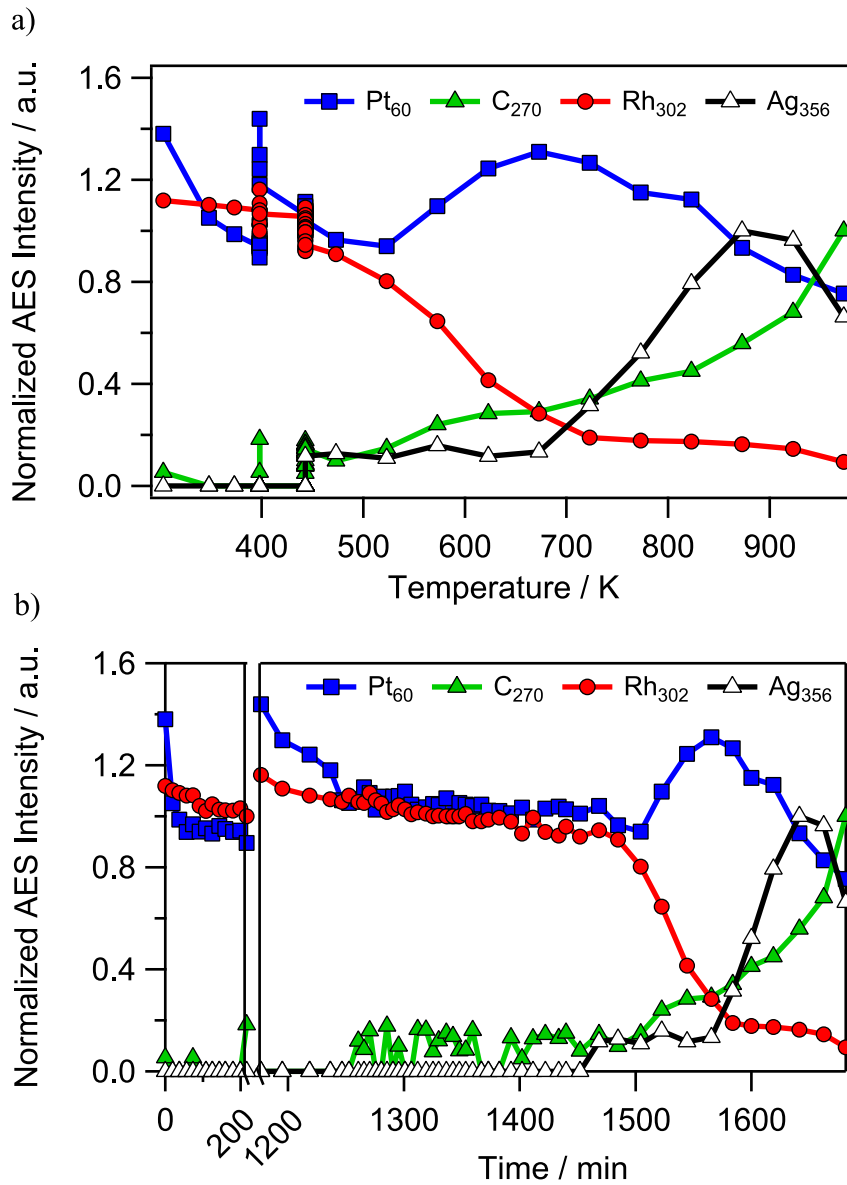


Figure 8.6: Thermally induced diffusion of 3 ML Rh into polycrystalline Pt on LiNbO₃ monitored with AES. a) Normalized Pt₆₀, C₂₇₀, Rh₃₀₂ and Ag₃₅₆ intensity as a function of temperature. The average intensity of Pt and Rh at 445 K is set to one, as well as the maximum intensity of C and Ag. b) Normalized AES intensity as a function of time (split x -axis).

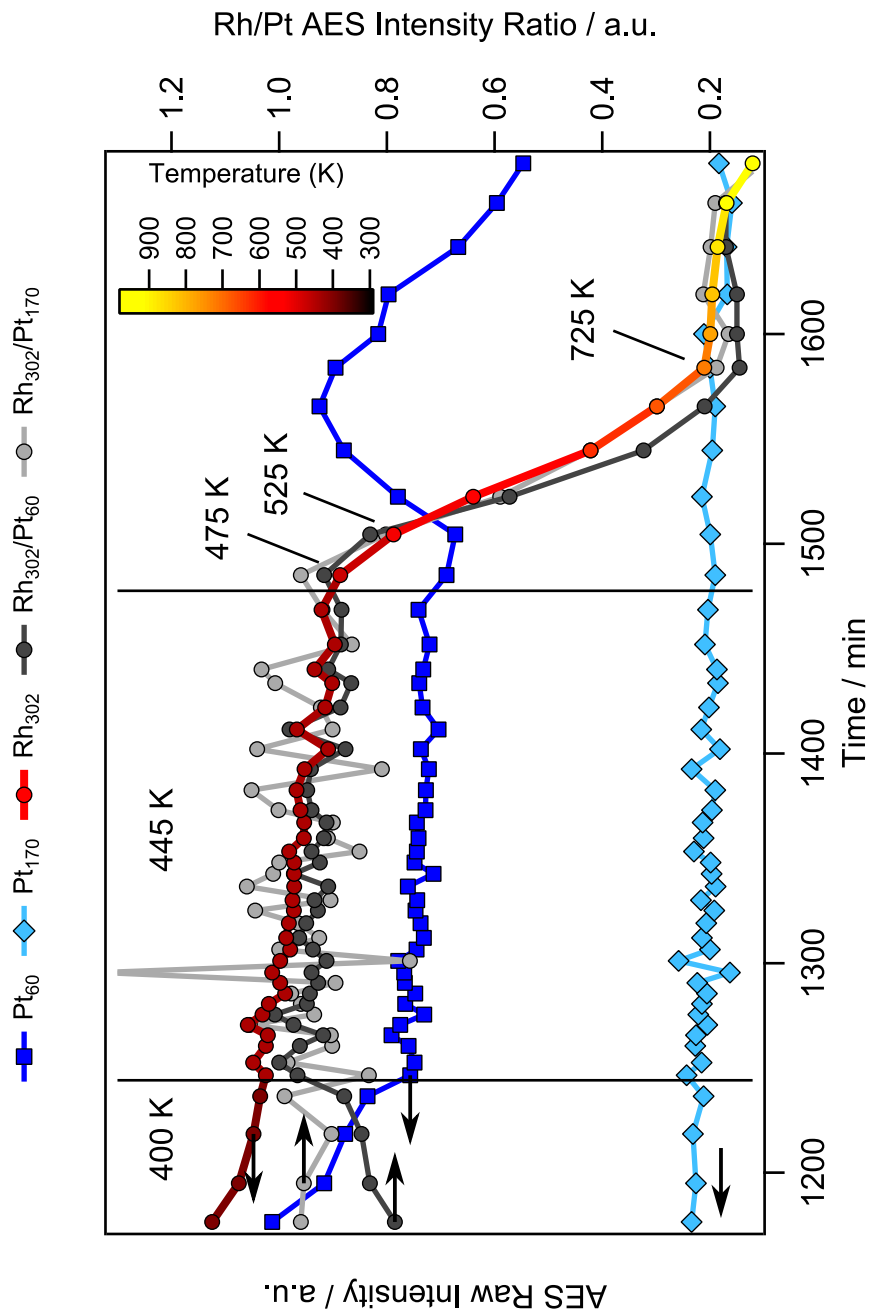


Figure 8.7: Thermally induced diffusion of 3 ML Rh into polycrystalline Pt on LiNbO₃ monitored with AES. The raw intensity of Pt₆₀, Pt₁₇₀ and Rh₃₀₂ is shown, together with the Intensity ratios Rh₃₀₂/Pt₆₀ and Rh₃₀₂/Pt₁₇₀. The substrate temperature is indicated by the color scale.

signal appears at around 1600 min experiment time, when the sample temperature is further increased to 475 K. The sudden appearance of silver may most likely be explained by a sample movement due to the temperature increase, which leads to an (partial) overlap of the probing electron beam with silver resin located at the edges of the LiNbO₃ crystal. Since the sample is mounted to the sample holder only by two Ta wires used for heating, the sample position reacts very sensitive to changing currents running through the heating wires. This is also a possible explanation for the decreasing Ag signal at temperatures above 900 K.

8.6 Thermal inter-diffusion of Rh and Pt for Rh/Pt(110)

The diffusion of Rh into the Pt bulk, or of Pt through the Rh overlay, can occur by different mechanisms. Preferentially, diffusion may occur along grain boundaries or lattice defects of the poly-crystalline film. In order to estimate the effect of such a facilitated diffusion, the thermal diffusion of thin Rh layers of varying thickness on a Pt(110) single crystal is studied in a comparative experiment. The single crystal, by definition consists of a single grain, although small angle grain boundaries still may exist. Also the number of lattice defects should be much lower compared to the poly-crystalline Pt film on the LiNbO₃ substrate.

Carbon accumulates on the sample surface during experiments of several hours length, due to the (photon or electron induced) dissociation of carbon monoxide from the residual gas, and due to C segregation of the sample bulk to the surface at elevated temperature. Therefore also the influence of varying amounts of co-deposited C on the segregation of Rh on Pt(100) are studied.

The AES intensity evolution as a function temperature is shown in figure 8.8a, b and c for 1.5 ML and 3 ML Rh co-deposited with C, and of 3 ML of “clean” Rh, respectively. In the graphs, the Auger raw intensities are displayed, together with the Rh₃₀₂/Pt₆₀ and Rh₃₀₂/Pt₁₇₀ intensity ratios (light and dark grey, right axis). As already mentioned in section 8.5, the Auger ratios are less affected by experimental drifts. The Rh₃₀₂ spectra and the Rh/Pt intensity ratios of all three measurements have in common, that the intensity evolution as a function of temperature is characterized by three different segments. Starting at 300 K, the intensity shows a more or less constant value until a change in slope at around 500 to 550 K indicates the onset of Rh diffusion into deeper layers. However, the intensity variation with increasing temperature is quite small until at around 800 K a second change in the slope marks a drastic decrease of the Rh signal. Finally, at around 900 to 950 K the Rh concentration in the topmost surface layers is below the resolution limit of the Auger spectrometer.

In all three measurements, in the measurements of Rh co-deposited with C and in the measurements with pure Rh, a considerable C accumulation on the sample surface is detected at high temperatures above 800 K. In the measurements with co-deposited C (figure 8.8top and middle graph), the C signal already raises significantly at around 400 K. The drastic increase of the carbon concentration in the first two measurements leads to a strong attenuation of the Pt₆₀ and Pt₁₇₀ intensity, which can be recognized

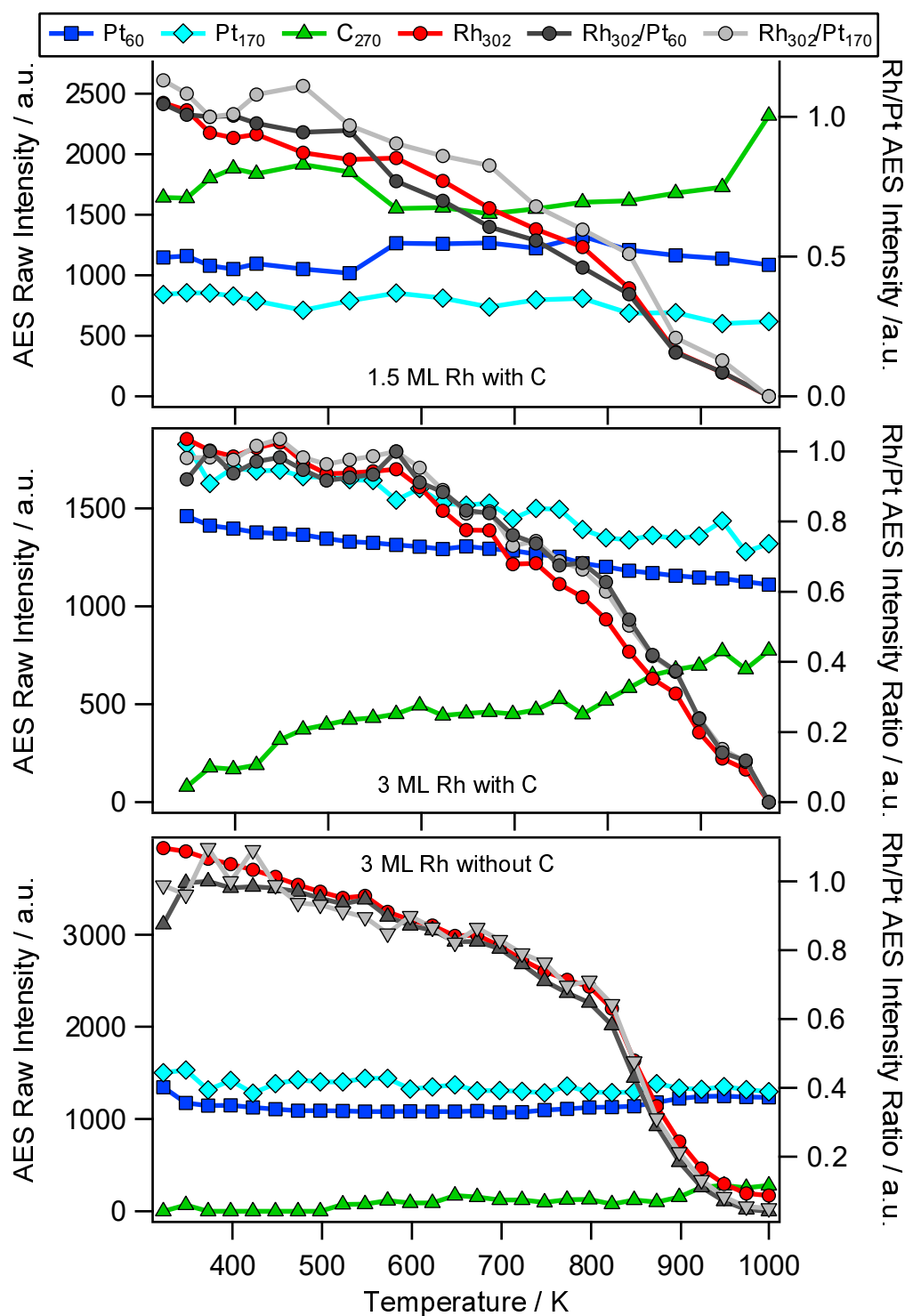


Figure 8.8: Thermal diffusion of Rh on Pt(100) monitored with AES. Shown are the Pt₆₀, Pt₁₇₀, C₂₇₀ and Rh₃₀₂ raw signals as acquired, together with the Auger intensity ratios Rh₃₀₂/Pt₆₀ and Rh₃₀₂/Pt₁₇₀ (right axis) of 1.5 ML and 3 ML Rh co-deposited with carbon (top and middle) as well as 3 ML Rh deposited without C (bottom). The average intensity ratios around 400 K have been set to unity.

by a constant decrease of both signals in the measurement of 3 ML Rh with C, displayed in the middle graph of figure 8.8(b). This effect obscures the expected Pt signal increase upon diffusion of Rh into deeper layers of the Pt crystal in the measurements with co-deposited C. In the last measurement shown in figure 8.8(bottom graph) a slight increase of Pt₆₀ and Pt₁₇₀ can be seen, starting at around 850 K.

8.7 Discussion

The results presented in section 8.4 demonstrate the diffusive intermixing of a 3 ML Rh film and the underlying poly-crystalline Pt film as a result of prolonged SAW treatment at 445 K. The comparison of the XPS data extracted from XPEEM measurements with and without the normalization for inhomogeneities of the MCP detector gives no indication for an experimental artifact being responsible for the Pt 4f ratio increase measured on the Rh covered and Rh free Pt surface. The Pt 4f intensity ratio exhibits no correlation with the drift of the incident X-ray beam. An initial correlation of the sample movement (which is caused by a temperature increase from 400 to 445 K as a result of the applied ultrasonic power) and the Pt intensity ratio is most probably caused by two related effects: The SAW treatment leads to the diffusive intermixing of Rh and Pt Pt, and simultaneously to a temperature increase of a sample, causing the sample movement. The fact that no direct connection between sample movement and intensity ratio exists is demonstrated by the missing correlation in the second half of the measurement.

With the applied ultrasonic power and frequency of approximately 0.1 W and 125 MHz, no SAW-induced-diffusion of Pt atoms through a \sim 5 ML thick Rh layer is measured at room temperature. At elevated temperature (445 K) instead, an increase by a factor 1.75 of the Pt 4f core level intensity ratio measured on a Rh covered and on a uncovered Pt area is observed.

AES experiments for comparison, which investigate the thermal diffusion of homogeneous, thin (\approx 3 ML) Rh layers into a 50 nm Pt film supported on LiNbO₃, and into a Pt(100) single crystal, indicate higher temperatures for the onset of thermal diffusion. On the Pt film on LiNbO₃ the onset of bulk diffusion is observed to occur at around 475 to 525 K. For the Rh diffusion into a Pt(100) crystal, the first Rh intensity decrease is measured around 550 K, followed by a steep decrease of the Rh intensity starting at 800 K.

These experimental findings are in accordance with density functional theory calculations of binary PtRh-alloys, which predict a Pt enrichment in the first surface layer at 1373 K [322]. The diffusion of Pt through the Rh overlayer is energetically favored due to the lower surface energy of Pt compared to Rh [317]. Ideal SAW should, however, have no influence on the composition of the surface, since all atoms remain in place. The observed diffusive intermixing might therefore be the consequence of anharmonic contributions of the SAW. Recently, in molecular dynamics simulations the SAW promoted surface diffusion was observed [316]. The anharmonic dissipation of energy during the dynamic coupling of acoustic waves with vibrational modes of the adsorbate turned

out to be important. Also adiabatic changes in surface temperature and a variation of diffusion barriers by surface stress were discussed [316].

The comparison of SAW-induced-diffusion experiments conducted at the CIRCE beamline with thermal-diffusion experiments conducted at Hannover indicates a temperature difference of about 30 - 80 K for the onset diffusive intermixing of Rh and Pt. In other words, the SAW have the same effect as a temperature increase by 30 - 80 K. Similar results were found in a combined PEEM and quadrupol mass spectrometry study Kelling and Cerasari et al. reported an increase of the CO₂ production rate in CO oxidation on Pt(110) upon application of SAW, corresponding to a temperature increase of 45 K [313,314].

The thermal-diffusion experiments have shown, that the system Rh/Pt reacts sensitive to C contamination, since C tends to segregate to the sample surface as the temperature is increased. This effect can already be observed at temperatures around 400 K, if a considerable amount of C is present. Since the measured intensity ratio variation of the Pt 4f core level intensities measured on Rh covered and pristine Pt areas is quite small, this effect has to be taken into account, when discussing the surface acoustic waves as the reason for Rh (or Pt) diffusion. However, surface segregation of C should affect the uncovered Pt surface as well as the Rh covered area in a similar manner, thus having only a minor influence on the Pt 4f ratio.

With the SAW-induced-diffusion experiments a first step is done towards a verification of the hypothesis, that SAW-induced surface defects are the main reason for a SAW-induced catalytic enhancement: it is shown, that SAW can alter the composition of a bimetallic surface. All the other elementary steps of adsorption, desorption and reaction need to be investigated as well. The most difficult problem will be to show under reaction conditions which effects are actually responsible for the observed increase in catalytic activity. A problem is to understand how SAW can promote the diffusion of surface atoms. Theoretical support will be essential here. First attempts in this direction have been made, showing that most likely it are the non-linear properties of such SAWs, i. e. properties that arise beyond a certain amplitude of the waves that are responsible for such promotion effects [316]. However, the measured temperature difference between pure thermal diffusion and SAW-induced diffusion is with 30 to 80 K quite small. The accuracy of the temperature measurement during the SAW experiments carried out in Barcelona should therefore be checked again in future experiments.

8.8 Summary

In the SAW-induced diffusion experiments carried out at Barcelona, the diffusive intermixing of Rh and Pt was observed at 445 K. In an experiment for comparison, the onset of pure thermal diffusion of Rh into the Pt bulk on an identical sample was measured to occur around 475 - 525 K, i. e. at a 30 - 80 K higher temperature. On a Pt(100) single crystal surface, diffusion of Rh into the Pt bulk was measured to start at around 550 K. A strong decrease of the Rh concentration on the Pt(100) surface sets in at around 800 K. In conclusion, a SAW facilitated diffusion of Rh into a poly-crystalline Pt film

was observed at 445 K. Due to the small temperature difference to the pure thermal diffusion a second experiment, which rules out the uncertainties related to temperature measurement and possible carbon contamination, is necessary.

Chapter 9

Conclusion and Outlook

In this study, the reaction-induced redistribution dynamics of vanadium oxide supported on Rh(111), Rh(110), and Pt(111) surfaces (inverse model catalysts) have been studied, as well as the influence of surface acoustic waves (SAW) on the composition of a bimetallic Rh/Pt surface.

Reaction-induced redistribution of VO_x

On the thermodynamically stable Rh(111) surface, the formation of macroscopic vanadium oxide stripe and island patterns during catalytic methanol oxidation is accompanied by a considerably increase in the formaldehyde production. A ripening mechanism, which involves the reversible polymerization/depolymerization of large vanadium oxide islands into mobile V_xO_y -clusters explains the movement and coalescence of neighboring oxide islands under reaction conditions [69, 70]. This mechanism is quite robust, since vanadium oxide island formation and coalescence can be observed in a number of catalytic reactions including ammonia and CO oxidation. The high catalytic activity of ultrathin VO_x layers on Rh(111) in methanol oxidation is probably caused by the existence of vanadyl groups in the two-dimensional VO_x phases [53, 56].

On the thermodynamically less stable Rh(110) surface, the catalytic activity of ultrathin VO_x films is below the activity of the bare Rh(110) surface. The formaldehyde production rate in methanol oxidation is beyond the detection limit of our experimental set-up. Whether the low catalytic activity is caused by the absence of vanadyl groups in the VO_x phases on Rh(110) has to be answered in future experiments.

Pattern formation in methanol oxidation is quite different on a $\text{VO}_x/\text{Rh}(110)$ surface. Even though macroscopic vanadium oxide islands form during methanol oxidation, no island movement or coalescence of islands can be seen. Instead, one observes an enormous variety of different chemical wave pattern ranging from traveling interface modulations and traveling wave fragments to chemical waves involving both, the Rh(110) substrate and macroscopic VO_x islands. The ability of the Rh(110) surface to undergo a number of different adsorbate-induced reconstructions is apparently crucial for the unusual chemical wave patterns. For comparison, no chemical wave pattern occurred on

$\text{VO}_x/\text{Rh}(111)$ catalysts.

If catalytic methanol oxidation is carried out on a $\text{VO}_x/\text{Pt}(111)$ catalyst, no pattern formation can be observed and the formaldehyde production rate is below the detection limit of our experimental set up. Some indications exist in literature, that the absence of vanadyl groups explains the low activity towards formaldehyde production [184, 308]. Whereas V can be stabilized by even small amounts of oxygen on the $\text{Rh}(111)$ and $\text{Rh}(110)$ surface up to 1000 K, a considerable loss of vanadium into the Pt bulk is encountered if the $\text{VO}_x/\text{Pt}(111)$ surface is annealed in a reaction atmosphere in the 10^{-4} mbar range.

The comparison of the systems $\text{VO}_x/\text{Rh}(111)$, $\text{VO}_x/\text{Rh}(110)$, and $\text{VO}_x/\text{Pt}(111)$ reveals, that the metallic support has an strong influence on pattern formation and on the activity and selectivity of the supported VO_x catalysts. The metallic support can stabilize two-dimensional VO_x phases that contain vanadyl groups and provides the oxygen needed for the oxidation reactions. In the system $\text{VO}_x/\text{Rh}(110)$ the adsorbate-induced reconstructions of the $\text{Rh}(110)$ substrate play a key role in the chemical wave patterns. In the system $\text{VO}_x/\text{Pt}(111)$ a diffusion of V into deeper layers of the Pt bulk can occur. The catalytic performance of ultrathin supported VO_x catalyst strongly depends on the supporting metal and the orientation of the substrate surface. Even slight changes like the crystallographic surface orientation of the supporting metal have a drastic impact.

PEEM yields no or only indirect chemical information. In order to obtain the chemical and structural information required for a mechanistic understanding, in situ spectroscopic low-energy electron microscopy (SPELEEM) measurements were conducted with nearly all systems investigated in this thesis. These results led to the formulation of the polymerization/depolymerization mechanism for the coalescence of vanadium oxide islands during methanol oxidation on $\text{VO}_x/\text{Rh}(111)$ [69, 70], and the defect mechanism, which explains the traveling interface modulations in catalytic methanol and ammonia oxidation on $\text{Rh}(110)$ and $\text{VO}_x/\text{Rh}(110)$.

Detailed chemical information is obtained for the hole patterns in the oxidation reactions with NO on $\text{VO}_x/\text{Rh}(111)$, and for the reactive phase separation on $\text{VO}_x/\text{Rh}(110)$ catalysts. On the basis of mathematical models and the structural and chemical characterization, it should be possible to develop mechanisms which successfully reproduce the experimental behavior.

Despite the enormous instrumental development of in situ and operando spectroscopy, there is still a lack of instruments that can chemically and structurally resolve the reaction dynamics under the conditions of real catalysis. A key problem in heterogeneous catalysis is the so-called pressure gap between UHV studies at 10^{-10} mbar and “real catalysis” at 1 to 100 bar. In this thesis a large part of the pressure gap could be bridged through near ambient pressure low-energy electron microscopy, which can operate up to 0.1 mbar. This instrument was recently developed by ELMITEC Elektronenmikroskopie GmbH and the first successful demonstrations were accomplished in a collaboration project with Elmitec [29]. With methanol oxidation on $\text{VO}_x/\text{Rh}(111)$ it is shown that the catalyst surface is different in different pressure ranges: from static VO_x islands at 10^{-7} mbar over coalescing and oscillating VO_x islands in the 10^{-4} mbar range to finally

turbulent redistribution dynamics in the 10^{-2} mbar range.

The influence of SAW on the composition of bimetallic surfaces

SAW are known to promote catalytic reactions, but the postulated electronic effects do not agree with the large time constants of the promotion effect. In order to explain the long time constants, a promotion due to the creation of structural defects was introduced as working hypothesis. Ideal SAW would leave all substrate atoms in their position, but in order to demonstrate that such a defect generation is in principle possible, a model system consisting of an ultrathin Rh layer on a Pt substrate was created.

SAW could successfully be applied to the bimetallic surface consisting of an 5 ML thick Rh layer on polycrystalline Pt. At room temperature, no changes in the surface composition are observed. If the sample is heated to 400 K, the diffusive intermixing of Pt and Rh can be observed as a consequence of SAW application. A thermal-diffusion experiment for comparison reveals, that the SAW have the same effect as a temperature increase of 30 to 80 K.

This result demonstrates that SAW can induce diffusion and that SAW can cause substrate atoms to change position. A first step in showing that SAW can generate surface defects seems to be taken, but first one needs to show in future experiments that one can clearly exclude thermally-induced diffusion as reason for the Pt/Rh intermixing. Furthermore, the influence of SAW on all elementary steps involved in a catalytic reaction needs to be investigated. By comparing the catalytic activity and adsorption properties of a pristine surface with the properties of a SAW promoted surface, it should be possible to come close to a mechanism that explains the promotion of catalytic reactions by SAW.

Bibliography

- [1] Ertl, G. *Angew. Chem. Int. Ed. Engl.* **2008**, *47*(19), 3524–3535.
- [2] Laidler, K. J. *Pure and Applied Chemistry* **1996**, *68*(1), 155.
- [3] Centi, G.; Perathoner, S. *Catal. Today* **2008**, *138*(1-2), 69–76.
- [4] Centi, G.; Perathoner, S. *Top. Catal.* **2009**, *52*(8), 948–961.
- [5] Armor, J. N. *Catal. Today* **2011**, *163*(1), 3–9.
- [6] Somorjai, G. A.; Li, Y. *Introduction to Surface Chemistry and Catalysis*; Wiley: Oxford, 2nd ed. ed., 2010.
- [7] Sinfelt, J. H. *Surf. Sci.* **2002**, *500*(1-3), 923–946.
- [8] Rupprechter, G. In *Surface and Interface Science*; Wandelt, K., Ed., Vol. 45; Wiley-VCH: Weinheim, 2012-2015; pages 459–528.
- [9] Prieto, G.; Schüth, F. *J. Catal.* **2015**, *328*, 59–71.
- [10] Schlögl, R. *Angew. Chem.* **2015**, *127*(11), 3531–3589.
- [11] Campbell, C. T.; Sauer, J. *Chem. Rev.* **2013**, *113*(6), 3859–3862.
- [12] Imbihl, R.; Behm, R. J.; Schlögl, R. *PCCP* **2007**, *9*(27), 3459.
- [13] Schloegl, R.; Schoonmaker, R. C.; Muhler, M.; Ertl, G. *Catal. Lett.* **1988**, *1*(6-7), 237–241.
- [14] Stoltze, P.; Nørskov, J. K. *Phys. Rev. Lett.* **1985**, *55*(22), 2502–2505.
- [15] Guerrero-Pérez, M. O.; Bañares, M. A. *Chem. Commun.* **2002**, (12), 1292–1293.
- [16] Frenken, J.; Groot, I. *Operando Research in Heterogeneous Catalysis*, Vol. 114; Springer International Publishing: Cham, 2017.
- [17] Weckhuysen, B. M. *Chem. Commun.* **2002**, (2), 97–110.
- [18] Rasmussen, P. B.; Hendriksen, B. L. M.; Zeijlemaker, H.; Ficke, H. G.; Frenken, J. W. M. *Rev. Sci. Instrum.* **1998**, *69*(11), 3879–3884.

- [19] Roobol, S. B.; Cañas-Ventura, M. E.; Bergman, M.; van Spronsen, M. A.; Onderwaater, W. G.; van der Tuijn, P. C.; Koehler, R.; Ofitserov, A.; van Baarle, G. J. C.; Frenken, J. W. M. *Rev. Sci. Instrum.* **2015**, *86*(3), 033706.
- [20] Creemer, J. F.; Santagata, F.; Morana, B.; Mele, L.; Alan, T.; Iervolino, E.; Pandraud, G.; Sarro, P. M. In *IEEE 24th International Conference on Micro Electro Mechanical Systems (MEMS), 2011*, pages 1103–1106, Piscataway, NJ, 2011. IEEE.
- [21] Vendelbo, S. B.; Elkjær, C. F.; Falsig, H.; Puspitasari, I.; Dona, P.; Mele, L.; Morana, B.; Nelissen, B. J.; van Rijn, R.; Creemer, J. F.; Kooyman, P. J.; Helveg, S. *Nat. Mater.* **2014**, *13*, 884 EP –.
- [22] Knop-Gericke, A.; Kleimenov, E.; Hävecker, M.; Blume, R.; Teschner, D.; Zafeiratos, S.; Schlögl, R.; Bukhtiyarov, V.; Kaichev, V.; Prosvirin, I. P.; Nizovskii, A. I.; Bluhm, H.; Barinov, A.; Dudin, P.; Kiskinova, M. *Adv. Catal.* **2009**, *52*, 213–272.
- [23] Toyoshima, R.; Yoshida, M.; Monya, Y.; Kousa, Y.; Suzuki, K.; Abe, H.; Mun, B. S.; Mase, K.; Amemiya, K.; Kondoh, H. *J. Phys. Chem. C* **2012**, *116*(35), 18691–18697.
- [24] DeCaluwe, S. C.; Grass, M. E.; Zhang, C.; Gabaly, F. E.; Bluhm, H.; Liu, Z.; Jackson, G. S.; McDaniel, A. H.; McCarty, K. F.; Farrow, R. L.; Linne, M. A.; Hussain, Z.; Eichhorn, B. W. *J. Phys. Chem. C* **2010**, *114*(46), 19853–19861.
- [25] Nguyen, L.; Tao, F. F.; Tang, Y.; Dou, J.; Bao, X.-J. *Chemical reviews* **2019**.
- [26] Donald, A. M. *Nat. Mater.* **2003**, *2*(8), 511–516.
- [27] Barroo, C.; Wang, Z.-J.; Willinger, M. G. *Acc. Chem. Res.* **2018**, *24*(S1), 660–661.
- [28] Ning, Y.; Fu, Q.; Li, Y.; Zhao, S.; Wang, C.; Breitschaft, M.; Hagen, S.; Schaff, O.; Bao, X. *Ultramicroscopy* **2019**, *200*, 105–110.
- [29] Franz*, T.; Boehn*, B. v.; Marchetto, H.; Borckenhagen, B.; Lilienkamp, G.; Daum, W.; Imbihl, R. *Ultramicroscopy* **2019**, *200*, 73–78.
- [30] Greeley, J.; Mavrikakis, M. *Nat. Mater.* **2004**, *3*(11), 810–815.
- [31] Suchorski, Y.; Rupprechter, G. *Catal. Lett.* **2018**, *148*(10), 2947–2956.
- [32] Surnev, S.; Fortunelli, A.; Netzer, F. P. *Chem. Rev.* **2013**, *113*(6), 4314–4372.
- [33] Barcaro, G.; Fortunelli, A. *PCCP* **2019**, *21*(22), 11510–11536.
- [34] Shapoval, O.; Hühn, S.; Verbeeck, J.; Jungbauer, M.; Belenchuk, A.; Moshnyaga, V. *J. Appl. Phys.* **2013**, *113*(17), 17C711.

- [35] Farstad, M. H.; Ragazzon, D.; Walle, L. E.; Schaefer, A.; Sandell, A.; Borg, A. *J. Phys. Chem. C* **2015**, *119*(12), 6660–6669.
- [36] Freund, H.-J. *Surf. Sci.* **2007**, *601*(6), 1438–1442.
- [37] Freund, H.-J.; Pacchioni, G. *Chem. Soc. Rev.* **2008**, *37*(10), 2224–2242.
- [38] Moulijn, J.; van Diepen, A.; Kapteijn, F. *Appl. Catal. A* **2001**, *212*(1-2), 3–16.
- [39] Zhang, J.; Medlin, J. W. *Surf. Sci. Rep.* **2018**, *73*(4), 117–152.
- [40] Liu, J. J. *ChemCatChem* **2011**, *3*(6), 934–948.
- [41] Lunkenbein, T.; Schumann, J.; Behrens, M.; Schlögl, R.; Willinger, M. G. *Angew. Chem. Int. Ed. Engl.* **2015**, *54*(15), 4544–4548.
- [42] Kuld, S.; Thorhauge, M.; Falsig, H.; Elkjær, C. F.; Helveg, S.; Chorkendorff, I.; Sehested, J. *Science* **2016**, *352*(6288), 969–974.
- [43] Schumann, J.; Eichelbaum, M.; Lunkenbein, T.; Thomas, N.; Álvarez Galván, M. C.; Schlögl, R.; Behrens, M. *ACS Catal.* **2015**, *5*(6), 3260–3270.
- [44] Rodriguez, J. A.; Liu, P.; Graciani, J.; Senanayake, S. D.; Grinter, D. C.; Stacchiola, D.; Hrbek, J.; Fernández-Sanz, J. *J. Phys. Chem. Lett.* **2016**, *7*(13), 2627–2639.
- [45] Schwab, G.-M. *Adv. Catal.* **1979**, *27*, 1–22.
- [46] Tauster, S. J.; Fung, S. C.; Garten, R. L. *JACS* **1978**, *100*(1), 170–175.
- [47] Tauster, S. J. *Acc. Chem. Res.* **2002**, *20*(11), 389–394.
- [48] Flege, J. I.; Grinter, D. C. *Prog. Surf. Sci.* **2018**, *93*(2), 21–45.
- [49] Andersson, M.; Bligaard, T.; Kustov, A.; Larsen, K.; Greeley, J.; Johannessen, T.; Christensen, C.; Nørskov, J. K. *J. Catal.* **2006**, *239*(2), 501–506.
- [50] Nørskov, J. K.; Abild-Pedersen, F.; Studt, F.; Bligaard, T. *PNAS* **2011**, *108*(3), 937–943.
- [51] Medford, A. J.; Vojvodic, A.; Hummelshøj, J. S.; Voss, J.; Abild-Pedersen, F.; Studt, F.; Bligaard, T.; Nilsson, A.; Nørskov, J. K. *J. Catal.* **2015**, *328*, 36–42.
- [52] van Santen, R. A.; Sautet, P. *Computational Methods in Catalysis and Materials Science*; Wiley, 2009.
- [53] Schoiswohl, J.; Sock, M.; Eck, S.; Surnev, S.; Ramsey, M. G.; Netzer, F. P.; Kresse, G. *Phys. Rev. B* **2004**, *69*(15), 1688.
- [54] Schoiswohl, J.; Kresse, G.; Surnev, S.; Sock, M.; Ramsey, M. G.; Netzer, F. P. *Phys. Rev. Lett.* **2004**, *92*(20), 206103.

- [55] Schoiswohl, J.; Surnev, S.; Sock, M.; Eck, S.; Ramsey, M. G.; Netzer, F. P.; Kresse, G. *Phys. Rev. B* **2005**, *71*(16), 086102.
- [56] Döbler, J.; Pritzsche, M.; Sauer, J. *JACS* **2005**, *127*(31), 10861–10868.
- [57] Romanyshyn, Y.; Guimond, S.; Kuhlenbeck, H.; Kaya, S.; Blum, R. P.; Niehus, H.; Shaikhutdinov, S.; Simic-Milosevic, V.; Nilius, N.; Freund, H.-J.; Ganduglia-Pirovano, M. V.; Fortrie, R.; Döbler, J.; Sauer, J. *Top. Catal.* **2008**, *50*(1-4), 106–115.
- [58] Göbke, D.; Romanyshyn, Y.; Guimond, S.; Sturm, J. M.; Kuhlenbeck, H.; Döbler, J.; Reinhardt, U.; Ganduglia-Pirovano, M. V.; Sauer, J.; Freund, H.-J. *Angew. Chem. Int. Ed. Engl.* **2009**, *48*(20), 3695–3698.
- [59] Mason, T. J.; Lorimer, J. P. *Sonochemistry: Theory, applications and uses of ultrasound in chemistry*; Wiley: New York, 1988.
- [60] Serpone, N.; Colarusso, P. *Res. Chem. Intermed.* **1994**, *20*(6), 635–679.
- [61] Suslick, K. S. *Science* **1990**, *247*(4949), 1439–1445.
- [62] Suslick, J.; Casadonte, D. J. *JACS* **1987**, *109*(11), 3459–3461.
- [63] Inoue, Y. *Surf. Sci. Rep.* **2007**, *62*(8), 305–336.
- [64] Inoue, Y. *Catal. Surveys Japan* **1999**, *3*(2), 95–108.
- [65] Denison, D. R. *J. Vac. Sci. Technol.* **1969**, *6*(1), 214–217.
- [66] Krischer, C.; Lichtman, D. *Phys. Lett. A* **1973**, *44*(2), 99–100.
- [67] Gruyters, M.; Mitrelias, T.; King, D. A. *Appl. Phys. A* **1995**, *61*(3), 243–251.
- [68] von Boehn, B. *Redistribution of Supported Vanadium Oxide Catalysts by Pattern Formation* Bachelor Thesis, Leibniz University Hannover, Hannover, **2014**.
- [69] Hesse, M.; von Boehn, B.; Locatelli, A.; Sala, A.; Montes, T. O.; Imbihl, R. *Phys. Rev. Lett.* **2015**, *115*(13), 136102.
- [70] Hesse, M. *Strukturbildung ultradünner Vanadiumoxid-Schichten bei der katalytischen Oxidation von Methanol an Rh(111)* PhD Thesis, Leibniz University Hannover, Hannover, **2019**.
- [71] von Boehn, B. *Restructuring of thin Vanadium Oxide layers on Rh(110) during the Formaldehyde Synthesis Reaction* Master Thesis, Leibniz University Hannover, Hannover, **2016**.
- [72] Bauer, E. *Surface Microscopy with Low Energy Electrons*; Springer New York: New York, NY and s.l., 2014.

- [73] Ertl, G.; Küppers, J. *Low Energy Electrons and Surface Chemistry*; VCH: Weinheim, 2., completely rev. ed. ed., 1985.
- [74] Van Hove, M. A.; Weinberg, W. H.; Chan, C.-M. *Low-Energy Electron Diffraction: Experiment, Theory and Surface Structure Determination*, Vol. 6 of *Springer Series in Surface Sciences*; Springer: Berlin and Heidelberg, 1986.
- [75] Fauster, T.; Hammer, L.; Heinz, K.; Schneider, M. A. *Oberflächenphysik: Grundlagen und Methoden*; Oldenbourg Verlag: München, 2013.
- [76] Nič, M., Jirát, J., Košata, B., Jenkins, A., McNaught, A., Eds. *IUPAC Compendium of Chemical Terminology*; IUPAC: Research Triangle Park, NC, 2009.
- [77] Niehus, H.; Heiland, W.; Taglauer, E. *Surf. Sci. Rep.* **1993**, *17*(4-5), 213–303.
- [78] Seah, M. P.; Dench, W. A. *Surf. Interface Anal.* **1979**, *1*(1), 2–11.
- [79] Meitner, L. *Z. Physik* **1922**, *11*(1), 35–54.
- [80] Auger, P. *J. Phys. Radium* **1925**, *6*(6), 205–208.
- [81] Weissmann, R.; Müller, K. *Surf. Sci. Rep.* **1981**, *1*(5), 251–309.
- [82] Hanke, G.; Müller, K. *J. V. Sci. Technol.* **1984**, *2*(2), 964–968.
- [83] Rye, R. R.; Madey, T. E.; Houston, J. E.; Holloway, P. H. *J. Chem. Phys.* **1978**, *69*(4), 1504–1512.
- [84] Feibelman, P. J.; McGuire, E. J.; Pandey, K. C. *Phys. Rev. B* **1977**, *15*(4), 2202–2216.
- [85] Rao, C. N. R.; d. Sarma, D.; Hedge, M. S. *Proc. Royal Soc. A* **1980**, *370*(1741), 269–280.
- [86] Sawatzky, G. A.; Post. *Phys. Rev. B* **1979**, *20*(4), 1546–1555.
- [87] Borkenhagen, B. *Oberflächen-Elektronenmikroskopie von anwendungsrelevanten Materialien für heterogene Katalyse, III-V-Heteroepitaxie und polykristalline Werkstoffe* PhD Thesis, Technische Universität Clausthal, Clausthal-Zellerfeld, **2012**.
- [88] Risley, J. S. *Rev. Sci. Instr.* **1972**, *43*(1), 95–103.
- [89] Heun, S.; Schmidt, T.; Ressel, B.; Bauer, E.; Prince, K. C. *Synchrotron Radiat. News* **1999**, *12*(5), 25–29.
- [90] Locatelli, A.; Bianco, A.; Cocco, D.; Cherifi, S.; Heun, S.; Marsi, M.; Pasqualetto, M.; Bauer, E. *J. Phys. IV France* **2003**, *104*, 99–102.

- [91] Amati, M.; Barinov, A.; Feyer, V.; Gregoratti, L.; Al-Hada, M.; Locatelli, A.; Mentès, T. O.; Sezen, H.; Schneider, C. M.; Kiskinova, M. *J. Electron. Spectros. Relat. Phenomena* **2018**, *224*, 59–67.
- [92] Aballe, L.; Foerster, M.; Pellegrin, E.; Nicolas, J.; Ferrer, S. *J. Synchrotron Radiat.* **2015**, *22*(3), 745–752.
- [93] Casalis, L.; Jark, W.; Kiskinova, M.; Lonza, D.; Melpignano, P.; Morris, D.; Rosei, R.; Savoia, A.; Abrami, A.; Fava, C.; Furlan, P.; Pugliese, R.; Vivoda, D.; Sandrin, G.; Wei, F.-Q.; Contarini, S.; DeAngelis, L.; Gariazzo, C.; Nataletti, P.; Morrison, G. R. *Rev. Sci. Instr.* **1995**, *66*(10), 4870–4875.
- [94] Grosvenor, A. P.; Biesinger, M. C.; St. Smart, R. C.; Gerson, A. R. In *Hard x-ray photoelectron spectroscopy (HAXPES)*; Woicik, J. C., Ed., Vol. 59 of *Springer Series in Surface Sciences*; Springer: Cham and Heidelberg and New York and Dordrecht and London, 2016; pages 217–262.
- [95] Cooper, J.; Zare, R. N. *J. Chem. Phys.* **1968**, *48*(2), 942–943.
- [96] Atomic Calculation of Photoionization Cross-Sections and Asymmetry Parameters. Elettra Sincrotrone Trieste S.C.p.A.. **2019**.
- [97] Yeh, J. J.; Lindau, I. *At. Data Nucl. Data Tables* **1985**, *32*(1), 1–155.
- [98] Yeh, J.-J. *Atomic Calculation of Photoionization Cross-Sections and Asymmetry Parameters*; Gordon and Breach Science Publ: Langhorne, PA, 1993.
- [99] Lander, J. J.; Morrison, J.; Unterwald, F. *Rev. Sci. Instrum.* **1962**, *33*(7), 782–783.
- [100] Oura, K.; Katayama, M.; Zotov, A. V.; Lifshits, V. G.; Saranin, A. A. *Surface Science: An Introduction*, Advanced Texts in Physics; Springer: Berlin and Heidelberg, 2003.
- [101] Altman, M. S. *J. Phys.: Condens. Matter* **2010**, *22*(8), 084017.
- [102] Locatelli, A.; Aballe, L.; Mentès, T. O.; Kiskinova, M.; Bauer, E. *Surf. Interface Anal.* **2006**, *38*(12-13), 1554–1557.
- [103] Mentès, T. O.; Zamborlini, G.; Sala, A.; Locatelli, A. *Beilstein J. Nanotechnol.* **2014**, *5*, 1873–1886.
- [104] Scholl, A.; Ohldag, H.; Nolting, F.; Stöhr, J.; Padmore, H. A. *Rev. Sci. Instr.* **2002**, *73*(3), 1362–1366.
- [105] Tonner, B. P.; Harp, G. R. *Rev. Sci. Instrum.* **1988**, *59*(6), 853–858.
- [106] Engel, W.; Kordesch, M. E.; Rotermund, H. H.; Kubala, S.; von Oertzen, A. *Ultramicroscopy* **1991**, *36*(1-3), 148–153.

- [107] Bauer, E. *Ultramicroscopy* **1985**, *17*(1), 51–56.
- [108] Bauer, E.; Mundschau, M.; Swiech, W.; Telieps, W. *Ultramicroscopy* **1989**, *31*(1), 49–57.
- [109] Hertz, H. *Ann. Phys. Chem.* **1887**, *267*(7), 421–448.
- [110] Hallwachs, W. *Ann. Phys. Chem.* **1889**, *273*(8), 666–675.
- [111] Einstein, A. *Ann. Phys. Chem.* **1905**, *322*(6), 132–148.
- [112] Rotermund, H. H.; Engel, W.; Jakubith, S.; von Oertzen, A.; Ertl, G. *Ultramicroscopy* **1991**, *36*(1-3), 164–172.
- [113] Fowler, R. H. *Phys. Rev.* **1931**, *38*(1), 45–56.
- [114] DuBridge, L. A. *Phys. Rev.* **1933**, *43*(9), 727–741.
- [115] Dushman, S. *Phys. Rev.* **1923**, *21*(6), 623–636.
- [116] Schindelin, J.; Arganda-Carreras, I.; Frise, E.; Kaynig, V.; Longair, M.; Pietzsch, T.; Preibisch, S.; Rueden, C.; Saalfeld, S.; Schmid, B.; Tinevez, J.-Y.; White, D. J.; Hartenstein, V.; Eliceiri, K.; Tomancak, P.; Cardona, A. *Nat. Methods* **2012**, *9*(7), 676–682.
- [117] SIS (SPELEEM Image Suite). Locatelli, A.; Mentęs, T. O. **08.05.2019**.
- [118] Locatelli, A.; Mentęs, T. O. In *Synchrotron Radiation*; Mobilio, S., Boscherini, F., Meneghini, C., Eds., Vol. 185; Springer Berlin Heidelberg: Berlin, Heidelberg, 2015; pages 571–591.
- [119] Bauer, E. *Rep. Prog. Phys.* **1994**, *57*(9), 895–938.
- [120] Schmidt, T.; Heun, S.; Slezak, J.; Diaz, J.; Prince, K. C.; Lilienkamp, G.; Bauer, E. *Surf. Rev. Lett.* **1998**, *05*(06), 1287–1296.
- [121] Locatelli, A.; Mentęs, T. O.; Niño, M. Á.; Bauer, E. *Ultramicroscopy* **2011**, *111*(8), 1447–1454.
- [122] Günther, S. *Prog. Surf. Sci.* **2002**, *70*(4-8), 187–260.
- [123] Locatelli, A.; Cherifi, S.; Heun, S.; Marsi, M.; Ono, K.; Pavlovska, A.; Bauer, E. *Surf. Rev. Lett.* **2002**, *09*(01), 171–176.
- [124] Baez, A. V. *J. Opt. Soc. Am.* **1961**, *51*(4), 405.
- [125] Gregoratti, L.; Barinov, A.; Benfatto, E.; Cautero, G.; Fava, C.; Lacovig, P.; Lonza, D.; Kiskinova, M.; Tommasini, R.; Mähl, S.; Heichler, W. *Rev. Sci. Instrum.* **2004**, *75*(1), 64–68.

- [126] Gregoratti, L.; Marsi, M.; Cautero, G.; Kiskinova, M.; Morrison, G. R.; Potts, A. W. *Nucl. Instr. Meth. Phys. Res. A* **2001**, *467-468*, 884–888.
- [127] Marsi, M.; Casalis, L.; Gregoratti, L.; Günther, S.; Kolmakov, A.; Kovac, J.; Lonza, D.; Kiskinova, M. *J. Electron. Spectros. Relat. Phenomena* **1997**, *84(1-3)*, 73–83.
- [128] Amati, M.; Abyaneh, M. K.; Gregoratti, L. *J. Inst.* **2013**, *8(05)*, T05001–T05001.
- [129] Sezen, H.; Al-Hada, M.; Amati, M.; Gregoratti, L. *Surf. Interface Anal.* **2018**, *50(10)*, 921–926.
- [130] Zeller, P.; Amati, M.; Sezen, H.; Scardamaglia, M.; Struzzi, C.; Bittencourt, C.; Lantz, G.; Hajlaoui, M.; Papalazarou, E.; Marino, M.; Fanetti, M.; Ambrosini, S.; Rubini, S.; Gregoratti, L. *Phys. Status Solidi A* **2018**, *215(19)*, 1800308.
- [131] Gregoratti, L.; Al-Hada, M.; Amati, M.; Brescia, R.; Roccella, D.; Sezen, H.; Zeller, P. *Top. Catal.* **2018**, *61(12-13)*, 1274–1282.
- [132] NIST Chemistry WebBook, NIST Standard Reference Database 69. Linstrom, P.
- [133] Paul, W. *Angew. Chem. Int. Ed. Engl.* **1990**, *29(7)*, 739–748.
- [134] Paul, W.; Raether, M. *Z. Physik* **1955**, *140(3)*, 262–273.
- [135] Campana, J. E. *Int. J. Mass Spectrom.* **1980**, *33(2)*, 101–117.
- [136] Falconer, J. L.; Schwarz, J. A. *Catal. Rev.* **1983**, *25(2)*, 141–227.
- [137] Zhang.; Lagally. *Science* **1997**, *276(5311)*, 377–383.
- [138] Venables, J. A.; Spiller, G. D. T. In *Surface Mobilities on Solid Materials*; Binh, V. T., Ed., Vol. 27 of *NATO Advanced Science Institutes Series, Series B*; Springer: Boston, MA, 1983; pages 341–404.
- [139] Frank, F. C.; van der Merwe, J. H.. *Proc. R. Soc. Lond. A* **1949**, *198(1053)*, 205–216.
- [140] Frank, F. C.; van der Merwe, J. H.. *Proc. R. Soc. Lond. A* **1949**, *198(1053)*, 216–225.
- [141] Frank, F. C.; van der Merwe, J. H.. *Proc. R. Soc. Lond. A* **1949**, *200(1060)*, 125–134.
- [142] Stranski, I. N.; Krastanow, L. *Monatsh. Chem.* **1937**, *71(1)*, 351–364.
- [143] Volmer, M.; Weber, t. *Z. Phys. Chem.* **1926**, *119U(1)*.
- [144] Bauer, E. *Z. Kristallogr. – Cryst. Mater.* **1958**, *110(1-6)*.

- [145] Gilmer, G. H.; Grabow, M. H. *JOM* **1987**, *39*(6), 19–23.
- [146] Ratsch, C.; Zangwill, A. *Surf. Sci.* **1993**, *293*(1-2), 123–131.
- [147] Baskaran, A.; Smereka, P. *J. Appl. Phys.* **2012**, *111*(4), 044321.
- [148] Argile, C.; Rhead, G. E. *Surf. Sci. Rep.* **1989**, *10*(6-7), 277–356.
- [149] Singh, H. P. *Acta Cryst. A* **1968**, *24*(4), 469–471.
- [150] Barbieri, A.; van Hove, M. A.; Somorjai, G. A. *Surf. Sci.* **1994**, *306*(3), 261–268.
- [151] Brault, P.; Range, H.; Toennies, J. P.; Wöll, C. *Z. Phys. Chem.* **1997**, *198*(1), 1–17.
- [152] Ganduglia-Pirovano, M. V.; Scheffler, M. *Phys. Rev. B* **1999**, *59*(23), 15533–15543.
- [153] Thiel, P. A.; Yates, J. T.; Weinberg, W. H. *Surf. Sci.* **1979**, *82*(1), 22–44.
- [154] Castner, D. G.; Somorjai, G. A. *Appl. Surf. Sci.* **1980**, *6*(1), 29–38.
- [155] Schwegmann, S.; Over, H.; de Renzi, V.; Ertl, G. *Surf. Sci.* **1997**, *375*(1), 91–106.
- [156] Köhler, L.; Kresse, G.; Schmid, M.; Lundgren, E.; Gustafson, J.; Mikkelsen, A.; Borg, M.; Yuhara, J.; Andersen, J. N.; Marsman, M.; Varga, P. *Phys. Rev. Lett.* **2004**, *93*(26 Pt 1), 266103.
- [157] Gibson, K. D.; Viste, M.; Sanchez, E. C.; Sibener, S. J. *J. Chem. Phys.* **1999**, *110*(6), 2757–2760.
- [158] Wider, J.; Greber, T.; Wetli, E.; Kreutz, T. J.; Schwaller, P.; Osterwalder, J. *Surf. Sci.* **1998**, *417*(2-3), 301–310.
- [159] Ganduglia-Pirovano, M. V.; Reuter, K.; Scheffler, M. *Phys. Rev. B* **2002**, *65*(24), 472.
- [160] Root, T. W.; Schmidt, L. D.; Fisher, G. B. *Surf. Sci.* **1983**, *134*(1), 30–45.
- [161] Brault, P.; Range, H.; Toennies, J. P. *J. Chem. Phys.* **1997**, *106*(21), 8876–8889.
- [162] Gustafson, J.; Mikkelsen, A.; Borg, M.; Lundgren, E.; Köhler, L.; Kresse, G.; Schmid, M.; Varga, P.; Yuhara, J.; Torrelles, X.; Quirós, C.; Andersen, J. N. *Phys. Rev. Lett.* **2004**, *92*(12), 126102.
- [163] Ganduglia-Pirovano, M. V.; Scheffler, M.; Baraldi, A.; Lizzit, S.; Comelli, G.; Paolucci, G.; Rosei, R. *Phys. Rev. B* **2001**, *63*(20), 165.
- [164] Wohlgenuth, H. *Über die Wechselwirkung von Sauerstoff mit einer Rh(110)-Oberfläche* PhD Thesis, Freie Universität Berlin, Berlin, **1993**.
- [165] Kiskinova, M. *Chem. Rev.* **1996**, *96*(4), 1431–1448.

- [166] Comelli, G.; Dhanak, V. R.; Kiskinova, M.; Pangher, N.; Paolucci, G.; Prince, K. C.; Rosei, R. *Surf. Sci.* **1992**, *260*(1-3), 7–13.
- [167] Comelli, G.; Dhanak, V. R.; Kiskinova, M.; Paolucci, G.; Prince, K. C.; Rosei, R. *Surf. Sci.* **1992**, *269-270*, 360–364.
- [168] Schwarz, E.; Lenz, J.; Wohlgemuth, H.; Christmann, K. *Vacuum* **1990**, *41*(1-3), 167–170.
- [169] Dudin, P.; Barinov, A.; Gregoratti, L.; Kiskinova, M.; Esch, F.; Dri, C.; Africh, C.; Comelli, G. *J. Phys. Chem. B* **2005**, *109*(28), 13649–13655.
- [170] Dhanak, V. R.; Baraldi, A.; Comelli, G.; Paolucci, G.; Kiskinova, M.; Rosei, R. *Surf. Sci.* **1993**, *295*(3), 287–294.
- [171] Marbrow, R. A.; Lambert, R. M. *Surf. Sci.* **1977**, *67*(2), 489–500.
- [172] Baraldi, A.; Dhanak, V. R.; Comelli, G.; Prince, K. C.; Rosei, R. *Surf. Sci.* **1993**, *293*(3), 246–253.
- [173] Arblaster, J. W. *Platinum Metals Review* **1997**, (41), 12–21.
- [174] Sandy.; Mochrie.; Zehner.; Grübel.; Huang.; Gibbs. *Physical review letters* **1992**, *68*(14), 2192–2195.
- [175] Starke, U.; Barbieri, A.; Materer, N.; van Hove, M. A.; Somorjai, G. A. *Surf. Sci.* **1993**, *286*(1-2), 1–14.
- [176] Derry.; Ji-Zhong. *Phys. Rev. B* **1989**, *39*(3), 1940–1941.
- [177] Steininger, H.; Lehwald, S.; Ibach, H. *Surf. Sci.* **1982**, *123*(1), 1–17.
- [178] Niehus, H.; Comsa, G. *Surf. Sci. Lett.* **1981**, *102*(1), L14–L20.
- [179] Derry, G. N.; Ross, P. N. *J. Chem. Phys.* **1985**, *82*(6), 2772–2778.
- [180] Heilmann, P.; Heinz, K.; Müller, K. *Surf. Sci.* **1979**, *83*(2), 487–497.
- [181] Pennemann, B.; Oster, K.; Wandelt, K. *Surf. Sci.* **1991**, *249*(1-3), 35–43.
- [182] Schoiswohl, J.; Eck, S.; Ramsey, M. G.; Andersen, J. N.; Surnev, S.; Netzer, F. P. *Surf. Sci.* **2005**, *580*(1-3), 122–136.
- [183] Schoiswohl, J.; Surnev, S.; Netzer, F. P.; Kresse, G. *J. Phys.: Condens. Matter* **2006**, *18*(4), R1–R14.
- [184] Tang, Z.; Wang, S.; Zhang, L.; Ding, D.; Chen, M.; Wan, H. *PCCP* **2013**, *15*(29), 12124–12131.
- [185] von Boehn, B.; Menteg, T. O.; Locatelli, A.; Sala, A.; Imbihl, R. *J. Phys. Chem. C* **2017**, *121*(36), 19774–19785.

- [186] Píš, I.; Skála, T.; Cabala, M.; Šutara, F.; Libra, J.; Škoda, M.; Matolín, V.; Nehasil, V. *J. Alloys Compd.* **2012**, *543*, 189–196.
- [187] Koch, H. P.; Krenn, G.; Bako, I.; Schennach, R. *J. Chem. Phys.* **2005**, *122*(24), 244720.
- [188] Píš, I.; Stetsovych, V.; Mysliveček, J.; Kettner, M.; Vondráček, M.; Dvořák, F.; Mazur, D.; Matolín, V.; Nehasil, V. *J. Phys. Chem. C* **2013**, *117*(24), 12679–12688.
- [189] Haken, H.; Mikhailov, A. S. *Foundations of Synergetics I*, Vol. 51; Springer Berlin Heidelberg: Berlin, Heidelberg, 1990.
- [190] Haken, H.; Mikhailov, A. S.; Loskutov, A. Y. *Foundations of Synergetics II*, Vol. 52; Springer Berlin Heidelberg: Berlin, Heidelberg, 1991.
- [191] Mikhailov, A. S.; Ertl, G. *Chemical Complexity*; Springer International Publishing: Cham, 2017.
- [192] Meschede, D. In *Gerthsen Physik*; Meschede, D., Vogel, H., Gerthsen, C., Eds., Springer-Lehrbuch; Springer: Berlin, 2010; pages 211–249.
- [193] Rinzel, J.; Terman, D. *SIAM J. Appl. Math.* **1982**, *42*(5), 1111–1137.
- [194] Kuznetsov, Y. A. *Elements of Applied Bifurcation Theory*, Vol. 112 of *Applied Mathematical Sciences*; Springer: New York, NY, third edition ed., 2004.
- [195] Imbihl, R. *Catal. Today* **2005**, *105*(2), 206–222.
- [196] Makeev, A.; Imbihl, R. *Phys. Rev. E* **2019**, *100*(4).
- [197] Bär.; Nettesheim.; Rotermund.; Eiswirth.; Ertl. *Phys. Rev. Lett.* **1995**, *74*(7), 1246–1249.
- [198] Makeev, A.; Hinz, M.; Imbihl, R. *J. Chem. Phys.* **2001**, *114*(20), 9083–9098.
- [199] Turing, A. *Phil. Trans. R. Soc. Lond. B* **1952**, *237*(641), 37–72.
- [200] Lovis, F.; Hesse, M.; Imbihl, R. *Catal. Lett.* **2010**, *136*(3-4), 171–176.
- [201] Lovis, F.; Imbihl, R. *J. Phys. Chem. C* **2011**, *115*(39), 19141–19148.
- [202] Lovis, F.; Hesse, M.; Locatelli, A.; Mentès, T. O.; Niño, M. Á.; Lilienkamp, G.; Borckenhagen, B.; Imbihl, R. *J. Phys. Chem. C* **2011**, *115*(39), 19149–19157.
- [203] Weckhuysen, B. M.; Keller, D. E. *Catal. Today* **2003**, *78*(1-4), 25–46.
- [204] Granger, P.; Parvulescu, V. I. *Chem. Rev.* **2011**, *111*(5), 3155–3207.
- [205] Surnev, S.; Ramsey, M.; Netzer, F. *Prog. Surf. Sci.* **2003**, *73*(4-8), 117–165.
- [206] Kosuge, K. *J. Phys. Chem. Solids* **1967**, *28*(8), 1613–1621.

- [207] Goering, E.; Schramme, M.; Müller, O.; Paulin, H.; Klemm, M.; denBoer, M. L.; Horn, S. *Physica B: Condens. Matter* **1997**, *230-232*, 996–998.
- [208] Toledano, D. S.; Metcalf, P.; Henrich, V. E. *Surf. Sci.* **2000**, *449*(1-3), 19–30.
- [209] Czekaj, I.; Hermann, K.; Witko, M. *Surf. Sci.* **2003**, *525*(1-3), 33–45.
- [210] Czekaj, I.; Witko, M.; Hermann, K. *Surf. Sci.* **2003**, *525*(1-3), 46–56.
- [211] Schoiswohl, J.; Sock, M.; Surnev, S.; Ramsey, M.; Netzer, F.; Kresse, G.; Andersen, J. *Surf. Sci.* **2004**, *555*(1-3), 101–117.
- [212] Kresse, G.; Surnev, S.; Schoiswohl, J.; Netzer, F. *Surf. Sci.* **2004**, *555*(1-3), 118–134.
- [213] Hermann, K.; Witko, M.; Druzinic, R.; Tokarz, R. *Appl. Phys. A* **2001**, *72*(4), 429–442.
- [214] Metcalfe, I.; Sugi, Y.; Groppi, G.; Sheldon, R.; Wachs, I. E. *Catalysis: James J. Spivey*, Specialist periodical report; Royal Society of chemistry: Cambridge, 2007.
- [215] Wachs, I. E. *Dalton Trans.* **2013**, *42*(33), 11762–11769.
- [216] Sauer, J.; Zehl, A.; Limberg, C.; Schomäcker, R. *Structure, Dynamics and Reactivity of Aggregates of Transition Metal Oxides*; Deutsche Forschungsgemeinschaft: Bonn, 2011.
- [217] Tepper, B.; Richter, B.; Dupuis, A.-C.; Kuhlenbeck, H.; Hucho, C.; Schilbe, P.; bin Yarmo, M. A.; Freund, H.-J. *Surf. Sci.* **2002**, *496*(1-2), 64–72.
- [218] Kröger, E. A.; Sayago, D. I.; Allegretti, F.; Knight, M. J.; Polcik, M.; Unterberger, W.; Lerotholi, T. J.; Hogan, K. A.; Lamont, C.; Woodruff, D. P. *Surf. Sci.* **2007**, *601*(16), 3350–3360.
- [219] Dupuis, A.-C.; Abu Haija, M.; Richter, B.; Kuhlenbeck, H.; Freund, H.-J. *Surf. Sci.* **2003**, *539*(1-3), 99–112.
- [220] Baron, M.; Abbott, H.; Bondarchuk, O.; Stacchiola, D.; Uhl, A.; Shaikhutdinov, S.; Freund, H.-J.; Popa, C.; Ganduglia-Pirovano, M. V.; Sauer, J. *Angew. Chem. Int. Ed.* **2009**, *48*(43), 8006–8009.
- [221] Ganduglia-Pirovano, M. V.; Popa, C.; Sauer, J.; Abbott, H.; Uhl, A.; Baron, M.; Stacchiola, D.; Bondarchuk, O.; Shaikhutdinov, S.; Freund, H.-J. *JACS* **2010**, *132*(7), 2345–2349.
- [222] Asmis, K. R.; Meijer, G.; Brümmer, M.; Kaposta, C.; Santambrogio, G.; Wöste, L.; Sauer, J. *J. Chem. Phys.* **2004**, *120*(14), 6461–6470.
- [223] Sauer, J.; Dobler, J. *Dalton Trans.* **2004**, (19), 3116–3121.

- [224] Feyel, S.; Döbler, J.; Schröder, D.; Sauer, J.; Schwarz, H. *Angew. Chem. Int. Ed. Engl.* **2006**, *45*(28), 4681–4685.
- [225] Sturm, J. M.; Göbke, D.; Kuhlenbeck, H.; Döbler, J.; Reinhardt, U.; Ganduglia-Pirovano, M. V.; Sauer, J.; Freund, H.-J. *PCCP* **2009**, *11*(17), 3290–3299.
- [226] Romanyshyn, Y.; Guimond, S.; Göbke, D.; Sturm, J. M.; Kuhlenbeck, H.; Döbler, J.; Ganduglia-Pirovano, M. V.; Sauer, J.; Freund, H.-J. *Top. Catal.* **2011**, *54*(10–12), 669–684.
- [227] Rodríguez, J. A.; Hrbek, J. *Surf. Sci.* **2010**, *604*(3–4), 241–244.
- [228] Schoiswohl, J.; Surnev, S.; Netzer, F. P. *Top. Catal.* **2005**, *36*(1–4), 91–105.
- [229] Krenn, G.; Schoiswohl, J.; Surnev, S.; Netzer, F. P.; Schennach, R. *Top. Catal.* **2007**, *46*(1–2), 231–238.
- [230] Schoiswohl, J.; Sock, M.; Chen, Q.; Thornton, G.; Kresse, G.; Ramsey, M. G.; Surnev, S.; Netzer, F. P. *Top. Catal.* **2007**, *46*(1–2), 137–149.
- [231] Schoiswohl, J.; Surnev, S.; Sock, M.; Ramsey, M. G.; Kresse, G.; Netzer, F. P. *Angew. Chem. Int. Ed. Engl.* **2004**, *43*(41), 5546–5549.
- [232] Zinke-Allmang, M.; Feldman, L. C.; Grabow, M. H. *Surf. Sci. Rep.* **1992**, *16*(8), 377–463.
- [233] Kukushkin, S. A.; Osipov, A. V. *Phys.-Usp.* **1998**, *41*(10), 983.
- [234] Voorhees, P. W. *Annu. Rev. Mater. Sci.* **1992**, *22*(1), 197–215.
- [235] Elofsson, V. *Nanoscale Structure Forming Processes*, Vol. v. 1804 of *Linköping Studies in Science and Technology. Dissertations*; Linköping University Electronic Press: Linköping, 2016.
- [236] Wei, T.-C.; Phillips, J. *Adv. Catal.* **1996**, *41*, 359–421.
- [237] Zhou, Y.; Jin, C.; Li, Y.; Shen, W. *Nano Today* **2018**, *20*, 101–120.
- [238] Hansen, T. W.; Delariva, A. T.; Challa, S. R.; Datye, A. K. *Acc. Chem. Res.* **2013**, *46*(8), 1720–1730.
- [239] Vayssilov, G. N.; Lykhach, Y.; Migani, A.; Staudt, T.; Petrova, G. P.; Tsud, N.; Skála, T.; Bruix, A.; Illas, F.; Prince, K. C.; Matolín, V.; Neyman, K. M.; Libuda, J. *Nat. Mater.* **2011**, *10*(4), 310–315.
- [240] Matte, L. P.; Kilian, A. S.; Luza, L.; Alves, M. C. M.; Morais, J.; Baptista, D. L.; Dupont, J.; Bernardi, F. *J. Phys. Chem. C* **2015**, *119*(47), 26459–26470.
- [241] von Boehn, B.; Preiss, A.; Imbihl, R. *PCCP* **2016**, *18*(29), 19713–19721.

- [242] von Boehn, B.; Mehrwald, S.; Imbihl, R. *Chaos* **2018**, *28*(4), 045117.
- [243] von Boehn, B.; Imbihl, R. *PCCP* **2017**, *19*(28), 18487–18493.
- [244] von Boehn, B.; Imbihl, R. *J. Phys. Chem. C* **2018**, *122*(24), 12694–12703.
- [245] von Boehn, B.; Menteş, T. O.; Locatelli, A.; Sala, A.; Imbihl, R. *J. Phys. Chem. C* **2018**, *122*(19), 10482–10488.
- [246] LEEDpat4 Version 4.2. Herrmann, K.; van Hove, M. A. **2019**.
- [247] Storp, S. *Spectrochim. Acta B* **1985**, *40*(5-6), 745–756.
- [248] Wu, Q.-H.; Thissen, A.; Jaegermann, W.; Liu, M. *Appl. Surf. Sci.* **2004**, *236*(1-4), 473–478.
- [249] Nakao, F. *Vacuum* **1975**, *25*(9-10), 431–435.
- [250] Bartmess, J. E.; Georgiadis, R. M. *Vacuum* **1983**, *33*(3), 149–153.
- [251] Silversmit, G.; Depla, D.; Poelman, H.; Marin, G. B.; de Gryse, R. *J. Electron. Spectros. Relat. Phenomena* **2004**, *135*(2-3), 167–175.
- [252] Abe, Y.; Kato, K.; Kawamura, M.; Sasaki, K. *Surf. Sci. Spec.* **2001**, *8*(2), 117–125.
- [253] Ibach, H. *Surf. Sci. Rep.* **1997**, *29*(5), 195–263.
- [254] Imbihl, R.; Ertl, G. *Chem. Rev.* **1995**, *95*(3), 697–733.
- [255] Rotermund, H. H.; Haas, G.; Franz, R. U.; Tromp, R. M.; Ertl, G. *Science* **1995**, *270*(5236), 608–610.
- [256] Rotermund, H. H. *Surf. Sci.* **1997**, *386*(1-3), 10–23.
- [257] Murray, P. W.; Thorshaug, S.; Stensgaard, I.; Besenbacher, F.; Lægsgaard, E.; Ruban, A. V.; Jacobsen, K. W.; Kopidakis, G.; Skriver, H. L. *Phys. Rev. B* **1997**, *55*(3), 1380–1383.
- [258] Werfel, F.; Brümmer, O. *Phys. Scr.* **1983**, *28*(1), 92–96.
- [259] Demeter, M.; Neumann, M.; Reichelt, W. *Surf. Sci.* **2000**, *454-456*, 41–44.
- [260] Kasperkiewicz, J.; Kovacich, J. A.; Lichtman, D. *J. Electron. Spectros. Relat. Phenomena* **1983**, *32*(2), 123–132.
- [261] Meisel, A.; Hallmeier, K. H.; Szargan, R.; Müller, J.; Schneider, W. *Phys. Scr.* **1990**, *41*(4), 513–516.
- [262] Powell, C. J. *J. Electron. Spectros. Relat. Phenomena* **2012**, *185*(1-2), 1–3.

- [263] Comelli, G.; Dhanak, V. R.; Kiskinova, M.; Prince, K. C.; Rosei, R. *Surf. Sci. Rep.* **1998**, *32*(5), 165–231.
- [264] Mertens, F.; Imbihl, R. *Chem. Phys. Lett.* **1995**, *242*(1-2), 221–227.
- [265] Mertens, F.; Imbihl, R. *Surf. Sci.* **1996**, *347*(3), 355–366.
- [266] Mertens, F.; Schwegmann, S.; Imbihl, R. *J. Chem. Phys.* **1997**, *106*(10), 4319–4326.
- [267] Rafti, M.; Uecker, H.; Lovis, F.; Krupennikova, V.; Imbihl, R. *PCCP* **2012**, *14*(15), 5260–5264.
- [268] Rafti, M.; Borkenhagen, B.; Lilienkamp, G.; Lovis, F.; Smolinsky, T.; Imbihl, R. *J. Chem. Phys.* **2015**, *143*(18), 184701.
- [269] Dhanak, V. R.; Comelli, G.; Cautero, G.; Paolucci, G.; Prince, K. C.; Kiskinova, M.; Rosei, R. *Chem. Phys. Lett.* **1992**, *188*(3-4), 237–240.
- [270] Africh, C.; Lin, H.; Corso, M.; Esch, F.; Rosei, R.; Hofer, W. A.; Comelli, G. *JACS* **2005**, *127*(32), 11454–11459.
- [271] Bellman, A. F.; Cvetko, D.; Morgante, A.; Polli, M.; Tommasini, F.; Prince, K. C.; Rosei, R. *Surf. Sci.* **1993**, *281*(1-2), L321–L325.
- [272] Mikhailov, A. S. *Foundations of Synergetics I: Distributed Active Systems*, Vol. 51 of *Springer Series in Synergetics*; Springer: Berlin and Heidelberg, 1994.
- [273] Pismen, L. M. *Patterns and interfaces in dissipative dynamics*, Springer Series in Synergetics; Springer: Berlin, Heidelberg, 2006.
- [274] Stokbro, K.; Baroni, S. *Surf. Sci.* **1997**, *370*(2-3), 166–178.
- [275] Nieuwenhuys, B. E.; Bouwman, R.; Sachtler, W. *Thin Solid Films* **1974**, *21*(1), 51–58.
- [276] Schwarz, E.; Ernst, K. H.; Gonser-Buntrock, C.; Neuber, M.; Christmann, K. *Vacuum* **1990**, *41*(1-3), 180–184.
- [277] Michaelson, H. B. *J. Appl. Phys.* **1977**, *48*(11), 4729–4733.
- [278] Makeev, A.; Imbihl, R. *J. Chem. Phys.* **2000**, *113*(9), 3854–3863.
- [279] Schütz, E.; Esch, F.; Günther, S.; Schaak, A.; Marsi, M.; Kiskinova, M.; Imbihl, R. *Catal. Lett.* **1999**, *63*(1/2), 13–19.
- [280] Schaak, A.; Shaikhutdinov, S.; Imbihl, R. *Surf. Sci.* **1999**, *421*(1-2), 191–203.
- [281] Rafti, M.; Lovis, F.; Imbihl, R. *Catal. Lett.* **2012**, *142*(1), 16–21.

- [282] Smoluchowski, R. *Phys. Rev.* **1941**, *60*(9), 661–674.
- [283] Hesse, M.; Günther, S.; Locatelli, A.; Menteş, T. O.; Santos, B.; Imbihl, R. *J. Phys. Chem. C* **2016**, *120*(47), 26864–26872.
- [284] Hagberg, A.; Yochelis, A.; Yizhaq, H.; Elphick, C.; Pismen, L.; Meron, E. *Physica D: Nonlinear Phenomena* **2006**, *217*(2), 186–192.
- [285] Hagberg, A.; Meron, E. *J. Chem. Phys.* **1994**, *7*(3), 805–835.
- [286] Kai, S.; Muller, S. C.; Mori, T.; Miki, M. *Physica D: Nonlinear Phenomena* **1991**, *50*(3), 412–428.
- [287] Horváth, D.; Tóth, Á. *J. Chem. Phys.* **1998**, *108*(4), 1447–1451.
- [288] Szalai, I.; de Kepper, P. *J. Phys. Chem. A* **2004**, *108*(25), 5315–5321.
- [289] Dri, C.; Africh, C.; Esch, F.; Comelli, G.; Dubay, O.; Köhler, L.; Mittendorfer, F.; Kresse, G.; Dudin, P.; Kiskinova, M. *J. Chem. Phys.* **2006**, *125*(9), 094701.
- [290] Africh, C.; Esch, F.; Comelli, G.; Rosei, R. *J. Chem. Phys.* **2001**, *115*(1), 477–481.
- [291] Gottschalk.; Mertens.; Bär.; Eiswirth.; Imbihl. *Phys. Rev. Lett.* **1994**, *73*(25), 3483–3486.
- [292] Mertens.; Gottschalk.; Bär.; Eiswirth.; Mikhailov.; Imbihl. *Phys. Rev. E* **1995**, *51*(6), R5193–R5196.
- [293] Campbell, C. T.; Ertl, G.; Kuipers, H.; Segner, J. *Surf. Sci.* **1981**, *107*(1), 220–236.
- [294] Petukhov, M.; Andrea Rizzi, G.; Granozzi, G. *Surf. Sci.* **2001**, *490*(3), 376–384.
- [295] Petukhov, M.; Rizzi, G.; Granozzi, G. *Thin Solid Films* **2001**, *400*(1-2), 154–159.
- [296] Asensio, M. C.; Kerkar, M.; Woodruff, D. P.; de Carvalho, A. V.; Fernández, A.; González-Elipe, A. R.; Fernández-García, M.; Conesa, J. C. *Surf. Sci.* **1992**, *273*(1-2), 31–39.
- [297] Sedona, F.; Rizzi, G. A.; Agnoli, S.; Llabrés i Xamena, F. X.; Papageorgiou, A.; Ostermann, D.; Sambì, M.; Finetti, P.; Schierbaum, K.; Granozzi, G. *J. Phys. Chem. B* **2005**, *109*(51), 24411–24426.
- [298] Sedona, F.; Agnoli, S.; Granozzi, G. *J. Phys. Chem. B* **2006**, *110*(31), 15359–15367.
- [299] Barcaro, G.; Sedona, F.; Fortunelli, A.; Granozzi, G. *J. Phys. Chem. C* **2007**, *111*(16), 6095–6102.
- [300] Barcaro, G.; Agnoli, S.; Sedona, F.; Rizzi, G. A.; Fortunelli, A.; Granozzi, G. *J. Phys. Chem. C* **2009**, *113*(14), 5721–5729.

- [301] Leisenberger, F. P.; Surnev, S.; Vitali, L.; Ramsey, M. G.; Netzer, F. P. *J. Vac. Sci. Technol. A* **1999**, *17*(4), 1743–1749.
- [302] Surnev, S.; Vitali, L.; Ramsey, M. G.; Netzer, F. P.; Kresse, G.; Hafner, J. *Phys. Rev. B* **2000**, *61*(20), 13945–13954.
- [303] Sambì, M.; Petukhov, M.; Domenichini, B.; Rizzi, G. A.; Surnev, S.; Kresse, G.; Netzer, F. P.; Granozzi, G. *Surf. Sci.* **2003**, *529*(1-2), L234–L238.
- [304] Agnoli, S.; Menteş, T. O.; Niño, M. A.; Locatelli, A.; Granozzi, G. *PCCP* **2009**, *11*(19), 3727–3732.
- [305] Khaliullin, R. Z.; Bell, A. T. *J. Phys. Chem. B* **2002**, *106*(32), 7832–7838.
- [306] Goodrow, A.; Bell, A. T. *J. Phys. Chem. C* **2007**, *111*(40), 14753–14761.
- [307] Kim, H. Y.; Lee, H. M.; Metiu, H. *J. Phys. Chem. C* **2010**, *114*(32), 13736–13738.
- [308] Zheng, Y.; Zhang, L.; Wang, S.; Ding, D.; Zhang, H.; Chen, M.; Wan, H. *Langmuir* **2013**, *29*(29), 9090–9097.
- [309] Nishiyama, H.; Inoue, Y. *Surf. Sci.* **2006**, *600*(13), 2644–2649.
- [310] Nishiyama, H.; Inoue, Y. *J. Phys. Chem. B* **2003**, *107*(34), 8738–8741.
- [311] Nishiyama, H.; Inoue, Y. *Surf. Sci.* **2005**, *594*(1-3), 156–162.
- [312] Kelling, S.; Mitrelias, T.; Matsumoto, Y.; Ostanin, V. P.; King, D. A. *Faraday Disc.* **1997**, *107*, 435–444.
- [313] Cerasari, S. *Kinetic and Nonlinear Effects Associated with the Catalytic CO Oxidation on Pt Surfaces* PhD Thesis, Freie Universität Berlin, Berlin, **2000**.
- [314] Kelling, S.; Cerasari, S.; Rotermund, H. H.; Ertl, G.; King, D. A. *Chem. Phys. Lett.* **1998**, *293*(5-6), 325–330.
- [315] Shugaev, M. V.; Manzo, A. J.; Wu, C.; Zaitsev, V. Y.; Helvajian, H.; Zhigilei, L. V. *Phys. Rev. B* **2015**, *91*(23), 8.
- [316] Wu, C.; Zaitsev, V. Y.; Zhigilei, L. V. *J. Phys. Chem. C* **2013**, *117*(18), 9252–9258.
- [317] Wen, Y.-N.; Zhang, J.-M. *Solid State Commun.* **2007**, *144*(3-4), 163–167.
- [318] Slobodnik, A. J. *Proc. IEEE* **1976**, *64*(5), 581–595.
- [319] Shibayama, K.; Yamanouchi, K.; Sato, H.; Meguro, T. *Proc. IEEE* **1976**, *64*(5), 595–597.
- [320] Foerster, M.; Statuto, N.; Casals, B.; Hernández-Mínguez, A.; Finizio, S.; Mandziak, A.; Aballe, L.; Hernández Ferràs, J. M.; Macià, F. *J. Synchrotron Radiat.* **2019**, *26*(Pt 1), 184–193.

- [321] Foerster, M.; Prat, J.; Massana, V.; Gonzalez, N.; Fontserè, A.; Molas, B.; Matilla, O.; Pellegrin, E.; Aballe, L. *Ultramicroscopy* **2016**, *171*, 63–69.
- [322] Yuge, K.; Seko, A.; Kuwabara, A.; Oba, F.; Tanaka, I. *Phys. Rev. B* **2006**, *74*(17), 392.

Appendix A

Vanadium oxide phases on Rh(111) reported in literature

Table A.1: Ordered vanadium oxide phases on Rh(111) reported in literature.

LEED pattern	Composition	Oxidation state	V coverage / MLE	Reference
$(\sqrt{13} \times \sqrt{13})R13.8^\circ$	VO ₃	+5	0.46	[53]
$(\sqrt{7} \times \sqrt{7})R19.1^\circ$	VO ₃	+5	0.43	[53]
$(5 \times 3\sqrt{3})$ -rect	V ₁₃ O ₂₁	+3 / +5	0.43	[55]
(5×5)	V ₁₁ O ₂₃	+3 / +5	0.44	[55]
Moiré	VO ₂	+4	0.85	[53]
(9×9)	V ₂ O ₃	+3	0.44	[55]
(2×2)	V ₂ O ₃	+3	≤ 0.5	[53, 202]
(2×2) -split	V ₂ O ₃	+3	≤ 0.5	[202]
$(\sqrt{3} \times \sqrt{3})R30^\circ$	V ₂ O ₃	+3	-	[53]
”Wagon wheel“	VO	+2	0.73	[55]
$(\sqrt{3} \times \sqrt{3})$ -Moiré	-	-	-	[70]

Appendix B

List of abbreviations

AES	Auger electron spectroscopy
AFM	Atomic force microscopy
ALA	Angle limiting aperture
ARPES	Angle resolved photoemission electron microscopy
AS-t	Auger signal vs. time
CA	Contrast aperture
CCD	Charge coupled device
CMA	Cylindrical mirror analyzer
CMOS	Complementary metal-oxide-semiconductor
CVD	Chemical vapor deposition
ESEM	Environmental scanning electron microscopy
FL	Field lens
FLA	Field limiting aperture
HREELS	High resolution electron energy loss spectroscopy
IL	Illumination aperture
IMFP	Inelastic mean free path
LEED	Low-energy electron diffraction
LEEM	Low-energy electron microscopy
MCP	Micro-channel plate
MEM	Mirror electron microscopy
NAP-LEEM	Near ambient pressure low-energy electron microscopy
NAP-PEEM	Near ambient pressure photoemission electron microscopy
NAP-XPS	Near ambient pressure X-ray photoelectron spectroscopy
OBJ	Objective lens
OSA	Order selecting aperture
PEEM	Photoemission electron microscopy
PD	Phase Diagram
PVD	Physical vapor deposition
QMS	Quadrupol mass spectrometry
SEM	Single electron multiplier

SPELEEM	Spectroscopic low-energy electron microscopy
SPEM	Scanning photoemission electron microscopy
STM	Scanning tunneling microscopy
STV	Start voltage
TEM	Transmission electron microscopy
TL	Transfer lens
TPD	Temperature programmed desorption
TPR	Temperature programmed reaction
UHV	Ultra-high vacuum
UV-VIS	Ultraviolet-visible spectroscopy
XPS	X-ray photoelectron spectroscopy
XPEEM	X-ray photoemission electron microscopy
ZP	Zone plate

Curriculum vitae

Persönliche Informationen

Bernhard von Boehn

Geboren am 04.01.1990 in Großburgwedel

Schulbildung

- 1996 - 2000: Grund und Hauptschule I Burgdorf
- 2000 - 2002: Michael-Ende-Schule Burgdorf
- 2002 - 2009: Gymnasium Burgdorf

Zivildienst

- 2009 - 2010: Medizinische Hochschule Hannover, Kinderchirurgie

Studium

- 2011 - 2011: Johannes Gutenberg-Universität Mainz: Biomedizinische Chemie
- 2011 - 2014: Leibniz Universität Hannover: Chemie
- 2014 - 2016: Leibniz Universität Hannover: Material- und Nanochemie

Promotion

- 2016 - 2020: Wissenschaftlicher Mitarbeiter in der Gruppe von Prof. Dr. R. Imbihl am Institut für Physikalische Chemie und Elektrochemie der Leibniz Universität Hannover

Hannover, den 6. April 2020

Publikationsliste

Peer-Review-Publikationen

1. L. Jacobs¹, B. von Boehn¹, M. Homann, C. Barroo, T. Visart de Bocarmé, and R. Imbihl. On the importance of the structure in the catalytic reactivity of Au-based catalysts. *Applied Surface Science*, **2020**, accepted manuscript.
2. B. von Boehn, C. Penschke, X. Li, J. Paier, J. Sauer, J.-O. Krisponeit, J. I. Flege, J. Falta, H. Marchetto, T. Franz, G. Lilienkamp, and R. Imbihl. Reaction dynamics of metal/oxide catalysts: Methanol oxidation at vanadium oxide films on Rh(111) from UHV to 10^{-2} mbar. *Journal of Catalysis*, **2020**, *385*, 255 - 264.
3. T. Franz¹, B. von Boehn¹, H. Marchetto, B. Borckenhagen, G. Lilienkamp, W. Daum, R. Imbihl. Catalytic CO oxidation on Pt under near ambient pressure: a NAP-LEEM study. *Ultramicroscopy* **2019**, *200*, 73 - 78.
4. M. Homann, B. von Boehn, A. Malhotra, L. Gregoratti, M. Amati, P. Zeller, R. Imbihl. Large nucleation barrier for Ni oxide on Rh(110) driving Ni into subsurface sites upon oxidation. *Surface Science* **2019**, *679*, 56 - 63.
5. B. von Boehn, S. Mehrwald, R. Imbihl. Hole patterns in ultrathin vanadium oxide layers on a Rh(111) surface during catalytic oxidation reactions with NO. *Chaos: An Interdisciplinary Journal of Nonlinear Science* **2018**, *28*, 045117.
6. B. von Boehn, T. O. Montes, A. Locatelli, A. Sala, R. Imbihl. Reactive phase separation during methanol oxidation on a V-oxide-promoted Rh(110) surface. *The Journal of Physical Chemistry C* **2018**, *122*, 10482 - 10488.
7. B. von Boehn, R. Imbihl. Chemical wave patterns and oxide redistribution during methanol oxidation on a V-oxide promoted Rh(110) surface. *The Journal of Physical Chemistry C* **2018**, *122*, 12694 - 12703.
8. T. Smolinsky, B. von Boehn, R. Imbihl. Chemical waves in the $O_2 + H_2$ reaction on a Rh(111) surface alloyed with nickel. I. Photoelectron emission microscopy. *The Journal of Chemical Physics* **2018**, *148*, 154704.

¹Beide Autoren haben zu gleichen Teilen an dieser Arbeit mitgewirkt.

9. T. Smolinsky, M. Homann, B. von Boehn, L. Gregoratti, M. Amati, M. Al-Hada, H. Sezen, R. Imbihl. Chemical waves in the $O_2 + H_2$ reaction on a Rh(111) surface alloyed with nickel. II. Photoelectron spectroscopy and microscopy. *The Journal of Chemical Physics* **2018**, *148*, 154705.
10. U. N. Fagioli, B. von Boehn, M. Rafti, R. Imbihl. Kinetics of low pressure ammonia oxidation over Rh(111). *Latin American Applied Research* **2018**, *48-1*, 27 - 30.
11. B. von Boehn, T. O. Menteş, A. Locatelli, A. Sala, R. Imbihl. Growth of vanadium and vanadium oxide on a Rh(110) surface. *The Journal of Physical Chemistry C* **2017**, *121*, 19774 – 19785.
12. B. von Boehn, R. Imbihl. Large amplitude excitations traveling along the interface in bistable catalytic methanol oxidation on Rh(110). *Physical Chemistry Chemical Physics* **2017**, *19*, 18487 – 18493.
13. B. von Boehn, A. Preiss, R. Imbihl. Dynamics of ultrathin V-oxide layers on Rh(111) in catalytic oxidation of ammonia and CO. *Physical Chemistry Chemical Physics* **2016**, *18*, 19713 – 19721.
14. M. Hesse, B. von Boehn, A. Locatelli, A. Sala, T. O. Menteş, R. Imbihl. Island ripening via a polymerization-depolymerization mechanism. *Physical Review Letters* **2015**, *115*, 136102.

Conference Proceedings

1. L. Jacobs, C. Barroo, B. von Boehn, M. Homann, R. Imbihl, T. Visart de Bocarmé. Understanding fundamental processes on Au-Ag catalysts during oxidation reactions: a correlative microscopy approach. *Microscopy and Microanalysis* **2019**, *25*, 310 - 311.

Konferenzbeiträge - Vorträge

1. Dynamics in inverse catalyst systems: Restructuring of vanadium oxide supported on Rh(111) during methanol oxidation. DPG Frühjahrstagung, Sektion Kondensierte Materie: Post-Deadline-Session **04.2019**, Regensburg.
2. Dynamics of V-oxide catalysts from UHV to near ambient pressure. 23. Harzseminar: Strukturbildung in Chemie und Biophysik **03.2019**, Goslar–Hahnenklee.
3. Islands vs. holes: regular and inverse VO_x distribution patterns controlled by the oxygen supply in catalytic oxidation reactions on Rh(111)/ VO_x . 117. Bunsentagung: Kinetics in the Real World **05.2018**, Hannover.
4. Interface instabilities in catalytic reactions on Rh(110). 21. Harzseminar: Strukturbildung in Chemie und Biophysik **02.2017**, Goslar–Hahnenklee.

5. Wave pattern and anisotropic growth in catalytic methanol oxidation over Rh(110) / VO_x. 20. Harzseminar: Strukturbildung in Chemie und Biophysik **02.2016**, Goslar–Hahnenklee.
6. Polymerization mechanism for travelling vanadium oxide islands. 19. Harzseminar: Strukturbildung in Chemie und Biophysik **03.2015**, Goslar–Hahnenklee.
7. Travelling vanadium oxide islands in a catalytic reaction. Frühjahrstagung der Deutschen Physikalischen Gesellschaft **03.2015**, Berlin.
8. Long-range attraction between macroscopic vanadium oxide islands. 18. Harzseminar: Strukturbildung in Chemie und Biophysik **02.2014**, Goslar–Hahnenklee.

Konferenzbeiträge - Poster

1. Surface acoustic wave-activated diffusion of surface atoms. LEEM / PEEM-11 Conference **10.2018**, Chongqing (China).
2. Restructuring and redistribution of ultrathin V-oxide layers on Rh(111) during catalytic reactions. LEEM / PEEM-11 Conference **10.2018**, Chongqing (China).
3. Vanadium oxide redistribution on Rh(111) and Rh(110) during methanol oxidation. 7th Humboldt Award Winners' Forum "Fundamental Concepts and Principles of Chemical Energy Conversion" **10.2017**, Bonn.
4. Island ripening via a polymerization/depolymerization mechanism. ECSCD2015: European Conference on Surface Crystallography and Dynamics **10.2015**, Trieste (Italien).
5. Island ripening via a polymerization/depolymerization mechanism. Volkswagen Symposium: Complexity and Synergetics **07.2015**, Hannover.